LEVEL III
A046917

AFML-TR-78-55

AD A060783

PROCEEDINGS OF THE ARPA/AFML REVIEW OF PROGRESS IN QUANTITATIVE NDE

SCIENCE CENTER, ROCKWELL INTERNATIONAL
1049 CAMINO DOS RIOS
THOUSAND OAKS, CALIFORNIA 91360

DDC FILE COPY

MAY 1978

TECHNICAL REPORT AFML-TR-78-55
Third Annual Report 4 September 1976 – 30 June 1977

DDC
RECEIVED
NOV 3 1978
D

Approved for public release; distribution unlimited.

AIR FORCE MATERIALS LABORATORY
AIR FORCE WRIGHT AERONAUTICAL LABORATORIES
AIR FORCE SYSTEMS COMMAND
WRIGHT-PATTERSON AIR FORCE BASE, OHIO 45433

78 10 26 046

NOTICE

When Government drawings, pecifications, or other data are used for any purpose other than in conjunction with a definitely related Government procurement operation, the United States Government thereby incurs no responsibility nor any obligation whatsoever; and the fact that the government may have formulated, furnished, or in any way supplied the said drawings, specifications, or other data, is not to be regarded by implication or otherwise as in any manner licensing the holder or any other person or corporation, or conveying any rights or permission to manufacture, use, or sell any patented invention that may in any way be related thereto.

This report has been reviewed by the Information Office (OI) and is releasable to the National Technical Information Service (NTIS). At NTIS, it will be available to the general public, including foreign nations.

This technical report has been reviewed and 's approved for publication.

THOMAS J. MORAN
Project Monitor

DONALD M. FORNEY, Jr., Chief
Nondestructive Evaluation Branch
Metals and Ceramics Division

"If your address has changed, if you wish to be removed from our mailing list, or if the addressee is no longer employed by your organization please notify AFML/LLP, WPAFB, OH 45433 to help us maintain a current mailing list."

Copies of this report should not be returned unless return is required by security considerations, contractual obligations, or notice on a specific document.

AIR FORCE/86780/8 October 1978 — 480

UNCLASSIFIED

SECURITY CLASSIFICATION OF THIS PAGE (When Data Entered)

REPORT DOCUMENTATION PAGE	READ INSTRUCTIONS BEFORE COMPLETING FORM
1. REPORT NUMBER: AFML TR-78-55	2. GOVT ACCESSION NO. / 3. RECIPIENT'S CATALOG NUMBER
4. TITLE (and Subtitle): PROCEEDINGS OF THE ARPA/AFML REVIEW OF PROGRESS IN QUANTITATIVE NONDESTRUCTIVE EVALUATION	5. TYPE OF REPORT & PERIOD COVERED: Third Annual Report 09/04/76 thru 06/30/77
	6. PERFORMING ORG. REPORT NUMBER: SC595.24AR
7. AUTHOR(s): Donald O. Thompson, Program Manager	8. CONTRACT OR GRANT NUMBER(s): F33615-74-C-5180
9. PERFORMING ORGANIZATION NAME AND ADDRESS: Science Center, Rockwell International, 1049 Camino Dos Rios, Thousand Oaks, California 91360 389 949	10. PROGRAM ELEMENT, PROJECT, TASK AREA & WORK UNIT NUMBERS: 7351-09-43 17 09
11. CONTROLLING OFFICE NAME AND ADDRESS: Advanced Research Projects Agency, 1400 Wilson Boulevard, Arlington, Virginia 22209	12. REPORT DATE: MAY 1978 / NUMBER OF PAGES: 394
14. MONITORING AGENCY NAME & ADDRESS (If different from Controlling Office): Air Force Materials Laboratory (LLP), Air Force Systems Command, Wright-Patterson Air Force Base, Ohio 45433	15. SECURITY CLASS. (of this report): UNCLASSIFIED / 15a. DECLASSIFICATION/DOWNGRADING SCHEDULE

16. DISTRIBUTION STATEMENT (of this Report)

Approved for public release; Distribution Unlimited.

12 393 p

17. DISTRIBUTION STATEMENT (of the abstract entered in Block 20, if different from Report)

9 Annual rept. no. 3, 4 Sep 76-30 Jun 77,

18. SUPPLEMENTARY NOTES

19. KEY WORDS (Continue on reverse side if necessary and identify by block number)

nondestructive evaluation; nondestructive testing; qualitative ultrasonics; signal processing; adhesive bonds; composites' residual stress; acoustic emission; reliability; quality

20. ABSTRACT (Continue on reverse side if necessary and identify by block number)

The edited transcripts of the ARPA/AFML Review of Quantitative NDE held on June 14-17, 1977, at Cornell University, Ithaca, New York, are presented in this document. Several key topics form the core of these presentations and discussions. They include quantitative ultrasonics, adhesives and comoosites, emissions related to failure prediction, residual stress, and reliability of ceramics. It is believed that this document provides a reasonable summary of NDE research and development currently underway.

DD FORM 1 JAN 73 1473 EDITION OF 1 NOV 65 IS OBSOLETE

UNCLASSIFIED

SECURITY CLASSIFICATION OF THIS PAGE (When Data Entered)

78 10 26 046

389 949

PREFACE

This report contains the edited transcripts of the Review of Progress in Quantitative NDE held at Cornell University, June 14-17, 1977. The Review was sponsored by the Advanced Research Projects Agency and the Air Force Materials Laboratory as a part of and at the conclusion of the third year of work on the Interdisciplinary Program for Quantitative Flaw Definition, Contract No. F33615-74-C-5180. Arrangements for the Review were made by the Science Center, Rockwell International, host organization for the Interdisciplinary Program, and the Materials Science Center at Cornell University, Prof. H. H. Johnson, Director.

The format selected for this Review was somewhat different from those of the past. For the first time in this series, a number of poster sessions were presented in addition to the traditional technical sessions. The poster sessions provided a good way to accommodate the growing momentum in the NDE research field (as evidenced by an increased number of papers) while maintaining a forum for technical exchange. The posters presented at the Review are included in this report as well as the technical papers. As a further means of stimulating this exchange, several papers related to the main technical interests of the ARPA/AFML program were included in the Review and are presented even though they were not directly sponsored by ARPA/AFML.

In addition to the technical presentations, two overview papers of significance were presented. One of these was given by Mr. W. J. Willoughby, Jr., Deputy Chief of Naval Material, in the opening session. Mr. Willoughby provided a very timely and vivid description of current actions within Naval Material aimed at the promotion and improvement of overall reliability. The second of these was given in the closing session by Dr. F. N. Kelley, Director, Air Force Materials Laboratory. In his paper, Dr. Kelley described a format for the reduction to practice of new research results as well as pitfalls to avoid in the process. He also outlined several features which are necessary for the establishment of a steady flow of new technology, one of which is the injection of "real world" problem awareness to the researcher. This was also a very timely paper, for a number of research efforts have reached maturity under this and other ARPA and AFML programs and may now be considered for reduction to practice through appropriate "windows" of opportunities and needs. The final session of the Review was, in fact, devoted to a presentation of these results.

The organizers of the Review wish to acknowledge the financial support and encouragement provided by the Advanced Research Projects Agency and the Air Force Materials Laboratory. Special thanks are due to both Mr. Willoughby and Dr. Kelley for their summaries. Both of these gentlemen took time from very busy schedules to be present at the Review. The organizers also wish to thank the speakers, session chairmen, authors of poster presentations, panel members, and participants who collaborated to provide a stimulating meeting. They wish to acknowledge with thanks the assistance of Mrs. Diane Harris who managed the organizational matters of the meeting from the Science Center, and Ms. Shirley Dutton and Mrs. Lana Eriksson for the preparation of the Proceedings. They are indebted to Prof. H. H. Johnson, Director of the Materials Science Center at Cornell University, and his staff for their excellent cooperation in the conduct of the Review, to Ms. Kris Molt and her staff at Cornell University who ably assisted Mrs. Harris in the management of local arrangements, and to Prof. J. A. Krumhansl, who has been a participant in the ARPA/AFML program since its inception, for the initial invitation to hold the Review at Cornell.

Donald O. Thompson
Director
Structural Materials
Rockwell International, Science Center

ACCESSION for
NTIS White Section
DDC Buff Section
UNANNOUNCED
JUSTIFICATION
BY
DISTRIBUTION/AVAILABILITY CODES
Dist. AVAIL. and/or SPECIAL
A

LEVEL II

DDC
RECEIVED
NOV 3 1978
D

PRECEDING PAGE BLANK

ADVANCED RESEARCH PROJECTS AGENCY/AIR FORCE MATERIALS LABORATORY

REVIEW OF PROGRESS
IN
QUANTITATIVE NDE

June 14 - 17, 1977
Cornell University

TABLE OF CONTENTS

SESSION I - INTRODUCTORY — D. O. Thompson, Chairman — PAGE

INTRODUCTORY REMARKS
H. H. Johnson, Cornell University, and
D. O. Thompson, Science Center, Rockwell International 1

COMMENTS FROM ARPA/AFML
E. van Reuth and M. J. Buckley, Advanced Research Projects Agency, and
D. M. Forney, Jr., Air Force Materials Laboratory 3

RELIABILITY BY DESIGN
W. J. Willoughby, Jr.
Assistant Deputy Chief of Naval Material
Reliability and Engineering 5

SESSION II - DEFECT CHARACTERIZATION BY QUANTITATIVE ULTRASONICS — D. A. Lee, Chairman

INTRODUCTION
R. B. Thompson
Science Center, Rockwell International 15

LONG WAVE SCATTERING OF ELASTIC WAVES FROM VOLUMETRIC AND CRACK-LIKE DEFECTS OF SIMPLE SHAPES
J. E. Gubernatis
Los Alamos Scientific Laboratory 21

EXPERIMENTAL MEASUREMENTS AND INTERPRETATION OF ULTRASONIC SCATTERING BY FLAWS
B. R. Tittmann and R. K. Elsley
Science Center, Rockwell International 26

IDENTIFICATION OF FLAWS FROM SCATTERED ULTRASONIC FIELDS AS MEASURED AT A PLANAR SURFACE
L. Adler, K. Lewis, P. Szilas, and D. Fitting
University of Tennessee 36

UTILIZATION OF PHYSICAL FEATURES OF SCATTERED POWER FOR DEFECT CHARACTERIZATION
E. Domany
University of Washington, Seattle 44

INVERSION OF ULTRASONIC SCATTERING DATA TO MEASURE DEFECT SIZE, ORIENTATION, AND ACOUSTIC PROPERTIES
R. Shankar, A. N. Mucciardi, M. F. Whalen, and M. D. Johnson
Adaptronics, Inc. 50

APPLICATION OF A NEW INVERSE METHOD TO NONDESTRUCTIVE EVALUATION
N. Bleistein and J. K. Cohen
University of Denver 73

IMPLEMENTATION
"PRESENT STATUS AND FUTURE DIRECTIONS"
R. B. Thompson
Science Center, Rockwell International 81

PRECEDING PAGE BLANK

SESSION III - MINISYMPOSIUM ON SCATTERING THEORIES AVAILABLE FOR FUTURE APPLICATION — J. A. Krumhansl, Chairman — PAGE

MATCHED ASYMPTOTIC EXPANSIONS APPLIED TO SCATTERING CALCULATIONS
S. K. Datta
University of Colorado 86

SPECTRAL ANALYSIS OF ELASTIC WAVES SCATTERED BY OBJECTS WITH SMOOTH SURFACES
Y. H. Pao and V. Varadan
Cornell University 92

RECIPROCITY THEORIES FOR FLAW ANALYSIS
G. S. Kino and B. A. Auld
Stanford University 99

APPLICATION OF GEOMETRICAL DIFFRACTION THEORY TO SCATTERING BY CRACKS
J. D. Achenbach, A. K. Gautesen, and H. McMaken
Northwestern University 102

SESSION IV - NEW TECHNIQUES AND PHENOMENA (POSTERS)

NEW METHODS OF DETECTION AND CHARACTERIZATION OF SURFACE FLAWS
B. A. Auld
Stanford University 108

SURFACE WAVE TECHNIQUES FOR PREDICTING THE REMAINING LIFE OF FATIGUE DAMAGED METALS
O. Buck, W. L. Morris, and R. V. Inman
Science Center, Rockwell International 112

MECHANISM OF PHOTOSTIMULATED EXOELECTRON EMISSION
W. J. Pardee
Science Center, Rockwell International 117

MEASUREMENT OF PHASE AND GROUP VELOCITIES OF DISPERSIVE WAVES IN SOLIDS
W. Sachse
Cornell University 122

MEASUREMENT OF STRESS PROFILES BY PHASE CONTRAST TECHNIQUES
D. Barnett, G. Herrmann, J. Hunter, G. Johnson, G. Kino, W. Leung, A. Selfridge, C. Steele, J. Shaw, and T. Waugh
Stanford University 127

MAPPING RESIDUAL STRESS FIELDS BY ULTRASONIC TOMOGRAPHY
B. P. Hildebrand and D. E. Hufford
Battelle Northwest 131

QUANTITATIVE ULTRASONIC TOMOGRAPHIC IMAGING
J. D. Young and F. L. Lederman
General Electric Company 137

ACOUSTIC IMAGING OF JOINED SURFACES
C. S. Teat, S. K. Wang, and C. C. Lee
Carnegie-Mellon University 141

ULTRASONIC INSPECTION OF NEAR NET SHAPE DISKS
J. E. Doherty and J. M. LaGrotta
Pratt & Whitney Aircraft 146

A PHASE INSENSITIVE ULTRASONIC RECEIVER
J. S. Heyman
NASA/Langley Research Center 151

INTEGRATED ULTRASONIC TRANSDUCER
S. H. Kwan, R. M. White, and R. S. Muller
University of California, Berkeley 157

OPTICAL DETECTION OF ACOUSTIC EMISSION SIGNALS
C. H. Palmer and R. E. Green, Jr.
Johns Hopkins University 161

SESSION IV - NEW TECHNIQUES AND PHENOMENA (CONTINUED) PAGE

APPROACH TO ACOUSTIC EMISSION SIGNAL ANALYSIS - THEORY AND EXPERIMENT
N. Hsu, J. A. Simmons, and S. C. Hardy
National Bureau of Standards 166

DEFECT SPECIFIC PENETRANTS
R. L. Crane and S. Allinikov
Air Force Materials Laboratory 170

OPTICAL INTERFEROMETRY FOR THE EVALUATION OF MATERIAL AND STRUCTURAL CHARACTERISTICS
B. W. Maxfield
Lawrence Livermore Laboratory 172

SESSION V - NDE FOR ADVANCED MATERIALS W. D. Bascom, Chairman

FRACTURE MECHANICS OF JOINTS
K. L. DeVries, University of Utah, and
G. P. Anderson, Thiokol Chemical Corporation 178

MICROSCOPIC FEATURES OF ADHESIVE BONDS FOR NONDESTRUCTIVE MEASUREMENTS
H. W. White, L. M. Godwin, and T. Wolfram
University of Missouri 186

BOND STRENGTH MEASUREMENTS BY ULTRASONIC SPECTROSCOPY
G. A. Alers, and R. K. Elsley,
Science Center, Rockwell International, and
P. L. Flynn, General Dynamics 191

FRACTURE MECHANICS OF FIBER-REINFORCED COMPOSITES
E. M. Wu
Lawrence Livermore Laboratory 198

FAILURE MECHANISMS IN FIBER-REINFORCED COMPOSITES
I. M. Daniel
IIT Research Institute 205

CHARACTERISTICS OF ACOUSTIC EMISSION SIGNALS FROM COMPOSITES
L. J. Graham and R. K. Elsley
Science Center, Rockwell International 219

MOISTURE DIFFUSION ANALYSIS OF COMPOSITE STRENGTH DEGRADATION
D. H. Kaelble
Science Center, Rockwell International 226

SESSION VI - RELIABILITY OF STRUCTURAL CERAMICS A. G. Evans, Chairman

OVERVIEW OF RELIABILITY IN STRUCTURAL CERAMICS
A. G. Evans
Science Center, Rockwell International 233

HIGH FREQUENCY ULTRASONICS
G. S. Kino and B. T. Khuri-Yakub, Stanford University, and
B. R. Tittmann, Science Center, Rockwell International 237

FRACTURE INITIATING DEFECTS AND THEIR CHARACTERIZATION (POSTERS)

HIGH RESOLUTION REAL TIME ACOUSTIC MICROSCOPY
L. W. Kessler and D. E. Yuhas
Sonoscan, Inc. 241

MICROWAVE TECHNIQUES FOR NDE OF CERAMICS
A. J. Bahr
Stanford Research Institute 245

HIGH FREQUENCY LONGITUDINAL AND SHEAR WAVE INSPECTION OF GAS TURBINE CERAMICS
T. Derkacs
Thompson-Ramo-Wooldridge 251

SESSION VI - RELIABILITY OF STRUCTURAL CERAMICS (CONTINUED) PAGE

FAILURE CAUSING DEFECTS IN CERAMICS
"WHAT NDE SHOULD FIND"
R. W. Rice, J. J. Mecholsky, S. W. Freiman, and S. M. Morey
Naval Research Laboratory 257

QUANTITATIVE FAILURE PREDICTION
"ARE ALL THE WICKETS COVERED?" (PANEL DISCUSSION)
A. G. Evans, Moderator
Science Center, Rockwell International 273

Panel Members: N. Mann, E. Lence, T. Derkacs, R. Rice, N. Tallan, J. Schuldies

COMMENTS ON NDE
Prof. Dr. P. Höller
Fraunhofer-Gesellschaft, Institut für Zerstörungsfreie Prüfverfahren, Saarbrücken, Germany 280

SESSION VII - NEW TECHNOLOGY ROOTS H. M. Burte, Chairman

STEADY STATE REQUIREMENT FOR TECHNOLOGY TRANSITION
F. N. Kelley
Air Force Materials Laboratory 282

"NEW" CANDIDATES FOR ULTRASONIC NDE STANDARDS
AND CALIBRATIONS
G. Birnbaum
National Bureau of Standards 289

TRI-SERVICES NDE CAPABILITIES REQUIREMENTS
AIR FORCE/ARMY/NAVY
D. N. Feeney, Jr., Air Force Materials Laboratory
S. Lorber, Army Material Development & Readiness Command
J. J. Kelly, Naval Material Command 294

NEW TECHNOLOGY FROM ARPA/AFML
D. O. Thompson, Science Center, Rockwell International, and H. Burte, Air Force Materials Laboratory 303

(POSTERS)

PROGRAMMABLE FILTER FOR ULTRASONIC NDE SYSTEMS
R. M. White
University of California, Berkeley 307

DECONVOLUTION PROCESSING FOR FLAW SIGNATURES
E. S. Furgason, R. E. Twyman, and V. L. Newhouse
Purdue University 312

CHARACTERIZATION FACILITY FOR NDE TRANSDUCERS
K. M. Lakin
University of Southern California 319

COMPUTER AIDED INTERPRETATION OF NDE SIGNALS
R. K. Elsley
Science Center, Rockwell International 326

NEW ULTRASONIC STANDARDS
B. R. Tittmann and N. E. Paton
Science Center, Rockwell International 331

DIGITALLY CODED ELECTROMAGNETIC TRANSDUCERS
T. Moran
Air Force Materials Laboratory 336

NEW ELECTROMAGNETIC TRANSDUCER APPLICATIONS
R. B. Thompson
Science Center, Rockwell International 340

SESSION VII - NEW TECHNOLOGY ROOTS (CONTINUED) PAGE

(POSTERS CONTINUED)

ARTILLERY PROJECTILE INSPECTION WITH EMAT's
C. M. Fortunko
Science Center, Rockwell International 345

STEAM GENERATOR TUBE INSPECTION WITH EMAT's
C. Vasile
Science Center, Rockwell International 350

BURIED GAS PIPELINE INSPECTION WITH EMAT's
G. Alers
Science Center, Rockwell International 355

ULTRASONIC IMAGING SYSTEMS
G. S. Kino, T. M. Waugh, and D. Corl
Stanford University 359

MEASUREMENT OF STRENGTH OF ADHESIVE BONDS
G. A. Alers and R. K. Elsley,
Science Center, Rockwell International, and
P. L. Flynn, General Dynamics 365

WETOMETER FOR MEASUREMENT OF MOISTURE IN COMPOSITES
D. H. Kaelble
Science Center, Rockwell International 371

ATTENDEES 377

WELCOME AND INTRODUCTORY REMARKS

H. H. Johnson
Cornell University
Ithaca, New York

and

D. O. Thompson
Science Center, Rockwell International
Thousand Oaks, California 91360

D. O. Thompson: It's a pleasure to welcome you to the ARPA/AFML Review of Progress in Quantitative NDE. I'm Don Thompson, Director of the Structural Materials Department at the Rockwell International Science Center, and have had the privilege of serving as the Program Manager for the Program in Quantitative NDE which is under discussion for the next three days here. I'd like to introduce Prof. Herbert H. Johnson, Director of the Materials Science Center at Cornell University, and our host for the next three days. Herb, I'm sure that Dr. Peter Cannon, Vice President of the Science Center, Mrs. Diane Harris, who has served as our conference coordinator, myself, and all my colleagues join to thank you and your staff--Mr. Noel Desch, Mrs. Sharon Wells, Ms. Kris Molt, and many others--for all the cooperation you have given us. Special mention should also be given to Prof. J. A. Krumhansl for taking the initiative in suggesting that this meeting be held at Cornell. We appreciate the many courtesies and hospitality that you at Cornell have shown us.

H. H. Johnson: On behalf of the Materials Science Center and the University in general, we're very pleased that you've chosen to come here for your review meeting. For the last two or three years the Materials Science Center has been trying to encourage the holding on campus of major meetings in materials and materials related topics so that when Jim Krumhansl came and said, "Why not have the NDT meeting here?" it seemed to be a natural. Consequently, we plunged right in. We hope you enjoy your stay. In view of the fact that we're starting just a little bit late, I don't think I'll say any more just now. I hope you have a good meeting.

D. O. Thompson: Thank you very much, Herb. The good will and the courtesies that you have extended are much appreciated. Before proceeding with a program summary, I'd like to recognize two guests from overseas who are with us. They are Prof. Höller, Director of the NDE Institute at Saarbrucken, West Germany, and Mr. Robert Dokes of the British Navy Admiralty Materials Laboratory. We're glad that you could join us in this review.

I'd like to take a few minutes to tell you a little bit about the program. During it's three-year history, the ARPA/Air Force program has pursued four objectives. I think it's worthwhile to take a brief look at them so one can better measure over the next three days where we are, what we have done, and where we have come from over these last three years. The objectives are:

- To pursue advanced research in selected areas
- To establish a focal point for NDE research
- To enhance communication between the research community and the NDE user
- To improve the scientific base for NDE in selected areas.

The research referred to in the first objective has been divided into three projects. These projects are:

1. Flaw characterization by acoustic techniques.
2. Bond strength of bonded materials.
3. NDE characterization of failure related material properties.

Projects 2 and 3 have lately been combined under the heading of strength-related properties. Approximately two-thirds of our efforts have been spent in the ultrasonic topic, that is, the first one, and the remaining one-third in projects two and three.

I think that a number of exciting things have developed in these projects over the three years. Two related approaches have been pursued in Project 1 in an effort to develop a quantitative capability. The first is an ultrasonic scattering approach which has involved the development of new samples suitable for scattering experiments, theoretical treatments of the scattering which are amenable both to ultrasonic system design and to the development of a physical "feeling" of the behavior of scattering, experimental verification of these theories, and inversion procedures for the deduction of quantitative results from ultrasonic signals. The second approach has emphasized acoustic imaging and a transferral of work from the medical imaging field into the material NDE area. Underlying these efforts (and a necessary adjunct to them) are a number of ultrasonic improvements that also possess a stand-alone identity. These include a transducer characterization capability which provides a convenient method for the characterization of NDE transducers and two new options for inverse filtering to provide ways to improve transducer fidelity. The new technology of non-contact transducers has been significantly advanced. As a result of the work done to date, a number of applications are now in progress. Several software packages have also

been produced which aid significantly in the improvement of ultrasonic responses. Two other important applications areas have been generated from the ultrasonic scattering work in this project. These are a candidate procedure for ultrasonic standards and developments in the ultrasonic NDE of ceramic materials. As you recall, one of the program objectives is aimed at the improvement of the scientific base for NDE. As a physicist, I am particularly pleased with the closure that has been obtained in the ultrasonic work. By closure is meant the cycle whereby well characterized scattering samples were designed and fabricated, ultrasonic scattering theories were developed to describe them, the theories were independently experimentally verified, and the results then inverted to extract quantitative flaw parameters which agreed reasonably well with the known parameters. The successful development of this loop required other noteworthy advances, as indicated above, and, I believe, represents the first time in ultrasonic NDE that this traditional scientific loop has been closed.

In Projects 2 and 3 we have several other successes. These include the development of NDE procedures for the characterization of strengths in simple (single-phase) adhesively bonded materials. Another is a technique for the measurement for moisture in composites. Advances have also been made in the analysis of acoustic emission signals from which they can be correlated with the strength of the composite. Techniques for residual stress detection in ferrous materials utilizing the non-contact transducer technology is also ready for an application.

I would like to say a few words about the nature of the work in these projects that will be reported in the next three days. Our efforts have been aimed primarily at the generic core that underlies and is common to many specific applications. We believe that this is the most cost-effective way to spend the major part of the research funds entrusted to us. Specific application problems can then be addressed utilizing this knowledge.

Finally, I'd like to make some comments about work that supports the last three objectives. As of January, 1977, the program had produced some 55 technical papers, and another eleven or twelve had been submitted to editors. Program participants had given 67 seminars and professional society papers, as of that time, and ten patent disclosures as of that time had been written. That number will probably be doubled when everything is caught up. There have also been some fifteen or more graduate students involved in our work, a very important element of bringing new thoughts into the NDE area. Two special journal issues have been produced, and a number of review papers are in preparation. One of the major points of the program has been the annual meetings, like this one. They have grown from about 65 attendees at the first to about 200 at this one. We appreciate very much the cooperation demonstrated by colleagues doing related research at these meetings and from users who need new tools. This cooperation has aided significantly in establishing a focal point for NDE research activities.

Again, I welcome and thank you for coming to the meeting. I sincerely hope that you'll find it worthwhile, and that you will contribute freely to an exchange of ideas and information.

COMMENTS FROM ARPA/AFML

E. van Reuth and M. J. Buckley
Advanced Research Projects Agency
Arlington, Virginia 22209

and

D. M. Forney, Jr.
Air Force Materials Laboratory
Wright-Patterson Air Force Base
Dayton, Ohio 45433

E. van Reuth (ARPA): I thought it would be appropriate to make a few comments tonight since this week is the third anniversary of this program. I was pretty new with ARPA and these two guys by the name of Don Thompson and this guy he had gotten to, Mike Buckley from the Air Force Materials Laboratory, came in with blazing six guns. They painted such a picture that I was putty in their hands. So we started this program. I went out on thin ice for it with a pretty sizeable sum of money. I have found that it has been worth it over these three years. There have been, however, over these three years some ambivalent feelings on my part. How do you measure success? What am I going to say to myself 10-20 years from now; was this program successful or not? I see some signs of success, but I wonder if these successes would have occurred had not ARPA put an investment into the area. I like to feel they wouldn't have been accomplished, but it remains for posterity to show that. We have been fairly successful in getting things implemented into certain services. We have asked Mr. Willoughby to come here tonight from the Navy because the Navy has not been the most successful of the three services. They're not coming in first or second in my book as far as NDE is concerned, but I think when you hear Mr. Willoughby, you're going to hear that Mr. Willoughby has some interesting thoughts on this and I'm convinced if anyone can have an effect, he has a good shot at it.

I am stepping down tonight as the ARPA manager of this program. If there is a moment at which I step down, it is right now. During the last year or year and a half I have looked around for someone to come to ARPA who could manage an aggressive program like this and maximize the benefits. That person is Mike Buckley.

M. J. Buckley (ARPA): This program, I think, has been very successful, but as Ed has said, it is hard to measure the progress. We're working in a broad area. Some of you may not know how much money has been spent. To date about 2.4 million dollars shared by the Air Force and ARPA has been expended for three years of the program. I can say that the Director of ARPA has signed an ARPA order to extend the program to 27 months at a higher level of effort and the Air Force is negotiating, or will be, with Rockwell for that in the near future. Coming back here, this is the fourth meeting for that contract and there are a lot of faces that are now part of the group in NDE who three years ago didn't really know what it was except that it was a source of funding. I think now we have some real excitement in the field and I think we're facing some of the real critical questions. In particular, the inversion question intrigues me. How do we take a measurement and go back to the source? I expect over the next two years to focus down on some more specific problems in a broad sense so that we can demonstrate new capabilities and yet build some fundamental blocks to get there so that we have a solid base in which to expand and then solve specific problems. From the ARPA viewpoint, I think we're going to be looking in the future towards specific test beds on which to demonstrate technology to show that this quantitative capability, as we bring about pieces of it, can be applied to particular problems with a return on investment. That's really the name of the game in DoD. It's hard to convey how unusual this program is at ARPA. I didn't realize it until I got there. But to run a program for five years of this broad a nature is very unusual. In fact, I don't think there's anything else like that at ARPA at all right now. So, it has been rather unique in many ways and very successful. As the next two years come about I think we are going to be under a lot of pressure to focus in on some specifics that really demonstrate what this technology can do. I'm looking forward to the meeting and to seeing and talking with you again; hopefully, two years from now we really will have done something very impressive. Thank you.

D. O. Thompson (Rockwell International Science Center): Thank you, Mike. I just want to say that I have sincerely appreciated and enjoyed the working relationship that we've had with both yourself and Ed during the course of the three years. It is unusual, I think, to find Program Monitors who contribute technically as well as philosophically to a program, but both of these people have. Right now I'd like to introduce Mr. Don Forney from the Air Force Materials Lab. As you have heard, Mike has left the Air Force and has proceeded on to ARPA, leaving the program monitorship in one of his colleagues' hands, Dr. Rod Panos, at the Air Force Materials Laboratory. Unfortunately, Rod can't be with us tonight, but fortunately, it's because of a good reason. He's expecting an addition to his family. In place of Rod, I'd like to introduce Mr. Don Forney who is head of the NDE branch at the Air Force Materials Laboratory.

D. J. Forney, Jr. (AFML): I think the ultrasonic inspection of Mrs. Panos indicated that the birth would take place at any time now, and Rod, being a good NDE scientist, didn't want to believe that any false predictions could come from that

inspection; so he decided to stay at home. It's interesting to follow Mike on this podium because he normally would be making the remarks that I'm going to now make; I'll have to check with him later to find out if I said what he would have said. I'd like to comment that from the Air Force's point of view we also feel that this program is an important one. We think it's a unique project in that it's evolving a science base, if you will, to undergoad a fairly old technology area--one which we think was reaching its asymptote in new development opportunities until, as Ed pointed out, Don and Mike undertook the task of trying to develop some activity to put some science under this so-called art area that has evolved over the last 30 or 40 years with totally inadequate progress being made. I'd like, therefore, to add my comments that I think that we can be very happy that people like Don and Mike decided to attack that dragon. I think the success of this program and other science based activities in the future will all owe beginnings to these two guys and the thing that they did. I think that the success and productivity of this program is very important to the future of this kind of activity. A generic project, if I can describe it that way, is very unusual in DoD. It took a large measure of faith in the prospect of success for our management to fund a sizeable program of this type for a considerable length of time. I think productivity and success in the program is very important to its future. The idea of funding institutes or center type programs, if I can characterize them this way, is very out of character in a service organization. Over the years we've tried and failed in many technical subjects to generate interest on the part of our management to put money over the long term to pay for institutional kinds of R&D; yet, we feel that the focus that has been put together on a program like this will create real progress. I think that what has happened in this program is that there's been a lot of stimulation in new thinking within the NDE community. Many science-based people who are not NDE scientists, if there is such a thing, have applied their energies and their thoughts and have stimulated thinking among NDE engineers to think of things as possible that weren't thought possible before. The approaches to typical engineering solutions have been vastly broadened by the science-based kind of work that is represented in this program. Finally, and I think perhaps importantly, renewed expectations on the part of the funding management has come about. NDE was an area that management thought could never face up to the task that it was being called upon to handle. I think that the scientific progress made in this program has really renewed the faith on the part of funding management indicating that, after all, there may be a solution out there. I think that the fact that this program is proceeding on and in the near term has a lot of help is a gratifying thought in the terms of what we might be able to accomplish in NDE and the kind of management attention that we'll get in the future. I'd really like to say that the Air Force has a strong commitment to continue efforts in the science-based area and we hope that other parts of DoD will feel the same way and maybe increase their energies in that direction. We certainly invite the participation on the part of our sister services in focusing their attention toward the fundamental solution to the problem. Again, on behalf of the Air Force part of the program we are very happy to see so many people here; the fact that the program audience grows each year is gratifying to us. Thank you.

RELIABILITY BY DESIGN

W. J. Willoughby, Jr.
Assistant Deputy Chief of Naval Material
(Reliability and Engineering)

Headquarters Naval Material Command
Washington, DC 20360

With Introduction
by
Hans Vanderveldt
Department of the Navy
Naval Sea Systems Command

Good evening. The keynote address tonight addresses a topic in which all of you are extremely interested. That topic is reliability by design. To present to you some thoughts on the Navy's approach to this idea, we have with us probably the foremost authority in the Navy for the establishment of policy and programs in this area, a man who is the Deputy Chief of the Navy Materials Command for reliability and maintainability. Mr. Willis J. Willoughby is exceedingly well qualified for this position. He has some 22 years of experience that ranges from basic engineering to design to engineering management, a very important function itself, and prior to accepting this position with the Navy, he was Director of reliability, quality, control, and safety for the manned spaceflight program of the National Aeronautics and Space Administration's Apollo Program. It was the success of this program which brought Mr. Willoughby to the Navy's attention and to Admiral Isaac Kidd in particular. Admiral Kidd, who was the commander, the Chief of Naval Material, invited him to come with the Navy to establish the program, the policies, and the procedures necessary to improve the reliability and maintainability of our fleet afloat. He has been able to bring a new look to the Navy in this area quite successfully, and he is getting a lot of attention. He has formalized, and this is a very important step in the Navy, a new approach for building vehicles and issuing an instruction which deals with reliability of naval material. He has received the Apollo Group Achievement Award and the NASA Exceptional Service Medal. I think I have talked long enough, so without further delay, it is my privilege to introduce to you Mr. Willis J. Willoughby.

RELIABILITY BY DESIGN

W. J. Willoughby, Jr.
Assistant Deputy Chief of Naval Material
(Reliability and Engineering)

Headquarters Naval Material Command
Washington, DC 20360

Gentlemen, it is my privilege to spend a few minutes with you tonight. I'd like to thank ARPA, the Air Force, and the Rockwell Science Center for the invitation to share a little bit of what I call the "new look" in the Navy. I'm really here tonight on behalf of the Navy, and particularly on behalf of Admiral Michaelis who is the Chief of Naval Material. The story I have to tell you is one that I think you will find somewhat enlightening. I know you'll find some of it amusing, but I hope that the overall message will be that the Navy has undertaken a program to improve its fleet readiness and has undertaken it as a very serious proposition.

A story comes to mind that I think is appropriate to this particular gathering, especially since I've seen a number of you before in various places as you represent companies, universities, or the Government. This story came to me recently. It relates to an old lady who is getting ready to get on a train. She saw the conductor making signals to the engineer. The lady walked up to him and said she would like to know what he was doing. He was pretty grumpy and the train was late, so he turned to her and said, "Lady, when I do that kind of a thing, I'm telling the engineer to get the hell out of here." So with that, he walked off in a huff. The little lady got on the train and sat down. A little later, the conductor began thinking about it and realized that he had been a little rude. He decided he would apologize to her. As he approached the lady and started to say that he was sorry, she made the same signals he had made to the engineer. In some respects, I think that's the way I approach some of you--It's time to get the hell out of here.

Nondestructive testing came to me a long time ago and I never really knew what it was. My father was an executive with the Atlantic Coast Line Railroad. Back in the 30's, I can remember my pride when my father took me out to the railroad shops one day and showed me a thing called the Sperry Car. That's, of course, the device that the railroads run up and down the tracks to check the rails. I had never seen it. I took a little ride out on it. I didn't know what was so impressive about it except for its being so small. I could see papers being run through something and wiggles being made. From that, somebody was telling me, it was a remarkable thing. I later encountered the same kind of an experience, only this time it was much more serious.

On the Apollo program, we learned a lesson about titanium and methanol. As you know by now, titanium and methanol don't mix. We didn't know it at the time. One night at home I got a telephone call at 11:00 p.m., and it was similar to the story of the train, only they were telling me to get the hell out to Downey. A titanium tank had exploded. A launch tank had it on board. Actually, it was a dock tank, but nobody quite knew what had happened. We were all scared because we were approaching launch date. We didn't know what was really going on, but when we found out what happened we were even more scared because we heard of things for the first time called flaw sizes, growth rates, progression rates, all sorts of things--eventually termed stress corrosion. Most frightening to us at that time was that we had bought all the titanium tanks we were going to buy. So there we were with a buy of titanium tanks on our hands and an Apollo launch pretty nearly at hand.

A lot of excited people began to get into the act, and I found myself facing some very learned people who very quickly became even more learned about a thing called stress corrosion in titanium. They finally wound up convincing us that they understood the fracture mechanics well enough that they could tell us not only the flaw size, but the growth rate. We were being assured as we were putting that thing together on the pad that for every pressure cycle we put on it, the growth rate would be thus and so. The people would stand up in front of our flight readiness reviews and say the growth is thus and so, and when we get to the moon it will be this big, and when you get back home it will be this big. "But don't worry, fellows, it isn't going to hurt you," they said. That was news to me and I went home every night saying, "I wonder if those fools know what they're talking about?" I didn't know, NASA didn't know, but the more data we collected, the more we became convinced that that was what was happening.

We could live with a flaw of a particular size, and as a matter of fact, we did. Before every mission we flew, we determined what flaw sizes we had in the tanks and the projected time they were going to last and how many pressure cycles we could put on them. After that experience, I came to have a very deep appreciation for the science of stress corrosion, metal fatigue, and nondestructive testing. It was a "bath" that I had never taken before; it was a "bath" I never want to take again because it was a very worrisome thing for us all. There was just no way we could demonstrate completely that we were right. We had a very fine group of engineers and a very fine group of industrial support people who, I think, did an outstanding job; and we learned to live in their confidence. It was hard to do at first because we

weren't trained for that. When we had things that weren't right, we simply stomped them out.

With that memory in mind, I'd like to share with you tonight what I think to be an exciting evolution, or revolution, that's taking place within the Naval Material Command and within the Navy as a whole. I would like to bring to your attention what it can mean to the nondestructive test community, and later on will summarize some of the observations that I have made.

I came to the Navy at their invitation kicking and screaming all the way. I became involved with the Navy by accident, strictly by accident. A friend of Admiral Isaac Kidd, then Chief of Naval Material, had known Alan Shepard. Alan came to me one day and said, "Will, the Navy's having an awful lot of trouble with fleet readiness and reliability. I think you should go over there and talk to them a little bit and just see if there's any way you can shed light on their problem." So I went over there one day during lunch and spent some time with them. The result was that I agreed to do a quick study for the Navy--to say to them that if we, NASA, were doing this job, this is how we would be doing it versus how they were doing it. That was the gist of the thing. I took about seven people (this was just before Apollo 17 so I had to hurry) and spent three days on this project. We picked a sample of equipment that the Navy selected and reviewed it at the contractor's site. We reviewed their procurement cycle and their contract. The result was that we told the Navy we just wouldn't have done it that way. "We don't believe that the hardware you get is really going to do the job for you when you do it this way."

As a result of that, I was asked to give a presentation to what the Navy calls the "General Board," which is a large group of the admiralty who gather periodically to pay homage to the Navy. I stood before that group not knowing what was really in store for me. At the end of that presentation, Admiral Kidd said to me, "Will, I expect you to report on board in two weeks." Not being too swift, I thought a minute and said, "The Navy's here, NASA's there; I don't think you can really say that." I smiled and said, "That's a very kind invitation, thank you," and left. The Navy continued insistent, and letters flew back and forth between NASA and the Navy. I can remember vividly when the letters kept coming from higher and higher authorities. Finally, they were on secretarial levels and White House levels. My management came to me each time saying, "What do you want us to do about this?" I said, "Let's use Navy terminology. Let's tighten up the line, let's throw out an anchor; but whatever you do, fellows, don't turn loose of me." I said, "I've seen those guys over there and, believe you me, they couldn't win if they had to." That went on for awhile. Finally, the NASA administrator came to me and said, "Really, I don't know what you've done over there, but you don't have to go to work for the Navy." From that point on, things looked black. I agreed to go on a loan basis for 18 months to see what could be done in that time. My secret ambition in that 18 months was simply to prove that nothing could be done and so go back to NASA.

That, of course, is where a part of the story I want to tell you tonight really lies because Admiral Kidd came back from the fleet at that time. He was new to the Naval Material Command as its Chief. He came back with some very, very deep concerns about readiness, about the Navy's fighting ability. He expressed it to me in many terms, but I think it can best be expressed to you simply that he didn't believe the Navy could do the job with its current state of reliability of readiness. He was very worried. He had been side-by-side with the Russian Navy. He had seen it and he worried. He had come from the Mediterranean. When he saw me fighting coming to the Navy, he asked me to please keep an open mind. He said, "I'll give you access to all the files, the systems, whatever you'd like to have in order to learn and understand what our problem really is."

Early in my life a lead engineer had told me of an equation for success that I've always kept in mind. It came to mind then, and I used it primarily as one of the basis for assessing "Why me?" in the Navy; why couldn't it be somebody else? This equation for success goes something like this.

First, you must know the problem. I went through the Navy files; and as nearly as I could see, they knew the problem of fleet readiness, of unreliability, of trouble with equipment, as long as ten years ago. They couldn't have been after me just to learn the problem. They already knew what the problem was; it's well documented.

The second part of this equation for success is that you must have the proper tools. I looked through the system once again for tools. In this case there would be instructions, procedures, directives, specifications, etc. What I saw there was an abundance; it wasn't a lack.
Later, I came to believe that the abundance I saw was really a part of the problem; it's called a Military Specification. I'd never seen a MIL-SPEC before. (I've lead a sheltered life, you see. I'll explain to you later.) MIL-SPECS were an anomaly in my life. As I look at them more and more, I've become a sworn advocate of stamping out MIL-STDS. They just aren't what they claim to be. As I said, the second part of the equation is tools, and I'd seen them.

The third part of the equation was discipline. In other words, if you know the problem, have the tools, and have the discipline, you'll always succeed. I've followed that all my life and found it to be a very successful, simple equation. When I looked at discipline in the Navy, there's where I got my surprise. In Washington, where I'd worked in NASA, we were across the river from the DOD complex. I could look out my window and see the Navy's bright braids shining in the sunlight, and I could see them smartly marching up and down the streets. Discipline was the last thing in the world that I thought would be missing in the equation. But I did find that discipline was missing, and when I was relating this story to Admiral Kidd one day, he told me to look completely. I decided that the first place to look was in the Chief's own office, to see if he knew how to carry it out, because that's what he's in charge of--Naval Material. I went in to Ike one day and told him two stories which I'll relate to you one at a time.

The first one involved this business of discipline. I said, "Ike, I've looked through Naval Material Command records and I can relate it to you this way--I can remember as a youngster when the Mighty Mo ran aground in the Chesapeake. All they did was to wait for the high tide and float it off again, but the skipper of that ship never saw the light of day again." I also said, "Ike, there's one other thing that's obviously apparent to me. If you run a procurement aground, the only thing that happens to you is that you 'make flag.' That's absolutely a matter of record." Now I don't say that derogatorily. What is really meant is this: The experience for promotion in the Navy comes from operational experience, not experience in Washington. There's not a program manager in Washington that's not anxious to get out of there as fast as he knows how; and he's rated on his ability to fly an airplane, sail a ship, or whatever it is he does from an operational point of view. His stay in Washington is as minimal as he can make it. He doesn't want to be there long, and he knows he's not going to get much of a rating out of his performance in Washington. So when I say he "makes flag," what I really mean is his interlude in the procurement world doesn't in any way have a lot to do with his promotion. It all comes from his operational ability. Following on with this little litany a minute, what I also want to point out to you is a part of the looking that I did.

The focus that the Navy has in front of it today was set by a study I did with three or four people I brought from NASA. We reviewed about 180 contracts. I asked for 180 contracts, at random, of Naval procurements (some large items, some small items, some very small items) and looked through those. From this review we really found the major problem in the Navy's acquisition program. The Navy, today, is committed to change it, based on the visibility of that particular study. Of the 180 contracts, I found three particularly significant things. First, there wasn't one contract that had an enforceable reliability requirement in it. Any reliability requirements in the contracts could not be enforced; not a single one. There were two reasons: First, most of them were stated as goals. Having worked in industry long enough, I can tell you what a goal is. I just love contracts written with goals that say you'll do the best you can and someday you'll get the answer whenever they give you enough money. Watch out for goals because nothing ever happens. That is very quantifiable. Second, those that weren't written in terms of goals were stated in terms of probability and statistics. You have to realize right away that anybody in the Naval Material world who deals in terms of probabilistics is intellectually dishonest. He's fooling himself, and he's fooling everybody because the population size is too small. It just doesn't work. I can give you a point estimate with engineering judgment that has more accuracy e to the minus lambda t carried to nine decimal places with a sample size of 500. It just doesn't work; it's speculation.

But the even more damaging aspect of probabilistics is that they're nonuseful to engineers. Back in the 1950's when I was designing electronics, I can remember when reliability came into vogue. We had never heard of the word. In 1953-55 reliability started popping up. I can remember the lead engineer coming to me and saying, "Will, this has got to be a reliable system here." I said, "Gee, what does that mean?" It was .99, .98, whatever the thing was. I said, "Chief, what does that mean?" He said, "It's got to be good." Probabilistics just don't do you any good; what we want is MTBF. MTBF is a useable item. It's just as useable as volume, weight, space, velocity, etc. But these contracts had none of that in them. So our first observation was that they just weren't enforceable. None of the 180! It didn't matter who you wrote them with, who they were for, what equipment they were for; they just were not enforceable.

The second finding, and equally interesting, was that all the contractors in these 180 contracts gave the Government what it bargained for in performance. As a matter of fact, more than thirty percent of the contractors gave us more performance than we wanted. From a performance point of view, the records that Packard left behind seem to make a lot of sense. You can almost leave a contract alone when it comes to performance. It seems as though we can generally get what we want when it comes to performance.

Out of this contract review came the third part of the equation which is really the one we're going to focus on tonight. Any reliability given to the Navy in the equipment, and any reliability that was achieved, was an accident. It was serendipity. It was what was left over after the performance specification had been set. Any other attempt to put reliability in it was fallacious. It was just somebody picking a number out of thin air and writing it down, without basis. That led me to the real fundamental thing that we're talking about here tonight, and that is that <u>reliability must be a function of design.</u> It can't come by chance. One of the first things I found when I came to DOD is that you have to have a slogan such as "design to cost." There's life cycle cost, all sorts of slogans, so the one we used was "reliability by design, not by chance." The contract review showed that all the reliability that came to the Navy in its equipment was strictly by chance. The program manager primarily was being motivated by performance and a budget and schedule. Most of the time, he was in trouble in some way that you could trace back to the fact that the equipment wasn't reliable. It was taking him more time in the test program, running his budget up, giving him trouble in the fleet. He was having to go out and do some fixing and that was running his budget up. Primarily, though, the schedule/cost/budget problems he was having could be attributed to the fact that reliability was not part of his design. That puzzled me because, you see, in my experience (tracing backwards, before I came to NASA, I was at ARINC) reliability was a first requirement. When I was with the airlines, reliability was a first requirement. I had led a sheltered life because, in every case, reliability was desired and, as a matter of fact, required. In the case of Bell Labs, that was profit and loss and they designed 30 years in MTBF equipment; not 30 hours or 30 minutes. Repeaters that go under the ocean have 35 to 40 years demonstrated MTBF today. Profit and loss: they don't have to pull those things up. Cables are very hard to service; they're trouble. What motivated that design was

profit and loss. With the airlines it was profit and loss again; but in this case, safety was thrown in. The equipment the airlines dealt with had to be reliable; they had to be careful. In Apollo we were in a goldfish bowl and all of us, whether we wanted to or not, became very well acquainted with the astronauts. We loved them like brothers and took extra care simply because of our appreciation of the astronauts. All in all, we were motivated. When I looked at the Navy and their program managers and their procurement system, I saw nothing motivating reliability--not a thing. There is where I saw the root cause of the problem: motivation.

When I told Ike this, he asked me what I was going to do. I said, "The first thing I'm going to do is focus attention on the subject. I'm going to embarass people. I'm going to cause them to take second thoughts and ultimately we're going to require that performance and reliability be given equal consideration in RFP's, in Navy thinking, in the Office of the Chief of Naval Operations, in the whole equation." We have recently begun this in our institutionalizing process. We've issued a reliability instruction in which it is required that reliability and performance be equally considered in every aspect. Do not consider it second. If you can't make it reliable, don't start.

I have a little card in my pocket that I think is down-right amazing. This is called the Realistic story, but it's Radio Shack. In it, Radio Shack has a very interesting paragraph that I think goes for anybody dealing in the equipment world. I found it remarkable for a manufacturer like this to state it quite this way, but this is how they stated it: "Our people who design and build our products approach their task differently from conventional makers. We build to achieve three things in the following order. First, reliability; second, performance; third, competitive price. We're not interested in price unless the product is reliable. We're not interested in price unless the performance meets our criteria for the way things work, look, feel best, and sound." So here's a little manufacturer just making equipment who has a better motto for reliability than I found in the Navy. As a matter of fact, it really fits the motto that I have now brought to the Navy. The Navy has now taken this on board with great vigor.

At first, there was a lot of trouble. We did have a lot of problems in getting it understood. I think the main thing we had trouble with was the snapshot I took of what reliability really meant to the Navy when I went there. It was simply this: measurement, measurement. It was e to the minus lambda t. That was reliability. It was a cultist organization run by statisticians with the engineers completely out of the loop. It was done at the end of the development cycle. Sometimes, it was done after the production had stopped. I saw a squadron of airplanes going on a carrier. They were already on the carrier and production had already been turned off. I reviewed the contract and saw in it a reliability demonstration program: 3.5 million dollars. I said we don't need to spend that money. There's nothing you can do about it; they're already on the deck of the carrier. Why do we want to demonstrate it? The flyers will tell us what it's all about pretty quick. It doesn't take them long. I saw that measurement was what we were primarily doing. Measurement is all right providing it's a closed loop measurement cycle. You have to realize in a military procurement cycle that it isn't closed loop. There's no time for it to be closed loop. If a measurement takes place at the end, then you do not have sufficient money to make the fundamental corrections you should make to the equipment. The time you have for delivery is paramount because contractors who are building ships will charge you for every day the equipment is delayed in delivery to them, so they find themselves in a bind. The equipment comes up for test and, guess what, it's a bust. It doesn't make any difference; they deliver it anyway. I can show you record after record of Navy materials flunking their demonstration tests and being delivered with a fix kit for the fleet. Of course, that's the box you're in and I don't blame anybody for that.

If you wait to that point in time to get your snapshot of what reliability really is, then you've lost the game unless you just happen to pass. In a lot of cases the passing is rigged. I've seen equipment that demonstrated 22 hours MTBF in a six-month scenario of "fleet environment." When it went out to the fleet, it was one-tenth of an hour MTBF demonstrated. Why? Because it really never saw the fleet environment until it got there no matter how hard we tried. I don't think anybody necessarily did it wrong on purpose. It's just impossible to demonstrate that kind of a thing that late in the program. It's got to be in a designer's mind; it's got to be part of the "mission profile" he designs to. That's the way we've always done it in our lifetime. We never waited on a demonstration to do it. What I really saw was that the present approach for reliability was really by chance.

I thought that the only thing we could really do was to start an intellectual discourse with the engineers, with the managers, with everybody involved, as to what they were really doing. We could cause them to start thinking a little bit and see if the thinking process wouldn't really lead them to the right answer. Over the past years, that's what I've done. I issued an instruction in April. I could have issued that instruction when I first came two and one half years ago. Of course, it wouldn't have looked the same as it does today because I learned a little and they learned a little. So together I think they have an instruction that is going to be supportable and which will cause an improvement in our reliability.

Let me talk to you just a minute about that same snapshot involving military standards. I blamed the problem of some of our fleet on military standards. I haven't found a more damaging standard than MIL-STD-781B, which is an environmental test specification for reliability demonstration and acceptance. We're better off to stomp it out, to get rid of it. What I have now promoted is a change to MIL-STD-781C. MIL-STD-781C has a lot of the good things in it I think we ought to have. Military standards aren't really wrong; it's the way we use them. Most people have become so used to boilerplating with military standards that they simply say if I'm

going to have a reliability program, it's going to be in accordance with MIL-STD-785A. MIL-STD-785A tells you how to build everything from bullets to ships. You have to use your mind the minute you see a military specification, to tailor it. There is a paragraph in these military specifications that says to tailor the design to the situation and use what's applicable in the specification, but I haven't seen that done. Most people have gotten into the habit now of just taking the military specification and using it as is, without much intelligence and without much thinking about it. What we've had to do is to pull our reins in on the military specifications in those areas that are bothering us and say "You can't use them unless you come to us and tell us about the military specification you intend to implement; what parts of it are applicable to this design and what parts aren't?"

One of the things I have in my office that makes all this possible (while I was still working for NASA, I did negotiate with the Navy what I considered to be something that was very necessary if we were really going to get on with the job with the Navy) is the authority to carry it out. I have a thing called a business clearance review which simply says that you don't go to contract with Navy unless you go through my office. When those contracts come through, we send them back if they haven't got the right requirements in them and we haven't said the right things. This has caused a little bit of controversy, a little bit of a problem. As I told someone at supper time, you may have noticed that the crime rate in Washington has gone down according to the records. There is no doubt in my mind this is true because the Navy has hired all the hit men out of Washington to see what they can do about me.

There is no doubt we do have a problem which we're trying to solve; part of it being to get attention focused in the right places. The main thing we have found is that combat effectiveness is really a function of economic effectiveness. We're finding that the greatest economic level for reliability improvement in the fleet comes in the design process. It uses less money and involves less time. You can erase a resistor on a drawing board whereas if you replace it in the fleet, it costs you millions and millions of dollars. Without really knowing what I was doing, I recently approved a no-cost Engineering Change Proposal (ECP) to change a capacitor in a piece of equipment that was out in the fleet. When we were done, it cost three million dollars because we had to change publications, training, standards, and test equipment. All I did was approve the no-cost ECP for a capacitor. There is no such thing, fellas. When it gets in the fleet it's a costly process. This is what the Navy is finding out. The economic leverage isn't where it was. That is today, of course, the biggest asset I think we have in helping us get this reliability equation solved--the economics of the budget. We are finding ourselves with a shrinking budget, and we're not able to buy what we could buy before; you have to realize that the large majority of the Navy's money goes into spare parts and product support.

When I first came to the Navy, what worried me most was how to get attention focused on design when by admission of every contractor, his main money making source was parts and support. That worried me greatly. I went out to see a few contractors. Not long ago Harry Graves, President of United Technology, even put it in writing in Aviation Week, that 30 to 40 percent of United Technology's profit structure was parts and support. While that equation got changed (not due to anything I did) because of inflation shrinking the ability to buy with the dollar, what we found ourselves doing more and more was buying less and less new equipment. This means no new starts for the industry. This means a technological base freeze, literally. We just can't do anything new; all we can do is support what we've got. In briefing industry, I have called their attention to starting to design for reliability now if you intend to keep a technological base because it's going to stop. We're just not going to buy any new equipment. If you look through the Navy's records, you will find there is very little new equipment being bought. Most of it is reprocurement and update of old equipment. There is some new equipment, of course, but not nearly to the extent we ought to have. We have set into being what we call a "new look," a new way of doing business. In that new way of doing business, we've published a little thing for public relations or public information. It says in one word what the Navy is going to do. It says what you must do in terms of RFP's, bids, designs, etc. It says to contractors that unless you follow these, you're just not going to do business with the Navy. At first there was a little doubt about that, but it soon went away. We have it pretty well understood now that this is the method by which we're going to do business. As I said before, the biggest thing we have to do is get the reliability decision-making process up early. We have to decide if it's going to be a reliable device early in the design. We have to lose this infatuation with performance.

The commercial industry has lost its infatuation with performance. When you go out to buy something in the commercial world or your wife goes to buy something, you don't ask how many times the washing machine jiggles up and down or what kind of a defrosting cycle your refrigerator has, etc. The main thing you ask the commercial industry is whether it's durable, is it reliable, how long will it last? You've seen the ad for Maytag washing machines where the poor maintenance guy is just out of business and crying because he has nothing to do (a little exaggerated because I own one). Nevertheless, in principle, it is focused about right. They have done a good job. The RCA XL-100 is a good example, and I happen to know that RCA didn't get there by accident. That set was held off the market for quite awhile while they worked on limited life. I don't know whether you have had any bad experiences with them or not, but the basic concepts are there. Most of the industry is trying to work on a product life. The only people who aren't working on it right now (who weren't working on it, I should say) is the Navy. We're working on it right now. The new approach says that we are going to design it in and we are going to make sure that the concepts have been considered early in the game. The reason we want to do this is to reduce what

Admiral Kidd called an "umbilical to the beach."

I stand here tonight and very sincerely say to you that I worry in terms of our defense posture with the U. S. Navy after having seen some of the Russian technology through the Soyez Visibility. I have come to a personal conclusion I want to express to you tonight. The thing that motivates me to continue under all the stress and duress in the Naval Material Command is to make sure that this project does get carried out and that the Navy does change its way of doing business. I'm motivated simply by this: I'm convinced that our sophistication is the problem we have in our equipment. The Russian technology is not very sophisticated; it is very unsophisticated equipment. If you simply take a quick snapshot of what that means if the two forces were engaged, you have to come to the following conclusion: If it's a short engagement we would be the superior; if it's a long engagement, I think we'll have a problem. Sophistication without life gives you only the original big bang. For instance, we can have a plane that can leave an aircraft carrier and go do a mission and come back, but he can't do it twice. Oh, I may rectify it while he's down; however, some of their equipment can go up over and over and over again. They can't do as sophisticated a mission and they can't track multiple targets, but the point is that they have the sustaining power. What I'm dedicated to doing is seeing that this performance, which is so good, also has life. If you put life into our performance equation, it's unbeatable; it's absolutely unbeatable. When things get tough and I get tired, I always reflect back to that particular snapshot that I had and I come on again with new vigor to see to it that we carry out this new Navy program.

In order to do that, we've also created another slogan which we call "Big R, Little m." In other words, we want reliability in our equipment and we want it to have minimum maintenance because I saw in my snapshot of the fleet that our maintenance problem is truly bad. It's tough. I went out on the carrier, the AMERICA, and before I knew the Navy's reliability problems were for real, I even agreed to fly in an F-14. It was only later that I woke up to my indiscretion. Since this is a technological symposium, let me tell you something. The Navy does do things they don't take credit for. I am completely convinced that the Navy has invented the elusive time machine that everybody talks about. When I went on the F-14, while we were sitting on the catapult waiting to leave the deck, the pilot up front gave the catapult officer a salute; and he said to me, "Will, if you're comfortable back there, you give a thumb's up." While we were sitting there on the catapult, the pressure was raised, the engines were run up, the pilot gave his salute, and I raised my thumb. Even though only one second passed, it seemed like days because I looked at that finger and said, "You fool, what have you done?" It was a valuable experience. I learned a lot.

What I saw out there were tired people, maintenance people who had lost their enthusiasm for maintenance because, as one fellow said, "It doesn't do any good to repair it; it'll be back the next day." I put an "X" on the box and said let's look at that one when you're done. He finished testing it; I stood right there and said "Okay, I'll put my initials right here." I told him I'd be back tomorrow night. I went back the next night and he was grinning. There it was. This is bad motivation for maintenance people. How would you like to keep repairing something over and over again and just see it fail, see it come back. Pretty soon you just have an "I don't give a heck" attitude. I am also dedicated to helping those fellows change their attitude because, as I told them, they're our stewards. We dedicate that equipment to them and yet part of what we give them is junk, just pure junk. We say to them take care of it, treat it right. You and I wouldn't buy it if we went to the marketplace to buy some of that equipment; it would never get sold because we know better. What we have done is to emphasize reliability by design. We've now brought the process up to the front end of the contract and said "Measurement is not very important any more." We are going to have measurements for contractual reasons; there is no way a contractor can be released unless he has demonstrated he did what you asked him to do. What we're not going to do is make decisions based on that measurement data. We're simply going to release him from his obligation if he did the demonstration like he was supposed to, and we're not going to put a lot of bucks in it.

Instead, we are transferring the money up to the front end of the contract and we are asking them to do things that are on this particular card. This little card was really made as a flyer for the instruction that came out so that some people who didn't want to read the whole instruction could see it right here on one card. In this thing, we have the requirement "design to minimize failure." That is really what it is all about. First of all, you have a mission profile which is a Navy responsibility. This one you don't lay at the feet of the contractors. Most of the equipment I saw in the Navy didn't have a fighting chance because no one had said what the mission profile was going to be. We had simply told the contractor to make it so it will operate in some unknown environment for some unknown number of cycles. He can't do that. The designer must know what you intend to do with the equipment, how you intend to use it. We have had a very difficult problem getting this ironed out, but we finally got the specifications, etc., out, and people are responding to the mission profile. Some of them are a little weak, but they are getting better. For a while I didn't think I had a chance, to be honest with you. It looked like it just couldn't be done. I've seen responses in the last year that have shown that people are starting to think and are recognizing the same thing I recognize. If we do want a Navy, we want it to be a good Navy. Therefore, we have to put some time into product life. We have also said that we want you to do environmental profiles. We want to know the environment in which the equipment is going to be operating. We want not only the performance profile, but the environmental profile. Following up on that, we are now asking the contractor to give us a design that is understressed, not overstressed. Reliability is simply a function of stress. Once you realize that, there is nothing else to the problem. All you have to do now is figure out a way to solve it.

Reliability is a function of stress, so in order to get the stress levels understood and to minimize the stress on equipment, we have set standards. We have said you will derate all of your components to our standards and we have the list of standards you will use. For instance, we have set junction temperatures inside of semiconductors. A junction temperature is what governs the life of a semiconductor. For every ten degrees you derate a junction temperature, you double its life. In studies they did years ago, NASA and Bell Labs set certain junction temperatures. Bell Labs' junction temperatures run between 50-60°C. NASA said because of weight limitations, space environment, etc., we must have 100°C junction temperature. Would you care to guess what I found the Navy's junction temperatures to be running. They were 170-240°C. Just remember that for every ten degrees you double the life of the device. Just like a light bulb, you cannot stress it too hard. What we have now done is said to the designer, "We want you to follow our derating criteria; we want you to follow our design criteria, but we also want you to make stress analyses." It's funny that you talk about nondestructive testing here, and yet for some reason your electronic community has known for years that electrons running through the wires are just as damaging to components as cars are to bridges. I could find reams of mechanical stress analyses for all the equipment we bought, but I couldn't find the first piece of data for electronic stress analyses. It is very well known and understood.

We have told the contractor to make a stress analysis on every decision, mechanical and electrical. Not only that, we will sit down and review it to see if he did it right. Now there lies the hooker because the Navy has to be able to review it to see if it is right. We do have the manpower and the talent, and we must run them together right now to see that it all gets done properly. We've also done sneak circuit analysis which NASA originated. It isn't too well known, but it is a very worthwhile tool for understanding what stresses you have on your circuits. I'll give you an example of one that you may have in your automobiles right now. I will give you two because I just read another one from Detroit the other night.

A sneak circuit is an unplanned event that takes place due to a malfunction in a component part or a misoperation which opens up a path that had not been normally analyzed to be there. An example is in your automobile. If you own a 1975 Ford or General Motors product, here's a sneak circuit. You know that when you get in your car and your ignition is turned off on the post, nothing will happen when you turn on your radio because you haven't got the column turned on. What you have to do in this case is to turn on your radio, leave the column turned off, reach underneath the key and pull out the emergency flasher (the thing that makes all sorts of lights go on your car). Now put on your brakes and your car radio will play. That's a fact! I've had people rush out and run back in while I was talking to them and say yep, that's right. That's a fact!

Yesterday I read another one that says all owners of Cadillacs are asked to bring their Cadillacs back in. (I'd say anybody that owns a Cadillac deserves it.) All Cadillac owners were asked to bring their cars back in to have a printed circuit board replaced. If you have an electric door lock on your Cadillac, when you move the transmission from neutral into drive, it pulses it into the unlocked position. Now you're asked to bring it back and they'll give you another PC board. In the technical note it says that it keeps the electrons from being confused. Well, they're right. The electrons do become confused.

All I was trying to summarize here in this little bit on reliability by design is simply the fact that it's the place where the money is to be made in the world today if you're interested in seeing to it that reliable systems are brought on board. There is another part of this that worried me; and because I talked about it too much, I found it in my shop not too long ago. I got a call from Admiral Michaelis one night and he said, "Will, we've been listening to what you've said and we've decided to give you that responsibility too." There are a lot of indications that we are having success in the design world, but the thing that I'm worried about now is quality assurance, or quality control. What I'm worried about is whether it's built to print. I've worked in plants where we would do the thing right in design, but it wasn't built like that. I thought it was in another shop and it was, but it just simply melted into mine. Maybe I should not have said anything, but I had a very sincere motivation. You can design it right, but if you don't build it to print you've got a problem. I saw all the indications that our build-to-print visibility wasn't working very well. I went out to contractor's plants (with them kicking and screaming), picked up boards, and brought them home just to show defects on them, to the Material Command personnel, to let them know what we've got to worry about. That's another part of the equation: build-to-print. I now have reliability, quality, maintainability, production and engineering. I don't know quite how to handle all that yet because my focus is still on reliability which I think is the principal problem the Navy is facing.

In closing, let me give you a little bit of insight into some of the things I think would interest you tonight. I said earlier in my opening remarks that I was going to give you some snapshots of what I thought was an exciting period in the Navy right now and what it meant to nondestructive engineering and nondestructive testing. In this world today I see that reliability has to be the focal point of just about everything for awhile because there are a lot of things happening in the world that aren't in the Naval Material Command. We've seen what happens in coal when fuel and gasoline, fossil fuels, etc., start to get scarce. I see that we are also going to find a scarcity of some of our natural resources. Not long ago, Don wrote a paper that elegantly put that in perspective. It says something like "At the current rate of use, we have 40 to 70 years before our natural resources are gone." Why? Because we're in a throwaway society. Because we're at a place where reliability hadn't been understood; but in some of the lesser complicated

things where a lot of money is being spent, it is understood; but in some of the lesser complicated things, we tend to build anew. We say throw it away. I'm raised with a mind that tells me that isn't the right way to do business. Waste not, want not. I learned that years ago, but I find that today's society may be cultivating something that is going to cause us want later on. We haven't focused on the fact that reliability is an important equation in any design, and I'm pushing it very hard. The fix-the-fleet business, as the Navy calls it, is a serious problem for me. I don't like to see them waste all that money going out there and fixing the fleet. It costs millions of dollars to fix something in the fleet when we could do it very cheaply when we're designing it. I am reminded of something here that I'd quickly like to tell you on fix-the-fleet. It's a story that I think will emphasize it to you very carefully.

At one time, this town had what was known as the town drunk. The wife of this particular person was very much embarassed over the situation, and for a number of years she tried to convince Charlie to go on the wagon and stop drinking. Finally, he accepted the challenge. For a long time he stayed on the wagon until one night he went out with the boys. They convinced him to have a few, and then he knew he was in trouble. All the way home he devised a plan for how he was going to get into the house without his wife knowing he had been drinking. He very carefully devised a plan. He went up to the front door and looked and listened. The house was quiet, no lights were on, so he said okay, I can get in the house. If I can get in the house without her hearing me, I'll be all right. He got in the front door, stood in the hallway, and everything was quiet. Then he had a set of stairs to go up, and he decided that the best way to go up the stairs was to take off his shoes because then he could go up more quietly. He took off his shoes and started up the stairs. Being in his stocking feet and with the stairs being a little slippery, he fell. When he did, he had a bottle in his pocket and it cut his north side right badly. So he got up again and listened and everything was quiet. He said well now, I'll just go in the bathroom and patch myself up and I've got it made. So he goes into the bathroom, opens up the medicine chest, gets out the bandaids, backs up to the mirror and fixes himself up. He goes on to bed very quietly, turns out the light, and his wife hasn't heard him because she was asleep. He says, I have it made; she didn't know. The next morning she gives him holy hell. She wants to know why he'd been out drunk last night. He said how could you possibly know I was out drunk last night. She said why else would those bandaids be all over the bathroom mirror? I submit to you tonight, even though you're laughing, that when we go out to the fleet, we're putting bandaids on the bathroom mirror. That is what we're trying to stop. We don't want any bandaids on the bathroom mirror.

Part of the problem has been the staying power within the Navy which has caused this to happen. I happen to be the focal point for this in the Navy. I know it so well for the simple reason that about a year after I was there, as I was going out of my office to see Ike Kidd a minute, I saw a piece of paper on the hall floor which I reached down and picked up. It was a little square sheet of paper that had my name across the top and had a matrix on it. There were a lot of numbers written on it and dates, etc. I said to myself, what in the world is this? I went in to see Ike. When I was there I said, "Hey, I found this on the floor. What is this, Ike? Do you know what it is?" He looked at it a minute and broke out laughing. He said, "Well, this is an anchor pool." Now I don't know if you know what an anchor pool is, but I didn't. The Navy has a custom; when a ship goes into a harbor, you make wagers on the exact time (day, hour, second, whatever) that the anchor goes over the side; and the one closest to the exact time collects the pool. I said, "Well, that's interesting, Ike; but what's that got to do with me?" He said, "This is an anchor pool on when you're leaving." That wasn't too bad until several days later when I got a telephone call. The telephone call went like this. The caller wouldn't identify himself, but he wanted to know if I knew there was an anchor pool out on my leaving. I said yes; it has come to my attention several times now. He said, "I just wanted to know if you'd do me a favor. If you plan on leaving in the month of May, would you make it on the 23rd?" I haven't seen any anchor pools lately because I think people have taken me more seriously. I believe the Navy has mustered its best effort. I believe they really are charging on down the right road now. I believe we have a few years before we are going to get there; but we are going to get there. There is no doubt in my mind about it. I am determined to see it through, and I think it takes determination to see it through. I have had an experience in my life that gave me an awful lot of determination.

In the early 1970's, the doctors told me I had three months to live. I was diagnosed as having cancer, articular cell sarcoma. They said, "That's such a fast disease you won't even make it around the corner." Through the good Lord and the science of medicine, I am still here today. I haven't got all my health back, but enough that I am satisfied.

The point I am trying to make is that this is a part of what I am determined to do. I am determined to see the Navy get what they want because they want it so badly. Sure, there are forces that try not to let it happen, but it is going to happen.

I want to give you one more illustration. It has been a long road over the past four years, and it has been a long hard road. With the issuance of that instruction, I now see that there is some light at the end of the tunnel. To illustrate it to you in a more remarkable way, I would like to tell you the story of the farmer who crossed a chicken with a cow. When he crossed a chicken with a cow, he got a funny looking animal. They couldn't figure out what to call the animal; so the son of the farmer said, "We ought to call it a raribird. It's an unusual looking animal." Through the years they were raising the raribird; they kept feeding it and feeding it; and it got bigger and bigger. Finally, they discussed the matter one night and said, "We've got to get rid

of this raribird. It's just eating us out of house and home." They tried to figure out just how they would do this. Finally, they devised a plan to take the raribird to a cliff. They put him in a truck one night, drove to a cliff, and said, "We're going to push the raribird over the cliff." They pushed and pulled and tugged, and the raribird wouldn't get out of the truck. While they were doing that, the kid said, "I know what we've got to do. We've got to get a big stick so we can tip this fellow out of here. We've just got to pry him out." While the kid had gone to get the stick, the farmer's neighbor came up and saw the raribird in the truck. He walked up to the edge of the cliff and asked the farmer what he was going to do. The farmer said, "We've got to get rid of this raribird. The kid has gone to get a stick so we can tip him out of the truck and push him over the cliff." Then the farmer's neighbor looked up at the raribird, looked over the cliff and said, "That's a long way to tip a rari."

Gentlemen, it has been my pleasure to be here tonight to talk to you and to try to share with you a little enthusiasm. I believe the Navy does have enthusiasm for what they are doing. I know I have enthusiasm for what I am doing. I believe that reliability is an integral part of nondestructive engineering; and I believe that you play a large part in that equation because it is through you that we have assurance of our product. I believe that if you are fighting a tough road, join the crowd. Any time we try to change man's mind, try to introduce new thought, we automatically have a problem and it takes time. I submit to you that from what I have heard tonight, and from what I have read of your proceedings, you are making progress. I believe that if you continue, you will get there. When you do, I am sure we will have a more reliable product; and we, in the Navy, promise to support you. Thank you.

DEFECT CHARACTERIZATION BY QUANTITATIVE ULTRASONICS

INTRODUCTION

R. B. Thompson
Science Center, Rockwell International
Thousand Oaks, California 91360

"Flaw Characterization by Ultrasonic Techniques" is the subject of this morning's session. The ultimate goal is to predetermine the in-service failure probability of a structural component with the best possible confidence. To achieve such a comprehensive goal there are a number of parts that are needed, as is schematically illustrated in Fig. 1. One first needs a measurement system. In this set of talks, ultrasonic techniques are being discussed. One needs a transducer or transducer array to gather ultrasonic information, coupled with techniques for processing this information. In this session, attention will be focused on ultrasonic scattering techniques and the types of signal processing and signature identification operations that can be used to identify the nature of the defect; e.g., its size, shape, and orientation. Imaging techniques will be discussed in later sessions. To achieve the ultimate goal of prediction of failure probability, of course, one must combine this information with fracture mechanics or other failure predictions schemes to develop some sort of an accept/reject criteria that would lead to a go/no-go decision. However, the scope of the ARPA/AFML program has not included fracture mechanics, only those elements on the left-hand side of the figure--the gathering, the processing, and the interpretation of the ultrasonic data in terms of geometric characteristics of the defects--have been considered.

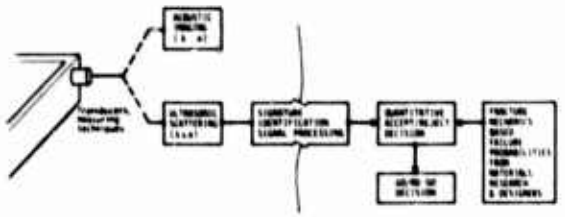


Figure 1. Steps required to incorporate quantitative accept/reject criteria with ultrasonic NDE to make GO/NO-GO decisions.

The papers to be presented in this morning's session were all prepared as a part of Project I of the ARPA/AFML Program for Quantitative NDE. Before presenting a specific overview of the flaw characterization studies, I would like to indicate that there are a number of other related activities that have been a part of the project that will be presented later on in the program. Figure 2 is a summary of this work. These are items that will be needed in a flaw characterization system in addition to the defect characterization results to be discussed today. For example, improvements in transducers, imaging systems, new ultrasonic standards, and filters for NDE systems are all included. In each area, the advances reported can have immediate impact on today's NDE systems as well as being an integral part of a future defect characterization system. There has also been a new effort recently started dealing with extending the bulk defect work discussed today to the case of surface flaws. Finally, some very successful applications of the scattering techniques to the development of techniques for the inspection of ceramic components will be presented. All of these elements will be needed in the development of a fully integrated defect characterization system.

ELEMENTS OF PROJECT I TO BE PRESENTED IN OTHER SESSIONS

VIII "NEW TECHNOLOGY ROOTS"

POSTER SESSION, FRIDAY MORNING

ELECTROMAGNETIC TRANSDUCERS, OPTIMIZATION & APPLICATION
R. B. THOMPSON, C. M. FORTUNKO, C. F. VASILE, G. ALERS

CHARACTERIZATION SYSTEM FOR NDE TRANSDUCERS
K. M. LAKIN

PROGRAMMABLE FILTER FOR ULTRASONIC NDE SYSTEMS
R. M. WHITE

NEW ULTRASONIC STANDARDS
B. R. TITTMANN AND N. E. PATON

ULTRASONIC IMAGING SYSTEMS
G. S. KINO

IV "NEW TECHNIQUES AND PHENOMENA"

POSTER SESSION, WEDNESDAY AFTERNOON

NEW METHODS OF DETECTION AND CHARACTERIZATION OF SURFACE FLAWS
B. A. AULD

VII "RELIABILITY OF STRUCTURAL CERAMICS"

THURSDAY EVENING

OVERVIEW OF RELIABILITY IN STRUCTURAL CERAMICS
A. G. EVANS

HIGH FREQUENCY ULTRASONICS: A CASE IN POINT
G. S. KINO, P. T. KHURI-YAKUB, B. R. TITTMANN

Figure 2. Elements of Project I to be presented in other sessions.

Returning to this session on Flaw Characterization. the immediate goal that we have adopted is to develop techniques and procedures to determine the size, shape, and orientation of defects in metal parts. The philosophy of the technical approach adopted to accomplish this goal is shown in Fig. 3. We have wished to establish a set of procedures, whereby a defect characterization capability is built up from fundamental building blocks involving an understanding of the basic interaction of the ultrasound with the flaw. This will not only establish an immediately useful result, but will also illustrate a method that can be generalized in the future as needed for specific cases. The first element is an understanding of the details of the ultrasound defect interaction. This is accomplished by a close interaction between the development of theories and the performance of verifying and/or guiding experiments. These experiments should be performed on controlled samples in which there are defects of predetermined sizes and shapes. In this program, the development of approximate theories has been emphasized because the number of flaw shapes which can be treated by exact techniques is extremely limited. We wish to develop techniques which can be generalized to the complex shapes of real flaws. Even if one has developed a complete understanding of this ultrasound-defect interaction, it does not immediately follow that one can identify a flaw from a set of experimental data. In order to do so, one needs to develop inversion techniques. That's the second half of the procedure, the one that's going to produce the ultimate payoff. We have made use of an analogy to an integral equation. The theory can be viewed as the kernel of this integral equation which relates ultrasonic measurements to physical parameters of the flaw. By solving the equation by whatever means is appropriate, one develops a relationship that predicts the size, shape, and orientation of the defect in terms of certain measureables. In order to verify this relationship, one must put real experimental data into these mathematical expressions and compare the predictions with independent knowledge of the flaw parameters. This completes the loop of the demonstration of the defect characterization capability. The predictive relationship is then available for use coupled with fracture mechanics or other failure predictions disciplines to develop accept-reject criteria.

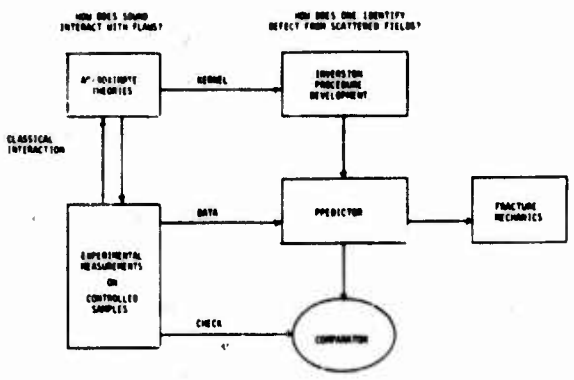


Figure 3. Philosophy of development of quantitative defect characterization techniques.

This is the methodology being followed in Project I. The remainder of this paper briefly describes some of the philosophies that were taken in filling each of these boxes as a preview for the in-depth presentations by the individual investigators.

We have used the diffusion bonding technique to fabricate samples with defects of controlled shapes. Figure 4 illustrates this. One starts out with two cylindrical pieces of titanium. In each is machined half of the desired defect shape. They are then diffusion bonded together. Grain growth takes place across the interface and there is virtually no memory of the bonding plane. One then has a homogeneous piece of material with the desired defect in the center. The choice was dictated by two reasons. Most of the defects had an ellipsoidal shape. This makes it possible to develop theories in a relatively simple manner and hence is a very good place to start to develop our understanding and test the methodology shown in Fig. 3. In addition, you will notice that in the oblate spheroid case as the aspect ratio becomes large the defect shape more and more closely models a planar shape which is an idealization of a crack, a very real defect of great practical concern. The dimensions were chosen to be typical of the sizes of flaws typically sought in aerospace systems. In such cases the ultrasonic measurement frequency is often on the order of 1 to 10 MHz. As a scale factor, we have shown the range of wavelengths of these frequencies as compared to the defect size. As you see we are in a difficult regime in which the wavelength is comparable to the defect size. The very successful results that will be reported in later papers illustrate some of the power of the defect characterization techniques.

As a physical example, Figs. 5 and 6 show pictures of experimental configurations that have been used. Figure 5 shows the experimental apparatus that Tittmann and Elsley have used. In this case, the diffusion bonded samples with the defects at the center have been machined with a spherical exterior surface. It is clear this doesn't represent any practical situations except a ball-bearing with a defect exactly in the center. Nevertheless, it is a very important configuration for experimental measurements as needed in the development of understanding of scattering phenomena. It allows the experimenter to arbitrarily vary the angle of incidence of the ultrasound as well as the angle at which the ultrasound is detected. In one sample, one can simulate all possible orientations, and this flexibility has been used to great advantage as will be discussed in much greater detail during subsequent papers. Since this is a very unrealistic configuration from a practical point of view, a second set of samples have been used as shown in Fig. 6. These have identical defects imbedded on the interior. However, they have a planar surface. The figure shows the immersion measurement configuration which has been used by Adler. It is very similar to an on-line inspection station at many industrial laboratories around the country. By studying the same flaw geometries in the two sample shapes, it has been possible to directly compare the more basic and practical approaches.

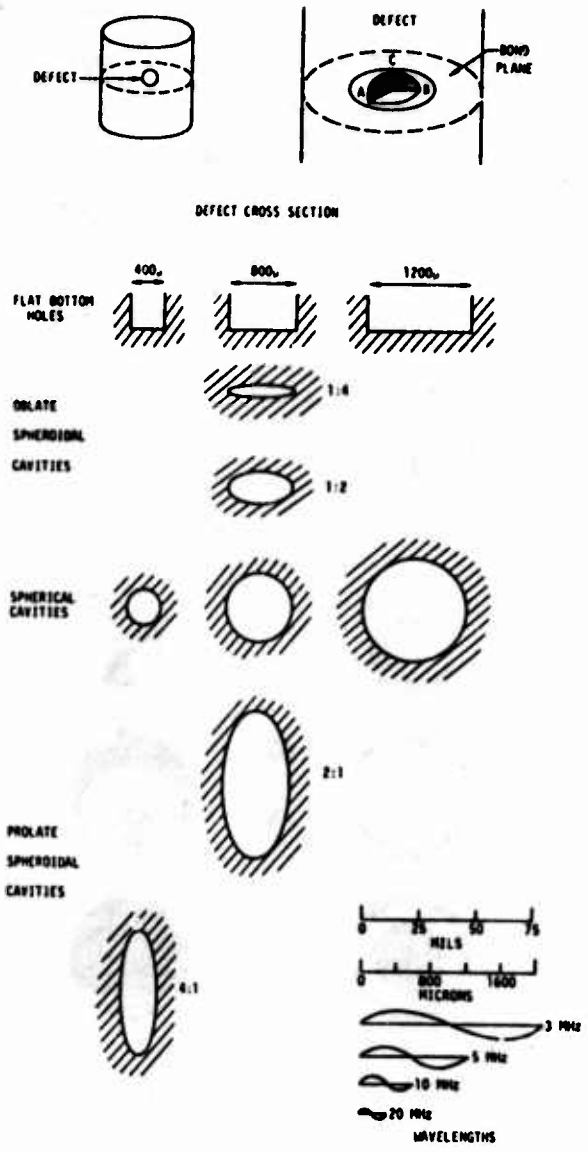


Figure 4. Defect shapes in diffusion bonded samples.

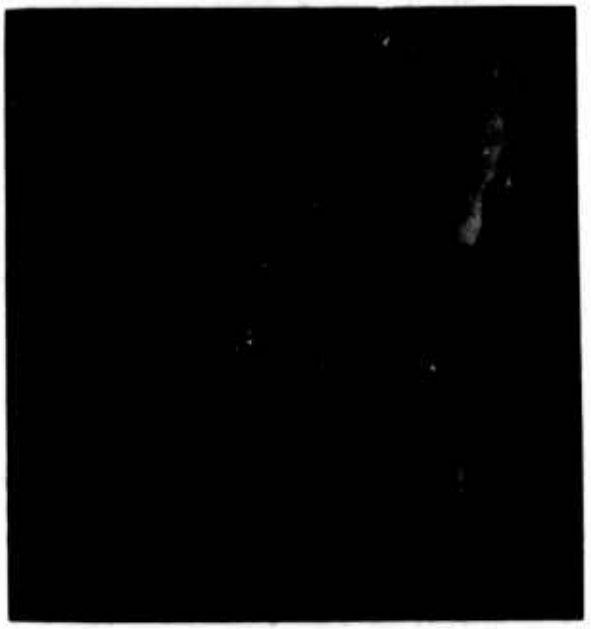


Figure 5. Photograph of sample holder.



Figure 6. Apparatus used for immersion testing of samples with flat faces.

During the first two years of the program primary attention was placed on the development of the experimental and the theoretical building blocks needed for an understanding of the ultrasound-defect interaction. During the third year, the focus has shifted to the inversion problem. The first question one must ask is, "How much information am I going to be able to use?" If one can assume that one can measure the ultrasonic scattering at all frequencies and at all angles, one has a tremendous amount of information about the flaw, but one could never hope to realize this in a real situation. We have therefore restricted ourselves as is schematically illustrated in Fig. 7. We considered the situation in which the defect is on the interior of a part having a geometry such that ultrasonic waves can enter or leave the part at angles no greater than 60° with respect to the surface normal. Although the spherically shaped samples allow full axis from any angle, we have restricted ourselves to use only that information obtainable with transducers in a cone of 60° half-angle. No use is made of large angle scattering information or of any through transmission signals. In terms of the frequencies available, we have taken the natural attenuation of the titanium samples to be the limit. Thus we are considering frequencies in the range of 1-10 MHz. We do allow ourselves to look at mode converted signals. When a longitudinal wave strikes a defect, both longitudinal and shear waves are scattered. Since these can both be detected and differentiated in a standard water bath configuration, such information could be used in an industrial setup. Given the information available within this experimental window, we have sought techniques to characterize the size, shape, and the orientation of the ellipsoidal flaws. The next question was what sorts of measurements would we like? The details of how we developed these techniques will be presented in the following papers.

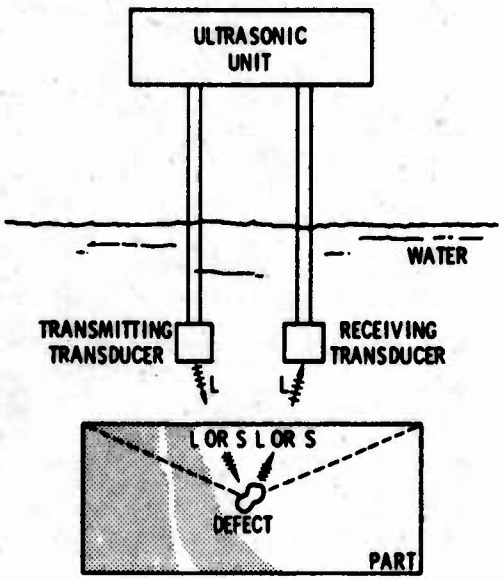


Figure 7. Schematic ultrasonic immersion configuration illustrating geometrical limitations and mode converted signals.

Figure 8 shows a result presented at the Asilomar meeting last year. Here, equal contours of scattered ultrasonic power are shown for two defect geometries as calculated by Krumhansl and a number of his colleagues here at Cornell using the Born approximation. The plots are orthogonic projections of a frequency average of the scattered ultrasonic power for: (1) a spherical inclusion, and (2) an oblate spheroidal inclusion tilted at 45° with respect to the angle of incidence of the ultrasonic energy. Both the direct L→L scattering and the mode converted L→T scattering are shown. From such information it is possible to design experiments which will distinguish between the two types of defects. Strictly speaking, the Born approximation is only accurate for cavities. However, direct experiment has shown that many of the features shown in these plots apply to strongly scattering defects such as cavities as well.

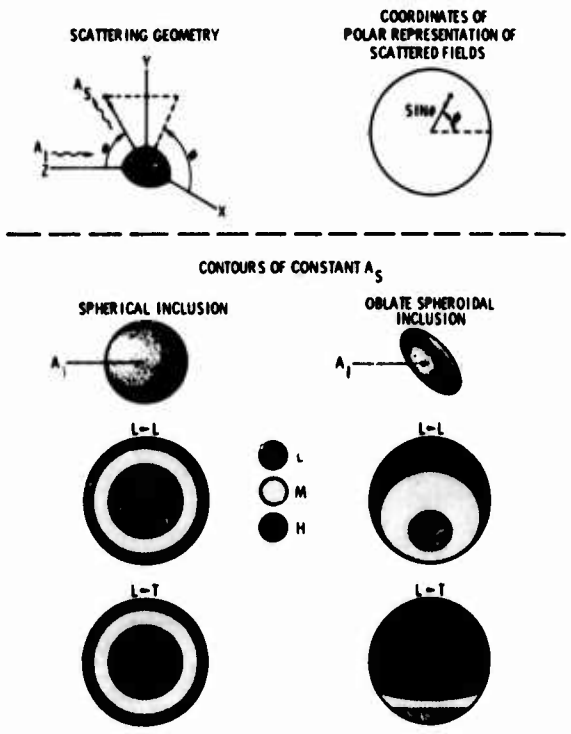


Figure 8. Variations in equal amplitude scattering contours for two defect types.

The simplicity of the Born approximation, plus the fact that it predicts the results of many experiments performed on cavities, suggest that it may be useful as a model in the design of experiments. For example, one can consider in detail the inverse problem. Figure 9 illustrates the various relationships involved. In the Born approximation, simple expressions are derived for the amplitude of a scattered longitudinal wave A and a scattered transverse wave B in terms of the properties of the scattering object. The expression is a product of two terms. One is a rather slowly varying angular function which depends only on the change of the elastic constants and the density within the inclusion, but which is independent of its shape.

COMPARISON OF DIFFERENT SCATTERING CONFIGURATIONS BASED ON BORN APPROXIMATION



$$U_s = \frac{\vec{A}}{r} e^{ik_L r} + \frac{\vec{B}}{r} e^{ik_T r}$$

$$\vec{A} = \frac{k_L^2}{4\pi}\left[\frac{\delta\rho}{\rho}\cos\theta - \frac{\delta\lambda+2\delta\mu\cos^2\theta}{\lambda+2\mu}\right] F\left[\frac{f\sin\theta}{V_L}, 0, \frac{f(\cos\theta-1)}{V_L}\right]$$

$$\vec{B} = \frac{k_T^2}{4\pi}\left[\frac{2\alpha\delta\mu\cos\theta\sin\theta}{\mu\rho} - \frac{\delta\rho\sin\theta}{\rho}\right] F\left[\frac{f\sin\theta}{V_T}, 0, f\left(\frac{\cos\theta}{V_T} - \frac{1}{V_L}\right)\right]$$

where

$$F(u,v,w) \triangleq \int_{-\infty}^{\infty} dx \int_{-\infty}^{\infty} dy \int_{-\infty}^{\infty} dz\, f(x,y,z) e^{-i2\pi(ux+vy+wz)}$$

$$f = \begin{cases} 1 & \text{INSIDE OBJECT} \\ 0 & \text{OUTSIDE OBJECT} \end{cases}$$

Figure 9. Comparison of different scattering configurations based on Born approximation.

This shape information is contained in the second factor, F, which is the spatial Fourier transform of the shape of the object. In other words if f(x,y,z) is defined to be 1 inside the object and 0 outside the object, then F is the spatial Fourier transform of f. To solve the inverse problem, one must obtain enough components of F from scattering experiments so that the shape function f can be reconstructed by taking the inverse transform. Within this framework, one can determine how much data is needed to determine the shape of an object and can compare the performance of systems, spectroscopic systems, and other approaches to defect characterization.

Figure 10 presents a specific example. Here the region of Fourier transform space which is sampled by different experiments is indicated for a two-dimensional example. One can see that in a spectroscopic system at a single angle, one is essentially measuring components along a line passing through the origin. If one uses the angular variation of direct L→L scattering with a central transmitter and moving receiver at a fixed frequency, one measures components along an arc. If one measures L→L backscattering over the same aperture, one obtains information over a considerably greater range in Fourier transform space. Still more informaton is obtained if one is able to measure the mode converting signals. Examples of each of these approaches will be presented in the papers that follow. They can be compared to a common framework by an analysis such as this. In the next two years of the program, emphasis will focus on the inverse problem, and a much more extensive analysis of this type will be carried out.

INVERSE PROBLEM

$$f(x,y,z) = \int_{-\infty}^{\infty} dx \int_{-\infty}^{\infty} dy \int_{-\infty}^{\infty} dz\, F(u,v,w) e^{+i2\pi(ux+vy+wz)}$$

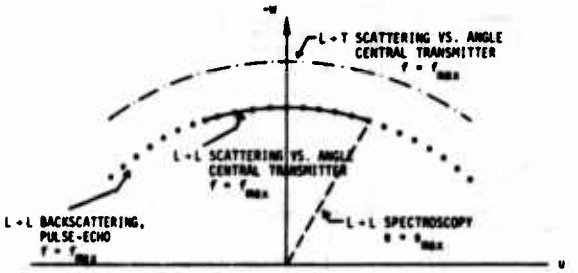


Figure 10. Inverse problem.

Figure 11 summarizes the work that has been done on inversion techniques at this time. Papers will be presented on three distinct techniques for inverting ultrasonic data. Dr. Mucciardi will discuss empirical, derived, nonlinear predictions which have been developed using the adaptive learning capability of Adaptronics. These have been derived using a new concept. In order to develop and verify the predictive relationships, one needs to have a training set of data and a second, independent set of data against which the results can be checked. In this program, theoretical solutions have been used to train the network, and then experimental data has been used to test the network. This is important because one does not need to construct a large training set of samples of every possible configuration if one has an adequate model. Other defect characterization procedures have also been quite sucessfully pursued by Domany based on symmetry principles, physical observations of the natures of the scattered fields, and again incorporating some of the theoretical scattering data. A third paper by Bleistein presents a more formal inversion procedure which has been recently developed based on previous experience in electromagnetics and geophysics and incorporating ideas similar to those presented in Fig. 11.

In conclusion, it should be emphasized that all of the results that will be presented have been the direct product of many detailed interactions between all of the investigators and represent their cooperative interaction. Several meetings have been held at the Science Center and all participants involved have contributed substantially to the ideas developed.

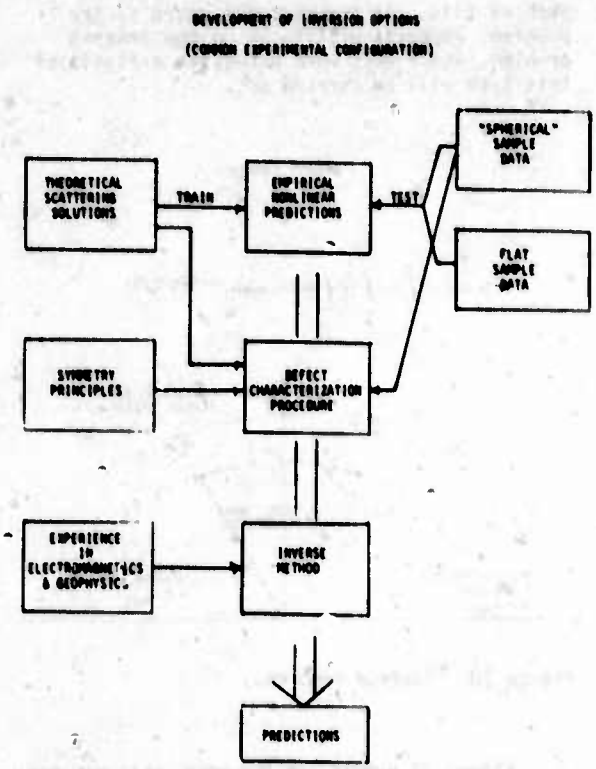


Figure 11. Development of inversion options (common experimental configuration).

LONG WAVE SCATTERING OF ELASTIC WAVES FROM VOLUMETRIC AND CRACK-LIKE DEFECTS OF SIMPLE SHAPES

J. E. Gubernatis
Los Alamos Scientific Laboratory
Los Alamos, New Mexico 87545

ABSTRACT

The development of several approximations appears to permit accurate and practical calculations of the scattering of elastic waves from volumetric and crack-like defects of simple shapes if the wavelength of the incident wave is larger than the characteristic length of the shape. These approximations, which I call the quasi-static and extended quasi-static, use static solutions of defects in uniform strains to predict scattered (dynamic) fields. Since static solutions for several simple defect shapes (oblate and prolate spheroid, ellipsoid, and circular and elliptical cracks) are available, scattering predictions are possible, and the results of such calculations are presented.

Introduction

I was asked to preface my presentation with a few words about the current state of ultrasonic defect characterization studies in the ARPA/AFML program compared to their state at its start. Consequently, my presentation has two distinct parts: One part I call "Past to Present" in which, emphasizing the role played by theoretical studies, I try to assess what I regard as benchmarks in ultrasonic flaw characterization studies. The other part I call "Long Wave Scattering from Simple Shapes" in which I discuss my recent work.

Past to Present*

A Chronology

Zeroth Year (Krumhansl, Gubernatis)

At the start of the ARPA/AFML program, the existing literature on the scattering of elastic waves from defects was not properly oriented to the problem of flaw characterization. No systematic way existed to study the scattering from shapes more complicated than a sphere (or an infinite cylinder). Since the sphere is the only shape of finite volume solvable in closed form, a need for the development of efficient numerical techniques or approximations existed.

First Year (Krumhansl, Gubernatis, Domany, and Huberman)

As a first step, a formal theory of the scattering of elastic waves was developed.[1,2] This theory has a strong analogy to scattering theories used in quantum mechanics and thus has the potential susceptibility to a variety of numerical and approximate techniques. A decision was made to avoid costly numerical solutions and concentrate on less costly and simple approximate techniques, which would perhaps reveal some physical insight. An approximation, called the Born Approximation in quantum mechanics, was studied and was compared to exact scattering results from a sphere. With some limitations, the approximation appeared quite useful.[3] A special usefulness was the fact that the shape of a defect enters through easily calculable factors involving the Fourier transform of the volume V occupied by the defect (the shape factor)[2,3], i.e.,

$$\int_V d\underline{r}\, e^{i\underline{q}\cdot\underline{r}}$$

where $\underline{q}$ is the difference between the scattered and incident wave vectors.

Tittmann[4], meanwhile, measured the scattering of elastic waves from a sphere and found a good comparison between measured values and results calculated by exact theory. I regard the agreement as significant because I personally find as unconvincing explanations why what experimentalists measure is what theorists calculate.

In short, a useful and simple approximation now existed.

Second Year (Krumhansl, Domany, Teitel, Muzikar, and Wood)

The Born Approximation was now applied to a spheroid[5], and the scattering was measured by Tittmann[6] and Adler and Lewis[7]. Although the theory worked better for an oblate than for a prolate spheroid, when theory and Tittmann's experiment were compared, a correlation between the aspect ratio of spheroidal shapes and measured results was found; a definite relationship was established between scattering data and an identifying geometrical feature of a defect (a non-spherical one). In part, a flaw was characterized.

The theorists began to examine other approximations, and the scattering from crack-like flaws was computed.[5]

Third Year (Krumhansl, Domany, Rose, Teitel)

The purpose of this meeting is to report the results for the third year; thus, I will conclude my view of the past after making several remarks that are difficult to time-sequence.

*This research was sponsored by the Center for Advanced NDE operated by the Science Center, Rockwell International, for the Advanced Research Projects Agency and the Air Force Materials Laboratory under contract F33615-74-C-5180.

Comments and Opinions

The program has benefited greatly from a strong interaction between theory and experiment. This interaction is not accidental, but is indebted to the foresight shown in establishing the program when diffusion bonded samples containing identifiable defects of simple shapes (spheres and spheroids) were constructed. If the theorist had to work with the "flat bottom hole", I doubt as much progress would have occurred.

Theory needs experiment, but can (and in some cases it has) progressed to the point where it is considerably cheaper to do the calculations than it is to make the measurements. For example, the Born Approximation, and to some extent another approximation I discuss below, produce a data point for a fraction of a penny and a data base (about 1000 points) for several dollars. A comparably sized data base with experimental uncertainty currently takes several days to measure which is several hundred dollars in salaries. This cost-effectiveness is germane to the work of Tony Mucciardi[8] and of Eytan Domany.[9] Tony needs a large data base on which to train his computer. Eytan, by being able to compute cheaply and examine a variety of scattering cases, is seeing systematics translatable to experimental procedures for identifying flaw shapes. The cost-effectiveness of theoretical studies cannot be emphasized strongly enough.

Longwave Approximations for Simple Shapes**

Introduction

Completed studies used integral equation methods to describe the scattering. Recently, the theory of the scattering of elastic waves from flaws by use of integral equations was developed systematically.[1,2] Previously, nearly all theoretical studies of the scattering of elastic waves have used partial differential equations. With this approach the exact equations for scattering from a spherical flaw were found; however, the methods of partial differential equations have not been successful for shapes of finite volume other than the sphere: Boundary conditions are very difficult to apply, and a systematic development of a perturbation theory for general finite volumes is equally difficult. By contrast, the boundary conditions, at least at the start, are automatically built into the integral equation for all volumes, and a variety of systematically developed approximations is possible.

Some Technical Details

The basic scattering equation is[1,2]

$$u_i(\underline{r}) = u_i^0(\underline{r}) + \int d\underline{r}' g_{ij}(\underline{r},\underline{r}')\, v_{jk}(\underline{r}')\, u_k(\underline{r}') \quad (1)$$

where repeated subscripts imply summation. The vector field $u_i(\underline{r})$ represents the displacement field, and the vector u_i^0 is the incident displacement field. The flaw is hosted in an infinite elastic medium assumed isotropic and described by the Lamé parameters λ and μ. The Green's function for this medium $g_{ij}(\underline{r},\underline{r}')$ equals

$$g_{ij} = \frac{1}{4\pi\rho\omega^2}\left[\beta^2\delta_{ij}\frac{e^{i\beta R}}{r} - \frac{\partial}{\partial x_i}\frac{\partial}{\partial x_j}\left(\frac{e^{i\alpha R}}{R} - \frac{e^{i\beta R}}{R}\right)\right] \quad (2)$$

where ω is the frequency of the incident wave, ρ the density of the host material, α the wave number of the longitudinal mode (P wave), β the wave number of the transverse mode (S wave), and $R = |\underline{r}-\underline{r}'|$. The tensor field operator $v_{ij}(\underline{r})$ represents the flaw and is equal to

$$v_{ij} = \delta\rho\omega^2\delta_{ij} + \frac{\partial}{\partial x_k}\,\delta C_{ikj\ell}\,\frac{\partial}{\partial x_\ell}\,. \quad (3)$$

The quantity $\delta\rho$ is the difference between the density of the flaw and its host; correspondingly, $\delta C_{ijk\ell}$ is the difference between the elastic constants tensor of flaw and its host. Although the flaw is hosted in an isotropic medium, the flaw can have an arbitrary density and elastic properties; however, the case of particular interest is the scattering from a void ($\rho = C_{ijk\ell} = 0$).

Equation (1) describes the scattering of vector fields by a tensor "potential", and the scattered fields propagate from $\underline{r}$ to $\underline{r}'$ by a tensor Green's function (2). Additionally, because an isotropic elastic medium has two modes of propagation, the far field displacement is of the form

$$u_i \sim u_i^0 + A_i\frac{e^{i\alpha r}}{r} + B_i\frac{e^{i\beta r}}{r}$$

where the vector A_i represents the amplitude of the longitudinal scattered wave and B_i the transverse. As a consequence, for a given frequency, the differential cross-section is

$$\frac{dP}{d\Omega} = \frac{\alpha(\lambda+2\mu)\,|A_i|^2 + \beta\mu|B_i|^2}{\alpha(\lambda+2\mu)\,|a_i|^2 + \beta\mu|b_i|^2} \quad (5)$$

where a_i and b_i are the vector amplitudes of an incident longitudinal and a transverse displacement field. From Equation (5) it is apparent that even if $|a_i|^2$ or $|b_i|^2$ equals zero, the cross-section always involves contributions from two modes of scattering associated with the same frequency (mode conversion).

Because of the differential operators appearing in the "potential", the scattered vector amplitudes can be regarded as functionals both of the displacement and strain fields internal to the flaw:

$$A_i = A_i[u_i;\, \epsilon_{ij}]$$

$$B_i = B_i[u_i;\, \epsilon_{ij}]$$

**Supported by USERDA.

The Born Approximation corresponds to replacing the displacement field by the incident displacement and the strain field by the strain field e^0_{ij} associated with the incident displacement field:

$$A_i = A_i[u^0_i;\ e^0_{ij}]$$

$$B_i = B_i[u^0_i;\ e^0_{ij}]$$

The results of this approximation have been computed for a variety of spherical flaws and compared to the exact solution.[3] This approximation is found to describe backscattering well when the wavelengths are larger than the radius of a sphere. This observation was verified experimentally.[6]

For long wavelengths, the system is in a quasi-static condition. An alternative approximation, called the quasi-static approximation,[10] is to replace the displacement fields by the amplitude u^0_i of the incident mode and to replace the strain field by the associated static strain field e^σ_{ij}.

$$A_i = A_i[u^\sigma_i;\ e^\sigma_{ij}]$$

$$B_i = B_i[u^\sigma_i;\ e^\sigma_{ij}] \qquad (6)$$

The results of this approximation are, for long wavelengths, identical to the exact results for a sphere,[11] i.e., it is not limited to backscattering. By a systematic study of the iterative solution of the integral equation, it was recently shown that the approximation represented by Equation (6) is exact for any finite shape at long wavelengths.[12] This result permits the exact calculation of the scattering of elastic waves from a flaw other than a sphere, albiet at long wavelengths. The approximation determines exactly the ω^4 contributions (the Rayleigh limit) to the scattering cross-section. Solutions of e^σ_{ij} are available for a number of geometries. The most famous and the most convenient is Eshelby's solution[13] for a spheroid and ellipsoid. These shapes are extremely important, for by varying aspect ratios of the shapes one can distort them to resemble needle and disc crack-like geometries, types of flaws that one is most eager to detect.

A more powerful approximation is the extended quasi-static approximation.[14] In this approximation

$$A_i = A_i[u^\sigma_i\, e^{i\underline{k}_0\cdot\underline{R}};\ e^\sigma_{ij}\, e^{i\underline{k}_0\cdot\underline{R}}]$$

$$B_i = B_i[u^\sigma_i\, e^{i\underline{k}_0\cdot\underline{R}};\ e^\sigma_{ij}\, e^{i\underline{k}_0\cdot\underline{R}}] \qquad (7)$$

where $\underline{k}_0$ is the wave vector of the incident wave. An important point is that for ellipsoids and spheroids this approximation also uses Eshelby's solutions. This approximation, in contrast, to the Born and the quasi-static, is not well-defined in terms of a perturbation expansion.

A description of the full details of these approximations is in preparation.[12] What is more useful to present interests are calculated results for the variously shaped defects.

Results

Figure 1 illustrates the manner in which the scattering angles θ and ϕ are defined with respect to the direction of the incident wave $\underline{k}_0$. The incident direction is always chosen along the z-axis, and the defects are always hosted in Ti-6Al-4V. The differential cross-section is in decibels, and zero is equated to -100 db.

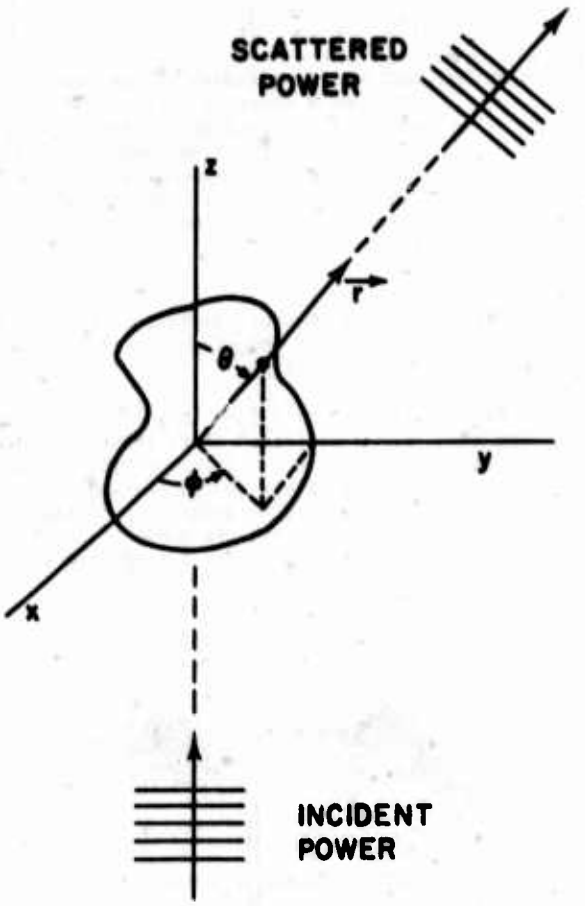


Figure 1. The basic scattering picture. Incident power scatters from a flaw into a receiver in the direction $\underline{r}$.

In Fig. 2 is a comparison of three approximations, the Born, quasi-static, and extended quasi-static, with exact results for a sphere. The incident wave is a longitudinally polarized plane wave, the defect is a spherical void, k is the wavenumber of a longitudinal wave, and a is the radius of the sphere. The range of ka is to 2. For a void, the extended quasi-static approximation appears to be quite useful up to ka $\simeq$ 1.5.

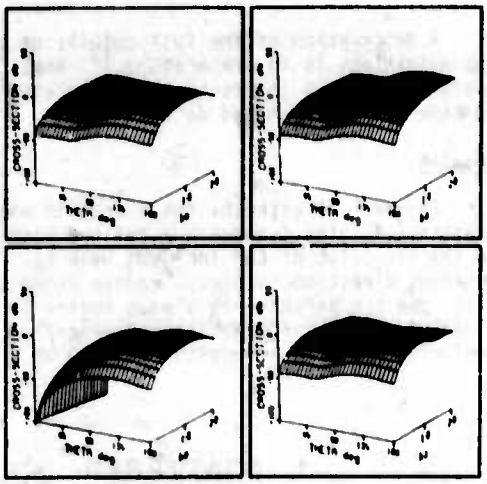


Figure 2. Incident longitudinal plane wave scattering from a spherical void. The differential cross-section is calculated four ways: clockwise from lower left-hand corner, the Born Approximation, the extended quasi-static approximation, the quasi-static approximation, and the exact calculation.

The remaining figures, because of the absence of exact results, were computed with the extended quasi-static approximation.

The scattering of a longitudinally polarized plane wave from a stainless steel prolate spheroid is shown in Fig. 3. k is still the longitudinal wave number, but a refers to the semi-major axis. The axis of symmetry is perpendicular to the incident direction and along the y-direction. The major axes, along x and y, are 4 times the minor axis.

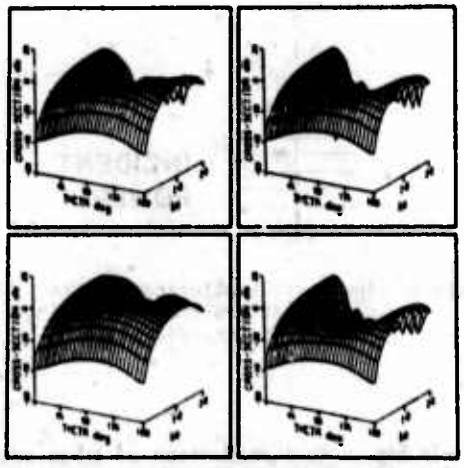


Figure 3. Incident longitudinal plane wave scattering from a prolate spheroidal void calculated from the extended quasi-static approximation. The incident direction, along the z-axis, and the axis of symmetry are perpendicular, along the y-axis. The ratio of the z-axis to the y-axis is 1/4. Clockwise from lower left, θ equals 0, 30, 60, 90 degrees.

By letting the short axis of an ellipsoid or oblate spheroid go to zero, one produces elliptical and circular disc-like cracks.[16] Figure 4 shows the scattering of a longitudinal plane wave incident normal to the face of a crack lying in the xy-plane. k is the longitudinal wave number, and a is the radius of the crack. On the left is the longitudinal-to-longitudinal scattering; on the right, longitudinal-to-transverse (mode converted) scattering.

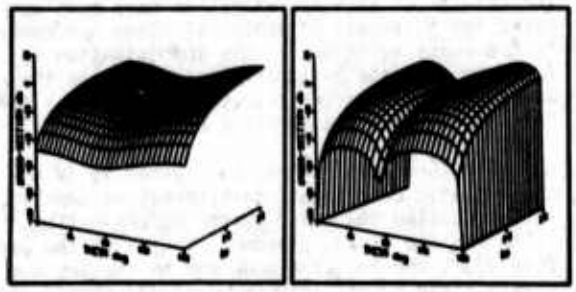


Figure 4. Incident longitudinal plane wave scattering from a circular crack. The incident direction, along the z-axis, is normal to the crack plane. On the left is longitudinal-to-longitudinal scattering; on the right, longitudinal-to-transverse scattering.

In Fig. 5, a transversely polarized plane wave is scattered off the edge of an elliptical crack. The cracks lie in the xz-plane the semi-major axis, along x, is twice the semi-minor axis. The angle $\phi = 90°$. On the left is the transverse-to-longitudinal scattering (mode converted); on the right the transverse-to-transverse scattering.

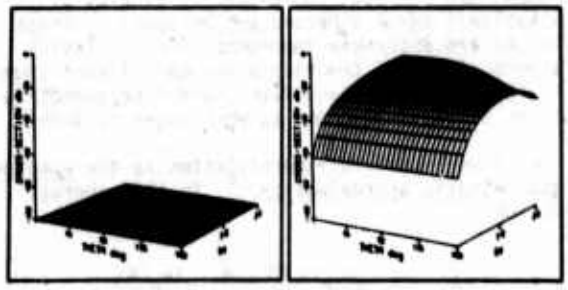


Figure 5. Incident transverse plane wave scattering from an elliptical crack. The incident direction is along the z-axis, and the polarization is along the x-axis. The crack is in the xz-plane; its major axis, along x, is twice its minor axis. $\theta = 90°$. On the left is transverse-to-longitudinal scattering; on the right, transverse-to-transverse scattering.

Several conclusions are evident. The scattering is not isotropic. Different shapes produce different angular distributions. For acoustic and many quantum mechanical problems the scattering at long wavelengths is isotropic. This illustrates the fact that the elastic wave scattering problem has distinguishing features which can prevent the blind adoption of techniques and concepts successful in these other areas. Scattering signatures exist, but there is a need for systematic study to exploit them fully. The amount of data that can be easily generated is enormous, but it can be done cheaply.

Time and space permit the showing of only a small sample of nearly 100 calculations. The complete set of calculations is being prepared as a Los Alamos Report.[15]

References

1. J. E. Gubernatis, E. Domany, M. Huberman, and J. A. Krumhansl, in 1975 Ultrasonics Proceedings, (IEEE, New York, 1975), p. 107.

2. J. E. Gubernatis, E. Domany, and J. A. Krumhansl, J. Appl. Phys., June 1977.

3. J. E. Gubernatis, E. Domany, J. A. Krumhansl, and M. Huberman, J. Appl. Phys. June 1977.

4. B. R. Tittmann, AFML technical report, AFML-TR-75-212, p. 195.

5. J. A. Krumhansl, E. Domany, J. E. Gubernatis, P. Muzikar, S. Teitel, and D. Wood, Rockwell International (Science Center) technical report, "Interdisciplinary Program for Quantitative Flaw Definition; Special Report, Second Year Effort", p. 102

6. B. R. Tittmann, Rockwell International (Science Center) technical report, "Interdisciplinary Program for Quantitative Flaw Definition; Special Report, Second Year Effort", p. 102.

7. L. Adler and D. K. Lewis, Rockwell International (Science Center) technical report, "Interdisciplinary Program for Quantitative Flaw Definition; Special Report, Second Year Effort", p. 140

8. A. Mucciardi, this proceedings.

9. E. Domany, this proceedings.

10. In Ref. 5, this approximation was called Mal and Knopoff.

11. A. K. Mal and L. Knopoff, J. Inst. Math. Applic. 3, 376 (1967).

12. J. E. Gubernatis, unpublished. S. K. Datta has shown this for ellipsoids ["Report on the Workshop on Application of Elastic Waves in Electrical Devices, Non-Destructive Testing, and Seismology", Northwestern University, May 24-26, 1976, ed. by J. D. Achenbach, Y. H. Pao, and H. F. Tierstein, p. 355].

13. J. D. Eshelby, Proc. Roy. Soc. A241, 376 (1957).

14. In Ref. 5, this approximation was called quasi-static.

15. J. E. Gubernatis, unpublished.

16. The work on disc-like cracks was done with E. Domany.

EXPERIMENTAL MEASUREMENTS AND INTERPRETATION OF ULTRASONIC SCATTERING BY FLAWS

B. R. Tittmann and R. K. Elsley
Science Center, Rockwell International
Thousand Oaks, California 91360

ABSTRACT

Experimental measurements have been carried out in previous efforts on the scattering of elastic waves from ellipsoidal and spherical cavities embedded in titanium on alloy by the diffusion bonding process. The scattering data have been compared with calculations from exact theory and those from the Born approximation. The results demonstrated that the new concept of sample fabrication by the diffusion bonding process is successful, and that the approximate scattering models developed to date are both useful and correct within acceptable limits for many applications. Efforts have been expended this year to provide a scheme and useful data base for the development of inversion techniques (i.e., deterministic, probabilistic, or adaptive schemes) from which quantitative properties of the scattering center can be rapidly extracted. The work has provided a preliminary definition of the minimum quantity and type of data acquisition needed for a "smart" NDE system.

Introduction

The objective of the third year was a coordinated effort among the various investigators to integrate the results of all the studies into a demonstration of defect characterization capability. This has focused upon the problem of identifying the size, shape, and orientation of a spheroidal cavity embedded in a solid by inversion techniques. A part of the effort is focused on the utilization of the adaptive learning capabilities developed by Mucciardi at Adaptronics (see this proceedings) to develop predictive relationships inverting measured ultrasonic fields to obtain the geometric properties of the spheroidal cavities. Thus theoretical models developed by Krumhansl, Gubernatis, Domany, et al. (see this proceedings) were tested against the experimental data obtained in the contract mode on idealized spherically shaped samples in the study described in detail below and against data obtained in the immersion mode on samples with flat surfaces by Adler (see this proceedings).

Data Acquisition Plan for Inversion

A data acquisition plan was formulated to provide a base of experimental data for use in developing scattering inversion techniques (i.e., deterministic, probabilistic, or adaptive learning schemes). In order to simulate a realistic NDE situation, the plan limited the range of angles from which the defect could be "viewed" by the ultrasonic transducers. Each defect was located at the center of a sphere built in the form of a "trailer hitch" described below. A "viewing window" was defined on the surface of the sphere in terms of intersections of the surface with a cone centered on the defect and having a half-angle of 60° (see Fig. 1). The shaded area in Fig. 1(a) is the area within the viewing window. The window was placed at a variety of positions on the sphere to simulate defects of various orientations. Figure 1(b) is a stereographic projection of the viewing window. A grid of transducer positions is seen laid out in the window with circles indicating receiver positions and squares indicating transmitter positions. For a given window position and for each transmitter position within the window, the scattered ultrasound waveform is recorded at each of the 17 receiver positions (one of the receiver positions is the same as the transmitter position and the data is taken as a pulse echo measurement).

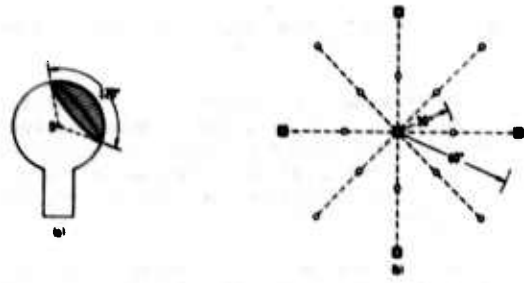


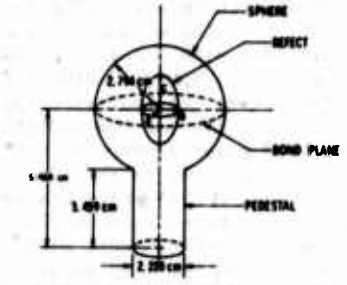
Figure 1. (a) "Trailer hitch" spherical sample with ellipsoidal void defect at center (D). Shaded area is "viewing window" available to ultrasonic transducers.

(b) Stereographic projection of viewing window showing receiver positions (circles) and transmitter positions (squares).

Sample Fabrication and Measurement Apparatus

As described in detail by Paton,[1] in the sample fabrication two cylinders of Ti alloy were machined and then their bases diffusion bonded together in such a way that the final longer cylinder contained a spheroidal cavity at its center. Then this cylinder was machined into a configuration of a sphere on a pedestal such as shown in Fig. 2 with the center of the defect coinciding with the center of the sphere. In this way ten (10) samples were fabricated, as listed in Fig. 2, with defect geometries, including prolate and oblate spheroids and thin discs. The motivation for machining the samples into a spherical configuration was to provide the simplest geometry possible for probing and

analyzing the three-dimensional far field scattering patterns for the obstacles with the goal of measuring phase as well as amplitude.



DESCRIPTION	a (cm)	b (cm)	c (cm)	STAND OFF
PROLATE SPHEROID	200	200	800	60
PROLATE SPHEROID	400	400	800	41
SPHERE	200	200	200	35
SPHERE	400	400	400	36
SPHERE	800	800	800	37
OBLATE SPHEROID	400	400	200	39
OBLATE SPHEROID	400	400	100	38
CIRCULAR DISC	800	800	100	62
ELLIPTICAL DISC	2500	800	250	61
SIMULATED CRACK	800	800	-	67

Figure 2. Sample configuration and list of samples.

The measurement fixture, shown in Fig. 3, was designed and constructed to allow arbitrary motion of two transducers across the surface of the sphere, as well as another transducer mounted to the bottom of the pedestal. Figure 4 establishes the coordinate system for the various transducers with respect to the defect and defines the polar angle α and the azimuthal angle β for the two moving transducers.

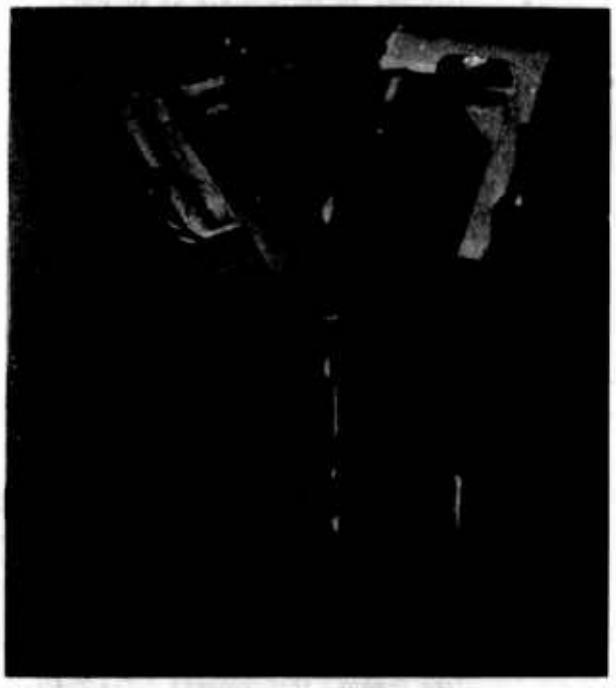


Figure 3. Photograph of sample holder.

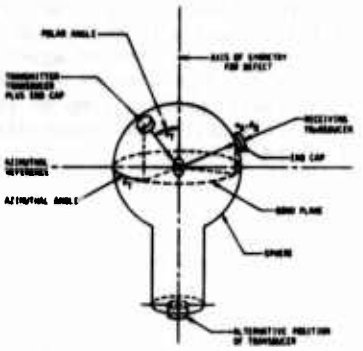


Figure 4. Measurement coordinate system.

The measurement apparatus is outlined in Fig. 5. The transducers used are 5 MHz broadband Panametrics units and are pulsed by either a UM721 Reflectoscope or a Panametrics 5052PR. The coupling between the flat transducer wear plates and the spherical sample surface was accomplished with the aid of end caps constructed from the same stock Ti-alloy as the sample and polished to conform to the mating surfaces. R.F. waveforms are captured by a Biomation 8100 transient recorder and the experiments are controlled and signal processing performed on an Eclipse mini-computer using the Science Center's Interpretive Signal Processor language. The frequency range studied has been chosen to be 2-10 MHz in order to give a range of ka = 0.5-10.

Scattering Data Base for Use in Inversion

With the techniques described above, scattering data were collected on defects for which the current theoretical approximation work the best, i.e., cavities in the shape of oblate spheroids. This data was added to the computerized ultrasonic scattering base at the Science Center and is available on 9-track 800 BPI magnetic tape for use in developing scattering inversion techniques. A copy of the data has been sent to Adaptronics, Inc., and is discussed by Mucciardi (see this proceedings).

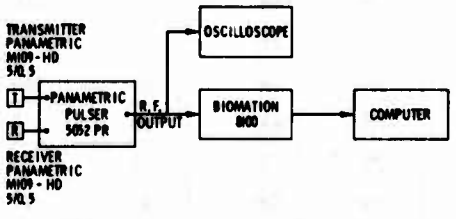


Figure 5. Schematic - Data Acquisition System.

Figure 6 shows a sample waveform and its Fourier transform (absolute value) on specimen No. 39 containing a cavity in the shape of an oblate spheroid. Complete sets of waveforms have now been obtained for four windows (see Fig. 1(b)) on each of two oblate spheroid samples (Nos. 38 and 39) for directly scattered longitudinal waves and are summarized in Table I.

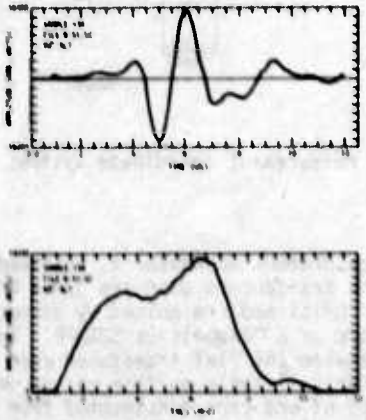


Figure 6. Sample waveform and its Fourier spectrum (magnitude) for pulse-echo data on oblate spheroid at a polar angle of 40° from axis of symmetry.

TABLE I

DEFECT SIZE AND ORIENTATION

ALIAS NAME	RADIUS ALONG AXIS (μm)	RADIUS PERP. AXIS (μm)	ELEV. (POLAR) ANGLE α	AZIM. ANGLE β
1Q	200	400	0	0
2Q	200	400	30	225
3Q	100	400	80	160
4Q	100	400	0	0
5Q	200	400	80	160
6Q	100	400	30	0
7Q	200	400	30	0
8Q	100	400	30	225

Figure 7 and 8 demonstrate some of the qualitative features in the data. In Fig. 7 the scattered waveform peak-to-peak amplitude is written in dB at each receiver site for a transmitter 60° away from the window axis, which in this case coincides with the axis of symmetry for the defect, an oblate spheroid with a 2 to 1 aspect ratio. Contour lines are indicated approximately in order to demonstrate how the radiation pattern for the scattered power appears to tilt away from the transmitter position, in agreement with intuition. In Fig. 8 similarly obtained data are plotted on a computer contour plot developed by Domany (see this proceedings) with reasonable agreement considering the 1 dB accuracy of the data (which corresponds to two integers on the contour plot).

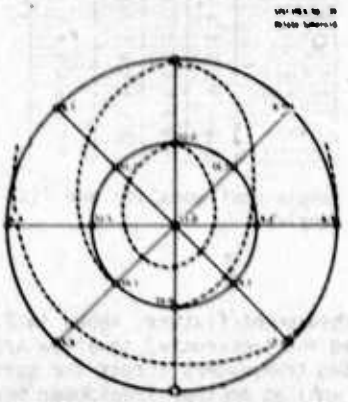


Figure 7. Sample data from data set 1Q (see Table I) for transmitter positioned at (60°, 180°) the bottom of the window. The numbers are relative power in dB recorded by a receiver moved successively to the other window positions. The dashed lines are rough estimates for 12.0 dB, 10 dB, and 6.9 dB contours.

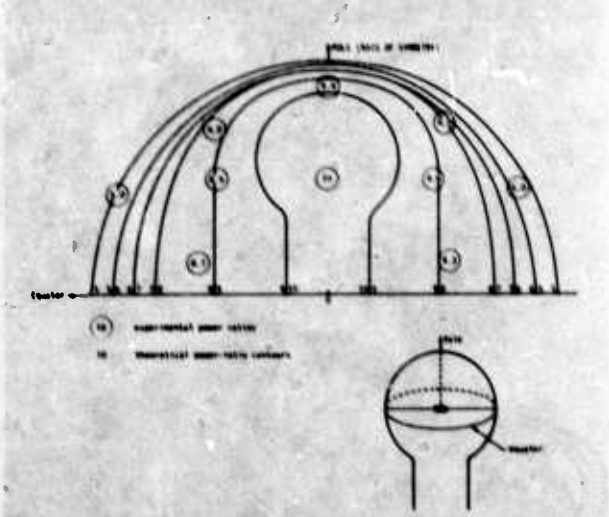


Figure 8. Comparison between calculated (from Born approximation) and observed power ratios for scattering from oblate spheroid No. 39. The results obtained for the surface of the spherical sample are plotted in the form of a projection (see Domany, this report). The transmitter is at "0". The maximum power scattered is arbitrarily chosen as 10.

Angular Dependence for Spheroidal Defects

A scatterer of irregular shapes reflects different amounts of sound in different directions. This makes possible the estimation of shape (i.e., "out-of-roundness") and orientation by observing the peak height of the pulse-echo video signal when the defect is viewed from a variety of directions.[2]

Figure 9 surveys some of the theoretical and experimental results in order to draw attention to the qualitative differences between the various defects.[3] The figure shows backscattered power as a function of the polar angle for a sphere, an oblate spheroid, a prolate spheroid and a circular disc. Both the experimental curves (dashed lines) and the theoretical curves (solid lines) are normalized along the symmetry axis (polar angle $\alpha = 0$). The theoretical curves are results of Born approximation calculations.

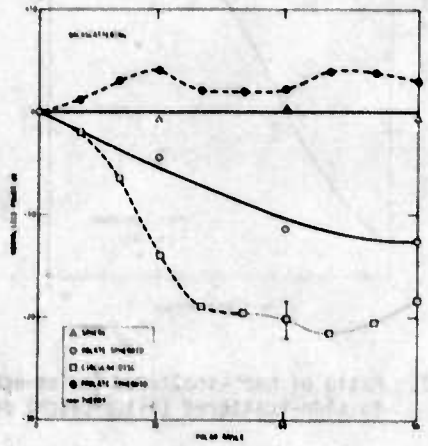


Figure 9. Angular dependence of pulse-echo power (data normalized at zero polar angle α).

The plot demonstrates the dramatic differences in the angular dependence for the various shapes when the sizes of the objects are approximately comparable. Measurement of the backscattered power for a few angles near $\alpha = 0$ is clearly sufficient to classify the scattering object according to shape. Furthermore, to the extent that quantitative calculations have been applied to the data at this time, good agreement between theory and experiment is observed. All the salient features of Fig. 9 are in quantitative agreement with the Born approximation, see Fig. 10 for the spheroidal shape and with Keller's theory for the discs (see Adler, this proceedings).

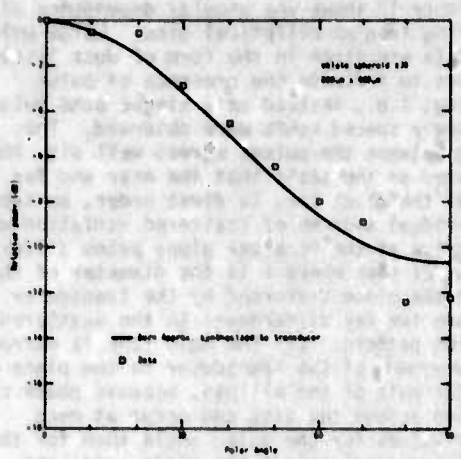


Figure 10. Comparison of pulse-echo data as a function of polar angle α with predictions of Born approximation. (The calculations take into account the transducer characteristics.)

Figure 11 presents more detailed results for a number of shapes and sizes in an unnormalized way and focuses attention on the quantitative differences between the defects. For example, the 600 μm radius sphere gives an approximately 4 dB higher backscattering than the 400 μm radius sphere. This is in agreement with physical intuition and in good quantitative agreement with scattering theory which scales the intensity by ρ^2 where ρ is the radius of curvature--(in this case $\rho = a$) and predicts a difference of 3.5 dB.

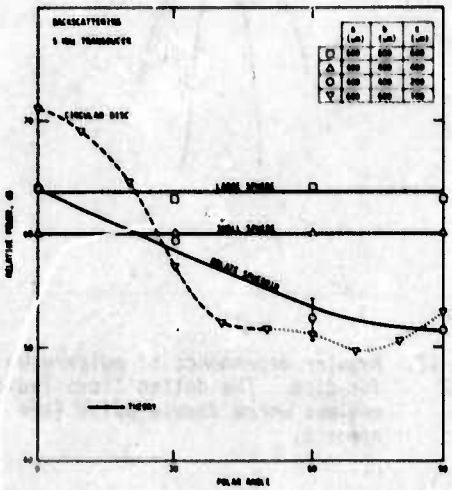


Figure 11. Angular dependence of pulse-echo power.

Figure 12 shows the angular dependence of the scattering from an elliptical disc. Large polar angle data are given in the form of dots instead of dashes to indicate the presence of pulse splitting; i.e., instead of a single echo pulse, two closely spaced echos were observed. The spacing between the pulses agrees well with that calculated on the basis that the near and far edges of the discs can, to first order, be treated as individual sources of scattered radiation which then arrive at the receiver along paths differing by about $2\ell \sin\ell$ where ℓ is the diameter of the disc in the plane traversed by the transducer. There are two key differences in the scattered radiation pattern: (1) the main lobe is narrower for traversal of the transducer in the plane of the major axis of the ellipse, because phase cancellation across the disc can occur at much smaller values for the polar angle than for the case of traversal across the minor axis; and, (2) the narrow lobe data (traversal across major axis) shows a lower side-scattered ($\alpha = 90^\circ$) power level, because the transducer at that angle faces the smaller cross section of the disc. Calculations predict a difference of 12.4 dB which is in good agreement with the observed ~12 dB. These features, as well as the degree of splitting in the echo pulse, are thus seen to provide powerful indicators of the size and shape of defects approximating penny-shaped cracks. The lack of symmetry in the plots is thought to result from distortions of the disc-shaped cavity incurred during the bonding process.

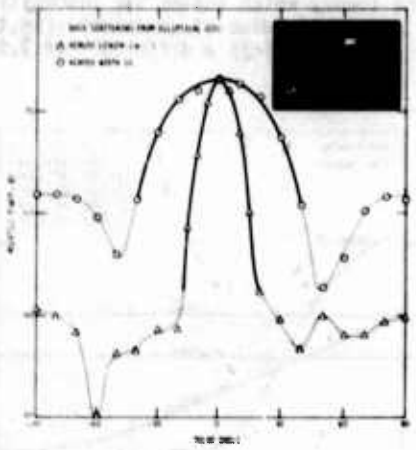


Figure 12. Angular dependence of pulse-echo power for disc. The dotted lines indicate regimes where double pulse (see insert) appears.

Figure 13 presents data obtained on the spheroidal cavities as a function of the aspect ratio. The measurement was in part motivated by calculations made available for this problem by the use of the Born approximation. The theoretical curve was obtained by averaging the calculations over $0 \leq kc \leq 2$, where k is the wave vector of the ultrasonic wave and 2c is the length of the ellipsoid axis in the direction of the incident wave. To accomplish a comparison with the available samples, a different transducer set (i.e., with different center frequency) had to be used with each sample. This ensured that kc would be approximately constant throughout the experiment. Furthermore, wide-band transducers were used so that some averaging could be accomplished approximating the theoretical averaging over the range of kc values described above. As seen in Fig. 13, the agreement between theory and experiment is good, and in view of the difficulties in the experiment, remarkably close. The significance of this study is that it allows a qualitative extrapolation to the case of the penny-shaped crack which is one of the geometries frequently encountered in commercial NDE applications.

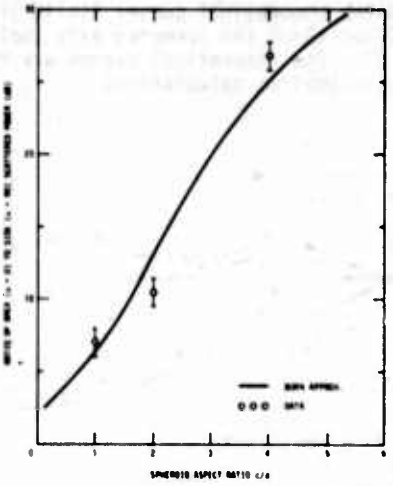


Figure 13. Ratio of back-scattered (pulse-echo) to side-scattered (pitch-catch) power.

Figure 14 presents preliminary data on the angular dependence of the pulse-echo peak height from a simulated crack 1200 μm in diameter. As described by Paton,[1] the defect was made by placing a small amount of non-metallic compound (yttria) on the mating surface and inhibiting the bonding process in that area. As expected, the measurements were very difficult to carry out because most of the signal passed through the flaw and special techniques of signal averaging yet to be developed are required to remove the competing signals from scattering off metallurgical second phases. Nevertheless, these preliminary data are interesting because they display a rapid roll-off at small polar angles (faster than the data for the circular disk of the same diameter) in good agreement with Adler's calculations from Keller's theory (see this proceedings).

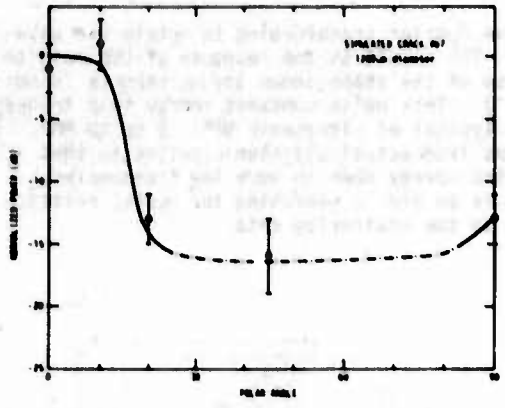


Figure 14. Angular dependence of pulse-echo power for simulated crack.

A number of measurements were carried out to see how the frequency dependence of pulse-echos (backscattering) from an oblate spheroid vary with polar angle. These data were obtained by spectrum analyzing the waveforms of broad-band pulse-echos. As reference, Fig. 15 presents the frequency dependence for longitudinal backscattering from a spherical cavity 800 μm in diameter and shows good agreement between experiment and classical scattering theory. Also shown in Fig. 15 (top graph) is the calculated frequency dependence for a sphere with half the diameter (400 μm). The key difference is that the graph appears to have been stretched out so that the oscillations exhibit a larger period and the first (low frequency) hump has been pushed to higher frequencies. This observation is equivalent to noting that the backscattering may be described by a single curve with ka as abscissa and that the first peak occurs at ka = 1. Because of the symmetry for the sphere, these results remain unchanged as a function of angle, and it is of interest to study the effects of deviation from symmetry.

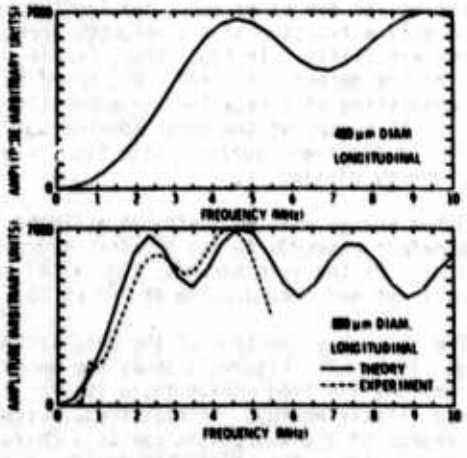


Figure 15. Comparison of "exact" theory and data for spherical void. The data is obtained by Fourier analyzing the pulse-echo waveform and dividing by transducer spectrum.

Figure 16 shows representative data and calculations from approximate models for the backscattering from an oblate spheroid with a 2:1 aspect ratio (sample 39) at two polar angles $\alpha = 10^\circ$ and $\alpha = 60^\circ$. Among the main features noticeable is a qualitative similarity of Fig. 16 with Fig. 15, in that at low polar angles, the oblate spheroid behaves as if it had a small effective radius a, i.e., first peak at high frequencies, large period of oscillation. As the polar angle is allowed to increase, the frequency dependence changes smoothly--as if contracting--until at large polar angles, the location of the first (low frequency) peak and the period of oscillations suggest a large effective radius. To a limited extent this result is borne out by the approximate theoretical models in accurately predicting the location of the first (low frequency) peak, and suggests that angular dependence data could be used very effectively in determining the size of the flaw in addition to shape and orientation.

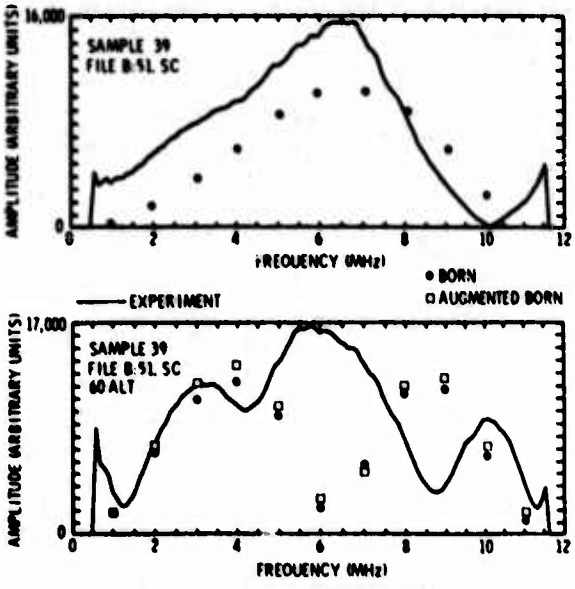


Figure 16. Comparison of approximate theories and data for back-scattering from an oblate spheroid for 10° (upper figure) and 60° (lower figure) off the axis of symmetry.

Time and Frequency Domain Analysis

A short ultrasonic pulse contains a wide band of frequencies. Because each frequency interacts differently with a defect, the scattered frequency spectrum is a signature of the defect. By studying the time-domain RF waveforms and the frequency spectra of the ultrasound backscattered from spherical scatterers, a number of techniques have been developed to determine size and impedance of the scatterers.

Waveforms - Figure 17 shows typical frequency spectral data. Figure 17 (upper left) shows the ultrasonic pulse produced by a broadband 5 MHz transducer. Figure 17 (upper right) shows the magnitude of the frequency spectrum of this pulse. Depending on the signal to noise ratio of the measurements, there is usable signal from 1 to 9 MHz. Figure 17 (middle left) shows the ultrasonic pulse which resulted when the above pulse was backscattered off of a 0.12 cm diameter spherical void in Ti-6Al-4V. The altered shape contains information about the scatterer. Figure 17 (middle right) shows the frequency spectrum of this scattered pulse. Here also there is structure characteristic of the scatterer. Finally, the effects of the transducer, pulser and medium can be removed by normalizing the scattered spectrum (middle right) by the pulse spectrum (upper right). This normalized spectrum is shown in Fig. 17 (lower right). Because of the small amount of energy present in the pulse at very low and very high frequencies, the normalization was cut off below 1/2 MHz and above 9 MHz. In the intervening region, the normalized spectrum is an accurate representation of the scattering properties of the defect.

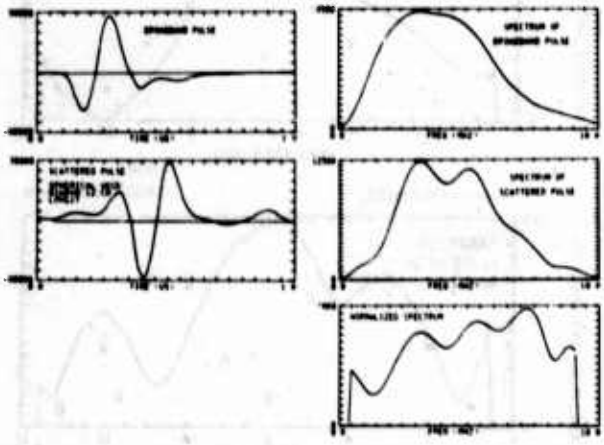


Figure 17. Time domain (left) and frequency domain (right) waveforms for a broadband ultrasonic pulse (top), the same pulse after scattering from a spherical void (middle), and after original pulse is normalized out of scattered pulse (bottom).

In order to find relationships between scattered signals and the properties of the scatterers, we have first studied theoretically calculated waveforms. For spherical voids and inclusions (though not for more complicated shapes), it is possible to calculate exactly the scattered ultrasonic waveforms. Calculations have been made using the method of Tittmann and Cohen for spherical scatters in a variety of sizes and material content.

Consider first the RF waveform. Figure 18(a) shows the backscattered waveform of a spherical void. It was calculated by first calculating the scattering as a function of frequency and then inverse Fourier transforming to obtain the waveform. The result is the response of the void to a pulse of the shape shown in Fig. 18(b) (a "Hanning pulse"). This pulse contains energy in a frequency range typical of ultrasonic NDE: 0 to 10 MHz. It differs from actual ultrasonic pulses in that it contains energy down to very low frequencies, which is an aid in searching for useful relationships in the scattering data.

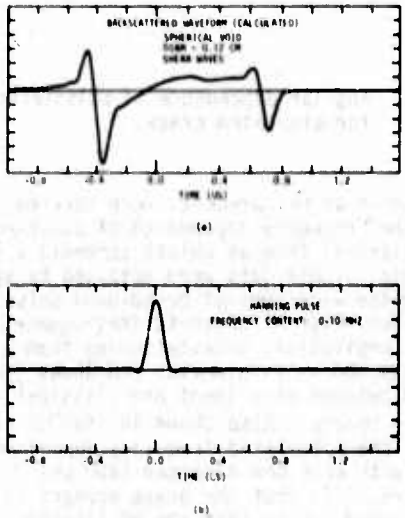


Figure 18. (a) Calculated time-domain response of 0.12 cm diameter spherical void to incident hanning pulse.
(b) Hanning pulse.

At high frequencies, the front surface of the void will be approximately flat over an area several wavelengths across and will therefore reflect a substantial amount of sound. At low frequencies, on the other hand, the front surface will be only a fraction of a wavelength across and will reflect little. In Fig. 18(a), T=0 is at the center of the defect. At T=-0.4 US, there is pulse consisting of a negative and a positive peak. It is a copy of the input Hanning pulse, at the time of the front surface, with its low frequency energy missing.

Other energy will be scattered at later times as the defect responds to the incident sound pulse. In the case of the void shown in Fig. 18(a), there is a well defined second pulse at T=0.65 US.

The frequency spectrum of the void is shown in Figs. 19 and 20. Figure 19 shows the magnitude spectrum. At low frequencies there is, as expected, little energy. At high frequencies, the interference of the two pulses causes a characteristic oscillation whose period is inversely proportional to the size of the void.

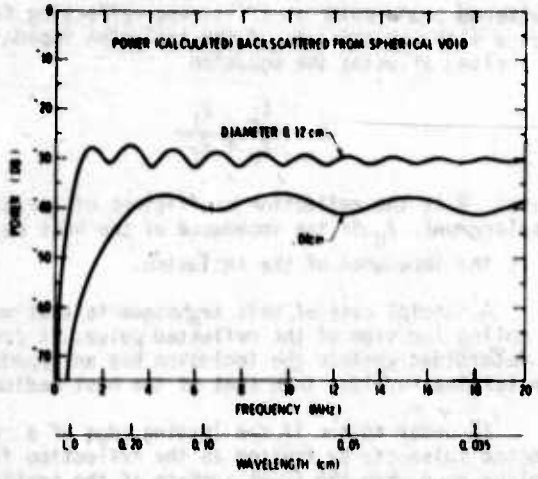


Figure 19. Calculated pulse-echo magnitude spectra for two spherical void scatterers.

The phase spectrum is shown in Fig. 20. To interpret the phase spectrum, recall that the effect of varying the arrival time of a pulse is to add to the phase spectrum a ramp of the form $\theta = 2\pi fT$ where T is the arrival time.

Figure 20 shows an upward slope corresponding to the arrival time of the front surface echo. The oscillations on this ramp are caused by the arrival time of the second echo. At low frequencies, the slope is zero, indicating that long wavelengths sense primarily the enter of the defect (T = 0).

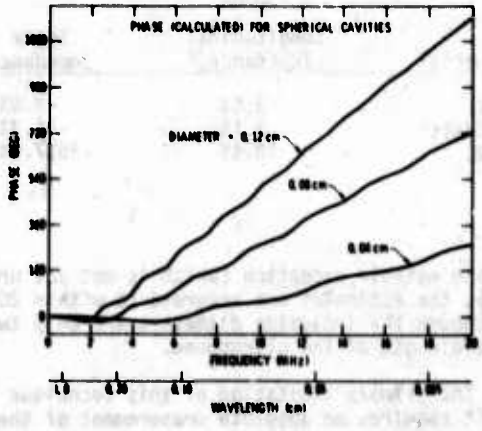


Figure 20. Calculated phase spectrum of 0.12 cm, 0.08 cm, and 0.04 cm diameter spherical void. Upward slope at high frequencies indicates that front face of void is nearer than its center. Flat slope at low frequencies indicates position of center.

Because the frequency spectrum stretches and shrinks, but does not change shape as the size of a scatter of fixed shape varies, the frequency of any feature of the frequency spectrum could be used as a measure of size. Thus, for longitudinal wave inspection of spherical voids, the first or second peaks of the magnitude spectrum predict diameter via the following relationships:

First peak:

$$\text{diam (mils)} = \frac{74.25 \text{ mils} * \text{MHz}}{\text{Frequency}}$$

Second peak:

$$\text{diam (mils)} = \frac{150.9 \text{ mils} * \text{MHz}}{\text{Frequency}}$$

Applying these formulae to experimentally measured spectra yields the following estimates:

Actual Diameter	Estimated Diameter	Difference
31.5	30.0	5%
47.24	47.13	1/4%

For a tungsten carbide sphere in Titanium-6-4, the first peak of the spectrum predicts diameter according to:

First peak:

$$\text{diam (mils)} = \frac{127 \text{ mils} * \text{MHz}}{\text{Frequency}}$$

For an experimental spectrum:

Actual Diameter	Estimated Diameter	Difference
31.5	31.36	1/2%

A more systematic approach is to measure the period of the oscillations of the magnitude spectrum by calculating a spectrum and noting the position of its maximum. This approach will be limited for very small defects, where the spectrum will consist of only the first part of Fig. 19 and there will be no oscillations to measure. As reported in the second annual report, this technique should give 30% accurate estimates down to diameters as small as 1/2 wavelength of sound.

The features of the spectrum which have been used in the preceding paragraphs are not independent of the material contained within the sphere. A technique which promises to be material independent makes use of the phase spectrum and is based on the following strategy:

1) Locate the front face of the defect using high frequencies (short wavelengths)

2) Locate the center using low frequencies (long wavelengths)

3) Subtract (1) from (2) to find defect size.

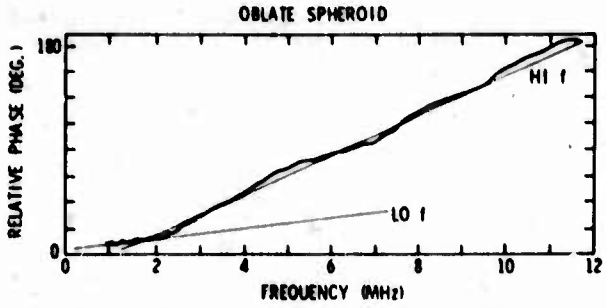
It was noted above that the high frequency part of the phase spectrum has a slope which indicates the location of the front surface of the defect, while the low frequency part has a slope which indicates the position of the center. Therefore, the difference of the slopes indicates size:

Diameter = velocity in host medium x

$$\frac{1}{4\pi}\left(\frac{d\phi}{df}\,\middle|\,\text{low freq.} - \frac{d\phi}{df}\,\middle|\,\text{high freq.}\right)$$

This method is independent of the material included within the defect and independent of the shape of the defect.

Figure 21 shows the results for experimental data from an oblate spheroid of semi-axes 100 and 400 microns viewed along the 100 micron axis. The phase slope method predicts a semi-axis of 114μm, in excellent agreement with the actual value of 100μm.



$$HI\ f\ \frac{d\phi}{df} = \frac{3.4\ \text{rad}}{11\ \text{MHz}} \qquad \tau_{HI} = \frac{1}{4\pi}\frac{d\phi}{df} = .0246\ \mu\text{sec}$$

$$LO\ f\ \frac{d\phi}{df} = \frac{1\ \text{rad}}{2\ \text{MHz}} \qquad \tau_{LO} = .0066\ \mu\text{sec}$$

$$\tau_{HI} - \tau_{LO} = .018\ \mu\text{sec} \qquad R = v\Delta\tau = .0114\ \text{cm}$$

Figure 21. Observed phase spectrum for back-scattering from oblate spheroid cavity along axis of symmetry and calculation of minor axis.

Finally, a technique has been developed which estimates the acoustic impedances of spherical solid inclusions in solids. It is based on the idea that the front surface of the scatterer is approximately flat, at least over a suitably small area. Therefore, when a pulse of ultrasound first encounters the scatterer, it will reflect in a manner similar to the way it would from a flat semi-infinite slab of the included material. By treating the back-scattered sound pulse as if it were reflecting from such a slab, an estimate of the inclusion impedance is arrived at using the equation

$$R = \frac{Z_H - Z_I}{Z_H + Z_I}$$

where: R is the reflection coefficient of acoustic displacement, Z_H is the impedance of the host medium, Z_I is the impedance of the inclusion.

A special case of this technique is that merely by noting the sign of the reflected pulse, it can be determined whether the inclusion has an impedance greater than or less than that of the host medium.

In order to see if the leading edge of a reflected pulse can be treated as the reflection from a plane even when the front surface of the scatterer has a large curvature (e.g., for a small scatterer), and even when only a limited range of frequencies is available, theoretically calculated waveforms have been used to make estimates of the longitudinal and transverse impedances of spherical (1.2 mm dia.) aluminum, brass, and tungsten carbide inclusions in Ti-6-4. The procedure consisted of using theoretically calculated frequency spectra covering the range 0 MHz to 10 MHz to construct the (time domain) reflected pulse that would result from an incident Hanning pulse which contains energy from 0 MHz to 10 MHz. To estimate the impedance of an inclusion, we need the reflection coefficient from its front surface. For this, we have used the height of the first peak of the waveform divided by the height of the first peak of the waveform from a void. In Fig. 18(a), this peak is the positive going one at t = -0.45μs. The accuracy of impedance estimates made using this technique is shown below.

Material	Error: Longitudinal Impedance	Error: Shear Impedance
Al	-3.6%	-9.5%
Brass	2.1%	-14.7%
WC	10.4%	-2537.0%

With one notable exception (which is not yet understood), the estimates are accurate to within 20%, even though the inclusion diameters are only twice the wavelength of the ultrasound.

The primary limitation of this technique is that it requires an absolute measurement of the scattered acoustic amplitude, and a knowledge of the inclusion diameter. The test to which the method has thus far been put is limited by the lack of noise (electrical or metallurgical) in the data, the absence of the band limiting effects of an ultrasonic transducer, and the application of the method only to spheres. It is expected that the addition of these factors will degrade the results somewhat, but not invalidate the technique.

Conclusions

One of the challenges facing ultrasonic NDT is the need to quantitatively evaluate defects so as to reduce the number of parts rejected unnecessarily. It is, therefore, desirable to obtain accurate measure of size, shape, orientation, and content of defects. To do this, we should collect as much information as needed and process that information by suitable methods. With this goal in mind, we have investigated small voids and inclusions of simple shapes in solids. The diffusion bonding process has been found most useful and has been used to make Ti-6-4 samples containing voids in the shape of spheres, ellipsoids of revolution, and disks. The r.f. waveforms of ultrasound scattered from these defects have been captured in real time and processed by a digital computer. With the aid of theoretical models based on both exact and Born approximation methods, signal processing algorithms have been developed which rapidly estimate, from experimental data, the geometrical properties of defects. The use of signal processing techniques on ultrasonic NDE waveforms can reveal much about the nature of small scatterers within a part. Angular dependence of the scattering gives information about the shape and orientation of the scatterer. Frequency analysis of pulse echo signals provides techniques for estimating the size and material content of the scatterers. Several of these techniques have been tested to void defects in titanium and show high promise of being usable in practical NDE applications. The work may be summarized by concluding that the new techniques in sample fabrication, measurement procedures, and data processing have provided a preliminary definition of the minimum quantity and type of data acquisition needed for a "smart" NDE system. The work has provided a useful data base for use in developing scattering inversion techniques (i.e., deterministic, probabilistic, or adaptive schemes) from which quantitative properties of the scattering center can be rapidly extracted. The scattering data have been found to be a valuable test for the evaluation and refinement of scattering theories which treat scattering from ellipsoidal cavities on an approximate basis. These results have been possible primarily because the new concept of sample fabrication by the diffusion bonding process was proven to be successful.

Acknowledgement

This research was sponsored by the Center for Advanced NDE operated by the Science Center, Rockwell International, for the Advanced Research Projects Agency and the Air Force Materials Laboratory under contract F33615-74-C-5180.

References

1. "Interdisciplinary Program for Quantitative Flaw Definition, Special Report Third Year Effort," Rockwell International Science Center, pp. 59-62.

2. R. K. Elsley and B. R. Tittmann, NDT Conference Proceedings (Southwest Research Institute, San Antonio, Texas, 1977), in press.

3. B. R. Tittmann, Proc. of 1976 IEEE Ultrasonics Symposium, IEEE Catalog #76 CH 1120-5SU, 74, 74-79 (1976).

IDENTIFICATION OF FLAWS FROM SCATTERED ULTRASONIC FIELDS AS MEASURED AT A PLANAR SURFACE

L. Adler, K. Lewis, P. Szilas, and D. Fitting
The University of Tennessee
Knoxville, Tennessee 37916

ABSTRACT

Ultrasonic wave scattering from ellipsoidal and cylindrical cavities embedded in titanium was measured and analyzed with a newly designed signal processing system. Using an immersion system and samples with flat faces, the range for waves incident, at certain polar and azimuthal angles, was determined for both L-L and L-S scattering. Attempts were made to define key parameters from both amplitude and phase spectra for characterizing cavities. Results are compared to predictions of Born approximations (developed by Krumhansl et al. at Cornell) and to experimental results taken by a contact system (Tittmann et al. at Rockwell). A new (Keller type) theory for crack-like defects which includes mode conversion will also be presented.

Introduction

The objective of the third year was to concentrate efforts among the various investigators upon the inverse problem. In an effort to obtain size and orientation of cavities from scattering data, our specific goal was to design system and data processing to obtain optimum information for scattering data within the experimental limitations of an immersed system using flat samples. Then by taking a large number of scattering data: (a) provide Adaptronics with this data to test their adaptive technique which is trained based on Born approximations, and (b) direct comparisons of the data to available models.

Experimental Technique

In previous investigations one of two techniques was used. These are: (a) normal incidence pitch-catch method, and (b) pulse-echo at various angles. Since both of these techniques have advantages, they were utilized in combination. Figure 1 illustrates the new experimental technique used in the third year. The transmitter launches a longitudinal wave to the liquid-solid interface at an angle such that both L and S waves are generated. The cavity can be insonified either by an L wave or by an S wave. Only L waves incident to the cavity are considered, which is mode converted into L and S waves. The configuration of the receiver is shown to receive only scattered L or scattered S waves. The transmitter can also be used to receive scattered L waves (this special case is the pulse-echo technique). This arrangement has the flexibility to vary the incident angle α and the scattered polar angle θ. The coordinate system used is shown in Fig. 2. The right side of the coordinate system is attached to the sample and used as experimental parameters. On the left the coordinate system is attached to the cavity and this is used by the Born approximation theory. One set of angles can be expressed in terms of the other by using a coordinate transformation. The system was also modified to receive in different planes; i.e., for fixed incident angle α and polar angle θ we have the capability to study the dependence on azimuthal angle ϕ. The new multiplane goniometer is shown in Fig. 3. The receiver is rotated about a fixed axis while keeping the transmitter in the same plane. For each value of the incident angle α (0°, 10°, 20°, 30°) the receiver was placed in four different planes, i.e., $\phi = -45^\circ$, 0°, 45°, 90°. In each plane the polar angle was adjusted up to 60°. Because of the transducer's dimension, the smallest angle between transmitter and receiver was always 30°. Altogether for L-L and L-S scattering we took approximately 120 data points for a given cavity. By reversing the transmitter and receiver or by using the pulse-echo mode, additional data points could be taken.

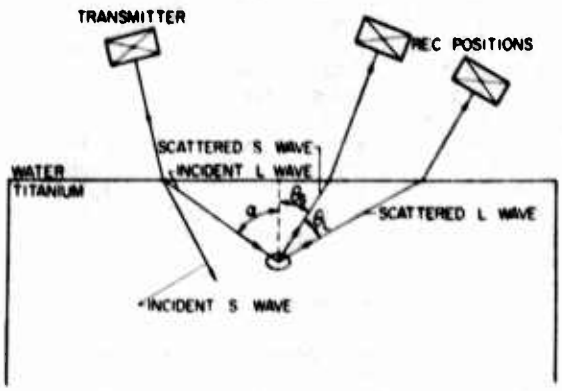


Figure 1. Experimental technique.

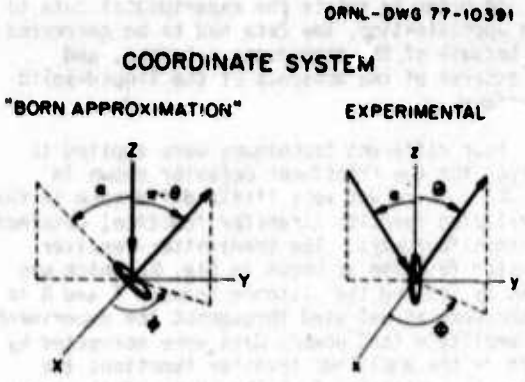


Figure 2. Coordinate system.

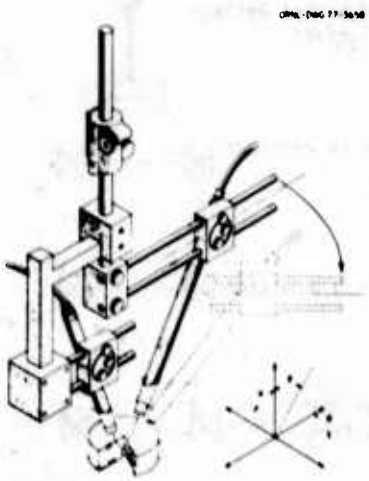


Figure 3. Multiplane ultrasonic goniometer

Modified Experimental System and Signal Processing

Our previous measurements of the frequency spectra of ultrasonic pulses were made by using a commercially available analog spectrum analyzer. This process limited out capabilities since: (1) it does not give phase information, and (2) it is not in suitable form to transfer and process the data to other investigators. Our new modified system is shown in Fig. 4. The essential feature of the system is a boxcar integrator which provides a low frequency equivalent of the rf waveform and permits digitizing the signal at an effective rate. The boxcar integrator allows one to recover and analyze signals which are far too small for data acquisition by a digitizing system. This is illustrated in Fig. 5 where the RF signal for a 40° shear wave scattered from a 200 x 400μ oblate spheroidal cavity in titanium is displayed with and without the boxcar integrator. The microprocessor is responsible for controlling the A to D converter and for conversion of the binary data to code format which is compatible with the selected peripheral device. Programs have been written which allow the data to be printed on paper tape displayed on a CRT terminal and stored on magnetic tape. The data from magnetic tape are processed by an IBM 360-91 using a FFT program. Thus one can obtain both amplitude and phase in frequency space. Figure 6 is the spectrum of a scattered wave for L-L scattering for a 500μ (diameter) disk-shaped cavity in titanium taken from the analog spectrum analyzer. The RF wave form and the processed amplitude and phase spectrum are shown in Fig. 7. In addition to phase information, the computed amplitude spectrum gives much more detail.

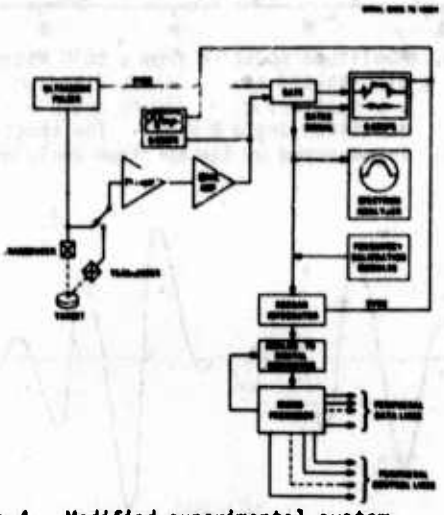


Figure 4. Modified experimental system.



Figure 5. 40° shear wave scattered from a 200 x 400μ oblate spheroidal cavity. (a) Before processing. (b) After processing.

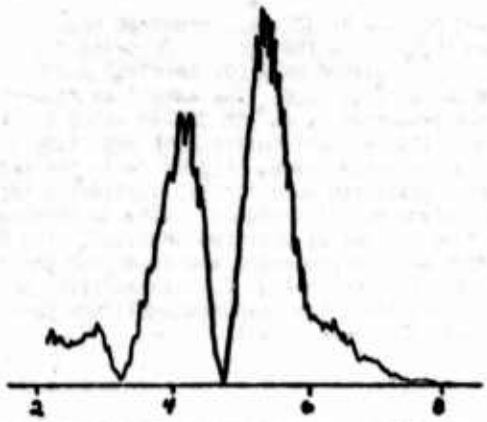
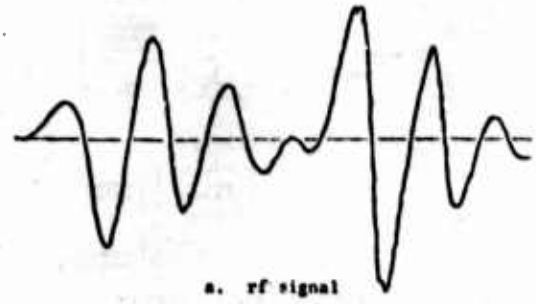
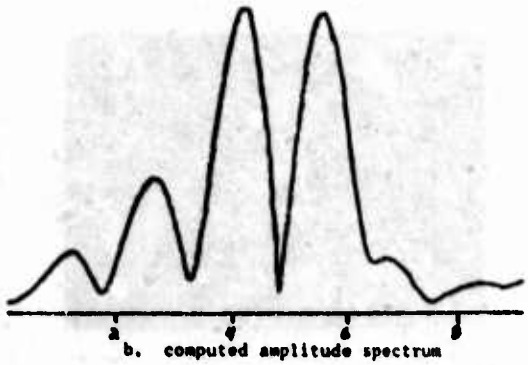


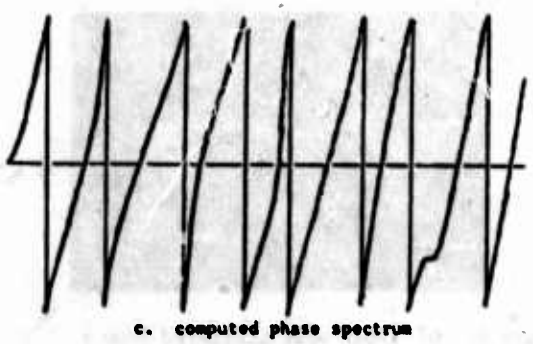
Figure 6. Amplitude spectrum from a 5000 micron disc-shaped cavity inside titanium, L-L scattering. Incident angle $\alpha = 0^{\circ}$; scattered angle $\theta = 60^{\circ}$. The spectrum is measured by the spectrum analyzer.



a. rf signal



b. computed amplitude spectrum



c. computed phase spectrum

Figure 7. Scattered L-L signal obtained from a 5000 micron disc-shaped cavity inside titanium. Incident angle $\alpha = 0^{\circ}$; scattered angle $\theta = 60^{\circ}$.

Correction of Data

In order to relate the experimental data to Born approximation, the data had to be corrected: (1) because of the transducer response, and (2) because of the presence of the liquid-solid interface.

Four different techniques were applied to correct for the transducer behavior shown in Fig. 8. There was very little difference in the normalizing function (transfer function) obtained in these four ways. The transmitter-receiver transfer function is shown in Fig. 9, which was taken by setting the distance between T and R to be the same as was used throughout the experiment. The amplitude (and power) data were corrected by dividing the amplitude transfer function; the phase was subtracted from the phase of the transfer function.

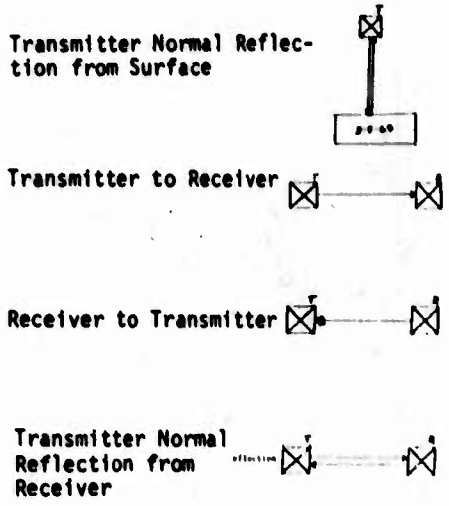


Figure 8. Normalization signals.

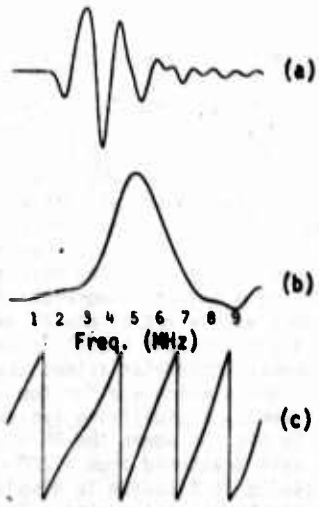


Figure 9. Transducer transfer function. (a) RF wave form; (b) amplitude spectrum; (c) phase spectrum.

The theory assumes an infinitely extended solid surrounding the cavities. The experiment, however, uses the information obtained in the liquid. The data, therefore, had to be corrected for the transmission of waves from titanium to water. In Fig. 10 the transmission amplitude vs. angle is given for L and S waves calculated by assuming infinite plane waves.

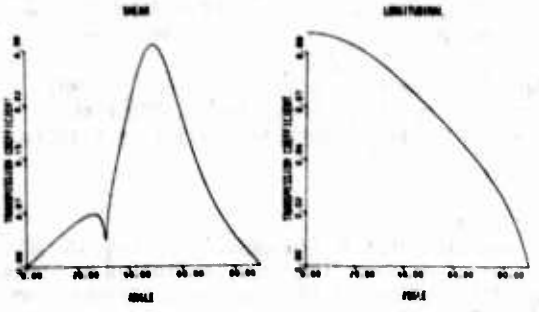


Figure 10. Transmission curve for Ti-6Al-4V water.

Procedures and Key Parameters

The different cavities used in this experiment were the following: 100 x 400μ and 200 x 400μ oblate spheroids; 200μ, 400μ, and 600μ spheres, 800 x 400μ prolate spheroid, and a 2500μ disk (the radii are given). The experimental parameters studied were the: (1) integrated power for the whole frequency region, (2) power spectra, (3) phase spectra, (4) amplitude of the center frequency, and (5) position of the center frequency. These parameters were studied for different α, θ, and ϕ for L-L and L-S scattering. The data are not complete. A complete data set is taken only on the 200 x 400μ oblate spheroid (both L-L and L-S). This was sent to Adaptronics for analyzing by their techniques of measuring size and orientation. Some data taken on the other cavities, however, are giving some understanding of the elastic wave interaction with defects.

Results

Power vs. Polar Angle Oblate Spheroid - Stereographic projection of the Born approximation, together with the experimental data,are shown in Fig. 11. For $\alpha = 0$ at the center of the concentric circles,the integrated power of the pulse echo is given. Each concentric circle corresponds to a given θ and for 360° variation of ϕ. On the left the angles θ are given. The small numbers correspond to the calculated values and the larger numbers (in dB) are the measured experimental points for $\phi = 0$, 45 and 90°. The drop of power with polar angle is followed by both experiment and theory. There are some uncertainties due to alignment. The data points are much better for individual frequencies. In Fig. 12 the variation of power for individual frequencies is shown. The least scatter in the data is obtained for 5.1 MHz. This is the center frequency of the input signal. There is also an increasing slope with increasing frequency.

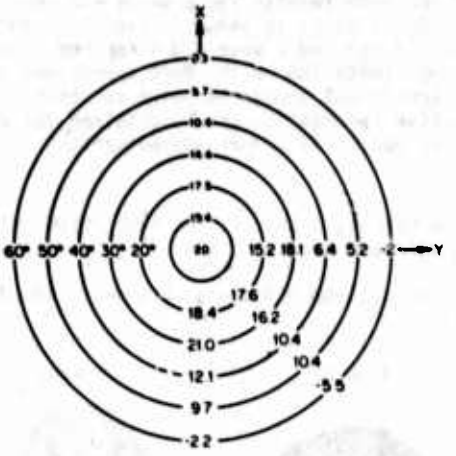


Figure 11. Stereographic projection of integrated power of L scattering for oblate spheroid $\alpha = 0$. Small numbers along +X axis are calculated from Born approximation. Large numbers are measured values at $\phi = 0°$ (along Y) $\phi = 45°$ and $\theta = 90°$.

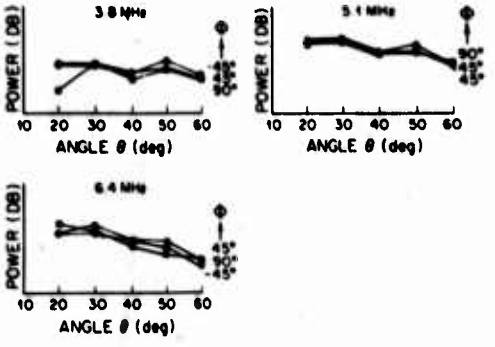


Figure 12. Scattering of longitudinal waves from a 200 x 400μ oblate spheroidal cavity in titanium, $\alpha = 0°$

Scattered Field Profiles - In order to visualize some details of the predicted Born approximation we have designed a 3D plot of the scattered energy behavior based on Born approximation. In Fig. 13 the scattered power is plotted for a 200 x 400μ oblate spheroidal cavity both for L-L and L-S scattering. Here $\alpha = 0$ and θ is varied from 0° to 60° and ϕ for 360°. The calculation is for a single frequency component which is 5 MHz. Now notice that from about 30° to 60° the the power falls off much faster for shear waves than for longitudinal waves (L waves and S waves

behave differently). Figure 14 shows the experimental results for the integrated power scattered from this oblate spheroid for L-L and L-S scattering. This variation from 30° to 60° is about 4 times faster for S waves than for L waves. Quantitative comparison between theory and experiment gives good results for L waves and poor results for S waves as shown in Fig. 15. The fact that ka = 2 for the L wave and 4 for the S wave gives the limitation on the Born approximation. It is significant though to point out that qualitative information can be obtained for even larger ka values from Born approximation.

Spheroid height, diameter, incident angle, minimum polar angle and frequency are:

400.0 microns, 800.0 microns, 0.0 deg., 120.0 deg., 5.1 MHz.

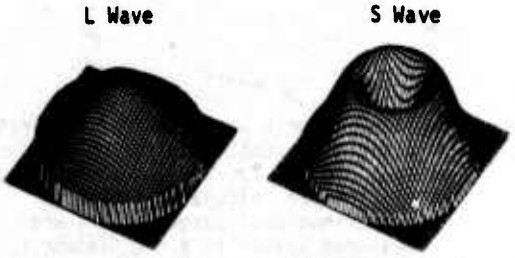


Figure 13. Calculated scattered field profile of a 5.1 MHz wave from a 400 x 800μ (diameter) oblate spheroidal cavity in titanium. α = 0°.

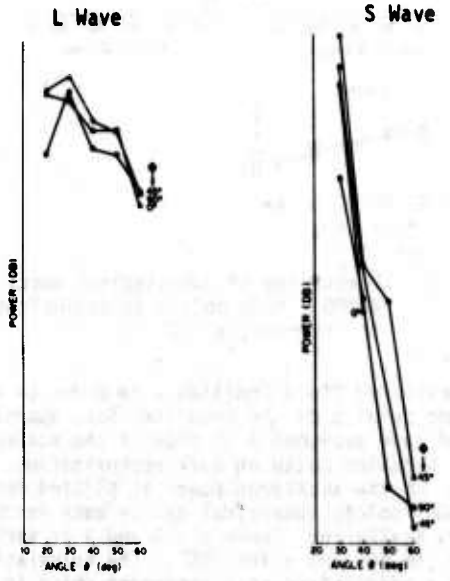


Figure 14. Integrated power vs. polar angle for scattered waves from 200 x 400μ oblate spheroidal cavity in titanium. α = 0°.

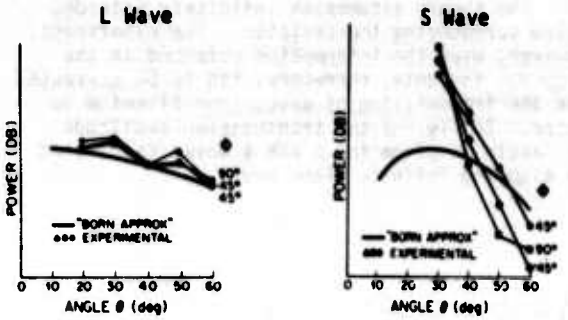


Figure 15. Power vs. polar angle for 5.1 MHz scattered waves from a 200 x 400μ oblate spheroidal cavity in titanium. α = 0°.

Position of Peak Frequency - In Fig. 16 the position of maximum frequency is plotted vs. polar angle for L waves and for S waves scattered from a 100 x 400μ oblate spheroid. The position of the maximum frequency for L waves is unchanged, but for S waves it varies down to about 3 MHz. Born approximation again predicts this behavior, qualitatively, given by the solid lines. It may be pointed out that the variation (slope) of frequency shift is half as much for the 200 x 400μ oblate spheroid as for the 100 x 400μ oblate spheroid. This information may be used to determine size.

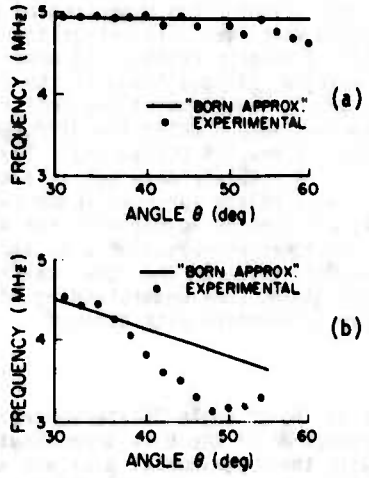


Figure 16. Maximum frequency shift as a function of polar angle for scattered (a) longitudinal and (b) shear waves from a 100 x 400μ oblate spheroidal cavity in titanium.

Normal Incidence - For non-normal incidence (or for α ≠ 0) the data for a given θ should have some φ dependence, as shown in Fig. 17, where the scattered L and S wave is given for α = 30 for

a 200 x 400μ oblate spheroid. This information may be used to determine orientation. Experimental results are shown in Fig. 18 for $\alpha = 20°$ for a scattered S wave from an oblate spheroid. The power varies with ϕ for constant θ and varies with θ for constant ϕ. For the peak frequency, 5.1 MHz, the variation in power is shown for both L and S waves in Fig. 19 for $\alpha = 20°$, $\theta = 20°$, 30°, and 40°. It appears that the ϕ dependence agrees better with theory for S waves than the θ dependence.

Spheroid height, diameter, incident angle, minimum polar angle and frequency are:

400.0 microns, 800.0 microns, 30.0 deg., 120.0 deg., 5.0 MHz.



Figure 17. Calculated scattered field for non-normal incidence $\alpha = 30°$ for 400 x 800μ oblate spheroidal cavity in titanium.

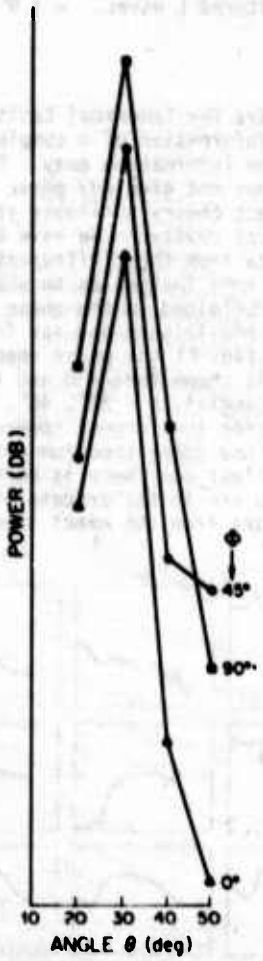
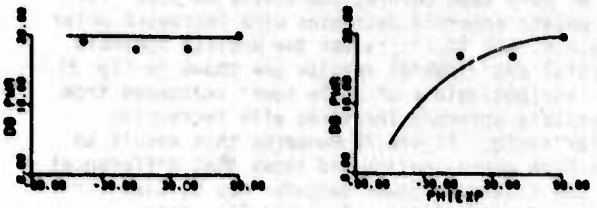


Figure 18. Integrated power vs. polar angle for S wave scattered from a 200 x 400μ oblate spheroidal cavity in titanium. $\alpha = 20°$.

Height, diameter, frequency, incident and polar angles are:

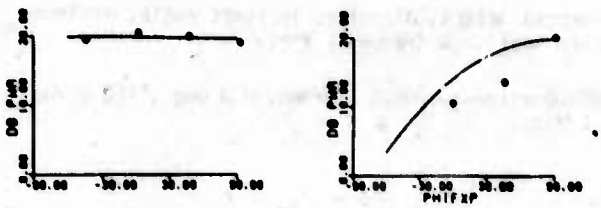
400.0 microns, 800.0 microns, 5.1 MHz, 20.0 deg., 20.0 deg.



1(a) 1(b)

Height, diameter, frequency, incident and polar angles are:

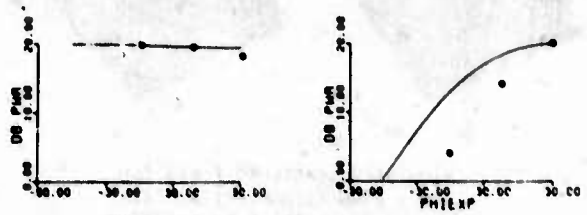
400.0 microns, 800.0 microns, 5.1 MHz, 20.0 deg., 30.0 deg.



2(a) 2(b)

Height, diameter, frequency, incident and polar angles are:

400.0 microns, 800.0 microns, 5.1 MHz, 20.0 deg., 40.0 deg.



3(a) 3(b)

Figure 19. Comparison between theory and experiment for variation of scattered amplitude vs. azimuthan angle for a 400 x 800μ oblate spheroidal cavity in titanium. $\alpha = 20°$.

1. $\theta = 20°$ (a) L wave (b) S wave

2. $\theta = 30°$ (a) L wave (b) S wave

3. $\theta = 40°$ (a) L wave (b) S wave

Comparison of Scattered L Field for Oblate and Prolate Spheroid - In Fig. 20 the scattered L wave and S wave for a 800 x 400μ prolate spheroid are shown for α = 0. The behaviors are quite different than for the oblate spheroid. As we have seen before, the scattered power for an oblate spheroid decreases with increased polar angle θ, but increases for the prolate spheroid. Initial experimental results are shown in Fig. 21. For various values of ϕ the power scattered from a prolate spheroid increases with increasing polar angle. Figure 22 compares this result to the Born approximation and shows that differences in the scattered power behavior may be used for shape identification. Incidentally, this observation is in agreement with physical intuition. The oblate spheroid behaves like a piston source and the end of the prolate spheroid would behave like a point source following the observed behaviors. Further insight may be gained by taking data on L-S scattering from prolate spheroids.

Spheroid height, diameter, incident angle, minimum polar angle and frequency are:

1600.0 microns, 800.0 microns, 0.0 deg., 120.0 deg., 5.1 MHz.

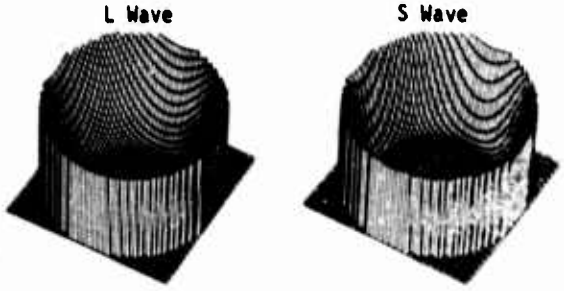


Figure 20. Calculated scattered field for 1600 x 800μ (diameter) prolate spheroidal cavities in titanium. α = 0°.

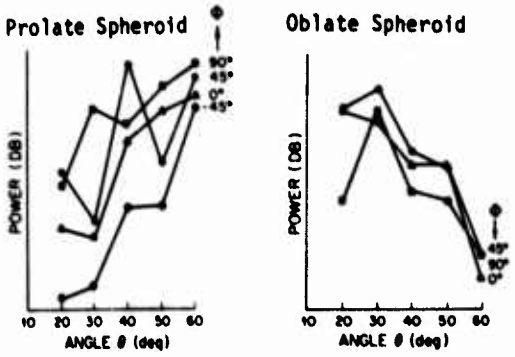


Figure 21. Integrated power vs. polar angle for L wave scattering.

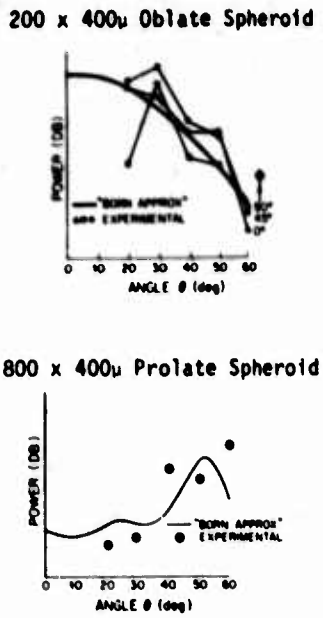


Figure 22. Integrated power vs. polar angle for scattered L waves. α = 0°

Phase Spectra for Spherical Cavities - Not to consider phase information of a complex signal is throwing half the information away. The Born approximation does not give any phase information and the only exact theory available at the moment is for a spherical cavity.[1] We have been taking L scattering data from three different sizes of spheres to gain some insight as to what type of information is contained in the phase spectra. Our results are preliminary and far from conclusive. In Fig. 23 the phase spectra for L-L scattering is shown for α = 0 and for three different polar angles, θ = 20°, 40°, and 60°. It appears that for the largest sphere there is no variation of the phase spectrum with angle and for the smallest one there is variation with polar angle. We are in the process of calculating this phase spectra from the exact theory.

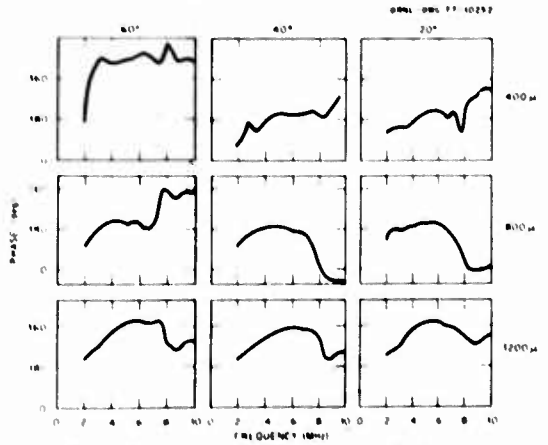


Figure 23. Phase spectra vs. polar angles for three different diameter spherical cavities in titanium.

Elastic Geometrical Theory of Diffraction for the Region ka $\geq$ 1 - As stated before, the L-L scattering for planar flaws and for ka $\geq$ 1, Keller's geometrical theory for electromagnetic waves, was successfully applied. By gaining more insight into the mode conversion problem we learned there are different types behavior from L-L and L-S scattering. We decided to tackle an elastic theory for geometrical diffraction. On the one hand, the semi-infinite plane for elastic problems was solved by Maue.[2] This result was taken and, following the concept of Keller, it was assumed that an incident L ray produces an S ray and an L ray (see Fig. 24). It is further assumed that the incident ray is proportional to the diffracted rays through D_L and D_S which are the diffraction coefficients for L waves and S waves, respectively. These diffraction coefficients are evaluated by comparing the exact solution from the half plane to a planar crack of arbitrary curvature. The solution is given in the far field. A similar procedure can be used to determine L and S diffracted fields for an incident S wave. Figure 25 gives a theoretical plot of the scattered L amplitude and phase spectrum for a 2500μ circular flaw. The dotted lines are the experimental amplitude spectrum which agrees well with theory. The calculated phase spectrum indicates that there is a sudden change in phase each time there is a minimum in the amplitude spectrum. Further experimental verification of this elastic diffraction theory is needed.

Conclusions

We have designed an experimental system which is capable of collecting a data base for quantitative flaw evaluation. The system is such that it can be used directly for a realistic NDT environment. Signal processing techniques have been applied to obtain information from scattering centers as small as 100μ in titanium--which may not be the lower limit. It has been established that both L-L and L-S scattering can be studied on an immersed system. These two types of scattering mechanisms provide useful and different information. With the same system, S-L and S-S scattering mechanisms will be studied. A data base is collected for several cavities with symmetrical geometry. Several key parameters of scattering have been identified which relate to size, orientation, and shape of the cavity such as variation of integrated power with polar angle and azimuthal angle, shift of frequency peak position with polar angle, the shape of this variation, phase spectra, etc. Direct comparison between theory and experiment establishes that the Born approximation holds well for ka < 2. On the other hand, for planar flaws and for larger ka geometrical theory of diffraction holds a lot of promise.

More experimental work and the development of a theory covering a large range of ka for crack-like flaws should be continued. Special emphasis should be placed on phase data which contain 50% of the information on scattering center.

ORNL-DWG 77-10253

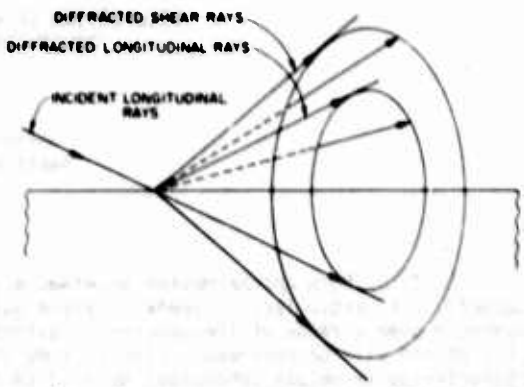


Figure 24. Schematic diagram for diffracted ray formation at an edge.

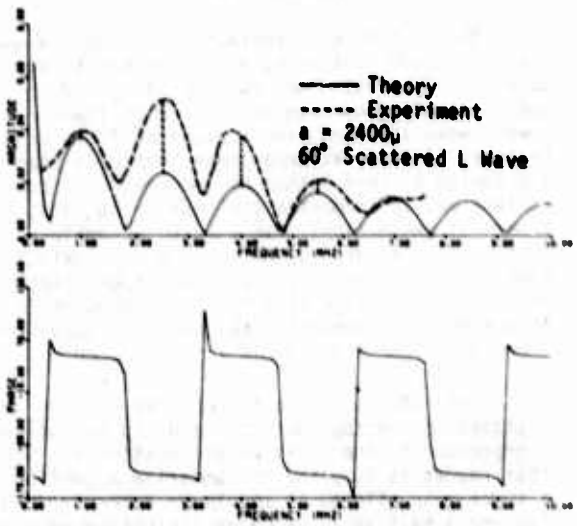


Figure 25. Plot of the scattered L amplitude and phase spectrum for a 2500μ circular flaw.

In summary, I would like to point out that in the last three years' effort the first attempt was made to supply NDT with a scientific base which can make the field a reliable quantitative tool of modern technology.

Acknowledgement

This research was sponsored by the Center for Advanced NDE operated by the Science Center, Rockwell International, for the Advanced Research Projects Agency and the Air Force Materials Laboratory under contract F33615-74-C-5180.

References

1. C. F. Ying and R. Truell, J. Appl. Phys., 27, 1086 (1956).

2. A. W. Maue, Z. Für Angew. Math. U. Mech., 33, 1 (1953).

UTILIZATION OF PHYSICAL FEATURES OF SCATTERED POWER FOR DEFECT CHARACTERIZATION

E. Domany
University of Washington
Seattle, Washington 98195

ABSTRACT

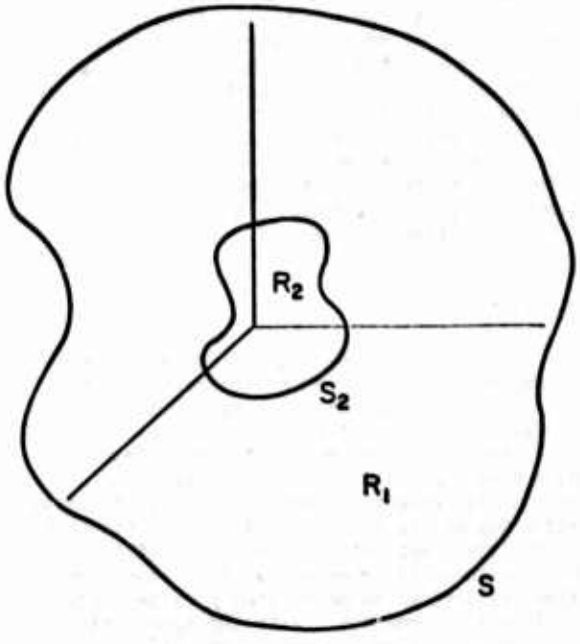
The first Born approximation provides a useful means to study scattering of ultrasound by various defects. In particular, it seems to yield qualitatively good results for the scattered power, when averaged over a range of frequencies. Features of the scattered power that have been discovered by this method will be reviewed. Closer study of some of these features leads to a step procedure to characterize an oblate spheroidal defect; to determine its orientation and shape. Procedures for extension to other shapes can also be given. Areas of future development will be indicated.

Introduction

The first Born approximation provides a useful means to study scattering of ultrasound by various defects. In particular, it seems to yield qualitatively good results for the scattered power when averaged over a range of frequencies. Features of the scattered power that have been discovered by this method are reviewed. A convenient way to summarize the scattering data, by numerical projections, was used to assemble a library of scattered power from various defects. Addressing the particular problem of an oblate spheroidal cavity, a step-by-step procedure to determine its orientation and shape is suggested. Areas of future development are indicated.

I will discuss some features of elastic waves scattered by various defects, and try to outline a procedure to characterize the scatterer. Since this report is supposed to summarize a portion of a three-year effort, it should be remembered that two and a half years of my participation were at Cornell, and only the last five months at the University of Washington. Thus most of the results that I will list were obtained in collaboration with various present and past members of Jim Krumhansl's group.[1] The last part of my presentation (Procedure to Determine Orientation and Shape) deals with new developments. Thus some of what I will say has been presented before.

Let me briefly review the general philosophy of the approach we chose to take. We started out with very little understanding of the scattering of elastic waves. We were quickly impressed by the mathematical complexity of the problem. The basic situation is depicted in Fig. 1; an incident elastic wave scattered by a defect. Exact solutions to this problem are available only for a limited class of scatterers. For scatterers of finite volume, only the spherical defect is soluble! Since deviations from spherical geometry were an important aspect of the program, we decided to consider various approximate treatments. The idea was to check the approximations against theory and experiment, and try to use them to provide us with some qualitative insight into the scattering mechanism.



$$R = R_1 + R_2$$
$$S_1 = S + S_2$$

Figure 1. The basic scattering situation, with scatterer R.

We hoped to characterize a general defect by an effective ellipsoid. Thus we were led to consider the simplest ellipsoid, i.e., a spheroidal cavity. Although we did concentrate on this object, we have also looked at cylindrical defects, prolate spheroids, and more recently extended our study to various cracks. The methods used were based mainly on the Born approximation,[2] and later on a quasi-static approximation.[3]

Our main concern was to try to isolate a few qualitative features, present those to experimentalists, and urge them to verify or discard them. We have benefited from those interactions, especially with Dr. B. Tittmann and Dr. L. Adler.

Another aspect I should mention was our collaboration with Dr. A. Mucciardi and R. Shankar of Adaptronics, whom we supplied with the Born approximation program to help train their computer.[4]

The structure of this report is as follows. In the discussion of "Physical Features of the Scattered Fields," a step-by-step procedure to characterize an oblate spheroidal cavity is presented. The second on "Areas of Future Development and Summary" summarizes and indicates areas of future development.

Physical Features of the Scattered Fields

By comparing the BA results with the exact solutions, we saw that for cavities the BA has a chance of being useful mainly in the backscattered regime. We also noticed that the BA misses the detailed frequency dependence of the scattered power, and does not contain any phase information. Thus we are led to consider the angular distribution of frequency averaged power.

Consider a scatterer characterized by two lengths, a,b (an oblate spheroid of width 2a and radius b is an example, but similar considerations hold for cylinders and "flat" objects of more general shape). Choose the axis a (the symmetry axis of the spheroid) as the direction of incidence of longitudinal waves. Within the integral equation formulation,[2,3] the defect is the source of the scattered waves. When viewed along the a-axis, an area $\sim b^2$ of the source is seen; while when viewed from the side (at 90° to the a axis) the area is $\sim ab$. Thus the ratio $R_1 = P_{180}/P_{90}$ of the backscattered frequency averaged power to that scattered at 90° is expected to increase with increasing b/a (or "flatness"). This qualitative picture was obtained by analyzing the results of the Born approximation for various scatterers. Within the approximation this behavior is predicted to hold quite independently of the detailed shape (i.e., for cylinders as well as spheroids). Experimentally,[5] it was checked for spheroids only - comparison of experiment and the Born approximation prediction is given in Fig. 2.

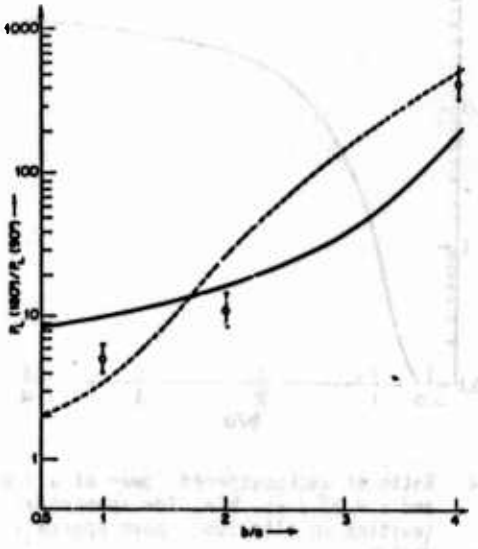


Figure 2. The ratio P(180)/P(90) for longitudinal power with longitudinal wave incident along symmetry axis of spheroidal cavities in Ti, vs. b/a of the scatterer. Uniform averages of $0<ka<1$ (full lines) and $9<ka<2$ (broken lines) were used. The circles are experimental results.

The experimental procedure involved in measuring this feature is a two transducer (pitch-catch) mode. An alternative mode of operation uses a single transducer (pulse-echo). This mode is useful to investigate the dependence of backscattered power on the angle of incidence. Obviously, for a spherical scatterer there is no preferred direction, and the backscattered power is independent of the direction of incidence. For a flat object, however, we expect more backscatter when the incidence is along the a-axis, than when along the b-axis. Thus, a variation of the backscattered power with angle of incidence, α, is another measure of the b/a ratio. Experiment and theory are compared on Fig. 3. On Fig. 4 we plot $R_2 = P_{180}(\alpha=0)/P_{180}(\alpha=90)$ as a function of b/a, for various spheroids.

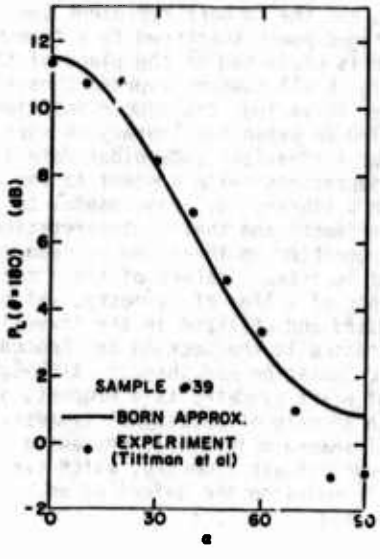


Figure 3. Backscattered longitudinal power P_L ($\theta=180°$), as a function of angle of incidence, α, for spheroidal cavity ($b=400\mu$, $a=200\mu$) in titanium. Rockwell transducer characteristics were used for the frequency averaging. The line is the Born approximation; dots are measurements (Tittmann, et al.).

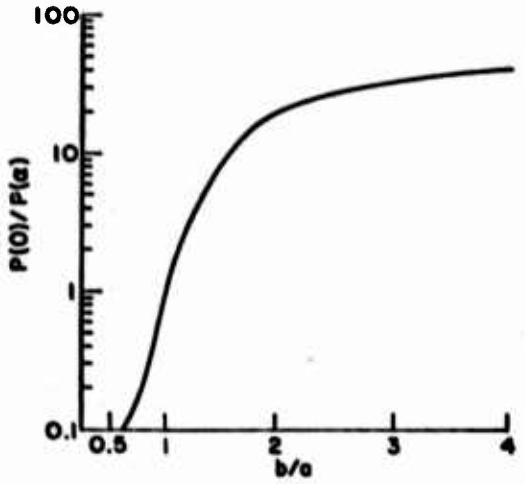


Figure 4. Ratio of backscattered power at $\alpha = 0$ and $\alpha = 90^\circ$, vs. b/a, for spheroidal cavities in titanium: Born approximation.

Both kinds of operational modes are most conveniently summarized in intensity projection maps. Figure 5 is an example of a pitch-catch mode experiment, and Fig. 6 is the same for a pulse-echo mode. In both cases the circle is the projection of an experimentally accessible "window." In Fig. 5 the source is at the center of the window, and the numbers represent the frequency averaged power scattered to a transducer whose position is projected to the plane of the figure. In Fig. 6 all numbers represent backscattered power to various transducer positions. We have compiled an extensive library of such projection maps for various spheroidal defect shapes and orientations (with respect to the window). Such a library may prove useful to decide on experiments and their interpretation, and also in suggesting an inversion procedure. One simple but important feature of these maps is the existence of a line of symmetry, which will be discussed and utilized in the inversion procedure discussed in the section on "Procedure to Determine Orientation and Shape." Although such a line of exact symmetry is a property of an object with an axis of rotational symmetry, a more general shaped object will possess a best line of approximate symmetry, which can be instrumental in modeling the defect by an effective spheroid.

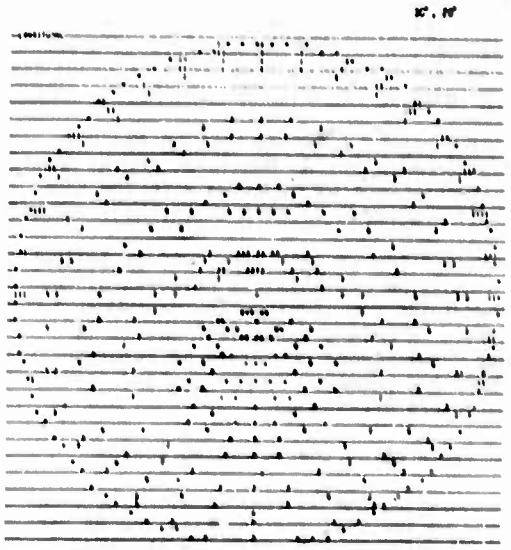


Figure 5. Projection map of frequency averaged longitudinal power. The transmitter is at the center of the circle, the perimeter corresponds to scattering at 90°. The defect is an oblate spheroid with b/a = 2, oriented at $\alpha = 30^\circ$ (α is the angle between the incident wave and the symmetry axis of the spheroid).

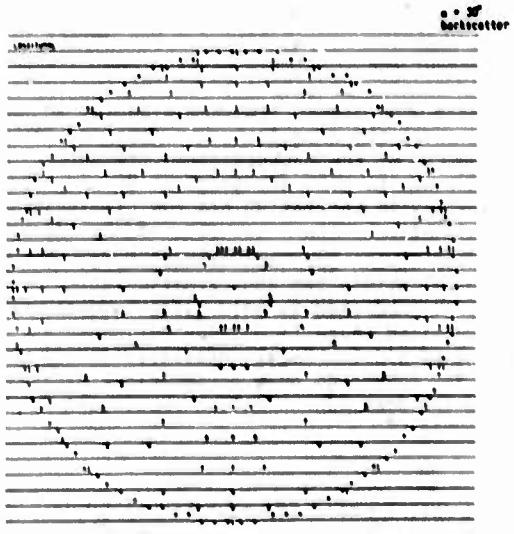


Figure 6. Same scatterer as Fig. 5; each number represents the backscattered power to a transducer operated in pulse-echo mode.

Procedure to Determine Orientation and Shape

Here we narrowed our attention to oblate spheroidal defects, viewed in a "window" of a 60° cone.

The geometry of the window and the defect is shown in Fig. 7. Since the same problem was treated by Mucciardi et al.[4] using an adaptive learning procedure, it seems appropriate to emphasize the difference between the two approaches. In the adaptive method one or more sets of measurements taken within the accessible window are analyzed in an empirical way. This approach aims at taking a fixed set of measurements, and performing the analysis after these were taken.

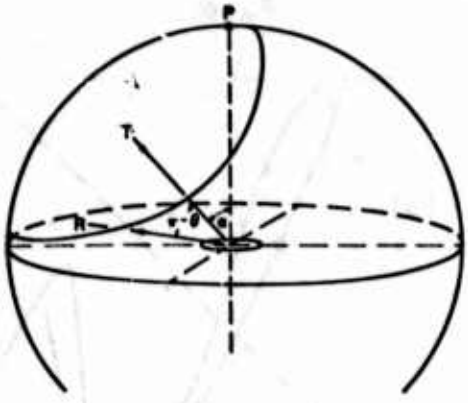


Figure 7. Geometry of experimental setup used to determine line of symmetry. The transmitter, T, is at the center of the window; α is the angle between the direction of incidence and the symmetry axis of the defect. This axis intersects the window at P. R is position of receiver, θ is the scattering angle. To determine the orientation we want to locate P. The line of symmetry connects P and T.

In contradistinction, the approach I follow is more interactive in character: the first set of measurements is analyzed, and the results of this analysis determine which second set of measurements to take. Since the analysis turns out to be quite simple, it is hoped that it can be performed "on line," and the resulting optimization of further measurements to be made compensates in terms of time and expenses.

The shortcoming of this approach is that it is harder to verify directly at this stage, since it requires closer interaction between analysis and experiment. One cannot take a complete set of measurements and assign them to analysis as a "homework exercise." Let us proceed now to outline the procedure step by step.

Orientation - (Step 1) When the central transducer of the array is used as the source, the scattered power is symmetric about the plane defined by the direction of the incident power and the symmetry axis (Fig. 1). We considered three sets of measurements taken by B. Tittmann, and tried to determine the plane of symmetry by a best-fit method based on three Legendre polynomials.[6] In two cases we were able to determine the symmetry plane to within 2°; in case 3 to within 20°. Note that this is not a check on theory, but rather on experimental accuracy. I would conclude that improved analysis (taking measurement errors into account) will provide a scheme to determine the line of symmetry to within 5-10°. Since this line runs through the center of our array and the symmetry axis of the defect, we can proceed to find the exact location of the axis.

(Step 2) Having found the line that contains the symmetry axis, we proceed utilizing one of the features that were discussed previously in "Physical Features of the Scattered Fields." We operate transducers in the pulse-echo mode along this line. Plotting backscattered power vs. positions, we get a curve like Fig. 3. The window specification is such that we either have access to both the major and minor axes, or at least to one of them. Thus the measured curve will exhibit either both a minimum and maximum, or one of these. In any case it is sufficient to pin down the orientation of the defect.

Shape and Size - I have tried to use various features of the scattered power to determine shape and size. This, however, seems to be a hard problem: we need two features at least to determine the two unknowns (b/a and absolute size). Various pairs of features that I considered did not provide sufficient resolution to make possible a reliable determination for any arbitrary position of the experimentally accessible window. If we have a reasonable estimate of the absolute size, using features from Fig. 2 or 4, b/a will be determined. But when both absolute size and b/a are unknown, the geometrical restriction and experimental error make a simultaneous determination of both quite unreliable (i.e., with large uncertainty).

However, seeing some of Bernie Tittmann's data, a most intriguing possibility emerged.[7] Consider the two curves in Fig. 8. These are backscattered amplitudes vs. frequency, taken at two angles of incidence, $\alpha = 0$ and $\alpha = 60°$, $A_0(f)$ and $A_{60}(f)$.

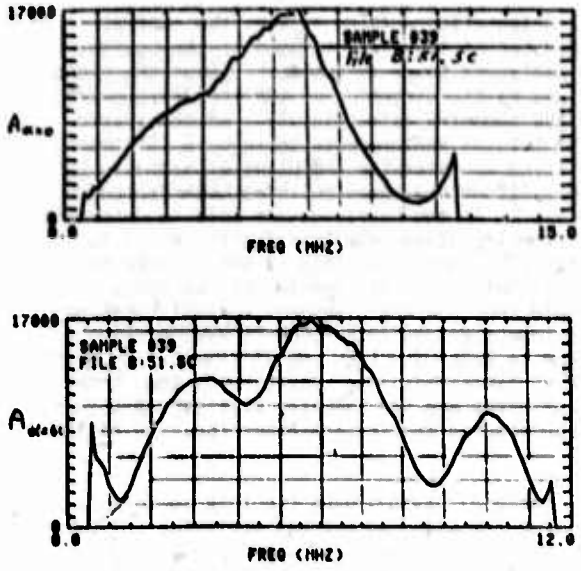


Figure 8. Amplitude vs. frequency of backscattered wave from oblate spheroid (b = 400μ, a = 200μ) in Ti, for angle of incidence α = 0°, and α = 60°.

We can now plot A_0 vs. A_{60}, using f as a parameter (see Fig. 9). This way we produce a universal curve for a spheroid of a given shape (i.e., b/a). Absolute size will determine only how far, for a given transducer, we can trace the curve. Note that for a sphere we obtain the straight line $A_0 = A_{60}$. Similar analysis of phase information will make this method even more powerful. Again, this prediction is independent of any approximation.

For comparison, we presented a similar plot for a spheroid of large b/a ratio. Clearly, the extent of deviations from a straight line is different: thus we can use these curves to predict b/a, and then from the length of the curve obtain the absolute size.

Areas of Future Development and Summary

As indicated by the last section, development of approximations that yield reliable frequency and phase information seem to be the most important issue at hand; although development of sophisticated inversion schemes based on currently available approximations does seem to be fruitful. I believe that the inversion problem will also be much simplified if one has a good handle on frequency and phase information.

Approximations with this aim in mind are currently developed,[10] and will be discussed by others. My main effort will be directed towards developing the distorted wave Born approximation, utilizing the exact solution for spheres to study scattering by ellipsoidal defects.

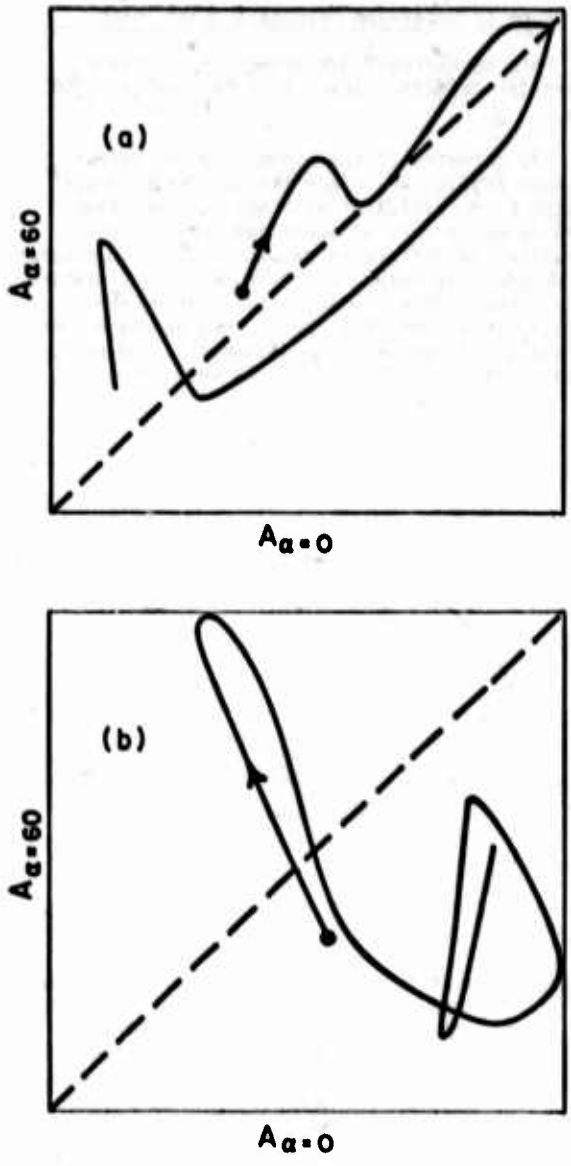


Figure 9. Plot of equally normalized amplitude, $A_{60}(f)$ vs. $A_0(f)$, using the frequency f as a parameter. The heavy dot indicates f = 2 MHz, and the arrow the direction of increasing f. The dashed line is the expected curve for a spherical defect.

(a) b = 400μ, a = 200μ
(b) b = 400μ, a = 100μ

Acknowledgements

I have greatly benefited from advice and encouragement from J. A. Krumhansl, J. E. Gubernatis, D. O. Thompson, B. Thompson, L. Adler and many others. I enjoyed a particularly pleasant and fruitful interaction with B. Tittmann, whose experiments provided both stimulus and insight, and shaped my approach to the problem. B. Delaplain helped me in developing and programming the best fit analysis of the symmetry line.

This research was sponsored by the Center for Advanced NDE operated by the Science Center, Rockwell International, for the Advanced Research Projects Agency and the Air Force Materials Laboratory under contract F33615-74-C-5180.

References

1. J. A. Krumhansl, E. Domany, J. E. Gubernatis, P. Muziku, S. Teitel, D. Wood, Interdisciplinary Program for Quantitative Flaw Definition, Special Report Second Year Effort, p. 102.

2. J. E. Gubernatis et al., J. Appl. Phys., to be published.

3. See J. E. Gubernatis, this report.

4. R. Shankar, A. N. Mucciardi, M. F. Whalen, and M. D. Johnson, this report.

5. The experiments quoted here and elsewhere in this report were performed by B. R. Tittmann and R. K. Elsley, Science Center, Rockwell International; see this report and references therein.

6. B. Delaplain and E. Domany, unpublished.

7. E. Domany and B. R. Tittmann, to be published.

8. N. Bleistein and J. K. Cohen, this report.

9. J. Rose and J. A. Krumhansl, to be published.

10. Y. H. Pao, previous work; Y. H. Pao and V. Varadan, "Proceedings, ARPA/AFML Review of Progress in Quantitative NDE," Cornell University, June 14-17, 1977, and references therein (to be published).

INVERSION OF ULTRASONIC SCATTERING DATA TO MEASURE DEFECT SIZE, ORIENTATION, AND ACOUSTIC PROPERTIES

R. Shankar, A. N. Mucciardi, M. F. Whalen, M. D. Johnson
Adaptronics, Inc.
McLean, Virginia 22101

ABSTRACT

Empirical solutions via the adaptive learning network methodology have been obtained to measure characteristics of three-dimensional defects (spherical and spheroidal) from the analysis of theoretically-modeled scattered waveforms. The solutions have been successfully applied to measure defects from actually observed ultrasonic scattering data. Spherical voids and inclusions in Ti-6-4, varying in diameter from 0.02 cm to 0.12 cm, and varying in acoustic impedance ratio [with respect to the host alloy (Ti-6-4)] from zero for air cavities to four for tungsten-carbide inclusions, can be directly measured via: (i) The phase cepstrum - which yields an unambiguous measurement of defect diameter and is independent of its acoustic impedance ratio; (ii) Adaptive Learning Networks (ALN) - synthesized from the amplitude spectrum and which yield accurate measurements of defect diameter and the acoustic impedance ratio of the included material. The two empirical solutions, synthesized from the scattering data from an exact model for spheres, yield similar accurate results when applied to actual scattering observed from the defects. Spheroidal defects (oblate spheroids) varying in aspect ratio from 1.67 to 6, varying in volume from 20 to 310 millionths of a cubic centimeter, and varying in orientation from 0° to 360° in azimuth and 0° to 90° in elevation, can be measured by adaptive learning networks synthesized from scattering data produced by the Born approximation as the theoretical model. Scattering data used to train the ALNs were obtained via computer simulation. As in the case of spheres, the ALNs were trained--using the synthetic waveforms--to predict the defect size and orientation. Once the empirical models were obtained, eight actual defect sizes and orientations were found via the models and these results compare well with the true values. This paper will describe the means by which the inversion of ultrasonic scattering to defect characteristics was accomplished and its NDE implications.

Introduction

The determination of the characteristics of subsurface defects in materials by non-invasive techniques is an important and challenging task in the non-destructive evaluation (NDE) of materials. This report presents results of a study in which characteristics of spherical and spheroidal defects, imbedded in a Ti-6-4 alloy, were measured accurately by analysis of the ultrasonic energy scattered from these defects.

The description of the scattering wave equations for defects of known geometries and material properties--the "forward" problem--has been a topic of several investigations. Ying and Truell[1] derived the equation for defects with spherical symmetry. Gubernatis and Domany[2] have used the Born approximation to the exact equations to describe spheroidal defects. From the NDE standpoint, the interest has been in the solution of the "inverse problem"; namely, how can the defect characteristics be described knowing the theoretical, or observed, scattering wave function. Studies by Tittmann and Cohen[3] and Sachse and Chian[4] show some measure of success in the solution of the inverse problem. Tittmann[3] concluded that the Born approximation to the exact theoretical scattering by spheroidal defects matches insufficiently the observed scattering from actual defects. Sachse and Chian[4] identified "echoes" in the scattered signature and related the arrival times of these echoes to defect geometry.

The specific objectives of this research were to:

(1) Synthesize adaptive learning network (ALN) models to measure the size (i.e., diameter) and acoustic impedance of spherical defects from the analysis of theoretically scattered waveforms.

(2) Evaluate the spherical defect ALN models for observed scattering from actual spherical defects.

(3) Synthesize ALN's to estimate the size and orientation of spheroidal defects from the analysis of the Born approximation to the exact theoretical scattering model.

(4) Evaluate the spheroidal defect ALN models for observed scattering from actual spheroidal defects.

In accordance with the above objectives, empirical solutions via the adaptive learning network methodology were obtained to measure the size and orientation of three-dimensional defects (spherical and spheroidal) from the analysis of theoretically-modeled scattered waveforms. The solutions were successfully applied to measure real defects from actually observed ultrasonic scattering data.

Spherical Defect Measurement from Theoretical Scattering

Spherical voids and inclusions in Ti-6-4, varying in diameter from 0.02 cm to 0.12 cm, and varying in acoustic impedance ratio (with respect to the host alloy Ti-6-4) from zero, for air

cavities, to four, for tungsten-carbide inclusions, were directly measured from their theoretically scattered waves via:

(1) The phase cepstrum - which yielded a measurement of defect diameter that was independent of its acoustic impedance ratio.

(2) Adaptive Learning Networks (ALN) - synthesized from the amplitude and phase spectra and which yielded accurate measurements of the acoustic impedance ratio of the included material independent of defect diameter.

The first solution means that defect diameter can be measured from a phase cepstral analysis of the theoretically scattered waveform. The phase cepstrum is a transformation of the phase of the scattered signal and was developed by Adaptronics during the course of this study.

A plot of the measured diameter as a function of the true diameter is displayed in Fig. 1. The results show an excellent agreement. The diameter was measured to within the spatial resolution imposed by the data collection system. Additionally, the measurement was independent of the acoustic impedance of the defect--at least over the range of impedance values present in the theoretical data set.

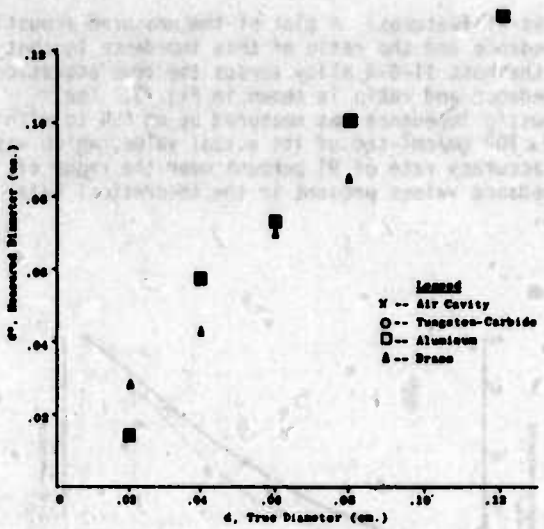
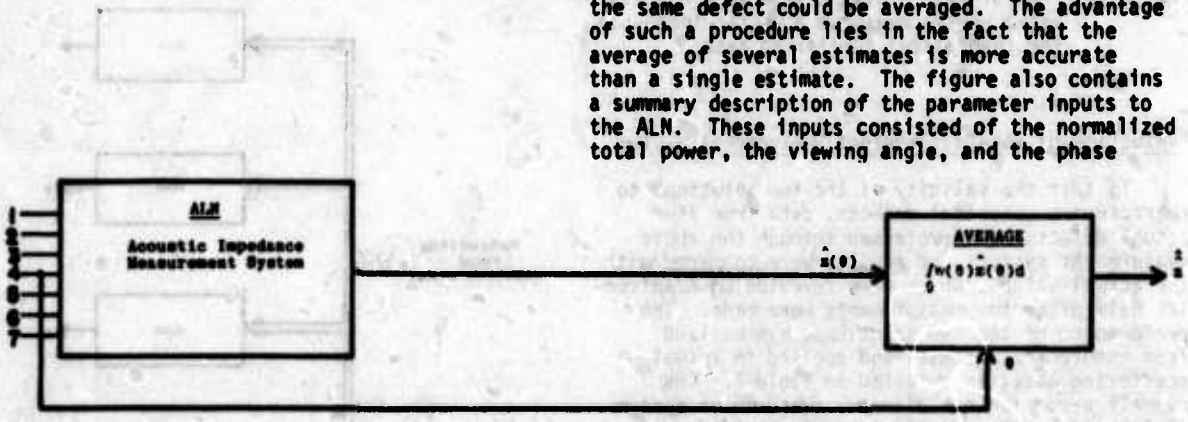


Figure 1. Plot of measured diameter versus true diameter based on phase cepstral analysis of theoretically scattered ultrasonic wave from spherical defects.

The second solution to the measurement of spherical defects provides a means of quantifying the acoustic impedance independent of defect size. A procedure, illustrated in Fig. 2, was devised wherein multiple acoustic impedance estimates of the same defect could be averaged. The advantage of such a procedure lies in the fact that the average of several estimates is more accurate than a single estimate. The figure also contains a summary description of the parameter inputs to the ALN. These inputs consisted of the normalized total power, the viewing angle, and the phase



CANDIDATE INPUTS FOR ALN

SOURCE	PARAMETER	FORMULATION	DESCRIPTION
Magnitude Spectrum	x_1	$\int_f \frac{A^2(f,d,\theta)}{A^2_{max}(d,\theta)}\,df$	Total energy in scattered signal, normalized by its maximum power
-	x_2	π/θ	Ratio of back-scatter to viewing angle
-	x_3	$\sin(\pi - \theta)$	-
-	x_4	θ	Viewing angle
Magnitude Spectrum	x_5	$\int_f \frac{x_1}{\frac{A^2(f,d,\pi)}{A^2_{max}(d,\pi)}}\,df$	Ratio of $x_1(\theta)$ to $x_1(\pi)$
Phase Spectrum	x_6	$q(\theta)$	Peak location (in micro-seconds) in phase cepstrum
Phase Spectrum	x_7	$1/q(\pi)$	Inverse of x_6 at π, back-scatter

Figure 2. Quantitative spherical defect acoustic impedance measurement system.

cepstral features. A plot of the measured acoustic impedance and the ratio of this impedance to that of the host Ti-6-4 alloy versus the true acoustic impedance and ratio is shown in Fig. 3. The acoustic impedance was measured by an ALN to within 5.0×10^5 gm/cm^2-sec of its actual value, which was an accuracy rate of 91 percent over the range of impedance values present in the theoretical data set.

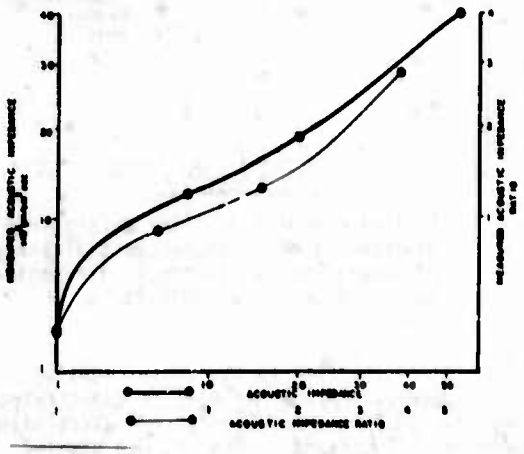


Figure 3. Plot of true acoustic impedance and its ratio versus measured acoustic impedance for theoretical scattering data.

Evaluation of Spherical Defect Measurement System

To test the validity of the two solutions to characterize spherical defects, data from four actual defects were processed through the above measurement systems and results were compared with the actual values, which were revealed to Adaptronics only after the measurements were made. The performance of the two solutions, synthesized from theoretical studies and applied to actual scattering data, is detailed in Table 1. The overall error for the diameter measurement system (0.015 cm) compared well with the resolution of the data collection system. The average absolute error in the acoustic impedance measurement was 7.6×10^5 gm/cm^2-sec over the range of impedance values, which compared satisfactorily with the accuracy rate for the theoretical data set (91%).

Table 1. Performance of spherical defect measurement system, synthesized from theoretical studies, on sample real spherical defects.

Sample	Solution 1: Phase Cepstral Analysis (Diameter (in cm)) True	Measured	Error	Solution 2: ALN Measurement System (Impedance (in 10^5 gm/cm^2-sec)) True	Measured	Error
Air Cavity	.04	.030	0.010	0.0	10.0	10.00
Air Cavity	.08	.076	0.004	0.0	0.0	0.00
Air Cavity	.12	.120	0.000	0.0	0.0	0.00
Tungsten-Carbide Inclusion	.08	.030	0.050	35.0	34.3	20.70
	Average Absolute Error		0.015			7.68

Spheroidal Defect Measurement from Theoretical Scattering

Spheroidal defects (oblate spheroids) varying in aspect ratio from 1.67 to 6, varying in volume from 20 to 310 millionths of a cubic centimeter, and varying in orientation from 0° to 360° in azimuth and 0° to 90° in elevation, were measured by adaptive learning networks synthesized from scattering data produced by the Born approximation to the theoretical model. As in the case of spheres, the ALN's were trained using the theoretical waveforms to predict defect size and orientation.

The spheroidal defect size and orientation measurement system is illustrated schematically in Fig. 4. The measurement system consists of four ALN's which compute, for oblate spheroids:

- minor axis, A (ALN1)
- major axis, B (ALN2)
- elevation orientation, α (ALN3)
- azimuthal orientation, β (ALN4).

These networks were synthesized from a vector of parameters computed from the theoretically scattered spectral waveforms observed at a circular array of receivers located symmetrically around the defect region.

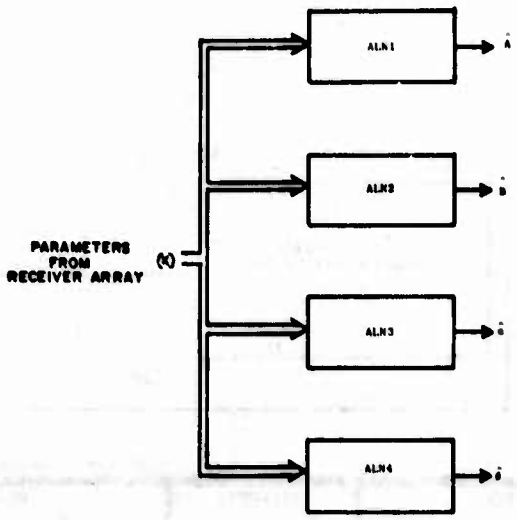


Figure 4. Quantitative spheroidal Adaptive Learning Network (ALN) defect measurement system.

The performance of the ALN's in measuring defect size and orientation from the theoretical scattering studies is summarized in Table 2. Each entry in the table corresponds to the absolute error in the appropriate component of the measurement system when averaged over defect orientation variations in both elevation and azimuth. An overall percentage error for each

component is indicated in the last row. The defect size was measured to within 21.7 percent of the true value for A (ALN1) and to within 9.2 percent of the true value for B (ALN2). These error rates translate to an average discrepancy in size measurement of the order of 55 microns (the average of the first two entries in the penultimate row). The defect orientation was measured with a 14 percent error in elevation, α (ALN3), and a 5 percent error in azimuth, β (ALN4). Since the elevation angle was restricted to variations in a single quadrant (0-90°), the error rate in α is an angular discrepancy of 12.6 However, the azimuthal orientation, β, varied over a 360° span and a 5 percent error rate translates to an angular discrepancy of 18°. The average angular discrepancy is 15° (average of last two entries in penultimate row).

Table 2. Performance of spheroidal defect measurement system for theoretically scattered waveforms from defects.

True Size (A x B)	Average Absolute Error: Size — ALN1 A, Minor Axis	Size — ALN2 B, Major Axis	Orientation — ALN3 α, Elevation	Orientation — ALN4 β, Azimuth
50 x 300	77.0	53.0	11.0	19.3
150 x 300	36.0	36.0	13.0	20.0
100 x 400	71.3	40.0	7.0	17.7
300 x 400	65.7	36.0	13.4	16.3
100 x 500	87.4	60.0	18.0	14.0
300 x 500	110.0	66.0	17.1	16.0
Average Absolute Error (All Sizes)	65.3	48.0	13.6	16.8
Percent Average Absolute Error (All Sizes)	21.7	9.2	14.0	9.0

Errors are averaged over different elevation and azimuth orientations.

The performance of the spheroidal defect measurement system on theoretical scattering data indicates that the inverse problem was solved with excellent accuracy using a family of ALN's.

Evaluation of Spheroidal Defect Measurement System

As in the case of spherical defects, the spheroidal defect measurement system was applied to actual scattering data from a variety of sample, real, oblate-spheroidal defects. The computed size and orientation were compared to their actual values. These actual values were revealed to Adaptronics only after the measurements were made.

In spite of the several deficiencies existent in the Born approximation to the theoretical scattering model when compared to the actual scattering phenomenon[2,3]--and the fact that the measurement system was synthesized from the former --a remarkable agreement was found between the actual values and the measured values, as listed in Table 3. The defect size was measured to within 15 percent of the true value of A and to within 37 percent for B. Thus, the size measurements differed from the true values by an average of 26 percent. In terms of length, the average error was 90 microns, which compared fairly well with the theoretical data set (50 microns). The orientation was measured to within 26 percent of the true value of α and to within 2.2 percent of β. In other words, the average angular error for both of these measurements was approximately 15 degrees, which matched exactly the error obtained for the theoretical data set.

Table 3. Performance of spheroidal defect measurement system, synthesized from theoretical data on actual scattering data from real defects.

	SIZE (In Microns)				ORIENTATION (In Degrees)			
	ALN1*		ALN2		ALN3		ALN4	
DEFECT NO.	TRUE A	MEAS. $\hat{A}$	TRUE B	MEAS. $\hat{B}$	TRUE α	MEAS. $\hat{\alpha}$	TRUE β	MEAS. $\hat{\beta}$
1	200	184	400	488	0	37	-	197
2	300	169	400	688	30	3	288	218
3	100	100	400	500	60	68	180	188
4	100	114	400	381	0	0	-	-
5	200	208	400	530	60	28	180	174
6	100	128	400	588	30	60	180	198
7	200	114	400	500	30	21	180	178
8	100	130	400	648	30	48	288	218
AVERAGE ABSOLUTE ERROR		30		148		22		8
PERCENT AVERAGE ABSOLUTE ERROR		15.0		37.3		26.6		2.2

* See Figure 4

The performance of the spheroidal defect measurement system on actual scattering data proves conclusively that not only does a family of ALN's invert theoretical scattering data, but it also has been successfully applied to invert actual scattering data from real defects.

Description of Data Base Used to Synthesize and Evaluate ALN Defect Models

Four categories of ultrasonic scattering data were used throughout the course of this study for the design and evaluation of ALN models to estimate the characteristics of sub-surface defects in metals:

(1) Theoretically generated complex Fourier spectrum from spherical defects.

(2) Experimentally observed time waveforms from spherical defects.

(3) Theoretically generated power spectrum from spheroidal defects.

(4) Experimentally observed time waveforms from spheroidal defects.

The data from Category 1 originated from studies by Tittmann and Cohen[3] and were computerized by Elsley, all of the Rockwell International Science Center. For spherical defects, it was possible to obtain exact scattering relationships. For spheroidal defects (i.e., prolate or oblate spheroids

with one axis of symmetry), the Born approximation was used to generate data of Category 3. A computerized version of the Born model was developed by Krumhansl, Gubernatis, and Domany of Cornell University.[2] This program was later modified by Johnson and Whalen of Adaptronics to enable spheroidal scattering to be obtained for any given transmitter and receiver position and defect spatial orientation. The data of Categories 2 and 4 were collected in experiments performed by Tittmann and Elsley at the Rockwell International Science Center. The details of the data generation procedure are described in the remainder of this chapter.

Theoretical Sphere Data Generation - A spherical defect (either an air cavity or one of three metal inclusions) of diameter, d, was ultrasonically illuminated by a transmitter. Five diameters were considered: 0.02, 0.04, 0.06, 0.08, and 0.12 cm. The scattered energy was generated and recorded by transducers equidistant and coplanar with the defect. The location of the transmitter, referred to as the back-scatter position ($\theta = 180^\circ$), remained fixed but the receivers could be placed anywhere in an arc extending from 180 degrees to 62.2 degrees (in 6.2-degree increments) for a total of 20 different positions. The transducer position relative to the spherical defect and the "pitch-catch" data recording arrangement are illustrated in Fig. 5.

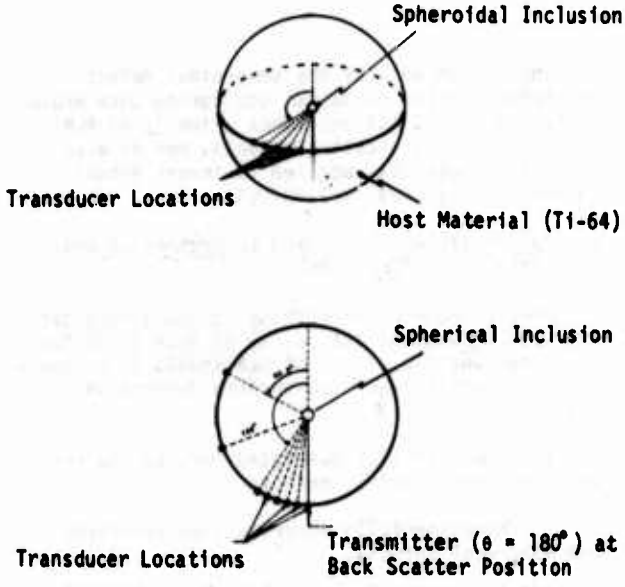


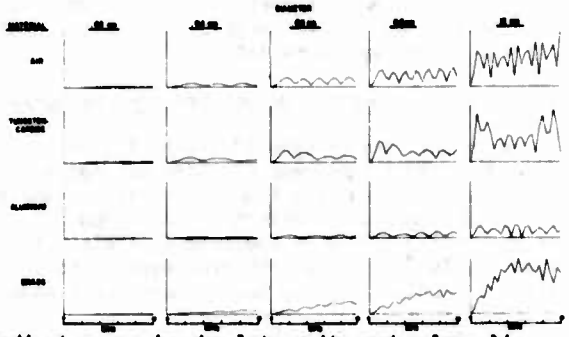
Figure 5. Perspective and stereographic view of data collection procedure for spherical defects.

The transmit signal was an ideal broadband pulse with equal energy from 0 to 10.156 MHz, sampled every 0.39 MHz, for a total of 27 frequency values. The transmitter and receiver responses were assumed to be ideal (flat spectrum in this frequency range). Thus, the digitized spectrum consisted of 27 complex values (cosine and sine coefficients) for each of the 20 angular locations of the receiver transducers.

The experiment further simulated the condition in which the transmitter and receiver could be in any of four different polarization modes. In Mode P = 1, the transmitter sent longitudinal waves and the receiver collected the scattered longitudinal waves. In Mode P = 2, the transmit wave was longitudinal and the receiver wave was the mode-converted shear wave. Mode P = 3 represented one shear wave to another shear wave for perpendicular polarizaiton, and Mode P = 4 represented parallel shear wave polarization.

The total back-scattered energy is determined by both the size of the defect and its material properties; the latter is characterized by the acoustic impedance which is defined as the product of wave velocity and defect-material density. It is known that, for a given defect-material, a larger defect produces larger total back-scattered energy. Conversely, for a given defect size, the amount of impedance "mismatch" between the defect and host materials influences the total back-scattered energy. Thus, "strong" and "weak" scatterers are distinguished by the defect impedance values being significantly different from and similar to, respectively, the host impedance.

The theoretical back-scatter spectral plots from the five different defects are displayed in Fig. 6 for each of the four defect materials. The transmitter and receiver are in Mode 1 polarization. The ordinates are in absolute units and vary from 0 to 0.003 and the abscissae signify frequency variations from 0 to 10 MHz. The first two rows in the figure contain responses from the strong scatterers--air cavities and tungsten-carbide inclusions--which have impedance values markedly different from the host. The last two rows contained spectral responses from the weak scatterers --aluminum and brass inclusions.

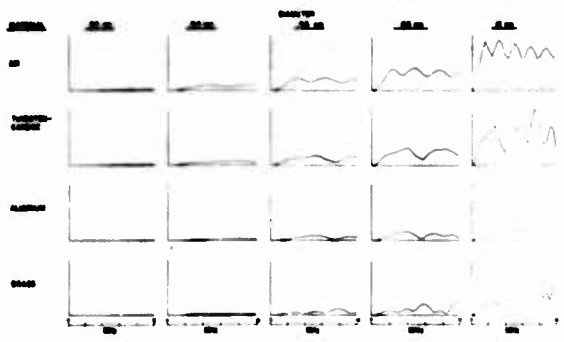


Ordinates are in absolute units and values lie between 0 and .003. Abscissae are frequency variations from 0 to 10 MHz.

Figure 6. Theoretical back-scatter spectral plots - polarization mode 3.

For a given size, the strong and weak scatterers have a noticeable difference in the energy levels, as evidenced in the plots. (For 0.02 cm defects, the spectra of scattered energy from brass and aluminum inclusions were too small to be represented.) In addition to variations in energy levels for different type scatterers, periodicities or "interference patterns" are noticed in the spectrum; these periodicities are much more frequent for larger defect diameters. This confirmed observations made by Sachse and Chian,[4] who postulated that interference patterns were manifest because components of the scattered wave were in-phase or out-of-phase with the primary reflection--depending on the defect diameter being an even or an odd multiple, respectively, of the half-wavelength. Adjacent "troughs" or "crests" in the interference patterns were discovered to occur for wavelength differences equal to the diameter. Thus, the frequency spacing of the patterns was inversely proportional to defect diameter.

A further confirmation of this phenomenon is provided by the plots in Fig. 7 (which is similar to Fig. 6, except that the transmitter and receiver are in Mode 3 shear wave polarization). The interference patterns are more evident in this figure because, for the same frequency range, wavelengths present in a shear wave are twice as small as those in longitudinal wave. Availability of the smaller wavelengths causes interference patterns to be manifest for smaller defect diameters. For example, the smallest half-wavelength in Mode 3 is 0.015 cm (shear wave velocity in Ti-6-4 of 3.03×10^5 cm/sec divided by twice the highest frequency, 20 MHz) and is comparable to the smallest defect size (0.02 cm). However, the smallest half-wavelength in Mode 1 (0.03 cm) precludes its existence of interference patterns for smaller defects.



Ordinates are in absolute units and values lie between 0 and .003. Abscissae are frequency variations from 0 to 10 MHz.

Figure 7. Theoretical back-scatter spectral plots - polarization mode 1.

In conclusion, the energy level of the scattered signature was an indicator of the type of scatterer (defect material), although not independent of size. The frequency spacing of the spectral interference patterns was an indicator of the defect size--again not independent of defect type. Methods by which spectral parameters can be computed that exploit either defect size or material characteristics exclusive of the others which are described in "Spherical Defect Data Signal Preprocessing and Feature Extraction."

Experimental Sphere Data Description - Experimental waveforms from spherical defects were recorded and digitized following the same measurement protocol as described in "Theoretical Sphere Data Generation" (Fig. 5). Each experimentally recorded waveform consisted of 5 microseconds of amplitude data samples at a 100 MHz rate. Thus, the highest frequency of 50 MHz was five times larger than the highest frequency available in the theoretical data base (which was 10.156 MHz). Moreover, the experimental waveform consisted of the scattered signature in only one mode of polarization--the longitudinal-to-longitudinal, P = 1 Mode--whereas the theoretical set consisted of four separate modes.

Composite plots of the actually observed back-scatter time signatures and their power spectra for two sample air cavities and a tungsten-carbide inclusion are presented in Fig. 8. The dotted line on each spectral plot shows the transducer response. The ordinate for each plot has been normalized between 0 and 1 by dividing each point on the original waveform by its maximum value. The abscissae for the time signatures extends from 0 to 1.2 microseconds, and, for the spectra, from 1 to 13 MHz. Unlike the theoretical spectra, the actual spectra peak at approximately 3 MHz--the nominal transducer rating. However, the interference patterns observed in theory are evident on the spectral envelope (indicated by the dotted curves).

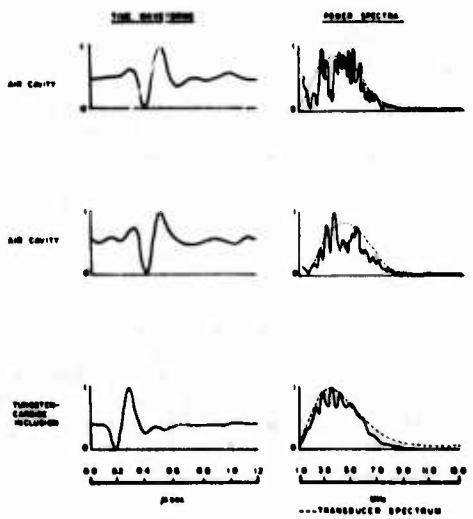


Figure 8. Experimentally observed signatures and their power spectra from sample real defects.

Therefore, to make a valid comparison between the theoretical and actual scattered spectra, a necessary precondition is the removal of the band-limited transducer response from the actual. This can be effected by deconvolution of the transducer spectra from the actual response. Conversely, the theoretical spectra could be convolved with the transducer response for comparison purposes.

For spherical defects, the former course of action was chosen to render the actual data relatively free of transducer modifications. Further, the larger bandwidth of the experimental data (50 MHz) was reduced to 10 MHz to make valid comparisons between theory and experiment.

Thus, as an initial preprocessing step, both the theoretical and experimental data were placed on a comparable basis: (i) transducer response ideal, and (ii) equal bandwidths of 10 MHz.

Theoretical Spheroid Data Generation - The transmitter and receiver spatial configurations for spheroids differed from those for spherical defects because a spheroid exhibited scattering patterns dependent on its orientation relative to the transmitter. Here the objectives were to determine both the size and orientation parameters of the spheroid, given the received spatially-distributed scattering information. The following definitions describe the spatial positions of the transmitters, receivers, and the spheroid; a spherical coordinate system was used.

A = minor axis radius (i.e., half the height of the scatterer); measured in microns.

B = major axis radius (i.e., half of the width of the scatterer); measured in microns.

α = elevation angle of the scatterer, measured between positive Z-axis and axis of symmetry of defect (i.e., along A); measured in degrees.

β = azimuthal angle of the scatterer, measured in the X-Y plane, between the positive X-axis and the projection of spheroid axis of symmetry onto the X-Y plane; measured in degrees.

θ = elevation angle of the transmitters and receivers, measured from the negative Z-axis, measured in degrees.

ϕ = azimuthal angle of the transmitter and receivers, measured from the positive X-axis, measured in degrees.

An oblate spheroid with the above size and orientation parameters is shown in Fig. 9. Both A and B are measured from the center of the defect. The four values shown (A, B, α, and β) are the size and orientation descriptors, and it is these that were modeled during ALN synthesis, as described in "Inverse Solution for Description of Spheroidal Defects."

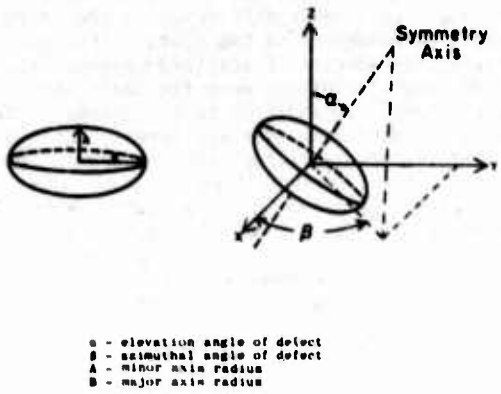
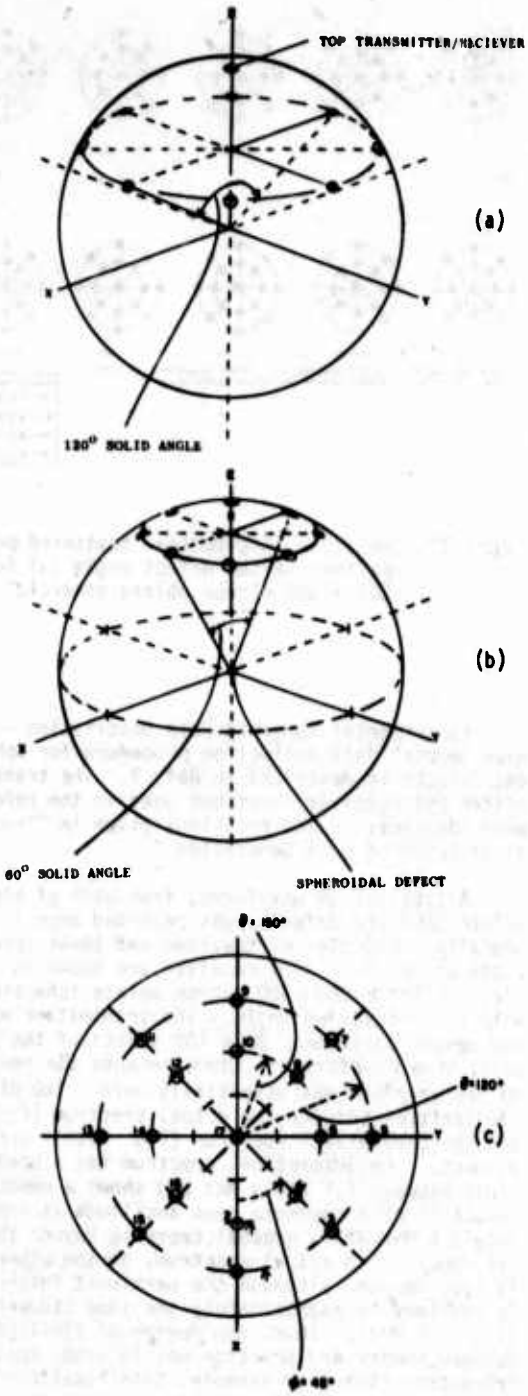


Figure 9. Oblate spheroid showing size (A and B) and orientation (α and β) parameters.

A total of 17 transducer positions was used in creating the theoretical spheroid data base. Five of the transducers operated both in the transmit and receive modes, while the others acted only as receivers. These positions are depicted in Fig. 10, where the circles indicate receiver only and the filled-in circles represent both transmit and receive positions. It can be seen that the transducer configuration consisted of two circular arrays and a top center receiver. The "outer" array covered a 120 degree solid angle and the "inner" array covered a 60 degree solid angle. Throughout the remainder of this report, these arrays will be called the "outer ring" and "inner ring," respectively. A stereographic view of these two rings (Fig. 10(c)) depicts two concentric circles with a transmitter/receiver in the middle. This middle transducer is referred to in this report as the "top center" transducer. The angular locations of the 17 transducer positions are given in Table 4.



○- Receiver only

●- Transmitter and receiver

Figure 10. Perspective and stereographic view of transmitter and receiver locations for spheroidal defect data generation. (a) Outer ring transmitters and receivers (120° solid angle); (b) inner ring receiver (60° solid angle); (c) polar view of transmitter and receiver location.

Table 4. Angular locations of the 17 transducer positions.

Transducer Number	Transducer Positions θ (degrees)	φ (degrees)	
1	120	0	•
2	180	0	
3	120	45	
4	180	45	
5	120	90	•
6	180	90	
7	120	135	
8	180	135	
10	180	180	•
11	120	225	
12	180	225	
13	120	270	•
14	180	270	
15	120	315	
16	180	315	
17	180	0	•

*Indicates both transmit and receive positions.

For each transmitter, the longitudinal and shear power spectra of the 17 receivers were generated via the Born approximation. For each defect of a given size and orientation, a total of 85 waveforms was available for each mode (17 received signals for each of five transmitter positions). The theoretical spectral bandwidth was chosen, for each waveform, to lie between 1.0 and 8.8 MHz in incremental steps of 0.39 MHz. Hence, each waveform contained 21 points. Only the received longitudinal waves were considered in this study (to conform with the available experimental data which were only recorded in the L→L mode).

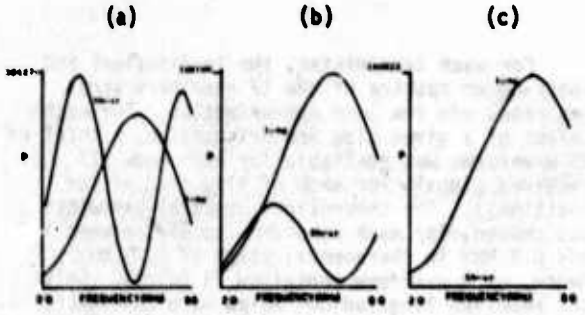
A total of 240 computer-simulated waveforms was generated from the Born approximation program to design and evaluate ALN models. These models provided estimates of sizes and orientations of the spheroidal defects. Six sizes, each at 40 orientations, were represented, as shown in Table 5. Only oblate spheroids were considered. The "ka" ranges exceeded unity for the highest frequencies (8 MHz), but were usually less than unity for the useable experimental bandwidth. ["ka" is the product of the wave number ($2\pi a/\lambda$, λ = wavelength) and a the defect diameter. If $ka < 1$, the wavelength is smaller than the defect diameter.]

Table 5. Six spheroidal defect sizes selected for the theoretical data base.

Size A x B (microns	ka Range	Orientation α (degrees)	β (degrees)
50 x 300	0 - 2.51	1.	60.
150 x 300	0 - 3.51	10.	150.
100 x 400	0 - 3.35	20.	330.
200 x 400	0 - 3.35	30.	
100 x 500	0 - 4.19	40.	
300 x 500	0 - 4.19	50.	
		60.	
		70.	
		80.	
		90.	

The Cornell program for the Born approximation, as received by Adaptronics, required the addition of several coordinate transformations to simulate arbitrary transmitter locations and defect orientations.[2] A description of these transformations is given in Appendix A.

Examples of Born generated longitudinal and shear power spectra, at each receiver, are shown in Fig. 11. These plots resulted when a 200 x 400 micron oblate spheroidal cavity was insonified by the top transmitter ($\theta = 180°$). The defect elevation angle, α, was zero, hence the spectra at all eight receivers in a given ring were identical. The receiver spectra in the outer ring, inner ring, and back-scatter are displayed. The ordinate, for each plot, is the spectral amplitude in absolute units, and the abscissae represent the frequency variation from 2 to 8 MHz.



Transmitter is at top center position and defect orientation is at zero elevation ($\alpha = 0$)

Figure 11. Longitudinal and shear power spectrum plots from Born approximation program for 200 x 400 micron oblate spheroid. (a) θ=120° (Outer Ring Receiver); (b) θ=150° (Inner Ring Receiver); (c) θ=180° (Top Ring Receiver - backscatter)

Note the frequency shift in the longitudinal wave as the receiver moves into the backscatter position. The peak for the longitudinal wave is 5.8 MHz at $\theta = 120°$, 6.3 MHz at $\theta = 150°$, and 6.7 MHz at $\theta = 180°$ (backscatter position).

The relative scattered power from a 200 x 400 oblate spheroid is presented in Fig. 12 for varying defect elevation angles. Each diagram shows a polar view of the receiver array. The level of shading on each receiver position indicates the relative longitudinal power. The incident beam originates from the center transmitter, and the defect is varied from 0 to 90 degrees, in elevation, along the $\beta = 202$-degree plane. Except for $\alpha = 0$ and $\alpha = 90$ degrees, β can be estimated by locating the receiver detecting maximum reflected power. The elevation angle, α, on the other hand, cannot be determined so easily. This fact was to influence the accuracies of α and β measurements, as will be shown in "Inverse Solution for Description of Spheroidal Defects."

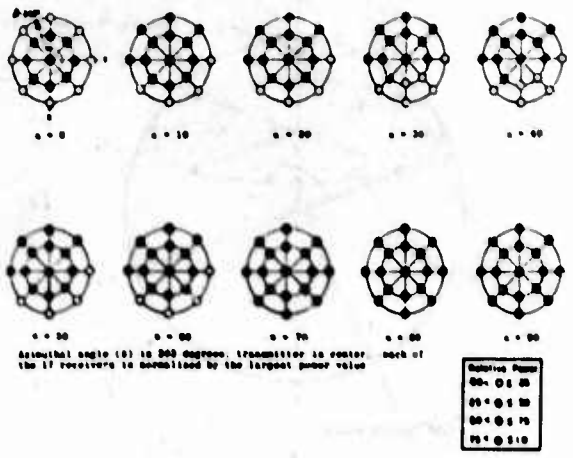


Figure 12. Relative longitudinal scattered power pattern versus defect angle (α) for a 200 x 400 micron oblate spheroid.

Experimental Spheroid Data Description - The experimental data collection procedure for spheroidal defects is described in Ref. 7. The transmitter and receiver locations used in the reference were identical to the positions given in "Theoretical Spheroid Data Generation."

A total of 85 waveforms, from each of eight oblate spheroid defects, was recorded experimentally. Examples of the time and power spectrum plots at an inner ring receiver are shown in Fig. 13 for a 200 x 400 micron oblate spheroid with zero elevation angle. The transmitter was at top center position. Only 100 points of the 501-point time waveform are shown because the remainder of the waveform was essentially zero. The dissimilarities between the actual spectrum (Fig. 13) and the theoretical spectrum (Fig. 11(b)) are evident. The theoretical spectrum has a bandwidth between 2.5 and 8 MHz and shows a smooth monotonic rise toward a peak amplitude at approximately 6 MHz and a gradual tapering beyond that frequency. The actual spectrum, on the other hand, is less smooth, although the pertinent information is confined to approximately the same bandwidth (2.5 to 6 MHz). Thus, any degree of similarity between theory and practice was in gross spectral characteristics (for example, total scattered energy) rather than in precise spectral shape.

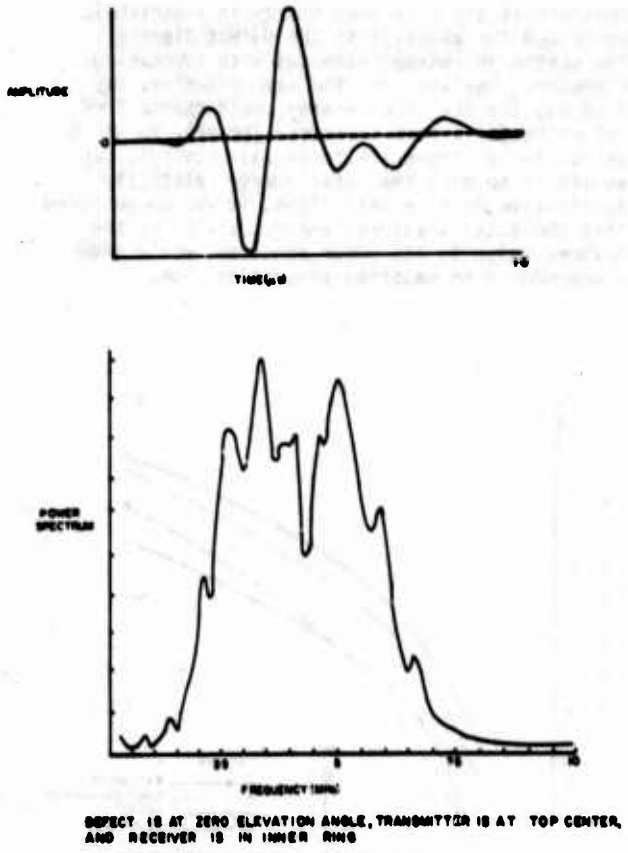


Figure 13. Time and frequency plots for 200 x 400 micron real, oblate spheroid.

Discussion - The theoretical signature of energy scattered from spheroids was considerably different from that observed in practice. Efforts in synthesizing an ALN from theory and expecting it to perform well for actual data will fall short if the parameter inputs to the ALN do not have a degree of "likeness" in theory and in practice. Theory assumes an ideal transducer with a flat spectrum and zero phase shift at all frequencies. However, in practice, the total scattered energy is altered considerably because transducers are not ideal.

The designed ALN measurement system should not be sensitive to variations in transducers used in data collection. Deconvolution of transducer response, prior to computing total energy, may make the measurement system less sensitive--but deconvolution itself may induce uncertainty because of its imprecise nature at frequency values beyond the transducer bandwidth.

Thus absolute quantities such as total scattered energy or the frequency at which maximum power was observed were susceptible to variations in the data collection system. Indeed, this reason was the prime consideration for computing relative parameter values; an example is the total energy scaled by some reference value intrinsic to the waveform.

The parameterization of these waveforms is explained in greater detail in the sections on "Spherical Defect Data Signal Preprocessing and Feature Extraction" and "Spheroidal Defect Data Signal Preprocessing and Feature Extraction."

Spherical Defect Data Signal Preprocessing and Feature Extraction

As discussed in the objectives at the beginning of this report, the major research goal in this project was to synthesize ALN's from parameters of a theoretical scattering model, and to evaluate these ALN's independently on actual scattering data from spherical defects.

The signal preprocessing objective was to derive parameters which were sensitive to the defect size and the defect material. It was found that the phase cepstrum of the signal was relatively insensitive to defect material properties but was a good indicator of defect size. The magnitude spectrum, on the other hand, was found to be a key source of information to determine material properties independently of defect size. This section presents these two transformations.

Presence of Echoes in Scattered Wave - The works of Sachse and Chian[4] and Cohen and Tittmann[3] indicate that the scattered wave from a spherical defect consists of the following components:

- The primary reflection, called the P-P wave.
- The circumferential or "creep" wave, which skirts around the periphery of the defect, called the PCP wave.
- The refracted ray propagating back and forth across the defect diameter, called the PFFP wave.

The PCP wave is a function of the properties of the host material and the diameter of the defect, whereas the PFFP wave is, in addition, dependent on the acoustic impedance of the defect. If one could isolate uniquely the times of occurrence of the PFFP and PCP waves in the scattered time signal, both the acoustic impedance of the defect material and its diameter could potentially be inferred.

Cepstral Analysis of Scattered NDE Waveforms - The cepstrum is a powerful signal processing tool which has found wide applications in echo detection, echo removal, and inverse filtering procedures.[5] A detailed discussion of the various forms of the cepstrum, their relationships, and implementations was described previously.[5] The primary reason for analyzing signal waveforms by the cepstrum is that the time delays between two or more similar events manifest themselves as peaks. Therefore a search for the location of peaks in the cepstrum will reveal the relevant time delays. However the search is compounded in difficulty by the fact that multiple time delays result in several peaks which are harmonics of, and sums and differences of, all possible delays. The peak(s) of interest can be potentially smeared by the presence of multiple echoes, and one can be misled as to their true location(s). Thus due to its inherent computational problems,[5] the cepstrum must be used with care.

Echo Time Detection by Power Cepstral Analysis - The power cepstrum is the inverse Fourier transform of the power spectrum of the scattered signal. The time delays in the signature should cause a "rippling" in the magnitude (power) spectrum. A further transformation on the magnitude spectrum should cause delta functions (peaks) to be manifest at those time delays. Since large defects have large scattered energy values, the rippling in the magnitude spectrum may be obscured by the large magnitudes. Magnitude shifts in the spectrum for defects of the same diameter but with different acoustic impedance ratios will lead to additional uncertainties in the measurement of true peak locations.

Echo Time Detection by Phase Cepstral Analysis - We have found that time delays in the scattered signature can be more easily detected in the phase rather than in the magnitude spectrum. The phase, at any particular frequency, is the arctangent of the ratio of the imaginary part and the real part of the complex Fourier transform. Both these parts are dependent on the frequency, the acoustic impedance ratio between the host and defect, and on the size of the defect. Larger acoustic impedance ratios create larger backscattered energies to be detected. Therefore, the magnitude component, which is the square root of the sum of the squares of the real and imaginary parts, is a function of the frequency and defect size, because the phase angle is independent of acoustic impedance ratio. Thus analysis of the phase--particularly the phase cepstrum--seemed more promising to determine diameter independent of material properties of the inclusion.

The formulation of the phase cepstrum appears in Ref. 5, and the reader is referred to it for the mathematical analysis; our interest is in the physical aspects of the mathematical formulation. The phase cepstrum is defined as the inverse Fourier transform of the complex exponential phase function rather than that of the phase function itself. Retaining the complex exponential of the phase function in computing the phase cepstrum has a threefold advantage. First, the complex exponential is a smooth function, and there are no discontinuities at the transition regions (-180° to 180° or 360° to 0°). Second, by encoding the phase angle in a manner similar to the basis functions of the Fourier transform, there are more opportunities for strong correlations between a given frequency and a given phase angle variation to result in a delta function. Third, the complex exponential avoids any detailed "unwrapping" procedure, which is necessary if one is to use the phase angle by itself.

Thus the phase cepstrum offers considerably more potential in detecting echo times than the power cepstrum and, as will be found later in the section on "Inverse Solution for Description of Spherical Defects," was a key indicator of defect diameter.

Magnitude Spectrum Processing - It was noted in "Theoretical Sphere Data Generation" that the total scattered energy was a function of defect material properties in addition to defect size. A plot of the total backscattered energy in polarization Mode 1 is presented in Fig. 14. The ordinate is the scattered energy in logarithmic units and the abscissa is the defect diameter. The scattered energy increases with increasing diameter. However, for the same diameter, say 0.08 cm, the scattered energy could change from -14 units for a weak scatterer (brass), to -11.5 units, for a strong scatterer (air-cavity). In an effort to make the total energy relatively insensitive to size variations, it was conjectured that the total scattered energy, scaled by the maximum value in its power spectrum, would show a dependence on material properties alone.

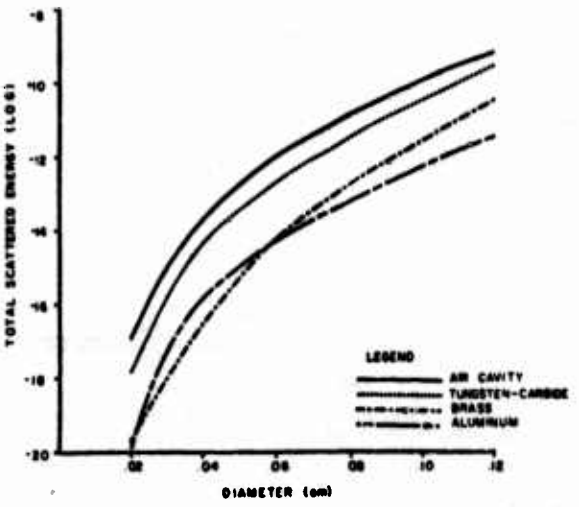


Figure 14. Theoretical total back-scattered energy from spherical defects as a function of defect diameter (mode 1 polarization).

The total scattered energy divided by the maximum value in the power spectrum is shown as a function of diameter in Fig. 15. The ordinate is, as before, in logarithmic units and the abscissa is the defect diameter. There is a high degree of insensitivity to defect diameter for all four materials. Although for smaller diameters it is not so evident, the scaled scattered energy is relatively constant for all sizes for a given material. Strong scatterers (air and tungsten carbide) have larger scaled total energy, whereas weak scatterers have lower scaled total energy.

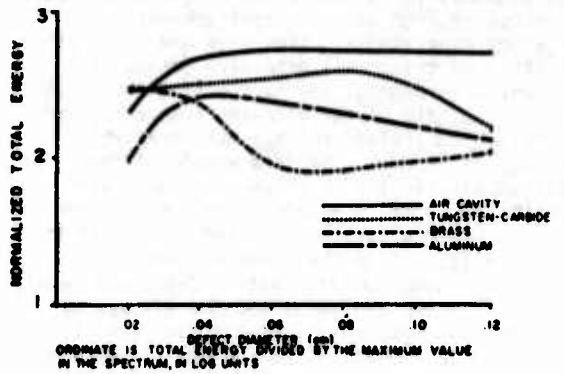


Figure 15. Theoretical total back-scattered energy, normalized by the maximum power, as a function of defect diameter (mode 1 polarization).

Thus the total energy scaled by the maximum power was relatively independent of defect size and also appeared to be a promising indicator of material properties.

Waveform Parameterization - The final candidate features (i.e., parameters) of the ultrasonic signature used as descriptors of defect size and its acoustic impedance are listed in Table 6. This list contains the total normalized total power (for reasons indicated previously in "Magnitude Spectrum Processing), the cepstral peak values (as explained earlier in this section on "Spherical Defect Data Signal Preprocessing and Feature Extraction"), and the viewing angle. The feature could be computed for either P = 1 or P = 3 mode of polarization. However, since the experimental data set consisted of a P = 1 polarization ultrasonic scattering wave (see "Experimental Sphere Data Description"), the list was compiled for the P = 1 mode to make a valid comparison between theory and experiment.

Table 6. Candidate features for describing spherical defects.

Parameter	Formulation[1]	Description
x_1	$\frac{\int A^2(f,d,\theta)\,df}{\int A^2_{max}(d,\theta)}$	Total energy in scattered signal normalized by its maximum power.
x_2	ϵ/θ	Ratio of back-scatter to viewing angle.
x_3	$\sin(\pi-\theta)$	Sine of viewing angle.
x_4	θ	Viewing angle.
x_5	$x_1/(\int_f \frac{A^2(f,d,\pi)df}{A^2_{max}(d,\pi)})$	Ratio of $x_1(\theta)$ to $x_1(\pi)$.
x_6	$q(\theta)$	Dominant peak-location in phase cepstrum, microsec.
x_7	$1/q(\pi)$	Inverse of x_6 at back-scatter.

[1] d = defect diameter, cm.
θ = viewing angle, radians.
f = frequency, MHz.
A = spectral magnitude.

The synthesis of ALN's to measure defect size and acoustic impedance, based on the above parameters, is detailed in the section on "Inverse Solution for Description of Spherical Defects."

Spheroidal Defect Data Signal Preprocessing and Feature Extraction

Comparison of Scattered Waveforms Obtained by Born Approximation and Actual Observation - Careful judgement was needed in the definition of candidate features for the spheroidal defect measurement system because there appeared to be little commonality between the two types of data (theoretical and empirical). Hence, from a rather large quantity of data per experiment, a total of only 32 candidate features was defined. There were four major differences between the two spheroidal data types.

First, the Born-generated receiver power spectra were very smooth curves somewhat similar to a half-cycle of a sine wave (Fig. 11). On the other hand, the real data power spectra were much less smooth (Fig. 13). The real data also exhibited sharper roll-off characteristics and were of a generally lower frequency than the Born data. Even after the theoretical spectra were multiplied by the actual transducer frequency response (to make the comparison on an equal basis), the real spectra were significantly different. Therefore, features sensitive to the shape of the individual spectra were excluded from consideration.

Second, it was observed that the difference in power between the inner and outer circular arrays was considerably greater for the theoretical data than for the real data in the case of defects with zero elevation ($\alpha = 0$) and transmitter location at top center. It was therefore decided to limit the feature types to those computed from powers within a given array rather than to those computed by combining powers from both arrays.

Third, it was discovered by personnel at the Rockwell International Science Center during the real data collection process that certain receiver powers may have been unavoidably corrupted by the transmitter signals. Specifically, the receiver collecting backscatter waveforms may still have been ringing from the transmit signal when the scattering waveform was received. Also, receivers in the hemisphere opposite to the outer ring transmitters may have responded to the direct transmit signal in addition to the scattered waveform. Accordingly, these receiver powers (which were in the outer ring only) were not used in the computation of features.

Fourth, real data always possess some degree of uncertainty, or "noise," whereas computer-generated data do not. Therefore, noise was added to make the Born spheroidal data resemble more closely the real data. This "corruption" process is described below.

Waveform Preprocessing: Born Data - As discussed in "Theoretical Spheroid Data Generation," each Born approximation (computer) experiment required 85 waveforms containing 21 words to be generated (although not all 85 were used in feature computation). The data were reduced to

a more manageable list of 32 features per experiment before synthesizing the ALN defect models.

In the generation of theoretical data, it was assumed that the transducer had an ideal response--flat magnitude spectrum and zero phase shift at all frequencies. The real data, however, were modified by a transducer response that was less than ideal. In fact, the nominally rated 5 MHz transducer used in the experiments had a bandwidth limited to the frequency range 1-9 MHz. Each of the 85 Born approximation waveforms was convolved with the transducer characteristics so that a higher degree of similarity between theoretical and experimental data could be attained. (Another means of obtaining similarity is by deconvolution of the transducer response from the experimental receiver data. However, this operation, although more general than convolution, is more difficult to implement and can require additional spectral smoothing. Although deconvolution was considered in this study, convolution was a more practical approach due to the time factor.)

Next, the 21-point spectra were integrated to determine the total power between 1.0-8.8 MHz. Preliminary comparison of the Born spectra to the corresponding experimentally-obtained spectra indicated very little similarity in their overall shapes. It was, therefore, decided to extract gross spatial features from the 85 receiver total powers rather than highly detailed features from the individual spectra. The single parameter of total power was just such a feature.

The total power was corrupted slightly by adding pseudo-random noise to give the Born and real data statistically similar properties. The "noisy" powers were computed by adding to the total power a uniformly distributed random number with zero mean and 0.33 variance, multiplied by 10 percent of the total power:

$$P_{noise} = P(1 + 0.1r)$$

where

$$r \in U(0, 0.33)$$

Note that it was established from an analysis of a limited amount of real data that there was approximately a 10 percent variation in the total power values in those cases where defect and transducer symmetry would allow no variation in theory (e.g., $\alpha = 0^\circ$ and the transducer in the top position--all the receivers in either circular array should detect equal scattered power).

After noise addition, the powers from the inner ($\theta = 150^\circ$) and outer ($\theta = 120^\circ$) rings were normalized separately by dividing each power in a ring by the total power in that same ring. Hence, after normalizing, the 8 receiver powers in either ring summed to unity. Normalization was performed in this manner for all five transmitting positions. The top position ($\theta = 180^\circ$, $\phi = 0^\circ$) receiver power was never used in computing any of the 32 features; only the normalized power around the inner and outer rings, for each transmitting position, was used.

Waveform Preprocessing: Real Data - A total of 85 time waveforms consisting of 501 points each was processed from each of eight spheroid scattering experiments. (The size and orientation identities of these real data were unknown to Adaptronics throughout the course of the study.) The sampling rate of the ultrasonic waveforms was 100 MHz, which yielded the highest observable frequency of 50 MHz. The data window of the scattered signal at each of the receivers was approximately 5 microseconds. The Fast Fourier Transform (FFT) algorithm was used to convert the receiver waveforms to the frequency domain. A 512-point power spectrum with a frequency resolution of 0.098 MHz per point (50 MHz divided by 512 points) was computed for each time signal. The bandwidth of interest was between 1.0-8.8 MHz, so the total power was computed by summing 80 amplitude spectral values in this frequency range. The same list of 32 features that was computed from the 240 Born program experiments was also computed from these eight real data experiments.

A comparison of the preprocessing steps for the Born and real data waveforms is shown in Fig. 16.

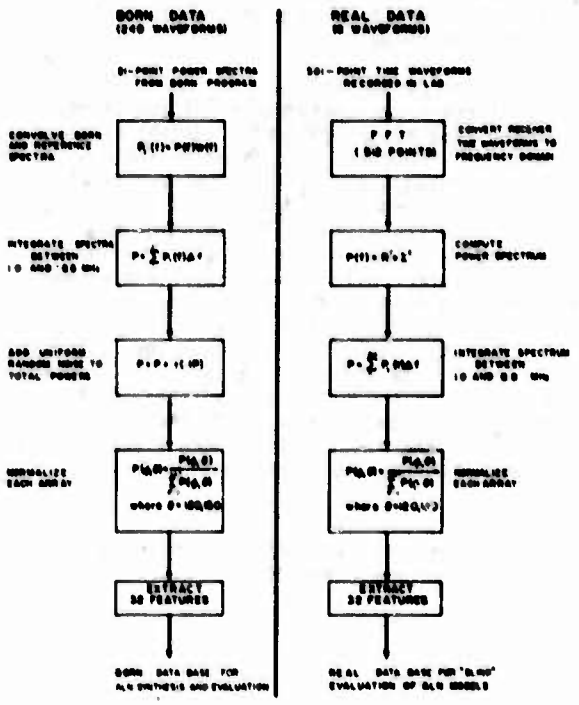


Figure 16. Spheroidal defect data pre-processing: Born data compared to real data.

Waveform Feature Extraction: Born and Real Data - Six types of feature were defined for each transmitter position:

CM = circular mean
CV = circular variance
ENT = entropy
MMR = min-max ratio
RI = inner ring ratio
RO = outer ring ratio

The circular mean was an angular feature which located the first moment of the scattered power around a circular receiver array. This feature was thought to be useful in determining β, the azimuthal defect orientation angle. Calculation of the CM was as follows:

$$CM = \tan^{-1}(S/C) + \gamma \qquad (2)$$

where:

$$S = \sum_{\phi=0}^{315^\circ} P(\phi,\theta) \sin \phi$$

$$C = \sum_{\phi=0}^{315^\circ} P(\phi,\theta) \cos \phi$$

and:

$\gamma = 0$ if $S > 0$, $C > 0$

$= \pi$ if $C < 0$,

$= 2\pi$ if $S < 0$, $C > 0$

$P(\phi,\theta)$ = longitudinal normalized total power at receiver position (ϕ,θ).

In the above computation, θ remained fixed at either 150° (inner ring) or 120° (outer ring); therefore, eight terms were summed in computing either S or C.

The circular variance feature is defined between zero and unity and was a measure of the power dispersion about the circular mean of a given circular array:

$$CVAR = 1 - \sum_{\phi=0}^{315^\circ} P(\phi,\theta) \cos(\phi - CM) \qquad (3)$$

The information-theoretic entropy feature is similar to the sample variance around a circular receiving array:

$$ENT = - \sum_{\phi=0}^{315^\circ} P(\phi,\theta) \log_2[P(\phi,\theta)] \qquad (4)$$

The min-max ratio is computed from the minimum and maximum powers around a given ring:

$$\frac{P(max) - P(min)}{P(max)} \qquad (5)$$

For each of the four outer ring ($\theta = 120$) transmitters, two more ratio features were computed, RI and RO, defined as follows:

$$RI(\phi) = \frac{[P(\phi-45,150) + P(\phi-90,150) + P(\phi-135,150)]}{[P(\phi+45,150) + P(\phi+90,150) + P(\phi+135,150)]}$$

$$RO(\phi) = \frac{[P(\phi-45,120) + P(\phi-90,120)]}{[P(\phi+45,120) + P(\phi+90,120)]} \qquad (6)$$

where:

ϕ = 0, 90, 180, and 270 degrees.

A list of the 32 candidate features is given in Table 7. This candidate list of inputs was used to synthesize the ALN's that measured spheroid defect size and orientation, as described in "Inverse Solution for Description of Spheroidal Defects."

Table 7. Candidate feature list for describing spheroidal defects.

FEATURE NUMBER	FEATURE TYPE	TRANSMITTER POSITION (ϕ,θ)	RING 1/
1	CM	0,180	IN
2	CVAR	0,180	IN
3	ENT	0,180	IN
4	MMR	0,180	IN
5	CM	0,180	OUT 2/
6	CVAR	0,180	OUT
7	ENT	0,180	OUT
8	MMR	0,180	OUT
9	CM	0,120	IN
10	CVAR	0,120	IN
11	ENT	0,120	IN
12	MMR	0,120	IN
13	CM	90,120	IN
14	CVAR	90,120	IN
15	ENT	90,120	IN
16	MMR	90,120	IN
17	CM	180,120	IN
18	CVAR	180,120	IN
19	ENT	180,120	IN
20	MMR	180,120	IN
21	CM	270,120	IN
22	CVAR	270,120	IN
23	ENT	270,120	IN
24	MMR	270,120	IN
25	RI	0,120	IN
26	RI	90,120	IN
27	RI	180,120	IN
28	RI	270,120	IN
29	RO	0,120	OUT
30	RO	90,120	OUT
31	RO	180,120	OUT
32	RO	270,120	OUT

1/ IN = Inner(θ=150°) Circular Array
2/ OUT= Outer(θ=120°) Circular Array

Inverse Solution for Description of Spherical Defects

Introduction - The measurement of defect diameter was performed via the phase cepstral analysis which yielded values independent of the acoustic impedance. The acoustic impedance was measured via an ALN model that was relatively independent of defect size. Both of these measurement schemes were tested with scattering data from actual defects and similarly accurate results were obtained.

Defect Diameter Measurement System-Phase Spectrum Processing of Theoretical Data - The defect diameter was measured by determining the peak location in the phase cepstrum (see section on "Spherical Defect Data Signal Preprocessing and Feature Extraction"), which is a signal transformation of the phase spectrum of the scattered ultrasonic waveform. Although the phase cepstrum may be

computed for any of the four modes of polarization, this investigation revealed that one of the modes, the vertical shear to vertical shear wave polarization (P = 3), offered the greatest resolution in the cepstral domain. To convert peak location in the cepstral domain to units of length, the following transformation was used:

$$d^* = \text{"characteristic length"} = v_s|t^*|$$

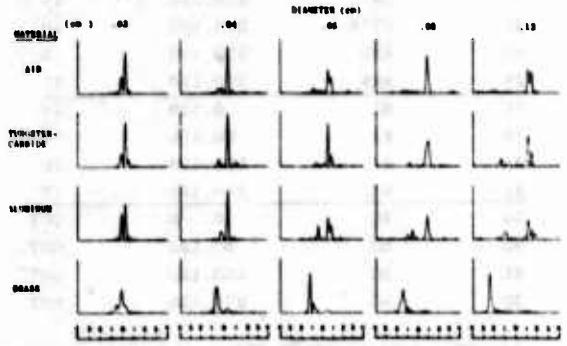
where

t^* = location of cepstral peak (sec)

and

v_s = (shear) wave velocity in Ti-6-4 = 3.03×10^5 cm/sec.

A composite plot of the theoretical P = 3 phase cepstra for the 5 different (theoretical) defects is displayed in Fig. 17 for each of the 4 different materials. The ordinates have been scaled between 0 and 1 by dividing by the largest observable peak. The abscissae represent quefrency, which varies from -1.3 to 1.3 microseconds (not shown). For ease of interpretation, quefrency values have been converted to length according to the above formula. Although quefrency can take on negative values, the length will always be positive.



Units on abscissae are in tenths of a centimeter. Peak location is indicative of diameter.

Figure 17. Phase cepstrum of theoretically scattered waveform at back-scatter position.

For each defect size, the peaks in the phase cepstra for three of the four materials coincided. However, the peaks for brass defects occurred in negative quefrency. If the transformation from quefrency to length is made, the peak location for brass nearly corresponded to the peak locations for the other three materials.

The phase cepstral analysis described above was equally valid for any other mode of polarization. The P = 3 mode was chosen instead of the P = 1 mode because the spatial resolution offered by the former is twice as small as the latter. The spatial resolution is given by the formula:

$$\Delta d = v\Delta t \,, \qquad (7)$$

where Δd is the spatial resolution, Δt is the quefrency resolution (sampling interval of time signal), and v is the velocity (which is twice as large for a P = 1 wave as it is for a P = 3 wave). Spatial resolution can be made smaller by decreasing Δt (sampling signal faster) or by decreasing v (using shear wave instead of longitudinal wave). The former technique was used to increase spatial resolution of the phase cepstrum of the experimental longitudinal wave.

A plot of the true versus measured diameter based on the phase analysis of the theoretically scattered wave is shown in Fig. 18. The relationship is not linear; however, it is monotonic and invariant (except for brass) with defect material.

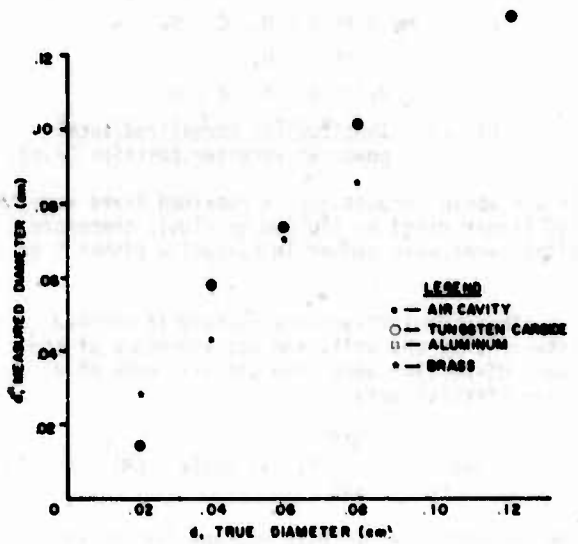


Figure 18. Measured diameter versus true diameter based on phase cepstral analysis of scattered P = 3 theoretical ultrasonic waveform.

Defect Acoustic Impedance Measurement System--Magnitude and Phase Spectral Processing of Theoretical Data - An ALN was synthesized from the theoretically scattered longitudinal-to-longitudinal (L→L) polarized (P = 1) spectral and cepstral parameters to measure acoustic impedance independently of defect size. It was decided to model the reflectance coefficient directly rather than the acoustic impedance. The former is expressed as the ratio:

$$r = \frac{Z_H - Z_D}{Z_H + Z_D} \,, \qquad (8)$$

where Z_H and Z_D are the acoustic impedances of the host material and the defect, respectively.

According to the above formula, the reflectance coefficient: (i) lies between -1 and +1, and (ii) exhibits a greater sensitivity for values close to zero, i.e., for defect materials which have acoustic impedance values similar to the host. It was therefore decided to model r for these two

desirable properties and then to obtain Z_D from the above formula. Since each defect size/defect constituent combination was scanned at 20 different viewing angles (θ's) a scheme was devised (illustrated in Fig. 19) wherein the acoustic impedance measurements at different angles could be averaged to yield one composite estimate value.

To compute the defect's acoustic impedance, $Z(\theta)$, the following transformation was used:

$$Z(\theta) = \left[\frac{1 - r(\theta)}{1 + r(\theta)}\right] Z_{Ti\text{-}6\text{-}4}, \qquad (9)$$

where $r(\theta)$ is the estimated reflectance coefficient at a particular viewing angle and $Z_{Ti\text{-}6\text{-}4}$ is the acoustic impedance of the host titanium alloy. The composite estimated ALN value so obtained was thus independent of the viewing angle. The list of candidate ALN inputs (Table 6) appears at the bottom of Fig. 19. To reiterate, the list contains normalized spectral power, viewing angle of the receiver with respect to the transmitter (which is always located at backscatter position), location of the phase cepstral peak at θ, and inverse of the phase cepstral peak at the backscatter position. The last two features were included to compensate for observed peak shifts in the phase cepstrum toward lower quefrencies as the receiver moved from backscatter to more forward scattering positions.

A diagram of the ALN network synthesized from the theoretical (L→L) spectral parameters is shown in Fig. 20. The resulting model is an eighth-degree (incomplete) polynomial equation in five of the seven inputs. It has among its principal inputs the normalized total energy, the ratio of normalized energy at θ to that at backscatter, and the phase cepstral features.

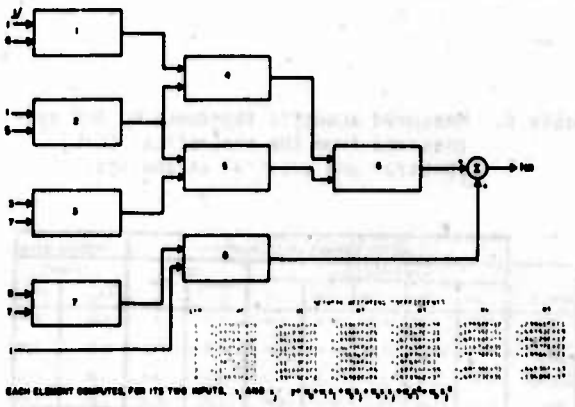
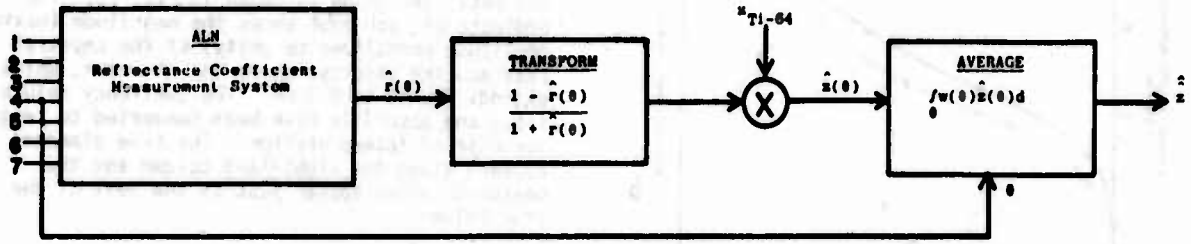


Figure 20. ALN spherical defect reflectance coefficient measurement model, synthesized from theoretically scattered parameters.



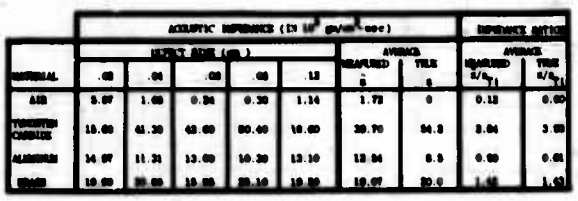
CANDIDATE INPUTS FOR ALN

SOURCE	PARAMETER	FORMULATION	DESCRIPTION
Magnitude Spectrum	x_1	$\int_f \frac{A^2(f,d,\theta)}{A^2_{max}(d,\theta)}\,df$	Total energy in scattered signal, normalized by its maximum power
-	x_2	π/θ	Ratio of back-scatter to viewing angle
-	x_3	$\sin(\pi - \theta)$	-
-	x_4	θ	Viewing angle
Magnitude Spectrum	x_5	$\frac{x_1}{\int_f \frac{A^2(f,d,\pi)}{A^2_{max}(d,\pi)}\,df}$	Ratio of $x_1(\theta)$ to $x_1(\pi)$
Phase Spectrum	x_6	$q(\theta)$	Peak location (in micro-seconds) in phase cepstrum
Phase Spectrum	x_7	$1/q(\pi)$	Inverse of x_6 at π, back-scatter

Figure 19. Quantitative spherical defect acoustic impedance measurement system.

The measured acoustic impedances for the variety of defects in the theoretical data set are shown in Table 8. Each entry in the table corresponds to the measured acoustic impedance for a given defect diameter. An overall average acoustic impedance measure can be obtained by summing across a row. This is indicated under "average measured impedance." The true impedance appears alongside, allowing a comparison to be made between the measured and true acoustic impedance ratios (with respect to Ti-6-4). These are shown in the last two columns and plotted in Fig. 21.

Table 8. Measured acoustic impedance by ALN synthesized from the theoretical (L→L) spectral and cepstral parameters.



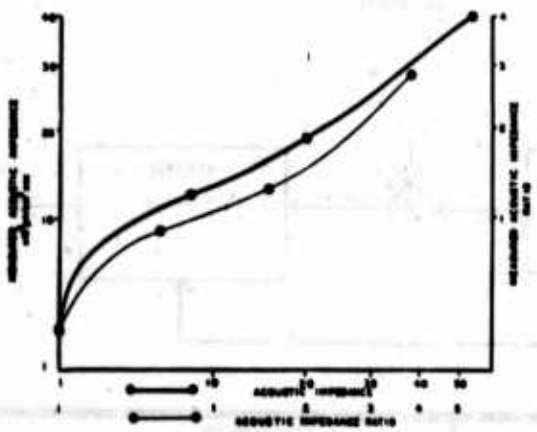


Figure 21. Plot of true acoustic impedance and its ratio versus measured acoustic impedance for theoretical scattering data.

Three observations can be made regarding these results:

- Acoustic impedance and the impedance ratio can be measured very accurately by the ALN for theoretical scattering data.
- The measurements are equally good for weak-scatterers (aluminum and brass) and for strong scatterers (air cavity and tungsten-carbide inclusions).
- The measurements are accurate and consistent for defect size variations from 0.02 cm to 0.12 cm, except for tungsten-carbide inclusions, which show a slightly greater variability.

Measurement of Spherical Defect Diameter and Acoustic Impedance from Experimental Data - As a test of validity of the synthesized solutions described in "Defect Diameter Measurement System-Phase Spectrum Processing of Theoretical Data," and "Defect Acoustic Impedance Measurement System-Magnitude and Phase Spectral Processing of Theoretical Data," experimental data from actual spherical defects were analyzed.

The experimental data consisted of the scattered L→L, P = 1 response, but the phase cepstral solution to measure diameter was synthesized from the scattered S→S, P = 3, response. So, to interpret the peak locations in the phase cepstrum of the experimental data, the longitudinal velocity--which is twice the shear wave velocity--was used. To convert the peak locations to length, one must use the transformation similar to the one in the "Introduction" to this section, i.e.,

$$d^* = \text{characteristic length} = v_\ell |t^*|$$

where

t^* = location of cepstral peak (secs.)

and

v_ℓ = longitudinal wave velocity in Ti-6-4 = 6.06×10^5 cm/sec.

A plot of the phase cepstrum of the recorded scattered data from the three air cavities and the one metal inclusion is shown in Fig. 22. The ordinate of each plot shows the magnitude (maximum amplitude normalized to unity) of the cepstral peak and the abscissa shows the diameter, which extends from 0 to 0.3 cm. The quefrency values along the abscissae have been converted to length for ease of interpretation. The true diameter appears along the right-hand column and the measured values appear just to the left of the true values.

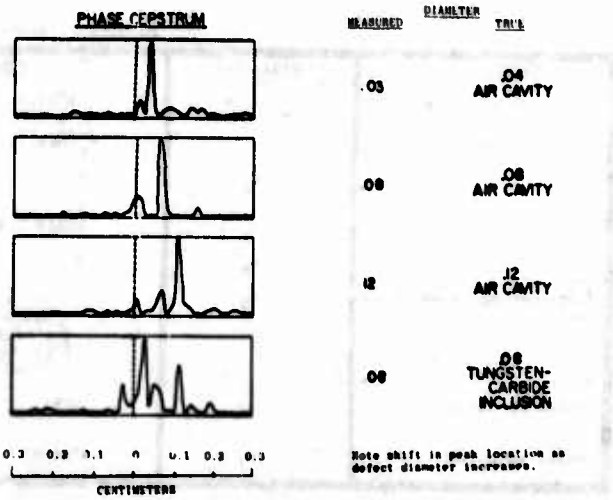


Figure 22. Phase cepstrum of experimental ultrasonic data from spherical defects.

There is very good agreement between the actual and estimated diameters for the three air cavities and reasonable agreement for the tungsten-carbide inclusion. The clarity of the peaks in the phase cepstrum compare (Fig. 22) with those obtained from the theoretical data (Fig. 18), in spite of the fact that:

- The polarizations were different.
- The bandwidth of the frequency spectra were mostly different.
- The cepstral resolutions were different.

To check the ability of the ALN network to measure acoustic impedance, the same after-deconvolution parameters of the spectral and cepstral waveforms (shown in the list in Fig. 19) were computed.

The true and measured acoustic impedances and their ratios (with respect to Ti-6-4) appear in Table 9. The acoustic impedances of two of the three air cavities were measured exactly. The first air cavity (0.04 cm diameter) yielded a value greater than actual. The measured acoustic impedances of the tungsten-carbide inclusion was 34.3 x 10^5 units versus the actual value of 55.2 x 10^5 un'ts.

Table 9. True and measured acoustic impedances of actual defects using ALN synthesized from theoretical waveforms.

DEFECT NO.	INCLUDED MATERIAL	DIAMETER	ACOUSTIC IMPEDANCE 1/ TRUE	ACOUSTIC IMPEDANCE 1/ MEASURED	ACOUSTIC IMPEDANCE RATIO TRUE	ACOUSTIC IMPEDANCE RATIO MEASURED
1	Air	.04	0.0	10.0	0.00	0.71
2	Air	.08	0.0	0.0	0.00	0.00
3	Air	.12	0.0	0.0	0.00	0.00
4	Tungsten-Carbide	.08	55.0	34.3	3.93	2.45

1/ 10^5 gm/cm^2-sec

The performance of two inverse solutions, synthesized from theoretical studies and applied to actual scattering data, is detailed in Table 10. The overall error for the diameter measurement system (0.015 cm) compares well with the resolution of the data collection system. The overall error in the impedance measurement system (of 7.64 x 10^5 gm/cm^2/sec) represents an error rate of 14% of the maximum impedance over the range of impedance values and compares favorably with the error rate for the theoretical data set (9%).

Table 10. Performance of spherical defect measurement system, synthesized from theoretical studies, on sample real spherical defects.

Sample	SOLUTION 1 PULSE COMPRESSION ANALYSIS (Diameter (in cm.) True	Measured	Error	SOLUTION 2 ALN SYNTHESIZED SYSTEM Impedance (in 10^5 gm/cm^2-sec) True	Measured	Error
Air Cavity	.04	.080	0.010	0.0	10.0	10.00
Air Cavity	.08	.070	0.004	0.0	0.0	0.00
Air Cavity	.12	.100	0.000	0.0	0.0	0.00
Tungsten-Carbide Inclusion	.08	.030	0.050	55.0	34.3	20.70
	Average Absolute Error		0.015			7.68

Conclusions - The defect diameter solution indicates that information for measuring defect size via the scattering of ultrasonic waves from spherical defects of varying composition exists mainly in the phase spectrum. Since the phase cepstrum is a measure of the dominant periodicity in the phase spectrum, the phenomenon of scattering is not unlike the phenomenon of acoustic resonance in cavities. A cavity resonates at a characteristic frequency which is linearly dependent on its diameter. (This is true for electromagnetic waves; it is assumed the same holds true for acoustical waves.) A plot of the measured diameter from the phase cepstral analysis (theoretical waveforms) versus the resonant wavelength for different defect sizes is displayed in Fig. 23. The resonant wavelength is related to the cavity diameter as:

$$\lambda = 1.14d \ , \qquad (10)$$

and it is independent of material properties. (The amplitude of the resonant wave is dependent on material properties, but not on the frequency of the wave.) The slope of the best-fitting line between the measured diameter ($\hat{d}$) and true diameter (d) in Fig. 23 is:

$$\hat{d} = 1.13d \ . \qquad (11)$$

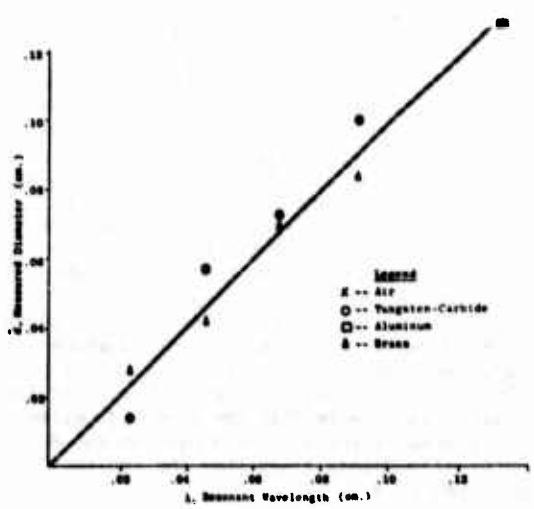


Figure 23. Measured diameter from phase cepstral analysis versus acoustic resonant wavelengths of spherical defects.

Comparing Eqs. (10) and (11), it is seen that the characteristic length being measured from the phase information, d, appears to be the resonant wavelength. This suggests that resonance is induced when the (broadband) pulse strikes the cavity. This argument is plausible, because the resonant frequency is contained in the 0-10 MHz pulse bandwidth for four of the five cavities:

Diameter, d (cm)	Resonant Frequency $= v_s/1.14d$ (MHz)
0.02	13.2
0.04	6.6
0.06	4.5
0.08	3.3
0.12	2.2

It can be seen that the resonant frequency of the 0.02 cm cavity is just outside of the 0-10 MHz band.

The second inverse solution showed that the acoustic impedance can be measured accurately by an ALN. The selected input parameters to the ALN--total normalized scattered energy and the viewing angle--are easily measureable quantities.

It is believed that these two empirical solutions (synthesized from theoretical studies to solve the inverse problem) are the first to measure sphere diameter and acoustic impedance accurately and independently of one another.

Inverse Solution for Description of Spheroidal Defects

The main objective concerning spheroids was to determine if the defect size and orientation could be estimated accurately from experimentally obtained scattering data when using ALN models synthesized from theoretical (Born) scattering data. Although this was the first attempt to solve the spheroid inversion problem, and also a first attempt at using artificial data as part of a solution, good estimates for three of the size and orientation parameters (A, B, and α), and an excellent estimate for the orientation parameter β were obtained.

Defect Size and Orientation Measurement System - Four parameters were estimated to describe defect size and orientation; A, B, α, and β. A fifth parameter, R, the radius of a sphere having the same volume as the spheroid (i.e., the cube root of the spheroid volume), was also estimated. Parameter A could be found indirectly, given R and B, but this estimate was not as accurate as the direct estimate of A. The defect measurement system is depicted in Fig. 24. During synthesis, each ALN had available the same set of 32 candidate input features during the training exercise (Table 7). Because the ALN synthesis algorithm determined which features were most relevant for each ALN, these networks use different features from the original candidate list. Note that the sine and cosine of the α network are used as inputs to the R network. The dashed lines show the indirect computation of A.

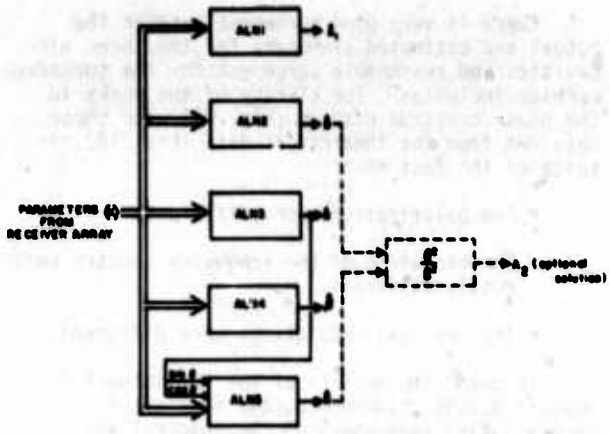


Figure 24. Quantitative spheroidal defect measurement system.

The network structures are given in Figs. 25 through 29. In each of these figures, the first layer elements (i.e., the left-most boxes) represent six-term quadratics of the form:

$$y = w_0 + w_1x_i + w_2x_j + w_3x_ix_j + w_4x_i^2 + w_5x_j^2 \qquad (12)$$

where the x's are the input features.

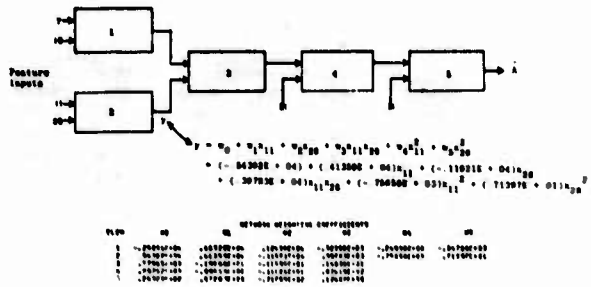


Figure 25. ALN structure and network coefficients to estimate size parameter "A" for spheroidal defects.

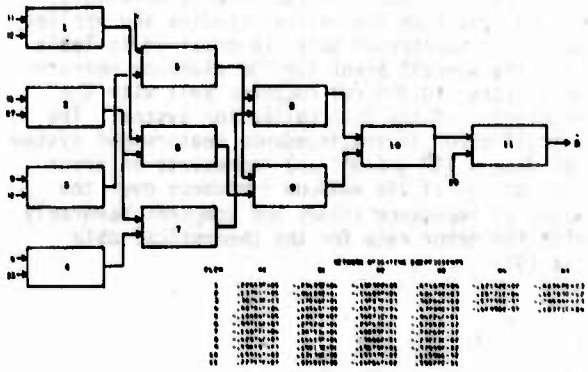


Figure 26. ALN structure and network coefficients to estimate size parameter "B" for spheroidal defects.

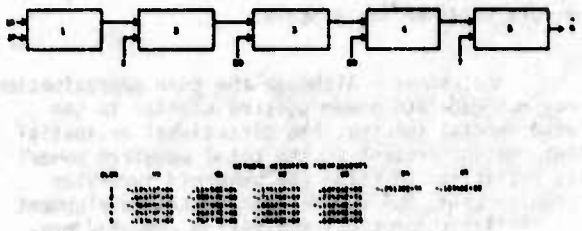


Figure 27. ALN structure and network weighting coefficients to estimate orientation parameter "α" for spheroidal defects.

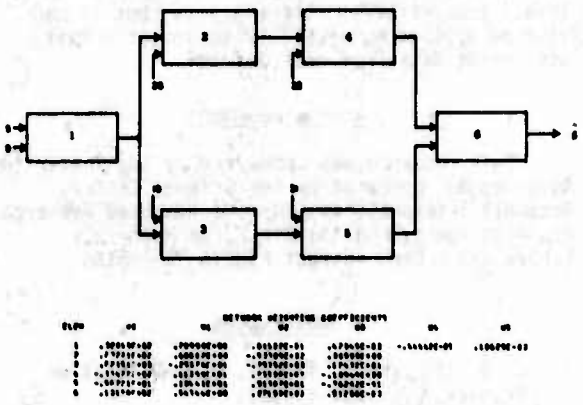


Figure 28. ALN structure and network coefficients to estimate orientation parameter "β" for spheroidal defects.

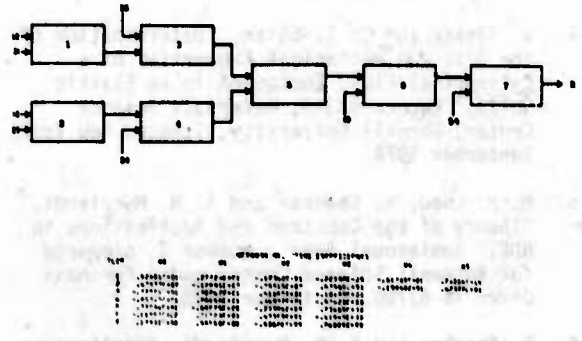


Figure 29. ALN and network coefficients to estimate size parameter "R" for spheroidal defects.

For each network, the input features are those listed in Table 11. For example, Input 7 in Fig. 25 is the entropy (ENT) in the outer ring when the transmitter is in the top position. Features 33 and 34 in Fig. 29 are the sine and cosine of the estimated angle $\hat{\alpha}$ from the net output shown in Fig. 27.

Table 11. Performance of spheroidal defect measurement system for theoretically scattered waveforms from defects.

True Size (A x B)	Average Absolute Error: Size ALN1 A, Minor Axis	Size ALN2 B, Major Axis	Orientation ALN3 α, Elevation	Orientation ALN4 β, Azimuth
50 x 300	77.9	83.9	11.6	19.3
150 x 300	25.9	38.0	13.0	20.0
100 x 400	71.3	40.0	7.8	17.7
200 x 400	42.7	35.0	12.4	16.3
100 x 500	57.4	40.0	12.9	11.9
300 x 500	116.0	66.6	17.1	16.0
Average Absolute Error (All Sizes)	65.2	45.9	12.6	16.0
Percent Average Absolute Error (All Sizes)	21.7	9.2	14.0	5.0

Errors are averaged over different elevation and azimuth orientations.

Measurement of Spheroidal Defect Size and Orientation from Theoretical Data - After ALN synthesis had been accomplished with a portion of the Born data, the models were evaluated with all of the 240 Born simulated experiments. A summary of the average absolute errors for each of the six defect sizes is shown in Table 11. Each entry in the table is the absolute error for a given size averaged over 32 orientations. That is, for each size, the absolute error was computed for 32 (eight α's times four β's) of the possible 40 defect orientations. (The α = 1 and 89 degree orientations were not used in computing the average errors as a matter of programming convenience.) An overall percentage error for each component of the measurement system is indicated in the last row. The defect size can be measured within 21.7 percent of the true value for A (ALN1) and within 9 percent of the true value for B (ALN2). These error rates translate to an average discrepancy in size measurement of the order of 55 microns (the average of the first two entries in the next to last row). The defect orientation can be measured with a 14 percent error in elevation, α, via ALN3 and a 5 percent error in azimuth, β, via ALN4. Since the elevation angle was restricted to variations in a single quadrant (0 to 90°), the error rate in α is an angular discrepancy of 12.6°. However, the azimuthal orientation, β, can vary in a 360° span and a 5 percent error rate is an average angular discrepancy of 18°. The average angular discrepancy in measurement is 15° (average of last two entries in the next to last row).

The performance of the spheroidal defect measurement system verifies that the inverse problem was solved with satisfactory accuracy using a family of ALN's.

Measurements of Spheroidal Defect Size and Orientation from Actual Data - As in the case of spherical defects, the spheroidal defect measurement system was applied to actual scattering data from a variety of sample, real, and oblate spheroidal defects. The computed size and orientation were compared to their actual values. These actual values were revealed to Adaptronics only after the measurements were made.

In spite of the several deficiencies existent in the Born approximation to the theoretical scattering model when compared to the actual scattering phenomena[2,3]--and the fact that the ALN measurement system was synthesized from the theoretical data--a remarkable agreement is found between the actual values and the measured values as shown in Table 12. The defect size is measured to within 15 percent of the true value for A and to within 37 percent for B. Thus the size measurements are, on the average, within 26 percent of their true values--in terms of length, within an average of 90 microns--and compare well with the theoretical data set (50 microns). The orientation can be measured to within 26 percent of the true value of α and to within 2.2 percent of the true β--in other words, an angular discrepancy of 15 degrees--which matches exactly the error obtained for the theoretical data set.

Table 12. Performance of spheroidal defect measurement system, synthesized from theoretical data, on actual scattering data from real defects.

DEFECT NO.	SIZE (In Microns)				ORIENTATION (In Degrees)			
	ALN5*		ALN6		ALN5		ALN4	
	TRUE A	MEAS. $\hat{A}$	TRUE B	MEAS. $\hat{B}$	TRUE α	MEAS. $\hat{\alpha}$	TRUE β	MEAS. $\hat{\beta}$
1	200	184	400	488	0	37	-	167
2	200	160	400	888	30	2	888	215
3	100	100	400	888	60	68	180	105
4	100	114	400	888	0	0	-	-
5	200	888	400	888	60	88	180	174
6	100	120	400	888	30	60	180	180
7	200	114	400	888	30	31	180	170
8	100	120	400	888	30	45	888	210
AVERAGE ABSOLUTE ERROR		90		148		20		8
PERCENT AVERAGE ABSOLUTE ERROR		15.0		37.3		22.6		2.2

* See Figure 4

In addition to measuring the size parameters A and B, it was decided to monitor the performance of ALN5 which measures the radius of a spherical defect having the same volume as the spheroidal defect. The use of ALN5 as an indirect estimator of A or B (each from a direct estimate of the other) was of questionable value, because the error in the indirect estimate was compounded by the error in the direct measurement. However, ALN5 provided a direct volumetric estimate and it was an additional piece of information to describe fully the defect characteristics.

The radius was measured to within 14.1 percent of the true value--an average error in length of 72 microns--which compared favorably with the errors obtained for A and B.

Conclusions - Although the Born approximation may not generate power spectra similar to the experimental spectra, the directional or spatial information present in the total waveform powers is sufficient to solve the spheroid inversion problem using ALN's. Hence, further development of similar theoretical scattering computer programs should be continued. Estimates for α, although quite good for Born data, are less accurate for the experimental data. Ways of lowering this error need to be investigated. Also, more effort is needed to determine why the estimated size parameter B was consistently biased for the real spheroid data. This may be due to a constant bias introduced in the Born approximation spectra which is not evident for experimentally observed spectra.

The performance of the spheroidal defect measurement system on actual scattering data demonstrates that not only can a family of ALN's invert theoretical scattering data, but it can also be applied successfully to invert actual scattering data from real defects.

Acknowledgement

This research was sponsored by the Center for Advanced NDE operated by the Science Center, Rockwell International, for the Advanced Research Projects Agency and the Air Force Materials Laboratory under contract F33615-74-C-5180.

References

1. C. S. Ying and R. Truell, Journal Applied Physics, 27, 1086 (1956).

2. J. E. Gubernatis, E. Domany, et al., "The Fundamental Theory of Elastic Wave Scattering by Defect in Elastic Materials - Integral Equation Methods for Application to Ultrasonic Flaw Detection," Report No. 2154, Materials Science Center, Cornell University, Ithaca, New York, May 1976.

3. B. R. Tittmann and E. R. Cohen, "Scattering of Longitudinal Waves Incident on a Spherical Cavity in a Solid," preprint SC-PP-75-130, Science Center, Rockwell International Corporation, December 1975.

4. W. Sachse and C. T. Chian, "Determination of the Size and Mechanical Properties of a Cylindrical Fluid Inclusion in an Elastic Solid," Report #2310, Materials Science Center, Cornell University, Ithaca, New York, September 1974.

5. M. H. Loew, R. Shankar and A. N. Mucciardi, "Theory of the Cepstrum and Applications to NDE," Semiannual Report Number 1, prepared for Rockwell Science Center under Purchase Order 76-62780, September 1976.

6. R. Shankar and A. N. Mucciardi, "Application of Adaptive Learning Networks to Establish Relationships Between Analytical and Empirical NDA Methods," Interim Progress Report No. 1, prepared for Rockwell Science Center under Purchase Order 76-62780, August 1976.

APPENDIX A

AXIS ROTATION ROUTINE FOR BORN PROGRAM

As received by Adaptronics, the Born approximation program was limited to simulating scattering from defects with axes of symmetry in the negative y-z plane. Also, the projector was assumed to be transmitting from positive to negative along the z axis, as shown in Fig. A.1.

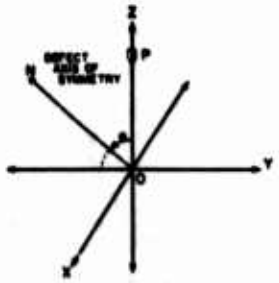


Figure A1: Orientation required by the Cornell Born computer program.

To simulate more realistic physical situations, the Born approximation program was modified to permit the defect, transmitter, and receivers to be located arbitrarily. For each arrangement, a new set of axes was constructed by rotating the old axes through three Euler angles about the "rigid network" of transducers and defect. In the new coordinate system, the line of transmission PO was along the z axis and the symmetry axis ON was in the negative y-z plane. The Born program calculated the reflected power at the redefined receiver points.

In the general case, the defect axis of symmetry ON could be oriented at angles (A,B) with respect to the original coordinate system, where A was measured from the positive z axis and B was measured azimuthally from the positive x axis, as shown in Fig. A.2. Similarly, the line of transmission of the projector could have angular coordinates (θ,ϕ), where θ was measured from the negative z axis and ϕ was measured azimuthally from the positive x axis. (The angles were defined to agree with the Born program conventions.)

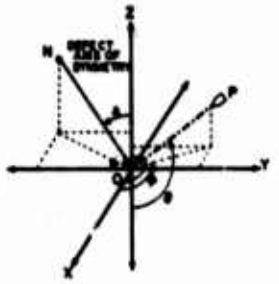


Figure A2: Illustration of sample orientation of A, B, θ, ϕ.

The axes underwent three Euler rotations to place the transmission line PO along the z axis and the symmetry axis ON in the negative y-z plane. Each Euler rotation was about a single axis (x, y, or z) and was defined as positive when the rotation was counterclockwise as viewed from the positive axis. The coordinates (x_1, y_1, z_1) of a point after one rotation were related to the old coordinates (x_0, y_0, z_0) by the expression $(x_1,y_1,z_1)^T = M(x_0,y_0,z_0)^T$, where M was a 3 x 3 matrix whose elements were determined by the angle and axis of rotation. After three rotations, the coordinates were further transformed to $(x_3,y_3,z_3)^T = LKM(x_0,y_0,z_0)^T$ where K and L were the 3 x 3 matrices corresponding to the second and third rotations, respectively. (The superscript "T" denotes matrix transpose.)

Rotation No. 1

The first rotation was about the z axis through an angle of ϕ-90° to place the line of transmission in the positive y-z plane. The 3 x 3 transformation matrix for a rotation through an angle γ about the z-axis is:

$$M = \begin{bmatrix} \cos\gamma & \sin\gamma & 0 \\ -\sin\gamma & \cos\gamma & 0 \\ 0 & 0 & 1 \end{bmatrix}$$

Here, $\gamma = \phi$-90°, so $\sin\gamma = -\cos\phi$ and $\cos\gamma = \sin\phi$. Therefore, maxtrix M becomes:

$$M = \begin{bmatrix} \sin\phi & -\cos\phi & 0 \\ \cos\phi & \sin\phi & 0 \\ 0 & 0 & 1 \end{bmatrix}$$

Rotation No. 2

To place the transmission line OP colinear with the z axis, the axes are rotated about the x axis through an angle θ-180°. The corresponding matrix for a rotation through an angle β is:

$$L = \begin{bmatrix} 1 & 0 & 0 \\ 0 & \cos\beta & \sin\beta \\ 0 & -\sin\beta & \cos\beta \end{bmatrix}$$

In the case, $\beta = \theta$-180°, $\sin\beta = -\sin\theta$, and $\cos\beta = -\cos\theta$, so L becomes:

$$L = \begin{bmatrix} 1 & 0 & 0 \\ 0 & -\cos\theta & -\sin\theta \\ 0 & \sin\theta & -\cos\theta \end{bmatrix}$$

The first two rotations place the z axis colinear with the line of transmission, as shown in Fig. A.3.

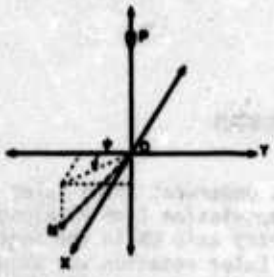


Figure A3: Orientation ψ after two Euler angle transformations.

Rotation No. 3

Following the first two rotations, the defect axis of symmetry (ON) is inclined at an angle ψ with respect to the negative y-z plane. Rotating the axes through an angle ψ about the z axis places the symmetry axis within the y-z plane.

The value of ψ is found by transforming the original Cartesian coordinates of point N through the first two rotations:

$$\begin{bmatrix} x_2 \\ y_2 \\ z_2 \end{bmatrix} = LM \begin{bmatrix} x_0 \\ y_0 \\ z_0 \end{bmatrix}$$

The quantities (x_0, y_0, z_0), assuming the point N to lie on a unit sphere, are:

$$x_0 = \cos A \ \sin B$$

$$y_0 = \sin A \ \sin B$$

$$z_0 = \cos B$$

The new Cartesian coordinates (x_2, y_2, z_2) determine ψ: $\psi = \tan^{-1}(x_2/-y_2)$. The FORTRAN function ATAN2$(x_2, -y_2)$ returns the proper sign of ψ). The rotation ψ, also about the z axis, has the general transformation matrix of the first rotation. The final rotation matrix becomes:

$$K = \begin{bmatrix} \cos\psi & \sin\psi & 0 \\ -\sin\psi & \cos\psi & 0 \\ 0 & 0 & 1 \end{bmatrix}$$

Result

The matrix product KLM transforms the original Cartesian coordinates of any point (such as a receiver location) to the corresponding values in the rotated system. Then, converted to spherical coordinates, the locations become the points at which the Born program calculates the reflected power. The defect orientation, as required by the program is specified by a single angle between the symmetry axis and the z axis. The value is: $\alpha = \tan^{-1}(-y_3/z_3)$, where $x_3 = 0$, y_3, and z_3 are the Cartesian coordinates of the symmetry axis in the final system, as shown in Fig. A.4.

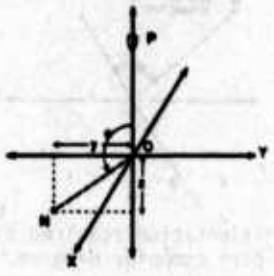


Figure A4: Orientation α after three Euler angle transformations.

APPLICATION OF A NEW INVERSE METHOD TO NONDESTRUCTIVE EVALUATION

N. Bleistein and J. K. Cohen
University of Denver
Denver, Colorado

ABSTRACT

When a wave impinges upon an irregularity in an otherwise homogeneous medium, the wave is deformed in a manner which is characteristic of the irregularity. This is the basis of a method of nondestructive evaluation of materials. Problems in which one seeks information about material properties from scattered waves are known as inverse problems. Traditionally, such problems are analyzed either by cataloging many solutions of direct problems and comparing the results of a given experiment with catalogs, or by attempting to solve the relevant equation of wave properties backwards in time. In contrast, we formulate the inverse problem as an equation or system of equations in which one of the unknowns is a function which directly characterizes the irregularity to be determined. Under the assumption of small sized anomalies or small changes in media properties, our system reduces to a single linear integral equation for this "characteristic" function. In many cases of practical interest, this equation admits closed form solutions. Even under the constraints of practical limitations on the data, information about the irregularity can be deduced. As an example, we consider the case of a void in a solid probed by acoustic waves. We show how high frequency data can be directly processed to yield the actual shape of the anomaly in a region of the surface covered by specular reflection of the probe. In the low frequency case, we show how to directly process the data to yield the volume, centroid, and "products of inertia" of the void.

Introduction

The application of a new inverse method to non-destructive evaluation is described. In particular, detection of a small hole in an otherwise homogeneous solid is discussed. The scattering of an acoustic probe by the hole is considered. It is shown that the scattered wave is proportional to the Fourier transform of the characteristic function of the domain occupied by the hole. The characteristic function is equal to unity in that domain, and zero outside. Thus, knowledge of this function characterizes the domain. The basic result is derived under the assumption that the scatterer is small - allowing use of the Born approximation - and "far" from the surface of the solid. Some features of aperture limited - band limited and aspect angle limited - observations are discussed. The applicability of this inverse method to non-destructive evaluation is demonstrated by this preliminary analysis.

When a wave (e.g., acoustic, elastic, electromagnetic) propagates through a medium, the wave is deformed by irregularities in that medium. The deformation of the probing wave is characteristic of the irregularity. This is the basis of a method for non-destructive evaluation of solid materials. A known probing wave is introduced into the medium. The wave "scattered" by the irregularity is observed. The nature of the irregularity is to be inferred from the nature of the scattered wave.

The type of problem we have described here is called an inverse problem. The corresponding direct problem would be to find the scattered wave given the "incident wave" (probe) and the irregularities of the medium. Inverse problems are often attacked indirectly; i.e., one solves direct problems for prescribed irregularities, seeking an irregularity for which the scattered wave most nearly approximates the data.

In contrast, we are engaged in research on direct solutions of the inverse problem. That is, we formulate an equation or system in which the solution is a function (or functions) which directly characterizes the "unknown" of the inverse problem. Recently, we have examined the non-destructive evaluation problem from the point of view of our inverse methods. Our conclusion is that our methods are most definitely applicable to this problem. The objective of this report is to describe our preliminary analysis.

Our basic model is as follows. We suppose that there is a small convex hole in an otherwise homogeneous solid. The size and shape of the hole are to be determined from observations of scattered waves on the surface of the solid. The waves are produced by acoustic sources on the surface.

We assume that the hole size is small compared to the distance to the boundary. This allows us to linearize an essentially non-linear problem. This linearization is equivalent to the Born approximation, Morse & Feshback.[8] Further exploitation of this scaling assumption allows us to reduce the inverse problem to a statement about the Fourier transform of the characteristic function of the region of the hole. The characteristic function is equal to unity inside the hole and equal to zero outside. Thus, knowledge of this function describes the hole.

In any practical problem, observations cannot be made over "all" frequencies, or over all directions of scatter. However, the vector variable in the Fourier transform introduced above has magnitude proportional to frequency and direction related to the source and receiver locations. Consequently, one must next examine the problem of extracting information about the characteristic function from its aperture limited - band

limited and aspect angle limited - Fourier transform. We discuss the low frequency and high frequency limits separately in the sections on "Low Frequency Analysis of the Characteristic Function" and "High Frequency Analysis."

Preliminary discussions focused on the low frequency limit only. However, analysis of magnitudes provided to us suggest that the high frequency limit might be exploited as well. To see why this is so, we note that the relevant parameter for high frequency approximation is:

$$\Lambda = 2\pi fa/c \quad , \tag{1}$$

where f is frequency in Hertz, "a" is a typical length, and c is soundspeed. Values provided to us were a maximum frequency of 8×10^6 Hz, a length scale of 50 mils, and a soundspeed of 21,000 ft/sec, for which $\Lambda = 10$. From the discussion of "High Frequency Analysis" it will become clear that such a value of Λ will produce "tolerable" results, while an increase in Λ by a factor of two will produce good results, and an increase by a factor of three will produce excellent results.

The advantage of high frequency data is that it can be used to produce a "picture" of the actual flaw. On the other hand, we show that from low frequency data we can find the volume, center of mass, and dimensions and orientation of an "equivalent" ellipsoid. Equivalence in this context means that the ellipsoid has the same centroid and mass-normalized products of inertia as the flaw to be detected. Orientation is then deduced by "diagonalizing" the matrix of products of inertia.

Basic Formulation

The mathematical formulation of the problem will be described with the aid of Fig. 1. A hole occupies a region D bounded by a surface S inside an otherwise homogeneous region A. The total field, inside the region D-A is assumed to satisfy the Helmholtz equation:

$$(\nabla^2 + \omega^2/c^2)U = 0 \quad . \tag{2}$$

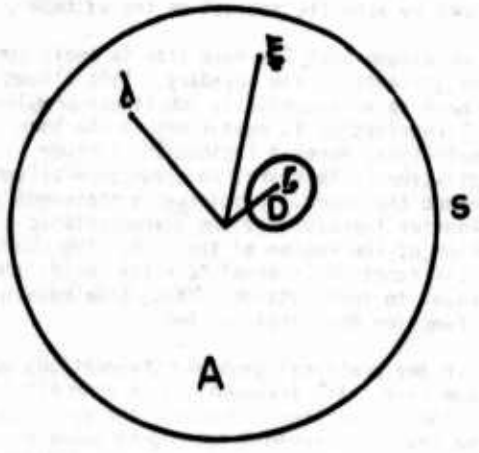


Figure 1. Basic model for analysis.

Here, ∇^2 denotes the Laplacian in three dimensions, ω is the frequency in radians/second, and c is the soundspeed. An impulsive source is located at $\underline{\lambda} = (\lambda_1, \lambda_2, \lambda_3)$ on S, the outer boundary of A. Thus, we take as boundary conditions:

$$\partial U/\partial n = (\underline{x} - \underline{\lambda}), \quad \underline{x} \text{ on } S; \tag{3}$$

$$\partial U/\partial n = 0, \quad \underline{x} \text{ on bdry } D. \tag{4}$$

Here, $\delta(\underline{x} - \underline{\lambda})$ is a two-dimensional Dirac delta function and $\partial/\partial n$ denotes the normal derivative directed into A-D. We remark here that this idealized problem applies to a real experiment only in the band limits of the Fourier transform of the time-shape of the source, and then only after normalizing the observed data at each frequency with respect to that source.

We set,

$$U = U_I + U_s \quad , \tag{5}$$

where

$$U_I(\underline{x},\underline{\lambda}) = \frac{\exp(i\omega|\underline{x} - \underline{\lambda}|/c}{2\pi|\underline{x} - \underline{\lambda}|} \quad . \tag{6}$$

Here, $\underline{x} = (x_1, x_2, x_3)$ denotes any point in D. The function U_I is the probe and the function U_s contains all of the response due to the hole, D, and due to the nature of S.

We shall observe the scattered field at $\underline{\xi} = (\xi_1, \xi_2, \xi_3)$ on S. We assume that, by "time-gating" the observations, the response due to D alone can be identified. Equivalently, we remove the boundary S and take U_s to be the response to the hole D alone due to the source U_I given by Eq. (6).

We introduce the Green's function:

$$g(\underline{x},\underline{\xi}) = 1/2\ U_I(\underline{x},\underline{\xi}) = \frac{\exp(i\omega|\underline{x} - \underline{\xi}|/c}{4\pi|\underline{x} - \underline{\xi}|} \quad . \tag{7}$$

We can then deduce the following integral representation for the response at $\underline{\xi}$ due to the source at $\underline{\lambda}$ (see, for example, Baker and Copson, 1950):

$$U_s(\underline{\xi},\underline{\lambda}) = \int_S [U_I(\underline{x},\underline{\lambda}) + U_s(\underline{x},\underline{\lambda})] \frac{\partial}{\partial n} g(\underline{x},\underline{\xi}) dS \quad . \tag{8}$$

Similarly, we can deduce that:

$$0 = \int_S [U_I(\underline{x},\underline{\xi}) \frac{\partial}{\partial n} g(\underline{x},\underline{\xi}) - g(\underline{x},\underline{\xi}) \frac{\partial U_I}{\partial n}(\underline{x},\underline{\lambda})] dS \quad . \tag{8}$$

Similarly, we can deduce that:

$$0 = \int_S [U_I(\underline{x},\underline{\lambda}) \frac{\partial}{\partial n} g(\underline{x},\underline{\xi}) - g(\underline{x},\underline{\xi}) \frac{\partial U_I}{\partial n}(\underline{x},\underline{\xi})] dS \quad , \tag{9}$$

which we shall use below.

For the small hole size (say, $9(\varepsilon)$), we expect that U_s will be small (also $9(\varepsilon)$), and thus the integral involving U_s in Eq. (8) will be even smaller. Thus we approximate U_s by:

$$U_s(\underline{\xi},\underline{\lambda}) = \int_S U_I(\underline{x},\underline{\lambda}) \frac{\partial g}{\partial n}(\underline{x},\underline{\lambda}) dS \quad . \tag{10}$$

This is the Born approximation.

We now use Eq. (9) to write this result in the more symmetric form:

$$U_s(\underline{\xi},\underline{\lambda}) = \tfrac{1}{4}\int_S [U_I(\underline{x},\underline{\lambda})\,\frac{\partial}{\partial n}\,g(\underline{x},\underline{\xi}) + g(\underline{x},\underline{\xi})\,\frac{\partial}{\partial n}\,U_I(\underline{x},\underline{\xi})]\,dS\,, \tag{11}$$

or

$$U_s(\underline{\xi},\underline{\lambda}) = \tfrac{1}{4}\int_S \underline{n}\cdot\nabla[U_I(\underline{x},\underline{\lambda})\,g(\underline{x},\underline{\xi})]\,dS\,. \tag{12}$$

By using the divergence theorem here, we find:

$$U_s(\underline{\xi},\underline{\lambda}) = \tfrac{1}{4}\int_D \nabla^2[U_I(\underline{x},\underline{\lambda})\,g(\underline{x},\underline{\xi})]\,dV\,. \tag{13}$$

Let us now suppose that we have some appropriate idea of where the flaw is located† and take that location to be $\underline{r}_o$ in or near D. By this latter phrase we mean that:

$$\frac{|\underline{x}-\underline{r}_o|}{|\underline{\lambda}-\underline{r}_o|} \ll 1, \quad \frac{|\underline{x}-\underline{r}_o|}{|\underline{\xi}-\underline{r}_o|} \ll 1, \quad \underline{x} \text{ in } D. \tag{14}$$

These estimates will be used to simplify Eq. (13), in which $\underline{x}$ is in D. To do so, we return to Eq. (6) and rewrite that equation as:

$$U_I(\underline{x},\underline{\lambda}) = \frac{\exp\,(i\omega|\underline{\lambda}-\underline{r}_o-(\underline{x}-\underline{r}_o)|/c)}{2\pi|\underline{\lambda}-\underline{r}_o-(\underline{x}-\underline{r}_o)|}\,. \tag{15}$$

We now apply the binomial theorem in the following form:

$$|\underline{\lambda}-\underline{r}_o-(\underline{x}-\underline{r}_o)| = |\underline{\lambda}-\underline{r}_o| \times \left\{1 - \frac{(\underline{\lambda}-\underline{r}_o)\cdot(\underline{x}-\underline{r}_o)}{|\underline{\lambda}-\underline{r}_o|^2} + O\left(\left|\frac{\underline{x}-\underline{r}_o}{\underline{\lambda}-\underline{r}_o}\right|^2\right)\right\} \tag{16}$$

By using this result in Eq. (15) we conclude that:

$$U_I(\underline{x},\lambda) = \frac{\exp\,(i\omega|\underline{\lambda}-\underline{r}_o|/c + i\omega\hat{\lambda}\cdot\underline{y})}{2\pi|\underline{\lambda}-\underline{r}_o|} \times \left\{1 + O\left(\frac{|\underline{x}-\underline{r}_o|}{|\underline{\lambda}-\underline{r}_o|}\right)\right\} \tag{17}$$

Here, we have introduced the notation:

$$\hat{\lambda} = \frac{\underline{\lambda}-\underline{r}_o}{|\underline{\lambda}-\underline{r}_o|}\,, \quad \underline{y} = \underline{x}-\underline{r}_o\,. \tag{18}$$

Similar approximations can be made in $g(\underline{x},\underline{\xi})$ given by Eq. (7) and for all of the derivatives appearing in Eq. (13). After some algebra, we conclude that:

$$U_s(\underline{\xi},\underline{\lambda}) = \frac{\exp[i\omega(|\underline{\lambda}-\underline{r}_o| + |\underline{\xi}-\underline{r}_o|)/c]}{(4\pi^2)|\underline{\lambda}-\underline{r}_o|\,|\underline{\xi}-\underline{r}_o|}\,I(\tfrac{\omega}{c},\hat{\lambda},\hat{\xi}). \tag{19}$$

Here, we have introduced the variable;

$$\hat{\xi} = \frac{\underline{\xi}-\underline{r}_o}{|\underline{\xi}-\underline{r}_o|}\,, \tag{20}$$

and

$$I(\omega/c,\hat{\lambda},\hat{\xi}) = -[\tfrac{\omega(\hat{\lambda}+\hat{\xi})}{c}]^2 \int_D \exp\,(i\omega(\hat{\lambda}+\hat{\xi})\cdot\underline{y})dV\,. \tag{21}$$

This function is the phase and range normalized far field scattering amplitude.

In order to interpret this result, we introduce $\Gamma(\underline{y})$, the characteristic function of the domain D, defined by:

$$\Gamma(\underline{y}) = \begin{cases} 1, & \underline{y} \text{ in } D \\ 0, & \underline{y} \text{ not in } D \end{cases}\,. \tag{22}$$

The Fourier transform of $\Gamma(\underline{y})$ is given by:

$$\gamma(\underline{k}) = \int_D \exp(-i\underline{k}\cdot\underline{y})dV\,. \tag{23}$$

We then conclude from Eq. (21) that;

$$I(\omega/c,\hat{\lambda},\hat{\xi}) = -k^2\,(\underline{k}) \qquad \underline{k} = \omega(\hat{\lambda}+\hat{\xi})/c,\ \ k = (\underline{k}\cdot\underline{k})^{\frac{1}{2}}\,. \tag{24}$$

In words, the far field scattering amplitude is proportional to the Fourier transform of the characteristic function of the scatterer. Knowledge of $\gamma(\underline{k})$ for "all" $\underline{k}$ (wideband and all directions of the vector) would provide a full description of the scatterer by Fourier inversion. Clearly, such information is not practically available. Thus, it is necessary to explore the question of extracting information about D from aperture limited - band limited and aspect angle limited - observations of the scattered field. Equivalently, we have reduced the problem to a question in Fourier analysis; namely, what sort of information about a characteristic (non-zero) function can be extracted from aperture limited information about its Fourier transform?

The identity, Eq. (24), has previously been derived under the assumption of high frequency[2-4,6,7,9-12] by using physical optics approximations instead of the Born approximation. This distinction is extremely important. In the present case, we may explore the possibility of extracting information about the scatterer from low frequency observations as well as from high frequency observations. In the earlier work, analysis of Eq. (24) for low frequency would have made no sense at all.

In the following ("Low Frequency Analysis of the Characteristic Function"), the low frequency limit is discussed and the question of high frequency information is addressed under "High Frequency Analysis."

†Delay time observations would suffice to produce this first approximation of the location of the hole.

Low Frequency Analysis of the Characteristic Function

For the characteristic function and its Fourier transform defined by Eq. (22) and Eq. (23), we define "low frequency" to mean that:

$$ky << 1, \quad \underline{y} \text{ in } D . \tag{25}$$

We assume that the provided observations of $\gamma(\underline{k})$ are sufficient for us to generate a spherical harmonic expansion of $\gamma(\underline{k})$ at least to the order $Y_{22}(\beta,\alpha)$. Here, we use the notation in Jackson, p. 66,[5] with (β,α) the spherical polar angles of $\underline{k}$. We further assume that sufficient observations are made at frequencies subject to Eq. (25) to allow a two-term power series expansion in k of the coefficients of the spherical harmonic expansion. Thus, while we are considering low frequency band limiting here, we are not considering aperture limiting in this case. The latter is a subject for further research not practicable under the present program.

We shall use spherical harmonic expansions to analyze Eq. (23). We begin, then, with the following spherical harmonic expansion of $\gamma(\underline{k})$:

$$\gamma(\underline{k}) = \sum_{\ell=0}^{\infty} \sum_{m=-\ell}^{\ell} Y_{\ell m}(\beta,\alpha) A_{\ell m}(k) . \tag{26}$$

Here, the coefficients $A_{\ell m}(k)$ are defined by:

$$A_{\ell m}(k) = \int_0^{\pi} d \int_0^{\pi} d\beta \, \gamma(\underline{k}) Y_{\ell m}^*(\beta,\alpha) \sin\beta \tag{27}$$

$$0 \le |m| \le \ell < \infty ,$$

with (*) denoting complex conjugate. These coefficients can be derived from our observations of $\gamma(\underline{k})$.

On the right side in Eq. (23), we substitute the spherical harmonic expansion of the exponential function:[5]

$$\exp(-i\underline{k}\cdot\underline{y}) = 4\pi \sum_{\ell=0}^{\infty} (-i)^{\ell} j_{\ell}(ky) \sum_{m=-\ell}^{\ell} Y_{\ell m}^*(\theta,\phi) Y_{\ell m}(\beta,\alpha). \tag{28}$$

Here, (θ,ϕ) are the spherical polar angles of the vector $\underline{y}$, j_{ℓ} is the spherical Bessel function of of the first kind and order ℓ. We conclude then, that

$$A_{\ell m}(k) = 4\pi(-i)^{\ell} \int_D j_{\ell}(ky) Y_{\ell m}^*(\theta,\phi) dV . \tag{29}$$

$$0 \le |m| \le \ell < \infty .$$

We define the coefficients in the power series expansions of Eq. (29) by the equations,

$$A_{\ell m}(k) = \sum_{n=0} k^n A^n_{\ell m}, \quad 0 \le |m| < \ell < \infty . \tag{30}$$

Below, we shall use only $A^0_{\ell m}$, $0 \le |m| \le \ell \le 2$ and A^2_{00}. We begin with:

$$I^0_{00} = \frac{1}{\sqrt{4\pi}} \int_D dV = \frac{1}{\sqrt{4\pi}} \text{ (Volume of D)} . \tag{31}$$

Here, we have used the fact that $j_0(ky) = 1$ to leading order and $Y_{00} = 1/\sqrt{4\pi}$. We shall continue below to use such facts about Bessel functions and spherical harmonics, without stating those facts explicitly.

From Eq. (31) we see that knowledge of I^0_{00} yields the volume of the hole. We now consider the order one terms in the set of $I^n_{\ell m}$.

$$\begin{aligned} A^0_{1,1} + A^0_{1,-1} &= -i\sqrt{8\pi/3} \int_D y_1 dV ; \\ A^0_{1,1} - A^0_{1,-1} &= \sqrt{8\pi/3} \int_D y_2 dV ; \\ A^0_{10} &= -i\sqrt{4\pi/3} \int_D y_3 dV . \end{aligned} \tag{32}$$

Thus, to leading order, the spherical harmonic coefficients of order (1, ±1) and (1, 0) provide the components of the centroid of the domain D. With reference to the observation of the preceding section, these coefficients provide a correction to the approximation $\underline{r}_0$ in Fig. 1.

We now consider all coefficients of order k^2.

$$\begin{aligned} A^2_{00} &= -\frac{2\pi}{3}(I_{11} + I_{22} + I_{33}) \\ A^0_{20} &= -\frac{1}{3}\sqrt{\pi/5}\, I_{33} + \frac{2}{3}\sqrt{\pi/5}\,(I_{11} + I_{22}) \\ A^0_{2,\pm1} &= \sqrt{2\pi/15}\,(I_{13} \pm i\, I_{23}) \\ A^0_{2,\pm2} &= \sqrt{2\pi/15}\,[I_{12} \pm \tfrac{i}{2}(I_{11} - I_{22})] \end{aligned} \tag{33}$$

Here

$$I_{pq} = \int_D y_p y_q dV, \quad p,q = 1,2,3 . \tag{34}$$

These coefficients are the products of inertia (more precisely, because of the lack of a mass density, these are "normalized" products of inertia) of the domain D with respect to the origin, $\underline{r}_0$, of the $\underline{y}$ coordinate system. Before discussing their significance, we remark that they can be determined by inverting the system (Eq. (33)). The result is:

$$\begin{aligned} I_{11} &= \tfrac{1}{2}(\sqrt{15/2\pi}\,(A^0_{2,2} - A^0_{2,-2}) - \frac{A^2_{00}}{2\pi} + \sqrt{5/\pi}\, A^0_{20}) ; \\ I_{22} &= \tfrac{1}{2}(\sqrt{15/2\pi}(A^0_{2,2} - A^0_{2,-2}) - \frac{A^2_{00}}{2\pi} + \sqrt{5/\pi}\, A^0_{24}) ; \\ I_{33} &= -\frac{A^2_{00}}{\pi} - \sqrt{5/\pi}\, A^0_{20} ; \\ I_{12} &= \sqrt{15/8\pi}\,(A^0_{2,2} + A^0_{2,-2}) ; \\ I_{13} &= \sqrt{15/8\pi}\,(A^0_{2,1} + A^0_{2,-1}) ; \\ I_{23} &= -i\sqrt{15/8\pi}\,(A^0_{2,1} - A^0_{2,-1}) . \end{aligned} \tag{35}$$

We shall now transform these products of inertia to a center of mass coordinate system. To do so, let us define the components of the centroid determined in Eq. (32) to be:

$$\bar{y}_p = \int_D y_p dV, \quad p = 1,2,3 . \tag{36}$$

We then define the products of inertia with respect to the centroid coordinate system to be:

$$J_{pq} = \int_D (y_p - \bar{y}_p)(y_q - \bar{y}_q)dV = Y_{pq} - \bar{y}_p\bar{y}_q, \tag{37}$$

$$p,2 = 1,2,3 .$$

To understand the significance of these functions, let us consider the case in which D is an ellipsoid with semi-axes of length, a,b,c, along the coordinate axes. Then the matrix of coefficients (J_{pq}) is diagonal with elements, a^2,b^2,c^2. For any other matrix (J_{pq}), let U be the orthogonal matrix which diagonalizes it. Then U^T, the transpose of U, is the matrix which transforms the coordinate system to principal axes. The diagonal elements of $U^T(J_{pq})U$ then provide the squares of the semiaxes of an equivalent ellipsoid, having the same centroid and products of inertia. Thus, from (J_{pq}) we are able to determine orientation and aspect ratio parameters for D.

High Frequency Analysis

We now address ourselves to the question of extracting information about the size and shape of the domain, D, from knowledge of $\gamma(\underline{k})$ defined by Eq. (23) only for high frequency. Here, by "high frequency" we mean that,

$$ky >> 1, \quad \underline{y} \text{ in } D . \tag{38}$$

As noted under "Basic Formulation," there is a more extensive literature on this problem. We shall outline the results of that analysis and demonstrate the results with computer graphics.

In the high frequency regime it has proven more desirable to process data for a first derivative of $\Gamma(\underline{y})$, rather than for $\Gamma(\underline{y})$ itself. When $\Gamma(\underline{y})$ is a characteristic function, the first derivative, $\partial\Gamma/\partial y_1$, for example, is proportional to a Dirac delta function. The proportionality factor is linear in the cosine of the angle between the normal and tye y_1 axis.* We note that,

$$\partial\Gamma/\partial y_1 = 1/(2\pi)^3 \int ik_1\gamma(\underline{k}) \exp i(\underline{k}\cdot\underline{y})dk^3 , \tag{39}$$

with the domain of integration being all of $\underline{k}$ space. Let us suppose that $\gamma(\underline{k})$ is known for all angles of $\underline{k}$, but only for $k_{MIN} < k < k_{MAX}$, with Eq. (38) true for k_{MIN}. This is the case of band-limited (but not aspect angle limited) data.

*For surface elements where cosine is near zero, one could use a derivative with respect to y_2 or y_3.

We denote this annular region in $\underline{k}$-space by B. We set $\gamma(\underline{k})$ equal to zero outside of B and define the band-limited derivative:

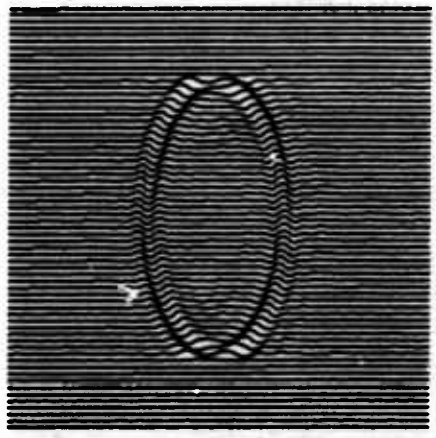
$$\partial\Gamma_B/\partial y_1 = 1/(2\pi)^3 \int_B ik_1\gamma(\underline{k}) \exp\{i\underline{k}\cdot\underline{y}\}dk^3 . \tag{40}$$

It has been shown by Mager and Bleistein[7] that, asymptotically, this function is proportional to the so-called "sin k function,"

$$\sin k(r) = \frac{\sin k_{MAX}r}{r} - \frac{\sin k_{MIN}r}{r} , \tag{41}$$

with r measuring minimum distance to the boundary of D. This function "peaks" at r = 0, thus distinguishing the boundary as an envelope of peaks.

We demonstrate the utility of this method through a series of pictorial examples beginning with Fig. 2. The examples are two-dimensional with D being an ellipse having semi-major axis of length, 2, semi-minor axis of length, 1. The Fourier transform of $\Gamma(\underline{k})$ is calculated by fast Fourier transform (FFT). The band limited inverse transform is then calculated using Eq. (40). The result is graphed (in Fig. 2, for example) with the third dimension (the function value) laid back down on the plane. On each line the height is normalized with respect to maximum height. Furthermore, the maximum on each line is tested against the absolute maximum. When this relative maximum falls below a critical value, the entire line is zeroed out. This insures, for example, that "noise" will not be enhanced outside of the vertical extent of the ellipse.



K Range 9-27

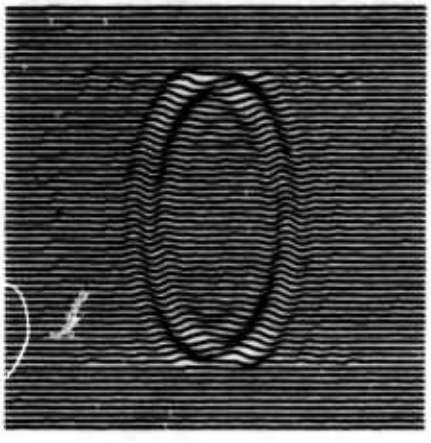
Figure 2. High frequency full aperture backscatter reconstruction.

Figure 2 depicts the result of very high frequency bandwidth processing, $9 \leq k \leq 27$. The characteristic main lobe-side lobe pair of the sin k function are observed on each line. The narrowness of the main lobe is a consequence of the high frequencies used. The relative height of the side lobes is a consequence of the percentage bandwidth,

$$\frac{k_{MAX} - k_{MIN}}{k_{MAX} + k_{MIN}} \times 100 ,$$

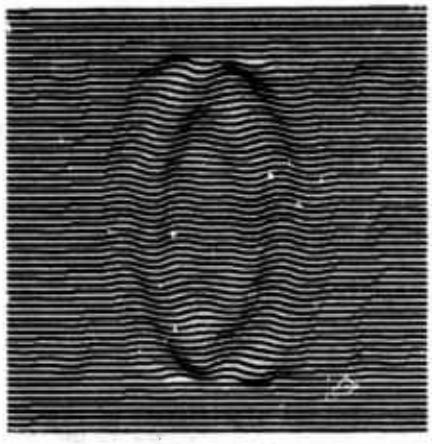
that was used here; namely 50%. This main lobe-side lobe configuration provides a characteristic signature. At this bandwidth, all further side lobes are virtually nil.

Figures 3 and 4 depict the results for lower frequency ranges 6 to 18 and 3 to 9, respectively, but the same 50% bandwidth. In Fig. 4, it is clear that visualization is becoming difficult. However, resolution can be improved by "curve fitting" the data to the known sin k function on each line. In Fig. 5, we repeat the frequency range of Fig. 4, but add the reference zero line at each level. The main lobe and two side lobes appear here as a characteristic triple of dark bands separated by two light bands produced by the zero crossings of the sin k function. The increased coherence in the picture is suggestive of the potential for analytical resolution enhancement. Figure 6 demonstrates the complete breakdown of this method when low to moderate frequency data is employed. We remark, however, that size and orientation are suggested by the figure, consistent with the conclusions of the discussion on "Low Frequency Analysis of the Characteristic Function."



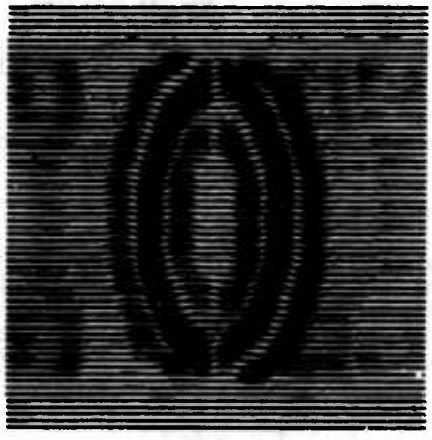
K Range 6-18

Figure 3. Medium high frequency full aperture backscatter reconstruction.



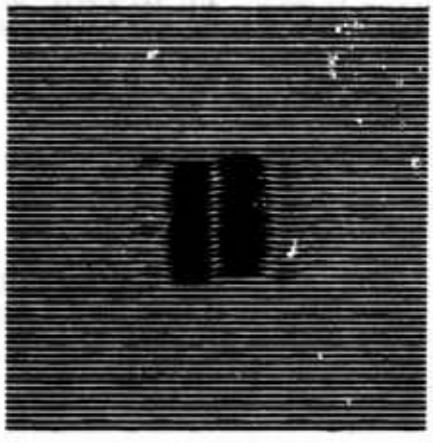
K Range 3-9

Figure 4. Medium frequency full aperture backscatter reconstruction.



K Range 3-9

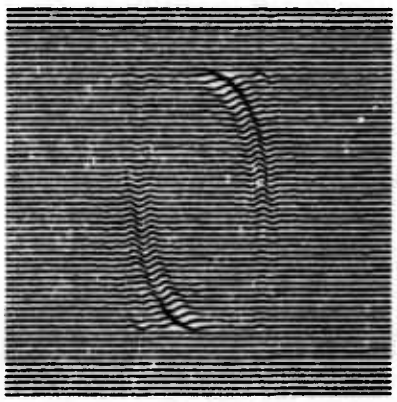
Figure 5. Medium frequency full aperture backscatter reconstruction and zero reference lines.



K Range .4-2.4

Figure 6. Low frequency full aperture backscatter reconstruction.

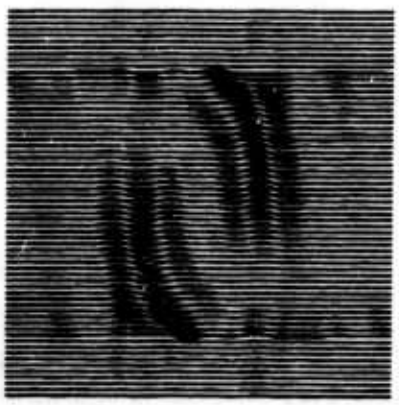
In Mager and Bleistein,[7] the problem of aspect limiting was considered as well. We showed that an angular aperture in $\underline{k}$-space defined an angular aperture in physical space in which the results were the same as for the full angular aperture case discussed above. The angular aperture in physical space is that one in which the normal direction of the boundary of D lies in the angular aperture in $\underline{k}$-space. Figures 7 and 8 demonstrate results for two symmetric 90° apertures. (Symmetric apertures are chosen for examples for convenience. They are not necessary for the theory.) In Fig. 8, considerable "spill-over" outside the predicted aperture is observed. This is well understood and discussed in the above cited paper.



K Range 9-27

Angular Range $\begin{matrix}0°-90°\\180°-270°\end{matrix}$

Figure 7. High frequency limited aperture reconstruction.



K Range 3-9

Angular Range $\begin{matrix}0°-90°\\180°-270°\end{matrix}$

Figure 8. Medium frequency limited aperture reconstruction.

In all of these examples, we have only demonstrated the extraction of information from an aperture limited (band limited and aspect angle limited) Fourier transform. In Mager and Bleistein,[7] the identity, Eq. (24), itself was verified in the high frequency case. This was done by determining I in the backscatter case, $\hat{\lambda} = \hat{\xi}$, by solving the scattering problem for a sphere numerically. The data was then phase and range normalized at 25 radii to produce I. We include one aperture limited diagram from that paper in Fig. 9. In that paper, we also showed that the same results will be obtained in three dimensions.

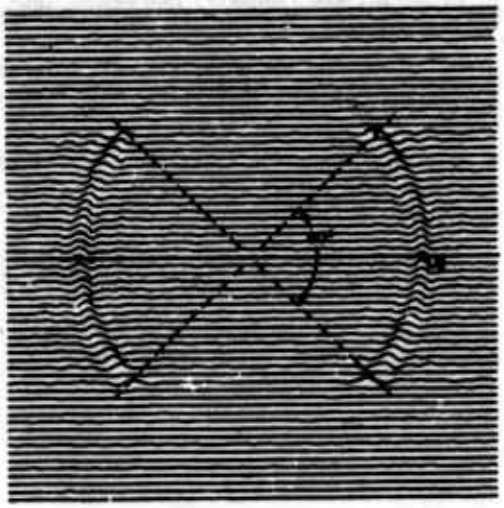


Figure 9. Limited aperture reconstruction from backscattered data at 25 radii.

Acknowledgement

This research was sponsored by the Center for Advanced NDE operated by the Science Center, Rockwell International, for the Advanced Research Projects Agency and the Air Force Materials Laboratory under contract F33615-74-C-5180.

References

1. B. B. Baker and E. T. Copson, The Mathematical Theory of Huygens Principle, 2nd Ed., Oxford (1950).

2. N. Bleistein, "Direct Image Reconstruction of Anomalies in a Plane via Physical Optics Forefield Inverse Scattering," J. Acous. Soc. Am., 59, 6, 1259-1264 (1976).

3. N. Bleistein, "Physical Optics Far Field Inverse Scattering in the Time Domain, J. Ac. Soc. Amer., 60, 6, 1249-1255 (1977).

4. N. N. Bojarski, "Three-Dimensional Electromagnetic Shortpulse Inverse Scattering," Syracuse University Research Corporation, Syracuse, New York (1967).

5. J. D. Jackson, Classical Dynamics, Wiley, New York (1962).

6. R. M. Lewis, "Physical Optics Inverse Diffraction," IEEE Trans. Ant. Prop. AP-17, 308-314 (1969).

7. R. Mager and N. Bleistein, "An Approach to the Limited Aperture Problem of Physical Optics Farfield Inverse Scattering," Denver Research Institute Report #MS-R-7704 (1976).

8. P. M. Morse, and Feshback, Methods of Theoretical Physics, McGraw-Hill, New York (1953).

9. W. L. Perry, "On the Bojarski-Lewis Inverse Scattering Method," IEEE Trans. Ant. Prop., Ap-22, 6, 826-829 (1974).

10. S. Rosenbaum-Raz, "On Scatterer Reconstruction from Farfield Data," IEEE Trans. Ant. Prop., AP-24, 66-70 (1976).

11. W. Tabbara, "On an Inverse Scattering Method," IEEE Trans. Ant. Prop., AP-21, 245-247 (1973).

12. W. Tabbara, "On the Feasibility of an Inverse Scattering Method," IEEE Trans. Ant. Prop., AP-23, 446-448 (1975).

IMPLEMENTATION: PRESENT STATUS AND FUTURE DIRECTIONS

R. B. Thompson
Science Center, Rockwell International
Thousand Oaks, California 91360

ABSTRACT

The previous papers present a number of techniques for quantitatively identifying the size, shape and orientation of defects in solid parts from the ultrasonic scattering information available at a single surface. This paper summarizes these results and discusses their interrelationships. A "decision tree" is presented which identifies the options that should be selected in various situations. Areas where future or in-progress work can be expected to have an impact on such procedures will be identified.

Figure 1 repeats Fig. 3 from my introduction because I want to again emphasize the methodology that has been involved in this program. We first were concerned with the development of both theoretical and experimental understanding of the interaction of an ultrasonic wave with a flaw. This is, to a great extent, complete and we are now attacking the inversion problem, whereby fracture related parameters of flaws are directly deduced from data obtained during ultrasonic measurement. This information will then be available for use in conjunction with fracture mechanics to define specific accept-reject criteria. In each of the general subject areas, there remain many things that we have not yet done. There are limitations on the accuracy of the theories that have been used; all possible types of defects have not been studied, and studies of certain inversion techniques have just begun. Nevertheless, we have made very significant progress by demonstrating how these individual building blocks fit together and by demonstrating successful inversion results for the case of ellipsoidal cavities. In this paper, I will summarize the progress that has been made and indicate the future directions that will be followed in order to ensure effective implementation of these ideas.

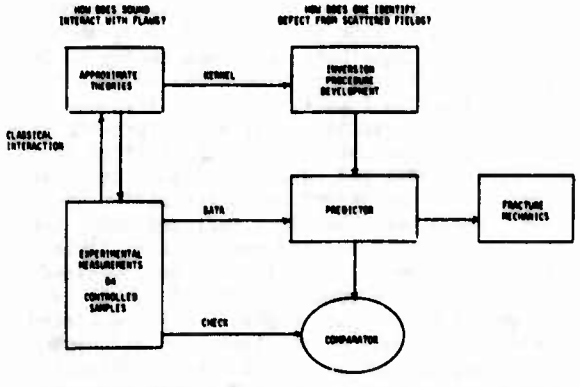


Figure 1. Philosophy of development of quantitative defect characterization techniques.

Figure 2 lists the specific technical approaches that have been used within each of the building block areas. Resources that are available, but not yet incorporated, are indicated by parentheses. In the theoretical area, much attention has focussed on the Born approximation because of its simplicity and the ease with which it can be generalized to complex shapes. Most of the experimental and inversion work has also been based on this model since it was the first available. Some additional more accurate models, the quasi static and extended quasi-static approximations have also been discussed; but these were developed relatively recently and there has not yet been time to fully integrate them into the program. These are available for future efforts. Experimentally, ellipsoidal cavities, disc shaped cavities, spherical cavities and inclusions, and some simulated cracks have all been studied. The effort primarily was concentrated on L→L scattering measurements. The adaptive learning work only utilized L→L scattering information as did the discussions of Domany and Tittmann. However, Adler did present some data on the mode converted L→T scattering which suggest that these signals contain important information that should be utilized. Most of the work utilized only the amplitude information. Phase does contain very important information, again as demonstrated by the work of Adler, and it should be incorporated in the future. For example, recalling the discussion of Bleistein which treats the shape reconstruction process as an inverse Fourier transform, it is clear that phase information is essential. Both the angular and frequency dependencies of the scattering have been discussed and used in detail. Inversion procedures have been developed based on adaptive learning, direct interpretation of observed physical features, and a direct mathematical solution of the inverse problem. The results of the adaptive learning procedure are very impressive in view of the fact that much of the available information was suppressed during the training phase because of systematic errors in the model. Incorporation of more accurate models in the future should yield further improvements in these encouraging results.

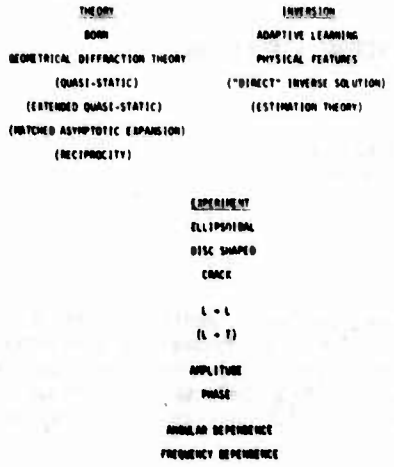


Figure 2. Specific technical approaches used within each of the building block areas.

Figure 3 repeats a comprehensive defect characterization scheme which Tittmann presented but did not have time to discuss in depth. On the right-hand side is shown the parameters one would like to know about a flaw, on the left-hand side the type of measurements that might be utilized in determining these parameters. The information is organized sequentially, starting at the top with an unknown flaw and ending at the bottom with an output for fracture mechanics. The time delay of an ultrasonic signal can first be utilized to determine the position of the defect. Then from backscattered data at a number of transducer positions, one can determine an orientation of the defect. The shape can then be deduced from certain observations of the angular dependence of scattering from a central transmitter to an array of receivers. (Alternatively, Domany would make use of the frequency dependence at two different angles in these determinations.) At this point, by looking at certain features of the ultrasonic fields one can determine whether it was an irregular crack-like defect or a smoother, ellipsoidal defect. For example, a T indicates that the ultrasonic signal is split and appears to be two distinct pulses. For crack-like defect with very sharp edges, one tends to see two signals that are produced by scattering from the edges whereas these edge signals are much less prominent in the ellipsoidal defect. After such observations have been used to make a separation between these two types, more quantitative size information can be produced by a phase measurement technique. As Tittmann briefly indicated, a comparison of the phases of the low frequency and the high frequency reflected signals can produce a quantitative measure of the dimensions of the defect. Once all of this is known, it is a relatively easy matter to obtain the acoustic impedance from the total scattered power. It is useful to look at the work of Mucciardi in the perspective of this defect characterization procedure. He assumed that the flaw had already been determined to be an ellipsoidal cavity. He then developed independent nonlinear networks which determined the two size parameters, the major and minor axes of the ellipsoids of revolution, and the two orientation parameters. This then provides us with a very powerful way of performing some of the operations in the more comprehensive procedure.

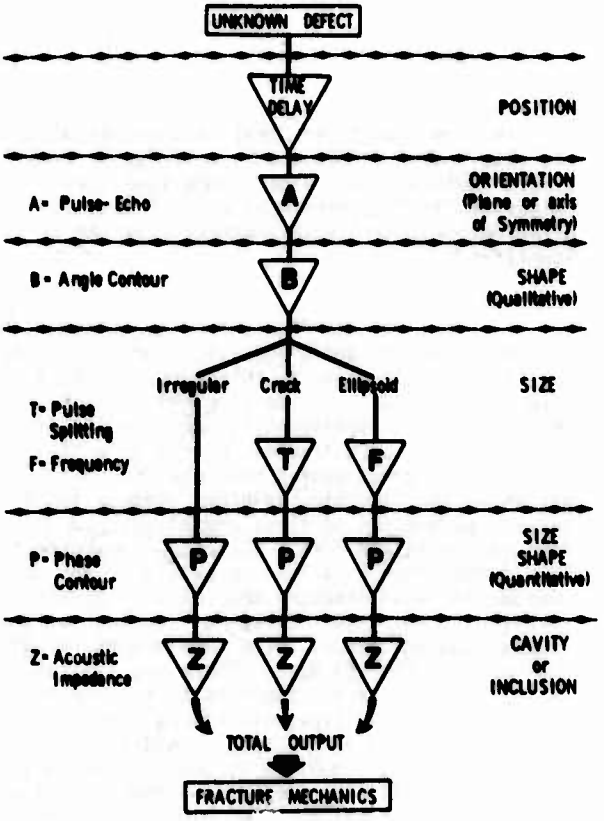


Figure 3. Defect characterization scheme.

Of course, there are many things one certainly needs to do in the future to refine this. Some of the tools that may be useful will be presented in the afternoon session. This work has been done under support outside the ARPA/AFML program but certainly can contribute very importantly to this flaw characterization problem. The matched asymptotic expansions, T matrix, reciprocity, and geometrical diffraction theories all provide means for extending the theoretical capabilities that we presently have and certainly should be incorporated in future defect characterization procedures. Hence they have been included under the category of unincorporated resources in Table I. Further experimental efforts will be addressed at considering a more general class of defect types. However, primary future emphasis will be placed on further development of the inversion techniques already discussed. In Fig. 2, one additional approach not discussed today has been included as a future resource. Richardson has been recently working on the application of estimation theory to NDE inversion problems. This provides an optimized

way to perform the inversion operation which is consistent with any pre-knowledge of the sorts of defects which may be present and the sources of noises in the experimental measurements.

Figure 4 summarizes what has been presented this morning. The building blocks of scattering theory, experimental observation and interpretation, and solutions of inverse scattering problems have been joined to demonstrate the capability to measure the size, shape, and orientation of ellipsoidal flaws. This, coupled with a number of things you will hear about in other sessions and which were summarized in Fig. 2 of my introductory talk, provides the basis for a defect characterization system which, in relatively simple cases, could be constructed in the near future. We hope to make such demonstrations in the next stages of this program. For some of the more complicated part geometries and defect types, there is need for additional theoretical, experimental, and inversion work. However, it is believed that this can be fitted into the framework indicated in Fig. 1 to provide an orderly and timely extension of capabilities.

JOINED THE BUILDING BLOCKS OF

- SCATTERING THEORY
- EXPERIMENTAL OBSERVATION AND INTERPRETATION
- SOLUTION OF INVERSE PROBLEM

TO DEMONSTRATE CAPABILITY TO MEASURE

- SIZE
- SHAPE
- ORIENTATION

OF ELLIPSOIDAL FLAWS

Figure 4. Summary of presentation.

DISCUSSION

IMPLEMENTATION: PRESENT STATUS AND FUTURE DIRECTIONS

R. B. Thompson, Moderator
Science Center, Rockwell International
Thousand Oaks, California 91360

B. P. Hildebrand (Battelle-Northwest): In all of this morning's session, and as far as I can see on the program, imaging is pretty well avoided. Is there a reason for it?

R. B. Thompson, Moderator (Rockwell International Science Center): I wouldn't say that imaging is avoided.

B. P. Hildebrand: Well, it's certainly not nearly as important, apparently, as the more indirect methods.

R. B. Thompson: I wouldn't necessarily want to say that. There are fewer papers on the program, but these represent a substantial effort. Gordon Kino will be presenting the work that he's done on imaging systems on Friday. He's also done some work that relates closely to imaging in ceramic materials. Also, the work to be presented by Lakin on transducer characterization makes use of imaging techniques. I think imaging is very important and I don't wish to minimize its importance.

There are some essential differences in the state of the art. As I see it, the imaging problem is primarily a technological problem. I think we know what we want to do with the signals. There are some very significant technological problems, of course. There's the problem of properly driving the elements, processing the received signals in real time, and so forth. The philosophy of this program has been to devote effort to understanding the generic physical principles underlying ultrasound-flaw interactions and to make use of these as appropriate in imaging or other signal processing schemes. We would like to see the "imaging" and "scattering" come closer together. For instance, I feel there is merit in trying to construct some sort of a hybrid system which would combine L→L and L→T scattering information to synthesize an image that might have higher resolution than an image formed in the classical way. One thing that does worry me about imaging in the context of certain production line applications is what one does once he has formed the image. How is it interpreted? How is it converted into a red light or a green light? Some of the scattering approaches may be simpler to convert into such an indication, but that's a personal opinion and you might well feel differently. I think those are the kinds of questions that are the key technical issues of the next few years.

G. S. Kino (Stanford University): ...but irrespective of that, how can you say that imaging doesn't give you more information? The eye is a tremendous recognition source--it's a hell of a good recognition source...

R. B. Thompson: Well, you're right and...

G. S. Kino: ...a sphere is a sphere and you can see it.

R. B. Thompson: You're absolutely right, Gordon. But the problem that I hear when I talk to a lot of people who are working on production lines is that the man gets tired. His eyeball doesn't say the same thing when he is bored after three hours that it said early in the morning. It is not that the information is not there, I certainly don't mean to say that because, it is. The real point is that an imaging system is a particular way to process ultrasonic fields. In the case of wavelengths that are small with respect to the size of the object, it's probably the optimum way. However, if experimental constraints are such that one cannot operate in those regimes, it may not be the optimum way and in fact I think it is probably not. But I really don't want to draw lines that clearly. Imaging is a fine way to go but what I'm trying to say is, "Let's find out what the basic principles are and determine in which regime each particular processing way is best."

V. L. Newhouse (Purdue University): One more comment to make about this question of imaging versus signal processing. We all believe in the validity of signal processing but we have to recognize that the human recognition ability is very superior and will be for a long time. To back up what Gordon said with regard to visual imaging, I'd like to point out that in the Tissue Characterization Conference (which has been cleverly arranged to take place yesterday and today at Gaithersburg, Maryland, which, of course, is unfortunate because there is a lot of overlap between the kind of topics that they're handling there and the kind of topics we're handling here), there have been suggestions made that it might even be advantageous to take the data that we get out of A-scan systems and frequency convert them to the audio range because it's known that the human audio pattern recognition capability is very, very powerful. So, what this means is that it's apparently even possible for people to recognize the bark of their dog from the bark of a pack of dogs.

So, audio recognition has been used a lot in medicine, for instance, for pattern recognition. Therefore, it would appear that we shouldn't ignore the human factor and we should try to do our signal processing in many cases so as to produce a pattern which is capable perhaps of being recognized by the audio or visual senses of the human operator. That may well be a very powerful technique. Possibly an alternative to the computer technique that Tony's been so ably working on at Adaptronics. Certainly it's something that shouldn't be ignored.

R. B. Thompson: Let me say one word in response to that. This issue was discussed at great lengths at one of the meetings we had a couple of years ago at the Science Center - I don't remember which one - and the point was made that in the medical field, the interpreter of data is a very highly paid individual and is, in general, highly skilled. In the nondestructive testing field, for whatever reason, that's often not the case. So there may be a difference in the approaches taken because of this external boundary condition that none of us can really address.

V. L. Newhouse: That is not so. I have a lot to do with the medical field because of our research programs. It turns out that the initial research is done by the highly paid physician but the routine examination is done by people who are called technicians. They are not highly paid but they are highly skilled.

R. S. Gilmore (General Electric): I'd like to come down on the side of Bruce, here. One of the problems in a practical environment where you apply an inspection is that usually you have to look at a large number of pieces. The problem is that humans are very unreliable under such conditions. We're working very hard to get people out of the decision making process so that we can improve the reliability of our inspections. When we consider imaging or medical applications, I would suspect that the number of decisions that have to be made are relatively few in comparison to the normal industrial production environment.

H. Guttwein (U. S. Army R&D Command, Dover, New Jersey): I'm jumping ahead, I realize here. Has any thought been given to the methodology in using this particular inversion data to correlate between your artificially produced defects and, say, some natural type defects that have occurred. Has there been any correlation work done?

R. B. Thompson: Not in what you've heard this morning. I think in the area of the ceramics, there's been some of that.

H. Guttwein: The second question is that I notice that all your standards are titanium. Is that by accident or is there a reason for it?

R. B. Thompson: There is a reason. It turns out that the diffusion bonding process works very well in titanium.

H. Guttwein: How does it work for aluminum or steel?

R. B. Thompson: We have done work in the program in developing diffusion bonding techniques for both of these materials. The basic problem is that if you do the bonding in a room atmosphere, there is an oxide formation which can inhibit bonding. This is soluble in titanium at bonding temperatures so there is no problem. In steel, we have found that when we do the bonding in a reducing atmosphere, we can, in fact, fabricate such samples. In aluminum we have also had success by sputtering off the oxide layer, then bonding the samples in vacuum. This has been done in the laboratory.

H. Guttwein: But it can be done?

R. B. Thompson: It can certainly be done. It is more expensive so we didn't choose to use it to prepare samples for this program.

H. Guttwein: My last comment is that, considering the industrial environment and the need for accurate and high volume type inspection, you have to eliminate the human being as the inspector. You have to make an electrical and mechanical inspection but not a human inspection. Thank you.

MATCHED ASYMPTOTIC EXPANSIONS APPLIED TO SCATTERING CALCULATIONS*

S. K. Datta
University of Colorado
Boulder, Colorado 80309

ABSTRACT

The diffraction of elastic waves by inclusions, cavities and cracks has been the subject of numerous studies in recent years. Because of analytical difficulties, however, most of these studies have dealt with spherical or circular inclusions and straight or circular cracks. In a series of recent papers we have shown that for long wavelengths it is possible to obtain an asymptotic expansion of the scattered field by the method of matched asymptotic expansions. These papers have dealt with ellipsoidal and elliptic inclusions. We also have been able to use this technique to solve scattering problems in a half-space. In this paper we present briefly the results that we have obtained in the course of this investigation. The results include scattering by ellipsoidal inclusions in three dimensions and elliptic cylinders in two dimensions, by buried circular cavities and elliptical inclusions in a half-space, and by an edge crack. In the context of the last problem it is shown that MAE together with analytic function techniques can be used to solve many (not necessarily straight) crack problems in two dimensions.

Introduction and Summary of the Results

The equation governing the displacement field $\underline{u}$ in a homogeneous isotropic linearly elastic solid is

$$c_1^2 \underline{\nabla}\underline{\nabla}\cdot\underline{u} - c_2^2 \underline{\nabla}\wedge\underline{\nabla}\wedge\underline{u} = -\omega^2\underline{u} \qquad (1)$$

where harmonic time dependence has been assumed. c_1, c_2 are the longitudinal and shear wave speeds in the medium. If an inclusion of different material properties is assumed to be embedded in this medium then the problem is to analyze the scattered displacement field, denoted by $\underline{u}^{(s)}$, when an incident wave, denoted by $\underline{u}^{(i)}$, impinges on the inclusion. We shall assume that the inclusion occupies a finite volume V (finite area in two dimensions) bounded by a closed surface S (closed curve in two dimensions). Let L be a characteristic linear dimension of the inclusion. Then it has been shown in References [1-6] that if $\epsilon = \omega L/c_1$ is small, the problem can be solved by a method of matched asymptotic expansions. In brief the technique is the following.

Let us introduce non-dimensional inner variables

$$\bar{\underline{x}} = \underline{x}/L \qquad (2)$$

Then equation (1) can be rewritten as

$$\bar{\underline{\nabla}}\bar{\underline{\nabla}}\cdot\underline{u} - \tau^{-2}\bar{\underline{\nabla}}\wedge\bar{\underline{\nabla}}\wedge\underline{u} = -\epsilon^2\underline{u} \qquad (3)$$

when

$$\underline{u} = \underline{u}^{(s)} + \underline{u}^{(i)}, \quad \underline{x} \in V$$

The boundary conditions for this inner problem are provided by the continuity of displacement and tractions across S. The solution to this inner problem is assumed to be of the form

$$\underline{u} = \underline{u}_0 + \mu_1(\epsilon)\underline{u}_1 + \mu_2(\epsilon)\underline{u}_2 + \ldots \qquad (4)$$

where $\mu_{n+1}/\mu_n \to 0$ as $\epsilon \to 0$. Substitution of (4) in (3) and equating the terms of the same order from both sides leads to a set of equations for u_n. Since the solutions to these equations would not satisfy the appropriate radiation conditions at infinity, the $\underline{u}_n$'s are not completely determined.

In order to complete the solution we formulate the outer problem in terms of the outer variables

$$\underline{x}' = \epsilon\bar{\underline{x}} \qquad (5)$$

and an assumed outer expansion

$$\underline{u} = \underline{u}^{(i)} + \nu_1(\epsilon)\,\underline{u}' + \ldots \qquad (6)$$

where $\nu_{n+1}/\nu_n \to 0$ as $n \to \infty$. The equations governed by $\underline{u}'_n$ are

$$\underline{\nabla}'\underline{\nabla}'\cdot\underline{u}'_n - \tau^{-2}\underline{\nabla}'\wedge\underline{\nabla}'\wedge\underline{u}'_n = -\underline{u}'_n, \qquad (7)$$

and u'_n satisfies the appropriate radiation condition. The solution is now completed by matching the nth order outer expansion of the mth order inner expansion with the mth order inner expansion of the nth order outer expansion.* It is found that in three dimensions $\mu_n(\epsilon)$ and $\nu_n(\epsilon)$ are integer powers of ϵ. However, in two dimensions they are of the form $\epsilon^{p}\ln^{q}\epsilon$ $(q<p)$. Using this approach we solved in Reference [1] the diffraction

*This research is supported in part by a grant (NSF-ENG76-04328) from the National Science Foundation

*The matching can also be done by introducing an intermediate variable as was done in Reference [2-6].

of elastic waves by a rigid spheroidal inclusion. For simplicity this analysis was confined to a plain longitudinal wave incident along the axis of symmetry. Results were presented for both the motion of the spheroid and the scattered far field. Figures 1-2 show the amplitudes of oscillation of different spheroids in comparison with the exact solutions obtained in References [7,8]. It is seen that the agreement is rather remarkable. In Figs.3-10 we show the angular dependence of the far-field displacement components for scattering from rigid spheroids of different shapes. Here

$$U_\xi^{S(T)} = iU_\xi \xi' e^{-i\xi'}/\tau a_1 \ , \ U_\eta^{S(T)} = iU_\eta \xi' e^{-i\tau\xi'}/\tau b_1 \quad (8)$$

for prolate spheroids, and

$$U_\xi^{S(T)} = -U_\xi \xi' e^{-i\xi'}/\tau a_1 \ , \ U_\eta^{S(T)} = -U_\eta \xi' e^{-i\tau\xi'}/\tau b_1 \quad (9)$$

The superscripts S or T stand for the cases when the spheroid is held fixed or not. a_1 is a normalization constant and

$$b_1 = a_1/\tau^2 \ , \ \epsilon_1 = \epsilon\xi_0/\pi$$

The Poisson's ratio has been taken to be 1/4. Later Sangster [9] considered the more general case of oblique incidence.

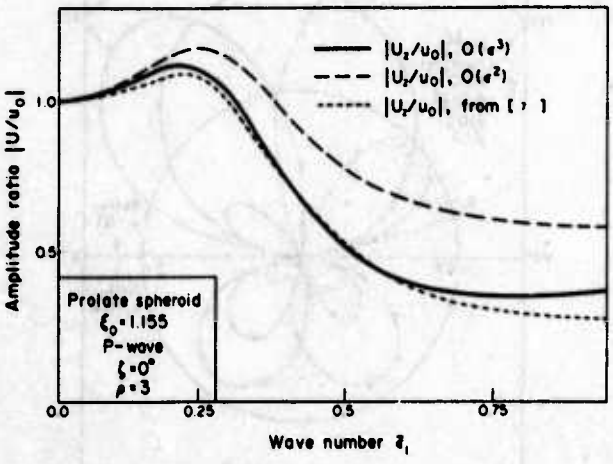


Figure 1. Amplitude of oscillation of a prolate spheroid $\epsilon_1 = \epsilon\xi_0/\pi$.

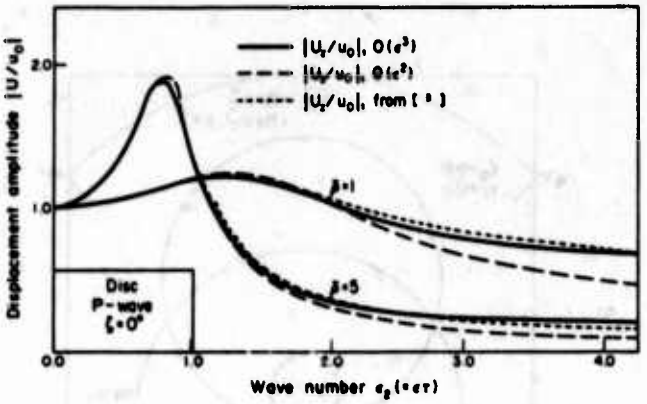


Figure 2. Amplitude of oscillation of a rigid disc.

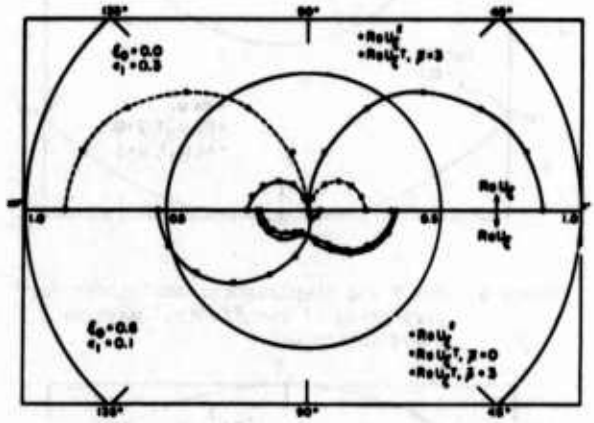


Figure 3. Far field displacement amplitudes for scattering of longitudinal wave by rigid spheroids.

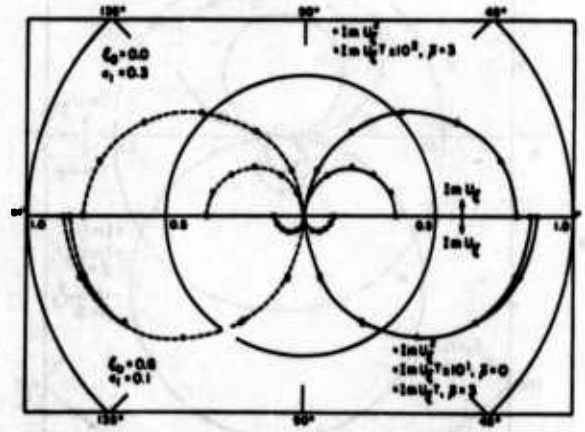


Figure 4. Far field displacement amplitudes for scattering of longitudinal wave by rigid spheroids.

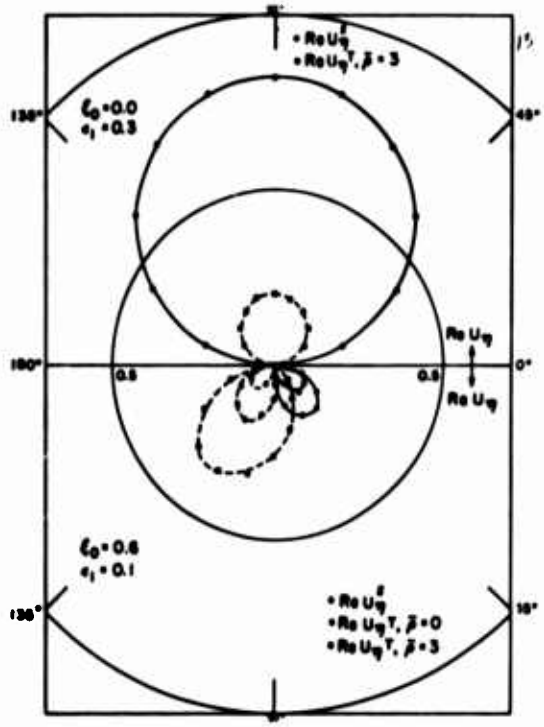


Figure 5. Far field displacement amplitudes for scattering of longitudinal wave by rigid spheroids.

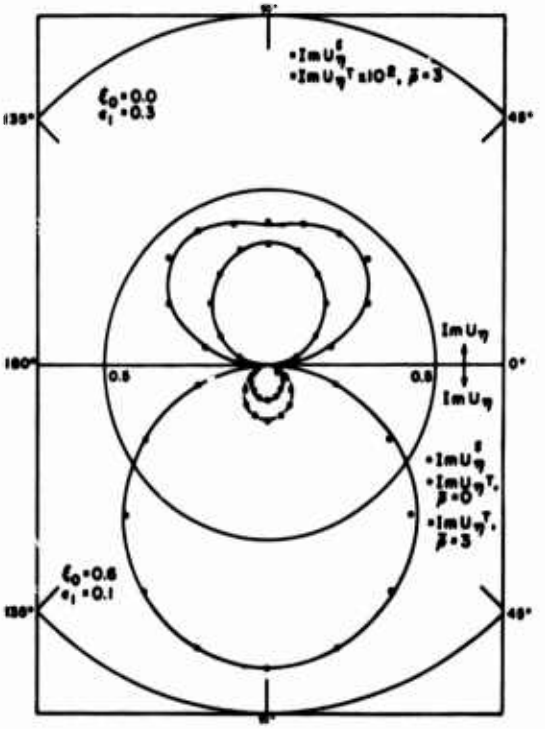


Figure 6. Far field displacement amplitudes for scattering of longitudinal wave by rigid spheroids.

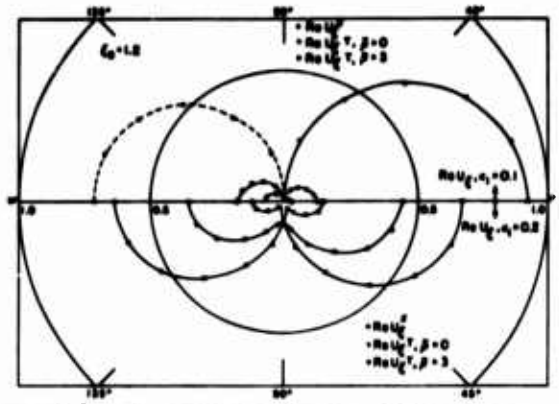


Figure 7. Far field displacement amplitudes for scattering of longitudinal wave by rigid spheroids.

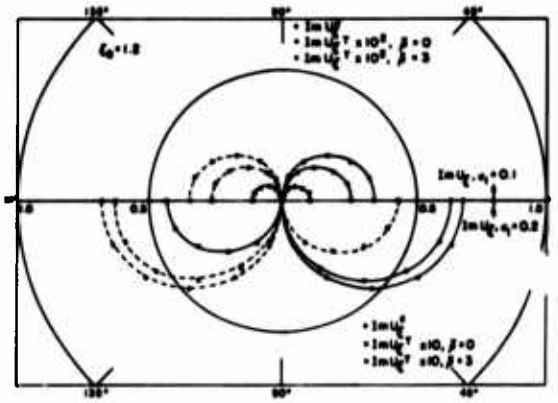


Figure 8. Far field displacement amplitudes for scattering of longitudinal wave by rigid spheroids.

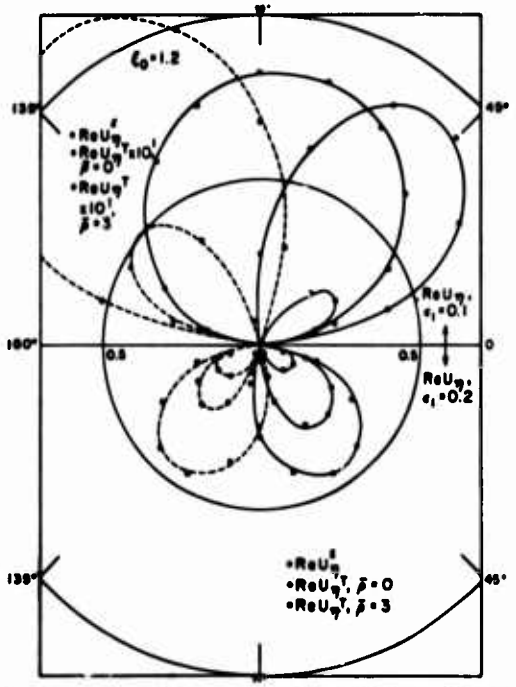


Figure 9. Far field displacement amplitudes for scattering of longitudinal wave by rigid spheroids.

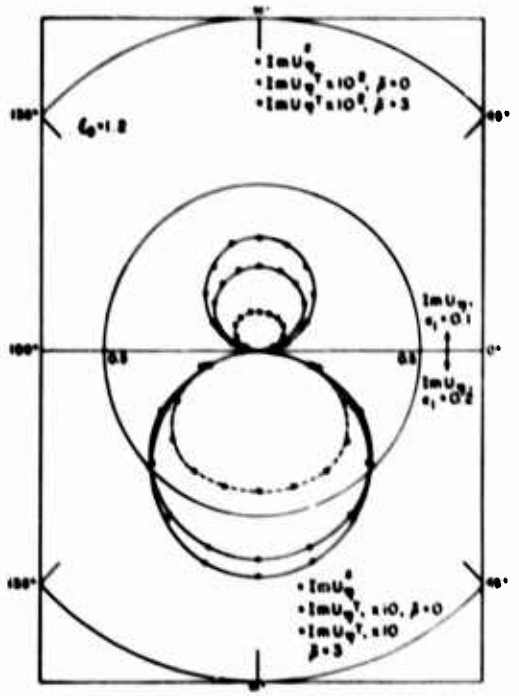


Figure 10. Far field displacement amplitudes for scattering of longitudinal wave by rigid spheroids.

In References [2,3] the analysis was confined to the diffraction of an antiplane shear wave by an elliptic cylinder and the far field was computed to $O(\epsilon^2)$ with $\epsilon = \omega L/C_2$ in this case. More recently [10] we have extended the calculations to $O(\epsilon^4)$ and the far field displacement amplitudes are shown in Figs. 11-12. In [11] we have analyzed the problem of a branched crack and have derived the results for an edge crack in a semi-infinite plane. Angular dependence of the amplitudes is shown in Fig. 13. It is shown in [11] that in two dimensions matched asymptotic expansions along with conformal mapping techniques can be used for arbitrarily shaped cavities. This is particularly useful for branched or curved cracks.

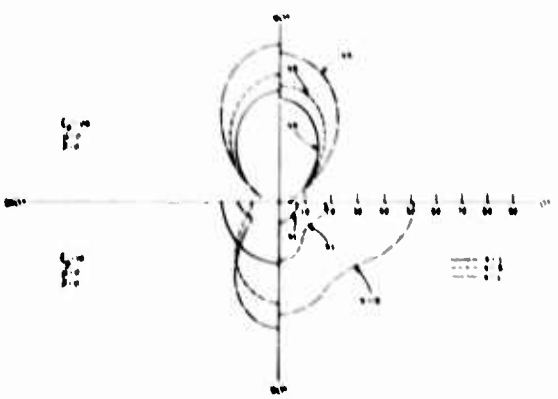


Figure 11. Back and forward scattered amplitudes for scattering of antiplane shear waves by an elliptic inclusion.

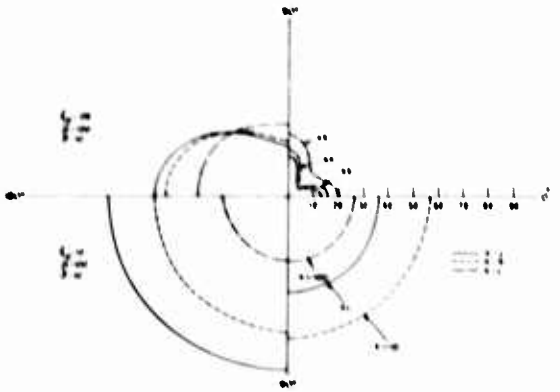


Figure 12. Back and forward scattered amplitudes for scattering of antiplane shear waves by an elliptic inclusion.

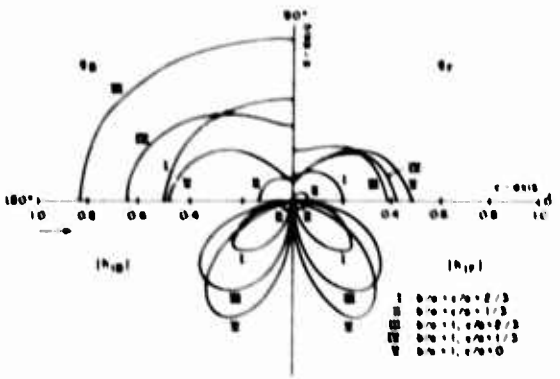


Figure 13. Far field displacement amplitude for scattering of antiplane shear waves by an edge crack.

Three dimensional diffraction by an elastic ellipsoidal inclusion has been solved in Reference [5]. The far field displacement amplitudes are shown in Figs. 14-17 for ellipsoidal cavities of various shapes. Since the calculations were confined to the lowest order in ϵ the normalized amplitudes defined as

$$g(\theta,\omega) = \frac{r' u_r^{(s)}}{\epsilon^3 u_0} e^{-ir'}, \quad h_1(\theta,\omega) = \frac{r' u_\theta^{(s)}}{\epsilon^3 u_0} e^{-ir'}$$

$$h_2(\theta,\omega) = \frac{u_\omega^{(s)} r'}{\epsilon^3 u_0} e^{-ir'} \tag{10}$$

do not depend on the frequency.

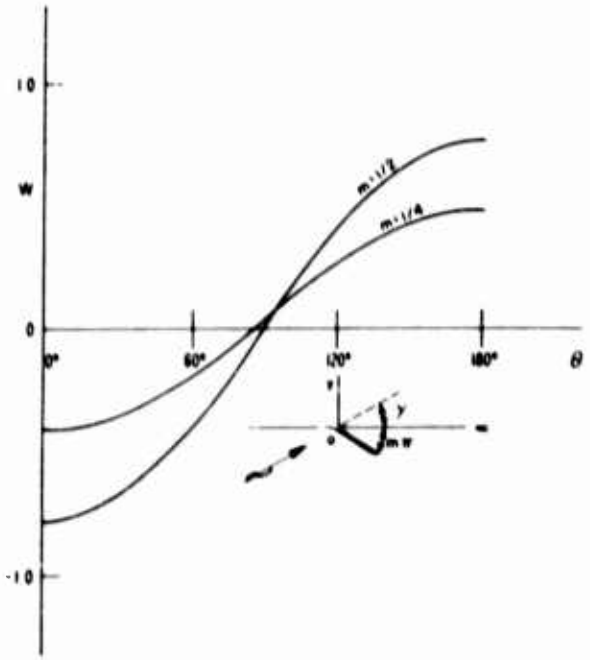


Figure 14. Back and forward scattered amplitudes of scattered longitudinal and shear waves for scattering by an ellipsoidal cavity (Incident longitudinal wave).

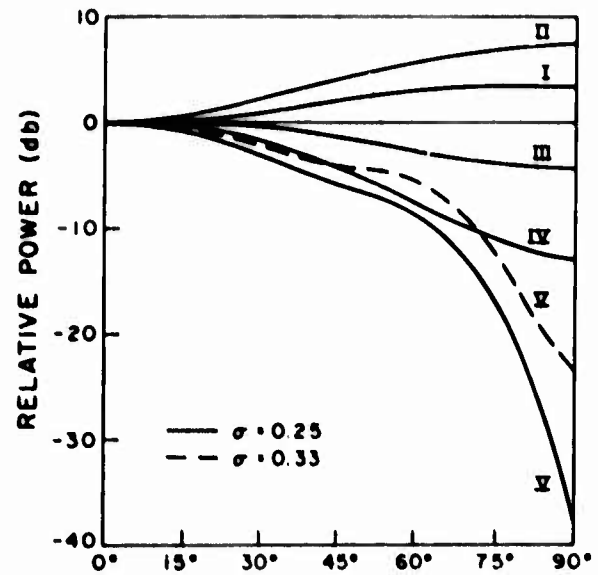


Figure 15. Backscattered power for an incident longitudinal wave.

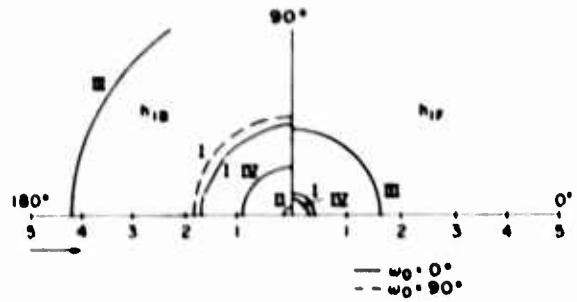


Figure 16. Back and forward scattered amplitudes of scattered shear wave (Incident shear wave).

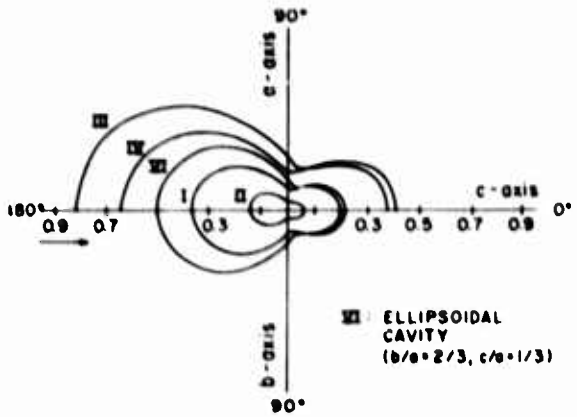


Figure 17. Far field displacement amplitudes for scattered longitudinal wave (Incident longitudinal wave).

In conclusion we would like to point out that MAE can also be used to solve diffraction problems in a half-space. This is discussed in Reference [12] in the context of diffraction by an elliptical inclusion and a circular cylindrical shell buried in a half-space. This extends the analysis for circular cavities presented in Reference [4].

References

1. Datta, S. K. and Sangster, J. D., SIAM J. Appl. Math., 26. 1974, 350-369.

2. Datta, S. K., Int. J. Solids and Str., 10, 1974, 123-133.

3. Datta, S. K., J. Appl. Mech., 42, 1975, 165-170.

4. Datta, S. K., Proc. 12th Annual Meeting of the Society of Engineering Sci., University of Texas, Austin, 1975, 49-55.

5. Datta, S. K., J. Acoust. Soc. Am., June 1977 (To appear).

6. Datta, S. K., Mechanics Today, vol. 4, Ed. S. Nemat-Nasser, Pergammon Press, 1977. 149-208 (To appear).

7. Oien, M. A. and Pao, Y. H., J. Appl. Mech. 40, 1973, 1073-1077.

8. Mal, A. K., Bull. Seismo. Soc. Am., 61, 1971, 1717-1729.

9. Sangster, J. D., The Scattering of Plane Elastic Waves by Rigid Spheroidal Inclusions, Ph.D. Thesis, Department of Mechanical Engineering, University of Colorado, Boulder, Colo., 1974.

10. Datta, S.K., "Scattering by a Random Distribution of Inclusions and Effective Elastic Properties," Report CUMER-77-5, June 1977. To be presented at the Second International Symposium on Continuum Models of Discrete Systems, Mont Gabriel, Quebec, June 26-July 2, 1977.

11. Datta, S. K., "Diffraction of SH-waves by a Brachned Crack," to be published.

12. Datta, S. K., and El-Akily, N., "Diffraction of Elastic Waves in a Half-space. I: Integral Representations and Matched Asymptotic Expansions," CUMER-77-6, June 1977. To be presented at the IUTAM Symposium on Modern Problems in Elastic Wave Propagation, Evanston, Ill., Sept. 12-15, 1977.

SPECTRAL ANALYSIS OF ELASTIC WAVES SCATTERED BY OBJECTS WITH SMOOTH SURFACES

Y. H. Pao and V. Varadan
Cornell University
Ithaca, NY 14853

ABSTRACT

This is a summary of the research on NDE performed during the last two years by the authors and Professor W. Sachse and Messrs. S. Sancar and G. C. C. Ku of the Department of Theoretical and Applied Mechanics at Cornell University. The report is divided into three parts: (1) Theoretical Spectra - Results based on the method of wave function expansion and the method of transition matrix (T-matrix) will be presented for the scattering by a circular cylindrical, elliptic cylindrical, spherical, and spheroidal (prolate or oblate) inclusions in solids. Additional results for the scattering by two circular cylindrical inclusions will also be shown. (2) Interpretation of Spectra - Spectra of a fluid inclusion may be interpreted on the basis of the theory of normal modes, and those of a cavity from the principle of interference. Spectra for two cylindrical cavities exhibit new features which are related to the interferences of waves diffracted by each cavity. (3) Comparison with Experiments - Some of the theoretical spectra are compared with experimental results obtained by Professor W. Sachse and his associates.

Introduction

As discussed in Ref. 1, the spectrum of the pulses scattered by an obstacle in an elastic solid equals the product of the spectrum of the incident pulse and the spectrum of responses of the obstacle when it is excited by monochromatic waves. In an experiment, the spectrum of the incident pulse can be isolated from the total spectrum; hence, we consider only the spectrum generated by the obstacle when radiated with monochromatic waves.

Let $u^i(\underset{\sim}{x},\omega)\exp(-i\omega t)$ be the displacement vector due to the incident harmonic waves of angular frequency ω, and $u(\underset{\sim}{x},\omega)\exp(-i\omega t)$ be the total wave field in the medium at the location $\underset{\sim}{x}$. The amplitude of the scattered waves can be expressed as

$$u^s(\underset{\sim}{x},\omega) = u(\underset{\sim}{x},\omega) - u^i(\underset{\sim}{x},\omega) \tag{1}$$

Our aim is to determine $u^s(\underset{\sim}{x},\omega)$ as a function of $\underset{\sim}{x}$ and ω. From u^s, all other quantities of interest like stresses, velocities and scattering cross-sections can be easily calculated.

Theoretical Spectra

The method which we developed to determine $u^s(\underset{\sim}{x},\omega)$ is an extension of the transition matrix (T-matrix) method originally developed by P. C. Waterman[2] for acoustic waves (scalar waves). Based on Huygens' principle for waves in an elastic solid, the waves scattered by a body with surface S are related to the secondary sources at S and the primary source by the following integral formula[3]

$$u^i(\underset{\sim}{x}) + \int_S [u(\underset{\sim}{x}')\cdot\underset{\sim}{n}'\cdot\underset{\sim}{\tau}(\underset{\sim}{x}|\underset{\sim}{x}') - \underset{\sim}{t}(\underset{\sim}{x}')\cdot\underset{\sim}{G}(\underset{\sim}{x}|\underset{\sim}{x}')]dS' \tag{2}$$

$$= \begin{cases} \underset{\sim}{u}(\underset{\sim}{x}); & \underset{\sim}{x} \text{ outside } S \\ 0; & \underset{\sim}{x} \text{ inside } S \end{cases}$$

In the above formula, $u(x')$ and $t(x')$ are respectively the unknown displacement and traction vectors at x', a point on S; n' is the unit outward normal to S at x' (Fig. 1). The functions $\underset{\sim}{G}$ and $\underset{\sim}{\tau}$ are respectively the Green's displacement tensor and the Green's stress tensor.

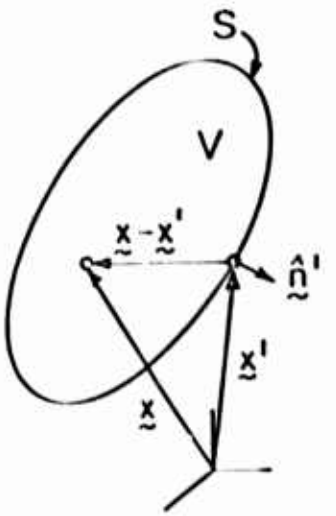


Figure 1. Mathematical model.

The essence of the transition matrix method is as follows: Select a set of vector basis functions $\phi_m^\sigma(x)$, $\psi_m^\sigma(x)$, and $\chi_m^\sigma(x)$ for vector waves in an elastic solid and then expand the unknown field $u^s(x)$ into a series of these basis functions.

$$u^s(x) = \sum_m \sum_{\sigma=1}^{2} [\alpha_m^\sigma \phi_m^\sigma(x) + \beta_m^\sigma \psi_m^\sigma(x) + \gamma_m^\sigma \chi_m^\sigma(x)] \quad (3)$$

The known incident field can be expanded into a series of the real parts of the basis functions denoted by $\hat{\phi}$, $\hat{\psi}$, $\hat{\chi}$.

$$u^i(x) = \sum_m \sum_{\sigma}^{2} [A_m^\sigma \hat{\phi}_m^\sigma(x) + B_m^\sigma \hat{\psi}_m^\sigma(x) + C_m^\sigma \hat{\chi}_m^\sigma(x)] \quad (4)$$

Since u^i is known, the coefficients A_m^σ, B_m^σ, and C_m^σ can be determined exactly. Substituting (3) and (4) into (2), we have shown that the unknown coefficients α, β, γ are related to A, B, C by an infinite matrix, known as the T-matrix[4].

$$\begin{pmatrix} \alpha_m^\sigma \\ \beta_m^\sigma \\ \gamma_m^\sigma \end{pmatrix} = \begin{pmatrix} T^{11} & T^{12} & T^{13} \\ T^{21} & T^{22} & T^{23} \\ T^{31} & T^{32} & T^{33} \end{pmatrix}_{mn}^{\sigma\nu} \begin{pmatrix} A_n^\nu \\ B_n^\nu \\ C_n^\nu \end{pmatrix} \quad (5)$$

Each element $(T^{ij})_{mn}^{\sigma\nu}$ represents an infinite sub matrix which depends on the choice of the basis function and the geometry of the bounding surface S. For a circular cylinder or a sphere, using circular cylindrical wave functions or spherical wave functions respectively, the T^{ij} can be determined exactly. For a body with a smooth, convex bounding surface, T^{ij} are determined from the surface integrals of the basis functions over S.

We note that P. C. Waterman[5] has given a matrix formulation for elastic waves beginning with a different integral representation.

Based on our formulation and a computer code developed by us, we can calculate $u^s(x,\omega)$ for a wide range of frequencies. Sample results are shown below (unless noted otherwise, inclusions are embedded in aluminum blocks):

(A)

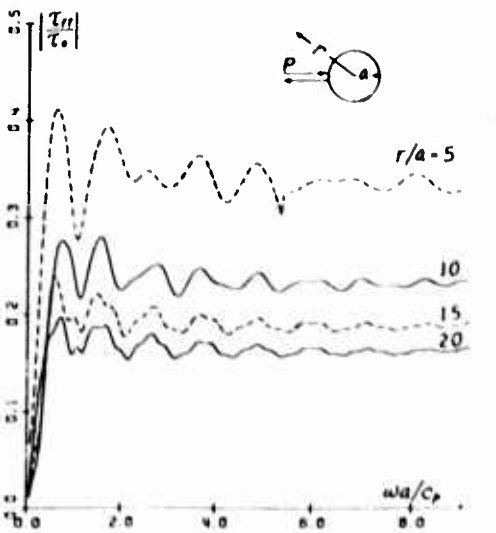


Figure 2. Backscattering of P-waves (longitudinal waves) by a circular cylindrical cavity (τ_{rr} is the radial stress, c_p the P-wave speed in solid).

(B)

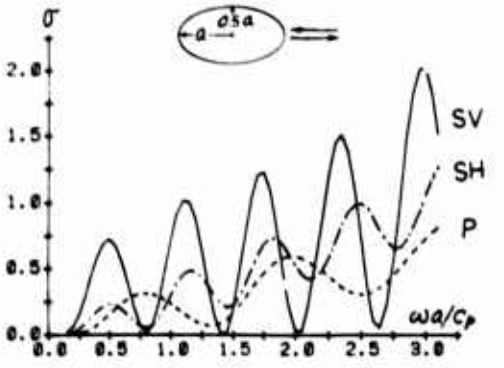


Figure 3. Backscattering by an elliptic cylindrical cavity for an incident P,SV (transversely polarized shear) and SH (horizontally polarized shear) wave along the major axis (σ is the differential cross section).

(C)

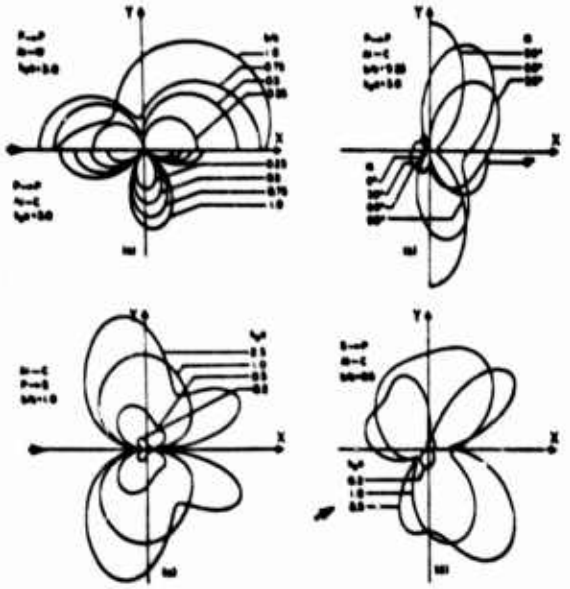


Figure 4. Angular distribution of far field scattered wave amplitudes by an elliptical cylinder with major axis 2a (along x-axis) and minor axis 2b. (Al-W indicates tungsten cylinder in aluminum matrix; Al-C indicates a cavity in aluminum solid; α the incident angle with respect to the x-axis)[7].

(D)

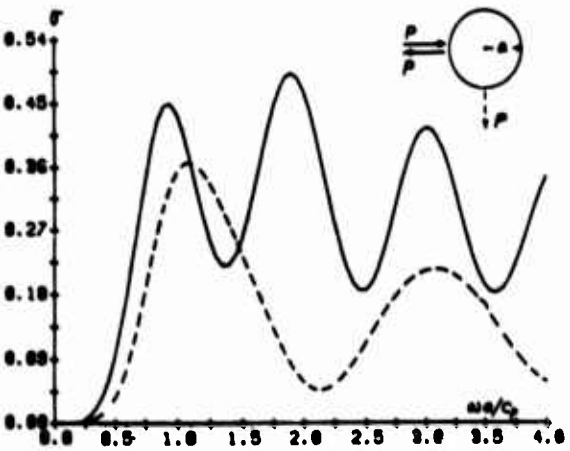


Figure 5. Backscattering and right-angle scattering of P-waves by a spherical cavity of radius 'a' (σ is the differential cross section)[8].

(E)

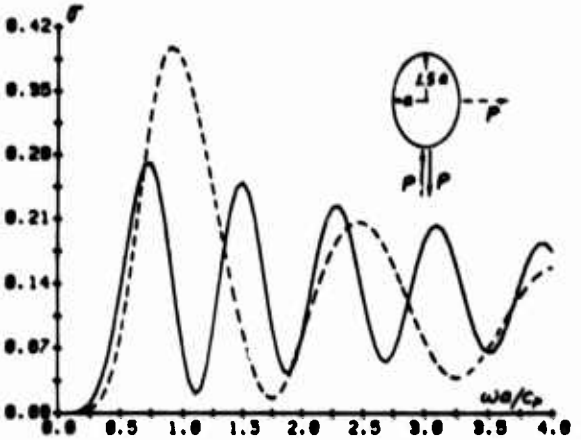


Figure 6. Backscattering and right-angle scattering of P-waves by a prolate spheroid (σ is the differential cross section)[9].

(F)

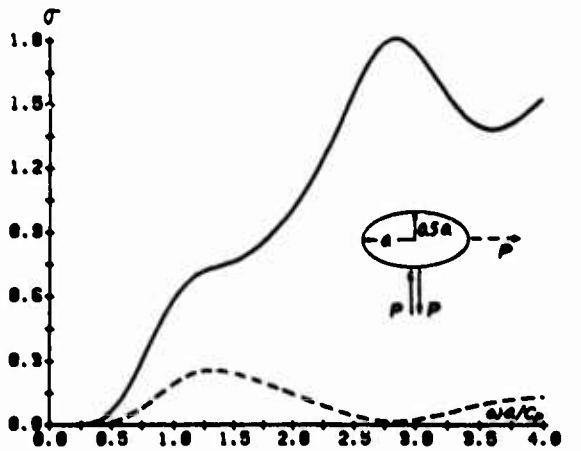


Figure 7. Backscattering and right-ang e scattering of P-waves by an oblate spheroid (σ is the differential cross section)[9]

(G)

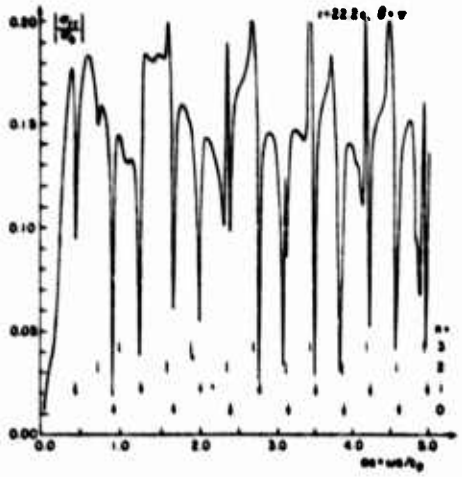


Figure 8. Backscattering of P-waves by a circular cylindrical cavity filled with water (σ_{rr} is the radial stress at distance r = 22.2a)[1].

In addition, we have made exact and approximate analysis of the multiple scattering of incident P-waves by two cylindrical cavities (Fig. 9) and two fluid cylinders (Fig. 10). The exact analysis is based on either the interactive method for multiple scattering developed by V. Twersky[11,12] or the T-matrix method for multiple scattering

(H)

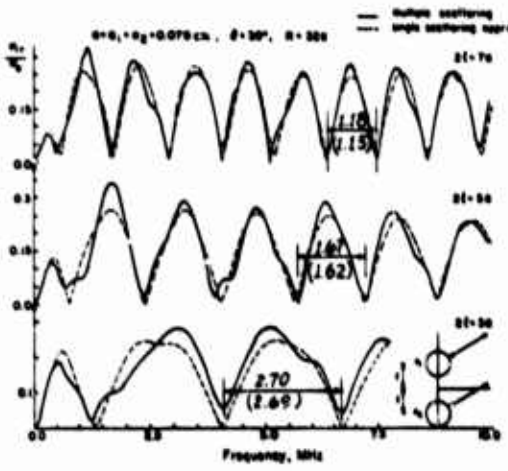


Figure 9. Backscattering of P-waves by two circular cylindrical cavities separated by a distance 2b, incident at an angle $\theta = 30^\circ$ with the horizontal axis (σ_{rr} is the radial stress at distance R = 32a from the mid-point of two circles)[13]

(I)

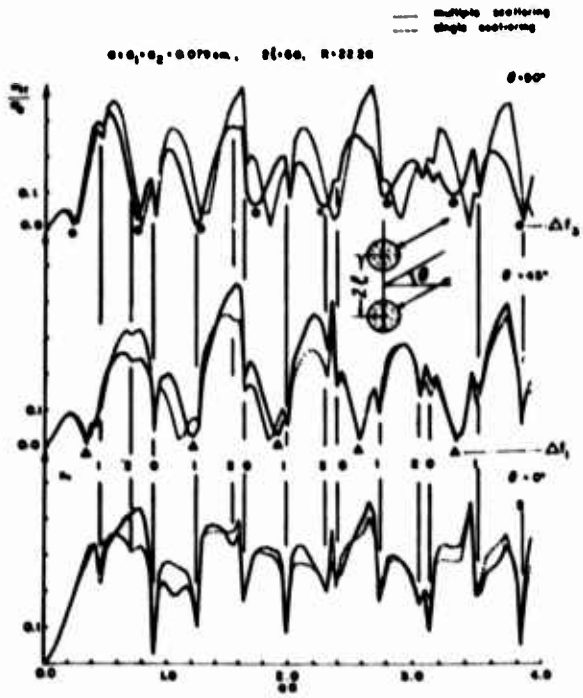


Figure 10. Backscattering of P-waves by two circular water cylinders at various angles of incidence (σ_{rr} is the radial stress, $\alpha a = \omega a/c_p$)[13].

Interpretation of the Spectra

We observe two features from these theoretical spectra: (1) all spectra of waves scattered by one or two cavities exhibit an obvious periodic structure; (2) the spectra of waves scattered by a liquid inclusion exhibits sharp peak and valley structure, which are quite different from those of a cavity. It is important to understand these features in order to apply spectral analysis to non-destructive evaluation of materials.

The periodicity of the spectra of a cavity may be understood from the interference of two rays of the scattered waves[6]. By a ray we mean the pulse propagating along a certain ray path connecting the receiver and the transmitter. Figure 11 shows an elliptical cavity and two ray-paths for backscattering. One is the direct reflected ray from the illuminated side of the cavity (PP or SS ray), the other is the creeping ray which runs around the shadow side of the cavity and then reaches the receiver (PP*P or SS*S ray).



Figure 11. Elliptical cavity and two ray-paths for backscattering.

The phase difference between these two rays is due to the different path lengths which is given by

$$\Delta(\text{Phase}) = 2a + 2aE(\tfrac{\pi}{2}, \epsilon) \qquad (6)$$

where $\epsilon = \sqrt{(1-b^2/a^2)}$ is the eccentricity of the ellipse and $E(\frac{\pi}{2}, \epsilon)$ is the complete elliptic integral of the second kind. Because of the interference of waves traveling along these two paths, the spectra exhibit periodic structures. For PP and PP*P rays the period along the αa-axis ($\alpha = \omega a/c_p$) is

$$\text{P-wave:} \quad \Delta_p(\alpha a) = 2\pi/[2+2E(\tfrac{\pi}{2}, \epsilon)] \qquad (7)$$

For SS and SS*S rays, we have

$$\text{S-wave:} \quad \Delta_S(\alpha a) = (c_S/c_p)\Delta_p(\alpha a) \; . \qquad (8)$$

Shown in Fig. 12 are three spectra of differential cross sections for the scattering of an incident SV, SH, and P-wave by an elliptical cavity in an aluminum solid. The spectra are the same as those shown in Fig. 3. On each graph, we measure the averaged periods in αa, which are marked above the dimension line. For the incident P-wave, we also calculated $\Delta_p(\alpha a)$ according to (7), which equals 1.428 and is marked below the dimension line inside parentheses. For the incident SV or SH wave, $\Delta_S(\alpha a) = 0.572$. We note that the agreement for the SH wave is very good, and the discrepancy for the SV and P-wave are not very large.

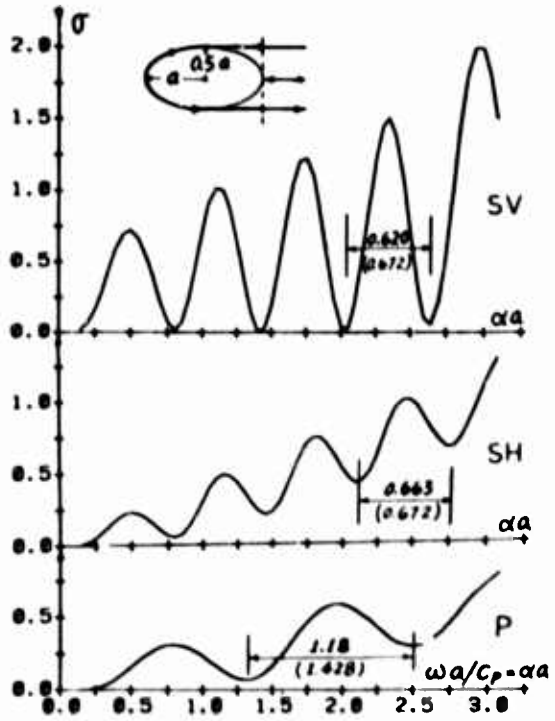


Figure 12. Spectra of differential cross sections for the scattering of an incident SV, SH, and P-wave by an elliptical cavity in an aluminum solid.

We also applied (6) to check the periods of spectra shown in Figs. 2, 3, and 5, 6. The agreement is always within 15 percent. The periods of the spectra for an oblate spheroid in Fig. 7 cannot be clearly determined.

On Fig. 9 we have indicated the periods 1.18, 1.67, and 2.70 (along frequency axis) of the spectra as measured from the thenetical spectra. In this case the periodicity is due to the interference of two rays reflected from each cylinder. The phase difference in length of these two rays is

$$\Delta(\text{Phase}) = 2(2\epsilon\sin\theta) \qquad (9)$$

Thus, along the frequency axis in Fig. .9, we expect to have a period of Δf,

$$\Delta f = c_p/(4\epsilon\sin\theta) \qquad (10)$$

The calculated values for Δf, 1.15, 1.62, and 2.69 are also shown in Fig. 9.

Since in all NDE work, we know in advance the values for c_p or c_s, knowing the periodicity of the spectra enables one to calculate the half-circumference of a cavity (Eqs. 7, 8) or the spacing between two cavities (Eq. 10).

For a cavity filled with fluid, the scattered spectrum is strongly affected by the natural frequencies of the fluid cylinder. The four lowest normal modes of a circular cylinder are shown in Fig. 13.[1] Each mode has a family of overtones (modes with additional modal circles). The natural frequencies of these modes and overtones can be calculated precisely, and the locations of the valleys of the backscattered spectra are formed to coincide with the overtone frequencies of modes n = 0 and n = 1. This has been thoroughly discussed in Ref. 1.

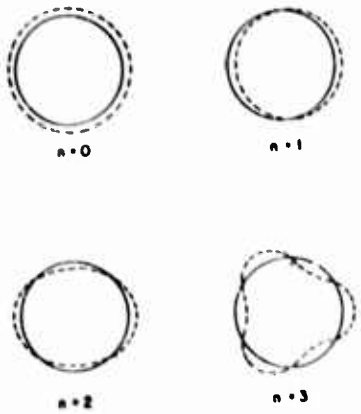


Figure 13. Four Lowest normal modes of a circular cylinder.

This theory of normal modes has been applied to interpret the spectra of the the scattering by two circular fluid cylinders. On Fig. 8 and 10, we show also the theoretical natural frequencies (in αa) for overtones of normal modes n = 0, 1 and 2. The four overtones of the zeroth mode (labeled with 0) and five overtones of the first mode (labeled with 1) all coincide with the valleys of all three spectra[1].

Since the natural frequencies depend on the radius of the cylinder and the speed of elastic waves in the fluid filling the cylinder it is possible to determine either from the detailed knowledge of the spectra.

Comparison with Experiments

Finally, we show a comparison between the theoretical spectra and the measured ones. In Fig. 14 are two measured spectra for the scattering of P-waves by a fluid cylinder in an aluminum block. Because the measured spectra include the spectra of the transducer, the magnitudes cannot be compared directly with the theoretical ones. However, the locations of the valleys (minima) coincide with the theoretical natural frequencies[14].

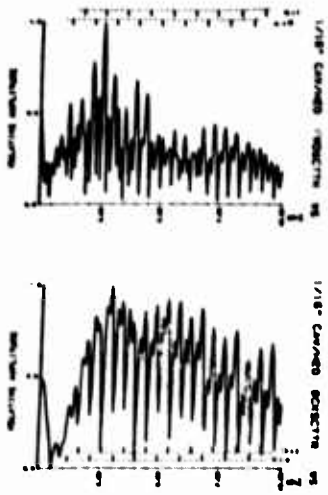


Figure 14. Comparison between the theoretical spectra and the measured ones.

On Fig. 15, we show both theoretical and experimental spectra of a P-wave scattered by two circular cavities in aluminum[13]. The spectrum of the incident pulse has been pre-determined and is divided from the scattered wave spectra. The agreement in the overall shape and the locations of maxima and minima is strikingly close.

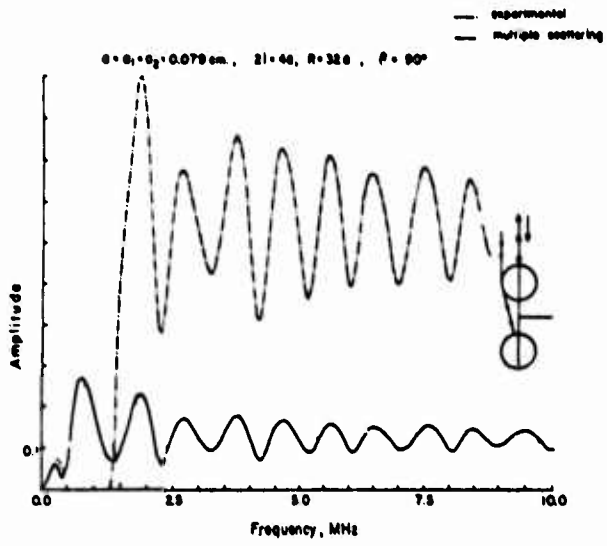


Figure 15. Theoretical and experimental spectra of a P-wave scattered by two circular cavities in aluminum.

In conclusion, we have shown that the transition matrix (T-matrix) method is very effective in calculating the theoretical spectra for waves scattered by an obstacle with smooth boundaries. The intricate structure of the spectra can be interpreted either by applying the principle of interference of two scattered rays, or from the theory of normal modes. Some of the theoretical spectra agree closely with experimentally determined ones.

Acknowledgement

This research was sponsored by the National Science Foundation (Grant No. ENG 75-13703) and the Material Science Center at Cornell University.

References

1. Y. H. Pao and C. C. Mow, J. Acoust. Soc. Am. 59, 1046 (1976).
2. P. C. Waterman, J. Acoust. Soc. Am. 45, 1417 (1969).
3. Y. H. Pao and V. Varatharajulu (V. V. Varadan), J. Acoust. Soc. Am. 59, 1361 (1976).
4. V. Varatharajulu (V. V. Varadan) and Y. H. Pao, J. Acoust. Soc. Am. 60, 556 (1976).
5. P. C. Waterman, J. Acoust. Soc. Am. 60, 567 (1976).
6. Y. H. Pao (to be published).
7. V. V. Varadan (to be published).
8. G.C.C. Ku, M.S. Thesis, Department of Theoretical and Applied Mechanics, Cornell University (1977).
9. V. V. Varadan (to be published).
10. V. Twersky, J. Acoust. Soc. Am. 24, 4245 (1952).
11. B. Peterson and S. Strom, J. Acoust. Soc. Am. 56, 771 (1952).
12. V. K. Varadan, V. V. Varadan and Y. H. Pao (to be published).
13. S. Sancar, Ph.D. Thesis, Department of Theoretical and Applied Mechanics, Cornell University (1977).
14. W. Sachse, F. Bifulco and Y. H. Pao, Material Science Report No: 2548, Cornell University (1975).

RECIPROCITY THEORIES FOR FLAW ANALYSIS

G. S. Kino and B. A. Auld
Stanford University
Stanford, California 94305

ABSTRACT

A new method of theoretical analysis based on the use of the reciprocity theorem has been developed. With this technique, one can predict the signal scattered by a flaw from one transducer to another in terms of the signals at the actual electrical terminals. The technique is particularly useful for dealing with focused beams and for taking account of near field and far field excitation and reception. We have applied this technique, using static assumptions, to determine scattering of a Rayleigh wave from a penny-shaped crack; by using the Born approximation we have determined the scattering of Rayleigh waves from a cylindrical hole. We have also used the theory to indicate the type of reflected signals we would expect from a focused beam illuminating a crack, and the peaks in the reflection characteristics as a function of frequency due to resonant modes of the flaws. The technique can be adapted for variational calculations. Basic variational theories have been derived but have not been applied to practical problems yet.

The scattering theories that are presently available generally consider plane wave excitation and reception by a point receiver. Basically the reason is historical. The first type of scattering theory was essentially that of Lord Rayleigh, who considered scattering of light from rain drops with plane wave excitation by the sun, the receiver being the eye, a point receiver.

We have developed a method of scattering analysis based on the use of the reciprocity theorem commonly employed in electromagnetic theory, which considers the transmitter to be a transducer, and the receiver to be the same transducer or another transducer located in a different position. The technique has the merit of great flexibility; it is particularly needed for our work in imaging systems, where both the transmitted and received beams may be focused. The technique is able to reproduce the results obtained by other methods, for the Green's function we employ is essentially that of the transducer, rather than that of a point source. With this approach we have been able to develop variational scattering formulae, elastostatic approximations, and normal mode expansions in terms of the resonant modes of a flaw.

The analysis follows from a generalization of the reciprocity theorem of electromagnetic theory:

$$\int_S (\underset{\sim}{E}^a \times \underset{\sim}{H}^b - \underset{\sim}{E}^b \times \underset{\sim}{H}^a) \cdot dS = \int_V (\underset{\sim}{J}^a \cdot \underset{\sim}{E}^b - \underset{\sim}{J}^b \cdot \underset{\sim}{E}^a)\, dV \qquad (1)$$

which relates two possible field solutions $\underset{\sim}{E}^a$, $\underset{\sim}{H}^a$, and $\underset{\sim}{E}^b$, $\underset{\sim}{H}^b$ within a volume V to each other. The terms J^a, J^b are current sources within the volume associated with the appropriate fields respectively. By using the piezoelectric constitutive equations, in addition to Maxwell equations, it is possible to generalize this reciprocity theorem to include both electromagnetic fields and acoustic fields.[1] In the problem of interest here it is convenient to carry out the analysis for the region shown in Fig. 1, including a flaw, whose volume is V_F and area S_F and whose outer surface is exterior to the sample and intersects the coaxial lines feeding the two transducers. We now take the field "a" to correspond to that which is present when one transducer is excited and no flaw is present, and the fields "b" to correspond to the situation when the other transducer is excited and there is a flaw present. In this case, we obtain the result

$$\int_{S_1+S_2} (\underset{\sim}{E}^a \times \underset{\sim}{H}^b - \underset{\sim}{E}^b \times \underset{\sim}{H}^a) \cdot dS + j\omega \int_{S_1+S_2} (\sigma_{ij}{}^b u_j{}^a - \sigma_{ij}{}^a u_j{}^b) n_i dS = j\omega \int (u_j{}^b \sigma_{ij}{}^a - \sigma_{ij}{}^b u_j{}^a) n_i dS \,, \qquad (2)$$

where n_i is the outward normal from the surface of interest into the interior of the medium, and the notation is standard since the surface $S_1 + S_2$ is exterior to the sample and the acoustic fields are zero (assuming a vacuum) or negligibly small (assuming a normal atmosphere). Consequently, only the electromagnetic terms are of interest and can be related to the voltage and current at the terminals of the coaxial line. By this means, we have managed to write the results in terms of scattering matrix formalism using acoustic fields corresponding to unit power excitation at the transducer. In this case, the expression for the reflection coefficient at the transducer, due to the wave scattered from a void, is

$$\Gamma = S_{11} = \frac{j\omega}{4} \int_{S_F} (\sigma_{ij}{}^i u_j - \sigma_{ij} u_j{}^i) n_i dS \,, \qquad (3)$$

where the superscript i corresponds to the incident unperturbed acoustic wave field due to the transducer when the flaw is not present.

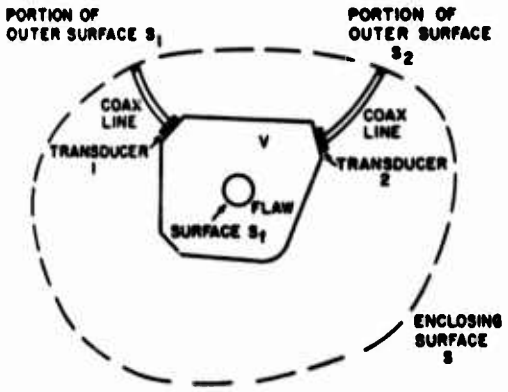


Figure 1. A schematic of the region of integration used for the reciprocity theorem.

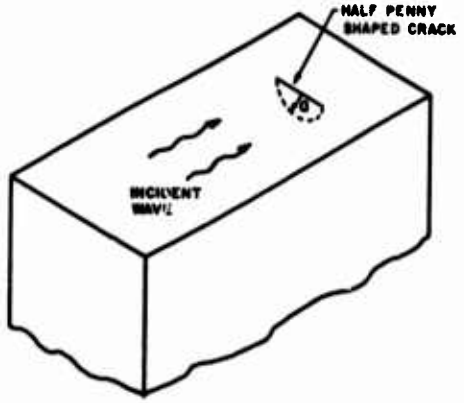


Figure 2. Schematic of half penny shaped crack.

One example which we have tackled is the scattering of a Rayleigh surface wave from a half penny shaped crack, whose radius a is much less than the wavelength λ, as shown in Fig. 2. In this case, only the longitudinal component of stress parallel to the surface is of importance and we can write

$$u_0 = \frac{\sigma_{zz}^{\,i}(1-\nu)}{\pi\mu}\sqrt{a^2 - r^2} \qquad (4)$$

where $\sigma_{zz}^{\,i}$ is the incident stress, ν is Poisson's ratio and μ the shear elasticity. Using this result in Eq. (3) we find that

$$S_{11}(\text{near field}) \approx \frac{a^3}{6\lambda^2 w}\,\eta\, g_z \,, \qquad (5)$$

$$S_{11}(\text{far field}) = \frac{a^3 w}{6\lambda^3 z}\,\eta\, g_z \,, \qquad (6)$$

$$\frac{S_{11}(\text{far})}{S_{11}(\text{near})} = \frac{w^2}{\lambda z} \,, \qquad (7)$$

where the transducer width is w; λ is the Rayleigh wavelength; the crack radius is $a \ll \lambda$; $g_z \sim 1$ and is a dimensionless calculable parameter; η is the tranducer efficiency; z the distance of the transducer from the crack. We note that this formula shows that the scattering depends on the radius cubed, i.e., it is as if the crack occupies a volume $V \sim a^3$. It will be observed that it is easy to carry out the two calculations of interest, one for the crack in the far field of the transducer, and one for the crack located in the near field of the transducer, it is assumed that the wave is straight crested in this region.

A similar analysis can be carried out for volume perturbations rather than for surface scattering. If we use the Born approximation for longitudinal waves, i.e., we assume $u_i = u_i^{\,1}$; $\sigma_{ij} = \sigma_{ij} = \sigma_{ij}^{\,i}$, it can be shown from Eq. (3) that the back scattered signal is

$$S_{11} = -\frac{j\omega}{4}\int\left(\omega^2(\Delta\rho)u_i e_{ij} - (\Delta c_{ijk\ell})e_{k\ell}\right)dV \qquad (8)$$

where $\Delta\rho$ and $\Delta c_{ijk\ell}$ are the perturbation in the density and elastic constants where the flaw is present. We can write this result for isotropic materials with a cross section much less than a wavelength in the form

$$|S_{11}| \approx \frac{\pi}{\lambda}\left(\frac{\Delta\rho}{\rho} - \frac{\Delta c}{c}\right)V_{\text{flaw}} \times \frac{\text{beam intensity at flaw}}{\text{power input to transducer}} \qquad (9)$$

The last term contains information on whether the flaw is in the near field or far field of the transducer, and determines how in large part $|S_{11}|$ varies with frequency.

In the opposite limit when the flaw size is large we can consider the specular reflections from it. In this case Eq. (4) enables us to write

$$S_{11} = \frac{1}{4}\int(\sigma_{ij}^{\,i}\sigma_j^{\,s} - \sigma_{ij}^{\,s}\sigma_j^{\,i})\,n_i dS \qquad (10)$$

where the superscript i stands for an incident wave, and s for the scattered waved. If we suppose that we know the reflection coefficient of a plane wave incident on the flaw surface from the transducer as illustrated in Fig. 3, we can write

$$S_{11} \sim \frac{\pi}{2} \int_{\text{flaw}} \Gamma(\theta)\, F(\theta) e^{-jkR\theta^2}\, \sigma_{33}^{i} v_z^{i} R^2 \theta d\theta \,, \quad (11)$$

where $\Gamma(\theta)$ is the reflection coefficient at the flaw and $F(\theta)$ is a slowly varying function of θ with $F(\theta) = 1$ at $\theta = 0$. Assuming that the main contributions to the integral are from regions where θ is small we find that

$$|S_{11}| \sim \frac{R\lambda}{2} F_{\text{flaw}}(\theta = 0) \times \frac{\text{Beam intensity at flaw}}{\text{Power input to transducers}} \,, \quad (12)$$

where R is the radius of curvature of the flaw at the point on the axis of the transducer. Thus the indication is that the return signal is proportional to the radius of curvature of the flaw.

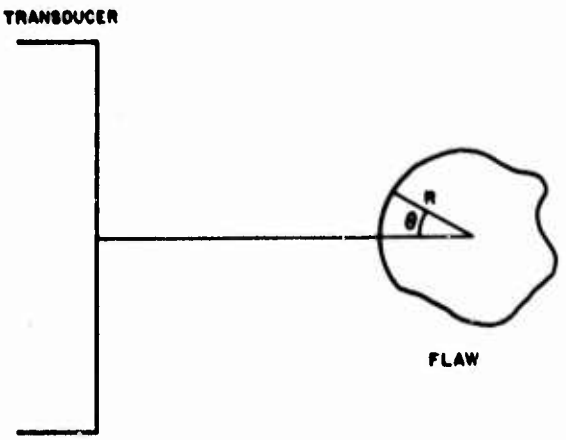


Figure 3. A schematic illustration of the notation used for the calculation of the specular reflection.

We shall not deal with other cases here, except to say that full variational scattering theorems have been derived using this technique and a start made on a scattering theorem in terms of the resonant modes of the flaw.

We believe that this technique is a simple but powerful method of analysis, and are carrying it further to examine a wide range of NDT problems of interest.

Acknowledgement

This work was originally supported by ARPA under contract No. MDA903-76-C-0250 with the University of Michigan and continued under research sponsored by the Center for Advanced NDE operated by the Science Center, Rockwell International, for the Advanced Research Projects Agency and the Air Force Materials Laboratory under contract F33615-74-C-5180.

Reference

1. B. A. Auld, "Acoustic Fields and Waves in Solids, Vol. II," pp. 152-154, Wiley-Interscience, New York, 1973.

APPLICATION OF GEOMETRICAL DIFFRACTION THEORY TO SCATTERING BY CRACKS

J. D. Achenbach, A. K. Gautesen, and H. McMaken
The Technological Institute
Northwestern University
Evanston, Illinois 60201

ABSTRACT

At high frequencies, the geometrical theory of diffraction provides useful and relatively simple approximations to diffracted fields. In this paper the theory is applied to the diffraction of time-harmonic longitudinal waves by a penny-shaped crack in an elastic solid.

Introduction

Methods to calculate the far fields when ultrasonic waves are diffracted by a crack, are essential to the scattering approach to QNDE. For diffraction of elastic waves by a penny-shaped crack, a considerable literature exists, which was summarized in a recent review article by Kraut[1]. Particularly interesting are simple approximate solutions which are useful for either high or low frequencies. A number of these approximations, including the Kirchhoff approximation, the adaptation of the Keller theory to shear-free media, and a new quasi-static approximation, were recently discussed by Domany, Krumhansl and Teitel[2].

In this paper, we will apply the geometrical theory of diffraction to ultrasonic diffraction problems. We will show that this theory provides useful and relatively simple approximations to diffracted fields.

The geometrical theory of diffraction is based on ray theory. Just as in other wave propagation phenomena, wavefronts are defined as surfaces of constant phase and the rays are normal to the wavefronts. In elastodynamic ray theory the amplitude of a high frequency mechanical disturbance is traced as the disturbance propagates along a ray. When a ray strikes an interface, reflected and refracted rays are generated. However, when a ray carrying a high frequency body wave strikes the edge of a crack, two cones of diffracted rays are generated. The surfaces of the inner and outer cones consist of rays of longitudinal and transverse motion, respectively. The half-angles of the cones are related by Snell's law. The groundwork for a three-dimensional geometrical diffraction theory for crack-like obstacles in an elastic solid has been presented in a paper by Achenbach and Gautesen[3].

For diffraction phenomena which are governed by a single wave equation, geometrical diffraction theory for a planar obstacle was developed by Keller[4]. The formulation of Ref. 4, and subsequent papers, e.g., Ref. 5, is, however, not applicable to diffraction by cracks in solids, since wave motions in solids are governed by two wave equations, which are coupled by the boundary conditions on the diffracting obstacle. Thus, although in first approximation it is useful to neglect this coupling, as was done in Refs. 6 and 7, it is appropriate to consider the problem in a mathematically more rigorous manner by taking the coupling into account.

For plane longitudinal and transverse waves, which are under arbitrary angles of incidence with a traction-free semi-infinite crack, the fields on the diffracted rays can be obtained by asymptotic considerations, as shown in Ref. 3. The results can be expressed in terms of diffraction coefficients which relate the diffracted fields to the incident fields. Geometrical diffraction theory provides modifications to the semi-infinite crack results, to account for curvature of incident wave-fronts and curvature of crack edges, and finite dimensions of the crack. In the usual terminology the results for diffraction of plane waves by a semi-infinite crack are the canonical solutions.

Geometrical diffraction theory is applicable if $\omega d/c_L >> 1$, where d is a characteristic dimension of the crack and c_L is the velocity of longitudinal waves. For some special problems where comparisons with mathematically exact solutions were possible, we found good agreement for $\omega d/c_L > 2$. For a crack with a cross-sectional dimension of 1 mm in steel ($c_L \sim 6.10^6$ mm/sec), the frequency should then be larger than about 1 MHz. This seems to be within experimental capability, see e.g. Ref. 6 and 7.

It should be noted that a slightly different interpretation renders the results of geometrical diffraction theory useful as wavefront results for propagating pulses.

Geometrical Theory of Diffraction-Basic Ideas

The basic ideas of geometrical diffraction can best be explained by means of an example. Figure 1 shows a planar crack with a smoothly curving edge in an elastic solid. The origin of a cartesian coordinate system (x, y, z) is in the plane of the crack, and the z-axis is normal to that plane. A time harmonic wave of the form

$$u_z = A_0 e^{i\omega(z/c_L - t)} \qquad (1)$$

is incident on the crack. This is a case of normal incidence, i.e., the wavefronts are parallel

to the z-axis. When a ray strikes the point P_2 on the edge of the crack, a fan of diffracted body wave rays is generated as shown in Fig. 1. Both longitudinal and transverse motions are carried by the diffracted rays. One ray of each kind emanating from two or more points on the boundary will pass through any point of observation. To keep the figure compact the point Q is shown closer to the crack than would actually be the case.

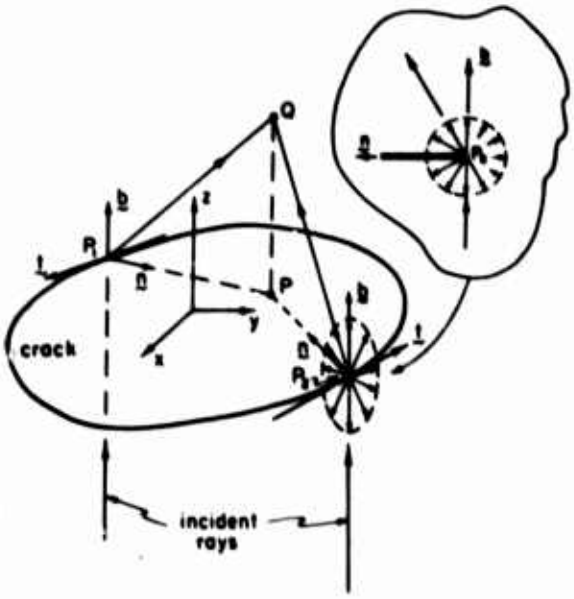


Figure 1. Normal incidence of a plane longitudinal wave on a planar crack in an elastic solid.

The diffraction problem described above belongs to a class of elastodynamic diffraction problems whose complete solutions are very difficult to obtain. The one problem in that class for which analytical results can be derived in a relatively simple manner is the diffraction of a plane incident wave by a traction free semi-infinite crack. In particular, for large values of $\omega r/c_t$ the fields on the diffracted rays emanating from the tip of the semi-infinite crack can be obtained by asymptotic considerations. These results can be expressed in terms of diffraction coefficients which relate the diffracted fields to the incident field. Geometrical diffraction theory for cracks of arbitrary shape is based on the semi-infinite crack results, in that it immediately provides first-order corrections to the semi-infinite crack results, to account for a curvature of incident wavefronts and curvature of crack edges. In the usual terminology the results for diffraction of plane waves by a semi-infinite crack are the canonical solutions. With some additional effort corrections for the finite dimensions of a crack can now be obtained, as described in this paper.

The total fields at point Q are, indeed, not just comprised of the fields on the "primary diffracted body wave rays" P_1Q and P_2Q. At the edge of the crack there are also rays of crack-face motion generated. These rays intersect the crack edges again and generate additional diffracted body wave rays. Some of these "secondary diffracted rays" will pass through point Q. This system of reflected and diffracted rays can become rather extensive. Fortunately, on the faces of the crack the main contributions to the diffracted fields are not coming from the diffracted rays of longitudinal and transverse motion, but rather from rays of surface waves. These rays, which have not been studied before, are important, because in the first approximation the diffraction coefficients for the body wave motions vanish on the crack faces, except for diffracted horizontally polarized transverse wave motions. In addition, surface wave motions suffer less geometrical decay than body wave motions. In a recent paper Gautesen, Achenbach and McMaken[8] have presented a theory for surface wave rays which are generated by the diffraction of body wave rays.

When a surface wave ray intersects the edge of a crack, a ray of reflected surface wave motion is generated, as well as cones of diffracted rays of longitudinal and transverse motions. The reflection coefficients can be computed. The cones of diffracted body rays can also be analyzed, and the associated diffraction coefficients can be obtained. With the aid of these results the stepwise radiation of energy which is temporarily trapped by the crack in the form of surface motion can be analyzed, and the scattered field can be computed as the sum of primary diffractions and a system of secondary diffractions.

For curved wavefronts and for curved edges of diffraction, the cones of diffracted rays have envelopes, at which the rays coalesce and the fields become singular. The envelopes are called caustics. The results of the geometrical theory of diffraction are not valid near caustics. It is, however, possible to extend the theory to the caustics. In the next section this is shown for the case of a penny-shaped crack which is under the normal incidence of a plane longitudinal wave. For this case the normal axis through the center point of the crack is a caustic. Uniformly valid expressions for the field on the body wave rays are obtained.

Some General Results for Diffraction of Longitudinal Waves

In this section we briefly summarize some pertinent expressions. The details can be found in a paper by Gautesen, Achenbach and McMaken[8].

Primary diffracted body wave rays. For an incident longitudinal wave the displacement fields on the diffracted body wave rays are

$$\underset{\sim}{u}^{\beta}_{d} = e^{i\omega S_\beta/c_\beta} \left[S_\beta\ (1+S_\beta/\rho^L_\beta\right]^{-1/2} D^L_\beta\ \underset{\sim}{i}^L_\beta\ U^L \qquad (2)$$

Here U^L defines the incident wave at the point of diffraction. In Eq.(2) the superscript β denotes the nature of the wave motion on the diffracted rays. Thus we will use $\beta = L$ and $\beta = T$ for longitudinal and transverse waves, respectively. The distances S_β are along the diffracted rays from the point of diffraction O to the point of observation. The unit vectors $\underset{\sim}{i}^L_\beta$ relate the displacement directions of the diffracted fields to those of the incident fields. The symbols ρ^L_β define the distance from O to the caustics and D^L_β are the diffraction coefficients. For an incident longitudinal wave we have

$$\rho^L_\beta = - a \sin^2\phi_\beta \left[a \, (d\phi_\beta/ds) \sin\phi_\beta + \cos\delta_\beta\right]^{-1} \quad (3)$$

where a is the radius of curvature of the edge at the point of diffraction, s is the distance measured along the edge, and δ_β are the angles between the relevant diffracted rays and the normal to the crack. The angles ϕ_L and ϕ_T are related by

$$c_T \cos\phi_L = c_L \cos\phi_T \quad (4)$$

The diffraction coefficients are obtained from the canonical problem of diffraction of a plane longitudinal wave by a semi-infinite crack.

Diffracted surface wave rays. For normal incidence, only symmetric surface wave motions are generated on the faces of the crack. The displacements on the diffracted surface wave rays then are

$$\underset{\sim}{u}^R_d = e^{i\omega S_R/c_R} \left(1+S_R/\rho_R\right)^{-\frac{1}{2}} D^L_R \, \underset{\sim}{i}^L_R \, U^L \quad (5)$$

The principal difference between Eqs. (5) and (2) is the additional term $S_\beta^{-\frac{1}{2}}$ in Eq. (2). This term reflects three dimensional (spherical) growth and decay in Eq. (2) versus two dimensional (cylindrical) growth and decay in Eq. (5). In Eq. (5) we have

$$\rho_R = - a \sin\phi_R \, (a \, d\phi_R/ds + 1)^{-1}, \quad (6)$$

where ϕ_R is related to ϕ_L by

$$c_L \cos\phi_R = c_R \cos\phi_L \quad (7)$$

Reflection of surface wave rays. A surface wave ray which intersects the edge of a crack gives rise to a ray of reflected surface waves, and to two cones of diffracted body rays. For a surface wave incident on the edge of a semi-infinite crack these reflection and diffraction processes were studied by Freund[9]. In the spirit of geometrical diffraction theory, we can immediately introduce the appropriate corrections for curvature of the incident wavefront and for curvature of the edge of the crack.

A surface wave ray is reflected such that the angle between the reflected ray and the tangent to the edge is just the same as the angle of incidence, ϕ_R, between the incident ray and the tangent to the edge. Moreover, rays of symmetric (antisymmetric) surface waves are reflected as rays of symmetric (antisymmetric) surface waves.

The incident field is defined by Eq. (5). Quantitatively, the fields on the reflected surface rays are given by

$$\underset{\sim}{u}^R_r = e^{i\omega s_R/c_R} \left(1 + S_R/\rho_R\right)^{-\frac{1}{2}} \mathcal{R} \, \underset{\sim}{i}^R_r \, u^R \quad (8)$$

The nature of the motions on the incident rays is the same as on the reflected rays. In Eq. (8) S_R is the distance from the point of reflection to the point of observation, $\mathcal{R}$ is the reflection coefficient, and ρ_R is the distance to the caustic where

$$\rho_R = - a \sin\phi_R \, (a \, d\phi_R/ds + 1)^{-1} \quad (9)$$

This is the same formula as given by Eq. (6), but here $\phi_R(s)$ is the given angle of incidence, while in Eq. (6), ϕ_R was computed from Eq. (7).

Body wave rays generated by diffraction of surface way rays. For this case the displacement fields are of the general form

$$\underset{\sim}{u}^\beta_d = e^{i\omega S_\beta/c_\beta} \left[S_\beta \, (1 + S_\beta/\rho^R_\beta)\right]^{-\frac{1}{2}} D^R_\beta \, \underset{\sim}{i}^R_\beta \, u^R, \quad (10)$$

where $\beta = L$ or $\beta = T$ for diffracted rays of longitudinal and transverse motion, respectively. Also D^R_β is the pertinent diffraction coefficient which can be computed, see Ref. 8. The distances to the caustics are given by ρ^R_L and ρ^R_T, respectively.

Diffraction by a penny-shaped crack. For normal incidence of a plane longitudinal wave of the kind given by Eq. (1), the incident and diffracted fields are axially symmetric with respect to the z-axis. Thus, only the radial distance $r = (x^2+y^2)^{\frac{1}{2}}$ and the axial distance z enter in the results. The geometry is shown in Fig. 2. The diffracted field at any point Q away from the crack can now easily be computed on the basis of the semi-infinite crack solution, as explained in the previous section. In cylindrical coordinates the radial and axial displacements for the diffracted field are obtained as

$$(u_d)_r = A_o \sum_{j=1}^{2} Q_j \, (-1)^j \, x$$

$$\left[G_L(\theta_j) \cos\theta_j \, e^{i\omega R_j/c_L} - G_T(\theta) \sin\theta_j \, e^{i\omega R_j/c_T}\right], \quad (11)$$

$$(u_d)_z = A_o \sum_{j=1}^{2} Q_j \, x$$

$$\left[G_L(\theta_j)\sin\theta_j\, e^{i\omega R_j/c_L} + G_T(\theta)_j \cos\theta_j\, e^{i\omega R_j/c_T}\right], \quad (12)$$

where $j = 1$ and $j = 2$ correspond to the contributions from P_1 (the point closer to Q) and P_2, respectively, while

$$G_L(\theta_j) = D_L^L\left(\theta_j;\tfrac{\pi}{2},\tfrac{\pi}{2}\right) + u_{inc}^{RS} D_L^{RS}\left(\theta_j;\tfrac{\pi}{2}\right) \quad (13)$$

$$G_T(\theta_j) = -D_T^L\left(\theta_j;\tfrac{\pi}{2},\tfrac{\pi}{2}\right) - u_{inc}^{RS} D_T^{RS}\left(\theta_j;\tfrac{\pi}{2}\right) \quad (14)$$

$$R_j = \left\{z^2 + \left[a + (-1)^j r\right]^2\right\}^{\frac{1}{2}}, \quad (15)$$

$$Q_j = R_j^{-\frac{1}{2}}\left[1 - (R_1/a)\cos\theta_j\right]^{-\frac{1}{2}}, \quad (16)$$

$$\cos\theta_j = a + (-1)^j r / R_j \quad (17)$$

In Eqs. (4) and (5), D_L^L and D_T^L are the diffraction coefficients for the primary diffractions, and the second terms in Eqs. (4) and (5) represent the contributions due to the motions of the crack faces. Explicit expressions are given in Ref. 8.

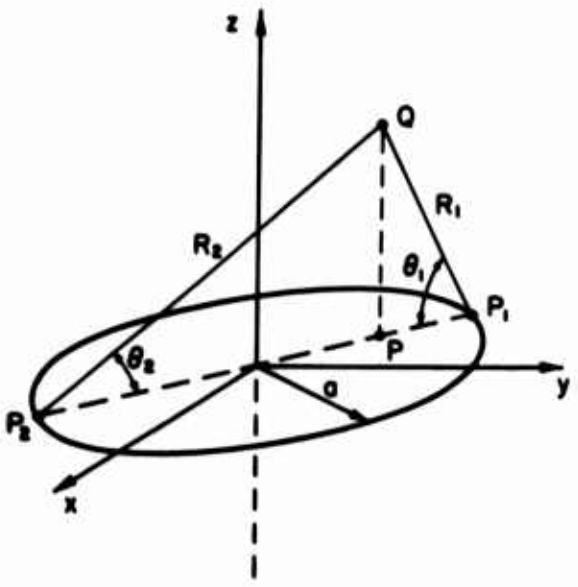


Figure 2. Normal incidence of a plane longitudinal wave on a penny-shaped crack.

The diffracted fields become singular at the caustic r = 0, and at the edge of the shadow zone. It is, however, not difficult to obtain fields which are also valid near r = 0, by the use of appropriate multiplication constants. The details are given in Ref. 8. The results are, for $r/a \ll 1$:

$$(u_d)_r = A_0\left(\frac{2\pi a}{rR}\right)^{\frac{1}{2}} e^{i\pi/4}\left[g_L^{\frac{1}{2}} G_L(\theta) J_1(g_L)\cos\theta\, e^{i\omega R/c_L} - g_T^{\frac{1}{2}} G_T(\theta) J_1(g_T)\sin\theta\, e^{i\omega R/c_T}\right] \quad (18)$$

$$(u_d)_z = A_0\left(\frac{2\pi a}{rR}\right)^{\frac{1}{2}} e^{-i\pi/4}\left[g_L^{\frac{1}{2}} G_L(\theta) J_0(g_L)\sin\theta\, e^{i\omega R/c_L} + g_T^{\frac{1}{2}} G_T(\theta) J_0(g_T)\cos\theta\, e^{i\omega R/c_T}\right] \quad (19)$$

where

$$\cos\theta = a/R, \quad R = (a^2 + z^2)^{\frac{1}{2}}, \quad (20)$$

$$g_L = (\omega r/c_L)\cos\theta, \quad g_T = (\omega r/c_T)\cos\theta. \quad (21)$$

In Eqs. (18) and (19), $G_L(\theta)$ and $G_T(\theta)$ are defined by Eqs. (13) and (14), and $J_0(g_T$ and $J_1(g_T)$ are Bessel functions of the first kind.

Some results for the penny-shaped crack. For the case of normal incidence the amplitudes of the axial and radial displacement components have been computed from Eqs. (11) and (12). The computations were carried out for fixed frequency and for fixed radial distance $\overline{OQ}$, as functions of the angle χ. The results are shown in Figs. 3 and 4, where the angle χ is defined in the insert in Fig. 3. The following numerical values were chosen: Poisson's ration: $\upsilon = 0.25$; frequency $\omega a/c_L = 3.5$; radial distance: $\overline{OQ}/a = 5$. The variation of the amplitudes with angle χ shows qualitative agreement with experimental results in the literature.

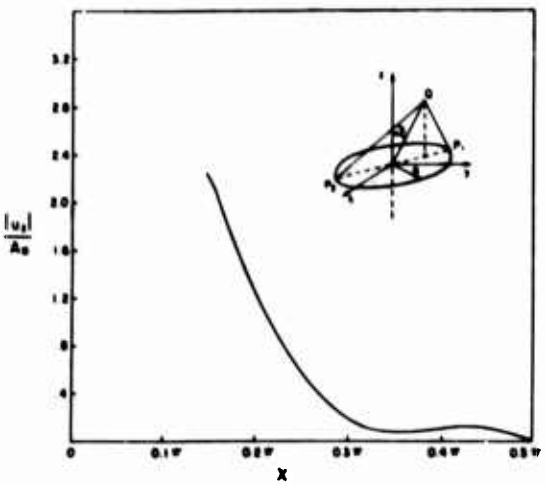


Figure 3. Axial displacement versus angle χ for $R/a = 5$ and $\omega a/c_L = 3.5$.

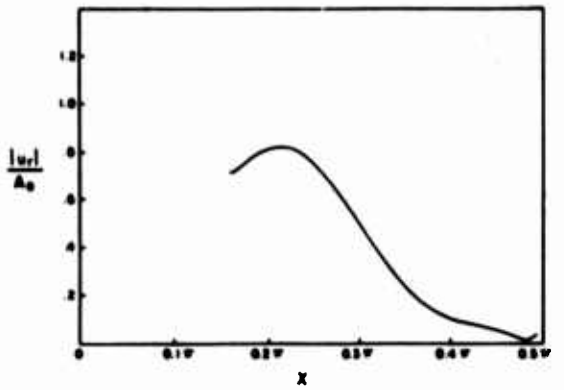


Figure 4. Radial displacement versus angle x for R/a = 5 and $\omega a/c_L = 3.5$.

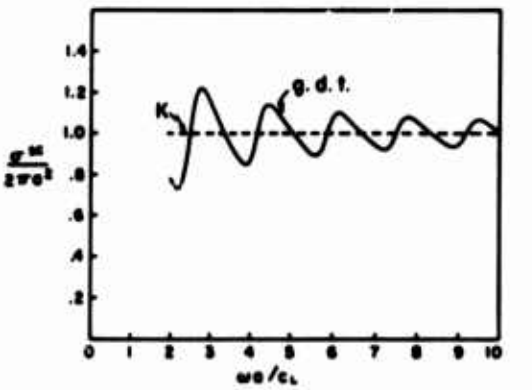


Figure 5. Scattering cross-section versus dimensionless frequency according to geometrical diffraction theory (g.d.t.), as compared with the Kirchoff (K) approximation.

A useful quantity to compute for diffraction of a longitudinal wave by a penny-shaped crack is the scattering cross section σ^{sc}. This quantity is defined as the ratio of the time-averaged scattered power over the intensity of the incident wave, I. For an incident wave of the form given by Eq. (1) we have:

$$I = \tfrac{1}{2}\omega^2 \rho c_L A_0^2 . \qquad (22)$$

The far field may in general terms be expressed as:

$$\underline{u}_d(\underline{s}_0) = A^L(\hat{\underline{x}}_0)\,\frac{\exp(i\omega|\underline{x}_0|/c_L}{4\pi|\underline{x}_0|} + A^T(\hat{\underline{x}}_0)\,\frac{\exp(i\omega|\underline{x}_0|/c_T}{4\pi|\underline{x}_0|} \qquad (23)$$

The interesting result, which was shown by Tan[10], now is that only the far-field diffracted wave amplitude which is of the same type as the incident wave, and computed for x_0 as a unit vector in the direction of wave incidence, occurs in the expression for σ^{sc}. For the problem at hand the simple result is:

$$\sigma^{sc} = \frac{c_L}{\omega}\,\frac{1}{A_0}\,\mathrm{Im}\,[A^L(\underline{i}_z)] \qquad (24)$$

It is easy to compute the right-hand side from Eq. (19). For $\nu = 0.25$ the result has been plotted in Fig. 5 versus the dimensionless frequency $\omega a/c_L$.

The result shown in Fig. 5 is valid for $\omega a/c_L$ sufficiently larger than unity. With results available in the literature, it is also possible to compute the corresponding result for $\omega a/c_L << 1$. With the low frequency approximations available in the literature, and with the high frequency approximations of the work proposed here, it seems very likely that enough information will be available to cover the whole frequency range.

Finally we present some computations for the amplitude of the axial displacement on the center axis of the crack for fixed z/a, as a function of $\omega a/c_L$. The results were computed from Eq. (19). The results are shown in Fig. 6.

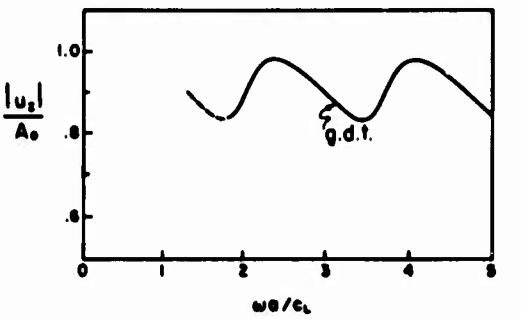


Figure 6. Axial displacement at r = 0 versus dimensionless frequency according to geometrical diffraction theory (g.d.t.) for z/a = 5.

References

1. E. A. Kraut, "Review of Theories of Scattering of Elastic Waves by Cracks," IEEE Trans. SU-23, 162 (1976).

2. E. Domany, J. A. Krumhansl, and S. Teitel, "Quasi-Static Approximation to the Scattering of Elastic Waves by a Circular Crack," to be published.

3. J. D. Achenbach and A. K. Gautesen, "Geometrical Theory of Diffraction for Three-D Elastodynamics," J. Acoust. Soc. Amer., 61, 413 (1977).

4. J. B. Keller, "A Geometrical Theory of Diffraction," in Calculus of Variations and its Applications, McGraw Hill, New York (1958).

5. J. B. Keller, "Diffraction by an Aperture," J. Appl. Phys., 28, 426 (1957).

6. L. Adler and D. K. Lewis, "Scattering of Broadband Ultrasonic Beams from Circular Disks," J. Acoust. Soc. Amer., 57, 59 (1975).

7. L. Adler and D. K. Lewis, "Scattering of a Broadband Ultrasonic Pulse by Discontinuities, IEEE Trans. Sonics and Ultrasonics, SU-23, 351 (1976).

8. A. K. Gautesen, J. D. Achenbach, and H. McMaken, "Surface Wave Rays in Elastodynamic Diffraction Theory," submitted for publication.

9. L. B. Freund, "The Oblique Reflection of a Rayleigh Wave from a Crack Tip," Int. J. Solids Structures, 7, 1199 (1971).

10. T. H. Tan, "Diffraction Theory for Time-Harmonic Elastic Waves," Doctoral Dissertation, Delft University of Technology, September 1975.

NEW METHODS OF DETECTION AND CHARACTERIZATION OF SURFACE FLAWS

B. A. Auld
Ginzton Laboratory, Stanford University
Stanford, California 94305

ABSTRACT

A new approach to microwave eddy current testing for surface cracks in metals involves the use of ferromagnetic resonance in a small garnet crystal placed close to the surface to be tested. It is well known in this case that the induced eddy currents on the metal surface cause a strong displacement of the ferromagnetic resonance frequency. The presence of a crack on the surface produces, by disturbing the eddy current pattern, a perturbation of the resonant frequency as the garnet sample passes over it. Theoretical detectability criteria for the garnet probe are developed on the basis of a magnetic perturbation relation and compared with calculations of Rayleigh wave and plate wave backward scattering and intermode scattering at a half-penny surface crack. Some experimental results are also given.

Up to this point the main thrust of research on methods for quantitative NDE has been directed toward internal flaws in materials using primarily ultrasonic methods of testing which provide the most easy access to the interior of an opaque body. In the case of surface flaws, a very important and critical branch of NDE, the flaw is accessible to probing by any one of a number of forms of energy. The purpose of this project is to investigate and evaluate at a fundamental level the use of different forms of energy - ultrasonic, electrical, magnetic, thermal, etc. - for the detection and characterization of surface flaws in materials, and then to explore in detail one or two of the more promising approaches.

After an initial investigation it was determined that eddy current and ultrasound techniques were the best candidates for further study, in that they have high sensitivity and offer the best possibilities for the development of novel approaches to search and characterization procedures. In the domain of eddy currents, microwave techniques have been studied using a ferromagnetic resonator as a probe that provides high sensitivity and spatial resolution, as well as the capability for novel array scanning techniques. The aspect of ultrasonic detection of surface flaws that has been emphasized is the use of guided wave modes to localize the probe on the surface and to deduce additional information about the flaw from intermode scattering.

Ferromagnetic Resonance in Eddy Current Testing

The change in the frequency of a microwave cavity resonator perturbed by a small slot or crack in the enclosing wall according to the Slater formula is

$$\frac{\Delta f}{f} = -\frac{1}{2}\frac{\text{magnetic stored energy in crack}}{\text{magnetic stored energy in resonator}} \quad (1)$$

This shows that the sensitivity of such a crack detection system is enhanced by reducing the volume of the resonator relative to the crack and by increasing the resonator Q.

The ultimate in this regard is a ferrimagnetic resonator, typically taking the form of a yttrium iron garnet (YIG) sample with a volume less than 10^{-4} in.^{3} and a resonance Q in the order of 1000. Such a resonator does not require an enclosing wall and is readily passed over the metal surface to be tested for cracks.

A resonator of this kind may be used for crack detection by measuring the input impedance at the coupling loop and observing the frequency shift as it passes over the flaw. This method is sensitive to lift off and a better technique is to use a balanced system with two YIG-controlled oscillators. The frequency difference is perturbed by the presence of a crack under one resonator, but is unaffected by changes in lift off d. From the Slater formula the detection sensitivity of a system with typical parameters

$$V_{\text{resonator}} = 10^{-4} \text{ in.}^3$$

$$d = 0.05 \text{ in.}$$

Short term oscillator stability: 1 part in 10^6 is

$$V_{\text{crack}} = 3 \times 10^{-11} \text{ in.}^3$$

corresponding to a half-penny shaped crack of radius 15 μm.

In our experiments we have easily detected a long crack 0.006" wide and 0.025" deep, by direct observation of the resonance curve on an oscilloscope. Measurements on cracks of other dimensions confirm that the frequency shift is proportional to the volume of the crack, as predicted by the Slater formula.

The ferrimagnetic resonance technique for surface crack detection provides greater spatial resolution than conventional eddy current testing and a high detection sensitivity. Ferrimagnetic resonators are readily tuned and switched with a small applied magnetic field and are therefore readily adaptable

to multi-frequency eddy current testing and scanning. The frequency shift method provides direct digital readout on a counter.

The resonant frequency of an isolated magnetic spin is determined by the restoring torque due to the dc bias field H_0.

In a small magnetic resonator, rf demagnetizing fields, arising from the magnetic poles produced at the boundaries, generate additional torques and shift the processional resonant frequency.

As shown below, the effect of placing a conducting plane in the vicinity of a magnetic resonator is equivalent to that of an image placed an equal distance on the other side of the plane. The torque resulting from action of the image field on the resonator induces an additional frequency shift that varies according to the lift off d.

In a normal bias field configuration the field pattern in (a) rotates without changing form and generates the rotating eddy current distribution in (b). Maximum frequency shift occurs when the crack is normal to the current flow, and cracks of any orientation may be detected directly underneath the resonator.

In a parallel bias field configuration the magnetic field and eddy current distributions alternate between the patterns shown directly above and those shown in the previous figure. Only cracks perpendicular to the bias field direction can be detected.

Resonant frequency detuning caused by a crack in the surface is due to perturbation of the eddy current pattern required to support this field.

Intermode Coupling of Guided Elastic Waves

Attention has recently been directed to the advantages of guided ultrasonic waves in NDE, where selective detection of certain types of flaws may be achieved by a suitable choice of wave mode (W. Mohr and Paul Holler, "On Inspection of Thin Walled Tubes for Transverse and Longitudinal Flaws by Guided Ultrasonic Waves," IEEE Trans. SU-23, pp. 369-374 (1976). By examining scattering between different guided modes one can also extract information about the lateral positions of a flaw in the structure.

Use of the piezoelectric reciprocity relation enables one to derive a simple expression for reflections measured at the electrical input of the ultrasonic transducer (B. A. Auld and G. S. Kino, in preparation) and this may be used to evaluate interscattering effects involving guided modes. An elementary example is normal incidence scattering of SH plate modes from a penny-shaped crack.

The general scattering formula may also be used to calculate normal incidence Rayleigh wave scattering from a half penny-shaped crack on a surface. For a crack of radius a on an aluminum surface, this gives an electrical reflection coefficient

$$\gamma = \frac{1}{2}\eta\,\frac{a}{w}\,(ka)^2$$

in the near field where η is the one-way conversion efficiency and w the width of the Rayleigh wave transducer.

For a state-of-the-art Rayleigh wave system this gives a theoretical detection sensitivity corresponding to a half penny-shaped crack with radius in the range of 15 μm. Experimentally cracks with a radius of several hundred μm have been observed.

Acknowledgement

This research was sponsored by the Center for Advanced NDE operated by the Science Center, Rockwell International, for the Advanced Research Projects Agency and the Air Force Materials Laboratory under contract F33615-74-C-5180.

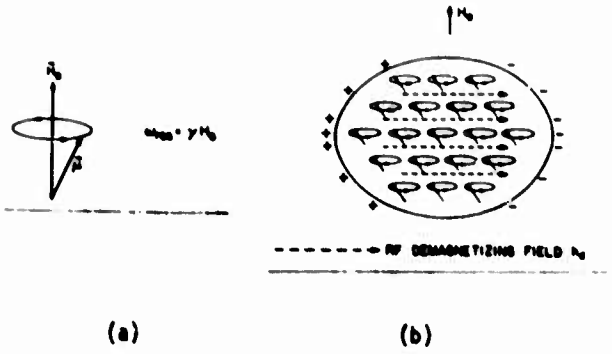


Figure 1. (a) Precessional resonance of single electron. (b) Resonance in a small ferrimagnetic sample.

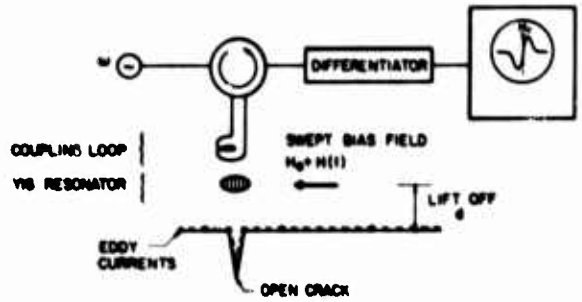


Figure 2. Crack detection in a single swept resonator system. The output indication is sensitive to variations in lift-off.

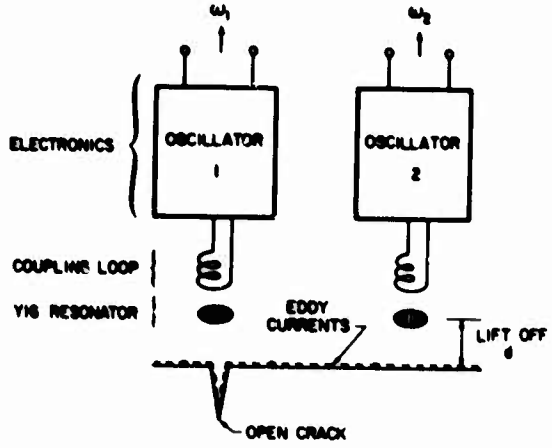


Figure 3. Double resonator system for discrimination against lift-off variations.

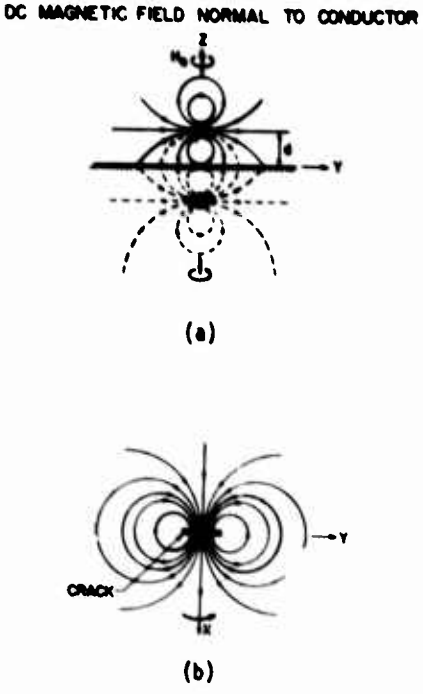


Figure 4. (a) Magnetic field distribution around resonator and its image. (b) Rotating eddy current distribution on conducting wall.

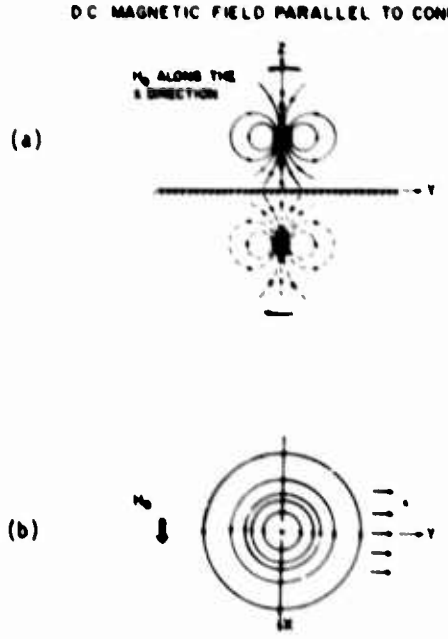


Figure 5. (a) Magnetic field distribution around resonator and its image. (b) Linearly traveling eddy current distribution.

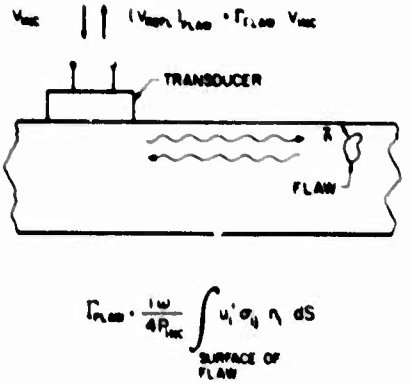
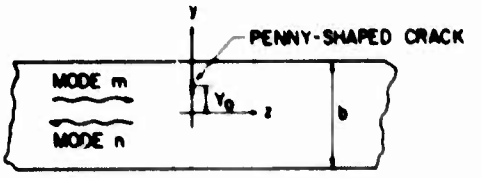


Figure 6. The basic formula for intermode scattering, obtained by reciprocity relation analysis relates the electrical reflection coefficient to a simple integral over the surface of the flaw.

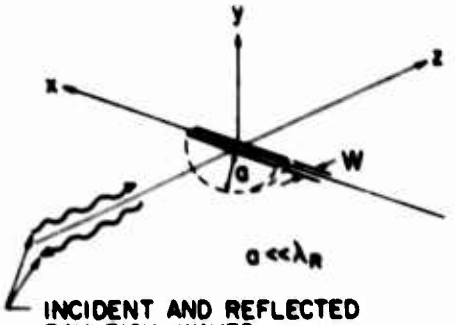
u_i' = displacement in the presence of the flaw due to an electrical input power P_{INC}

σ_{ij} = stress in the absence of the flaw with the same electrical input power.



$$\Gamma_{m\to n} \sim (\sigma_{zz})_m\,(\sigma_{zz})_n \sim \cos\frac{m\pi}{b}(y_0 + b/2)\cos\frac{n\pi}{b}(y_0 + b/2)$$

Figure 7. Intermode scattering of SH modes in plates: In the quasistatic approximation of the scattering coefficient is proportional to the product of the model stress at the position of the crack. Measurement of the relative amplitudes and phases of scattering from the m = 0 mode to three higher modes is sufficient to fix the distance Y_0.



$$u_z' \cong K\sigma_{zz}\,(a^2 - r^2)^{1/2}$$

$$\Gamma_{CRACK} \sim \omega^3 a^3$$

Figure 8. Long wavelength Rayleigh wave scattering by a penny-shaped crack: In this limit only the stress component σ_{zz} of the Rayleigh wave has non-negligible amplitude, and only a single stress intensity factor is required in the quasistatic approximation. The displacement distribution over the half-crack on the surface can be reasonably approximated by that of a full crack (George C. Sih, "Methods of Analysis and Solutions of Crack Problems," Nordhoff, 1973).

SURFACE WAVE TECHNIQUES FOR PREDICTING THE REMAINING LIFE OF FATIGUE DAMAGED METALS

O. Buck, W. L. Morris, and R. V. Inman
Science Center, Rockwell International
Thousand Oaks, California 91360

ABSTRACT

In our continuing efforts to investigate methods to characterize the state of fatigue nondestructively and to apply these observations to lifetime predictions, we have initiated acoustic surface wave studies using Al 2024-T351. A smooth bar specimen was designed which can be tested in tension-compression fatigue. Acoustic wedge transducers were mounted on the specimen to sample fatigue induced changes within the gauge section. Data on acoustic harmonic generation were taken as a function of applied external load at any point of the sample's fatigue life. An optical microscope was attached to the load frame to monitor microcrack formation in the gauge section. Significant changes of the second harmonic have been observed as a function of stress and fatigue. First results indicate a decrease of the second harmonic as a function of stress. At about 50% of the fatigue life microcracks initiated at surface intermetallics and a substantial increase of the second harmonic amplitude in the vicinity of zero external applied load was observed.

The objective of the present work is to investigate the potential of surface acoustic waves and, in particular, acoustic harmonic generation for surface stress measurements and for fatigue life predictions. Acoustic surface waves are particularly well suited for such measurements since the acoustic energy is highly localized at the materials' surface. The experimental setup for this work is exhibited in Fig. 1, which shows a fatigue sample of rectangular cross section (about 1 inch^2) installed in an electrohydraulic MTS machine. Also shown are acoustic wedge transducers with the transmitting transducers operating at 5 MHz and the receiving transducers tuned to 10 MHz to monitor changes in acoustic harmonic generation as the specimen is fatigued in the MTS machine. An optical microscope (not shown in Fig. 1) has also been used to observe microcrack initiation and growth. Figure 2, bottom, shows the electronics used for harmonic analysis of these acoustic surface waves. The finite amplitude signal is generated using a pulsed oscillator. A heterodyne receiver served as the frequency spectrum analyzer after detection of the signal by the 10 MHz transducer. The surface wave signals received were quite clean and disappeared completely by pressing a soft object against the specimen's gauge section. To demonstrate surface harmonic generation, several measurements on the dependence of the second harmonic amplitude (A_2) at 10 MHz on the first harmonic amplitude (A_1) at 5 MHz were performed with both A_1 and A_2 measured at the receiver transducer. As shown in Fig. 2, right-hand side, the theoretically expected $A_2 \propto A_1^2$ relation was observed. During the early stages of fatigue, harmonic generation was determined as a function of applied load during individual fatigue cycles. Figure 3 shows a typical example of such a measurement plotted in the quantity A_2/A_1^2 (to compensate for any variations in A_1 during the fatigue cycle) as a function of the applied stress. As can be seen from this figure, A_2/A_1^2 decreases with increasing applied stress. Such a dependence is expected theoretically, using non-linear theory of elasticity.

Harmonic generation as a function of applied load was also determined during the later parts of the fatigue life when the microcrack density, as initiated at intermetallics, became high. An example of such a harmonic generation result is shown in Fig. 4, top, with an example of one of the longer microcracks (about 15 μm, or 0.5 mils, long) shown in Fig. 4, bottom. The results given in Fig. 4 are clearly different from those in Fig. 3. Data similar to the ones shown in Fig. 4 for Al 2024-T851 were observed repeatedly on specimens with a large microcrack density. It is believed that the microcracks are the cause for the changed harmonic amplitude results, as explained qualitatively in the following.

As postulated by J. M. Richardson (Science Center, Rockwell International) recently, a stress induced crack opening and closing may be considered as an acoustic harmonic generator. Richardson considered a very simple system composed of an unbonded planar interface separating two semi-infinite linear media (see Fig. 5, top). By definition, the unbonded interface cannot support tension and thus it opens up during the tension phase of a wave propagating from one side of the interface to the other. The system is actually linear while the gap in the interface is closed. The origin of the nonlinearity is due to the fact that the time at which the gap opens and closes depends upon the ratio of the stress amplitude of the acoustic wave and the external stress that works to hold the gap closed (Fig. 5, bottom). In the case of a normally incident sinusoidal wave, the gap dynamics will be nonlinear and harmonics will be generated in a reflected or transmitted wave if the ambient stress is less than the stress of the incident wave.

From the above discussions it is expected that harmonic generation at cracks is a minimum both at maximum tensile and compressive stresses. In the vicinity of zero applied stress, however, harmonic generation should be a maximum. Indications for such an effect may be seen in Fig. 5, top. However, the origin of the large harmonic generation at +50 ksi is unknown at the present time. Further experiments to clarify this situation are underway.

The opening and closing of both microscopic and macroscopic cracks has been observed experimentally. Figure 6 shows the change in contact area of a macrocrack as a function of the applied stress. Microcracks, as shown in Fig. 4, will behave similarly and thus are thought to be a potential source for acoustic harmonic generation.

The conclusion of the present work is summarized in Fig. 7. After having generated strong and clean surface waves and Fourier analyzed the received signal, we have observed that the second harmonic decreases roughly by about 20% per ksi stress. Thus the sensitivity of this effect is one to two orders of magnitude larger than that of another acoustic technique, which uses the change of sound velocity as a stress indicator.

Harmonic generation also seems to be a very promising tool to detect microcracks as developed during fatigue. The nonlinearities occurring during opening and closing of microcracks have been considered by Richardson recently. The present results indicate that microcracks as little as 15 μm long (or about 0.5 mils) can be detected by harmonic generation if the density is high enough.

Acknowledgement

This research was sponsored by the Center for Advanced NDE operated by the Science Center, Rockwell International, for the Advanced Research Projects Agency and the Air Force Materials Laboratory under contract F33615-74-C-5180.

OBJECTIVE TO INVESTIGATE THE POTENTIAL OF SURFACE WAVES FOR SURFACE STRESS MEASUREMENTS AND FOR FATIGUE LIFE PREDICTIONS

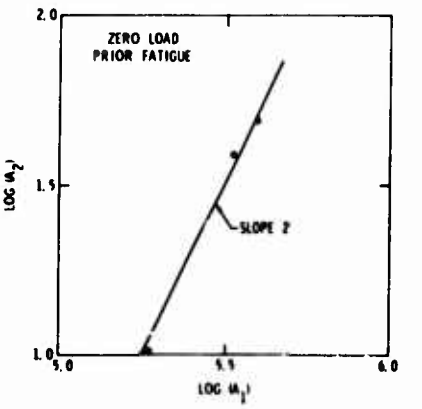
- ACOUSTIC WEDGE TRANSDUCERS, GENERATING ACOUSTIC SURFACE WAVES (AT 5 MHz), WERE MOUNTED ON THE SPECIMEN TO SAMPLE THE STATE OF STRESS AND THE STATE OF FATIGUE WITHIN THE GAUGE SECTION BY MEANS OF ACOUSTIC HARMONIC GENERATION. THE FIGURE SHOWS THE SPECIMEN WHICH WAS FATIGUED IN TENSION-COMPRESSION IN AN ELECTRO-HYDRAULIC MTS MACHINE.



Figure 1

- SHOWN IS THE EXPERIMENTAL APPARATUS FOR HARMONIC ANALYSIS OF ACOUSTIC SURFACE WAVES. SINUSOIDAL ULTRASONIC SURFACE WAVES OF FINITE AMPLITUDE AT 5 MHz WERE EXCITED BY A PZT TRANSDUCER. THE DISTORTED SIGNAL WAS DETECTED USING A 10 MHz PZT. A HETERODYNE RECEIVER SERVED AS THE FREQUENCY SPECTRUM ANALYZER BY VIRTUE OF ITS BROAD BAND MIXING STAGE.

- THE SECOND HARMONIC AMPLITUDE, (A_2), IS RELATED TO THE FIRST, (A_1), BY $A_2 = A_1^2$, AND WAS EXPERIMENTALLY VERIFIED USING THE ABOVE SYSTEM.



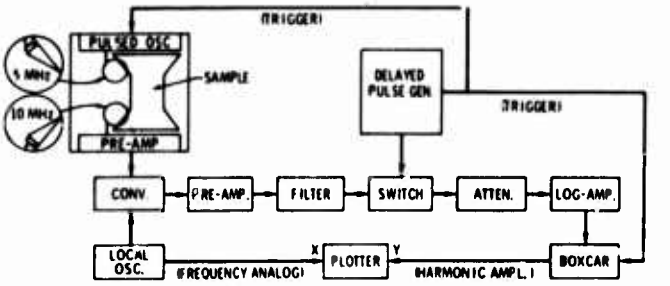


Figure 2

- DURING FATIGUE OF Al 2024 T351 THE QUANTITY LOG $\omega_2 A_1^2$ WAS DETERMINED AS A FUNCTION OF APPLIED STRESS
- THE OBSERVED LOG $\omega_2 A_1^2$ DECREASE WITH INCREASING STRESS CAN BE PREDICTED THEORETICALLY. SENSITIVITY OF THE EFFECT IS ABOUT 20% CHANGE IN ABSOLUTE SECOND HARMONIC FOR 100 ksi. INELASTIC EFFECTS PRODUCED SOME HYSTERESIS AT START OF TEST AS SHOWN IN THE EXAMPLE (AFTER 2000 CYCLES). MICROCRACK DENSITY WAS VERY LOW AT THIS TIME (~4% OF FATIGUE LIFE)

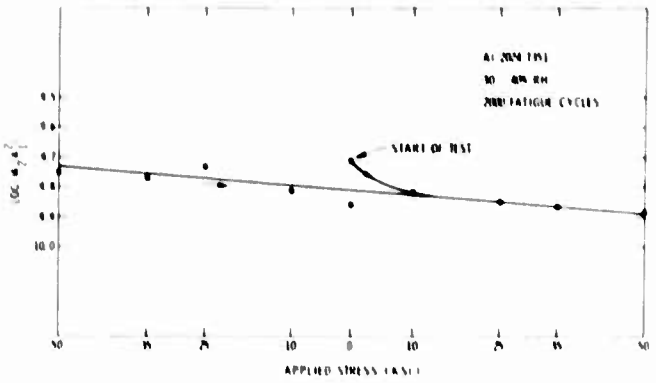
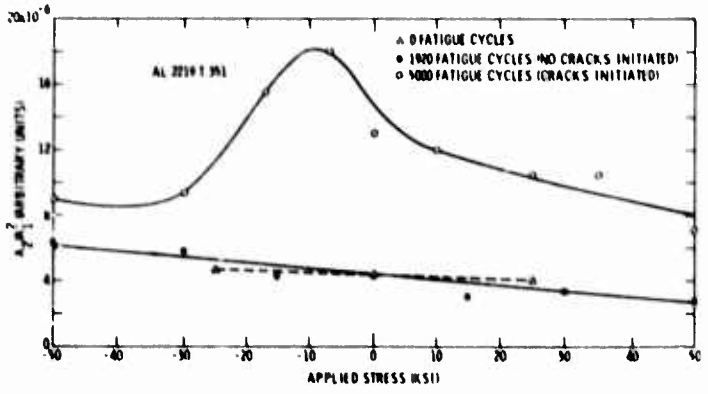


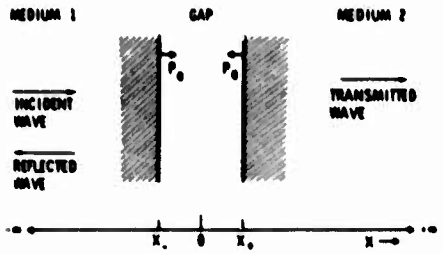
Figure 3

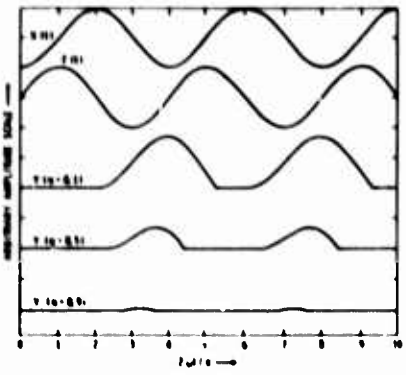




- MICROCRACK DENSITY AFTER FATIGUE OF Al 2024 T81 WAS QUITE HIGH WITH MAXIMUM CRACK LENGTH BEING ABOUT 15 μm (0.5 mils). CRACK TIPS ARE INDICATED BY ARROWS.
- IN THIS CASE THE QUANTITY LOG $\omega_2 A_1^2$ SHOWED A PRONOUNCED VARIATION AS A FUNCTION OF APPLIED STRESS WHICH IS ATTRIBUTED TO THE PRESENCE OF MICROCRACKS

Figure 4





- A POSSIBLE EXPLANATION FOR THE VARIATION IN LOG β_2/β_1^2 WITH STRESS MAY BE ACOUSTIC HARMONIC GENERATION AS THE CRACK OPENS AND CLOSES UNDER STRESS (J. M. RICHARDSON, SCIENCE CENTER)
- THE ORIGIN OF THE NONLINEARITY IS DUE TO THE FACT THAT THE TIME AT WHICH THE GAP OPENS AND CLOSES DEPENDS UPON THE RATIO (α) OF THE STRESS AMPLITUDE OF THE ACOUSTIC WAVE AND THE EXTERNAL STRESS WHICH TENDS TO CLOSE THE GAP.

Figure 5

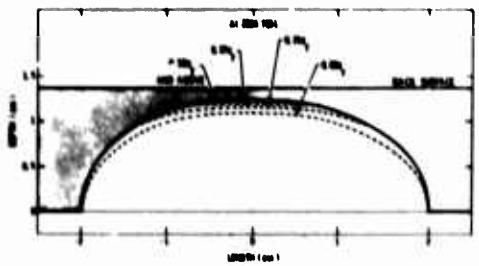


Figure 6

- STRONG AND CLEAN ACOUSTIC SURFACE WAVE SIGNALS HAVE BEEN PRODUCED ON SPECIMENS SUITABLE FOR TENSION-COMPRESSION FATIGUE.

(2) PRIOR TO MICROCRACK FORMATION HARMONIC GENERATION DECREASES WITH INCREASING APPLIED STRESS (SENSITIVITY ≈ 20%/100 Ksi). THUS THE TECHNIQUE IS POTENTIALLY USEFUL TO DETECT LONG RANGE INTERNAL STRESSES.

(3) MICROCRACKS ARE A POSSIBLE SOURCE FOR ACOUSTIC HARMONIC GENERATION. MICROCRACKS AS SMALL AS 19 μm (0.5 mils) MIGHT BE DETECTED. FURTHER RESEARCH IN THIS AREA IS NEEDED HOWEVER.

Figure 7. Conclusions

MECHANISM OF PHOTOSTIMULATED EXOELECTRON EMISSION

W. J. Pardee
Science Center, Rockwell International
Thousand Oaks, California 91360

ABSTRACT

This paper discusses the changes in photoyield of pure aluminum and binary aluminum alloys due to fatigue induced surface roughness in the energy range 5 to 11 eV. As evidenced by a surface replication technique, the roughness is caused by dislocation slip steps forming a near perfect grating on the surface. The grating causes a resonant coupling of incident photons to surface electromagnetic waves in the material, the decay of which can eject electrons if the resonance energy exceeds the material's work function. The theory of this roughness induced photoyield will be briefly reviewed. The effects of fatigue softening and hardening, of oxide layer thickness, and of alloying on the photoyield as a function of photon incident energy will be reported.

The term "exoelectron emission" is used in several different contexts. The phenomenon of interest is the mechanism by which fatigue increases the photoyield of aluminum. Typical results[1] are shown in Fig. 1 for work hardened and well annealed Al 1100. The photocurrent (electrons/incident photon) was measured with an electrometer to ground; the intensity of the incident light was measured by measuring the photocurrent from a gold sample and using the literature value for its photoyield. For both the well-annealed sample (for which internal stresses are increasing) and the work-hardened (for which internal stresses are decreasing) the effect of fatigue is to increase the photo-yield over the range of photon energy 5.7 to 8.5 eV, but the increase occurs much more rapidly with fatigue for the well-annealed sample.

Since photoemission is a surface effect (because the escape depth of the photoelectrons is only about 5nm), one expects changes in surface character with fatigue are responsible. Surface replicas of the two kinds of Al sample described above were prepared and examined in the transmission electron microscope. The results are shown in Fig. 2. Several conclusions can be drawn. Cracks are evidently not a factor, since none are visible on this scale, so any cracks must be much less than the wavelength of the light (about 0.16 μm). The most important result is that the slip steps are much greater on the well-annealed surface than they are on the work-hardened sample, suggesting that they are the source of the increased photoyield. Note that these slip steps have an approximate periodicity of about 50 nm.

The essential ingredients of the photoemission process are shown in schematic fashion in Fig. 3a. The calculations we present below demonstrate that there is a resonant coupling to the surface plasmon by the slip steps which increases the absorption of light, and that this increased absorption is sufficient to account for the increased photoyield without invoking any additional mechanism such as changes in the transport (oxide depth, for example) or escape probability (a change in work function, for example). The surface plasmon is a surface electromagnetic wave at the oxide-metal interface. It cannot couple to external radiation with a flat surface because it is impossible to match both the spatial phase ($2\pi f \sin x/c$) and the temporal phase (ft) across the boundary. However, the presence of the slip steps produce a weak spatially periodic term in the dielectric function, and this term results in induced fields containing (from the sum and difference of the incident field period with that of the dielectric function) long wavelength terms which can couple to incident light. The coordinate system for this model is shown in Fig. 3b. To test this conjecture, the absorption was calculated from Maxwell's equations.

The results of the theoretical calculation[2] are shown in Fig. 4. Figure 4a shows the absorption of p-polarized light by the oxidized aluminum for different values of the amplitude of the slip steps. The largest value considered, h=1.5nm, represents a slip step height of 3.0nm, or about 7-8 lattice constants, a reasonable maximum value. The effect of different slip step spacings is shown in Fig. 4b. The experimental value is about 50nm. The calculation shows that 80nm is inconsistent with the effect observed that 40 and 60nm are both consistent with the general wavelength dependence of the observed increase in photoemission, with 40nm in somewhat better agreement.

Figure 5 shows the experimental data of Fig. 1 replotted to show the change with fatigue and normalized by the calculated photoyield for a perface surface[2]. That is, this curve shows the photoyield after N fatigue cycles minus that at zero cycles, both divided by a normalizing factor. The spacing and magnitude of the two peaks seen here agrees well with theory for steps 2-3nm high and 50nm apart.

The preceding does not explain the gradual nature of the change with fatigue, but this can be understood from the micrographs shown in Fig. 6a and 6b. These show well-annealed Al at different stages in fatigue at different magnifications. Fig. 6a shows the development of slip on a 2μm scale, demonstrating that there is little change in the nature of the slip steps. Figure 6b, the same samples on a 40μm scale, shows that the area covered by plastic deformation does increase with fatigue. The change in photoyield is plotted against this increased area in Fig. 6c, demonstrating a linear growth.

The overall mechanism then is as follows. The photon beam used in these experiments covered a relatively large area of the sample. Those portions of the sample which had experienced plastic deformation permitted resonant coupling to the surface plasmon, increasing the photoyield by an amount proportional to the area covered by slip steps. These plasma oscillations then decayed to electrons which then had sufficient energy to escape, thereby increasing the photoyield.

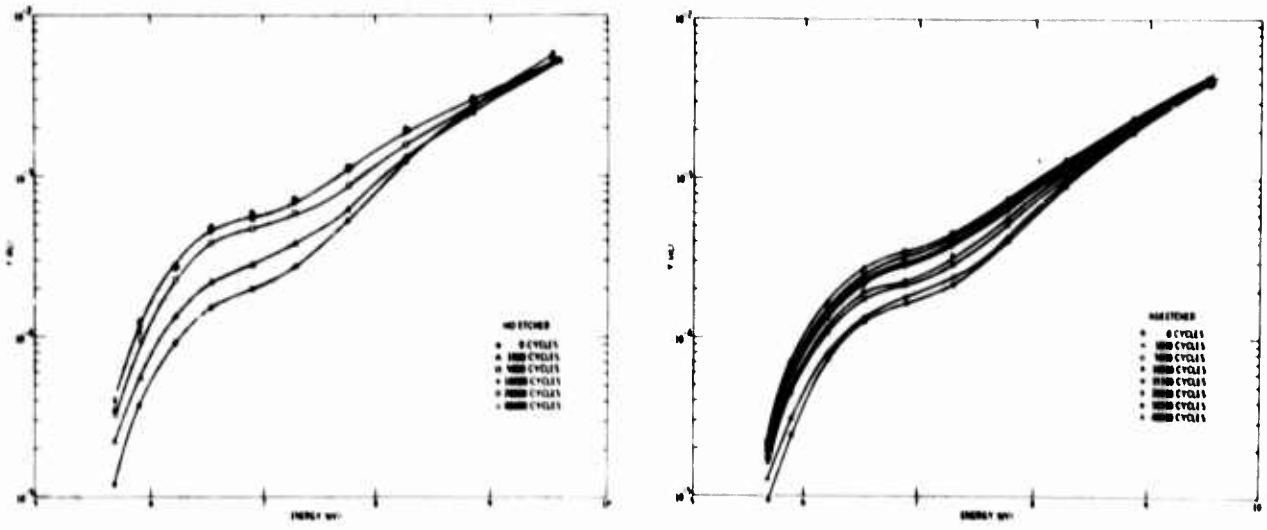
Acknowledgement

This work was sponsored by AFOSR Contract No. F44620-71-C-0043 and Rockwell International IR&D funds.

References

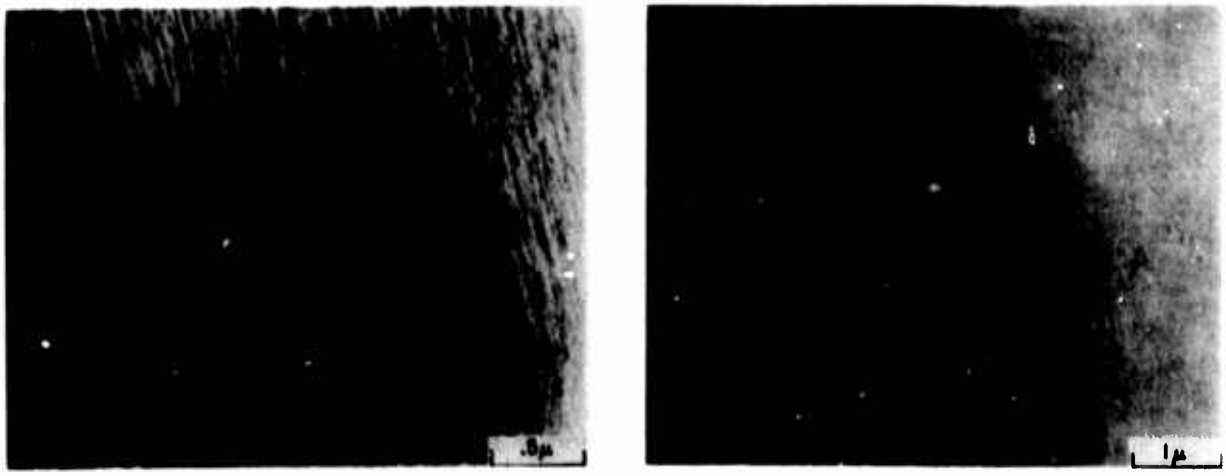
1. O. Buck, W. J. Pardee, F. J. Szalkowski, and D. O. Thompson, Appl. Phys. 12, 301-310, (1977).

2. W. J. Pardee and O. Buck, submitted to Appl. Phys.



(a) (b)

Figure 1. (a) Photoyield (electrons/incident photon) of well-annealed oxidized (12 nm oxide) Aluminum 1100 as a function of photon energies for various states of fatigue (4000 cycles = 10% fatigue life. (b) Photoyield (electrons/incident photon) of work hardened oxidized (12 nm oxide) Aluminum 1100 as a function of photon energies for various states of fatigue (4000 cycles = 10% fatigue life).



(a) (b)

Figure 2. (a) TEM micrograph of well-annealed Aluminum 1100 at 10% life; (b) TEM micrograph of work hardened Aluminum 1100 at 10% life.

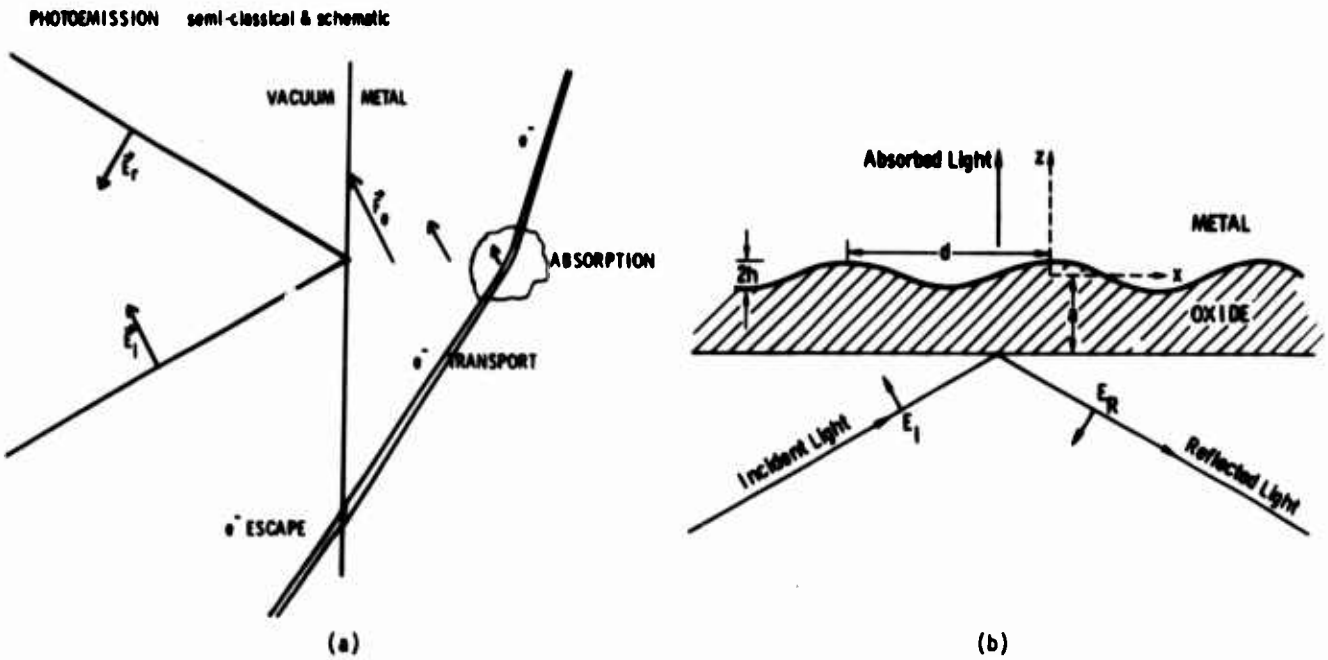


Figure 3. (a) A semi-classical illustration of the essential processes involved in photoemission. (b) Diagram (not to scale) of the model for which Maxwell's equations were solved (to leading order in h).

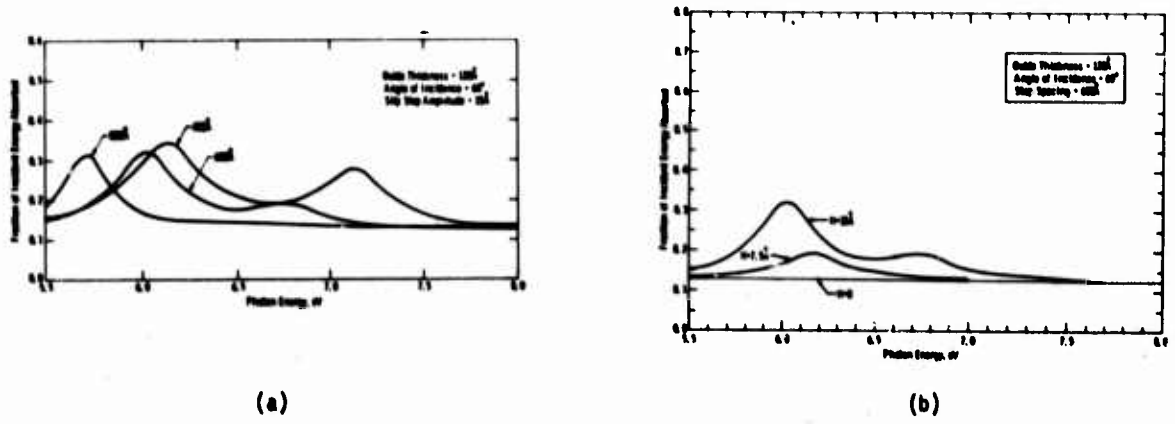


Figure 4. (a) Theoretical absorption of p-polarized light as a function of photon energy for various slip step amplitudes. (b) Theoretical absorption of p-polarized light for various slip step spacings.

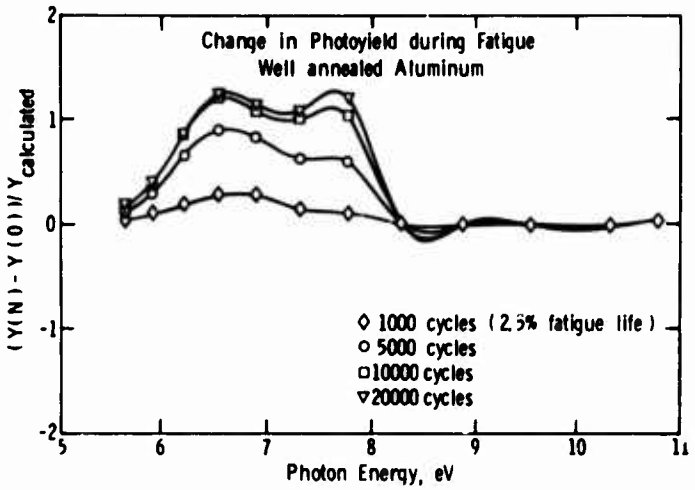


Figure 5. Experimental change in photoyield with fatigue, normalized by theoretical photoyield for a flat surface.

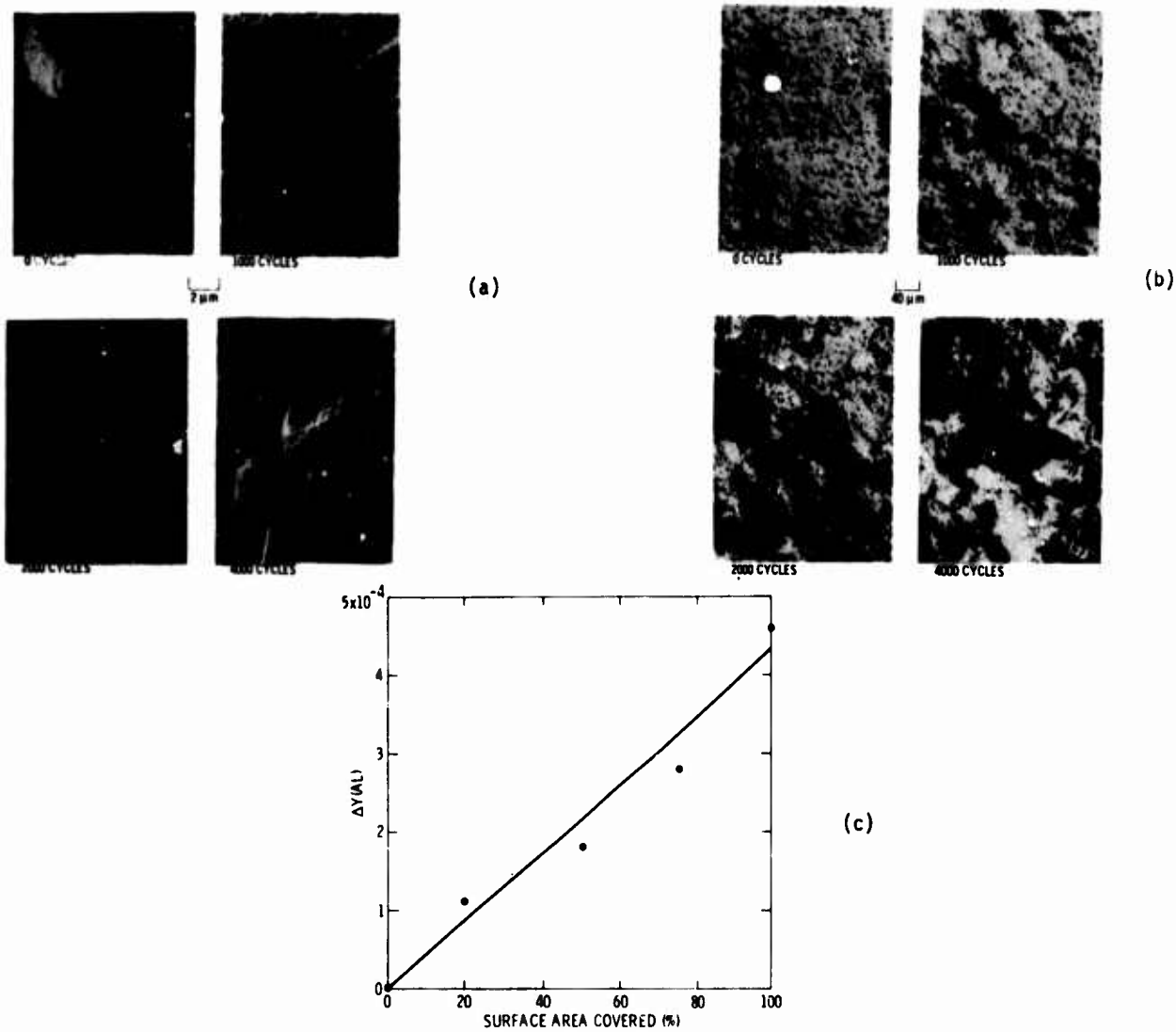


Figure 6. (a) Micrographs of well-annealed Aluminum 1100 at various stages of fatigue (2 μm scale).
(b) Micrographs of well-annealed Aluminum 1100 at various stages of fatigue (40 μm scale).
(c) Change in photoyield vs. area covered by slip step.

MEASUREMENT OF PHASE AND GROUP VELOCITIES OF DISPERSIVE WAVES IN SOLIDS

Wolfgang Sachse
Department of Theoretical and Applied Mechanics
Cornell University, Ithaca, New York 14853

ABSTRACT

The dispersion relation and the propagational speeds of waves in dispersive solids are determined by a newly developed technique in which the phase function of spectral analyzed broadband pulses is determined. The method is simpler than and in agreement with the continuous wave-resonance technique. Application is made to ultrasonic pulses propagating in fiber-reinforced composite materials and other dispersive wave propagation situations.

Theoretical Bases

A pulse $u(x,t)$ propagating in a linear medium $x > 0$ can be Fourier synthesized with harmonic waves $\exp[i\omega(t-x/v-\xi)]$ of all angular frequencies ω ($=2\pi f$) and phases ξ. Thus,

$$u(x,t) = \frac{1}{2\pi}\int_{-\infty}^{\infty} d\omega \int_{-\infty}^{\infty} A(\xi)e^{i\omega(t-x/v-\xi)}d\xi \quad (1)$$

Here v ($=\omega/k$) is the phase velocity which is a function of ω in a dispersive medium. For an arbitrary excitation pulse $u(0,t) = F(t)$ at the end $x = 0$, it follows from the Fourier theorem that

$$A(\xi) = F(\xi) \quad (2)$$

When $v = v(\omega)$, the input pulse changes its shape as it propagates through the medium. The signal received at $x = \ell$ is

$$u(\ell,t) = \frac{1}{2\pi}\int_{-\infty}^{\infty} \overline{F(\omega)}e^{i\,(t-\ell/v)}d\omega \quad (3)$$

where

$$\overline{F(\omega)} = \int_{-\infty}^{\infty} F(t)e^{-i\omega t}dt = |\overline{F(\omega)}|e^{-i\phi_0} \quad (4)$$

and $\phi_0 = \omega t_0$, t_0 being the time at which the excitation pulse enters the specimen at $x = 0$. The Fourier transform of the response $u(\ell,t)$ is

$$\bar{u}(\ell,\omega) = |\overline{F(\omega)}|e^{-i(k\ell+\phi_0)} = |\overline{F(\omega)}|e^{-i\phi(\omega)} \quad (5)$$

It is clear that from the measured phase spectrum, $\phi(\omega)$, of a dispersed pulse, one is able to determine the dispersion relation,

$$k(\omega) = [\phi(\omega) - \phi_0]/\ell \quad (6)$$

From this relation, one can easily calculate the phase velocity, v, and group velocity, v_g, as a function of frequency.

$$v(\omega) = \omega/k = \omega\ell/(\phi-\phi_0) \quad (7)$$

$$v_g(\omega) = d\omega/dk = \ell/(d\phi/d\omega - t_0) \quad (8)$$

Experiments

Method

Figure 1 shows two broadband ultrasonic transducers which are attached to both sides of a polished specimen. One transducer is excited by a voltage pulse, and the signals received by the second transducer are displayed by a sampling oscilloscope. Through an A/D converter interfaced with a PDP 11/40 digital computer, the signal is digitized and then Fourier transformed to yield both the amplitude (magnitude) spectrum and the phase spectrum. From the phase spectrum of the two transducers directly in contact (no specimen is between), we determine precisely the ϕ_0. The spectral analysis of the signal through the specimen of known length then yields $\phi(\omega)$.

Example: Undispersed 1 μsec Square Pulse

To check the operation of the signal analysis system, a simulated pulse shown in Fig. 2(a) of 1 volt amplitude and 1 μsec duration, centered at 2.0 sec was analyzed. In Fig. 2(b) is shown the magnitude of the Fourier transform and in Fig. 2(c), the phase spectrum, $\phi(\omega)$. This is a linear function of frequency. The dispersion relation, $k(f)$, was computed assuming that the propagation distance was 1 cm; the results being shown in Fig. 2(d). The computed phase velocity, $v(f)$, and group velocity, $U(f)$, are shown respectively, in Figs. 2(e) and 2(f). It is clear that v and U are independent of frequency and both equal the same value of 0.5 cm/μsec.

Applications

Broadband Pulse in 6061-T6 Aluminum

The results of experiments in a non-dispersive medium are shown in the figures. A broadband ultrasonic pulse, comprised mainly of frequency components from 3 to 12 MHz is propagated through a 1.9001 cm thick specimen of 6061-T6 aluminum. In Fig. 3(a) is shown the excitation pulse $u(o,t)$ and in Fig. 3(b) the first received pulse $u(\ell,t)$.

In Fig. 3(c) is shown the Fourier amplitude spectrum of $u(z,t)$ and in Fig. 3(d) the dispersion relation. The calculated phase velocity and group velocity of this specimen are shown in Figs. 3(e) and 3(f) respectively. It is clear from Fig. 3(d) that there is little dispersion in this material in the frequency range from 0 to 20 MHz.

The additional data points shown in Fig. 3(f) represent the values of group velocity measured with the continuous-wave, π-phase technique. For this specimen, no measurements were made below 1.5 MHz. At frequencies above 7 MHz data were recorded only at integer frequency points. The average group velocity measured using the continuous-wave technique was 0.618 ± 0.009 cm/μsec. For the pulse measurement, the average of 160 points which comprised the data in the frequency interval 0 to 20 MHz, the average was 0.609 ± 0.005 cm/μsec.

Composite Materials: Example--96-ply Boron-Epoxy

The results for a dispersive medium such as composite materials are shown in the figures. The pulse is propagated through a 0.546 cm thick specimen of 96-ply Boron-Epoxy. In this case, the wave propagation direction coincides with the fiber direction and the particle displacement direction is perpendicular to the fibers and tangent to the ply layers as shown in Fig. 4. The broadband shear excitation pulse is shown in Fig. 5(a). In Fig. 5(b) is shown the dispersed pulse detected at the receiving transducer. It is apparent that the high frequency components of the pulse propagate faster than the low frequency components. The relative amplitudes of the various frequency components in the pulse are shown in Fig. 5(c). As expected, the high-frequency components are markedly lower in amplitude than the low-frequency components. The dispersion relation is shown in Fig. 5(d), which is not a linear function of ω (or f). In Figs. 5(e) and 5(f) are shown the results of the phase and group velocity computation for the frequency range 0-10.0 MHz. Results for the spectral amplitudes beyond 10 MHz are not dependable. The data points on the group velocity curve are those obtained from continuous wave measurements.

Other Materials, Specimen Geometries, Etc.

Foamglas - Figure 6(b) shows the result of phase velocity measurements up to 1 MHz in Foamglas, an insulating material, shown in cross section in Fig. 6(a). Shown is a dependence on pore diameter--the larger the pore size, the lower the wave speed. Similarly, but not as clear is the porosity dependence. The curves are quite distinct from that found for bubble-free glass.

Thin Wires, Tubing - Figure 7(a) shows a longitudinal pulse propagating a 76.4 cm, 1.61 mm (OD) section of Remendur tubing. The received pulse has been delayed 135.7 μsec. Figure 7(b) is the amplitude spectrum of the pulse in Fig. 7(a), while Fig. 7(c) shows the determined dispersion relation, phase and group velocities.

Conclusions

Ultrasonic Pulse Phase Spectroscopy measurements yield results equivalent to continuous wave measurements of group velocity of elastic wave propagating in dispersive media.

The phase velocity and dispersion relation can be determined unambiguously with this technique.

The measurements are rapid. Only one received signal is required for analysis.

The technique is not restricted to elastic pulses.

Acknowledgements

This work was performed in conjunction with Professor Y. H. Pao through support provided by the National Science Foundation and the Air Force Office of Scientific Research. The specimen materials were donated by United Aircraft, U. S. Army Mechanics and Materials Research Center and Pittsburgh-Corning Glass Company. This paper was submitted for publication as Materials Science Center Report #2773, January 1977.

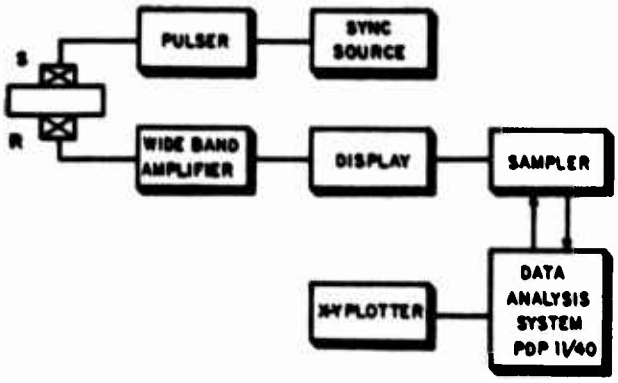


Figure 1. Schematic of experimental setup.

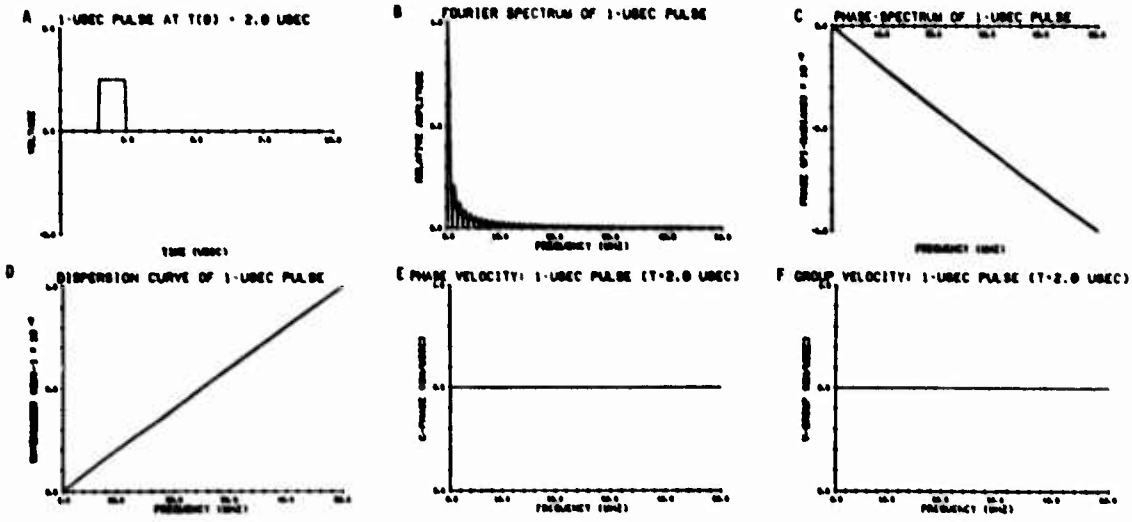


Figure 2. (a) 1-μsec pulse at T(0) = 2.0 μsec; (b) Fourier spectrum of 1-μsec pulse; (c) phase-spectrum of 1-μsec pulse; (d) dispersion curve of 1-μsec pulse; (e) phase velocity: 1-μsec pulse (T = 2.0 μsec); (f) group velocity: 1-μsec pulse (T = 2.0 μsec).

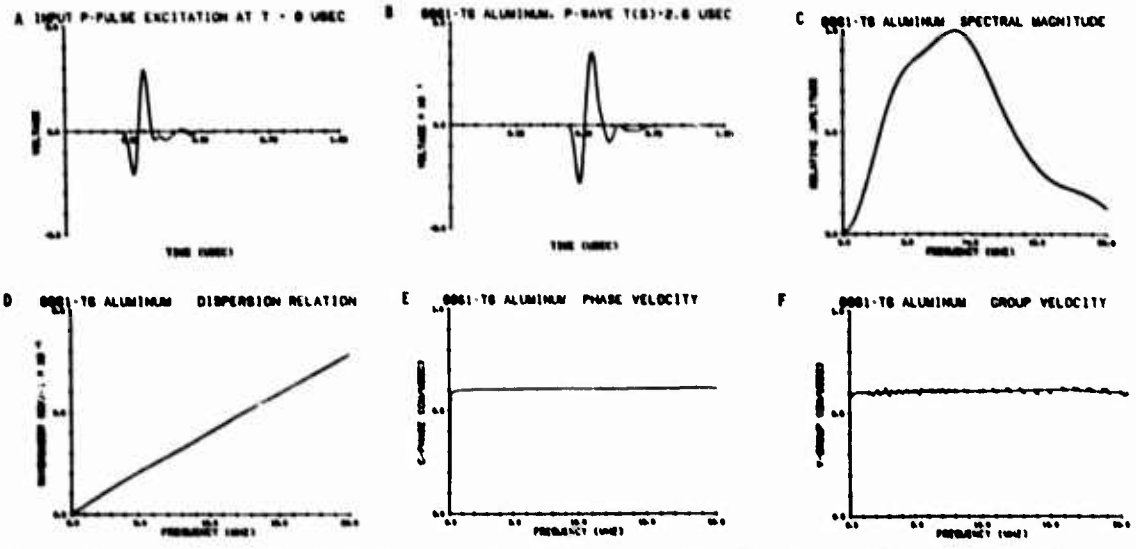


Figure 3. (a) Input P-pulse excitation at T = 0 μsec; (b) 6061-T6 aluminum, P-wave T(S) = 2.6 μsec; (c) 6061-T6 aluminum spectral magnitude; (d) 6061-T6 aluminum dispersion relation; (e) 6061-T6 aluminum phase velocity; (f) 6061-T6 aluminum group velocity.

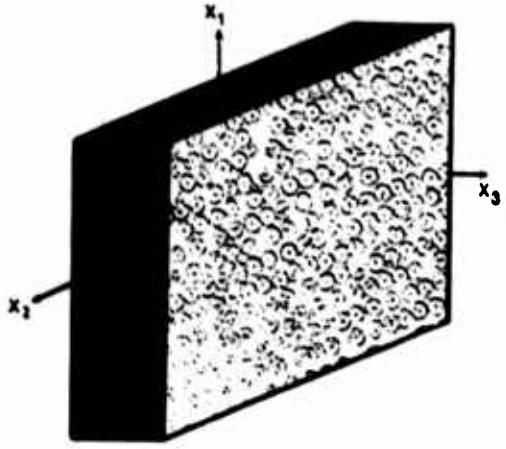


Figure 4. Boron-epoxy specimen.

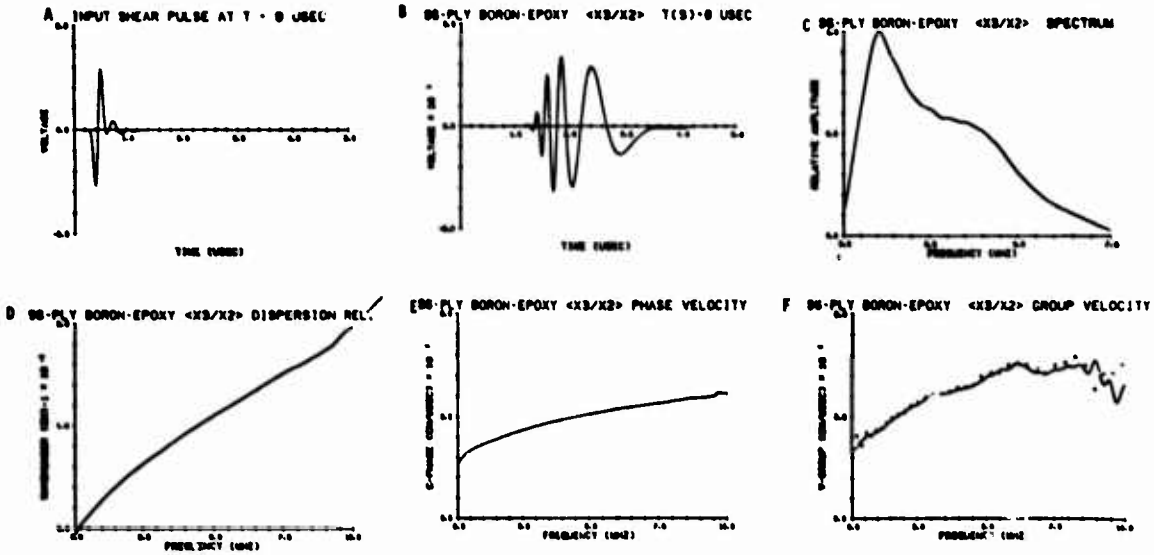
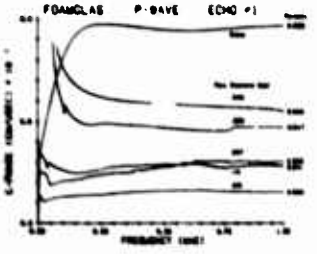


Figure 5. (a) Input shear pulse at T = 0 μsec; (b) 96-ply boron-epoxy <X3/X2> T(S) = 0 μsec; (c) 96-ply boron-epoxy <X3/X2> spectrum; (d) 96-ply boron-epoxy <X3/X2> dispersion rel; (e) 96-ply boron-epoxy <X3/X2> phase velocity; (f) 96-ply boron-epoxy <X3/X2> group velocity.

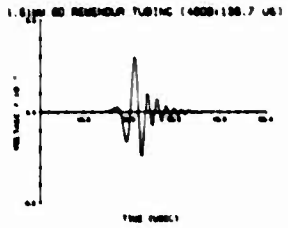


(a)

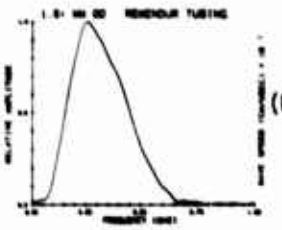


(b)

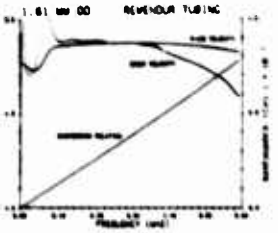
Figure 6. (a) Cross section of foamglas insulating material. (b) Foamglas P-wave echo 1.



(a)



(b)



(c)

Figure 7. (a) 1.61 mm OD remendur tubing (40 dB: 135.7 μs); (b) 1.6 mm OD remendur tubing; (c) 1.61 mm OD remendur tubing.

MEASUREMENT OF STRESS PROFILES BY PHASE CONTRAST TECHNIQUES

D. Barnett, G. Herrmann, J. Hunter, G. Johnson,
G. Kino, W. Leung, A. Selfridge, C. Steele, J. Shaw, and T. Waugh
Stanford University
Stanford, California 94305

ABSTRACT

An acoustic wave passing through a material has its velocity changed when stress is applied. This is due to changes in the third order elastic constant and the density of the material. By using a small diameter beam or a focused beam incident on a metal and reflected from both its front and back surfaces, it is possible to measure the difference in phase of the two reflected waves; the beam itself can be scanned over the surface of the material. Three kinds of measurements will be shown. The first relates the change of velocity of a compressional wave to the applied stress taken in an MTS testing system. The second shows a scan of the profile of the velocity change around a circular defect. The third is an image of the stressed region around a circular defect obtained with a scanned electronically focused system operating in a phase contrast mode.

A system has been implemented to make ultrasonic measurements of the state of stress in a metal sample. The basic technique determines the change in velocity of an acoustic wave passing through a sample when it is stressed. Scanned acoustic beams of small diameter are used also to determine the variation of the stress in an inhomogeneously stressed sample. One system uses mechanical scanning and is extremely accurate but slow in operation, the second system uses an array of transducers and is electronically scanned in one direction and mechanically scanned in the other. It is fast in operation but less accurate.

A block diagram for the accurate system is shown in Fig. 1. An acoustic transducer approximately 3 mm diameter is used to excite two rf tone bursts in water which are reflected from the front and back faces, respectively, of the sample so that the two received echoes from the front and back faces coincide. We measure the phase difference between the carriers of these tone bursts to determine the change in velocity of waves in the material. The advantage of this technique is that it eliminates errors due to the time delay of the wave in the water path between the transducer and the sample, for only the difference in time delays between waves reflected from the front and back face of the sample is determined. The output is gated so that only the coincident pulses are observed.

The phase relationship of the two echoes is a function of transit time through the sample and the carrier frequency of the tone burst. Thus, the frequency may be adjusted to create the minimum condition. It can be shown that if the transit time through the sample changes by ΔT, the required change in frequency Δf is given by the relation:

$$\frac{\Delta f}{f} = -\frac{\Delta T}{T} \qquad (1)$$

where f is the frequency and T is the transit time.

The experimental accuracy is 5 parts in 10^6 in a 20 mm thick aluminum sample. The measurement of the transit time of the pulse can be related to the stress state in the sample through nonlinear elasticity. The transit time is a function of the thickness of the sample and the acoustic velocity of the material. Thickness changes with stress can be accounted for by Poisson's ratio and can be measured independently by the use of strain gauges. Velocity changes with stress can be accounted for through use of third order terms in the strain energy function.

For plane states, changes in thickness and longitudinal wave speed are both proportional to the first stress invariant $\sigma_1 + \sigma_3$. Measurements have been made for calibration purposes in an MTS loading system with acoustic measurement apparatus attached to it. A stress strain curve for aluminum 6061-T6 is shown in Fig. 2. Corresponding values of relative velocity change are shown in Fig. 3. As far as we are aware, these are the first results of this type that have been obtained for both compression and tension; the curves are symmetric about the origin up into the plastic range.

Another sample tested was an aluminum disc which had a hardened steel punch pressed into it. The punch was removed and the surfaces of the disc were ground parallel. Acoustic scans were then taken over the region shown in Fig. 4. The disc was scanned in straight lines and then the results interpolated on the computer to give plots of lines of constant frequency change, which are approximately circular.

Another set of measurements were taken of an inhomogeneous state of plane stress in a plate with a circular hole drilled in it. The plate was loaded to produce a stress state which is predictable theoretically. Acoustic scans were made in one quadrant of the sample. Scan points were spaced 3 mm apart in one direction in the plots, the x and y dimensions are scaled with respect to the width of the plate so the edges are at $x = \pm 1$. An illustration of the plate used is given in Fig 5. The system was calibrated using the results obtained originally on the MTS testing system. Tension was applied to the sample using a special tension testing machine made for use in a small water tank; this is illustrated in Fig. 6. A set of results taken with a scan in the x direction was seen to compare closely to the theory. The calibration appears to be within 10% of the results obtained on the MTS testing rig. A second set of results, obtained with

a scanning system controlled by a computer and with scanning points only 1 mm apart, is shown in Fig. 7. Again, it is seen that the agreement between theory and experiment is excellent. Furthermore, the region of negative stress, i.e., compression on the top of the hole is measured experimentally, and it can also be seen that the stress near the side of the hole is approximately three times that of the uniform region far from the hole, as would be expected from the theory.

Another system for stress measurements has also been set up. This employs a 100 element electronically scanned and focused system with a long strip horizontal transmitting transducer. Again, two rf pulses are generated, and the resultant phase changes in the sample are measured. The receiver focuses on a point near the surface of the sample and operates in a transmission mode. A block diagram of the system is shown in Fig. 8.

The advantage of this system is the ability to rapidly scan a stressed sample. Changes in phase are now displayed as a change in amplitude of the output signal. The results for the entire sample can be displayed on an oscilloscope, thus giving immediate visual information on the stress state. The scan rate is approximately 100 times that of the purely mechanically scanned system, but the system is somewhat less sensitive to phase change than the first system. A photograph of an image of the disc sample, shown in Fig. 4 is illustrated in Fig. 9 using two different contrast levels. The stress region near the center of the sample can be clearly seen although the results are relatively crude as yet.

Acknowledgement

This work was supported by EPRI Contract No. RP-609-1 and NSF Contract No. DMK-76-00726 through the Center for Materials Research at Stanford University.

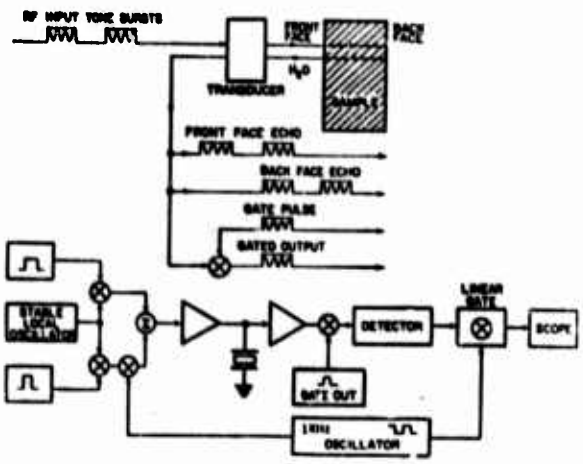


Figure 1. Block diagram of the precision phase measurement system.

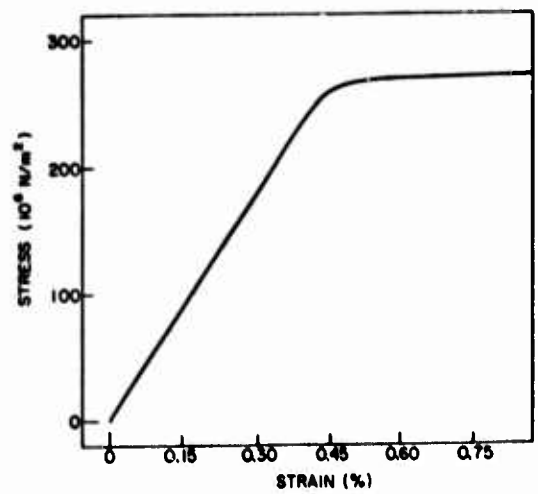


Figure 2. Stress strain curve for aluminum 6061-T6.

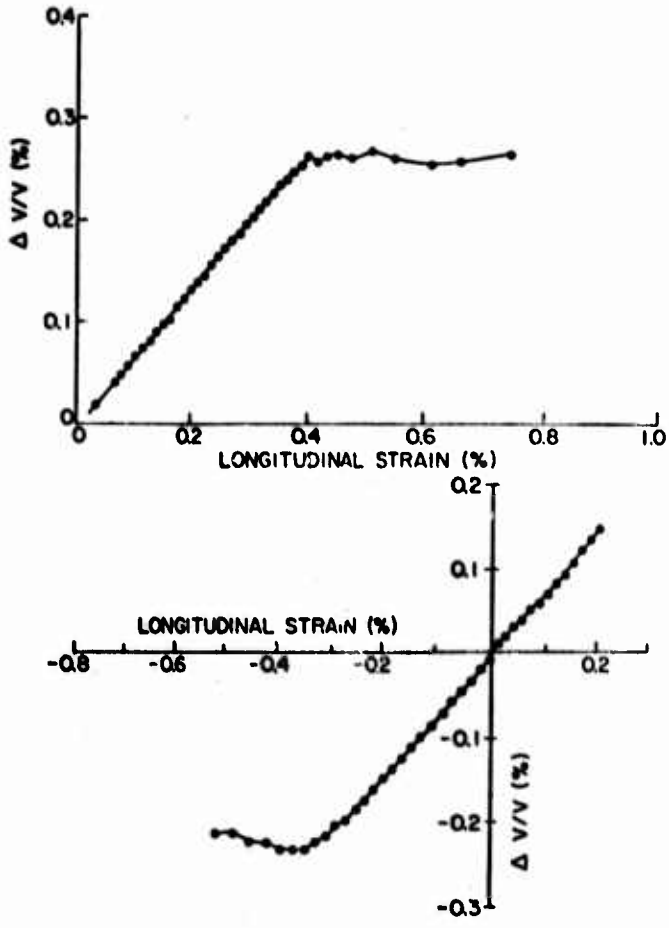


Figure 3. Relative velocity change versus longitudinal strain for aluminum.

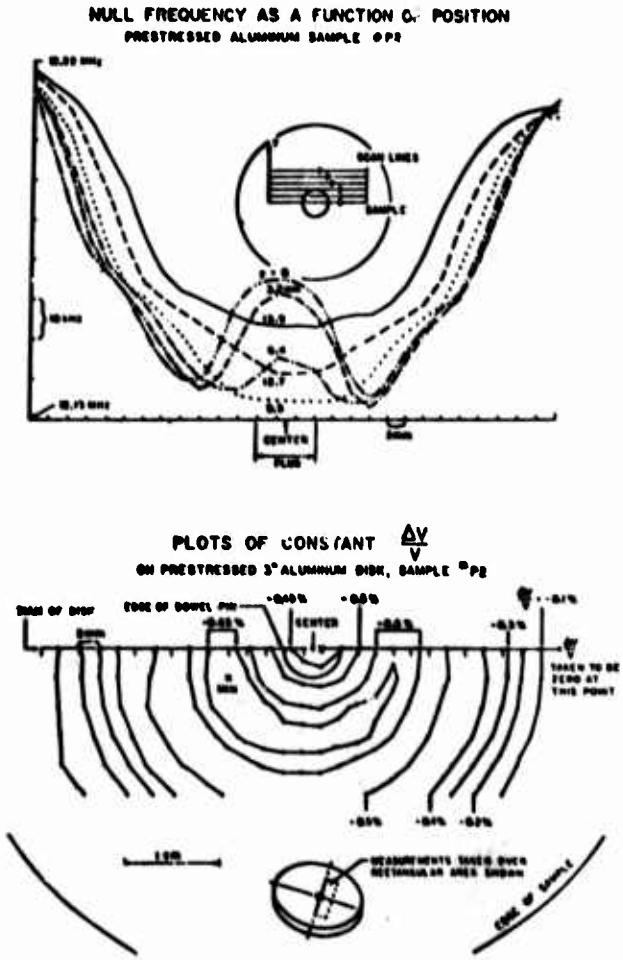


Figure 4. Results obtained by scanning a disk.

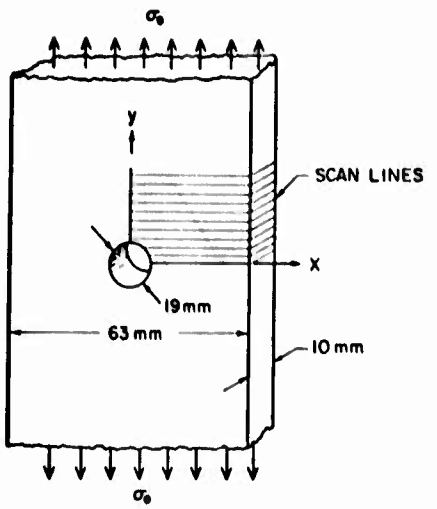


Figure 5. Geometry of the plate with a circular hole in tension.

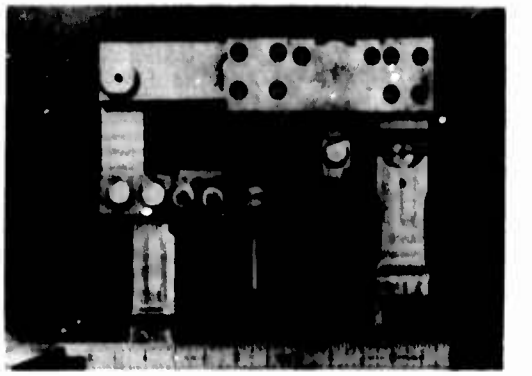


Figure 6. Tension testing machine made for use in small water tank.

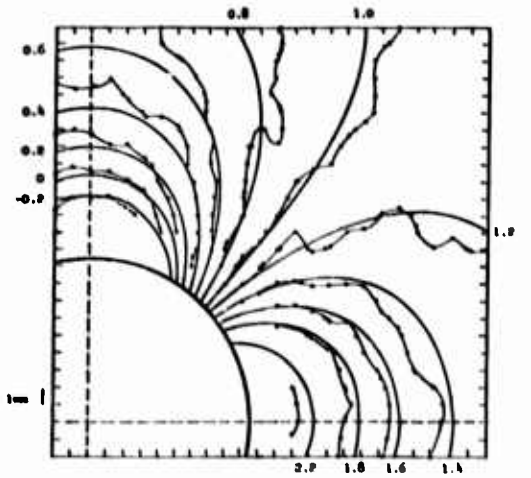


Figure 7. Scanned quadrant of plate with hole.

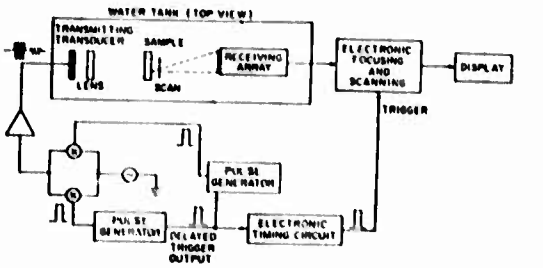


Figure 8. Block diagram of the electronically scanned and focused system.

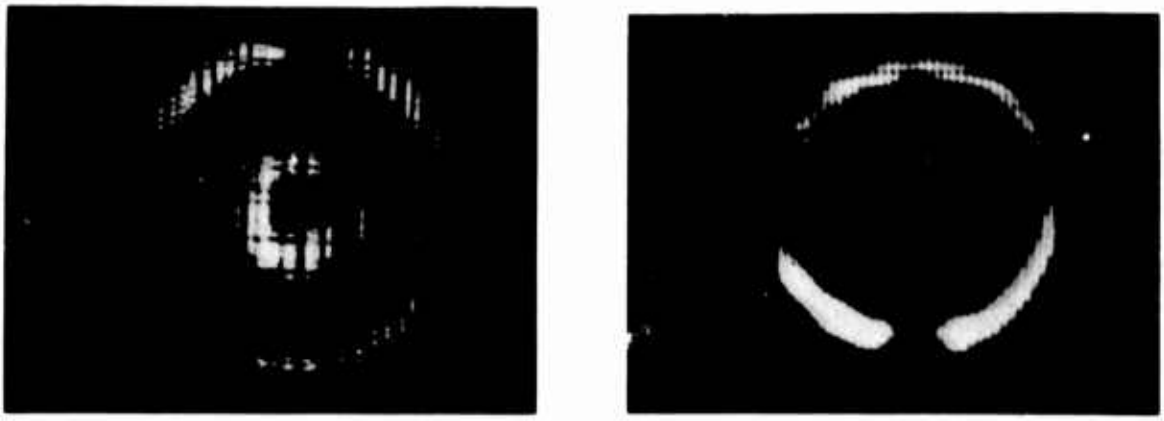


Figure 9. Photographs of stress state images of disk sample of Fig. 4 taken using the electronically scanned focusing system.

MAPPING RESIDUAL STRESS FIELDS BY ULTRASONIC TOMOGRAPHY

B. P. Hildebrand and D. E. Hufferd
Battelle Northwest
Richland, Washington 99352

ABSTRACT

It is well known that the velocity of sound in a solid is affected by stress. This phenomenon is a third order effect, and has been used primarily as a research tool to determine the Lamé amd Murnaghan elastic constants for various materials. A few preliminary attempts to use it for stress analysis have also been made. In this paper we describe the first attempt to combine this effect with the newly revived mathematical technique known as Computerized Axial Tomography (CAT) to provide quantitative maps of velocity within thick metal sections. From these maps it is possible to infer the state of residual stress within the material. The technique requires that time-of-flight profiles through a section of the solid be made in a number of angular directions. This is equivalent to measuring the velocity through the solid from many different directions in a single plane. The computer takes the set of data so gathered and inverts it to produce a cross-sectional plot of velocity versus position. We have succeeded in mapping velocity anomalies as low as 0.2% and estimate that 0.5% is technically feasible. This kind of sensitivity should allow us to map stress anomalies as low as 1000 psi/inch in steel. We will also describe an experiment with a mild steel section in which we inserted an oversized pin by shrink fitting. The reconstruction clearly shows the high compressive stress within the pin, and the tensile stress in the metal surrounding the pin.

Acknowledgement

This work was sponsored by the Electric Power Research Institute, Palo Alto, California.

References

1. B. J. Ratcliffe, "A Review of the Techniques Using Ultrasonic Waves for the Measurement of Stress Within Materials," British Journal of N.D.T., September 1969.

2. E. I. Crecraft, "Ultrasonic Measurement of Stresses," Ultrasonics, Vol. 6, April 1968.

3. N. H. Hsu, "Acoustical Birefringence and the Use of Ultrasonic Waves for Experimental Stress Analysis," Experimental Mechanics, May 1974.

4. R. T. Smith, "Stress-Induced Anisotropy in Solids - The Acousto-Elastic Effect," Ultrasonics, July-September 1963.

5. P. J. Noronha and J. J. Wert, "An Ultrasonic Technique for the Measurement of Residual Stress," J. of Testing and Evaluation, Vol. 3, March 1975.

6. Technical Digest of the Topical Meeting on Image Processing for 2-D and 3-D Reconstruction from Projections, August 1975, sponsored by Opt. Soc. Am.

7. D. S. Clark and W. R. Varney, "Physical Metallurgy for Engineers," C. VanNostrand, Princeton, N.J., 89-91 (1952).

$$\rho_0 V_L^2 = \lambda + 2\mu + \frac{T}{3K_0}\left[\frac{\lambda+\mu}{\mu}(4\lambda + 10\mu + 4m) + \lambda + 2\ell\right]$$

$$\rho_0 V_T^2 = \lambda + 2\mu - \frac{T}{3K_0}\left[\frac{2\lambda}{\mu}(\lambda + 2\mu + m) - 2\ell\right]$$

ρ_0 = DENSITY

V_L = VELOCITY OF LONGITUDINAL WAVES PROPAGATING IN DIRECTION OF STRESS

V_T = VELOCITY OF LONGITUDINAL WAVES PROPAGATING IN DIRECTION TRANSVERSE TO STRESS

λ, μ = SECOND ORDER LAME ELASTIC CONSTANTS

ℓ, m, n = THIRD ORDER MURNAGHEN ELASTIC CONSTANTS

T = UNIAXIAL TENSION

$K_0 = 1/3\,(3\lambda + 2\mu)$ = BULK MODULUS

FOR COMPRESSION, THE SIGN OF T IS REVERSED

Figure 1. Theoretical variation of longitudinal velocity as a function of stress.

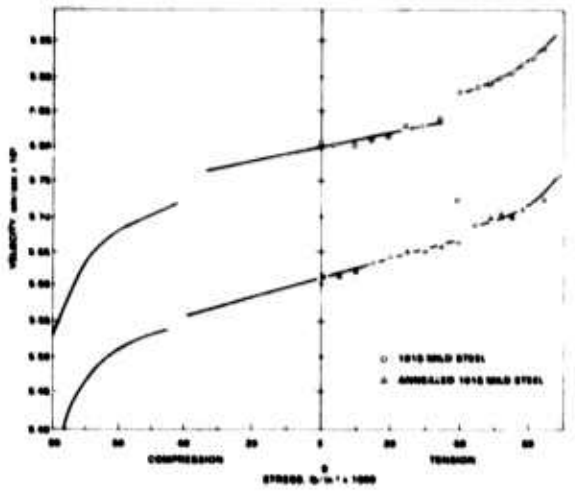


Figure 2. Experimental variation of longitudinal velocity with stress. The annealing was done by heading the sample to 1000°C and cooling at room temperature. Data was taken in tension only. The extrapolation to compression is valid in the linear region, but doubtful beyond the proportional limit.

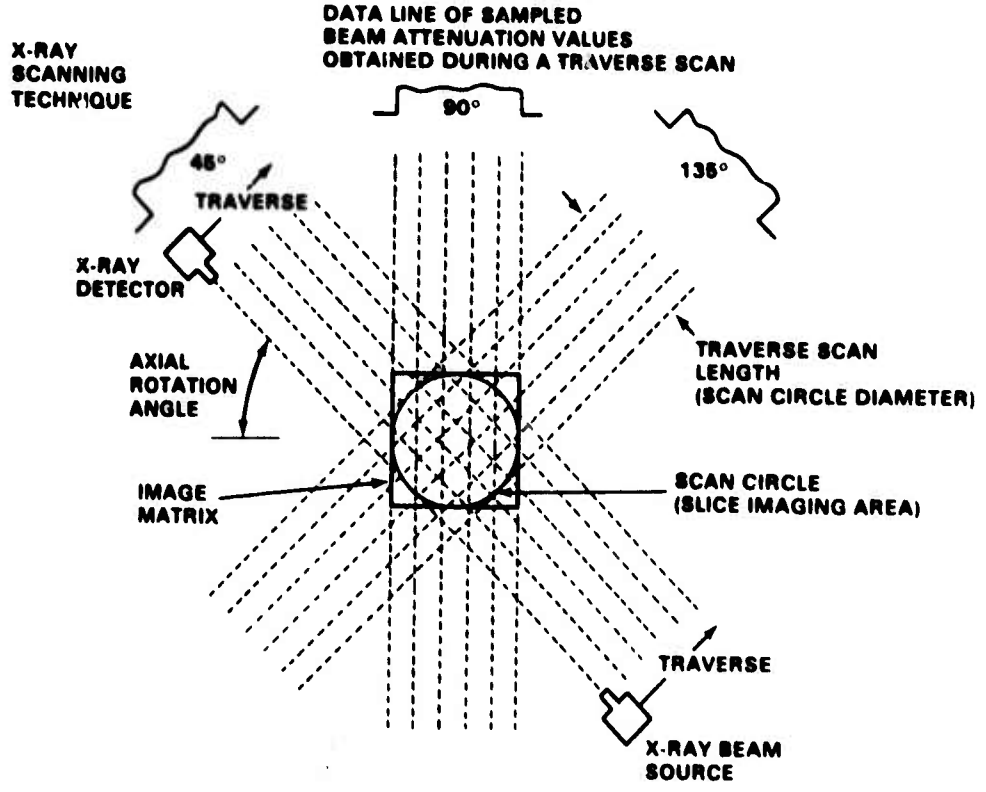


Figure 3. Principle of x-ray tomography. The source and receiver are on opposite sides of a moving frame. Each traverse produces a single projection at a single angle until 180 projections are collected.

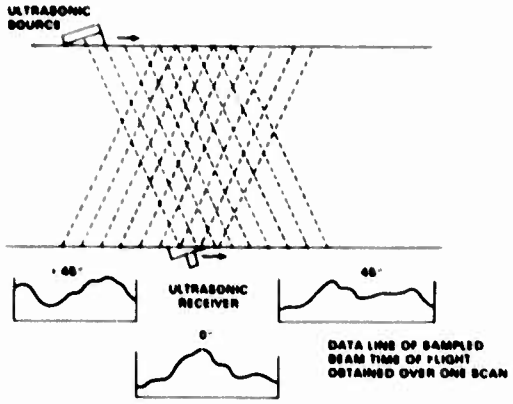


Figure 4. Principle of ultrasonic tomography for thick steel sections. Maximum practical field of view is 90°. This arrangement could be used if both sides of the section are accessible. The reconstruction will yield a cross-sectional plot of the ultrasonic velocity variations.

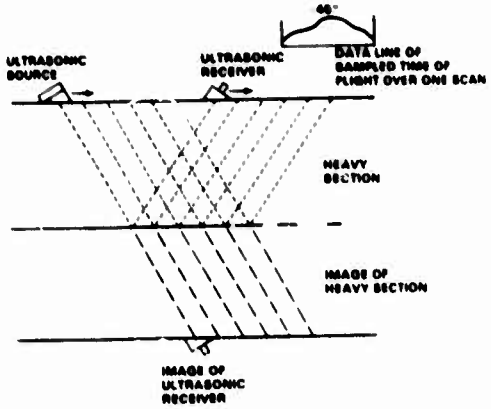
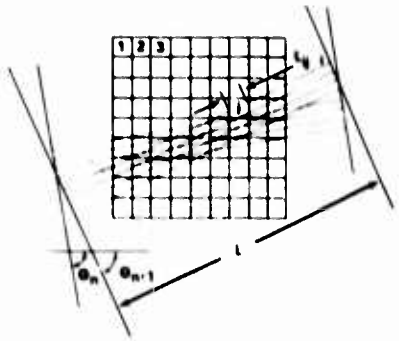


Figure 5. This arrangement could be used if only one side is accessible and the opposite side is smooth. Other angles would be obtained by changing the spacing between source and receiver. The reconstruction would then yield the object and its mirror image.



RECONSTRUCTION OF X-RAY TOMOGRAM

$$A_i = \sum_{j=1}^{K} a_j L_{ij} + a_0\left(L - \sum_{j=1}^{K} L_{ij}\right)$$

WHERE A_i = ATTENUATION ALONG i^{th} RAY (MEASURED)

a_j = ATTENUATION COEFFICIENT IN j^{th} CELL (UNKNOWN)

a_0 = ATTENUATION COEFFICIENT SURROUNDING MEDIUM (KNOWN)

L_{ij} = PATHLENGTH OF i^{th} RAY THROUGH j^{th} CELL (KNOWN)

L = TOTAL PATHLENGTH (KNOWN)

RECONSTRUCTION OF ULTRASONIC TOMOGRAM

$$T_i = \sum_{j=1}^{K} \frac{L_{ij}}{V_j} + \frac{1}{V_w}\left(L - \sum_{j=1}^{K} L_{ij}\right)$$

WHERE T_i = TIME OF FLIGHT ALONG i^{th} RAY (MEASURED)

V_j = VELOCITY IN j^{th} CELL (UNKNOWN)

V_w = VELOCITY IN SURROUNDING MEDIUM (KNOWN)

HENCE, WE HAVE P = NM EQUATIONS WHERE N = TOTAL NUMBER OF RAYS AND M = NUMBER OF ANGLES, AND K UNKNOWNS a_j OR V_j. IF K = NM WE CAN SOLVE FOR THE UNKNOWN ATTENUATION OR VELOCITY COEFFICIENTS

Figure 6. Reconstruction of x-ray and ultrasonic tomogram.

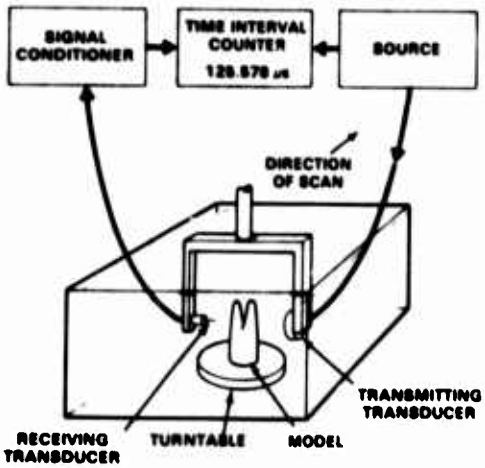


Figure 7. Experimental arrangement for obtaining time-of-flight profiles by through transmission. After each linear scan the model was rotated by 5°. A total of 19 scans were made for a total field of view of 90°. Time-of-flight measurements were made at 21 positions along the scan. Thus a total of 399 measurements were taken, and used to reconstruct 81 points yielding a system of equations having four-fold redundancy.

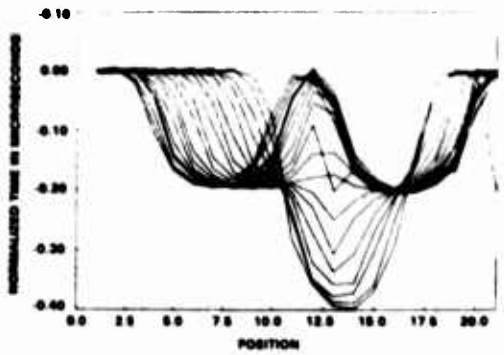


Figure 8. Plots of the time-of-flight profiles taken through the two-fingered glove model. Zero time-of-flight corresponds to the water path and negative times correspond to s-orter flight times. Minimum time occurs when the two fingers lie one behind the other resulting in maximum path through the faster liquid.

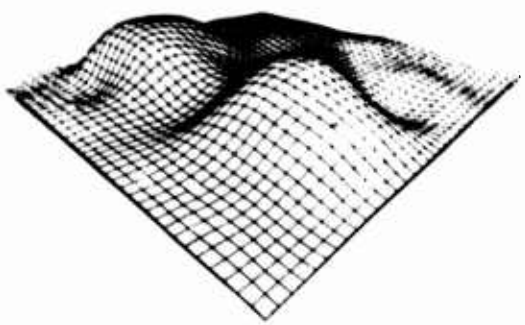


Figure 9. Reconstruction of velocity variation through the two-fingered glove model filled with a liquid whose velocity is 2% higher than that of the surrounding water. The reconstruction was done on a 9 x 9 grid and interpolated to a 40 x 40 grid.

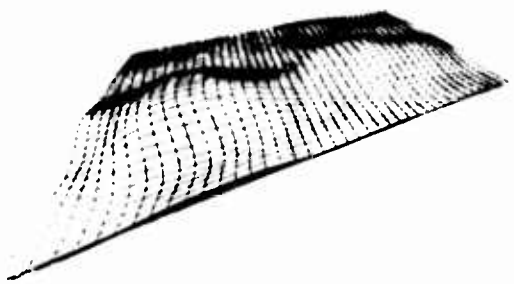


Figure 10. Reconstruction of velocity variation through the two-fingered glove model filled with a liquid who's velocity is 0.2% higher than that of the surrounding liquid.

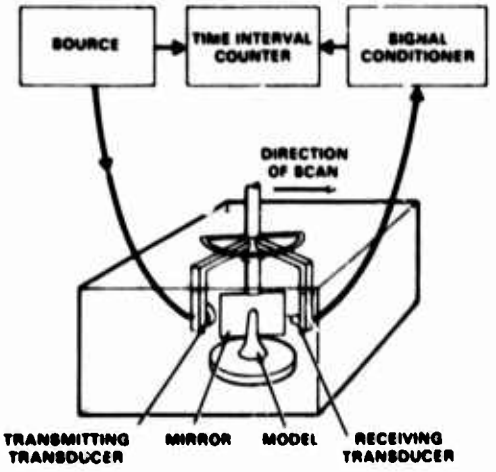


Figure 11. Experimental arrangement for obtaining time-of-flight profiles by reflection. After each linear scan the radial arms of the transducer holders were rotated 2.5° towards each other for a combined change of 5°. A total of 19 scans were made for a total field of view of 90°.

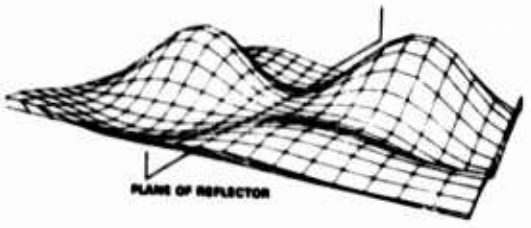


Figure 12. Reconstruction of velocity variation through the one-fingered glove model filled with a liquid who's velocity is 2% higher than that of the surrounding water. This reconstruction was done for the case where the data is taken by reflection, resulting in a mirror image.

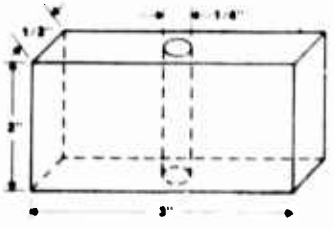


Figure 13. This is a steel model consisting of an oversized pin inserted into a hole. Both were fabricated from the same block of 1018 mild steel. The hole was 0.250 inches in diameter and the pin was 0.252 inches in diameter. The block was heated to 1000°C, the pin cooled in liquid nitrogen and then forced into the hole. The resulting compressive stress on the pin is estimated to be 108,000 psi.

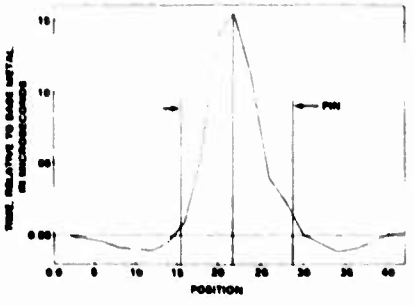


Figure 14. 0° profile through the steel model. Note the increased time-of-flight through the region containing the pin, and the decrease in the regions surrounding the pin.



Figure 15. Reconstruction of velocity variations in the steel model. Downward extension represents decreased velocity and, hence, compression. Note that in the surrounding block there is considerable tension stress. From the experimental calibration data we estimate average compressive stress in the pin to be 110,000 psi, maximum tension stress in the block to be 64,000 psi and maximum compression stress in the block to be 90,000 psi.

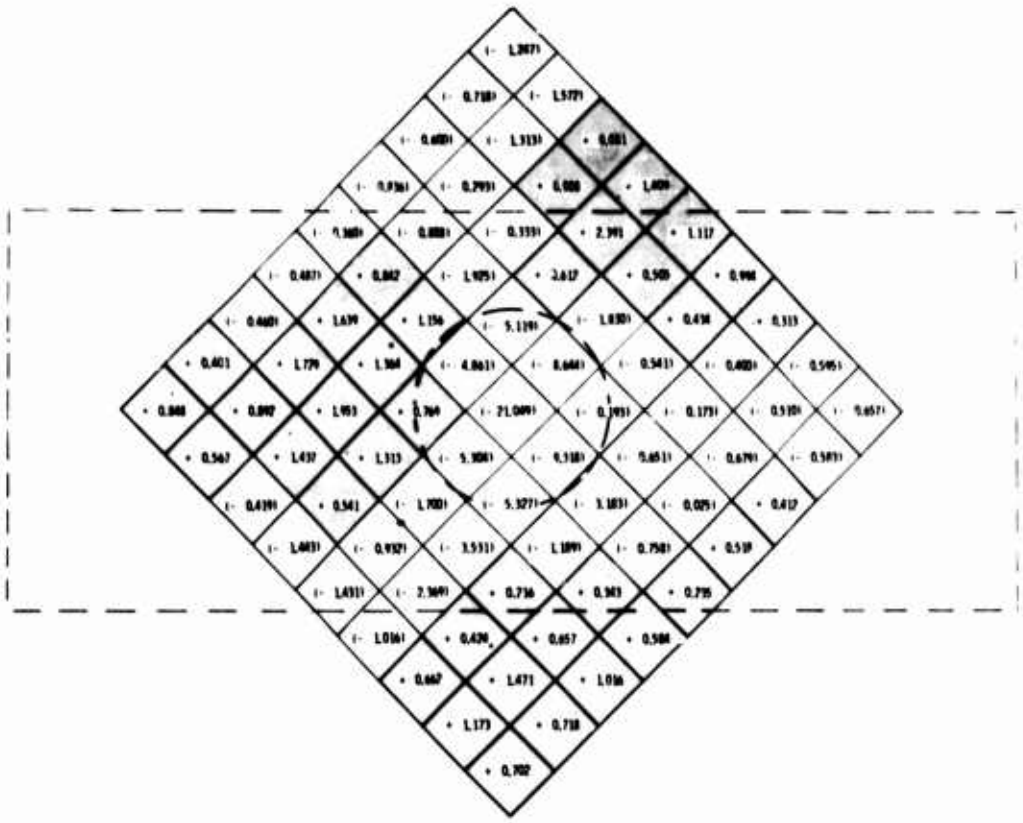


Figure 16. Numerical values for velocity changes in percent related to the geometry of the steel model. Shaded regions indicate velocity increase (tension) and white regions indicate velocity decrease (compression).

QUANTITATIVE ULTRASONIC TOMOGRAPHIC IMAGING

J. D. Young and F. L. Lederman
General Electric Research and Development Center
Schenectady, N.Y.

ABSTRACT

An ultrasonic transmission technique is described which images the velocity variation within metal parts. The arrival time of the first ultrasonic pulse to traverse the object is detected and displayed as a gray scale on a cathode ray tube while the part is being scanned horizontally and vertically. The velocity variation imaged within several cast turbine parts will be shown. The system can detect voids as small as 0.020 inch. With a more complex computer program and knowing the dimensions of the part, tomographic reconstruction of the velocity variation within parts with curved surfaces should be possible.

Introduction

In casted or pressed metal parts, it is desirable to achieve theoretical density without voids or microporosity. Voids, if large enough, can be detected by standard NDT techniques but microporosity may go undetected especially when it extends over a sizeable volume within the part. Ultrasonic velocity variations have been correlated with microporosity[1], but accurate velocity measurements have remained a laboratory procedure.

This paper describes an ultrasonic time of flight (TOF) system to accurately measure the velocity along a line through the part and displays the velocity variations as gray scale on a cathode ray tube. The accuracy of the velocity measurement is about 0.1% and our present display resolution capability is about 0.8 mm. If two orthogonal views are taken through the part, the location of the low velocity areas can be determined by scaling each view.

This TOF velocity profile imager was adapted for NDT from an ultrasonic breast scanner conceived by G. H. Glover[2].

System

A block diagram of the TOF velocity measuring system is shown in Fig. 1. The two 5 MHz transducers are mounted coaxially and spaced a fixed distance apart. Both transducer faces are restricted to form a small diameter pencil beam. Since the distance between transducers is fixed, the arrival time of the first ultrasonic pulse is a measure of the propagation velocity in the medium between the transducers. The arrival time is measured by making the width of a constant amplitude gate proportional to the TOF. A delay trigger from the repetition rate generator starts the gate and the threshold detector stops the gate. All later arriving ultrasonic pulses are ignored. The average value of this variable width gate is read on an analog meter and converted to a digital signal for tape recording and later transferred to the computer program file.

If a metal part is placed in the water tank between the two transducers, the average propagation velocity is increased, the arrival time is decreased and analog signal is reduced. Any velocity variation within the metal part will be recorded as a deviation from the composite water-metal average propagation velocity. The computer program simply expands any selected velocity window into 64 levels of gray and displays the results as intensity variations on a cathode ray tube.

The system can be calibrated by measuring the TOF with and without a sample of known thickness and velocity. The analog output meter reads ± 2000 counts; thus, the difference in counts can be read and, knowing the TOF in the sample, the time scaling for the system can be determined. With our present systems, the amplifier gain and threshold detector are set so that one count equals 2 nanoseconds. The signal-to-noise of our system is sufficient to reproduce the readings to within 5 nanoseconds. Since the TOF of a 1 1/4" thick steel part is 5 μsec, a velocity resolution capability of 0.1% is feasible. The repetition rate of our system is chosen so that several ultrasonic pulses are detected at each scan position to enhance the signal-to-noise ratio.

The horizontal scan is done with a stepping motor which advances both transducers and a TOF reading is taken every .04" or 1 mm. After one horizontal line is scanned, the part is withdrawn 0.0385" from the water tank and the horizontal line scanned in reverse direction. Our beam diameter is larger than the individual vertical displacement so that we have some overlap on each horizontal scan. The computer program takes this scanning geometry and the TOF data and makes a velocity variation intensity picture with the correct orientation. The pixel size is 0.03" or 0.8 mm which gives a maximum picture size of 2.4" by 2.3" with our present computer program. Each picture contains 3660 TOF data points.

Results

Figure 2 is a composite ultrasonic gray scale velocity image of a HIP René 95 sample. The sample is 6" in diameter and 2 1/4" thick with parallel ground faces. The part was too large to scan and image in one picture so that it was scannned in four sections and put together as a composite picture. The irregular imaging of the edge is caused by acoustic refraction which makes the ultrasonic image larger than the true dimension of the part and backlash in the scanning lead screw. This sample was known to have low average density and our results show that there is a large low velocity area in the center of the sample and a low velocity striation in the

lower right hand section. The entire lower right hand section has low average velocity. The black area has 16.4% lower velocity than the white area which is enough to account for the low density of the sample. A similar sample which was pressed to theoretical density had no detectable velocity variations. Clearly this imaging technique can show the location of low velocity (density) areas inside HIP parts and perhaps lead to improved process control during the design phase of the part's manufacture.

This imaging technique also has good spatial resolution as shown by Fig. 3 for a cast stainless steel turbine blade section. Fig. 3a is a full size front surface photograph of the turbine blade section. The area shown is the same as that imaged in Fig. 3b being 1.5" wide by 2.3" high. Note the two 0.02" diameter holes spaced about 1.1" apart on the center line of the sample. The ultrasonic gray scale velocity image is shown in Fig. 3b. The acoustic edge refraction has been masked to indicate the true dimensions of the sample. Black is low velocity and the black/white ratio in this case is 4%. The one pixel high and two pixel wide black strips spaced 1.1" apart on the center line are the images of the two 0.02" diameter holes. The hole image is horizontally elongated due to diffraction from the small diameter hole projected on the back face which is 0.67" behind the holes and also due to the horizontal scan speed which is too fast for the A/D converter used in this system. The larger black low velocity areas are internal defects. Figure 3c is the side view ultrasonic image of the same sample. Using Fig. 3b and 3c the position of the defect areas can be located. Thus, the lower black areas of Fig. 3b are mostly located near the back of the part, the middle black areas of Fig. 3b extend through the entire depth, while the upper black areas of Fig. 3b are very near the front surface.

Figure 4 is a different set of TOF data showing an expanded front view of the defects in the cast turbine blade section. This data was taken without scanning over the edges of the front surface, thus, enhancing the internal structure. The top hole is imaged in the center of the view. Note the tenicle structure emanating from the large low velocity areas. The defects imaged by ultrasonic TOF in this cast turbine blade section have not been identified. They do not show up with standard x-ray examination. The sample is now being sectioned for detailed metallurgical examination and some microporosity has been discovered but the examination is not complete.

Tomographic Imaging

The ultrasonic TOF imaging discussed above required samples with parallel faces. To image the internal structure of samples with complex surfaces, tomographic imaging must be used.

By using ray-tracing techniques, the time-of-flight method can be extended to include corrections for refraction in metals. This can be important in two ways. Firstly, correcting for refraction at the water-metal interfaces can be used to account for curved surfaces for imaging of odd-shaped specimens. Secondly, images can be enhanced by correcting for refraction of sound at boundaries of different acoustic velocity within the specimen.

In order to accomplish ray-tracing in odd-shaped metallic specimens, it is necessary either to have prior knowledge of the shape of the part (usually known) or to use a hardware scanning device which can follow surface contours (such as a state-of-the-art eddy current probe). Then the angles of the specimen boundaries can be determined. Finally, a small microprocessor and a simple algorithm can account for the odd shape of the specimen by reconstructing the path of the sound wave, and the velocity profile can be displayed with suitable gray scale. (See Fig. 5.)

Production of accurate time-of-flight profiles is the first step towards a full tomographic reconstruction. Tomography requires that many profiles or "projections" of the ultrasonic velocity be measured at different viewing angles. Then the ensemble of data is used by a minicomputer to reconstruct the image. The acoustic absorption can also be reconstructed using this technique without any major additions to the scanning hardware.

It is considerably more difficult to reconstruct quantitative images from ultrasound data measured in the reflective mode. However, this mode is desirable, because it has the advantage of one-port viewing. Only one transducer may be necessary, and it is possible to image specimens with obstructions that prevent imaging in the transmissive mode (such as very large specimens). The quantity to be imaged is generally either the acoustic impedance or the attenuation. For smaller specimens, reflective and transmissive techniques may be combined to provide more complete information about the material.

In the reflective mode, it is necessary to collect and analyze complete echo traces. Then these traces are converted into projections of the acoustic impedance or attenuation for input to the tomographic reconstruction programs. Another advantage of such an approach is that it provides the opportunity to obtain quantitative images of specimens where specular reflections are important. This can be accomplished in some specimens by using a deconvolutional procedure and a mapping algorithm.

Conclusion

A transmissive ultrasonic TOF quantitative velocity measuring system has been shown to image the internal structure of parallel face metal samples with good velocity and spacial resolution. The internal defects are probably density variations (microporosity) but their positive identification is not complete. Using a more complex computer program and the known dimensions of the sample, it should be possible to correct for variation in sample thickness and the effects of edge refraction to image the internal structure of samples with complex surfaces, tomographic reconstruction techniques must be used possibly with a contour following mechanism and wide angle receiving transducers or arrays. Tomographic reconstruction techniques open the possibility of imaging the sample using the measured values of velocity, impedance or attenuation in both the transmissive or reflective mode.

References

1. Krautkramer, J. and H., "Ultrasonic Testing of Materials," p. 97, Springer-Verlage, Berlin, (1969).

2 Glover, G. H., and Sharp, J. C. "Reconstruction of Ultrasound Propagation Speed Distributions in Soft Tissue: Time of Flight Tomography," IEEE Transactions of Sonics & Ultrasonics Vol. SU-24, p. 229 (1977).

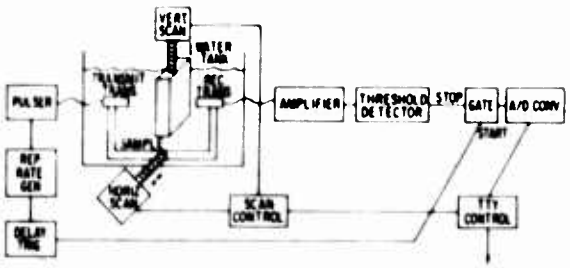


Figure 1. Block diagram of TOF velocity measuring system.



Figure 2. Composite ultrasonic gray scale velocity image of HiP Rene 95 sample. Black/white velocity ratio is 16.4%.



(a) (b) (c)

Figure 3. Cast turbine blade section. (a) Front surface photograph. Note the two 0.02" dia. holes on the center line. (b) Ultrasonic gray scale velocity image. Black is low velocity, white high velocity, B/W ratio 4%. The 0.02" dia. holes are clearly imaged. (c) Side view velocity image of same part.



Figure 4. Expanded front view of defects in cast turbine blade section. The top hole is imaged in the center of the view. Note the tenicle structure emanating from the large low velocity areas.

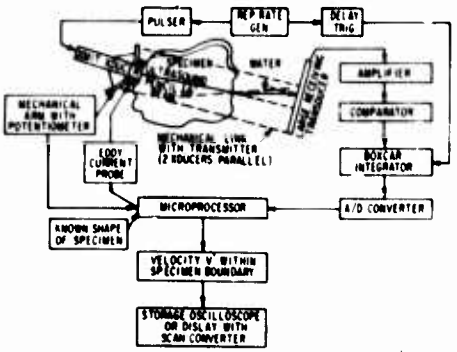


Figure 5. Block diagram of apparatus used for producing quantitative tomographic imaging in specimens of arbitrary shape.

ACOUSTIC IMAGING OF JOINED SURFACES

C. S. Tsai, S. K. Wang, and C. C. Lee
Center for the Joining of Materials

and

Department of Electrical Engineering
Carnegie-Mellon University
Pittsburgh, Pa. 15213

ABSTRACT

In this paper, the results of imaging experiments with the interfacial regions of representative solid material joints, using a transmission-type scanning acoustic microscope operating at 150 MHz, are reported. Voids and flaws in specially made joints as well as production-line silicon solder bonds (die bonded headers) have been detected using the transmission-mode of operation of the microscope. Acoustic velocity of epoxy in an organic adhesive bond has also been measured using a combination of transmission- and interference-mode of operation.

Introduction

The characteristics and strength of solid material joints, bonds, or composites are, to a large degree, influenced by the elastic properties of their interfacial regions such as stress distributions, microstructures, defects, voids, etc. It is thus desirable to visualize and ultimately characterize their interfacial regions using acoustic techniques[1]. A number of acoustic techniques capable of spatial resolution in the micron range have been developed in recent years[2-8], and some of them have been employed for the study of fracture and stress distribution in a single material[9,10]. We have employed a transmission-type scanning acoustic microscope[5] to image the interfacial regions of representative joints[11].

Key Components of the Transmission-Type Scanning Acoustic Microscope

The acoustic microscope consists essentially of an acoustic generator, two acoustic lenses, water cell, precision sample holder, mechanical scanning system, acoustic detector, signal processing electronics and storage CRT (Fig. 1). The acoustic waves are generated by a $LiNbO_3$ wafer transducer to which one end face of a sapphire rod is bonded. A spherical acoustic lens at the other end face of this rod allows the acoustic energy to be focused to a diffraction-limited spot. The focused acoustic beam is then reflected, refracted, scattered and attenuated at boundaries in the sample where variations in the elastic parameters occur. A second sapphire rod with an identical acoustic lens formed at one end face collects the transmitted acoustic energy. Another $LiNbO_3$ transducer bonded to the other end of this second sapphire rod converts the transmitted wave into an electrical signal which, after signal processing using a superheterodyne receiver, is fed to the CRT, resulting in an intensity-modulated image. By scanning the sample both laterally (in raster scan) and in depth, focused acoustic images for any cross section of the sample can be displayed on the CRT, and elastic inhomogenities in the sample mapped.

Figures 2 and 3 show, respectively, the photographs of the close-up and the whole set-up of the microscope.

Capabilities of the Acoustic Microscope

The key parameters of the acoustic microscope employed in this study are listed as follows:

- Spatial Resolution: 10 μm in water at 150 MHz
- Field of View for the Sample: 3x4 mm
- Magnification of Acoustic Images: 35
- Total Electrical Throughput Loss: 35 db
- Dynamic Range: 30 to 50 db at 1 mw (0dbm) input electric power, depending on the sample that has been examined
- Modes of Operation: Transmission mode and interference mode

The resolution capability of the microscope is demonstrated in the acoustic image of a 1000 mesh (25 μm periodicity and 10 μm thickness) copper grid which was inserted in the focal region of the acoustic beam in the water cell (see Fig. 4). Note that the bright areas correspond to larger transmission of acoustic energy and thus to the holes in the grid. Clearly, this microscope is capable of a spatial resolution of better than 10 μm in water at 150 MHz.

Acoustic Images of Solid Material Joints

A number of representative solid material joints, bonds, and composites have been examined using the transmission-mode and/or the interference-mode of operation. Some of the acoustic images that have been obtained are given in this paper. Additional acoustic images may be found in Ref. 11. Figures 5-7 and Fig. 8(a) show the acoustic images obtained using the transmission-mode of operation.

In the first specimen, a 400 mesh copper grid (2.5 mil periodicity and 1.75 mil thickness) was inserted between two brass sheets, each 2 mil thick, and glued into a composite using adhesive loctite 04L. The copper grid alone was first imaged and the resulting acoustic micrograph is shown in Fig. 5(a). Again, the bright areas correspond to the holes in the grid. A comparison of Fig. 5(a) with the optical image (not shown) indicates that the quality of the acoustic image is only slightly lower than that of the optical image. The acoustic micrograph for the composite is shown in Fig. 5(b). We see that some of the

bright areas have been lost, indicating that some debonding had occurred. We also note that the sizes of the bright areas are somewhat smaller than that of Fig. 5(a). This may possibly result from the imperfect contact at the edges of the holes and/or the effect of the adhesive through acoustic scattering. Thus, this particular specimen and the acoustic micrograph obtained serve to demonstrate that the acoustic microscope is capable of visualizing and detecting debonds of relatively thick joints/composites, consisting of both metallic and organic materials.

In the second specimen, a patch of epoxy was attached between two brass sheets, each 6 mil thick. In order to create a well defined variation in the thickness of the epoxy layer a fine metal wire was first laid at one end of the brass sheet to act as an uneven spacer before the epoxy has been applied. The acoustic micrograph obtained for the resulting bond is shown in Fig. 6. The dark dots in the image have been identified as resulting from the bonding flaws (in the form of air bubbles), and the fringe pattern as resulting from multiple acoustic reflections from the specimen. The first observation is confirmed by examination under an optical microscope after one of the brass sheets has been peeled off and the second observation is in agreement with the actual variation in the thickness of the epoxy layer as measured by a micrometer, namely, from 1.5 mils at one end to 4.5 mils at the other. Again, as in the first specimen, this particular bond and the acoustic micrograph obtained have clearly demonstrated the usefulness of the acoustic microscope for the inspection, identification and characterization of solid material bonds.

In the third specimen, a Motorola production-line die bonded header which consists of a 2.5x2.5 mm silicon wafer, Au-Sn solder and a copper plate as first polished to a suitable thickness from both end faces. The final thickness of the silicon wafer is 0.1 mm and that of the copper plate is 0.3 mm. The acoustic micrograph for the resulting bond is shown in Fig. 7. By scanning the specimen in depth it was found that the dark dots in the image reached the highest degree of focus as the focal region of the acoustic beam was brought to coincide with the solder region. Thus, it is concluded that the dark dots correspond to some voids in the bond. This particular bond and the acoustic micrograph obtained have clearly demonstrated that this acoustic microscope can be used to nondestructively observe voids in the semiconductor die bonds, one of the backbones of solid state electronics.

Note that the acoustic images shown in Figs. 4-7 were obtained using the transmission-mode of operation and, therefore, carry only amplitude information. However, phase information resulting from variations in the acoustic wave velocity and/or the thickness of the specimen is also important. For example, the strength of adhesive bonds have been shown to be closely related to the acoustic wave velocity of the adhesive[12]. We have employed a combination of the transmission-mode and the interference-mode of operation to measure the acoustic wave velocity of epoxy in a brass-epoxy-brass bond. In the interference-mode of operation the relative phase of the acoustic signals transmitted through the bond was obtained by comparing it with the phase of a reference electrical signal. Assuming that both brass plates are of uniform thickness and homogeneous in elastic parameters, we note that the relative phase of the transmitted acoustic signals is determined by the variation in the thickness of the epoxy layer and the acoustic velocities of both epoxy and water. Under this assumption, we see first that variation in the thickness of the epoxy layer is contained in the fringe pattern of the acoustic image obtained using the transmission-mode of operation. Next, the relative phase of the transmitted acoustic signals is contained in the fringe pattern of the acoustic image obtained using the interference-mode of operation. Thus, it is possible to deduce the acoustic wave velocity of the epoxy by counting the fringes in both acoustic images. The acoustic images obtained using the two modes of operation (for the same region of the brass-epoxy-brass bond) are shown in Fig. 8. By studying the fringe patterns in the acoustic images we have arrived at an acoustic wave velocity of 2.7×10^5 cm/sec for the epoxy in the bond. This measured value is in good agreement with the published data[12]. It is to be noted that spatial variation in the acoustic velocity may be determined by simply scanning the bond.

Conclusion

We have shown that the scanning acoustic microscope, operating in the transmission-mode of operation, is capable of detecting voids, flaws and defects in the interfacial regions of specially made joints/composites/bonds as well as production-line silicon solder bonds. We have also shown that the same microscope, when operating at a combination of transmission- and interference-mode of operation, can be used to measure the velocity of acoustic wave propagation in the bonding layer. Clearly, for each particular joint, bond or composite, more comprehensive study in which the individual parameter is independently controlled, is required to achieve a more detailed characterization.

Acknowledgements

We wish to thank Dr. E. Philofsky of Motorola for furnishing us the die bonded headers used in this study. Support from the Materials Research Laboratory Section, National Science Foundation, under Grant No. DMR72-03297-A03 is also gratefully acknowledged. S. K. Wang was also supported by an IBM Post Doctoral Fellowship.

References

1. See, for example, IEEE Trans. Sonics & Ultrasonics, Special Issue on Nondestructive Evaluation, SU-23, 283-374 (Sept 1976), Edited by D. O. Thompson.

2. L. W. Kessler, "Review of Progress and Applications in Acoustic Microscopy," (A) J. Acoust. Soc. Amer., 55, 909 (May 1974).

3. A. Korpel, L. W. Kessler, and P. R. Palermo, "An Acoustic Microscope Operating at 100 MHz," Nature, 232, 110 (1971).

4. B. A. Auld, R. J. Gilbert, K. Hyllested, C. G. Roberts, and D. C. Webb, "A 1.1 GHz Scanned Acoustic Microscope," Acoustical Holography, edited by G. Wade (Plenum, N.Y., 1972), 4, 73.

5. R. A. Lemons and C. F. Quate, "Acoustic Microscope-Scanning Version," Appl. Phys. Lett., 24, 163 (Feb. 1974).

6. R. A. Lemons and C. F. Quate, "Integrated Circuits as Viewed with an Acoustic Microscope," Appl. Phys. Lett., 25, 251 (Sept. 1974).

7. W. L. Bond, C. C. Cutler, R. A. Lemons, and C. F. Quate, "Dark-field and Stereo Viewing with the Acoustic Microscope," Appl. Phys. Lett., 27, 270 (Sept. 1975).

8. R. Kompfner and R. A. Lemons, "Nonlinear Acoustic Microscopy," Appl. Phys. Lett., 28, 295 (March 1976).

9. A. Madeyski and L. W. Kessler, "Initial Experiments in the Application of Acoustic Microscopy to the Characterization of Steel and to the Study of Fracture Phenomena," IEEE Trans. Sonics & Ultrasonics, SU-23, 373 (Sept. 1976).

10. J. Souquet and G. S. Kino, "Acoustic Phase Technique for Measuring Stress Region in Materials," 1976 Ultrasonics Symposium Proceedings, IEEE Cat. #76 CH1120-5SU, 582

11. C. S. Tsai, S. K. Wang, and C. C. Lee, "Visualization of Solid Material Joints Using a Transmission-Type Scanning Acoustic Microscope," to appear in Appl. Phys. Lett., (Aug. 1977).

12. G. A. Alers, P. L. Flynn, and M. J. Buckley, "Ultrasonic Techniques for Measuring the Strength of Adhesive Bonds," Materials Evaluation, 35, No. 4, 77-84 (April 1977).

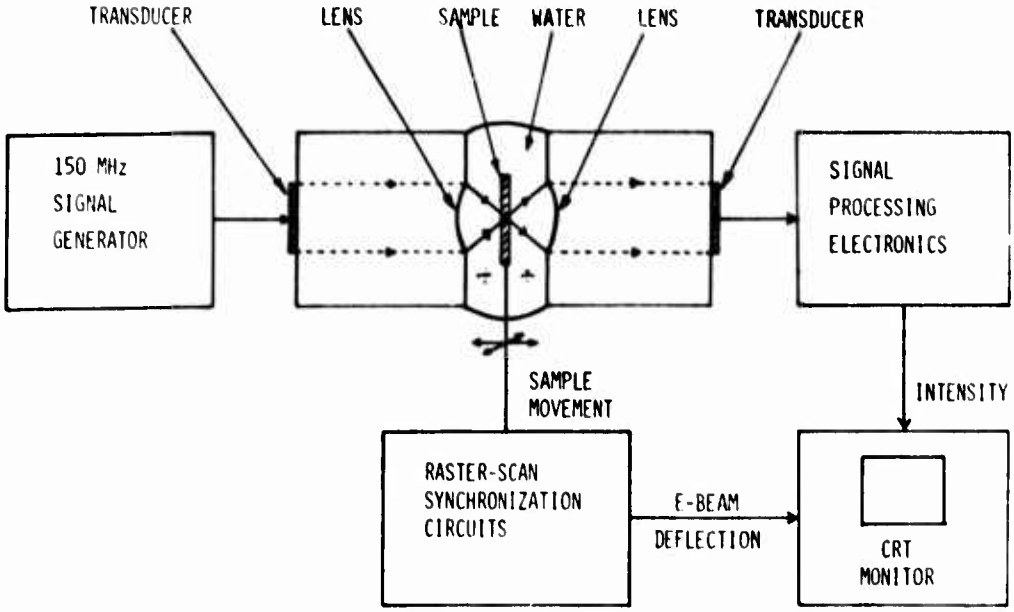


Figure 1. Block diagram.



Figure 2. Photograph of the acoustic microscope (the close-up).



Figure 3. Photograph of the acoustic microscope (the whole setup).

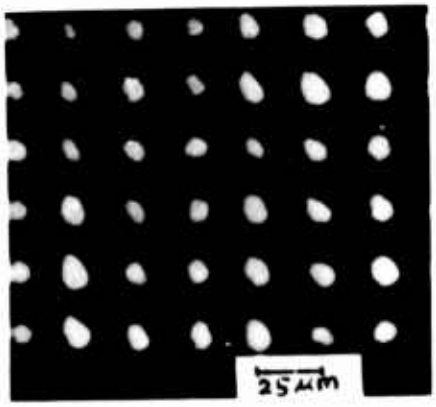


Figure 4. Acoustic image of a 1000-mesh copper grid (25 μm periodicity and 10 μm thickness).

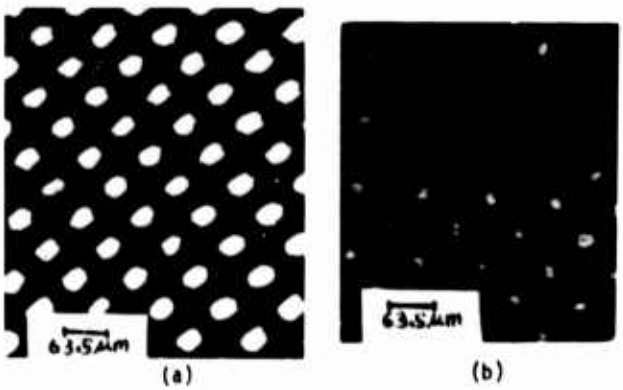


Figure 5. (a) Acoustic image of a 400-mesh copper grid (62.5 μm periodicity and 44 μm thickness). (b) Acoustic image of a brass-copper grid-adhesive-brass joint (the copper grid is that of (a), thickness of each brass sheet is 2 mils).



Figure 6. Acoustic image of a brass-epoxy-brass joint (thickness of each brass sheet is 6 mils, thickness of epoxy layer varies from 1.5 mils at one end to 4.5 mils at the other).

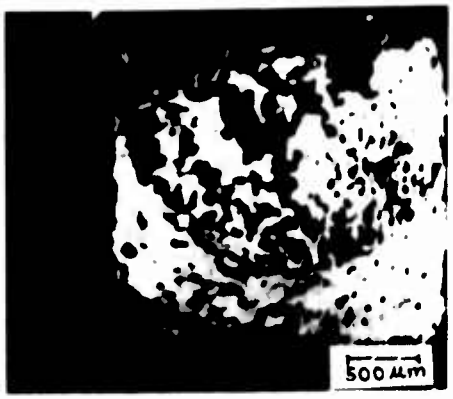


Figure 7. Acoustic images of solder bonds of silicon on copper. (Motorola production-line die bonded headers. The solder is Au-Sn preform; silicon dimensions are 2.5 x 2.5 x 0.1 mm; copper header is 0.3 mm thick).

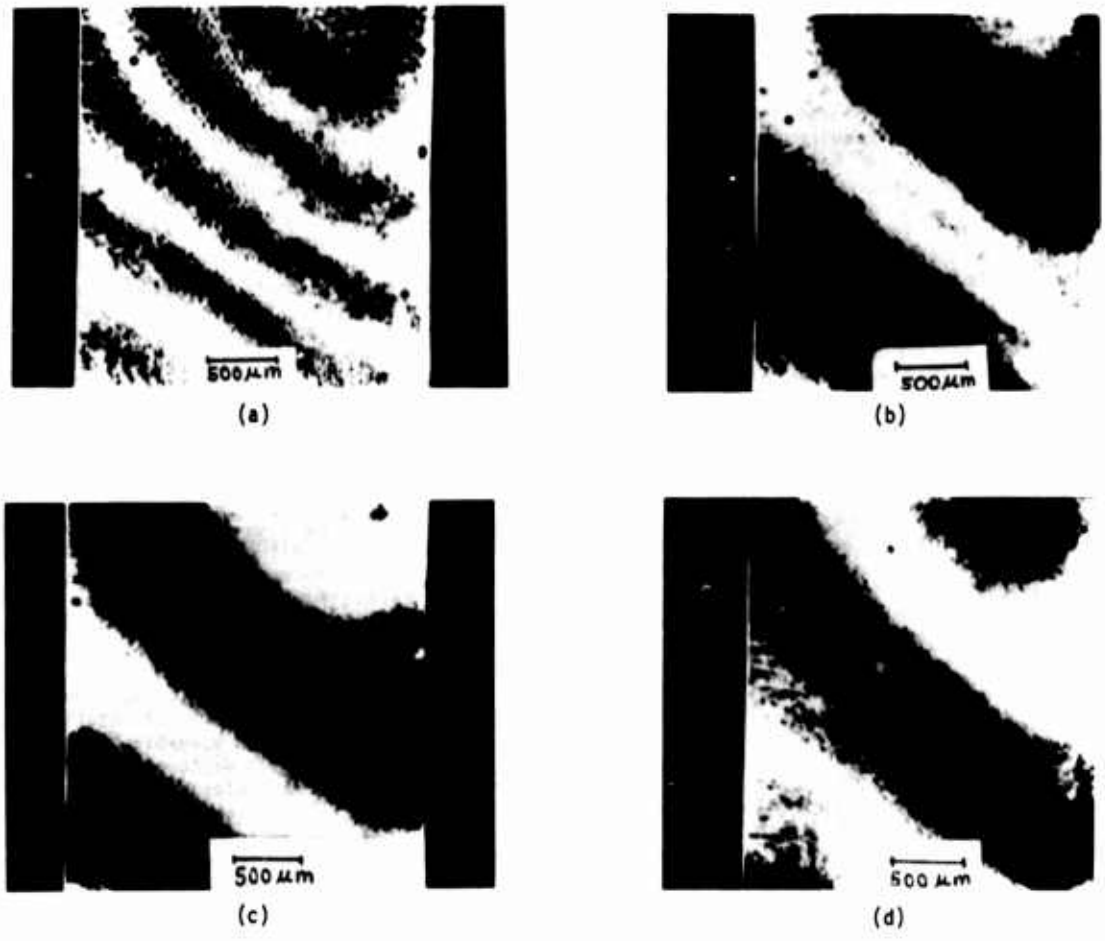


Figure 8. Acoustic images of brass-epoxy-brass bond (thickness of each brass sheet is 4 mils and that of epoxy layer is 1.0 mil).

(a) Acoustic image obtained using transmission-mode of operation.
(b) Acoustic image obtained using interference-mode of operation.
(c) Same as in (b), but with a change in phase reference by 90°.
(d) Same as in (b), but with a change in phase reference by 180°.

ULTRASONIC INSPECTION OF NEAR NET SHAPE DISKS

J. E. Doherty and J. M. LaGrotta
Pratt & Whitney Aircraft
Middletown, Connecticut 06547

ABSTRACT

With new fabrication technologies, disks for gas turbine engines can be manufactured from high strength materials with a substantial cost savings. Utilization of these technologies to their full potential is currently limited by the ability to perform a reliable high resolution, high sensitivity ultrasonic inspection. A computer automated inspection system is being developed to inspect near-net shape disks made by the new forming processes. The inspection system utilizes high resolution instrumentation and adaptive contour following techniques to detect small indications, such as those of concern in high strength powder alloys. The use life of components can be predicted from fracture mechanics principles if quantitative information about the type, size, shape, and orientations is known. The near-net shape disk inspection system has been configured to collect data necessary to use the new quantitative defect analysis techniques now being developed. The integration of advanced analysis methods into an automated ultrasonic inspection system will set the stage for an early application of quantitative life predictive schemes.

Introduction

In conventional practice, the forging weight of disks for gas turbine engine is considerably in excess of finished part requirements. Fabrication techniques such as HIP and Gatorizing® (isothermal forging) are currently being developed to permit the manufacture of disk preforms very close to their final shapes. These near-net shape techniques will permit considerable cost savings over the current techniques by reducing material input and machining requirements. (See Fig. 1.)

In current practice, the shape of a disk preform is constrained by ultrasonic inspection requirements. For example, to assure maximum ultrasonic inspection sensitivity, it is necessary to maintain the ultrasonic inspection beam normal to the surface of the component being inspected and, therefore, it is usually required that the "sonic" shapes needed for inspection have rectilinear surfaces. In addition, sonic shapes must have 0.125 to 0.250 inch overstock beyond the finished shape if complete inspectability is to be assured, since current ultrasonic instrumentation has poor sensitivity for defects near surfaces. If the low cost benefits of the new near-net shape processing are to be fully realized, the shape limitations of ultrasonic inspection must be eliminated. (See Fig. 2.)

The ultrasonic inspection of near-net shape disks will require an ultrasonic inspection system that can contour follow the inspection surface and maintain the inspection beam normal to the inspection surface by automatically correcting for the small changes in surface orientation associated with disk manufacturing tolerance. In addition, the inspection system must have improved near-surface resolution if overstock requirements are to be minimized. An ultrasonic inspection system for near net turbine disk shapes is currently under development at Pratt & Whitney Aircraft with Air Force support.

Inspection System Overview

The ultrasonic inspection system being developed for near-net shapes is an automatic inspection system controlled by a PDP 11/40 minicomputer, Fig. 3. Figure 4 is a schematic representation of the automatic contour following inspection system developed for the inspection of near-net shape turbine disks. This system is capable of sensing the contour of a disk and, with the aid of a limited preknowledge of the nominal near-net shape; it automatically follows the near-net shape disk geometry, keeping the appropriate separation and inspection angle. For special problem areas, the system can be entirely controlled by the computer. The system design provides for two transducer manipulators for greater flexibility in performing disk inspection and for conducting defect analysis. The manipulators are mounted on a turntable which is capable of 350° of rotation. This articulation is provided to permit collection of ultrasonic scattering data necessary to make quantitative defect characterization possible. The system has been constructed using close mechanical tolerances; all linear axes are ±0.1".

The primary contour-following transducer is located on the turntable axis of rotation. The secondary manipulator is moveable and can be made to stand off a variable distance from the primary manipulator. The manipulators have three degrees of freedom: vertical displacement, rotation and a gimbal movement. All three degrees of freedom are under direct computer control. Normalization of the contour-following transducer to the surface under inspection is controlled by the computer by sensing and maximizing the front face reflection. Normalcy can be maintained to within 0.5°; this is sufficient for good inspection sensitivity. The maximum scan speed that the system can operate at is determined by the variation in surface orientation, i.e., preform manufacturing tolerance, and by the rate at which the transducers can be

articulated. Currently, the system can scan the inspection surface at 4 in/sec if preform surface variations average 0.045 inch per inch; this is fast enough to give a fourfold improvement in inspection time over current methods using sonic shapes with machined surfaces. New advanced computer interfaced ultrasonic instrumentation and transducers have been developed to improve inspection sensitivity and near surface resolution. Some special features have been developed into the inspection system to assure a low cost and well controlled manufacturing process for near-net shape disks. These features extend the inspection systems capabilities to provide a direct link to computer aided machining (CAM) and to fabrication process control.

Computer Aided Dimension Inspection and CAM

The computer is becoming a key tool for improving manufacturing methods to reduce manufacturing costs. The advent of near-net shape forming philosophy offers an opportunity for further CAM innovations. Two new problems which must be addressed with near-net shape components are: dimensional inspection to determine whether the final desired disk shape can be machined from the disk preform, and the precision setup required for machining the preform to the final shape. These two tasks are easily performed manually when the generous overstock allowances of conventional practice are available; however, these tasks can be more difficult and more expensive when overstock allowance is reduced to 0.05 inch for near-net shapes unless computer aided approaches are adapted.

A primary feature of the near-net shape inspection system under development is that it follows the contour of the part under inspection with little or no pre-knowledge of the shape. In following the contour, the ultrasonic inspection system is producing information which can be used to determine the exact shape of the part being inspected. If this information is collected and stored, it can be used at a later time to define the preform shape. The measured shape can be then compared to an ideal shape to assess whether or not it is within tolerance and at the same time index points can be set to fix the preform on the turning machine for optimum metal removal.

The computer aided dimension inspection is done using a three-dimensional graphics display system which can present an isometric drawing made up of a collection of points and/or lines. With this system an operator can rotate, translate, tilt and enlarge the image of the object being displayed by simply turning controls, Fig. 5; all the while, the display system maintains the proper relationship between the group of points and/or lines which describe the object.

The three-dimensional shape data collected by the near-net shape inspection system is input into and displayed by the three-dimensional graphics system along with the final part shape. To avoid confusion, the system only allows the operator to see one dimetrical cross section at a time although the full three-dimensional image is stored within the machine. The operator simply translates, rotates and tilts, Fig. 6, until he arrives at the best fit of the final shape within the near-net shape preform. The fitting operation is done interactively on orthogonal cross sections similar to the method one might use in a mechanical setup. The display system has the capability for continuously rotating both shapes so that all cross sections can be evaluated.

When the operator is satisfied that an optimum fit has been made, the dimension inspection is completed on an IBM 370 computer which calculates and evaluates the closeness of the two shapes at all points. This is done to make sure that the human operator has not missed a low overstock area. Index set points to aid in setting the preform on the turning machine are also calculated by the 370 computer. With these set points the tedious and costly task of turning machine fixturing is eliminated.

The CAM inputs from the near net shape inspection system can reduce turbine disk procurement cost by automatically checking dimensions, minimizing setup time, reduce scrapping of parts due to improper indexing, and locating defects in areas which can be machined away.

Fabrication Progress Control

One of the most effective ways to assure that a fabrication process produces high quality components is to institute detailed methods of process control. Traditionally, information such as rejection rate at various inspection steps have been used to give an indication of how well a particular process was functioning. With the advent of computerized inspection, there are new opportunities for improved process control. With a computerized inspection system, large amounts of detailed inspection information can be collected and used to give an insight into the state of the fabrication process. This data can be used to give a precursor warning that component quality is declining long before actual rejections occur. Special features have been developed into the near-net shape inspection system to provide process control information for the material-consolidation process and the shape-forming process.

The ultrasonic response of a material is intimately related to the quality and internal structure of the material. Conventionally, the judgment of whether a material is acceptable is based on the absence of ultrasonic signals above a critical value. If rejection rates are low, there is little information available to evaluate whether or not the fabrication process is slowly changing. Things are different with a computerized inspection system, the presence of all indications, both above and below the critical level, can be recorded because of the speed and storage capacity of the computer. This data can be used to give an indication of the current status of the process because the large number of ultrasonic responses by the computerized inspection system that can be recorded permit statistical approaches to be used.

Figure 7 is a C-scan presentation of all indications found above the noise level on the inspection of a turbine disk. Figure 8 shows how this data can be ordered into distributions showing the number of indications with size or number of indications with location. On the average, these distributions will remain constant from part to part as long as no process change occurs. For example, if grain size, inclusion count were to

change, a corresponding change would occur in the number vs. indication size distribution. A change in the spatial distribution (e.g., the large density of indications at small radii in Fig. 8) might indicate the preferential formation of small forging defects in specific locations. The appearance of changes in the distribution of ultrasonic indications is a precursor warning that the process has changed, and if corrections are not made, there is increased likelihood of the occurrence of a rejectable indication. This same type of process control analysis has been developed for the CAM portion of the inspection system. In this case, the variation in the shape of the preform due to die wear and other shape process variables is monitored. Figure 9 is a schematic example of how this information would appear. The figure shows that there is a high variation in the average thickness at small radii and that the thickness in this region is above the expected value. This is one type of behavior which may be a manifestation of poor die closure.

The integration of process control features into the near-net shape inspection system will add to the advantages of near-net fabrication techniques for disks.

Conclusion

The development of computerized high resolution contour following ultrasonic inspection will yield a significant reduction in the cost of manufacturing turbine disks by permitting the use of near-net shape fabrication techniques. In addition, special features developed into the inspection system will permit further cost reductions by permitting the use of advanced computer added manufacturing and process control techniques.

Acknowledgements

This program is being supported by AFML Contract No. F33615-75-5193 entitled "Production Inspection of Near-Net Turbine Disk Shapes." The development of an inspection system to inspect near-net shape turbine disks is a major technical effort and, therefore, dependent on the contributions of many people. We would like to acknowledge the contributions of W. F. Adams, Jr., J. Becker, J. Bell, C. Fetheroff, J. S. Kunselman, T. Igielski, D. Johnson, I. M. Matay, R. H. McDaniel, A. R. Robinson, T. C. Walker, J. R. Williamson and B. G. W. Yee.

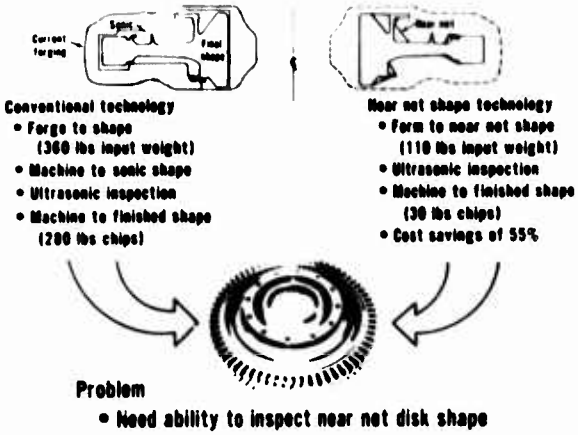


Figure 1. Manufacturing near net shape turbine disk for reduced cost.

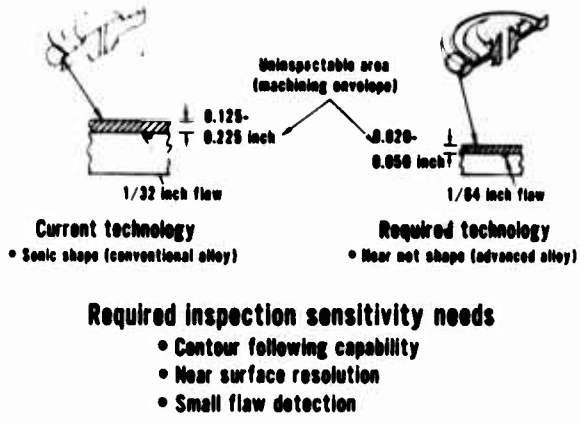


Figure 2. Production inspection requirements.



Figure 3. Near-net shapes inspection system.

Figure 4. Schematic diagram of the contour-following system.



Figure 5. Three-dimensional graphics display system.

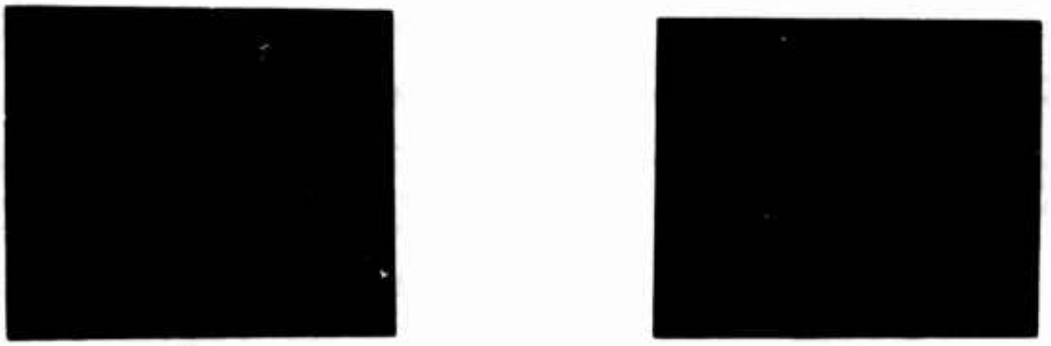


Figure 6. Photograph of three-dimensional graphic display screen.

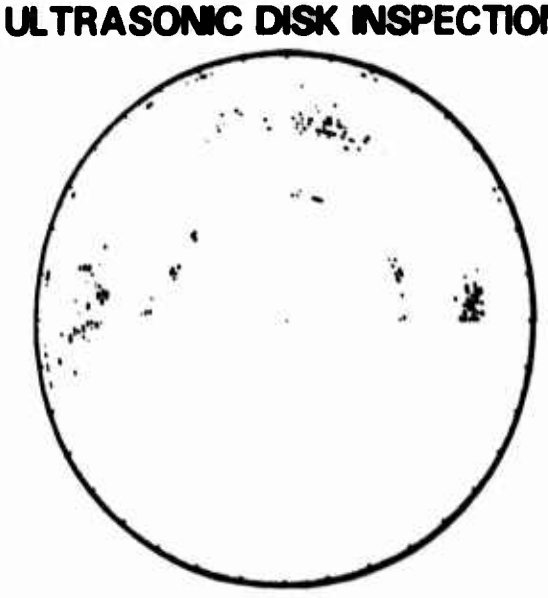


Figure 7. C-Scan presentation of ultrasonic data.

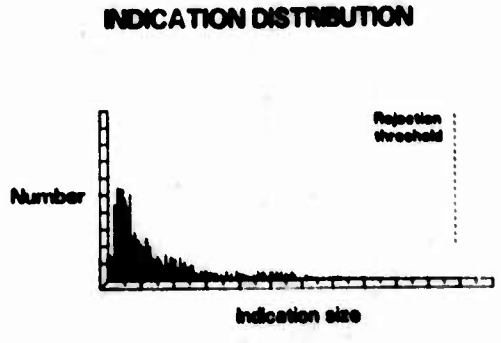


Figure 8. Indication distribution for ultrasonic data.

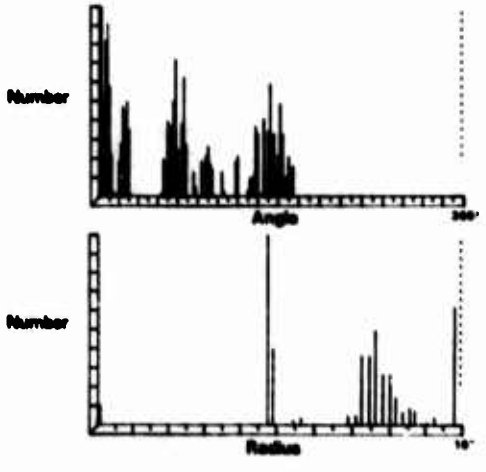


Figure 9. Indication distributions for ultrasonic data.

A PHASE INSENSITIVE ULTRASONIC RECEIVER

Joseph S. Heyman
NASA Langley Research Center
Laboratory for Ultrasonics
Hampton, Virginia 23665

ABSTRACT

Ultrasonic measurements of materials are usually obtained from an electrical conversion of an acoustic signal by a transducer. In this paper, a conventional (phase sensitive) transducer and a new phase insensitive acoustoelectric converter called an AEC are contrasted. In particular, the AEC is shown to exhibit superior characteristics for many typical experiments and appears to have many applications in the Nondestructive Evaluation (NDE) area.

Introduction

Transducers that are commonly used in ultrasonics are based on piezoelectric or magnetostrictive conversion of electrical energy into mechanical energy. Major advances in the state of the art of transduction have lead to electromagnetic and electrostatic devices which, although less efficient, have many beneficial attributes. One aspect these devices have in common is that they are phase sensitive. The significance of phase sensitivity is not apparent for laboratory studies on flat, parallel and homogeneous samples or for transducer diameters $d < \lambda$, the acoustic wavelength. But for the case where $d > \lambda$ (megahertz frequencies with conventional transducer geometries) and the "world" of study is not flat or parallel or homogeneous (NDE) phase sensitivity can be a real drawback.

In this paper, the problems of phase sensitivity are discussed and a new phase insensitive transducer called an Acoustoelectric Converter (AEC) is described. Data obtained with conventional and AEC transducers are contrasted for simple pulse-echo samples as well as for modified "C" scans of phantom flaws in metal as well as composite materials. The data indicate superior characteristics of the AEC for situations of phase complexity commonly found in a NDE environment.

The Importance of Phase in Ultrasonic Measurements

Recent papers have indicated the important effect phase can have in ultrasonic measurements of material properties.[1-4] In addition, measurements of non-parallel samples relate difficulty in determining real parameters in complex geometries causing a degradation of pulse echo data[5,6] as well as continuous wave line shapes.[7] Phase is important for some measurements, especially interferometric experiments where the velocity or thickness of material is significant and sample geometry can be controlled. However, for flaw detection in irregular shaped objects (or irregular shaped flaws) one must be careful in data interpretation.

Many NDE ultrasonic measurements of materials are obtained in a test setup such as shown in Fig. 1. A source of ultrasound is shown generating a propagating wave front through a material to an ultrasonic detector. Many variations of this geometry are possible including focusing, reflection detectors (using the source as the detector) and a complex combination of signal processing from simple gating and filtering to advanced computer analysis. But all techniques require a conversion from acoustic energy to an electrical signal. Figure 1 shows an idealized phase shifted wave emerging from the sample and results in a null signal out of a piezoelectric transducer. The incident energy to the detector is not zero - but the superposition of phases causes a zero output.

This problem is more clearly shown in the sequence of Figs. 2-4. Figure 2 shows two acoustic waves incident on a piezoelectric detector. The electrical output is the superposition of two waves. Since the waves are in phase, the resulting output is large. Figure 3, on the other hand, shows two waves entering out of phase so that the resulting output is decreased by the superposition. Two waves of slightly different frequency are shown in Fig. 4 with the resulting electrical signal severely modulated. The apparent effect of phase sensitivity is to produce a complex signal which may be difficult to interpret.

On the other hand, Fig. 5 shows the output of an ideal power detector to the three cases of in phase, out of phase, and frequency shifted incident acoustic waves. Since the power is equal in each case, the detector output is invariant. Thus, such a detector would result in an easily interpreted signal leading to higher resolution measurements of a material's attenuation.

Theory

A detailed account of the AEC has been submitted to JASA.[8] Therefore, only a brief review of the device will be presented here.

There are two mechanisms which determine the operation of the AEC. The first is related to theory developed by Hutson and White[9] to explain phonon-charge carrier coupling in piezoelectric semiconductors. Theory shows that the acoustic absorption α at a frequency ω due to free charge carriers in a material of conductivity σ can be expressed as:

$$\alpha = \frac{\omega}{D} \frac{\omega_c/\omega}{1 + (\omega_c/\omega)^2} \qquad (1)$$

where D is a material constant, $\omega_c = \sigma/\epsilon$ (ϵ is the material permativity). Therefore, acoustic energy is lost to the charge carriers.

The second mechanism is related to the Weinreich[10] relation which may be expressed as:

$$E_{ae} = \frac{\phi}{v} \frac{\mu}{\sigma} \alpha \qquad (2)$$

where ϕ is acoustic flux, v is the acoustic velocity and μ the mobility. This relationship predicts an electric field E_{ae} to accompany any mechanism which absorbs acoustic energy via free charge carriers. The electric field integrated through the AEC is the output of the device.

The first use of the acoustoelectric effect as a phase insensitive device is reported in Reference 11 by Southgate. Current work on the device at NASA Langley Research Center is focused on NDE while work at Washington University (J. G. Miller) is focused on medical applications.

AEC Characteristics

The directivity (measured with incident "plane" waves) of an AEC is related to its phase insensitivity and, therefore, is a good "yardstick" for comparison with conventional transducers. Therefore, an AEC was fabricated and compared to a piezoelectric transducer in a variable geometry water cell shown in Fig. 6. A conventional phase sensitive transducer was used to generate acoustic pulses as well as to receive the acoustic pulses after they reflected off the AEC face. A laser was used to measure the small angle through which the system rotated. The data obtained from these measurements is shown in Fig. 7. Since the phase sensitive device was used in reflection mode and, therefore, had energy incident at twice the rotated angle, the two transmission curves are the ones to be compared. The structure in the conventional transducer directivity curve is a result of phase modulation.

Another way of looking at the directivity using the water cell of Fig. 6 is to observe a pulse echo decay as a function of angle. This is shown in Fig. 8 for angles 0 degrees through 7 degrees. In each case, the upper trace is the AEC compared to a fixed electronically-generated expoenential while the lower trace is a conventional transducer compared to a fixed electronically-generated exponential. Note how rapidly the phase sensitive detector signal degrades with increasing nonparallelism while the AEC signal remains relatively constant. At 0.3 degrees the signal from the conventional device is almost 50 percent down from the parallel condition. No notcieable change is apparent at that angle for the AEC.

The last of the pulse echo pictures represents a nonparallelism of 7 degrees. The AEC response has dropped by about 50 percent. The piezoelectric detector response shows a larger second echo than the first due to phase superposition.

AEC Application

A scanning ultrasonic arrangement similar to the one shown in Fig. 1 was used to compare an AEC receiver to a conventional damped transducer receiver. Several test plates were examined containing phantom flaws. In each case identical conditions were set up with the exception of the receiver used.

The first item scanned is shown in Fig. 9 and is a resolution test plate for ultrasonics. It contains flat-bottomed grooves and holes of various depths with the smallest hole being 1/64th-inch in diameter. Figure 10 is a transmission ultrasonic scan with both traces obtained from a conventional highly damped piezoelectric transducer. The upper trace ued a "long" pulse echo excitation technique (narrow bandwidth) while the lower trace used a "short" pulse echo excitation technique (broadband). Both traces show the large grooves but the small holes are almost obscured. Figure 11 is identical to the top trace in Fig. 10 ("long" pulse echo excitation) but obtained with the AEC. Plate resonances are observable in two of the grooves whose thicknesses equalled an integer times $\lambda/2$. The small holes are clearly visible with a "clean" background and a superior image.

Figure 12 is a photograph of an angled slot resolution plate with three groups of four milled slots. The milling widths are 1/4 inch, 1/8 inch, and 1/16 inch. From the top of the plate down, the milling angles correspond to a depth difference along the slot of 2λ, λ, 0 and $\lambda/2$, respectively. Therefore, the top slot should contain four regions of resonance, the second two, the third none, and the last, one. As before, Fig. 13 was obtained with a conventional transducer. Although the slots are visible and resonances apparent, the complex structure is obscured. However, replacing the receiver with an AEC produced the picture shown in Fig. 14 which is quite clear shows a smooth entrance into the slots and clearly shows resonance conditions. The background signal is free of noise compared to the conventional transducer figure.

The last sample examined shown in Fig. 15 is an epoxy-graphite composite, a small region of which is internally bonded to a 0.002-inch thick Mylar film. The film acts as a "non-bond" region and shows up clearly in the ultrasounic pictures. Figure 16 shows the conventional transducer image of the composite structure. The background variation indicates considerable structure which most likely is caused by phase modulation. Actual variations in material properties leading to changes in attenuation are difficult to interpret. However, the composite plate as viewed by the AEC shown in Fig. 17 is more uniform. Recalling the directivity plot, the AEC is a "better" picture of the variability of the material. Since the AEC can be calibrated directly for attenuation, absolute measurements are possible thereby indicating more reliable information about the composite structure.

Conclusions

Although phase information can play an important role in some ultrasonic measurements, there are many situations where the phase superposition with amplitude superposition lead to data misinterpretation. The reason for this deficiency is the phase sensitive nature of conventional transducers. When the transducer diameter is larger than the acoustic wavelength, phase modulation can dominate the signal.

A new type of transducer has been developed which we call an Acoustoelectric Converter (AEC) and appears to have application to NDE. Since the AEC is almost a power detector, it is nearly phase insensitive with an output comparable to the sum of the "squares" of a conventional microarray. This provides a resolution enhancement, a high power enhancement and a low power loss. The net result of the AEC is to mow down the "grass" associated with conventional transducers with a on-parameter (attenuation) measurement.

Acknowledgement

The author wishes to thank Dr. John Contrell for many helpful discussions concerning this paper.

References

1. J. G. Miller, J. S. Heyman, A. N. Weiss, and D. E. Yuhas: "A Power Sensitive Detector for Echocardiography and Other Medical Ultrasonic Applications," presented at the American Institute of Ultrasound in Medicine, Seattle, WA, Oct. 8-10, 1974.

2. J. S. Heyman: "Ultrasonic Coupling to Optically Generated Charge Carriers in CdS; Physical Phenomena and Applications," Ph.D. Thesis, Washington University (1975) (also NASA TMX-68732).

3. Peter W. Marcus and Edwin L. Carstensen: "Problems with Absorption Measurements of Inhomogeneous Solids," J. Acoust. Soc. Am., 58, 1334-1335, (1975).

4. Joseph S. Heyman: "A Non-Phase Sensitive Transducer for Ultrasonics," Presented at the ARPA/AFML Annual Review of Progress in Quantitative NDE August 31 to September 3, 1976.

5. Rohn Truell, Charles Elbaum, Bruce B. Chick: Ultrasonic Methods in Solid State Physics, (New York, Academic Press, 1969).

6. R. Truell and W. Oates: J. Acoust. Soc. Am., 35. 1382, (1963).

7. D. I. Bolef and J. G. Miller: "Physical Acoustics," 8, W. P. Mason, ed., (New York, Academic Press, 1971).

8. Joseph S. Heyman: "A Phase Insensitive Acousto-Electric Converter," submitted to JASA May 1977.

9. A. R. Hutson and D. L. White: "Elastic Wave Propagation in Piezoelectric Semiconductors," J. Appl. Phys., 33, 40 (1962)

10. G. Weinreich: "Ultrasonic Attenuation by Free Carriers In Germanium," Phys. Rev., 107, 317 (1957).

11. P. D. Southgate: "Use of a Power-Sensitive Detector in Pulse-Attenuation Measurements," J. Acoust. Soc. Am., 39, 480, (1966).

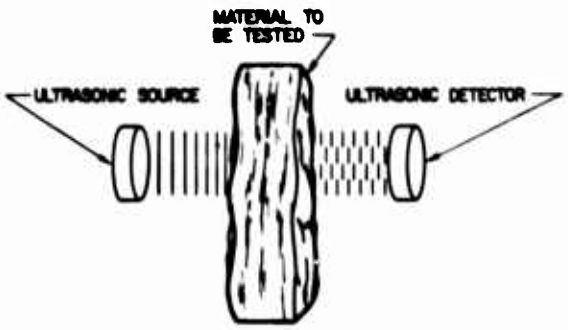


Figure 1. Typical arrangement for transmission ultrasonic imaging showing phase shifted plane waves exiting from the tested material.

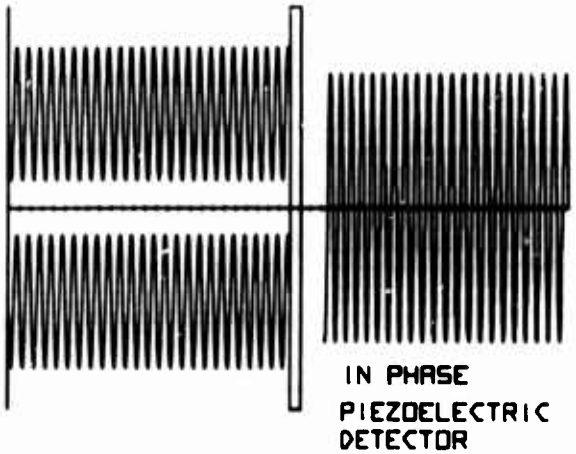


Figure 2. Two in-phase acoustic waves indident from the left on a conventional piezoelectric detector resulting in a large electrical output shown on the right.

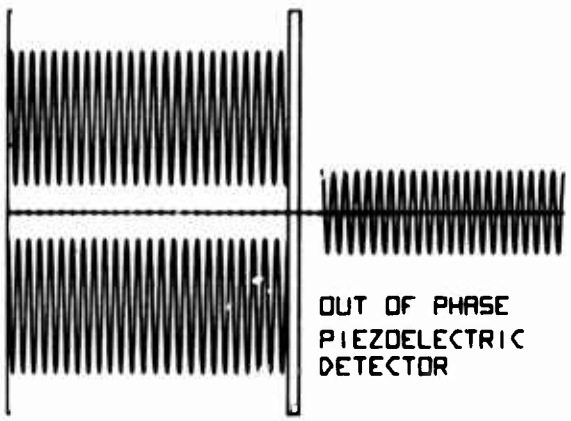


Figure 3. Two out-of-phase acoustic waves produce a reduced electrical output.

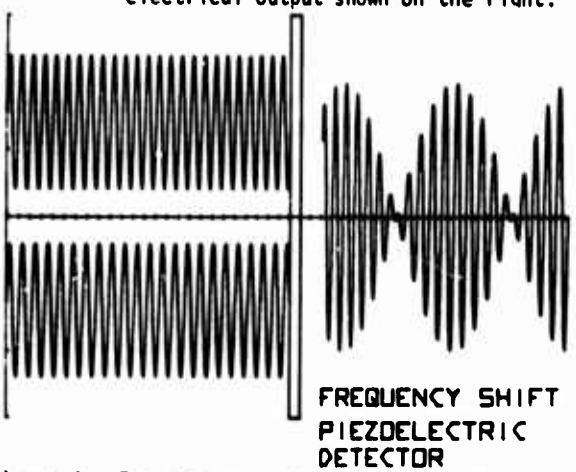


Figure 4. Two frequency shifted acoustic waves produce a severely phase modulated electrical output.

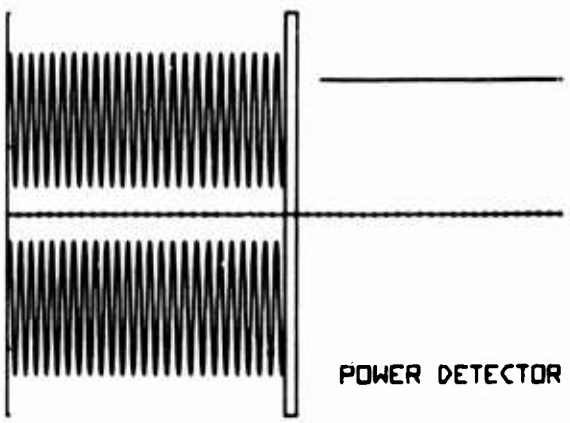


Figure 5. For cases of in-phase, out-of-phase, and frequency shift, the AEC (power detector) output is a constant since the incident power is constant.

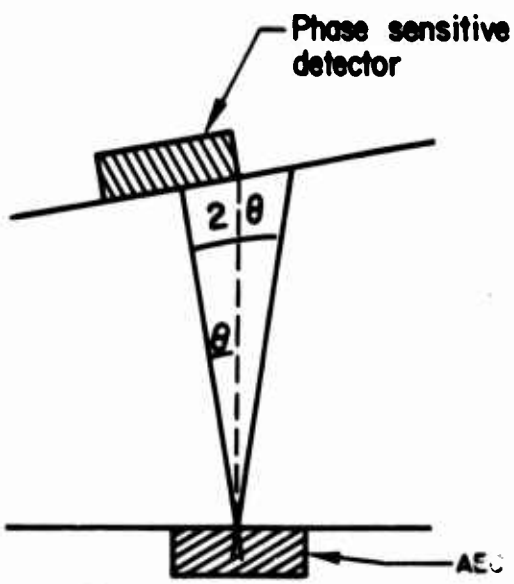


Figure 6. Block diagram showing variable geometry water cell.

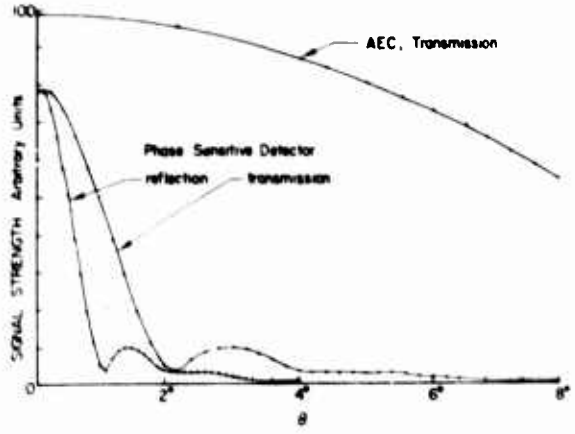


Figure 7. Directivity data of the AEC contrasted with that of conventional phase sensitive transducers. Both data were obtained in the water cell shown in Fig. 6.

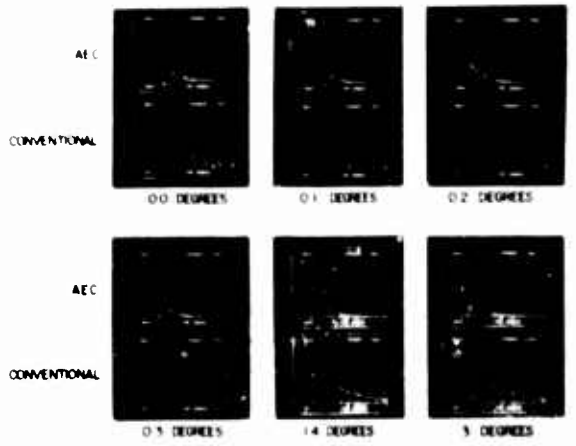


Figure 8. Pulse-echo data obtained in the water cell with angle varying from 0.0 degrees to 7 degrees. The upper traces are from the AEC (power signal) while the lower traces are from the conventional piezoelectric detector (pressure signal).



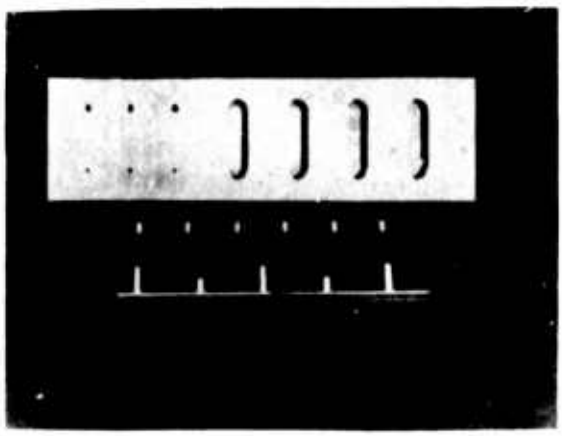


Figure 9. Resolution test plate containing flat-bottom grooves and holes, the smallest of which is 1/64-inch in diameter.



Figure 10. Transmission scanned ultrasonic picture of the plate shown in Fig. 9 using a conventional phase sensitive transducer. The upper figure (a) is long pulse echo excitation (narrow bandwidth) while the lower trace (b) is short pulse echo excitation (broad band).

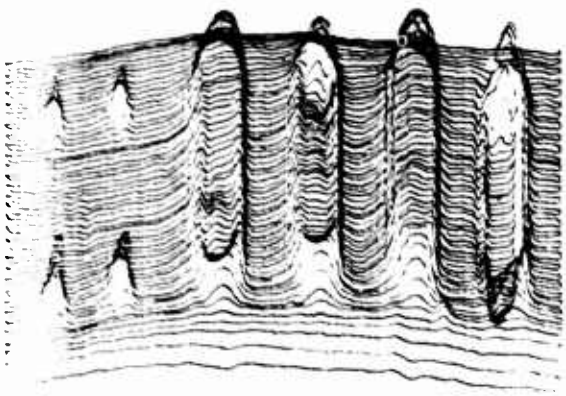


Figure 11. Same as Fig. 10(a), but using an AEC for the detector. The smallest holes are clearly visible as are plate resonances in the grooves.

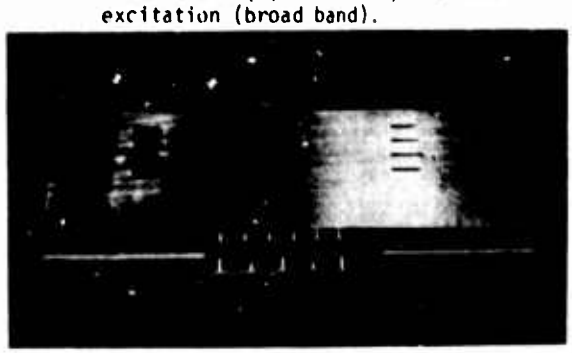


Figure 12. Angle resolution test plate (see text).



Figure 13. Conventional transducer scanned image of the plate shown in Fig. 12.



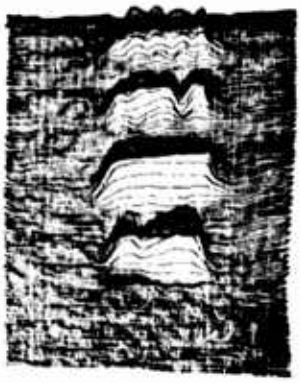


Figure 14. AEC scanned image of the plate shown in Fig. 12. The magnified region shows the small grooves which are on the left of both Figs. 13 and 14.



Figure 15. Photograph of an epoxy-graphite composite with a built-in regional "non-bond".



Figure 16. Conventional transducer scanned image of the plate in Fig. 15.

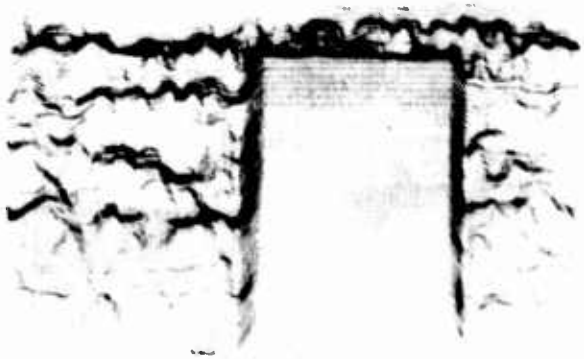


Figure 17. AEC scanned image of the plate in Fig. 15.

INTEGRATED ULTRASONIC TRANSDUCER

Sze-Hon Kwan, Richard M. White and Richard S. Muller
Department of Electrical Engineering and Computer Sciences
and the Electronics Research Laboratory
University of California, Berkeley 94720

ABSTRACT

Ultrasonic transducers composed of integrated assemblies of double-diffused MOS transistors (DMOST) and thin-film piezoelectric transducing elements are described. The entire transducer is built on a single-crystal silicon wafer and offers a number of attractive features including: small size and correspondingly precise localization of the sensitive element, a response that can be predicted by relatively simple theory, a large bandwidth, and a possibility of producing arrays of sensors together with other signal-processing elements in a single processing sequence. The piezoelectric film (zinc oxide) is sputtered either in the gate region of a double-diffused MOS transistor (making the so-called "PI-DMOST") or adjacent to the gate electrode of a double-diffused MOS transistor. The transducer may be excited in various ways: (1) in a thickness mode from the bare silicon surface opposite the piezoelectric-coated region; (2) in a flexural mode caused by bending the silicon wafer; (3) end excitation by surface motions either normal or transverse to the edge of the wafer; (4) by surface waves. Various of these modes are characterized by high sensitivity to strain, low conversion loss, large bandwidth, and good response at very low or very high frequencies.

Overview

Two different types of integrated ultrasonic transducers are illustrated: the piezoelectric-insulator-gate double-diffused MOS transistor (PI-DMOST) in which the piezoelectric material is located in the gate region of the transistor; and a transducer in which a piezoelectric film with electrodes is connected to the gate of an ordinary MOS transistor. Both types of transducer are highly sensitive and capable of being made quite small (strain sensitive regions about 1000 square microns in area have been made). The limiting frequencies of device operation for some modes of excitation can extend to the GHz region. Transducer fabrication procedures are compatible with present silicon planar integrated-circuit technology.

The figures below show the modes of excitation and responses observed. The PI-DMOST structure was used except where indicated otherwise.

Acknowledgement

This work was sponsored in part by the National Science Foundation under grant ENG76-21818, and in part by the Center for Advanced NDE operated by the Science Center, Rockwell International, for the Advanced Research Projects Agency and the Air Force Materials Laboratory under Contract F33615-74-C-5180.

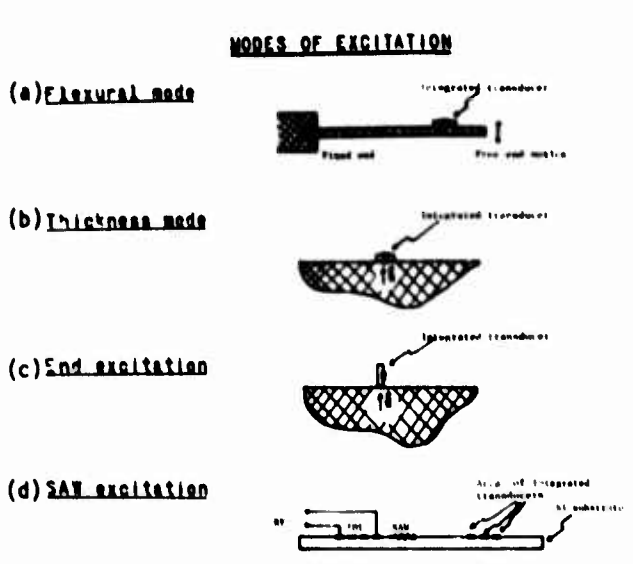


Figure 1. Modes of excitation of the integrated transducer. (a) Flexural mode, useful principally at low frequencies. (b) Thickness mode, in which the transducer is excited by motion of the surface on which it is placed. Response to displacements either normal or transverse to the surface may be observed. The silicon of which the transducer is made can serve as an integral wear plate for the transducer. (c) End excitation, with waves excited in the silicon by normal or tangential displacements and passing beyond the piezoelectric element of the transducer to an absorber which prevents reflections. (d) Surface-acoustic wave (SAW) excitation, of interest principally in making a signal processor employing an array of transducers.

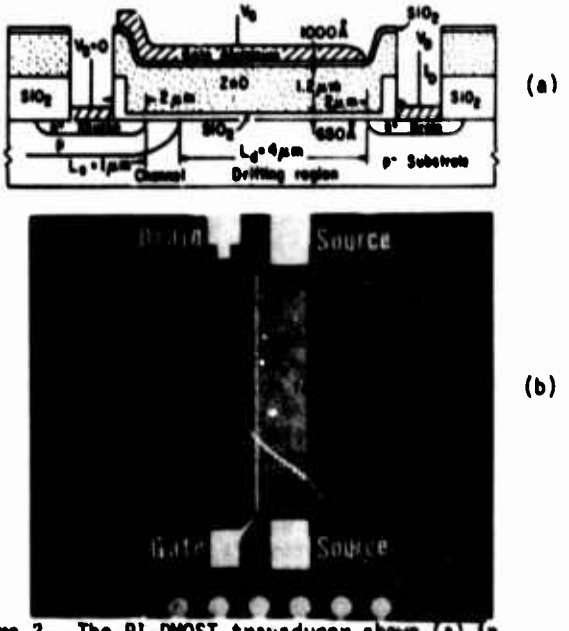


Figure 2. The PI-DMOST transducer shown (a) in cross-section (with exaggerated vertical scale) and (b) in a top view photograph of an actual device (area shown measures roughly 3 millimeters on a side).

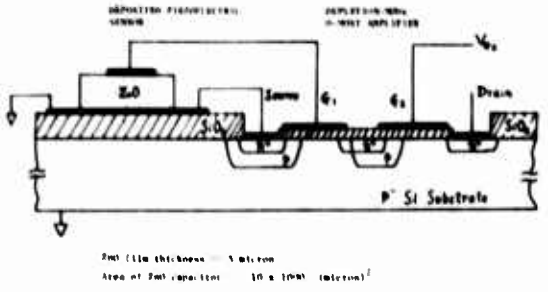


Figure 3. Transducer made with ZnO capacitor and dual-gate depletion-mode double-diffused MOS transistor. The separation of the ZnO and the transistor allows individual optimization of both acoustic and electrical performance, and avoids the necessity of sputtering over the channel region of the transistor. The dual gate structure of the D-MOST allows one to vary gain of the device by changing the bias voltage applied to the second gate.

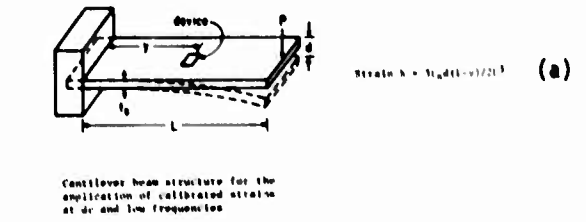




Figure 4. Flexural mode excitation. Mode used to verify responsiveness of a given device, typically with excitation at hundreds of Hz.

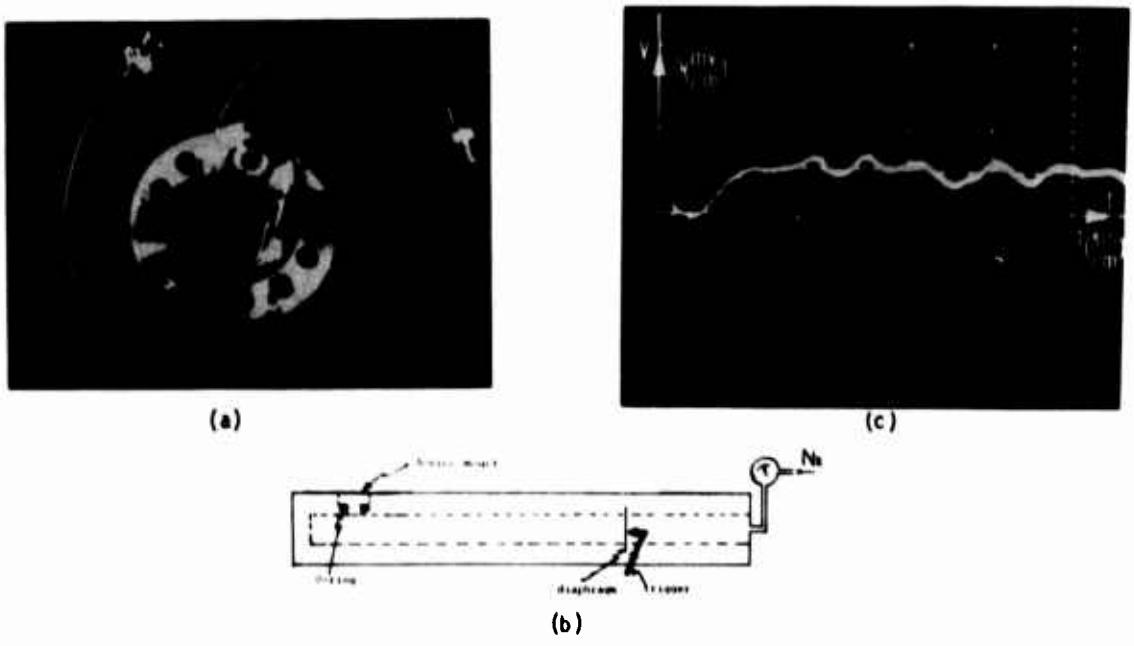


Figure 5. (a) Device mount for shock-wave experiment. (b) Schematic of the experimental setup. (c) PI-DMOST response to a shock wave with an equivalent strain of 10^{-6} at the wavefront.



Figure 6. Excitation of a PI-DMOST by displacements resulting from breaking of glass capillary to simulate an acoustic emission event (the initial response was not photographed owing to trigger delay problem).

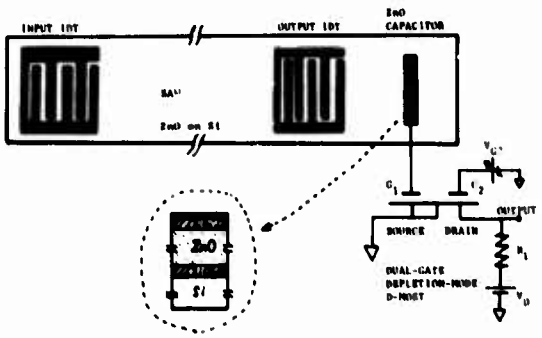
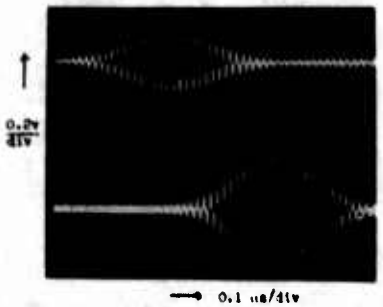


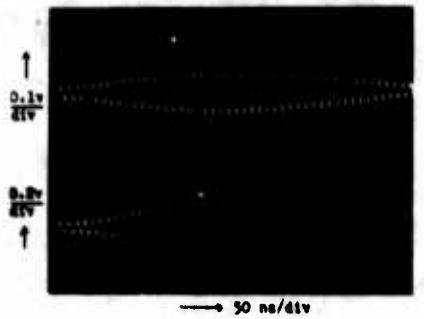
Figure 7. Experimental arrangement for excitation and detection of SAW with ZnO capacitor coupled to a dual-gate D-MOS transistor. Note that this sort of excitation could be used in making a signal processor. Also in either this mode or in end excitation mode one could use an array of transducer elements and transistors to perform signal processing the the transducer itself.



Top trace : output from interdigital transducer
delay time= 3.9 us
Bottom trace : output from D-DNOST
delay time= 4.2 us
V_{DD}=5v V_{G2}= 4.9v I_{Do}= 4mA

Response of a ZnO capacitor coupled D-DNOST strain transducer to excitation by SAW at 4[illegible] MHz.

(a)

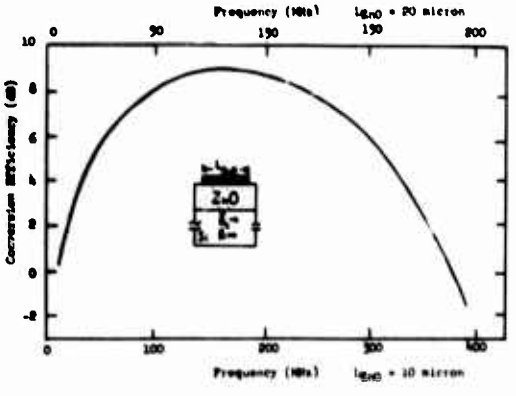


Top trace : output from interdigital transducer
delay time = 4.2 us
Bottom trace : response from D-DNOST
delay time = 5 us
V_{DD} = 11v V_{G2} = 7v I_{Do}= 9.4 mA

Response of a ZnO capacitor coupled D-DNOST strain transducer to excitation by SAW at 90 MHz.

(b)

Figure 8. Responses obtained from arrangement of Fig. 7. Comparison with IDT response is made at 46 MHz and at 90 MHz.



Conversion Efficiency = 10 Log (power delivered to load/ acoustic power)
(C.E.)

$$= 10 \log \left(A k_s \sin^2(k s l_{ZnO}/2) / (k_s l_{ZnO}/2)^2 \right)$$

R_L = 1 KΩ
A_{ZnO}/A_{ox} = 6
C_{ZnO}/C_{ox} = 1/30 (per unit area)

Figure 9. Computed conversion efficiency for device of Fig. 3 responding to SAW excitation. Note that for end excitation with a bulk wave, the response extends to low frequencies.

OPTICAL DETECTION OF ACOUSTIC EMISSION SIGNALS

C. Harvey Palmer
Department of Electrical Engineering
Johns Hopkins University, Baltimore, Maryland 21218
Robert E. Green, Jr.
Department of Mechanics and Materials Science
Johns Hopkins University, Baltimore, Maryland 21218

ABSTRACT

Piezoelectric transducers, long used in the generation and detection of ultrasonic waves, have more recently been the detector of choice for acoustic emission signals. Optical probing methods, however, have several important advantages for acoustic emission studies: (1) they have an inherent broad frequency response, free from mechanical resonances, (2) they do not interfere with the acoustic waves, (3) since the focused optical beam diameters are typically only a few hundredths of a millimeter, optical methods can probe very close to a crack or a twin, (4) they can probe internally in transparent media, and (5) they can be used over a very wide temperature range. In this paper we compare the response of an optical probe with that of a commercial acoustic emission transducer. Since the optical probe permits absolute calibration, we can not only measure acoustic emission amplitudes, but also determine the quantitative response of the piezoelectric transducer to known acoustic disturbances of various kinds over a range of frequencies. We include measurements of real acoustic emission from twinning in two metals and stress corrosion cracking in steel.

Introduction

Elastic waves are commonly used for the nondestructive evaluation of materials and structures. One method[1] employs transducer generated pulses of ultrasonic waves which are directed into the material and sensed either by the same transducer (pulse-echo) or by a separate transducer located at another point on the specimen (pitch-catch). By timing the return of the various echoes, we can determine the location of flaws. By monitoring the attenuation of the ultrasonic waves, we can determine changes in the microstructure of the material. Reception of the ultrasonic signals in this method is easy because with periodic signals of simple waveform, the required bandwidths are narrow and the echo return repetitive.

A second method[2] involves the passive reception of naturally generated bursts of elastic waves called acoustic emission. Acoustic emission signals may be characteristic of the generating mechanism, twinning, crack propagation, or dislocation motion and thus very informative. Such emission is known to increase dramatically prior to failure of the material -- hence its importance. However, because acoustic emission arises at unknown locations, at random times, and with an unanticipated waveform involving a relatively broad range of frequencies, it is much more difficult to detect than the ultrasonic pulses used for the first method.

Although optical methods have been shown to be invaluable for the detection of ultrasonic waves of all kinds, they have not been applied to the detection of acoustic emission bursts until now. Several optical techniques such as the knife-edge technique[3], diffraction technique[4,5], and differential interferometry[6] are unsuitable for various reasons. In this paper we describe an optical method which does work, and which has important advantages.

In Section II of the paper we briefly describe the instrumentation, show how it may be absolutely calibrated, and indicate the minimum disturbance amplitudes that we can measure. In Section III we demonstrate the similarity of optically detected and piezoelectrically detected signals when they are sensed under similar conditions. In Section IV we illustrate one of the several advantages of optical probing by showing waveforms obtained within a half millimeter of a crack.

Instrumentation

The optical probe used in our experiments is a modified Michelson interferometer having a stabilized optical path difference. As shown in Fig. 1, an expanded, collimated laser beam is incident from the left on a beam splitter. Light reflected downward is focused on a mirror at P and provides the reference path. Light transmitted by the beam splitter is focused on the specimen surface. The two returning beams, reference and sample, are recollimated and superimposed above the beam splitter where they form (ideally) a single, uniform interference fringe. The light focused on a photodetector, D, generates a photocurrent having both low frequency and high frequency components. The low frequency components, 0 to about 1 KHz, which result from room vibrations and atmospheric disturbances, drive the stabilization circuit. This circuit translates the mirror mounted on the piezoelectric drive in such a way as to maintain a quiescent optical phase difference $\pi/2 \pm 2N\pi$ between the reference and sample beams corresponding to the maximum sensitivity to small high frequency signals. The signal frequencies, typically 10 KHz to 1 MHz, are amplified, displayed on the oscilloscope, and generally recorded on video tape as well.

The interferometer is calibrated by substituting for the specimen a second piezoelectrically

driven mirror. This unit, driven at its resonant frequency, approximately 140 KHz, by a variable RF voltage of sufficient amplitude provides a large, controlled sinusoidal mirror displacement, $\delta = \delta_0 \cos \omega_a t$, where δ_0 is the amplitude and ω_a is the RF radian frequency. For a displacement from the quiescent $\pi/2$ phase difference, the photocurrent is given by

$$i_{photo} = (\alpha P_i/2) \ [1 - \sin(4\pi\delta/\lambda)]. \qquad (1)$$

In this expression, α is the sensitivity of the photodetector (amps/watt optical power), P_i is the laser beam power, and λ is the optical wavelength. The amplifier output voltage for a sinusoidal disturbance is then

$$V_{out} = K \sin[(4\pi/\lambda) \ \delta_0 \cos(\omega_a t)]. \qquad (2)$$

For sufficiently large disturbances, the peak-to-peak output voltage is 2K so that we have the required constant for absolute calibration. The minimum disturbance amplitude needed to give this voltage, V_{cal}, is evidently

$$4\pi\delta_0/\lambda = \pi/2 \text{ or } \delta_0 = \lambda/8 = 791\text{Å} . \qquad (3)$$

The waveform corresponding to this displacement is shown in Fig. 2; it is in excellent agreement with the theoretical curve given by Eq 2. Having determined the constant 2K, we now consider small signals, and thus approximate sin x by x in Eq. 2. Solving for the instantaneous displacement, we obtain

$$\delta = (\lambda/2\pi) \ v_{out}/V_{cal}. \qquad (4)$$

The minimum detectable displacement δ_{min} is easily calculated theoretically by observing that the noise level is determined by the shot current in the photodetector generated by the constant power $\alpha P_i/2$, the first term in Eq. 1. We find

$$\delta_{min} = \sqrt{2eB/\alpha P_i} , \qquad (5)$$

where e is the charge on the electron and B the amplifier bandwidth. For our instrument, B = 1 MHz, P_i = 1 mW, and α = 0.4 amp/watt, and we find that δ_{min} = 0.04 Å. The actual measured minimum detectable amplitude is about 1/2 Å.

For piezoelectric sensing we used a commercial piezoelectric acoustic emission transducer having a broad frequency response centered at 500 KHz. The signals detected by both the optical system and the piezoelectric transducer were fed through identical adjustable band-limiting filters for our comparisons. In the twinning experiments we set the bandpass at 10 KHz to 500 KHz, and in the stress corrosion experiments we used 10 KHz to 1 MHz. In addition, we used two identical video tape recorders to obtain a permanent record of the signals which we could later play back through the oscilloscope at any desired sweep speed or voltage gain. The audio portions of the two tapes were used to identify the particular events as seen on the oscilloscope used as a monitor during the recording process. We are thus able to compare the same event as detected by the two sensors.

Twinning Experiments - Optical System Tests

Our optical probe was first tested by sensing a variety of simulated acoustic emission signals. We also made a comparison with piezoelectrically sensed signals and found acceptable agreement. After these tests, we made a study of twinning in four different metals in which we detected the acoustic emission signals both optically and piezoelectrically at the same time. As shown in Fig. 3, the specimens were held in a clamp which was mounted on the interferometer base. The specimens all had a cross section area of 6 1/4 x 25 mm and were about 150 mm long. They were mechanically polished on one surface. The piezoelectric and optical sensors were arranged directly opposite each other across the small dimension of the specimen. Not shown in the figure is a special clamp which held the piezoelectric transducer on the specimen and allowed the optical probing beam to be focused directly opposite on the mechanically polished surface of the specimen.

Twinning emissions were generated by bending the specimen rather rapidly against the clamp. The signals passed between the aluminum clamping blocks and were detected by both sensors. Because the two sensors were close together and symmetrically placed, we assumed that the signals detected would be very similar, though they would probably differ somewhat in their high frequency components for which the specimen thickness is of the order of an acoustic wavelength or more.

Figure 4 shows a typical twinning event generated in a cadmium specimen. The upper trace shows the piezoelectric waveform; the lower one, the optical waveform. The sweep speed for the two traces was 50 μsec/div. The amplitude of the elastic disturbance is seen to build up rather rapidly in the first 50 μsec or so and then slowly decay in an oscillatory way which suggests specimen resonances. In any case, it is clear that the piezoelectric and optical waveforms are very much alike. The small high frequency component superposed on the piezoelectric signal that is absent in the optical signal may correspond to one of the strong resonant frequencies of the piezoelectric transducer. (We have not yet measured these resonances when the transducer is loaded by being in contact with the specimen surface.)

Typical acoustic emission amplitudes measured from direct oscilloscope photographs lie in the range 1 to 20Å. (Amplitudes as recorded on the video tape recorder were more difficult to determine, since the VTR gain was somewhat uncertain, and many signals were either lost in tape noise or were clipped when the tape became saturated.)

Figure 5 shows an interesting double twin signal in indium displayed at a sweep speed of

500 μsec/div. Here again, the upper trace is the piezoelectric signal, the lower one is the optical signal. The time spacing of the signals is almost exactly the same for the two sensors. The waveforms, though very similar, do differ slightly as seen when the first part of the first event is displayed at 50 μsec/div. The differences, as for the cadmium signals, differ mostly in the high frequency components.

We have also recorded a number of other signals, both in cadmium and indium and in zinc and tin as well. The similarity of the waveforms obtained optically and piezoelectrically is convincing.

Stress Corrosion Cracking in Steel

Acoustic emission due to stress corrosion cracking in steel was also studied both optically and piezoelectrically. The specimens were E4340 steel, austenitized in an argon atmosphere, oil quenched, and then tempered at 400°F for two hours. The specimens were 18 x 17 x 75 mm, mechanically polished on two sides, and had a v-bottomed slot about 25 mm deep machined in one end as shown in Fig. 6. The piezoelectric sensor was clamped to the specimen at the position shown; the clamp is not shown in the diagram. The first tests were done with the optical probe positioned opposite the piezoelectric transducer as shown in the drawing. In the tests reported here, the optical probe was positioned within 1/2 mm of the crack and moved along to keep abreast of the crack as it progressed.

After the loading bolt was tightened about a quarter turn, the specimen was aligned on the interferometer plate, and salt solution added. When the crack ceased to grow and the acoustic emission stopped, the specimen was removed, the bolt tightened further, and the specimen repositioned and more salt added.

Figure 7 shows two recorded events which occurred about a second apart. The upper two traces correspond to the first event, the lower two traces to the second event. The first and third traces, displayed at 20 μsec/div., are piezoelectric traces sensed at the position shown in Fig. 6. These two waveforms are very similar indeed. The other two traces, second and fourth, were sensed optically within 1/2 mm of the crack. These traces are also very much alike, but they are very different from the piezoelectric traces. We conclude that, not surprisingly, the signature of an event depends greatly on where it is sensed. However, since the minimum specimen dimension is 8 mm, we note that reflections begin to occur in less than 5 μsec. We could reasonably expect different resonances to be seen at different points on the specimen. Accordingly, many of the differences here could be attributed to specimen resonances. The higher attenuation at higher frequencies would also account for some of the differences in waveform.

Conclusion

In this paper we have shown that optical probing of acoustic emission signals is indeed possible, and that the waveforms sensed are in agreement with those sensed piezoelectrically insofar as a comparison is possible. We have verified the general belief that acoustic emission waveforms are highly dependent on the location of the sensor, and accordingly shown the usefulness of optical probes in being able to probe very locally, an impossibility with other types of probes, either piezoelectric or capacitive. We have determined that typical acoustic emission amplitudes lie in the range 1-20Å in many cases.

Acknowledgement

In addition to thanking our sponsors, we wish to thank our students, Steven E. Fick, Richard M. Claus, and Ronald A. Kline for their considerable help in various aspects of this project.

This work was supported by a grant from Army Research Office, Durham.

References

1. J. Krautkrämer and H. Krautkrämer: "Ultrasonic Testing of Materials," Springer-Verlag, Berlin and New York (1969).

2. J. C. Spanner: "Acoustic Emission, Techniques and Applications," INTEX Publishing Company, Evanston, Illinois (1974).

3. R. Adler, A. Korpel, and P. Desmares: "Instrument for Making Surface Waves Visible," IEEE Trans. Sonics and Ultrasonics, SU-15, 157 (1968).

4. R. L. Whitman and A. Korpel: "Probing of Acoustic Surface Perturbations by Coherent Light," Appl. Opt. 8, 1567 (1969).

5. G. I. Stegeman: "Optical Probing of Surface Waves and Surface Wave Devices," IEEE Trans. Sonics and Ultrasonics, SU-23 (1976).

6. C. H. Palmer, R. O. Claus, and S. E. Fick: "Ultrasonic Wave Measurement by Differential Interferometry," Appl. Opt. (to be published).

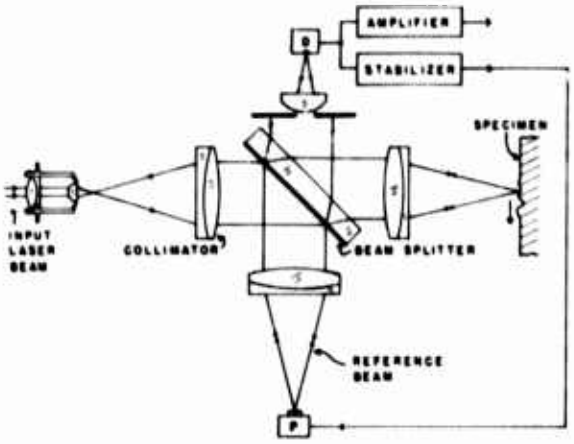


Figure 1. Stabilized optical path interferometer. Stabilizer removes low frequency, 0-1 kHz, disturbances; the high frequency signals, >10 kHz, are amplified and recorded.

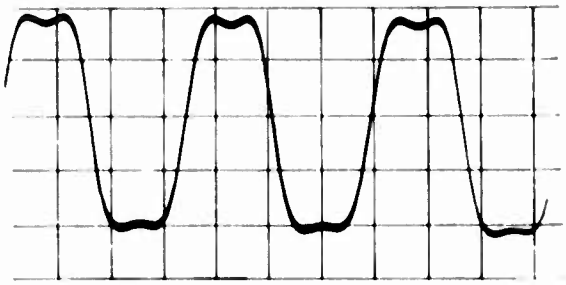


Figure 2. Experimental calibration curve corresponding to $\delta_0 = \lambda/8$. The vertical gain is 2 volts/div; sweep speed 2 μsec/div. The calibration frequency was 140 kHz, and $V_{cal} = 7.7$ volts.

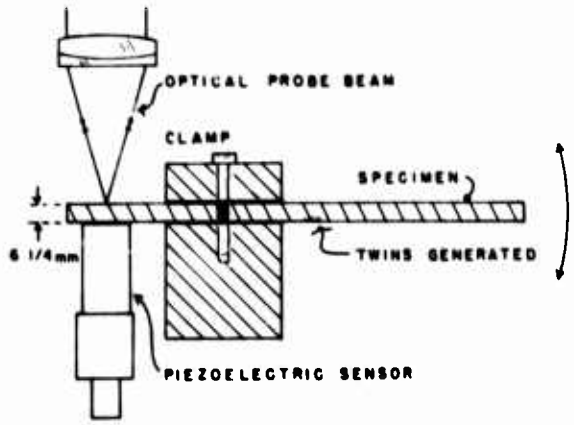


Figure 3. Mounting of specimens for twinning experiments to verify the performance of the optical and piezoelectric sensors.

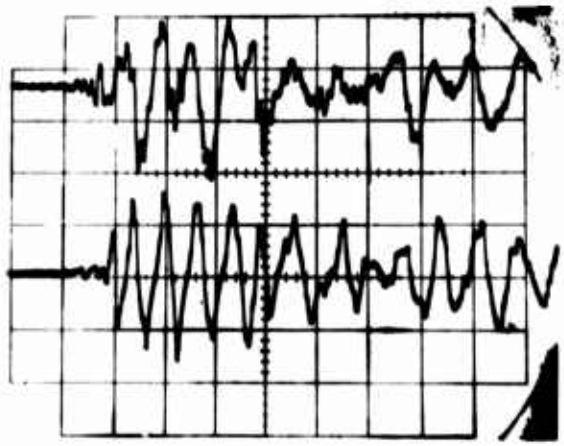


Figure 4. Acoustic emission in cadmium due to twinning. The sweep speed is 50 μsec/div. The upper trace is the piezoelectric signal, the lower trace the optical signal.

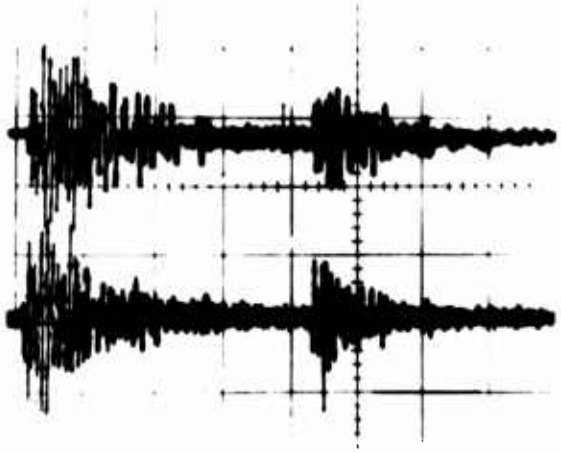


Figure 5. Double twin in indium; sweep speed 500 μsec/div. The upper trace is piezoelectric signal, the lower trace optical.

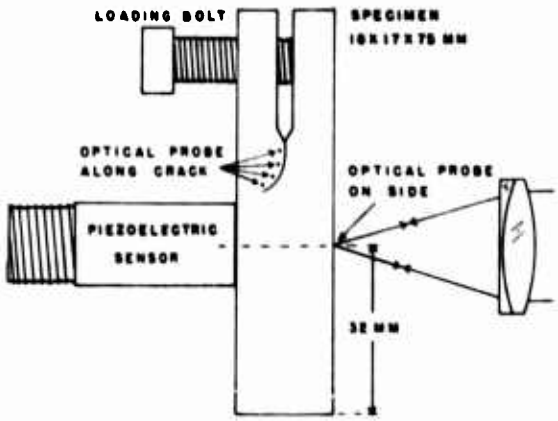


Figure 6. Arrangement of probes for study of E4340 steel specimens subjected to stress corrosion cracking. Here the optical probe was positioned along the crack.

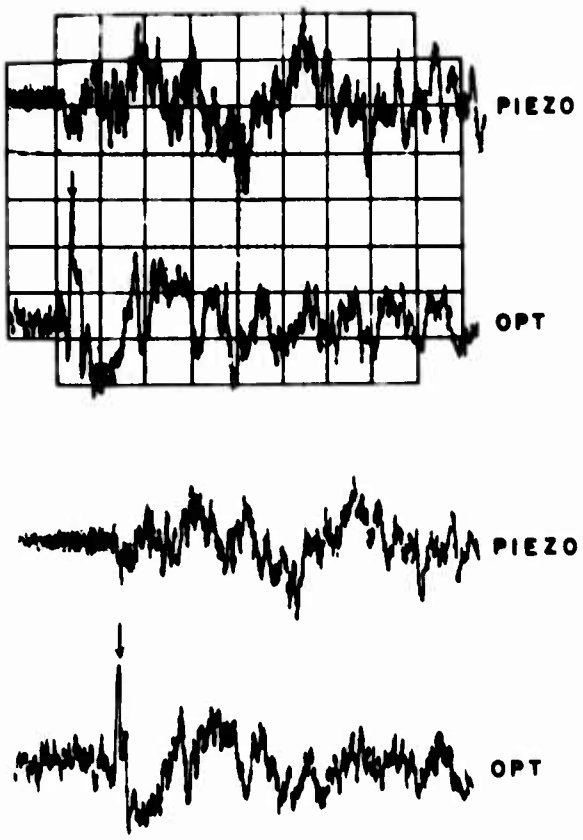


Figure 7. Two acoustic emission bursts in E4340 steel which occurred about a second apart. The two upper traces are for the first event, the lower two for the second event. The piezoelectric sensor on the specimen side gave the PIEZO traces, the optical sensor along the crack gave the OPT traces. Note the similarity of the two PIEZO traces and the similarity of the two OPT traces. The large differences between the piezo and optical traces results from sensor location. The sharp initial spike (see arrows) in the OPT traces is not recorded by the piezoelectric sensor only about 20 mm distant.

APPROACH TO ACOUSTIC EMISSION SIGNAL ANALYSIS - THEORY AND EXPERIMENT

Nelson N. Hsu, John A. Simmons and Stephen C. Hardy
Metallurgy Division
National Bureau of Standards

ABSTRACT

Acoustic Emission (AE) signals are notorious for their complexity and irreproducibility. Because AE source characteristics are virtually unknown and because the detected AE signals are colored by the propagation media, the sensor response and the instrumentation settings, interpretations of test results such as spectral analysis or correlation studies are mostly qualitative and sometimes controversial; theories either are empirically derived or cannot be verified by experiments. In this paper, we sketch an approach to the AE signal analysis problem. We first report the development of a theory which allows the computation of the displacement as a function of time at an arbitrary point on an infinite plate due to an arbitrary point source force function. The theory is based on a new Fourier inversion technique which yields exact formulas similar to those developed for seismological "ray" theories. We then report experimental results obtained on a 2.52 cm thick aluminum plate using a reproducible step function stress release pulse as a simulated AE signal and a wide band displacement capacitive transducer as a sensor. The measurements are in quantitative agreement with the predictions of theory. We also discuss applications wherein the simulated signal, capacitive transducer and plate theory are used for AE source signature analysis, and sensor calibration problems.

I. THE DETECTION OF INAUDIBLE SOUNDS EMITTED FROM A HIGHLY STRESSED REGION OF A STRUCTURE IS USED FOR LOCATING FLAWS IN SITU AND IN REAL TIME.

II. USUALLY THE SIGNIFICANCE OF THE SIGNAL CANNOT BE ASSESSED.

III. NO RELIABLE SYSTEM CALIBRATION TECHNIQUES ARE AVAILABLE.

IV. MOST REPORTED TEST RESULTS OF SIGNAL SPECTRAL ANALYSIS ARE STRICTLY QUALITATIVE, DIFFICULT TO REPRODUCE AND DIFFICULT TO INTERPRET.

Figure 1. Current Status

I. SOURCE CHARACTERISTICS ARE VIRTUALLY UNKNOWN.

II. DETECTED SIGNALS ARE COLORED BY:
   A. PROPAGATION PATH AND MEDIUM: THE MEDIUM'S GEOMETRY, MATERIAL PROPERTY, AND BOUNDARY CONDITIONS, ALL AFFECT THE DETECTED SIGNALS.
   B. SENSOR CHARACTERISTICS. THE OUTPUT VOLTAGE OF A TRANSDUCER IS FREQUENCY AND MODE DEPENDENT; IT IS NOT SIMPLY PROPORTIONAL TO PARTIAL DISPLACEMENT, VELOCITY OR FORCE.
   C. PROCESSING INSTRUMENTATION SETTINGS SUCH AS THRESHOLD LEVEL, FILTER PASSING BAND WIDTH, AND AMPLIFIER GAIN.

III. THEORIES ON ACOUSTIC EMISSION ARE EITHER BASED UPON EMPIRICAL RESULTS OR CANNOT BE VERIFIED EXPERIMENTALLY.

Figure 2. The Problems

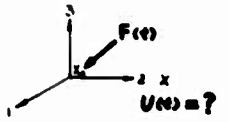
I. THEORY
   TO SOLVE THE PROBLEM OF A POINT SOURCE ARBITRARY TRANSIENT STRESS WAVE PROPAGATION IN A REALISTIC ELASTIC MEDIUM - A PLATE

II. EXPERIMENT
   DESIGN A TEST CONFIGURATION WITH SIMULATED AE SOURCE AND TRUE DISPLACEMENT TRANSDUCERS SUCH THAT ALL THE PARAMETERS INVOLVED CAN BE CHARACTERIZED, CONTROLLED, AND MEASURED.

III. DEVELOP METHODS FOR AE SYSTEM CALIBRATION

IV. DEVELOP COMPUTATION SCHEMES FOR SOLVING THE DECONVOLUTION PROBLEMS OF AE SIGNAL ANALYSIS.

Figure 3. Our Approach



FORMULATION: GIVEN A POINT FORCE FUNCTION $\vec{F}$ AS A FUNCTION OF TIME ACTING AT $\vec{\xi}_0$ IN OR ON AN INFINITE ELASTIC PLATE, TO FIND THE DISPLACEMENT AS A FUNCTION OF TIME AT $\vec{\xi}$

SOLUTION:

$$U_i(\vec{\xi}_0;\vec{\xi};t) = \int_0^{\infty} G_{ij}(\vec{\xi}_0;\vec{\xi};\tau) F_j(t-\tau)\,d\tau$$

G_{ij} ARE THE DYNAMIC GREEN'S FUNCTIONS OF THE PLATE DUE TO STEP-FUNCTION TIME DEPENDENCY.

REMARKS: G_{ij} HAVE BEEN DERIVED BY J. R. WILLIS USING A NEW FORM OF FOURIER INVERSION TECHNIQUES. THE NUMERICAL COMPUTATION OF G_{ij} HAS BEEN DONE FOR $0 \le \tau \le 7$. T DEPENDS ON THE REQUIREMENT AND NOT MUCH COMPUTING MONEY ONE HAS.

THE FOLLOWING THREE GRAPHS ARE EXAMPLES OF THE COMPUTED RESULTS.

Figure 4. Theory

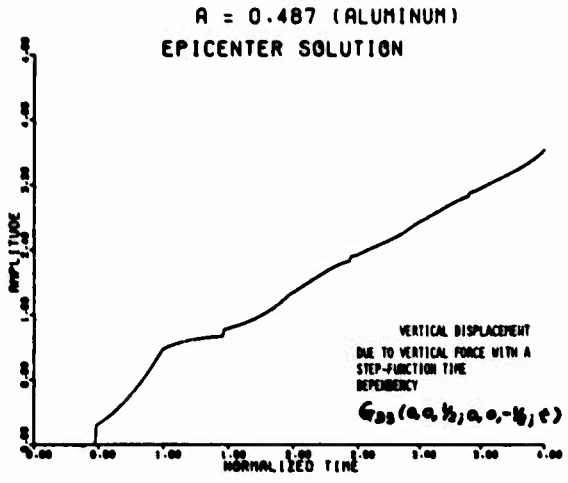


Figure 5

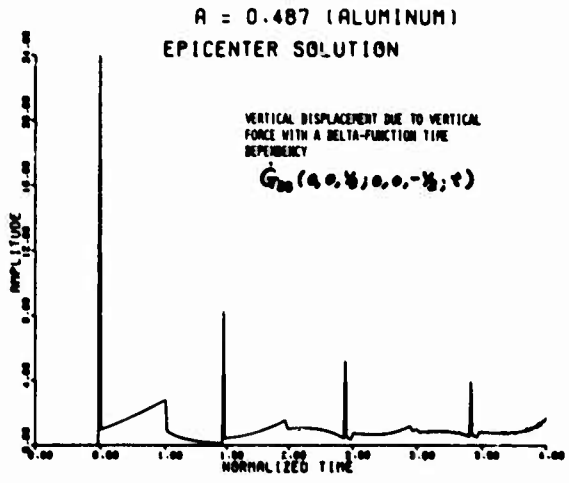


Figure 6

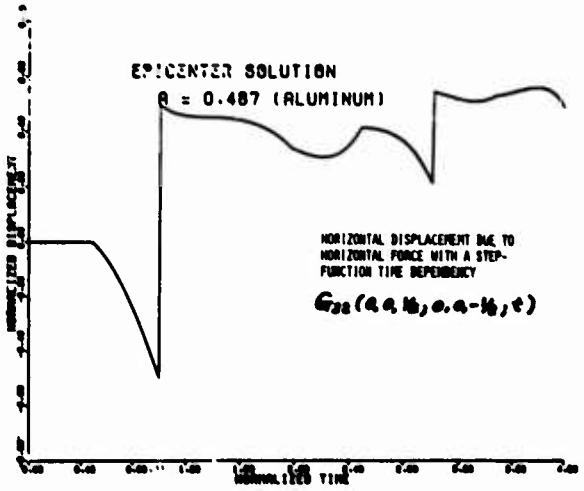


Figure 7

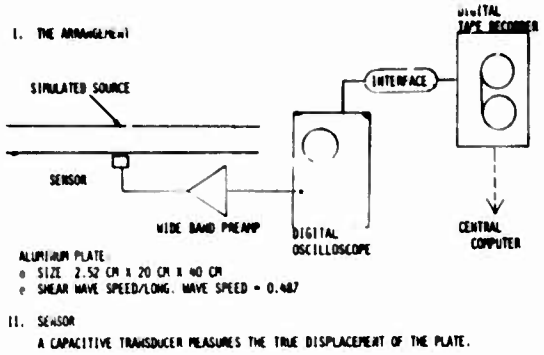


Figure 8. Experimental arrangement

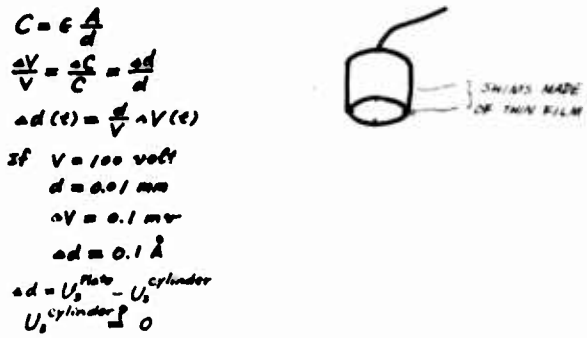


Figure 9. Capacitive transducer

III. SIMULATED SOURCE
A STATICALLY LOADED FAST RELEASE STEP-FUNCTION-LIKE STRESS PULSE PRODUCED BY BREAKING GLASS CAPILLARY OR PRODUCED BY A MECHANICAL DEVICE AS SHOWN IN THE FIGURE. THE SOURCE CHARACTERISTICS CAN BE CONTROLLED AND ARE REPRODUCIBLE.

F_{MAX} CAN BE DETERMINED BY MEASURING F'

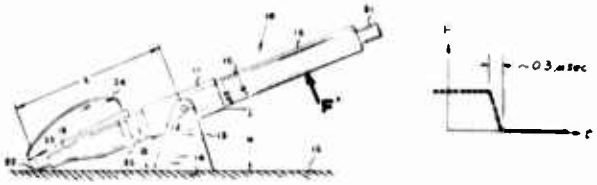


Figure 10. Acoustic emission source



Figure 11. Acoustic emission simulator

I. NEARLY PERFECT AGREEMENT BETWEEN THEORY AND EXPERIMENT AS SHOWN IN THE FOLLOWING FIGURE.

II. SOURCE CHARACTERIZATION CAN BE ACHIEVED BY REPLACING THE AE SIMULATOR WITH UNKNOWN SOURCES AND USING DECONVOLUTION METHOD WITH THE THEORETICAL CALCULATED DELTA-FUNCTION RESPONSE.

III. SENSOR CHARACTERISTICS CAN BE ACHIEVED BY REPLACING THE CAPACITIVE TRANSDUCER WITH THE SENSOR, USING SIMULATED SOURCE AND USING TRANSFER FUNCTION ANALYSIS.

Figure 12. Results

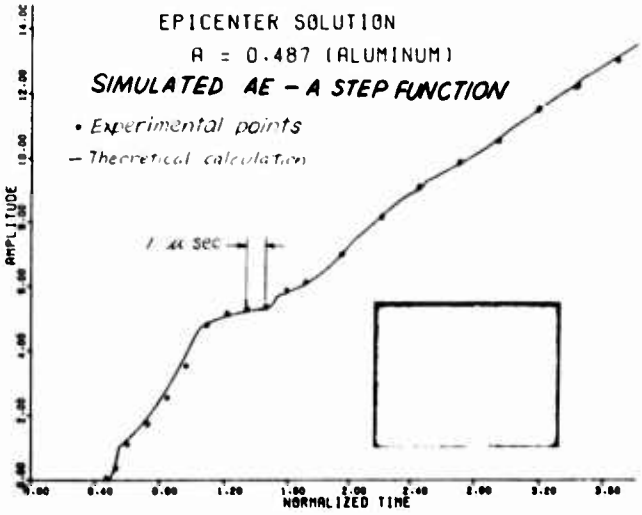


Figure 13. Simulated acoustic emission

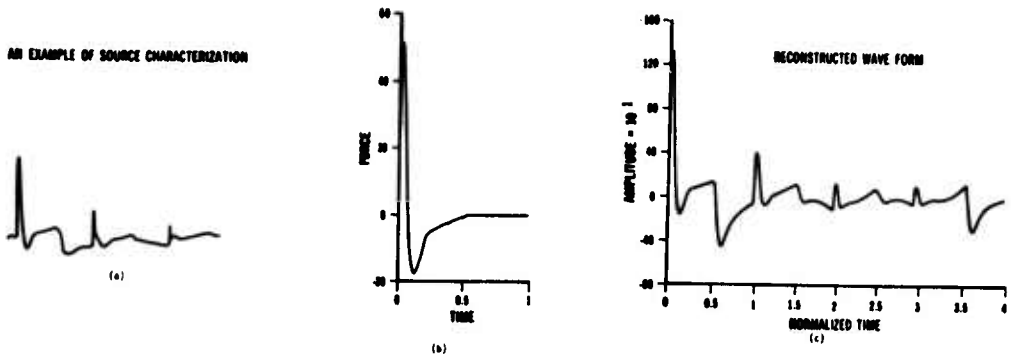


Figure 14. Acoustic emission characterizations

DEFECT SPECIFIC PENETRANTS

R. L. Crane and S. Allinikov
Air Force Materials Laboratory
Dayton, Ohio 45433

ABSTRACT

The failure to detect small through-the-thickness flaws in non-metallic coatings on metallic substrates can lead to corrosion rates several orders of magnitude greater than those of the bare metal. Therefore, the detection of such defects has high priority even though presently used inspection procedures are both expensive and difficult to perform. It has recently been shown that it is possible to make a penetrant that can detect those through-thickness flaws to the exclusion of all others. These penetrants are made by adding chelating agents to a carrier fluid such as an alcohol. The chelating agent becomes fluorescent when it contacts a metal substrate. Initial work utilized the chelating agent 8-hydroxy quinoline, and is sensitive to most metals. Current work is concentrating on chelating agents that are specific to certain metals. Thus, cracks in chromium coatings or steel can be detected if they penetrate on the steel base. Work on organic and biological agents show promise.

The failure to detect very small through-the thickness flaws in coatings on metal surfaces can result in corrosion rates several orders of magnitude greater than those for the bare metal.[1] Therefore the detection of these defects has a high priority, even though the inspection procedures currently in use are both expensive and difficult to perform. The recent development of a very sensitive penetrant which detects only corrosion initiating flaws could greatly simplify the inspection of coated metal components.[2]

The penetrants described in this article are based on the unique action of some organic compounds which chelate or combine with metal atoms and form fluorescent compounds. In the chelating process the organic molecule reacts with small amounts of metal by attaching itself to a metallic ion to form an organo-metallic complex. The ion is usually held at the center of this coordination complex making the structure rigid. This alters the fluorescent spectra of the original molecule, many times moving it into the visible spectrum. This action of chelating agents has been known for some time and is used to trace element analysis.[3]

Two distinctly different organic compounds were used in experiments to demonstrate the viability of this concept. The first compound, 8-hydroxy quinoline, was added in small amounts (0.1 to 1.0 weight percent) to isopropyl alcohol which served as carrier fluid. This material was applied to the surface of a boron epoxy F-4 rudder. Since this structure contains an aluminum honeycomb, any flaw that would permit water entry to the core could be detected with the penetrant. In the part examined, one flaw did exist and was detected as shown in Fig. 1.

Alcohol dehydrogenase, which is specific to zinc when converted to the apoenzyme form, was used to demonstrate the viability of using biological compounds as chelating agent in penetrants. Alcohol dehydrogenase is a metalloenzyme that contains zinc. The zinc atom can be removed from the protein structure by dialysis at pH of 5.5. This yields a zinc specific chelating agent. The specific action of the compound was tested by dissolving it in water and ethyl alcohol. When this fluid was exposed to zinc powder a faint yellow fluorescence was noted. Other enzymes contain different metal atoms and it may be possible to alter these protein structures to make iron, copper, etc. specific penetrants.

Several characteristics of these defect specific penetrants should be noted. First, they can be both inexpensive and easy to use. Second, the chelating agents are quite sensitive and must not contact their activators prior to use, i.e. the carrier fluid for the quinoline penetrant cannot be stored in a steel can. Third, they appear to be safe for human handling and in the case of the quinoline material, it has been used by law enforcement agencies to check criminal suspects for trace metal contamination.[4] Fourth, the dry fluorescence is often times much brighter than the wet fluorescence. Fifth, the fluorescence is visible only under proper ultraviolet illumination; in these experiments a Magnaflux ZB-26 light source was used. There are no doubt many other peculiarities to be noted in the use of this class of penetrants, and they will be reported in future work.

A new class of defect specific penetrants has been discussed. Two possible penetrant formulations were investigated, one based on an organic substance and the other based on a biological material. While it seems quite easy to detect through-the-thickness flaws in nonmetallic coatings on metal substrates, the design of penetrants that are activated by specific metals requires further work. Future work in this area should enumerate many possible specific penetrants, thus providing penetrants that provide the information about the depth as well as the length of surface connected flaws.

References

1. Evans, Ulick R., An Introduction to Metallic Corrosion, Edward Arnold Lt., London, 1963.

2. Crane, R. L., "A New Penetrant for Composite and Adhesively Bonded Structures," Materials Evaluation Vol. 35, No. 2, p. 54-55, 1977.

3. Welcher, F. J., ed., Standard Methods of Chemical Analysis, 6th edition Van Nostrand Co., New York, 1962.

4. "Trace Metal Detection Techniques in Law Enforcement," Pamphlet issued by the National Institute of Law Enforcement and Criminal Justice, 1970.

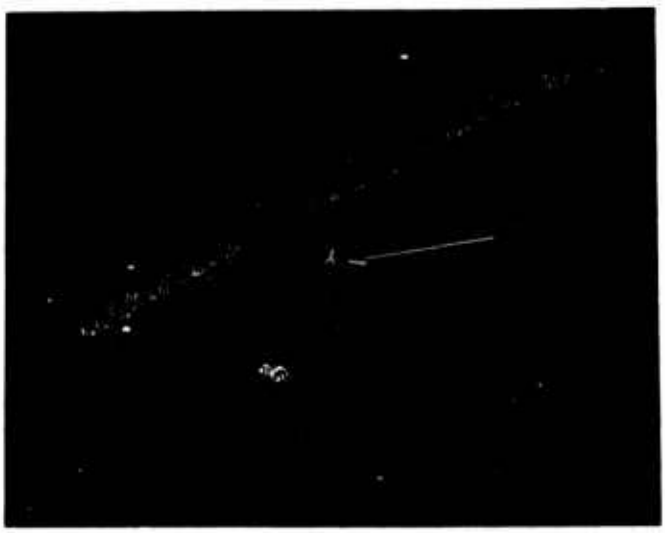


Figure 1. An indication of a through-the-thickness pore in the boron composite skin on an F-4 rudder. The extraneous indications are due to fingerprints.

OPTICAL INTERFEROMETRY FOR THE EVALUATION OF MATERIAL AND STRUCTURAL CHARACTERISTICS

B. W. Maxfield
University of California
Lawrence Livermore Laboratory
NDT Section
Materials Engineering Division
Livermore, California 94550

ABSTRACT

Of interest in many engineering applications is the change in shape of a body or the change in strain distribution within a body when it is subjected to altered external conditions. To be of maximum use, methods for evaluating these conditions should not affect performance of the body; that is, they should be nondestructive. Optical interferometric techniques have been used extensively to determine the displacement of the surface of a body between two differing states. They are both nondestructive and offer a wide field of view. Depending upon the particular method that is chosen, displacement resolution can range from about 10^{-2} μm (100 A) to 10^{3} μm (1 mm). Various forms of image shearing (displacement) interferometry are capable of measuring the derivative of the surface displacement between two states and hence can give directly the strain distribution. Many of these methods can be performed in real-time. In this case, an image of an appropriate reference state is formed and then used to compare with other states generated by a change in external conditions. We have found interferometric methods valuable for a number of specialized studies. Residual strain induced by cycling to increasingly higher pressures within the plastic flow regime has been measured in experimental pressure vessels. This information is being used to determine the optimum welding method and parameters for high energy rate forged stainless steel. Sub-surface defects and material inhomogenities frequently manifest themselves as an asymmetric or localized distortion of a body. We have used holography to search for localized deformation in fabricated components such as wound, fiber-epoxy pressure vessels. The elastic strain and thermal expansion of fabricated components have been measured using holography; this permits actual physical properties of the components to be compared with design or table values. These various applications of interferometry will be discussed in relation to practical problems and compared with other optical methods, in particular, speckle shearing interferometry.

Introduction

Optical methods for materials characterization are being used quite extensively; they are patricularly well suited for applications requiring non-contact sensing or when gathering information simultaneously over a large area is necessary . Visible light can only give direct information about the region very near the surface (about 1 μm). This direct surface information is frequently not sufficient. There are, however, conditions such as subsurface defects whose presence can cause a surface to behave different from that of a perfect body when subjected to an external stress. The usefulness of this procedure of comparing a body in a stressed and unstressed state (or at two different stress levels) depends upon the displacement produced by a given external stress: if a measurable displacement can be obtained using stresses much less than actual load conditions, then such a test can be considered non-destructive. In any case, this is an active test more like acoustic emission than the truly passive examination procedures of radiography or ultrasonics.

Most engineering structures are designed such that under normal operating stresses, the resulting displacement ranges over distances large compared to the wavelength of light (about 0.5 μm). Hence even though external stresses must be used, they can normally be considered non-destructive. Morever, various interferometric methods can give information about body performance under actual operating stress levels or in some cases can be used to determine the residual stress caused by a fatigue cycle.

In a typical measurement, the initial (relaxed or normal) state of the body is taken at the reference state. The body is then subjected to a deformation which establishes a new equilibrium surface. A variety of double exposure optical interferometric methods can be used to determine the difference between the initial and final surface.

Holography, the most sensitive of the interferometric methods, can be used to plot displacement contours separated by distances as small as one-hundredth the wavelength of light if the proper refinements are used . This means that surface deformations can be determined using an extremely small applied stress. If measurements at operating stress levels are desired, then it may be necessary to utilize some other interferometric method having reduced sensitivity to displacement. The remainder of this paper will discuss the use of holography with a comparison between holography and some other interferometric methods being given in the last section.

Holography

Figure 1 shows schematically how a hologram is produced[3]. Energy from a coherent light source (laser) is divided into two beams by a variable intensity beam splitter (BS). Each beam is focused onto a small aperature (diameter about 10 μm) to produce a good spherical wavefront over an angular spread of from 10 to 40 degrees (this so-called spatial filtering removes intensity variation from sources such as multiple reflections from optical surfaces, e.g. a beam splitter, and diffraction from dust on optical components). One of these beams illuminates the object which is often coated with a substance to make the surface a good diffuse scatterer. The other beam provides a phase coherent reference which is directed at the photographic plate where it adds vectorially with the light scattered from the object surface. The reference-to-scattered object beam intensity ratio is set to about 3:1 so that the scattered object beam varies the developed plate density about the reference level. This establishes a diffraction grating in the form of an interference pattern on the plate. When the developed plate is illuminated with a beam identical in form to the original reference beam (but usually brighter), light diffracted from this interference pattern reconstructs the original image which can then be photographed by a camera.

In order to view an object in its initial and final states, two holograms must be made and compared. This is most frequently done by exposing the first hologram, changing the external stress and then exposing the second hologram on the same photographic plate in exactly the same position. For the samll displacements of interest here, the two images appear to be precisely superimposed with a series of dark bands on or near the object. These bands result from interference of light scattered from identical points on the two, slightly displaced, images. The separation between dark bands represents about a half wavelength displacement between corresponding surface points. The exact relationship between true surface displacement and distance between dark bands depends upon the holographic setup and is derived later.

A quantitative interpretation is not as simple as might first appear. An external stress which deforms a body may also cause it to rotate or translate. These later effects must be removed from the former in order to deduce characteristics of the body material.

Interpretation of the interference pattern that results from double exposure holography has been the subject of many interesting papers[4,5]. It is readily demonstrated that the interference pattern is determined by the component of displacement bisecting the illumination and viewing directions. For other than parallel light illumination, the illumination direction will vary over the body surface. Thus, a general description of the pattern of dark bands must include, among other things, specifying the illumination and viewing directions. This makes it difficult to establish "standard" patterns.

Many problems are alleviated if one makes the viewing and illumination directions coincident[6]. A very practical setup that accomplishes this is shown in Fig. 2. The 1:1 beam splitter achieves the desired viewing and illumination but it does increase the exposure time by a factor of four for any given incident power level. Although having these directions coincident is not essential for quantitative holography, it greatly simplifies the interpretation. For instance, any symmetry in the object being viewed can show up in the interference pattern. For convenience, the analysis that follows is for the special case of coincident viewing and illumination directions.

Let $\vec{M}(\vec{r})$ be the displacement of a point on the surface of the object that occurred between two exposures and let $(\hat{i}, \hat{j}, \hat{k})$ be unit vectors in (x, y, z) coordinate system. Take $\hat{k}$ to be the illumination direction. The optical path difference caused by this displacement (assumed to be in air) is then $2\vec{M}(\vec{r}) \cdot \hat{k}$. Destructive interference (dark bands) will occur whenever the displacement between two points r_1 and r_2 satisfies the condition

$$2\,[M(r_1) - M(r_2')] \cdot \hat{k} = n\lambda \qquad (1)$$

where n is an integer.

In general, the displacement $\vec{M}(\vec{r})$ will have contributions from rigid body rotation and translation as well as that due to the desired deformation of the body being studied. As a case in point, let us consider the pressurization of a uniform elastic spherical metal shell, a segment of which is shown in Fig. 3. Here one has

$$\vec{M}(\vec{r}) = (a\hat{i} + b\hat{j} + c\hat{k}) + (\vec{r} \times \vec{\omega}) + (\kappa P\vec{r}) \qquad (2)$$

where the first term represents rigid body translation, the second rigid body rotation and the last uniform elastic expansion proportional to the internal pressure, P. Since all displacements are small, they add vectorially. The optical path difference is therefore

$$2\vec{M}(\vec{r}) \cdot \hat{k} = c + \alpha y - \beta x + \kappa P z \qquad (3)$$

where $\omega = (\alpha, \beta, \gamma)$. It is also useful to define a fringe density function

$$\vec{p} = \nabla(\vec{M}(\vec{r}) \cdot \hat{k}) \qquad (4)$$

which, for the case being considered, becomes

$$\vec{p} = -\beta\hat{i} + \alpha\hat{j} + \kappa P\hat{k} \qquad (5)$$

Already, many general statements can be made. Note that rigid body translation merely causes a constant phase shift over the entire body thereby neither changing the number of fringes nor the fringe density. Rotation produces a constant fringe density independent of the shape of the body. The only contribution to a fringe spacing that varies over the body is, in this case, the elastic deformation of the spherical shell upon pressurization.

For a sphere of radius a, $z = (a^2 - x^2 - y^2)^{1/2}$. Consequently, constant phase contours (that is, contours of constant z) are circles centered on the image of the sphere. If being viewed in the equitorial plane of the sphere, the fringes appear as concentric circles. In general, the fringes are projections of these circles on the plane normal to the viewing direction. Figure 4 is a photograph of the reconstructed image obtained from a double exposure hologram by changing the internal pressure of a spherical vessel. Rotation is almost completely absent. The circles are not quite concentric because the viewing direction (in this case, the orientation of the camera) is slightly above the equitorial plane of the sphere.

A small rotation gives interference patterns very similar to those of an anisotropic body with no rotation. There is not enough information in one view to determine anisotropic elastic properties. Two views of the same region taken simultaneously provide additional information (equations). Such a procedure has been used in evaluating welds in high energy rate forged (HERF) stainless steel pressure vessels. Figure 5 shows the reconstructed image viewing the weld region directly and by a mirror. The plastic strain distribution in the vicinity of the weld is shown in Fig. 6. The weld is rigid compared to the material in the heat affected zone (HAZ) on either side.

The thermal expansion coefficient of bodies of simple geometry can be measured quite easily using holography[7]. Typically, a 5°C temperature change between exposures is required. Coincident illumination and viewing makes data reduction much simpler but is certainly not necessary. Figure 7 shows the interference pattern obtained using the setup in Fig. 1 with about 25 degrees between illumination with parallel light and the viewing direction. This right circular cylinder was heated about 2°C between exposures. In the coincident geometry and with no rotation, one would obtain a series of vertical lines getting more closely spaced toward the edge of the cylinder. In Fig. 7 there is no indication of such an idealized pattern; this is due in part to the experimental geometry and in part to rigid body rotation.

Holography is also very useful for a qualitative examination of objects. Figure 8 shows the results of double exposure holography used to examine fiber epoxy pressure vessels[8]. Such bodies are highly non-uniform and quite anisotropic and hence yield a complex interference pattern. Good vessels, however, tend to have patterns that repeat so this can be used as a qualitative means of examining the entire surface of a body which is otherwise very difficult to inspect.

Summary

Optical methods have been used quite extensively in NDT for the qualitative inspection of components. The purpose of this paper is to point out that interferometry can be used for the quantitative determination of some useful engineering parameters of fabricated components. For example, we have measured the residual stress introduced by cycling a pressure vessel to its operating pressure and the variation of the thermal expansion coefficient over the surface of an isotropic body.

The examples discussed are applications of holography because that represents the majority of our experience to date. Other interferometric methods are being developed both here and elsewhere. Of particular interest are the various forms of speckle shearing interferometers.[9] These have two main advantages: they are less sensitive to rigid body rotation than holography and the contour interval can be set independent of the wavelength. Because two images are produced, one slightly displaced from the other, that is, sheared, the output is directly the derivative of the displacement, namely the strain. Hence, this is truly a wide field strain gauge. Disadvantages include effective loss of displacement information (although this can be obtained other ways) and a slightly more complex reconstruction process.

Our developments are motivated by the need to determine materials characteristics in finished parts and to be able to perform NDT inspections with the operator remote from the part (such as for tests in a high pressure or other hazardous environment). These are rather specialized applications but, in many cases, after proper development effort, the inspection procedures can be executed by good quality technical personnel. Quantitative as well as qualitative optical NDT methods should be considered as just some of the many tools in the NDT repertoire.

Acknowledgement

Much of the work reported here is a direct outgrowth of work begun by M. D. Meyer of this Laboratory.

Work performed under the auspices of the U. S. Energy Research and Development Administration under contract No. W-7405-Eng-48.

"This report was prepared as an account of work sponsored by the United States Government. Neither the United States nor the United States Energy Research & Development Administration, nor any of their employees, nor any of their contractors, subcontractors, or their employees, makes any warranty, express or implied, or assumes any legal liability or responsibility for the accuracy, completeness or usefulness of any information, apparatus, product or process dis-

closed, or represents that its use would not infringe privately-owned rights."

References

1. See, for example, Robert K. Erf, "Holographic Nondestructive Testing", Academic Press, NY 1974.

2. G. E. Sommargren, Applied Optics Vol. 16 (1977).

3. A very complete description is given in "Optical Holography", Robert J. Collier, Christopher B. Burckhardt and Lawrence H. Lin, Academic Press, New York 1971.

4. A. E. Ennos, J. Sci. Instrm. (J. Phys. E) Series 2 Vol. 16, 731 (1968).

5. Karl A. Stetson, J. Opt. Soc. of America, Vol. 64, 1 (1974).

6. M. D. Meyer and H. Spetzler, "Material Properties and Strain Determination Using Holographic Interferometry", Sandia Laboratories Report SLL-73-5325.

7. Lee O. Heflinger, Ralph F. Wuerker and Hartmut Spetzler, Rev. Sci. Instrm. Vol. 44, 629 (1973).

8. M. D. Meyer and T. E. Katayanagi, Journal of Testing and Evaluation, Vol. 5, 47-52 (1977).

9. Y. Y. Hung, R. E. Rowlands and I. M. Daniel, Applied Optics Vol. 14, 618 (1975).

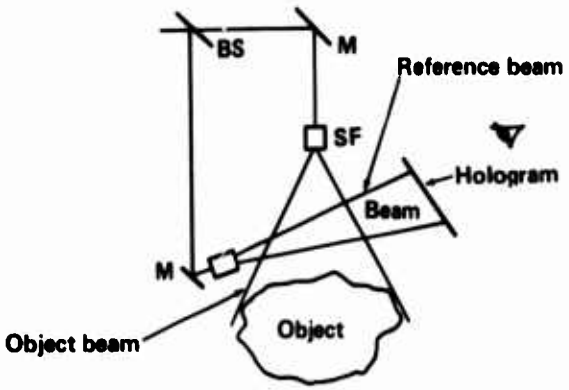


Figure 1. Typical minimum setup required to produce a hologram; components and their function are described in the test.

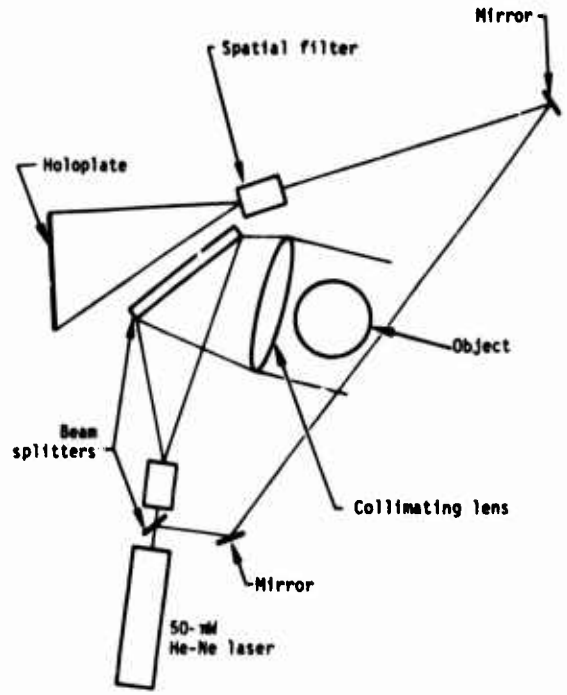


Figure 2. A holographic setup utilizing coincident illumination and viewing directions.

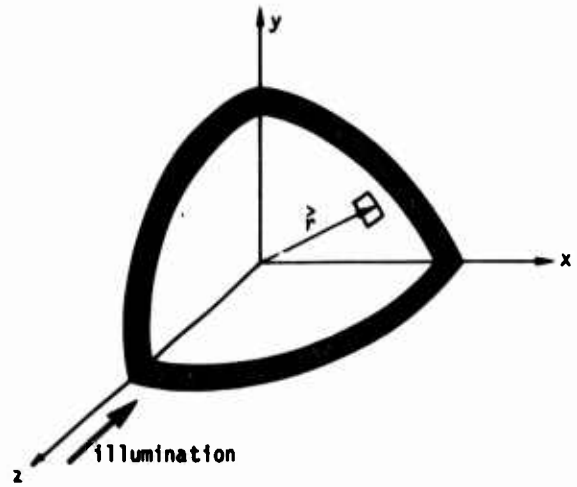


Figure 3. Coordinate system used to calculate the fringe pattern for coincident illumination and viewing of a pressurized spherical shell.

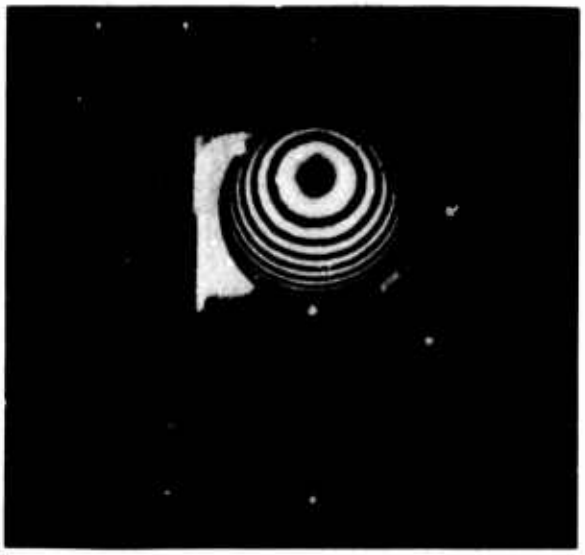


Figure 4. Reconstructed image of the interference pattern for the pressurization of a spherical vessel.

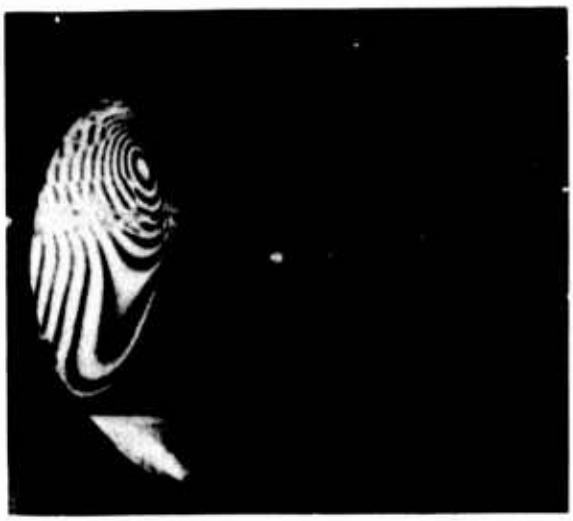
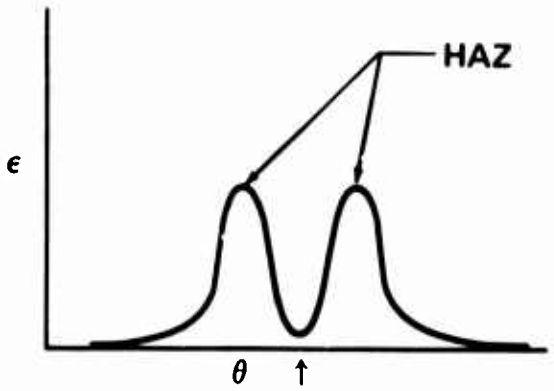


Figure 5. The reconstructed image of a two-view hologram of a portion of a diametrical weld in a stainless steel pressure vessel.



Plastic strain in the vicinity of a weld.

Figure 6. Plastic strain distribution in the vicinity of a diametrical weld after pressurization significantly above proof pressure; plastic flow has taken place in the heat affected zone (HAZ).

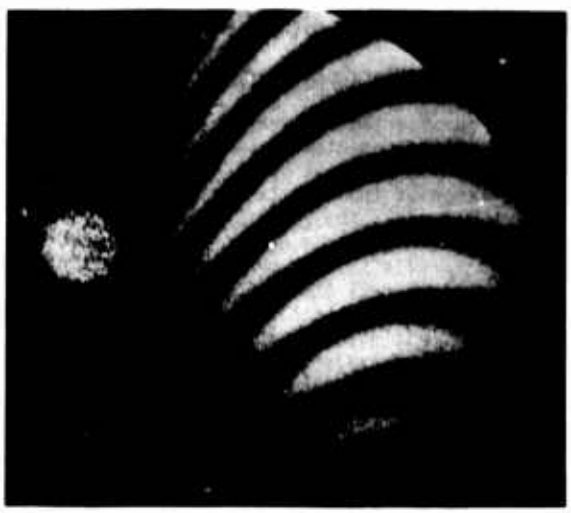


Figure 7. The interference pattern obtained by changing the temperature of a cylindrical specimen by about 2°C, but in this case coincident illumination and viewing was not used. Note that there is essentially no evidence of cylindrical geometry.

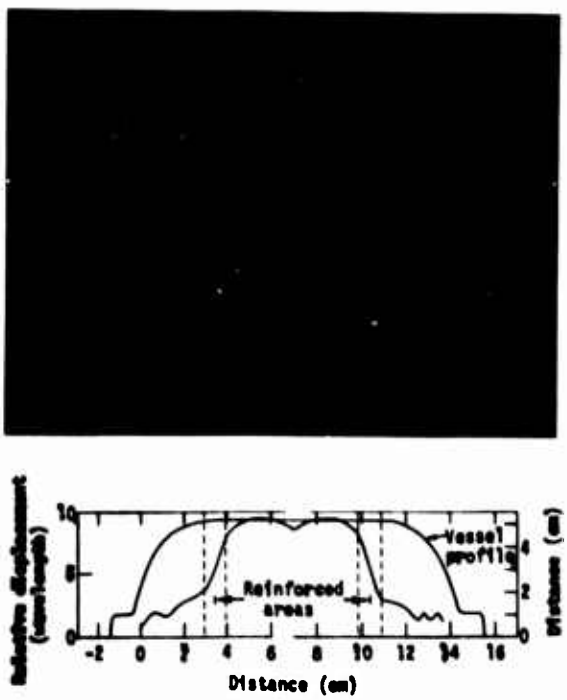


Figure 8. Reconstructed image of the interference pattern resulting from pressurization of a fiber-epoxy pressure vessel.

FRACTURE MECHANICS OF JOINTS

K. L. DeVries
University of Utah
Salt Lake City, Utah

Garron P. Anderson
Thiokol Chemical Corporation
Brigham City, Utah

ABSTRACT

Almost every engineering design requires that component members be connected. A disadvantage of mechanical connections such as bolts, screws or rivets is that they do not uniformly distribute the load; hence large local stresses result. This problem can often be reduced by joining the members adhesively. Major problems with adhesives that have tended to limit their wider usage include: (1) how the strength of an adhesive and the joint in which it is used can reliably be predicted, and (2) what factors tend to limit the strength of an adhesive joint and how they might be eliminated. It is the intent of the authors to show how fracture mechanics might be used to develop a rational philosophy and methodology that will aid in overcoming these problems. The adhesive fracture mechanics approach, in the opinion of the authors, holds the best potential of:

(1) Identifying and/or designing the best tests for evaluating a given adhesive
(2) Defining the best and most meaningful fundamental parameters by which adhesives might be characterized, and
(3) Making use of these parameters to systematically and optimally design joints and predict their strength and performance.

This presentation reviews the development of the fracture mechanics models, describes several tests that have been used to obtain model parameters, and reviews means by which these might be used to predict the strength of practical joints.

Introduction

The structural designer is often confronted with the question, "Under what conditions would this engineering element or part fail?" To answer this question, one must first decide what constitutes failure. While most of us normally associate failure with a part breaking into two or more pieces, conditions other than fracture can make a part inoperative or at least render its operation unsatisfactory. For example, floor joists may have such large elastic deflections that the floor is uncomfortably springy and soft at stresses far below that required to cause the joists to rupture. People walking or children playing on such a floor will cause chairs, tea cups, etc. to "dance" around annoyingly. As a consequence, floors are generally constructed much more sturdily than would be required from simple strength considerations. The designs of many such items are deformation-limited rather than strength-limited. Similarly, excessive plastic deformation may render many ductile machine elements inoperative. Plastic deformation often precedes fracture and may, in fact, nucleate the microscopic cracks that ultimately result in macroscopic fracture. Even when fracture is the primary mode of failure, the prediction of conditions under which it will occur is not always easy or straight-forward. We are, for example, aware that repeated loading at stresses of as little as 50% of that required to cause static failure can ultimately result in "fatigue" fracture. In the case of composite and bonded joints the concept of interfacial failure is introduced. Most of the past work has been done on cohesive failure; however, one of the central themes of this text will be that much of the knowledge and information obtained on cohesive failure is, in fact, directly transferable to adhesive conditions. They are, in our view, both special cases of the same basic phenomenon. Here we will attempt to develop a rational systematic approach to the analysis and design of adhesive interfaces.

The Continuum Approach to Design

It is important to realize that failure of structural components has been characteristically approached in two ways by the analyst.[1] Before recognition of the importance of inherent flaws in the material, the analyst relied upon one of several average stress or strain criteria, e.g., maximum tensile stress, maximum principal strain, maximum octahedral stress, or others, depending usually on experimental evidence and experience. While the existence of microscopic or atomistic "holes" in materials was recognized, it was generally assumed that their presence was of no design consequence and, as long as material production control techniques were sufficiently reliable to produce microvoids of a small mean size with a low dispersion around the mean size, the use of an average stress or strain criterion was justified.

Hence, thinking of the material as a continuum (and taking the case of a normal tensile specimen as an example), the maximum tensile stresses at failure measured in successive specimens of the same materials are likely to be quite consistent. There is always some reasonably uniform distribution of small flaws present, whose size is related to the type of material and method of material fabrication, e.g., casting voids, filler surfaces, boundaries of spherulites, grains, and other phases. A polymer which is mixed rapidly contains finely dispersed air bubbles; even with degassing some distribution of flaws will exist on some dimensional scale. The average tensile

strength, therefore, reflects the presence of flaws, and the dispersion of strength might be viewed as an indication of the uniformity of the flaw distribution. Because most standard materials are made under reasonably strict quality control conditions, it is not surprising to find that some sort of consistent (average) stress or stress-functional criterion can be used to predict failure.

Under more complicated conditions (such as the multiaxial stressing of a rotor disk), it is frequently customary to assume that the failure criterion is based on the octahedral shear stress (τ_{oct}), which includes the three principal stresses and is defined as

$$\tau_{oct} = c\sqrt{(\sigma_1-\sigma_2)^2 + (\sigma_2-\sigma_3)^2 + (\sigma_3-\sigma_1)^2} \qquad (1)$$

Assuming that this criterion (often called the Von Mises yielding criterion) applies, one predicts failure whenever a combination of principal stresses at any point in the part exceeds τ_{oct}. And how is τ_{oct} determined? If Equation (1) is a universal failure criterion, it must also apply to the failure of a simple uniaxial tensile specimen having stresses $\sigma_1 = \sigma_{tens}$, and $\sigma_2 = \sigma_3 = 0$. Thus, substituting into Equation (1), one finds that

$$\tau_{oct} = c\sqrt{2\sigma_{tens}^2} \qquad (2)$$

so that upon solving for the desired constant c and resubstituting into Equation (1), one finds that failure is expected under a multiaxial principal stress combination whenever at some point in the body

$$\sqrt{(\sigma_1 - \sigma_2)^2 + (\sigma_2 - \sigma_3)^2 + (\sigma_3 - \sigma_1)^2} \geq \sqrt{2\sigma_{tens}^2} \qquad (3)$$

In the more general average stress criterion case denoted as region I in Fig. 1, the failure criterion based upon average principal stresses would have the form

$$F(\sigma_1, \sigma_2, \sigma_2) \geq \sigma_{F_{cr}} \qquad (4)$$

where F is some function of the principal stresses at a point in the material and $\sigma_{F_{cr}}$ is the value of F at failure.

On the other hand, there are conditions in which discrete flaws, substantially larger than the uniform size distribution normally present, can exist in the material. Such inherent flaws may arise from localized corrosive attack, improper fabrication, micro-deformation associated with casting or forming operations, cyclic loading, accidental surface nicks or cuts or many other sources. Because they are discrete, usually relatively sharp, and larger than the surrounding voids, they may induce additional stress concentrations and provide loci of cohesive fracture initiation.

Ordinary elastic stress concentration factors are used if the flaw shape is not cracklike. However, if the inherent flaws are cracklike, stress concentration factors are useless, because linear elastic theory predicts an infinite concentration factor in the vicinity of a crack tip. Thus, the local stress value will exceed the finite allowable stress experimentally measured for the base material, containing only the reasonably uniform distribution of inherent voids. The strength degradation in such a situation is illustrated by region II of Fig. 1.

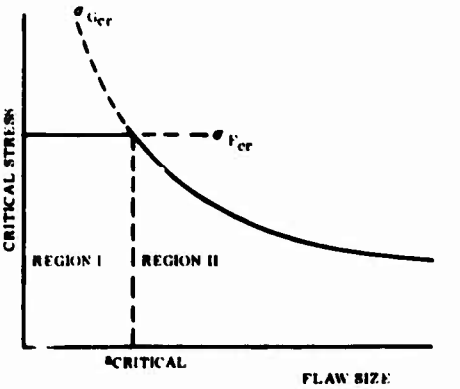


Figure 1. Failure surface as a function of flaw size.

Griffith [2] provided the first estimate of degradation as a function of the flaw size by considering the problem of a small, through-line crack in a thin sheet of brittle material (illustrated in Fig. 2a). Theoretically, the stress at the crack tips is (mathematically) infinite for an elastic body, thus giving rise to an infinite local stress at even small applied loadings--a degree of concentration for which Equation (4) is useless. Griffith avoided this problem by considering changes in the strain energy (volume integral of stresses squared), which remains finite. He proposed, in essence, that cohesive fracture would commence at a critical applied stress σ_{cr}, when the incremental loss of strain energy of deformation with increasing fracture area just equaled the work required to create a new fracture surface.* Hence in this case, with the elastic strain energy of deformation (U) due to the presence of the crack of length 2a being $U = \pi a^2\sigma^2/E$, one would have fracture whenever

$$\frac{\partial U}{\partial A}\Big|_{\sigma} \geq T \qquad (5)$$

* Actually, Griffith's original hypothesis was that the new criterion of rupture is obtained by adding to the theorem of minimum energy the statement that the equilibrium position, if equilibrium is possible, must be one in which rupture of the solid has occurred, if the system can pass from the unbroken to the broken condition by a process involving a continuous decrease in potential energy.

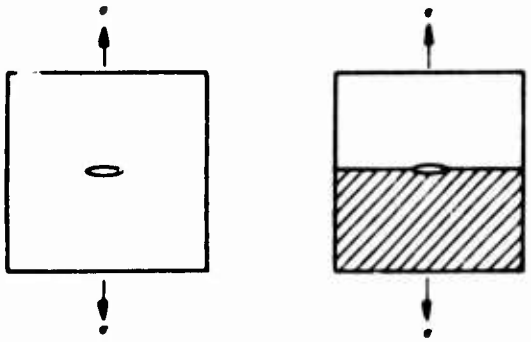
or

$$\frac{\partial}{\partial A}\left[\frac{\pi a^2 \sigma^2}{E}\right] > \frac{\partial}{\partial A}(4aT) \qquad (6)$$

where E is Young's modulus, A is fracture area (both debonded surfaces included), and T is the surface tension. That is to say, the strain energy of deformation lost in a brittle material as the crack extends is converted into the work to create the new fracture area. From Equation (6), the finite critical applied stress is determined as

$$\sigma_{cr} = \sqrt{\frac{2ET}{\pi a}} \qquad (7)$$

and applies in region II of Fig. 1.



(a) Cohesive fracture uniform material.

(b) Adhesive fracture bimaterial.

Figure 2. Comparison of adhesive fracture with cohesive fracture in a Griffith model.

Strictly speaking, the Griffith expression holds only for "brittle materials," where the only energy required to create new surface is that needed to rupture bonds (he experimented with glass). For most materials of structural interest in engineering, this is not the case.

Irwin [3] and Orowan [4] modified the original Griffith formulation by adding a term to account for the plastic energy dissipated as the crack grows. The condition for crack growth then becomes

$$\delta W + \delta U \geq \delta T + \delta \psi = \delta \Gamma \qquad (8)$$

where δU and δT are the elastic strain energy and increase in surface energy, respectively; δW is the change in external work during crack growth, δA; and $\delta \psi$ is the plastic flow energy dissipated during crack growth. $\delta \Gamma$, which we will call the fracture energy, then includes all terms required to create the fracture surface. For metals, plastics, and most other nonbrittle materials $\delta \psi$ is so much larger than δT that the latter can be neglected. Assuming the energy dissipated in crack growth is proportional to the new crack area, we can define a specific fracture energy G_c (often called the critical energy release rate) such that $\delta \Gamma = G_c \delta A$. G_c, of course has the units of energy per unit area, e.g., ergs/cm^2, in-lb/in.^{2}, etc. If we assume G_c is a material property which can be obtained from standard tests, the problem of linear elastic fracture mechanics becomes one of performing a stress analysis and solving for δU.

Williams [6] has suggested a related and very useful formulation of the Griffith problem; namely, that one might view G_c as a compilation of several effects. Thus

$$G_c = (G_c)_B + (G_c)_{KE} + (G_c)_p + (G_c)_{Ve} + \ldots$$

or

$$\gamma = \gamma_B + \gamma_{KE} + \gamma_p + \gamma_{Ve} \qquad (9)$$

where the subscripts B, KE, p, and Ve represent the contributions to G_c due to brittle (surface free energy), kinetic energy, plastic, and viscoelastic effects, respectively. In principle, any other contribution might likewise be added.

The combination of the region I and region II criteria, one flaw-insensitive (region I stress function) and the other dependent upon flaw size (region II fracture criterion), thus permits the designer to determine a maximum allowable design stress for either form of stress distribution.

Existing flaws of dimension greater than the critical flaw size illustrated in Fig. 1 become unstable at stresses lower than σ_{Fcr} in compliance with the region II criterion. Once it is recognized that Equations (4) and (5) are not competing failure criteria, but instead are complementary, it is possible to approach the design against failure in a more direct manner.

The energy balance to region II failure is described more fully in a recent text prepared by the authors. [7] We note that in the fracture literature one frequently encounters another approach based upon stress intensity factors K_i. The subscript i is used to designate direction of motion of crack surfaces relative to each other. We refer the reader to Reference 7 and 8 for a more complete discussion. However, it is appropriate here to establish certain basic relationships encountered in fracture mechanics.

We associate a mode I loading with displacements for which the debond surfaces in the debond tip vicinity move directly apart. Mode II is characterized by displacement in which the debond surfaces slide over one another perpendicular to the leading edge of the debond. In mode III, the debond faces slide over one another parallel to the leading edge of the debond. By superimposing combinations of these three modes, any debond surface displacement can be produced.

In terms of the coordinates shown in Fig. 3, the local stresses in the vicinity of a crack in a sheet of linear elastic material are

$$\sigma_{xx} + \frac{K_I}{\sqrt{2\pi r}} \cos\frac{\theta}{2}\left[1 - \sin\frac{\theta}{2}\cdot\sin\frac{3\theta}{2}\right], \quad (10)$$

$$\sigma_{yy} = \frac{K_I}{\sqrt{2\pi r}} \cos\frac{\theta}{2}\left[1 + \sin\frac{\theta}{2}\cdot\sin\frac{3\theta}{2}\right], \quad (11)$$

$$\tau_{xy} = \frac{K_I}{\sqrt{2\pi r}} \sin\frac{\theta}{2}\cdot\cos\frac{\theta}{2}\cdot\cos\frac{3\theta}{2} \quad (12)$$

for the state of plane stress

$$u = \frac{K_I}{\mu}\sqrt{\frac{r}{2\pi}}\cos\frac{\theta}{2}\left[\frac{1-\nu}{1+\nu} + \sin^2\frac{\theta}{2}\right], \quad (13)$$

$$v = \frac{K_I}{\mu}\sqrt{\frac{r}{2\pi}}\sin\frac{\theta}{2}\left[\frac{2}{1+\nu} - \cos^2\frac{\theta}{2}\right] \quad (14)$$

where μ is the shear modulus, ν is Poisson's ratio, and K_I represents the stress intensity factor for the crack opening mode. For the case of plane strain the displacement components are

$$u = \frac{K_I}{\mu}\sqrt{\frac{r}{2\pi}}\cos\frac{\theta}{2}\left[1 - 2\nu + \sin^2\frac{\theta}{2}\right] \quad (15)$$

$$v = \frac{K_I}{\mu}\sqrt{\frac{r}{2\pi}}\sin\frac{\theta}{2}\left[2 - 2\nu + \cos^2\frac{\theta}{2}\right] \quad (16)$$

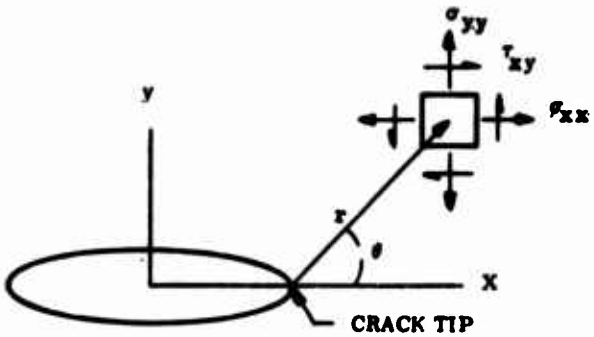


Figure 3. Crack tip coordinates.

The value of K_I depends on the exact nature and dimension of the crack. It has been proposed that the value of K_I at failure might be used as a failure criterion. It is hypothesized that failure occurs when the K_I for any crack and loading geometry reaches a critical value, K_{Ic}. This critical stress intensity factor K_{Ic} (now viewed as a material property) is sometimes referred to as the fracture toughness of a material and has the dimensions of stress x $\sqrt{\text{length}}$. It can be shown that this criterion is in all respects equivalent to the Griffith-Irwin theory and, in fact, G_{Ic} and K_{Ic} are related for linear elastic materials by

$$G_{Ic} = \frac{1-\nu^2}{E}\left[K_{Ic}^2\right] \quad (17a)$$

for plane strain and

$$G_{Ic} = \frac{K_{Ic}^2}{E} \quad (17b)$$

for plane stress. In addition, for linear elastic materials statically loaded, the following relationships exist:

$$2\frac{\partial U}{\partial A} = G = \frac{1}{E}\left[K_I^2 + K_{II}^2 + (1+\nu)K_{III}^2\right] \quad (18)$$

for plane stress and

$$2\frac{\partial U}{\partial A} = G = \frac{1-\nu^2}{E}\left(K_I^2 + K_{II}^2 + \frac{K_{III}^2}{1-\nu}\right) \quad (19)$$

for plane strain. At the critical loads Equation (18) becomes

$$2\gamma_c = G_c = \frac{1}{E}\left(K_{Ic}^2 + K_{IIc}^2 + (1+\nu)K_{IIIc}^2\right) \quad (20)$$

For more complicated geometries, energy balance concepts are normally preferred (at least by the authors) because of the direct association with the laws of physics.

In the previous equations we have used the convention that the surface area A refers to the surface area generated on both surfaces of the crack. This definition is, more or less, arbitrary and leads to no confusion as long as the material property, γ_c, and energy release rate in the body being analyzed have used a common definition of surface area. In fact we have adopted the convention that A refers to the surface area generated by one surface of debond when referring to adhesive fracture. In this case $\gamma_a = G_{ca}$.

Adhesive Fracture Energy

The previous remarks, and Fig. 1, were presented in the context of cohesive fracture. It can be demonstrated that a bonded joint can be treated in a similar manner. The similarity of adhesive and cohesive fracture (illustrated in Figs. 2a and 2b, respectively) from a continuum mechanics viewpoint, and particularly the energy concept of fracture, has been elucidated by Williams [5]. In both cases it is well known that an elastic stress singularity may exist at a sharp geometric discontinuity such as a wedge point, crack tip, or terminus of debond, which depends upon the local boundary conditions, method of loading, and properties of the material or materials. In principle, one finds that for either adhesive or cohesive fracture a general equation of the Griffith type can be written, namely,

$$\sigma_c = \sqrt{\gamma}\, f(E_i, \nu_i)g(a) \quad (21)$$

where g(a) includes geometric and stress intensity factors.

Although the adhesive fracture energy γ_a is in the purest sense a material property (e.g., it depends on surface preparation) within a continuum mechanics interpretation, it can denote an adhesive system parameter which may be used subsequently for predicting adhesive fracture

The restriction of a homogeneous system is certainly not necessary to apply energy methods to region II failure, as long as one can properly account for energy dissipation through the entire system. Thus the application to adhesively bonded systems is direct. In order for debond to propagate over an area δA for a given applied load, the following energy balance must be satisfied:

change in work input - change in stored energy - energy dissipated

$\geq$ energy required to debond an area δA

or, in symbolic form

$$\delta W - \delta U - \delta E_d \geq \gamma_a \delta A . \qquad (22)$$

A parameter called the adhesive fracture energy, γ_a, is included in the energy balance equation to account for the energy in a system that is required to separate two materials. If γ_a is interpreted as the energy per unit area required to break bonds, its magnitude will depend only upon the number of bonds existing per unit of debond surface area and the average energy required to break a single bond. Thus γ_a for a linear elastic system should be a property of the adhesive bond strength only, independent of loading mode. As with cohesive fracture energy, dissipative energy is included in the adhesive fracture energy, γ_a, and the debond surface area is assumed planar. The γ_a values obtained from laboratory testing, therefore, may be orders of magnitude greater than the energy required to break bonds. The γ_a values now represent the strain energy decrease per unit of planar (projected) debond surface area in the process of separating the two materials. This interpretation of γ_a is the one used throughout this paper.

In the absence of input work (fixed displacement boundary) and energy dissipation mechanisms such as plastic yielding or viscous flow remote from the debond tip as debond propagates, Equation (22) reduces to

$$-\delta U \geq \gamma_a \delta A . \qquad (23)$$

In the limit as the debond area approaches zero, the failure criterion is written in terms of energy release rate $\partial U/\partial A$, and adhesive fracture energy γ_a, in the form

$$-\frac{\partial U}{\partial A} \geq \gamma_a . \qquad (24)$$

As shown in Reference 7, if the boundary loads are in terms of surface tractions, the failure condition becomes

$$\frac{\partial U}{\partial A} \geq \gamma_a . \qquad (25)$$

Numerical methods for calculating the energy release rate are also discussed in Reference 7.

Combinations of mode I and mode II loading are very common in adhesive systems, since fracture may follow the bond line, take place within the adhesive or alternate between the two but in any case usually propagates approximately parallel to the bond surface. Several authors, including Anderson et al.[9], Chang[10], and Trantina[11] have noted a dependence of adhesive fracture energy (or critical stress intensity) on loading mode.

Chang[10] discusses test results using single lap shear joint specimens. By varying the length of overlap in this specimen, it is possible to vary the ratio of mode I and mode II loading at the adhesive adherend interface. It was found that the adhesive fracture energy for a mode II loading was greater than that for a mode I loading. A Griffith analysis of such a joint agreed well with the experiment if the adhesive fracture energy γ_a was assumed to be of the form

$$\gamma_a = K_s \gamma_a^{(s)} + K_t \gamma_a^{(t)} \qquad (26)$$

where K_t and K_s are the fractions of the total strain energy attributed to tensile and shear loading of the joint, respectively, and $\gamma_a^{(t)}$ and $\gamma_a^{(s)}$ are the adhesive fracture energies as measured with pure mode I and mode II loadings, respectively.

Trantina[11] used slant edge-cracked plate tests to induce different portions of mode I and mode II loading over a wide range of slant angles and cracklengths. By varying the angle between the adhesive layer and the load line in these specimens, combined-mode fracture toughness values were determined. The trend in these data clearly indicates: (1) a significant increase in the fracture energy as the mode II loading is introduced, (2) the mode II fracture energy is larger than that for mode I (perhaps by as much as a factor of two or more), and (3) a failure criterion that assumes a linear relation between mode I and mode II fracture energies is not applicable for Trantina's system.

Extensive testing has been completed by the authors[12,13] on one particular adhesive system to demonstrate the importance of mode dependency on evaluation of bond strenth. In this study, it is shown that the mode γ_a value is more than a factor of two greater than the mode I value and that the mode III value was greater by more than a factor of three.

Although the γ_a data show large changes due to loading mode, the engineering implications are not as severe as one might suspect, since the critical stresses are generally related to the square root of γ_a. Thus, if the actual γ_a value is somewhere between the modes I and II values (for instance, 40% higher than the mode I value), a critical stress predicted using the mode I value would be conservative by less than 20%.

A second complication which occurs in adhesive fracture mechanics is the apparent time and temperature dependency of adhesive fracture energy,

even for systems whose bulk behavior is nearly linearly elastic. In linear elastic cohesive systems, no time dependency is noted. However, as noted by Irwin[3], "time-effects are expected in adhesive-joint separation, both from the strain-rate sensitivity of high polymer adhesives and from the possible influence of moisture and other environments."

Thus, with the present state of the art, one must select laboratory tests for which temperature, loading rate, and loading mode duplicate as nearly as is possible those in the bondline being analyzed. If there is difficulty in obtaining the desired load rate and/or temperature in the laboratory, it is possible to test specimens at a number of different load rates and temperatures. Then by applying a time-temperature shift of the resulting γ_a data in a manner similar to that used in obtaining relaxation moduli for viscoelastic materials one can obtain a master γ_a versus log (reduced time) [log (time-temperature shift factor)] curve which may cover many decades of time.

Experimental Procedures

To this point we have attempted to develop the basic premises and analytical approach on adhesive fracture mechanics. A number of different sample configurations have been proposed and tested as means of determining critical adhesive parameters. In principle, any specimen for which the energy release rate can be calculated and the load at which debond propagates can be determined could be used to evaluate γ_a (or G_{ca}). In practice, however, certain geometries have the advantage of being more analytically tractable and/or more convenient in terms of experimental sample preparation and testing. Testing configurations that the authors and others have found particularly useful include, the blister test[14,15], cone tests (pull out and twist)[16], peel tests[17-20], lap shear[21], cantilever tests[22-24], tensile specimens with the adhesive joint at various angles to the tensile axis[25,26], parallel plates loaded in shear and cleavage[27] as well as several others[7].

Specific Applications

The fundamental framework of adhesive fracture mechanics have been developed and a number of potential test methods have been tested. We are now in a position to apply these to specific problems. In the time allocated for this presentation no attempt will be made to be all inclusive in giving a listing of some of the problems studied. (In the oral presentation, a few of the studies listed below will be very briefly described.) It is hoped that these problems will serve to show the versatility of the fracture mechanics approach to adhesive failure analysis. The authors like to feel that this approach is not a rigid, narrow set of rules for testing and analysis. Rather, it appears to them that it is a more systematic approach philosophy to adhesive problems that facilitates the acquisition of the most meaningful information from as simple, convenient, and straightforward a test as possible for the particular adhesive of interest. The information thus obtained may then be utilized for prediction of performance in other geometries that may be pertinent. It is hoped that the information thus obtained may then be utilized for prediction of performance in other geometries that may be pertinent. It is hoped that the examples given might act as a stimulus to help the readers design or choose tests well suited for their particular adhesive systems.

We would, therefore, like to list a few areas of past study with references so that those with sufficient interest might refer to the original publications for details of the study. This will be followed by brief fracture mechanics analysis for the conditions for debonding between the layers in a laminate composite.

Fracture mechanics methods have been applied to:

- the problem of mode dependence (16, 25, 28, 29)
- the effect of adhesive thickness (7)
- The evaluation of dental adhesives (30)
- an evaluation of barnacle cement (31)
- an evaluation of structural joints (32-33)
- the failure under fatigue of adhesive joints
- the failure of joints subjected to environmental effects (34)
- and many other studies (7, 30-35)

An example might be helpful to demonstrate the techniques of adhesive fracture mechanics, and in particular how it might be used to analyze the behavior of systems that do not readily lend themselves to closed form analytical solutions.

The procedure used to obtain an energy release rate was to calculate the strain energy stored in the laminate for two slightly different debond areas. The strain energy release rate is then approximately equal to the difference in the two strain energy values divided by the difference in total debond area. In equation form

$$\frac{\partial U}{\partial A} \sim \frac{\Delta U}{\Delta A} = \frac{U_1 - U_2}{A_1 - A_2} = \frac{1571.945 - 1570.950}{\pi[(0.100)^2 - (0.104)^2]} \tag{27}$$

$$= 2730 \text{ in. lb/in}^2$$

The adhesive fracture mechanics technique has been demonstrated here for a rather simple geometry and loading condition. However, with present finite element capability any geometry and loading system could be analyzed provided sufficient computer capacity is available. That is, with an arbitrary orthotropic geometry and a given set of displacement, stress, force, thermal or acceleration loads, an energy release rate can be found. If the γ_a value has been determined from a laboratory test, the size flaw which would propagate under the given loading system could then be determined.

The adhesive fracture mechanics approach can be briefly outlined with the aid of Figs. 4, 5 and 6. Figure 6 shows schematically a three-layer laminate composite with a small region of debond between two of the layers. Although this system is of a comparatively simple geometry, it does not readily lend itself to analytical stress

analysis. This does not pose a major problem, however, since numerical methods are available that (with the aid of a computer) make accurate determinations of stress and strain possible for almost any reasonable geometry. In the case of interest here a finite element analysis yielded the axial stress in the vicinity of the crack as shown in Fig. 5 and the crack opening displacement represented in Fig. 6. These can in turn be used to calculate the strain energy present in the system due to the applied loading and how this varies with crack (debond) size. If the material is linearly elastic (as we assume in the case here) only the stresses need be determined in order to calculate the strain energy. The method can, however, be applied equally well to other constitutive relationships as well.

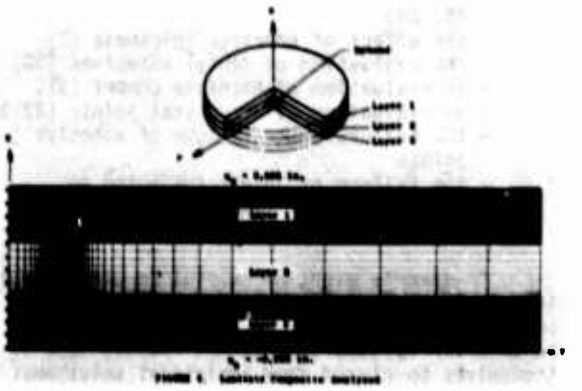


Figure 4. Laminate composite analyzed.

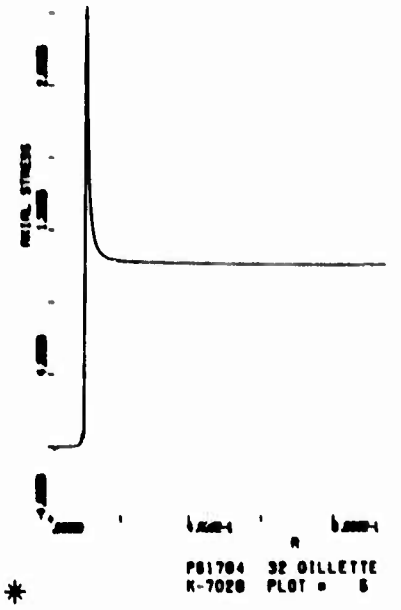


Figure 5. Axial stress in Layers 2 and 3 adjacent to debond plane.

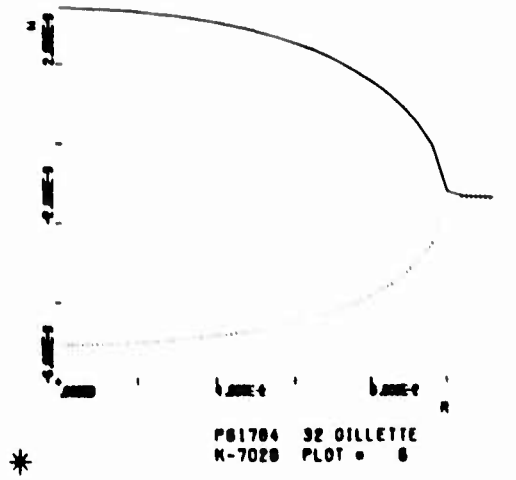


Figure 6. Crack opening displacement.

Since it is known that the strain energy release rate is proportional to the square of the applied displacement (0.01 in. in this case), the energy release rate for other applied displacements could be calculated for the geometry analyzed as

$$\frac{\partial U}{\partial A} = 2730 \left(\frac{U_z}{0.01}\right)^2 \qquad (28)$$

The adhesive fracture energy is equal to the value of energy release rate at the load which causes a debond to propagate. U_{crit}, the adhesive fracture energy is given by

$$\gamma_A = 2730 \left(\frac{U_{crit}}{0.01}\right)^2 \qquad (29)$$

One of the challenging problems associated with failure prediction is in determing the critical load as opposed to the maximum load. If tests are being conducted at a constant load rate (displacement or force), it is possible to build up considerable loads after debond initiation. Acoustic emission techniques have been used successfully for particular systems. However, in general, more definitive techniques are required.

We have attempted to outline and demonstrate the utility of adhesive fracture mechanics to: (1) evaluate and compare adhesives through a comparison of their fundamental material properties; (2) predict loading conditions for failure, if these properties are known (perhaps from standard tests); (3) optimize adhesive configuration and adhesive joint design for a given adhesive system; and (4) use as a quality assurance tool in conjunction with NDE flaw detection techniques.

In the latter case, if the adhesive system properties such as moduli and specific fracture energy are known, along with the loads to which the system will be exposed it should be possible to predict flaw sizes that will result in failure.

The problem then becomes one of locating and determining the size of flaws in the structure. Those with flaws larger than this critical size would either be discarded or repaired.

One of the authors is presently applying techniques similar to those described here for the space shuttle rocket motor case design. A critical problem is: What flaw size can be tolerated and can flaws of this size be reliably detected by NDE methods. It appears to the authors that a critical point for the satisfactory solution to problems of this type is improved NDE methods detection for small flaws or regions of debond.

Acknowledgements

Portions of the work described here were supported by the National Science Foundation Grant #DMR 74-03271 and Thiokol Chemical Corporation.

References

1. M. L. Williams, J. Adhes, 4, 307-332 (1972).

2. A. A. Griffith, Proc. Int. Congr. Appli. Mech., 1st, Delft, Holland, page 55-63 (1924).

3. G. R. Irwin, J. Appl. Mech. Trans., ASME 24, 361 (1957).

4. E. Orowan, Rep. Prog. Phys., 12, 185 (1949).

5. M. L. Williams, Proc. Int. Congr. Appl. Mech., 5th, 451-464 (1966).

6. M. L. Williams, Int. J. Fract. Mech., 1(4), 202 (1966).

7. G. P. Anderson, S. J. Bennett and K. L. DeVries, Analysis and Testing of Adhesive Bonds, Acad. Press, New York (1977).

8. P. E. Paris and G. C. Sih, ASTM-STP 381 (1964).

9. G. P. Anderson, K. L. DeVries, and M. L. Williams, J. Colloid Interface Sci., 47(3), 600 (1974).

10. M. D. Chang, Ph.D. Dissertation, Mech. Engr. Dept., University of Utah, Salt Lake City, Utah (1972).

11. G. C. Trentina, J. Compos. Mater., 6, 371 (1972).

12. G. P. Anderson, Ph.D. Dissertation, Mech. Engr. Dept., University of Utah, Salt Lake City, Utah (1973).

13. K. L. DeVries, M. L. Williams and M. D. Chang, Exp. Mech., 4(3), 89 (1974).

14. M. L. Williams, J. Appl. Polym. Sci., 13, 29-40 (1969).

15. H. Dannenberg, J. Appl. Polym. Sci., 5, 125-134 (1961).

16. G. P. Anderson, K. L. DeVries and M. L. Williams, Int. J. Frac., 10(5), 565 (1974).

17. J. J. Engel and R. N. Fitzwater, Adhesion and Cohesion, (T. Weiss, Ed.) 89-100, Elsevier, Amsterdam (1962)

18. T. Hata, M. Gamo, and Y. Doi; Kobunshi Kagaku, 22, 152 (1962); Chem. Abstr., 64(6), 833 (1966).

19. G. P. Anderson, K. L. DeVries, and M. L. Williams, Exp. Mech., 24, 109 (1976).

20. A. N. Gent and G. R. Hamed, J. Adhesion, 1, 91, (1975).

21. S. Mostovoy and E. J. Ripling, Final Report, Contract No. N0019-74-C-0274, Materials Research Laboratory, Glenwood, Illinois (1974-75).

22. W. D. Bascom and R. L. Cottington, J. Adhes., 1, 333-346 (1976).

23. M. D. Chang, K. L. DeVries and M. L. Williams, Effect of an Elastic Plastic Adhesive Layer on Adhesive Fracture, UTEC DO 71-188, University of Utah (1971).

24. W. D. Bascom, R. J. Jones and C. O. Timmous, Mixed Mode Fracture of Structural Adhesives In Adhesion Science and Technology (L. H. Lee, Ed.), 9B, Plenum Press, New York, 501 (1975)

25. A. N. Gent, Rubber Chem. Tech., 47 (1974).

26. E. J. Ripling, S. Mostovoy, and R. L. Patrick, Mater. Res. Std., 129, (1964).

27. E. J. Ripling, S. Mostovoy and R. L. Patrick, Am. Soc. Test. Mater., STP 360, 5 (1964).

28. M. L. Williams, K. L. DeVries and R. R. Despain, J. Dent. Res., 52(3), 517 (1973).

29. R. R. Despain, K. L. DeVries, R. D. Luntz and M. L. Williams, J. Dent. Res., 52, 674-679 (1973).

30. A. N. Gent, P. B. Lindley and A. G. Thomas, J. Appl. Polym. Sci., 8, 455 (1964).

31. W. D. Bascom, R. L. Cottington, R. L. Jones and P. Peyser, J. Polym. Sci., 19, 2545-2562 (1975).

32. A. N. Gent, R. L. Henry and M. L. Roxbury, J. Appl. Mech., 41, 855 (1974).

33. A. N. Gent, Proc. Int. Conf. Dynam. Crack Propagat., (G. C. Sih, ed.) Noordhoof, Leyden, 157 (1972).

34. A. N. Gent and R. P. Petrich, Proc. Roy. Soc., London, A310, 433 (1969).

35. A. N. Gent, J. Polym. Sci., Part A-2(9), 659 (1971).

MICROSCOPIC FEATURES OF ADHESIVE BONDS FOR NON-DESTRUCTIVE MEASUREMENTS

H. W. White, L. M. Godwin, and T. Wolfram
University of Missouri
Columbia, Missouri 65201

ABSTRACT

Inelastic electron tunneling spectroscopy, or IETS, provides an extremely sensitive method for monitoring the chemical and physical state of a molecular substance adsorbed onto an oxide surface. Inelastic tunneling data directly reflect the molecular vibrational frequencies of the first monolayer of adsorbed molecules and changes in the vibrational spectrum can be correlated with changes in the chemical state of the molecule/oxide interface. We have carried out IETS experiments on the components of the commercial adhesive, Hercules 3501. This epoxy system consists of two molecular components; diamino diphenyl sulfone (DPS) and tetraglycidycl 4,4' diamino diphenyl methane (DPM). IETS spectra of the individual components and of the epoxy mixture adsorbed on aluminum oxide have been obtained and the vibrational modes and frequencies assigned by comparison with computer calculations and existing infrared optical spectra. Some evidence for an aging effect has been observed for the adsorbed DPS. This effect appears as a dramatic change in the low frequency vibrational modes and may be associated with the formation of hydrogen bonds or the polymerization of the DPS. Further studies of this effect are in progress. The effects of water permeation may be studied using D_2O as a tracer. The vibrational modes of D_2O are easily distinguished from those of water which may be present as a contaminant. If the exchange reaciton $D_2O + HCR \rightarrow DHO + DCR$ occurs, it would be easily detected in the IETS spectrum. Initial experiments performed by simply immersing the tunnel junction into liquid D_2O for severl hours were unsuccessful because severe corrosion of the tunnel junction resulted. Experiments employing aluminum/aluminum oxide/adhesive/gold thin film junction for the study of H_2O permeation are in progress. Further studies are planned to monitor the effects of heat treatment on the adhesive components and mixture.

Introduction

The objective of this program is to assess the feasibility of utilizing Inelastic Electron Tunneling Spectroscopy, or IETS, to monitor the chemical state of an adhesive/adherend interface of the type encountered in the adhesive bonding of aluminum components. The goal of the project is to determine what changes occur at an adhesive bondline during thermal curing and in bond degradation resulting from hydrothermal aging. Through such studies we hope to determine some of the important mechanisms of adhesive bond failure. IETS provides an extremely sensitive method for monitoring the chemical and physical state of a molecular substance adsorbed onto an oxide surface. Inelastic tunneling data directly reflect the molecular vibrational frequencies of the first monolayer of adsorbed molecules. Changes in the vibrational spectrum can be correlated with changes in the chemical state of the molecule/oxide interface. Since aluminum and other metals used in adhesive bonds have an oxide covering, the molecule/oxide interface geometry in inelastic tunnel junctions closely approximates that found in real adhesive systems. The method of IETS is not directly applicable as an "on-line" NDE technique but specific information concerning the mechanisms of bonding and bond degradation is needed in order to devise more meaningful NDE procedures.

We have carried out IETS experiments on the components of the high performance commercial adhesive, Hercules 3501. This epoxy system consists of two molecular components; diamino diphenyl sulfone (DPS) and tetraglycidyl 4,4' diamino diphenyl methane (DPM).

IETS spectra of the individual components and of the epoxy mixture adsorbed on aluminum oxide have been obtained and the vibrational modes and frequencies assigned by comparison with computer calculations and existing infrared optical spectra. Some evidence for an aging effect has been observed for the adsorbed DPS. This effect appears as a dramatic change in low frequency vibrational modes and may be associated with the formation of hydrogen bonding of the NH_2 groups to the oxide layer.

The effects of water permeation are being studied. D_2O is being used as a tag molecule since it has vibrational modes which are easily distinguished from those of H_2O. Using a new and exciting technique called external doping, molecules of H_2O and D_2O can be introduced into or removed from an already fabricated tunnel junction.

Experimental Results

Figure 1 shows a schematic of a typical adhesive bond between two pieces of aluminum metal. The adhesive is in contact with the aluminum oxide rather than the metal since an oxide quickly forms an aluminum when it is exposed to air or cleaned with etching solutions prior to bonding. In commercial applications the oxide thickness is typically 100 to 200 angstroms. There is a fantastic need for information regarding the microscopic interface between the adhesive and the oxide. It is difficult, however, to obtain the information using conventional methods. Ultrasonic techniques give critically needed information about the bulk properties of the adhesive but give little information about the interface region. The wavelengths in ultrasonic studies are considerably longer than the several angstroms associated with the thickness of the interface layer.

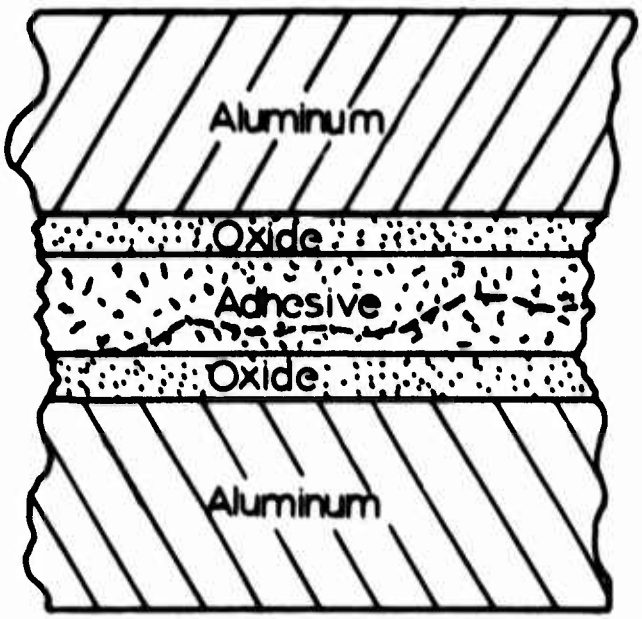


Figure 1. Schematic of an adhesive bond between two pieces of aluminum.

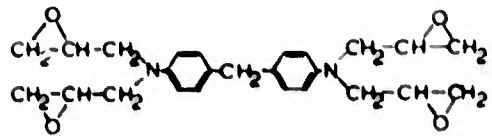
The chemical nature of the interface is very important to the integrity and service life of a bond. The dashed line in Fig. 1 shows a typical fracture line. Most of the fracture line surface is not at the interface; however, it often happens that the fracture line originates at the interface region. Black and Blomquist[1] have studied several metal adhesive systems and find that when they are exposed to a heat treatment the shear strength decreases significantly, often by more than a factor of two. They concluded that the primary reason for this decrease in shear strength is due to catalytic action at the bondline.

Hydrothermal aging is believed to be one of the most important causes for bond failure in service. Studies have been done on the bulk properties in order to determine how water which permeates a bond contributes to its degradation. The role of the water at the interface is considered to be very important, but to date there have been no good means of studying its effect.

The fact that an adhesive interface consists of a molecular layer bonded to an oxide suggests the possibility of inelastic electron tunneling spectroscopy as a useful tool. Our programs in both IETS and adhesives are relatively new and, as a consequence, most of the information presented is preliminary. The high performance Hercules 3501 epoxy system, distributed by Hercules, Inc.[2], was chosen for study during the third year.

The two molecules which form the epoxy system are shown in Fig. 2. The upper one is tetraglycidyl 4,4' diamino diphenyl methane (DPM). It has four identical arms, each with an epoxy ring. The other molecule shown is diamino diphenyl sulfone (DPS) which is the curative for the DPM epoxy molecule. The molecules are not planar. The atoms in the DPS molecule lie in two planes whose intersection is a line in the plane defined by the two oxygens and the sulphur. The DPM molecules are even more 3-dimensional. They form dimers relatively easily even at room temperature. Spectra must therefore be interpreted with an awareness of the fact that one or more of the arms may be joined to other molecules.

Tetraglycidyl 4,4' diaminodiphenyl methane
DPM



Diaminodiphenylsulfone
DPS

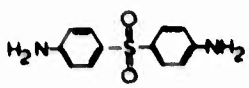
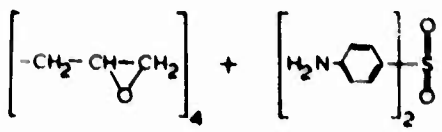
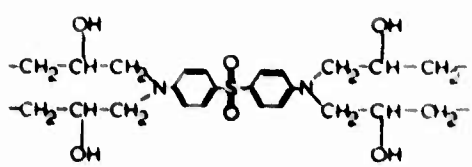


Figure 2. Schematics of the two molecules in the Hercules 3501 epoxy system.

The cross-link reaction for the DPM and DPS molecules is shown in Fig. 3. In the cross-link molecule there is an OH group on each arm. The arms in the cross-linked structure link with other arms in a somewhat disorganized fashion. The result is a very 3-dimensional structure. The methane group and rings are incorporated into the matrix.





Crosslink Reaction

Figure 3. The cross-link reaction for the Hercules 3501 epoxy system.

Bonding to the aluminum oxide probably occurs through the OH group, in much the same way in which phenol bonds to an aluminum oxide film, namely, as C_6H_5O-. [3] The OH groups make this molecule very polar and thereby susceptible to water permeation. The presence of water on the substrate could adversely affect the bonding properties.

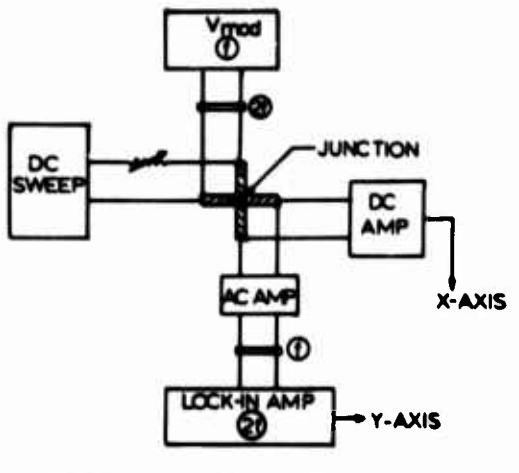
Aluminum/aluminum oxide/dopant/lead tunnel junctions were fabricated, where dopant refers to the molecules on which IETS spectra are to be obtained. The aluminum electrode was first evaporated at 10^{-6} Torr. A glow discharge was then used to form the oxide layer. A liquid doping technique was used to deposit approximately one monolayer of the molecules on the oxide. The process involves making a dilute solution of the molecular species to be studied, placing a drop of the solution on the electrode, and spinning off the excess. A lead counter electrode was then evaporated over the molecules.

The DPM resin was not easy to dissolve. Methyl ethyl ketone (mekol) and tetrahydrofuran (THF) worked best. These two solvents, and to a lesser extent chloroform, dissolved the DPS curative.

Figure 4 is a block diagram of the spectrometer system. The junction is cooled to 4.2K. A DC bias across the junction is slowly swept from 50 to 500 millivolts. An AC signal of 1000 Hz and approximately 1 millivolt (rms) is applied continuously. The amplitude of the second harmonic signal as generated by the tunnel junction is recorded on an XY recorder as a function of the DC bias. The second harmonic signal is proportional to:

$$\frac{d^2V}{dI^2} .$$

Peaks in this signal locate the energies of the vibrational modes as read from the bias voltage (energy) scale.



IETS SPECTROMETER

Figure 4. A block diagram of the inelastic electron tunneling spectrometer.

Spectra were first obtained on each of the molecules, then for the two molecules placed together on the same junction. This work is to be followed by studying the effects of heat treatment and hydrothermal aging on the observed spectra. Figure 5 shows two curves, A and B, taken on a junction doped with DPS using mekol as a solvent. The energy range is from about 50 to 500 millielectron volts (meV), which corresponds approximately to the wavenumber range 400 to 400 cm^{-1}. The OH stretch peak near 450 meV is observed in most IETS spectra. The CH stretch near 355 meV is found in all hydrocarbon spectra. The lower energy peaks for the DPS molecule were assigned by comparison with IR, other IETS data, and with normal mode frequencies calculated using literature values for the force constants. Both atomic motions and frequencies were obtained from the normal mode calculations. If an observed peak was more than 3 meV from a calculated vibrational energy a question mark was placed after its assignment label in Fig. 5. The measured locations, in meV, of the peaks are shown following the group assignment. The S=O stretch at 134 meV agree well with calculated vibrational energies and other data. The peak at 116 meV could be either a NH bend or an oxide phonon. Many doped junctions and nearly all undoped junctions show the presence of an oxide phonon at 117; however, the calculated vibrational energy for the NH bend is 115 meV. The peak at 102 meV was tentatively identified as an S=O bend since this group had a calculated frequency near 98 meV. The assignment at 52 meV was made in the same manner except that the S=O motion had a calculated frequency of 48 meV.

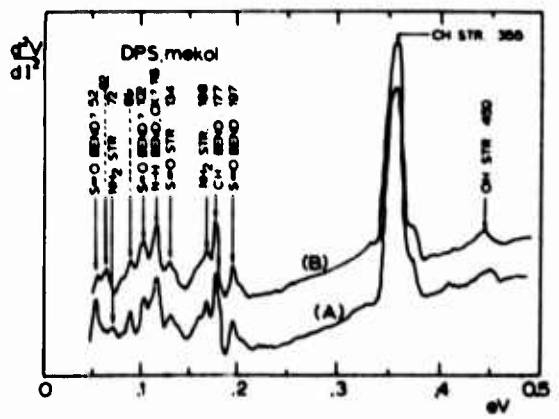


Figure 5. Two spectra taken on a junction doped with the curative DPS.

Until now the features discussed have been the same for both spectra A and B. In the energy range 55 to 75 meV the spectra are different. Spectrum A was taken on the junction soon after preparation. Spectrum B was taken nine days later, during which time the junction had been stored

in a clean, dry atmosphere. The junction resistance remained constant at 1500 ohms. Spectrum A shows a small peak at 72 meV which is within 2 meV of the value of the normal mode energy calculated for an NH_2 stretch in DPS. Spectrum B shows no evidence for a peak at 72 meV but shows a new distinct peak at 62 meV. An aging effect has occurred. There is very little evidence in the literature of any polymerization occurring inside of a tunnel junction, but there is evidence for chemisorption. We speculate that the NH_2 groups on the ends of the DPS molecule have chemisorbed to the oxide layer.

Figure 6 shows the spectra of four separate junctions. The lower curve is the spectrum for a junction doped with only the solvent THF. It serves as a background spectrum. Both THF and mekol spectra show a small peak near 174 meV which is undoubtedly due to CH bend modes and a small peak near 117 meV which is probably due to an oxide phonon. The second curve from the bottom, labeled "DPM, THF" is for the DPM epoxy molecule dissolved in the THF. Again, there is a large CH stretch peak located at 355 meV. The third curve labeled "DPM, mekol" shows essentially the same features as the second. The peak at 177 meV is probably a CH bend. The peak at 168 meV is probably due to NH_2 stretch modes. CH_2 rock modes are expected to be observed near 116 meV; however, the peak at that location could be due, at least in part, to an oxide phonon expected near 117 meV.

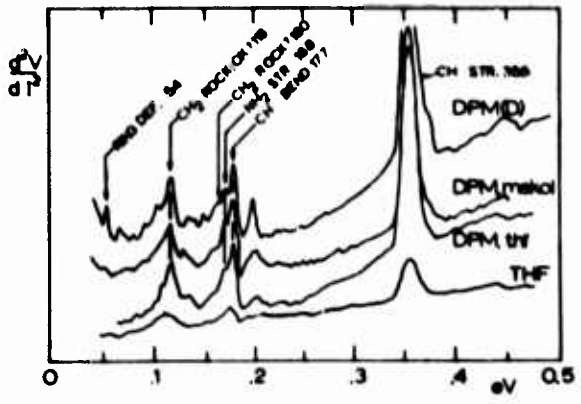


Figure 6. Spectra taken on junctions doped with the epoxy DPM.

The curve labeled "DPM (D)" is a spectrum for DPM which had been deuterated by an exchange reaction before placing in the junction. One of the goals of this project is to study the role of water at the interface of an adhesive bond. Water can be diffused into a junction and its presence can be monitored by using D_2O as tag molecules. The "DPM(D)" spectra was taken to provide information on the size and location of peaks associated with a deuterated DPM molecule. The spectrum has peaks not observed in the other spectra. We must be cautious in our interpretation of this spectrum since some structural changes may have occurred during the deuteration process.

At the First International Conference on Inelastic Electron Tunneling Spectroscopy held at the University of Missouri-Columbia during May 1977, Jeklevic and Gaerttner [4] reported the observation of IETS spectra of molecules which had been introduced into completely fabricated tunnel junctions. Curve A in Fig. 7 shows a clean junction made in the presence of H_2O vapor. Note the OH stretch at 450 meV. Curve B is the spectrum for a clean junction exposed to D_2O vapor after fabrication. The peak at 327 meV is an OD stretch mode indicating that D_2O penetrated into the junction. This new technique of external doping appears to be a very promising technique for studying the interaction of molecules with surfaces. Of particular interest to us is the diffusion of H_2O and D_2O into and out of tunnel junctions under the proper experimental conditions.

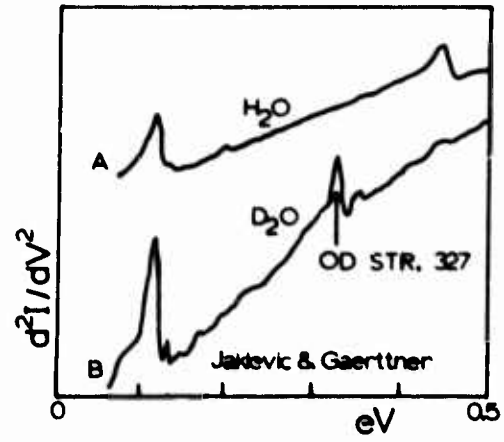


Figure 7. Curve A shows a clean junction made in the presence of H_2O vapor. Curve B is the spectrum for a clean junction exposed to D_2O vapor after fabrication. From R. C. Jaklevic and M. R. Gaerttner.

Figure 8 shows the spectrum for a junction containing both DPS and DPM molecules. The features are similar to those in spectrum A of the DPS molecule. One reason for this similarity may be due to the fact that the signature for the DPS molecule was always much stronger than that for the DPM molecule. Obtaining good noise-free junctions was considerably more difficult for the DPM molecule than for the smaller DPS. We are currently trying to improve spectral resolution and do some heat treatment and aging studies on the combined system.

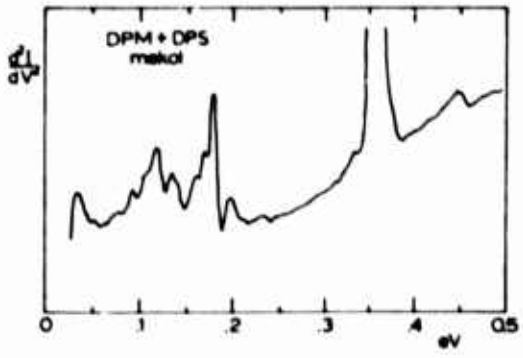


Figure 8. A spectrum on a junction containing both epoxy (DPM) and curative (DPS) molecules.

Our current activities are as follows:

(1) Improve spectral quality. A signal averaging system is needed to eliminate the effects of low frequency noise. The resolution in our spectra could be enhanced considerably.

(2) Investigate possible surface bonding mechanisms. The character of the bonding mechanisms for adhesive systems is not well known but is critical to an understanding of adhesive systems.

(3) Effects of heat treatment and hydrothermal aging. The recent advances reported in the external doping technique are being tried.

Conclusions

IETS (inelastic electron tunneling spectroscopy) is not directly applicable as a practical NDE technique and it is not trivial to apply IETS to the determination of adhesive-interface properties. However, at the present time, it is the only method available which allows an in situ study of adhesive/oxide interface bonding.

The feasibility of applying IETS to study changes in the molecular properties of an adhesive adsorbed on oxide due to time, temperature and permeating water has been demonstrated.

IETS offers a technique which, in the very near future, will become the most important (if not the only) method for determining the interface physics and chemistry of adhesive bondlines.

Information obtained from IETS studies will add greatly to the understanding of non-mechanical adhesive bond failure. Such knowledge should help in devising appropriate NDE measurements.

Initial studies using IETS should be applied to adhesives of simple molecular structure before proceeding to more complex systems.

Acknowledgements

The authors are grateful to C. Holmes and P. Corbin for their contributions to the design and fabrication of experimental apparatus.

This research was sponsored by the Center for Advanced NDE operated by the Science Center, Rockwell International, for the Advanced Research Projects Agency and the Air Force Materials Laboratory under contract F33615-74-C-5180.

References

1. J. M. Black, R. F. Blomquist, Ind. Eng. Chem., 50, 918 (1958).

2. Hercules, Inc., P.O. Box 98, Magna, Utah, 84044.

3. B. F. Lewis, W. M. Bowser, J. L. Horn, Jr., T. Luu, and W. H. Weinberg, J. Voc. Sci. Technol., 11, 262 (1974).

4. R. C. Jaklevic and M. R. Gaerttner, First International Conference on Inelastic Electron Tunneling Spectroscopy, University of Missouri, Missouri 65201, May 25-27, 1977.

BOND STRENGTH MEASUREMENTS BY ULTRASONIC SPECTROSCOPY

G. A. Alers, R. K. Elsley
Science Center, Rockwell International
Thousand Oaks, California 91360
and
P. L. Flynn
General Dynamics
Fort Worth, Texas 76101

ABSTRACT

The goal of this project has been to discover techniques for predicting the strength of a metal-to-metal adhesive bond from nondestructive measurements on the completed structure. Both the cohesive strength of the adhesive material itself and the adhesive strength of the metal-to-adhesive interface must be determined separately. In previous phases of the program, it was demonstrated that the Fourier transform of the ultrasonic echo returned from a metal-adhesive-metal sandwich structure immersed in a water bath contained sufficient information to obtain a prediction of the cohesive strength of the joint. Furthermore, certain features of the Fourier transform were shifted by thin layers of "different" materials at the metal-to-adhesive interfaces so that detecting poor adhesion was also a possibility. During the current phase of the program, more reliable mechanical tests and more accurate measurement techniques were developed. As a result, measurements of the wave velocity in FM-400 adhesive joints subjected to different degrees of cure correlated with the cohesive shear strength of the joints. Quantitative measurements of the standing wave resonant frequencies in Chemlok 304 adhesive joints showed a correlation with the strength of adhesion at the metal-to-adhesive interface.

Introduction

The nondestructive measurement of the strength of a completed adhesive bond between two pieces of metal is a major problem which is retarding the application of this very efficient method of joining to aerospace and other lightweight structures. Without a method of verifying the strength of a finished joint, the designer, the manufacturer, and the user are reluctant to utilize adhesive bonding for primary structures and thus heavy, complicated joints made with holes and bolts are still the dominant construction method. Over the past several years, various NDE techniques have been applied to this problem, and considerable success has been achieved at locating regions of disbonds or foreign objects whose dimensions are on a scale large compared to the bond line thickness. Such methods as ultrasonics and x-rays or neutron radiography can produce maps of the adhesive material which show these gross flaws in the joint. What is lacking are techniques which expose deficiencies in the intrinsic strength of the joint which arise from poor cohesive strength in the bulk of the adhesive itself or from the lack of adhesion between the adhesive and the metal. Poor cohesion within the adhesive can arise from an improper cure during manufacture, incorrect chemistry in the original adhesive material, or microscopic defects such as porosity. Poor adhesion can arise from incorrect preparation of the metal surfaces prior to bonding, aged adhesive material or an improper primer application to the metal. It has been the objective of this study to find ultrasonic techniques that can give a quantitative measure of the presence of these intrinsic deficiencies and provide a means for predicting the strength of adhesive bonds which do not show gross flaws under conventional radiographic or ultrasonic C-scan inspections.

Accomplishments to date include the development of computer programs to analyze the ultrasonic pulse signals reflected from adhesively bonded sandwiches in such a way that numerical values for the ultrasonic velocity and attenuation within the adhesive layer can be extracted. It was shown that both of these physical properties could be correlated with the strength of bonds made with a model adhesive system. Thus it appears that techniques are available for deducing the cohesive strength of a finished adhesive bond from quantitative measurements of its response to ultrasonic waves. The current program, reported here, has been to demonstrate this strength prediction capability on bonds made with commercial adhesives after being subjected to various environmental exposures and/or various fabrication technique modifications.

The detection and measurement of a reduction in quality of adhesion at the metal to adhesive interface has been a much more challenging problem for ultrasonic inspection. Theoretical investigations concerning the way in which the mathematical boundary conditions at the adhesive to metal interface effect the ultrasonic wave propagation modes in the sandwich structure have shown that standing wave resonances in the thickness dimension are sensitive to the state of the boundary. Therefore, the current program has been to detect these thickness mode resonances with the same type of computerized apparatus that was used in the cohesive bond strength measurements and to see if a correlation with the strength of adhesion could be demonstrated.

Experimental Techniques

In order to establish any quantitative relationship between a nondestructive measurement and

the strength of an adhesive joint, each step in the procedure must be performed in such a way that all uncertainties are minimized. The ultrasonic measurements must be made accurately at the location on the bond where the strength measurement is made. Likewise, the strength measurement must be made in such a way that small, localized defects (such as edge imperfections) do not dominate the mechanical failure process. In all cases, the chemistry and curing of the adhesive as well as the preparation of the metallic surfaces prior to bonding must be made in a uniform, consistent manner so that scatter in the results due to fabrication variations are minimized. Each of these three key elements were carefully developed for the present program and are discussed separately below.

Mechanical Tests

In previous studies, the lap shear specimen shown at the top of Fig. 1 has been used to provide a measure of the adhesive bond strength. Its primary drawback is that a stress concentration occurs along the edge of the bonded joint that is perpendicular to the stress and any weakness in this region is then likely to be the source of failure. Since the ultrasonic measurements on the joint must be made at points away from the edges, the standard lap shear test is unsatisfactory for accurate correlations between strength and NDE measurement, because the ultrasonic data comes from regions of the joint that are probably different from the regions that initiate failure. To overcome this problem, two new test procedures were introduced for the current program. These are the peel test and the compression shear test as shown in Fig. 1. The force necessary to cause a crack to propagate through the exact region where ultrasonic measurements have been made is measured in the peel test. Since the small compression shear test specimen is cut out of a larger bonded plate after a thorough inspection by ultrasonics, the region of failure initiation can be located exactly where precise ultrasonic measurements have already been made. For nearly all of the test results presented later in this report, the compression shear test was used on small specimens 1" long and 1/2" wide in which the shear was applied to a 1/4" x 1/2" area in the center of the specimen. These test specimens were cut from 1-inch wide by 6-inch long bonded strips of 1/8-inch thick aluminum or from 6" x 6" bonded plates of 1/8-inch thick aluminum which had been interrogated at an array of points by ultrasonic pulse-echo methods.

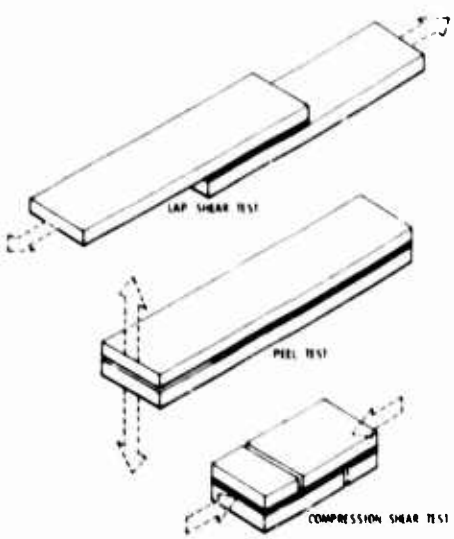


Figure 1. Various methods of testing the strength of adhesively bonded joints.

Adhesive Bond Preparation

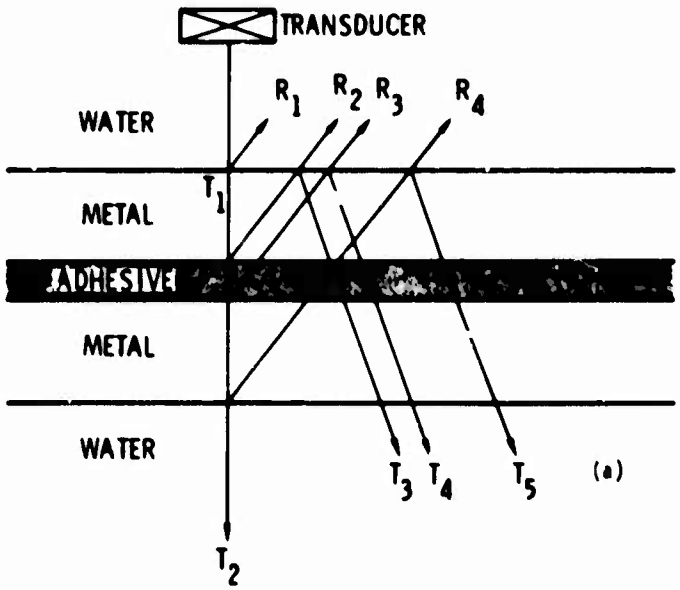
Two types of adhesive bonds were examined in this program. The first was designed to demonstrate the ability to measure deficiencies in the cohesive strength of a completed bond which had been made with a commercial adhesive material (FM 400) but cured at incorrect temperatures. This procedure was applied to the 6"x 6" square panels. The second bond type was designed to demonstrate the ability to measure strength reductions caused by poor adhesion between the adhesive and the metal. This latter class of defect was simulated by preceding the bonding process with the placement of a thin layer of contamination on the 6"x 1" aluminum peel test strips in such a way that the thickness of the contamination would vary slightly along the length of the strip in order to insure obtaining a distribution in strength values out of each long specimen. For these adhesion tests a model adhesive system (Chemlok 304) was used with surface contamination produced by wiping stopcock grease on the surface of the aluminum or by controlled precipitation of stearic acid onto the aluminum from a solution of pentane and stearic acid.

Ultrasonic Tests

Improvements in the ultrasonic test techniques were made to increase the accuracy of capturing the ultrasonic wave forms and placing them in the memory of the computer. Further improvements in the mathematical model which describes the reflection of ultrasonic waves by layered media were incorporated into the computer system so that direct comparisons between measurements of the reflected amplitude as a function of frequency could be made with detailed theoretical predictions of this same function. As a result of these changes, small shifts in the position of the resonant frequencies of the sandwich structure could be reliably measured and compared with theoretical expectations.

The existence of an accurate theoretical model for the ultrasonic signals has played a vitally important role in developing quantitative methods for adhesive bond strength determination. Figure 2(a) shows a schematic diagram of the metal-adhesive-metal sandwich immersed in a water bath and subjected to ultrasonic wave interrogation by a transducer mounted above the sandwich and oriented to send acoustic waves perpendicular to the layers. The reflected signals, labeled R_1, R_2, R_3 and R_4 in the figure, return along the normal to the specimen and are detected by the same transducer that launched them. These reflection signals are shown in Fig. 2(b), which demonstrates the importance of using very broad band (short time duration) ultrasonic signals in order to clearly separate the reflection from the top surface of the aluminum (R_1) from the reflection from the top of the aluminum-adhesive

interface (R_2) and from the reflection from the bottom of the adhesive layer (R_3). Figure 2(c) shows an enlarged version of the region of time containing only the reflections from the adhesive layer. This demonstrates that the digital computer analysis system is capable of performing very detailed analyses on specific events in the complex series of echos returned from the total adhesive bond sandwich. In particular, the ratio of the signal amplitudes reflected from opposite sides of the adhesive (the ratio R_3/R_2) is used to measure the ultrasonic attenuation in the adhesive layer. In order to measure the sound velocity in the adhesive layer or the frequencies of standing wave resonances within each of the layers, the computer generates the Fourier transform of the time domain signals shown in Fig. 2 to produce the reflected amplitude versus frequency graph shown in Fig. 3(a). This computation includes correcting the ultrasonic signal for the frequency response of the transducer to produce what is called the Normalized Reflection Spectrum. Because of the finite band pass of the transducer, the computer shows no information below 1 MHz and above 19 MHz, even though there are certainly reflection minima in these frequency ranges. Figure 3(b) shows the results of calculating the reflection spectrum of an aluminum-adhesive-aluminum sandwich with a small amount of attenuation included in the physical properties of only the adhesive. A comparison of the experimental and theoretical spectra demonstrates the high confidence with which various features in the experimental spectrum can be used for quantitative measurements and correlations. The splitting of the individual dips and the relative depths of the two minima are observed in both the theory and the experiments. These prominent dips, spaced at 2 MHz intervals, arise from the standing waves in the aluminum plates and are split into a pair of dips because the plates are of equal thickness and are coupled together by the adhesive layer. Thus their individual thickness resonant modes are shifted upward and downward along the frequency axis depending upon whether the metal surfaces on each side of the adhesive are moving in-phase or out-of-phase. The small dips near 5 and 10 MHz represent the standing wave resonance of the adhesive layer alone and can be used to determine the velocity of sound in the adhesive if the thickness of the layer is known.



ULTRASONIC INSPECTION
WITH NORMAL INCIDENCE WAVES

Figure 2(a). Schematic diagram showing the position of an ultrasonic transducer over the planar layers that form a common adhesive joint between metal plates.

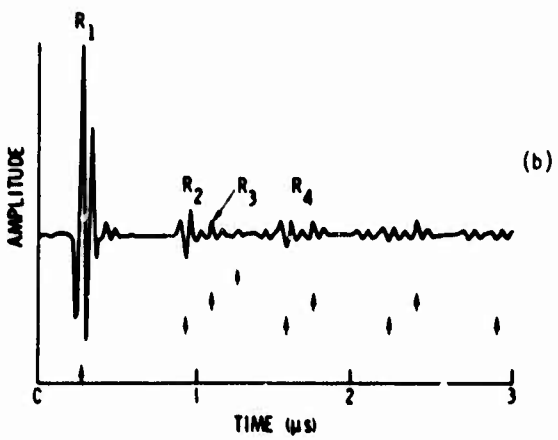


Figure 2(b). Signal amplitude versus time display for the echoes reflected from the multilayered adhesively bonded structure of Fig. 2(a).

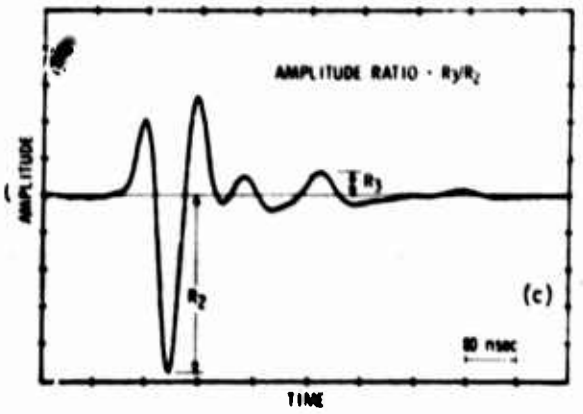


Figure 2(c). Expanded view of the time interval in which the reflections from the adhesive layer alone occur.

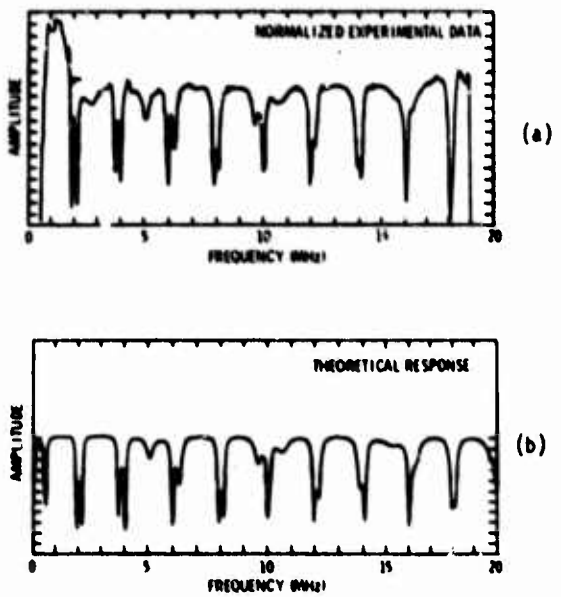


Figure 3. (a) Reflected amplitude versus frequency graph reduced by the computer taking the Fourier transform of the time domain signal shown in Fig. 2(b). Transducer effects have been normalized out of these data. (b) Theoretical prediction of the reflected signal versus frequency graph based on 1/8-inch thick aluminum adherends joined by a 10 mil adhesive layer with some attenuation in the adhesive.

Cohesive Bond Strength Measurement

Since both the elastic properties and the cohesive strength of the bulk adhesive are related to its internal chemical structure, a correlation between the cohesive strength of the bond and measured values of the velocity of sound and the attenuation of sound in the adhesive layer should exist. Figure 4 shows the good correlation observed in previous studies on a model adhesive system (Chemlok 304) which contained no scrim cloth and which cured without the evolution of any volatile materials. The various values of strength were obtained by changing the ratio of chemical constituants in the precured adhesive.

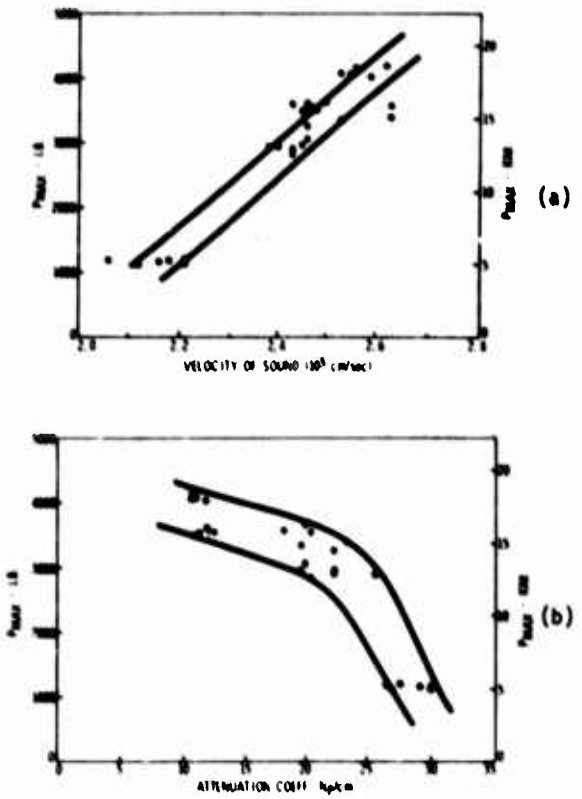


Figure 4. (a) Correlation observed between the velocity of sound in a model adhesive and the strength of the joint as measured by a lap shear test. (b) Correlation observed between the attenuation of sound in the model adhesive and the strength of the joint as measured by a lap shear test.

The current program has been directed at demonstrating this same correlation in a modern structural adhesive (FM 400) which contains both a scrim cloth as well as a metal particle filler and which cures with the evolution of a gas. Variations in the degree of cohesive strength were achieved by performing the cure at different temperatures - a common processing error. Figure 5 shows the data obtained when the ultrasonic measurements of sound velocity and attenuation were plotted against the compression shear strength of the many samples. To obtain these data, two 6"x 6"x 1/8" aluminum plates were bonded together and cured at a particular temperature. Then a computer automated inspection system was used to collect ultrasonic reflection signals and to deduce values for the velocity and attenuation at an array of points over the 36 square inches of bonded surface area. These points were chosen such that when the panel was cut up into a collection of compression shear samples (see the bottom of Fig. 1) the area subjected to the shear stress was identical with that which had been measured acoustically. Obviously the spread in both the acoustic measurements and strength measurements is quite large so that the scatter in the data overshadows any correlation in the case of the attenuation and makes a correlation between strength and velocity rather inaccurate. An examination of the fracture surfaces of the broken samples revealed the presence of scattered arrays of bubbles within the adhesive which had a wide distribution of sizes, although the largest did not exceed the spacing between the fibers of the scrim cloth. Since these bubbles should act as excellent ultrasonic wave scattering centers, they undoubtedly make a major contribution to the measured attenuation and cause it to vary considerably without changing the strength of the bond. Hence, the poor correlation between strength and attenuation. A surprising feature about the relationship between acoustic velocity and strength is the abruptness with which the strength changes as a function of curing temperature. Note that the strength jumps from zero to its maximum value when the cure temperature changes only from 120°C to 140°C. Also note that the values of the velocity corresponding to the uncured and fully cured states extend over the range of 2.5×10^5cm/sec to 3.2×10^5cm/sec - a spread of 25%. This spread is comparable to that which was observed with the model adhesive system when its chemical composition was changed and the good correlation between velocity and strength shown in Fig. 4(a) was observed. Thus, the present, real adhesive system differs from the model system only in the degree of uncertainty or scatter in the data. Presumably this scatter is associated with the hetrogeneous nature of commercial adhesives which contain scrim cloth, fillers and bubbles. Further effort should now be directed at understanding the origin of the scatter and correcting for it in the data processing or specimen preparation stages.

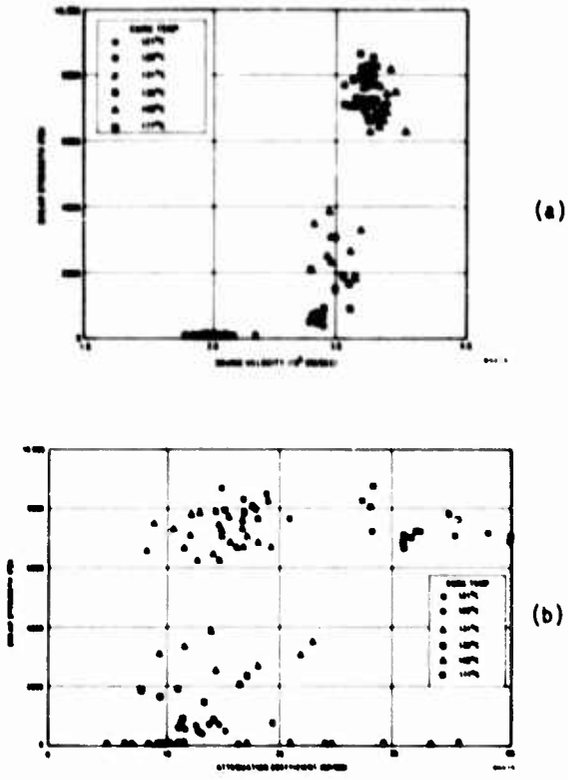


Figure 5. (a) Correlation observed between the velocity of sound and the compression shear strength measured on a joint made with FM 400 adhesive cured at different temperatures. (b) Correlation observed between the attenuation of sound and the compression shear strength measured on a joint made with FM 400 adhesive cured at different temperatures.

Adhesive Bond Strength Measurement

The task directed at a nondestructive measure of adhesion at the adhesive to metal interface concentrated on developing techniques for obtaining a distribution of bond strengths in the geometry of the peel test specimen using contamination on the aluminum adherends to adjust the strength values. It also concentrated on development of very accurate methods for extracting the resonant frequency values from the reflection amplitude versus frequency plots generated by the computer (see Fig. 3). Two methods of contamination were successful. One used a variable thickness layer of stop-cock grease to achieve different lap shear strengths on four specimens. The reflected amplitude versus frequency plots for these four samples are shown in Fig. 6 with the value of the measured shear strength of each sample recorded in the upper right hand corner. Obviously, the highest frequency at which the standing wave resonances are observed to be split increases as the strength of the bond increases. By making a graph of the strength versus the frequency at which the splitting disappears, one gets the excellent correlation shown in Fig. 7, which relates a nondestructive acoustic measurement with the strength of an adhesive bond that fails by weak adhesion. A physical basis for this correlation can be proposed to

arise from the fact that the weaker bonds are associated with a thicker layer of grease at the interface and this layer does not pass the high frequency sound waves from the aluminum into the adhesive. Thus the high frequency standing wave resonances show only the standing wave in the upper aluminum plate because no acoustic energy gets through the interface to excite the lower aluminum plate at its higher harmonics.

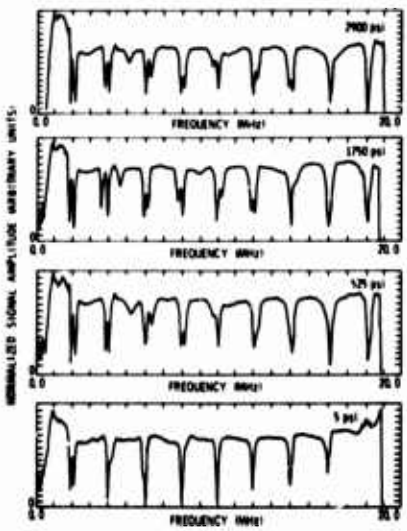


Figure 6. Reflected amplitude versus frequency plots measured on four samples whose lap shear strengths had been reduced by placing different thin layers of stopcock grease at the adhesive-to-metal interface.

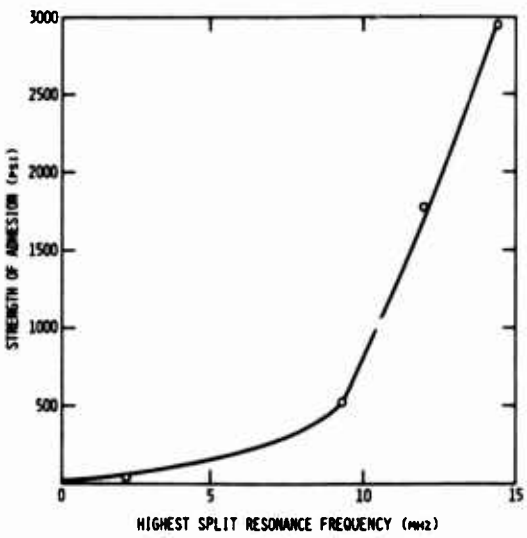


Figure 7. Correlation between the highest frequency for which a split resonance is observed and the adhesion strength observed in a lap shear test.

The other successful method of controlling the strength of adhesion was to put a variable thickness layer of stearic acid on the aluminum before preparing the bonded specimen. By placing a solution of the acid in pentane on one of the aluminum adherends and then allowing the pentane to evaporate, it was possible to deposit a very thin layer of stearic acid on the aluminum. When the ultrasonic signal amplitude versus frequency graphs for these specimens were produced, it was observed that the frequency at which splitting of the resonances appeared did not change when the strength of the bond changed. Thus the stearic acid layer at the interface does not show the same ultrasonic filtering response as the stopcock grease layer exhibited.

During the earlier theoretical studies on the effects of interfaces on the ultrasonic response of a sandwich structure, it was predicted that the lowest standing wave resonance of the total structure should be particularly sensitive to the conditions at the interface. Preliminary experiments verified this prediction by showing a strong correlation between strength measurements and the value of the lowest resonant frequency. To see if this correlation also existed for interfaces contaminated with stearic acid, special low frequency transducers were used to allow the computer system to display resonances in the frequency range from 0.3 to 0.6 MHz. Because this low frequency resonance is also sensitive to the thickness of the adhesive layer, special computer calculations were carried out to determine how all the standing wave resonances are shifted by a small change in bond line thickness. To determine the bond line thickness appropriate to a given test specimen, the computer system was used with a high frequency transducer to display the entire series of high frequency standing waves including the resonance of the adhesive layer alone (shown as the small dip near 5 MHz on Fig. 3). By assuming that the compliance of the bulk adhesive is constant over the length of a peel test specimen with stearic acid at the interface, the frequency of the adhesive resonance observed at an individual location can be used to calculate the effective thickness at that location. This value can then be used to correct the lowest frequency resonance to that which it would have for a standard thickness. In this way, all the lowest frequency resonances for any set of specimens can be compared to one another and correlations with other variables such as bond strength can be investigated. A comparison between the compression shear strength and the lowest frequency of resonance is shown in Fig. 8(a) for two specimen sets labeled 271 and 273, and a reasonably good relationship appears to exist. Figure 6(b) shows the correlation between the compression shear strength and the separation in frequency between the two minima, i.e. the splitting, of the lowest frequency split resonance at 1 MHz in Fig. 3. Here again, a normalization of the data to constant effective bondline thickness has been carried out. This second parameter seems to provide a somewhat more accurate correlation with strength and a smaller spread between the different initial specimens.

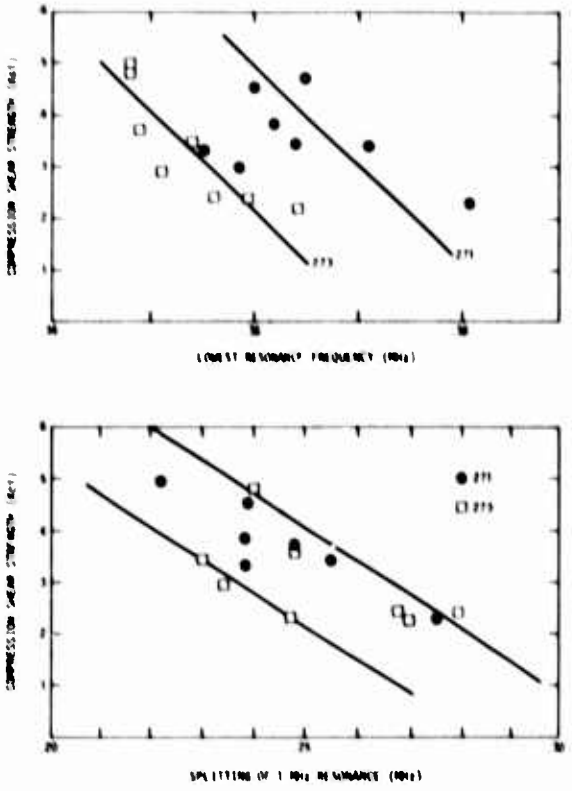


Figure 8. Correlation observed between the compression shear strength of two series of samples and two features of their amplitude versus frequency characteristics. Top curve: correlation with the lowest standing wave frequency for the entire sandwich. Bottom curve: correlation with the degree of splitting of the lowest frequency standing wave in one of the adherend plates.

Conclusions

Based on the postulate that the cohesive strength of a layer of adhesive should be related to its bulk physical properties, such as the velocity of sound and the attenuation of sound, a computerized system to rapidly analyze the ultrasonic signals reflected from an adhesively bonded pair of aluminum plates has been assembled. Using this system, it has been demonstrated that a good correlation between the cohesive strength of adhesive joints formed with a model adhesive and its velocity and attenuation can be obtained. On real, commercial adhesives the correlation is not as good because the inhomogeneous nature of this class of materials increases the spread in velocity and attenuation measurements. Methods for correcting the data for these inhomogeneity effects are now being developed.

For the case of measuring the quality of adhesion between the adhesive and the metal, techniques based on making quantitative measurements of the standing wave resonant frequencies of the bonded sandwich structure have been developed. After corrections are made for variations in the thickness of the adhesive bond layer from specimen to specimen, it has been shown that both the lowest standing wave resonant frequency of the entire sandwich and the magnitude of the splitting of the lowest standing wave frequency in the aluminum adherends can be used to predict the strength of the completed bond. Again, considerable scatter in the data points exists and an investigation into the origin of this effect is underway.

Acknowledgement

This research was sponsored by the Center for Advanced NDE operated by the Science Center, Rockwell International, for the Advanced Research Projects Agency and the Air Force Materials Laboratory under contract F33615-74-C-5180.

FRACTURE MECHANICS OF FIBER-REINFORCED COMPOSITES

E. M. Wu
Lawrence Livermore Laboratory
Livermore, California 94550

ABSTRACT

Quantitative understanding of the parameters which control composite fracture is imperative to the implementation of fail safe design and inspection of critical load bearing structures. For isotropic materials, fracture is essentially controlled by a single parameter, e.g., the fracture toughness or the stress-intensity factor. This one dimensional nature lends itself to experimental quantification. However, for anisotropic composites there are at least seven primary controlling parameters: 1) crack length; 2) crack orientation with respect to material axis of anisotropy; 3) nature of applied combined stresses; 4) lamination geometry; 5) deformational and strength responses of the constituent lamina; 6) three kinematically admissible modes of crack extension and 7) crack trajectory. Because of this large number of parameters, experimental quantification by systematic permutation of the parameters must be realistically viewed as intractable. This paper presents an analytical method of reducing these parameters from seven to two and furnishes experimental observations which lend support to the theoretical model. An experimental program is conducted on fiberglass reinforced epoxy where a centrally notched-crack is subjected to combined loading. Several lamination geometries are tested and by varying the external combined loading, different crack trajectories are predicted by the theoretical model. These predicted trajectories agree well with the experimental observed fracture mode. Such agreement suggests that with further refinement, the general condition of laminated fracture can be characterized.

Introduction

In contrast to isotropic metals and polymers, fracture of anisotropic composites is a multi-parameter problem because 1) the near-field stress distribution depends not only on the crack geometry but also on the relation of the crack to the material orientation, and 2) the material resistance to crack propagation is a strong function of the material orientation, e.g., it is more difficult to break fibers than to separate them. As a consequence of the multi-parameter characteristics, the prediction of crack initiation under biaxial loading and the prediction of crack trajectory become relevant to the fundamental understanding of fracture and to the rational analysis of composite engineering structures.

In the trend of current research practices, characterization of the strength of anisotropic multiphase composites is usually separated into two broad categories: 1) the composite strength in the absence of macroscopic flaws, and 2) the composite strength in the presence of macroscopic flaws (and stress-risers). These two categories are usually referred to as anisotropic failure criterion chracterization and fracture mechanics respectively, and they are treated as separate physical phenomena. Clearly, such arbitrary categorizing is a consequence of attempting to identify the critical paths of composite strength characterization through association with those experiences gained from isotropic solids. The one-parameter nature of isotropic fracture follows directly from the physical observation that isotropic crack extension is always perpendicular to the direction of maximum tension and the dissipation always occurs via a crack opening mode. Thus, the similarity between the mathematical model and physical observation is easily maintained. In contrast, composites, particularly in the laminated form, exhibit a large range of instability conditions involving various amounts of slow crack growth. First of all, the modes of energy dissipation are not limited to the opening mode but also include forward sliding and out-of-plane shear; the crack trajectories seldom follow the maximum tensile stress direction and often lead to non-self-similar crack extension including complex branching. The effects of the external loads (symmetric and stress-symmetric to the crack) as well as combined loading on crack instability also need to be documented. Finally, the size effect of flaws is far more dominant in composites than in homogeneous isotropic materials.

Whereas the one dimensional nature of isotropic fracture lends itself to experimental quantification in the form of a single critical stress-intensity factor or fracture toughness parameter, the multiple-parameter nature of crack extension in composites precludes empirical permutation of the parameters. For anisotropic composite laminates, there are at least seven primary parameters controlling the fracture characterisitics. These are:

1. Deformational and strength responses of the constituent lamina
2. Lamination geometry
3. Crack orientation with respect to the material axis of anisotropy
4. Crack length
5. Nature of applied stresses
6. Energy dissipation associated with the three kinematically admissible modes of crack extension
7. Crack trajectory

Theoretical Model

Because of this large number of parameters, experimental quantification by systematic permutation of the parameters must be realistically viewed as intractable. This paper presents an

analytical model which reduces the above parameter list from seven to two and furnishes experimental observations which lend support to the theoretical model.

The theoretical model is based on the hypothesis that, in the case of quasi-static crack extension, the necessary and sufficient condition for failure of a volume element around a macroscopic crack tip is similar to that condition for failure of a volume element in the absence of a macroscopic crack. Since the presence of a macroscopic crack gives rise to a combined complex state of stress in the neighborhood of the crack tip, it is necessary to know the condition of failure of the composite under complex loading, which is commonly referred to as the failure envelope or failure criterion. Thus, the major ingredients required in the implementation of the theoretical model are a) a mathematically operational anisotropic failure criterion for the composite lamina, and b) a suitable stress analysis technique through which the stress distribution in the neighborhood of the crack tip in a laminate can be computed. In recent years, numerous failure criterion have been proposed. Examination of their formulations, Ref. 1, reveals that they can be cast and compared in terms of tensor polynomials and that the majority of them are mathematically awkward; some even lack consistency of conversion between stress and strain. It was found that the tensor polynomial failure criterion, Ref. 2, encompasses maximum flexibility without redundancy and further, that it lends itself to the design of critical experiments, Ref. 3. The tensor polynomial failure criterion is used here, although it should be emphasized that other experimentally verified criteria may be substituted. The tensor polynomial failure criterion when expressed in terms of stress takes the form:

$$f(\sigma_i) = F_i\sigma_i + F_{ij}\sigma_i\sigma_j + F_{ijk}\sigma_i\sigma_j\sigma_k + \ldots = 1, \qquad i = 1,2,\ldots 6 \tag{1}$$

where in Eq. (1) contracted notation is used. For a typical engineering composite (graphite epoxy), the linear and quadratic terms in Eq. (1) provide sufficient correlation of the experimental data as shown in Fig. 1. These experimental data were obtained from tubular samples tested under combined stress conditions along radial loading paths by an axial-rotary-internal pressure mechanical testing machine controlled by an on-line digital computer. The experimental details have been reported in Ref. 4. The data actually populate a three-dimensional space in $\sigma_1\sigma_2\sigma_6$, but they have been convoluted (or projected onto the $\sigma_1\sigma_2$ plane for easy comparison. In Fig. 1, the same set of experimental data are convoluted onto the $\sigma_1\sigma_2$ plane by three different failure criteria. Better correlation by the tensor polynomial criterion exhibited both visually as well as by the lowest RMS (the root mean square) deviation of experiments from theory.

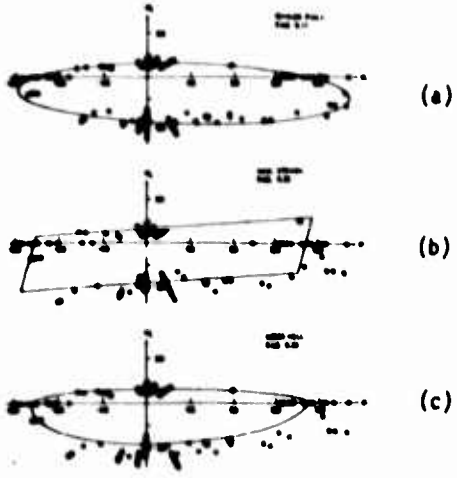


Figure 1. Failure data of graphite epoxy lamina convoluted onto $\sigma_1\sigma_2$ plane, stresses in (ksi). (a) By tensor polynomial failure criterion; (b) by maximum strain failure criterion; (c) by modified Mises-Hill failure criterion.

The physical interpretation of the failure envelope requires some attention, since the composite is assumed to be homogeneous, anisotropic, and contains a population of randomly distributed microscopic flaws C_1, C_2 ... C_i. While the flaws are small compared to the characteristic dimension D of the body as depicted in Fig. 2a, continuum analysis discloses that under arbitrary loads P_i the state of stress is unbounded at the location of the geometric singularities C_1, C_2 ... C_i, and thus would lead to immediate failure even for extremely small P_i. This is contrary to physical observations and the stresses appearing in Eq. (1) should be interpreted as the average stress acting on a small but finite characteristic volume (specified by a dimension r_c, Fig. 2a) which fully encapsulates one microscopic flaw. Thus, although the stress is singular inside this characteristic volume r_c, the average stresses external to r_c are bounded and may be used to characterize the failure of this volume through a failure criterion of the form

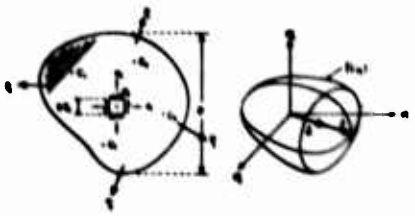
$$\mathcal{A} < \mathcal{F} \tag{2}$$

where $\mathcal{A}$ is the average stress vector acting external to the characteristic volume defined in terms of the unit vector e_i in the stress space of Fig. 2b as

$$\mathcal{A} = \sigma_i e_i \qquad i = 1,2, \ldots 6 \tag{3}$$

and $\mathcal{F}$ is the strength vector to the failure surface $f(\sigma_i)$ as determined by Eq. (1) and illustrated in Fig. 2b. Under an arbitrary loading P_i, the stress vector $\mathcal{A}$ at any location of the body can be determined through continuum analysis or numerical techniques. It follows that when criterion $f(\sigma_i)$ is known, then the location of a prevalent failure condition can be determined. Hence,

the problem of analyzing the crack initiation is possible with the availability of the second ingredient, i.e., the stress analysis of the crack.



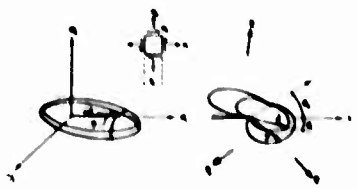
(a) (b)

Figure 2. (a) Homogeneous anistropic body with randomly distributed microscopic flaws. (b) Criticality of stress vector $\vec{\sigma}$ acting on characteristic volume r_c, the failure surface $f(\sigma_i)$ the strength vector $\vec{\mathcal{F}}$.

It has been found, Ref. 5, that for composite lamina the problems of biaxially loaded crack initiation and crack trajectory can be examined by introducing the criterion of comparing the stress vector $\vec{\sigma}$ around the crack tip to the strength vector $\vec{\mathcal{F}}$ of the parent material. The essentials of this concept are shown in Fig. 3, where 3b depicts a crack subjected to a system of biaxial loads, P_i. Through anisotropic stress analysis of the crack, the near-field stress σ_i around the crack tip can be computed as a function of material orientation as specified by compliance coefficients S_{ij}, Ref. 6.

$$\sigma_i = g_i(S_{ij}, 2a, r) \qquad i = 1,2,6 \qquad (4)$$

Here 2a and r are respectively the crack length and the distance from the crack tip. The crack tip stress is singular when r approaches zero. However, in accordance with our model, we only need to compute the average stress exterior to the critical volume which encapsulates the crack tip. Thus, Eq. (4) can be computed in terms of the critical volume r_c, and the stress vector $\vec{\sigma}$ can be expressed in the stress space $\sigma_1\sigma_2\sigma_6$ from Eq. (3). From Fig. 3a it can be seen that whether or not the material will fail under the influence of the stress vector $\vec{\sigma}$ (determined from Eq. (3)) can be determined by comparing the stress vector $\vec{\sigma}$ to the strength vector $\vec{\mathcal{F}}$ which is defined by the failure surface, i.e., Eq. (2). In Fig. 3a $\vec{\mathcal{F}} = \sigma_i^* \theta_i$ and σ_i^* are the roots of the lamina failure criterion (Eq. 1) in the direction of $\vec{\sigma}$. Thus, the coincidence of the stress and strength vectors determine both the initiation of failure and the trajectory of crack extension. This is graphically illustrated in Fig. 3b where the polar contours of the stress vector $\vec{\sigma}$ and the strength vector $\vec{\mathcal{F}}$ are plotted. It can be seen that the location of the maximum stress vector $\vec{\sigma}$, i.e., θ_i, in Fig. 3b, is not a sufficient condition for crack initiation; whereas the coincidence of $\vec{\sigma}$ and $\vec{\mathcal{F}}$ at θ_c defines initiation and crack extension along the θ_c direction. Extensive experiments on composite lamina (glass-epoxy) subjected to combined loading verified this concept (Fig. 4) where the characteristic dimension r_c was computed to be 0.076 inch for fracture under tension and 0.077 inch for fracture under shear. Futhermore a single characteristic $r_c = 0.077$ correlates all combined stress fracture results completely suggesting that r_c need not be an adjustable empirical constant. The net effect is that a formerly multi-dimensional fracture under complex stress problem can be completely characterized by two parameters, i.e., the characteristic volume r_c and one critical stress intensity factor.



(a) (b)

Figure 3. Relation between failure of characteristic volume r_c (a), and fracture of crack (b).

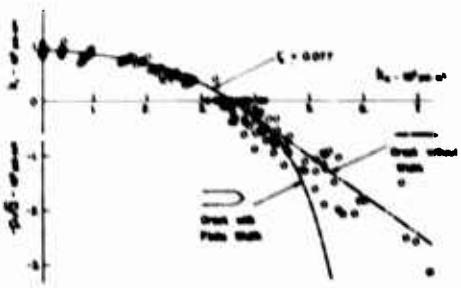


Figure 4. Crack extension of unidirectional composite (Scotch-ply 1002) under combined loading; k_1 - symmetric stress intensity factor (tension-compression), k_2, skew symmetric stress intensity factor (shear). Experimental results relatable by a single critical volume r_c.

It can be readily seen in the case where the anisotropic composite is a laminate that additional dimensions are introduced in the form of lamination angles and stacking sequences. If we are permitted to use classical linear laminated plate theory which appears to be a reasonable compromise, we can proceed to extend the above parameter reduction concept to the fracture of laminates by using

Eqs. (1,2,3,4) respectively. The basic equations for these computations are described in the following section.

Calculation of Stress and Strength Vectors For Laminate Composites

The following calculation of the stress and strength vector for a laminate is based on the assumptions that linear laminated plate theory is applicable and that the deformational and strength properties of the lamina are known, i.e.,

$$S_{ij} \qquad \text{known} \tag{5}$$

$$f(\sigma_i) = F_i\sigma_i + F_{ij}\sigma_i\sigma_j = 1 \text{ known} \tag{6}$$

The determination of S_{ij} and F_i, F_{ij} has been discussed in Refs. 7 and 1. With Q_{ij} for the lamina known, the stiffness matrix of the laminate can be computed from:

$$A_{ij} = \int_{-h/2}^{h/2} Q_{ij}\,dZ = \sum_{k=1}^{n} Q_{ij}^{(k)} (h_{k+1} - h_k), \tag{7}$$

where $Q_{ij}^{(k)}$ is the plane stress stiffness coefficient computed from S_{ij} and transformed to the orientation of the kth lamina. For the case of symmetrical stacking sequence the stress-strain relation for the laminate is

$$N_i = A_{ij}\epsilon_j^0 \tag{8a}$$

and

$$\epsilon_i^0 = A_{ij}^* N_j \tag{8b}$$

where ϵ_i^0 is the average strain through the thickness.

The general plane problem of a crack in the laminate then requires solution of the Airy's stress function x in the form, Ref. 6,

$$\frac{\partial^4 X}{\partial X_1^4} - \frac{2A_{26}^*}{A_{22}^*}\frac{\partial^4 X}{\partial X_1^3 \partial X_2} + \left(\frac{2A_{12}^* + A_{66}^*}{A_{22}^*}\right)\frac{\partial^4 X}{\partial X_1^2 \partial X_2^2} - \frac{2A_{16}^*}{A_{22}^*}\frac{\partial^4 X}{\partial X_1 \partial X_2^3} + \frac{A_{11}^*}{A_{22}^*}\frac{\partial^4 X}{\partial X_2^4} = 0 \tag{9}$$

For a crack oriented in an arbitrary direction in such a laminate (Fig. 5), the A_{ij}^* coefficients can be transformed from the principal direction to the direction of the crack. These coefficients can then be used in Eq. (9) to obtain the near field stress distribution around the crack tip. The solution is

$$\sigma_1 = 2R_e[S_1^2\phi_1'(Z_1) + S_2^2\phi_2'(Z_2)]$$

$$\sigma_2 = 2R_e[\phi_1'(Z_1) + \phi_2'(Z_2)]$$

$$\sigma_6 = -2R_e[S_1\phi_1'(Z_1) + S_2\phi_2'(Z_2)] \tag{10}$$

$$Z_1 = x_1 + S_1x_2$$

$$Z_2 = x_1 + S_2x_2$$

where for uniform stress σ^∞ and τ^∞ the stress functions are, Ref. 6,

$$\lim_{Z_1 \to a} \phi_1'(Z_1) = -\frac{(\tau^\infty\sqrt{a} + S_2\sigma^\infty\sqrt{a})}{2(S_1 - S_2)\sqrt{(2r(\cos\theta + S_1\sin\theta)}}$$

$$\lim_{Z_2 \to a} \phi_2'(Z_2) = -\frac{\tau\beta\sqrt{a} + S_1\sigma^\infty\sqrt{a}}{2(S_1 - S_2)\sqrt{(2r(\cos\theta + S_2\sin\theta))}} \tag{11}$$

and $S_1 = \alpha_1 + i\beta_2$, $S_2 = \alpha_2 + i\beta_2$ are the roots of the characteristic equation of Eq. (9). Thus, Eq. (10) is the laminate analogue of Eq. (4). From Eq. (10) for a given direction θ from the crack tip, the direction cosines of the stress vector can be obtained and the laminate analogue of Eq. (3) can be computed in the stress space as a function of distance r from the crack tip.

$$\vec{d} = \frac{N_1}{h}\vec{e}_1 + \frac{N_2}{h}\vec{e}_2 + \frac{N_6}{h}\vec{e}_6 \tag{12}$$

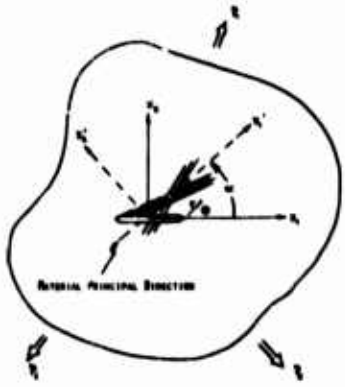


Figure 5. Definition of coordinates of a crack oriented in an arbitrary direction with respect to the principle direction of the laminate.

Now in order to compute the strength vector $\vec{F}$, the laminate analogue of a failure criterion is needed. This required laminate failure criterion can also be computed from the lamina failure criterion (Eq. (1)) through use of the linear laminated plate theory using the definition that 1st ply failure constitutes total failure of the laminate. This computation can be most efficiently performed by noting that every point in the lamina failure surface has a corresponding failure point in the laminate failure surface. We may then systematically choose a stress ratio

$$\frac{\sigma_1}{\sigma_2}, \frac{\sigma_1}{\sigma_6}, \sigma_1$$

in the lamina and obtain the failure condition $\sigma_1^*, \sigma_2^*, \sigma_6^*$ by Eq. (1). Substituting these stresses σ_i^* into

$$\epsilon_i^* = S_{ij}^{(k)} \sigma_j^*,$$

we obtain the failure strain condition. Assigning this failure strain condition to be the average strain of the laminate

$$\epsilon_{io}^* = \epsilon_i^*,$$

we can then compute the failure condition for the laminate by

$$N_i^* = A_{ij} \epsilon_j^*.$$

This procedure is summarized in the sequential solution of the following equations:

for kth layer subjected to

$$F_i^{(k)} \sigma_i^* + F_{ij}^* \sigma_i^* \sigma_j^* = 1, \qquad (13)$$

$$\epsilon_i^* = S_{ij}^{(k)} \sigma_j, \qquad (14)$$

$$\epsilon_{io}^* = \epsilon_i^*, \qquad (15)$$

$$N_i^* = A_{ij} \epsilon_{io}^* \qquad (16)$$

where * denotes failure conditions.

Systematic solution of Eqs. (13) to (16) for different ratios

$$\frac{\sigma_1}{\sigma_2}, \frac{\sigma_1}{\sigma_6}, \sigma_1$$

results in a laminate failure surface when discrete points are fitted with a third-order polynomial in the form, Ref. 8,

$$F_i \frac{N_i}{h} + F_{ij} \frac{N_i N_j}{h^2} + F_{ijk} \frac{N_i N_j N_k}{h^3} = 1 \qquad (17)$$

where

$$F_i, F_{ij}, F_{ijk}$$

are failure tensors for the laminate. A sample of the least square fit is shown in Fig. 6.

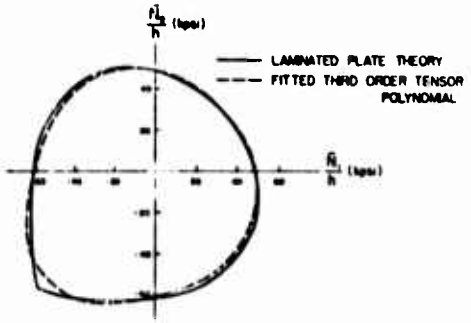


Figure 6. Third order tensor polynomial failure surface for 0/90/0/90/90/0/90/0 laminate.

In essence, Eq. (17) is the laminate correspondence of Eq. (1). Hence, for every stress vector determined by Eq. (12) a corresponding laminate strength vector can be computed from Eq. (17) by

$$\vec{F} = \frac{N_i^*}{h} \vec{e}_i \qquad i = 1,2,6 \qquad (18)$$

The above computation has the following meaning: For a given loading condition (Fig. 3) along each polar direction from the crack tip there exists a stress vector $\vec{\sigma}$ which is representative of the driving force in that direction. For such a stress vector the material resistance to rupture is represented by the strength vector $\vec{F}$. If the driving force is less than the resistance, no rupture can take place; hence, the stability for the crack is defined by

$$\vec{\sigma}_c = \vec{F}_c \qquad (19)$$

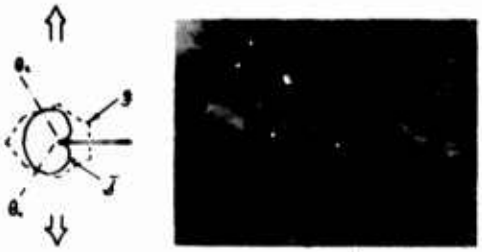
where the subscript c refers to the neighborhood of the crack tip.

Experimental Observations

The purpose of the experimental program is to examine the theoretical model to see if the coincidence of the stress vector $\mathcal{J}_c$ and the strength vector $\mathcal{J}_c$ defines the magnitude and direction of crack initiation trajectory.

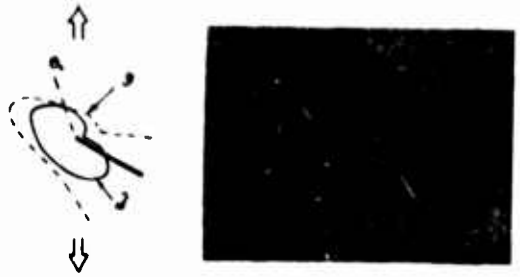
The samples are fabricated from 3M glass-epoxy pre-preg. Four variations of the lamination sequences are examined. The fracture samples are rectangular, 4.75" wide and 8" between grips. A centrally located initial crack is sawed in the sample by a jeweler's saw producing a crack width around .008". The specimens are tested in tension in a standard testing machine under displacement control. A motor driven 35 mm camera is triggered by the experimentalist and the event of each picture taken is also marked on the load-deformation recordings, thus providing a recording of crack length corresponding to different load levels.

We note that by varying the crack orientation with respect to the direction of tension, we can effectively apply combined tension and shear loading to the crack and, consequently, vary the contour of the stress vector $\mathcal{J}$. Furthermore, by varying the lamination geometry, we can vary the strength of the composite and, hence, the contour of the strength vector $\mathcal{J}$. In accordance with the method discussed in the previous section, the polar contour stress vector and strength vector are computed for four lamination geometries with different crack orientations as shown in Figs. 7 to 10. In Fig. 7a the crack is oriented perpendicular to the tensile load in an 0°/45°/90°/-45° laminate. The stress vector $\mathcal{J}$ and the strength vector indicate two critical orientations, θ_c, where crack initiation is predicted by the theoretical model. In Fig. 7b this predicted trajectory is clearly confirmed by experimental observation. In Fig. 8a, the crack is oriented at 60° to the tensile load in a 30°/60° laminate. The $\mathcal{J}$ and $\mathcal{J}$ contours indicate a single critical orientation $-\theta_c = 44°$ from original crack direction. Figure 8b shows that this predicted trajectory is substantiated by experimental observation. In Fig. 9a the crack is oriented at 45° to the tensile load in a 90°/45° laminate where the $\mathcal{J}$ and $\mathcal{J}$ contours predict a co-linear crack extension. Again, this is clearly substantial by the photograph shown in Fig. 10b.



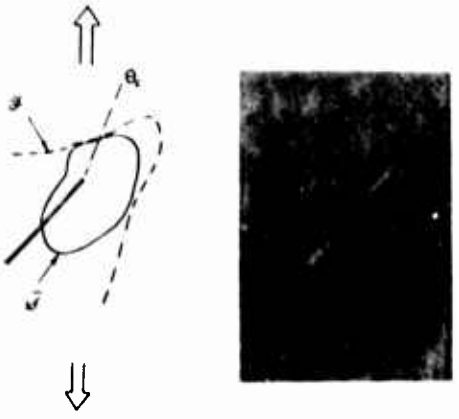
(a) (b)

Figure 7. (a) Computed stress vector $\mathcal{J}$ and strength vector $\mathcal{J}$ contour for 90/45/0/-45/-45/0/45/90 laminate. (b) Experimentally observed crack initiation.



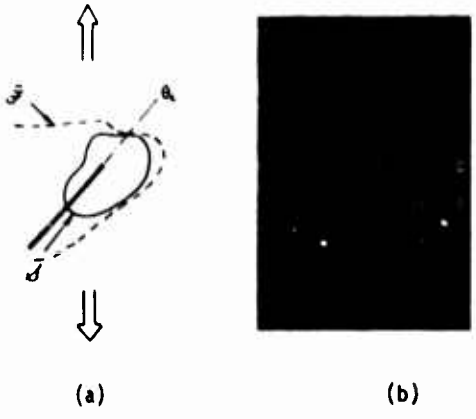
(a) (b)

Figure 8. (a) Computed stress vector $\mathcal{J}$ and strength vector $\mathcal{J}$ contour for 60/30/60/30/60/30/60 laminate. (b)Experimentally observed crack initiation.



(a) (b)

Figure 9. (a) Computed stress vector $\mathcal{J}$ and strength vector $\mathcal{J}$ contour for 45/45/45/0/45/45/45 laminate. (b) Experimentally observed crack initiation.



(a) (b)

Figure 10. (a) Computed stress vector $\mathcal{J}$ and strength vector $\mathcal{J}$ contour for 45/45/90/45/45/90/45/45 laminate; (b) experimentally observed crack initiation.

It is important to note that for a given laminate, both the contours of the $\bar{\mathcal{A}}$ and $\bar{\mathcal{F}}$ vectors are a function of external loading. Naturally, for different laminate configurations, the differences in these contours will be even more drastic. Furthermore, in the computation of the local stress around the crack tip, Eq. (10) is only applicable for a straight crack. If the crack extension is not self-similar, i.e., not co-linear with the parent crack then the mapping function changes in form and Eq. (10) is no longer applicable. Thus, for the cases of crack deflection, the above computation is only applicable for the point of initiation.

Finally, Eq. (19) checks the criticality of the stress and strength vector as modified in the neighborhood of the crack tip. It should be recognized that the criticality of the $\bar{\mathcal{A}}$ and $\bar{\mathcal{F}}$ vectors has to be checked for the far field or global condition where the stress distribution is not under the influence of the crack, i.e., whether the

$$\bar{\mathcal{A}}_g < \bar{\mathcal{F}}_g \qquad (20)$$

here the subscripts g refer to the far field global stress.

It is immediately apparent that if $\bar{\mathcal{A}}_g \ll \bar{\mathcal{A}}_c$, then crack extension will be confined completely to the crack tip. However, if $\bar{\mathcal{A}}_g \geq \bar{\mathcal{A}}_c$, global damage may occur in addition to the crack extension.

Conclusion

The characterization of the fracture responses of laminated composites is of great engineering importance not only for the prediction of the criticality of macroscopic flaws but also for the design of crack-arresting, fail-safe structures. Recent investigations of laminated composite fracture have utilized characterization methods established for isotropic solids and, hence, are revelant only to the particular lamination configuration tested. These results typically do not address the condition of combined loadings and the non-selfsimilar crack trajectory. Thus, these findings cannot be generalized to arbitrary lamination geometry and loading conditions for efficient structural design. A theoretical model has been presented herein to combine the lamina failure criterion with stress analysis of the crack. With this theoretical model, seven major parameters which control laminate fracture can be reduced to two, i.e., the lamina failure criterion and a critical volume characteristic to the composite. The reduction of controlling parameters to two makes quantification of the fracture of laminates a tractable task. Several lamination geometries are tested. By varying the external loading, different crack trajectories are predicted by the theoretical model. These predicted trajectories agree well with the experimentally observed modes. Such agreement suggest that, with refinement, the general condition of laminate fracture can be characterized within useful engineering accuracy.

Acknowledgment

This work has been initiated by the support of U.S. Air Force Materials Laboratory through Contract No. F 33615-72-C-1514 and is being continued by the support of Air Force Office of Scientific Research through Grant No. AFOSR-74-2687.

References

1. Wu, E. M. "Phenomenological Anisotropic Failure Criterion" in Composite Materials, 2 (Vol. ed. G. P. Sendeckyj, Series eds. L. J. Broutman and R. H. Krock) Academic Press, 1974.

2. Tsai, S. W., and Wu, E. M., "A General Theory of Strength for Anisotropic Materials," Journal of Composite Materials, 5, 1971.

3. Wu, E. M. "Optimal Experimental Measurement of Anisotropic Failure Tensors," Journal of Composite Materials, 6, 1971.

4. Wu, E. M. and Jerina, K. L. "Computer-Aided Mechanical Testing of Composites," Materials Research and Standards, 12, No. 2.

5. Wu, E. M., "Strength and Fracture of Composites" in Composite Materials (Vol. ed. L. J. Broutman, Series eds. L. J. Broutman and R. H. Krock) Academic Press, 1974.

6. Wu, E. M., "Fracture Mechanics of Anisotropic Plates," Composite Materials Workshop (eds. S. W. Tsai, J. C. Halpin and N. J. Pagano) Technomic Press, 1968.

7. Wu, E. M., Jerina, K. L. and Lavengood, R. E., "Data Averaging of Anisotropic Material Constants," ASTM STP 521, American Society of Testing and Materials, 1973.

8. Wu, E. M. and Scheublein, J. K., "Laminate Strength - A Direct Characterization Procedure," Composite Materials: Testing and Design (Third Conference), ASTM STP 546, American Society for Testing and Materials, 1974, pp. 188-206.

FAILURE MECHANISMS IN FIBER-REINFORCED COMPOSITES

I. M. Daniel
IIT Research Institute
Chicago, Illinois 60616

ABSTRACT

Failure mechanisms in fiber composites are a function of many parameters such as constituent properties, lamination geometry, state of stress, etc. They can be viewed at the microscopic level of fiber-matrix interaction, at the single lamina level and at the macroscopic laminate level. The basic failure mechanisms at the microscopic level include tensile, compressive or shear fracture of the matrix, bond failure of the fiber-matrix interface and tensile or compressive (buckling) failure of the fibers. In angle-ply laminates the first failure in the form of cracks parallel to the fibers occurs when the strain limit of the weakest ply (usually at 90-deg. to the load) is exceeded. This first ply failure is usually not catastrophic. The subsequent behavior of the laminate depends on its notch sensitivity and interlaminar shear strength. Failure patterns are highly influenced by free edges where a three-dimensional state of stress exists with high localized interlaminar shear and normal stresses. A variety of failure modes, not always predictable by theory, have been observed around notches in boron/epoxy, glass/epoxy and graphite/epoxy composites using experimental strain analysis techniques. In uniaxially loaded quasi-isotropic laminates with holes, regions of high strain concentration with nonlinear response develop at characteristic locations around 22.5-deg. off the horizontal axis. Failure starts at these off-axis points in the form of local delamination and fiber breakage and propagates across the width of the plate. The effects of lamination geometry, ply stacking sequence, biaxial stress and hole diameter on failure are discussed. In the case of cracks, failure at the top of the crack usually takes the form of a damage zone consisting of ply subcracking along fiber directions, local delamination and fiber breakage. Final failure occurs when this damage zone reaches some critical size. One noteworthy result was that the strength of quasi-isotropic graphite/epoxy laminates is independent of notch geometry and that there is a critical notch size below which the material becomes notch insensitive.

Introduction

A fiber reinforced composite laminate is made up of a number of variously oriented laminae or plies with each ply consisting of a layer of parallel fibers embedded in a matrix. Failure in composite laminates can be viewed from many levels. At the macroscopic level the laminate is viewed as a homogeneous anisotropic material and failure occurs when the average state of stress exceeds some failure criterion for the laminate. At the "mini" level each ply is regarded as a homogeneous anisotropic layer with its own anisotropic failure criteria. The state of stress in each ply can be determined. Failure of one ply affects the stiffness and remaining strength of the laminate but does not necessarily result in total failure. At the microscopic level, it is recognized that the overall behavior of the composite laminate is intimately related to the internal stress distributions and load transfer between the constituent matrix and fibers. The basic failure modes include tensile, compressive or shear fracture of the matrix, bond failure at the fiber matrix interface, and tensile or compressive failure of the fibers. These modes are not isolated or independent but can interact and trigger each other. Failures on the microscopic level within one ply can cause interply failures (delaminations) and result in through the thickness total laminate failure.

Failure mechanisms in fiber composites are a function of the constituent properties, lamination goemetry, structure geometry including geometric discontinuities, state of stress and environmental conditions. In the present paper failure mechanisms under uniaxial and biaxial stresses are discussed at the lamina level (unidirectional composite), for balanced angle-ply laminates and angle-ply laminates with holes and cracks.

Failure Modes in Unidirectional Composite

Longitudinal Tension

The composite in this case is governed by the ultimate strain of the fibers. The most likely initial failure is a fiber break accompanied by some loss of effective fiber length and high interfacial shear stress near the break (Fig. 1).[1] This fiber break can be followed by a number of failure mechanisms in the surrounding matrix, i.e., transverse cracking in the matrix extending up to the adjacent fibers, fiber debonding for some distance from the newly formed ends or conical shear fracture of the matrix.[2] As the load increases, the size of these failure sites remains relatively unchanged but their number increases throughout the composite causing cumulative weakening. Ultimate failure occurs when the number of localized fractures increases to provide a weak path for complete fracture.

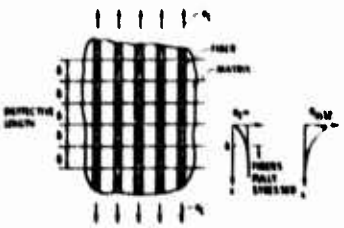


Figure 1. Failure model of unidirectional composite under longitudinal tension (Rosen, 1964).

In the lamina scale three basic failure modes can be distinguished:

(1) brittle
(2) brittle with filament pullout
(3) staggered failure, i.e., brittle failure with filament pullout and matrix shear or debonding along the fibers

These failure modes as discussed by Chamis[3] are illustrated in Fig. 2. Composites with low fiber volume ratio ($v_f \leq 0.4$) exhibit brittle failure, those with intermediate fiber volume ratio ($0.4 \leq v_f \leq 0.65$) exhibit brittle failure with fiber pullout. Plies with high fiber volume ratio ($v_f \geq 0.65$) exhibit the third mode of failure above.

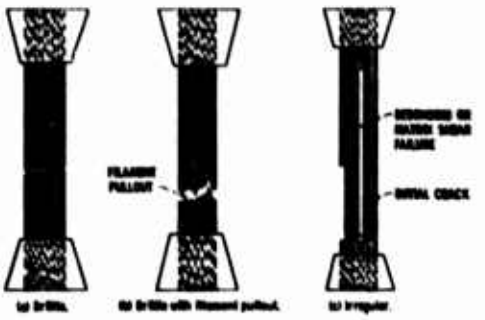


Figure 2. Longitudinal tensile failure model in unidirectional composite (Chamis, 1974).

The longitudinal tensile strength can be predicted reasonably well from the elementary rule-of-mixtures relation

$$S_{11T} + S_f V_f + \sigma_m (1-v_f) \qquad (1)$$

where S_f is the tensile strength of the fibers, and σ_m is the stress in the matrix at a strain equal to the fiber failure strain.

Longitudinal Compression

Compressive behavior of unidirectional composites has been discussed by Greszczuk[4] and Chamis[3]. The characteristic modes of failure in this case are:

(1) Filament microbuckling with matrix elastic and fully bonded.

(2) Matrix yielding or interfacial debonding followed by filament microbuckling.

(3) Panel microbuckling.

(4) Shear failure.

(5) Ply separation by transverse tension.

These failure modes are illustrated in Fig. 3. The first mode of failure occurs in composites with low fiber volume fraction. More realistic composites fail in the second mode above. Shear failure modes have also been observed experimentally. Expressions for the longitudinal compressive strength for microbuckling and interaction modes have been given by Greszczuk.[4]

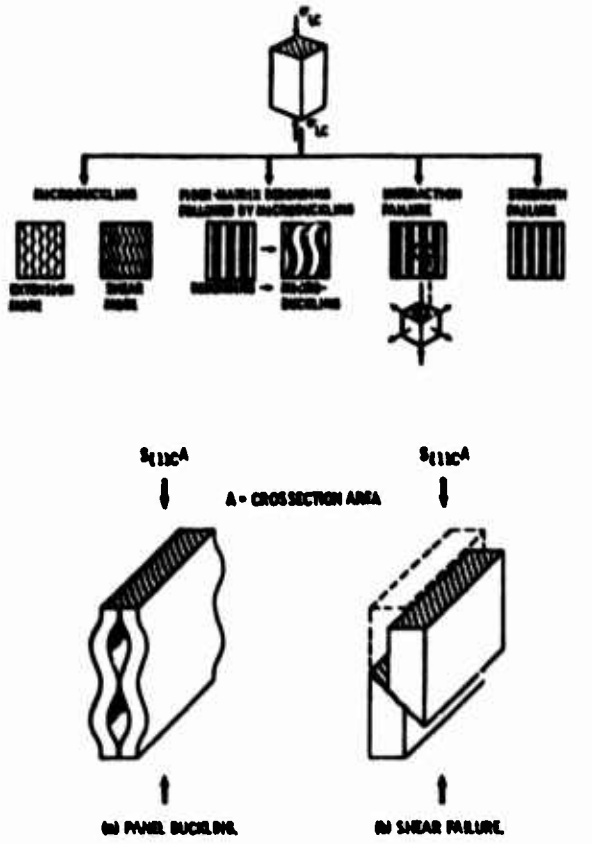


Figure 3. Longitudinal compressive failure modes in unidirectional composite (Greszczuk, 1974; Chamis, 19..

Transverse Tension

In this case, failure of the composite is dominated by the high strain concentration in the matrix. The primary failure modes are tensile matrix failure and fiber debonding. A great deal of analytical and experimental work has been reported on the stress distributions in transversely loaded unidirectional composites.[5-8] The most significant result is the strain concentration in the matrix at the fiber-matrix interface. An expression for this strain concentration is

$$k_\varepsilon = \frac{\bar{\varepsilon}_y}{\varepsilon_0} = k_\sigma \left(\frac{E_{22}}{E_m}\right) \frac{(1+\nu)(1-2\nu)}{1-\nu} \qquad (2)$$

where

ϵ_0 = average strain

$\bar{\epsilon}_y$ = maximum strain in the matrix

E_{22} = transverse composite modulus

E_m = matrix modulus

ν = matrix Poisson's ratio

k_σ = stress concentration factor

The stress concentration factor is obtained by analysis or experiment. The variation of the strain concentration factor as a function of fiber spacing is shown in Fig. 4, where it is seen that it rises sharply with increasing fiber volume ratio. Assuming a maximum strain failure criterion for the matrix, a simple expression for the transverse tensile strength is

$$S_{22T} \cong \frac{\epsilon_{mT}^u}{k_c} E_{22} \qquad (3)$$

where ϵ_{mT}^u is the ultimate tensile strain in the matrix. Groszczuk[4] has given more complex expressions involving three triaxial stress concentration factors.

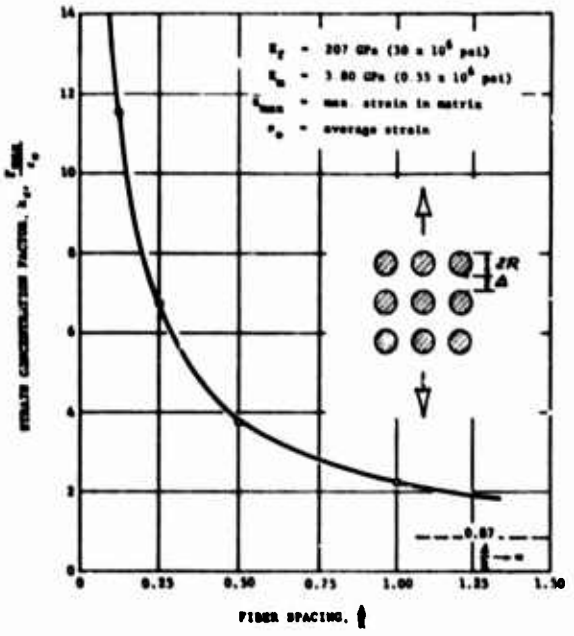


Figure 4. Strain concentration factor as a function of fiber spacing in a square array under transverse loading.

Transverse Compression

The primary failure modes under this type of loading are compressive failure and shear failure in the matrix, sometimes accompanied by fiber debonding. Compressive failure occurs in the matrix when the maximum compressive strain exceeds the ultimate compressive strain. An approximate expression for the strength under this mode of failure can be obtained by replacing ϵ_{mT}^u with ϵ_{mc}^u, the ultimate compressive matrix strain, in the compression for tensile strength. A correlation between transverse compressive strength and transverse modulus has been found experimentally.[4]

In-Plane Shear

Failure mechanisms under this loading are matrix shearing, fiber debonding or a combination of the two. The intralaminar shear strength can be determined by dividing the shear strength of the matrix by the shear stress concentrations due to voids and fibers.[4] In many composites the intralaminar shear strength is approximately equal to the interlaminar shear strength. A fairly good correlation has been found between the latter and the transverse tensile strength.[4]

Biaxial Loading

Under biaxial stress conditions one or more of the failure modes discussed before may be activated. Macroscopic and microscopic failure criteria have been proposed.[9,10,11] Macroscopic criteria are based on maximum strain or distortional energy. Heterogeneous microscopic failure criteria taking into consideration nonlinear response have been suggested by McLaughlin and Rosen.[11]

Failure Modes in Angle-Ply Laminates

In angle-ply laminates under uniform stress the first failure in the form of cracks parallel to the fibers of a ply occurs when the strain limit of the weakest ply (usually the one at 90-deg. to the tensile load) is exceeded. Such ply failures are not always detected easily on the macroscopic scale. For example, a change in slope is observed in the axial stress-strain curve of a $[0/90]_s$ graphite/epoxy laminate and a rather sudden change in Poisson's ratio.[12] The strain at the point of slope change equals the failure strain of the 90-deg. ply. The first ply failure is easily predictable and is not always catastrophic. The most challenging problem is the prediction of the subsequent behavior of the laminate following first ply failure.

When a [0/90] laminate, for example, is loaded in uniaxial tension the first cracks appear in the 90-deg. plies. Subsequently, three possible mechanisms of failure propagation can develop (Fig. 5).[12] If the adjacent 0-deg. plies are brittle and notch-sensitive the microcracks will propagate across these plies to cause catastrophic failure (Fig. 5a). This is associated with composites having a low fiber volume ratio and high interlaminar shear strength. If the ply interfaces are relatively weak, i.e., if the material has a low interlaminar shear strength, the cracks in the 90-deg. plies will turn along these interfaces, the initially

cracked ply will be isolated from the other plies and the laminate will continue carrying load with a slightly reduced stiffness and residual strength (Fig. 5b). If the adjacent 0-deg. plies resist crack propagation and if the interlaminar shear strength is high, the initial cracks in the 90-deg. plies do not grow but new similar cracks develop in this ply (Fig. 5c). The 90-deg. ply continues to carry some load through the intact interfaces. Its load carrying capacity is gradually depleted as these cracks become denser and the distance between them shorter.

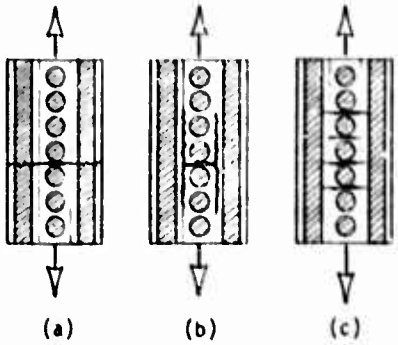


Figure 5. Failure mechanisms in composite laminate following first ply failure: (a) brittle failure, (b) delamination, (c) progressive degradation of 90-deg. ply. (Tsai and Hahn, 1975).

Failure patterns in angle-ply specimens of finite width are highly influenced by the free edges where a three-dimensional state of stress results in highly localized interlaminar shear and normal stresses.[13] Laminates of $[\pm\theta]$ layup under axial loading develop high interlaminar shear stresses which can reach values up to approximately half the normal axial stress. These stresses attenuate very quickly over a distance of approximately one laminate thickness from the edge. For a typical graphite/epoxy laminate they reach the highest value at the edge when $\theta \cong 35$-deg. Such high shear stresses near the free edge often cause progressive edge delamination especially under fatigue loadings. Symmetric angle-ply $[\pm\theta]$ laminates under axial tensile loading in the 0-deg. direction exhibit various failure modes depending on the angle θ. Rotem and Hashin[14] studied these failure modes for glass/epoxy laminates. Stress-strain curves for various values of the ply orientation are shown in Fig. 6. When $\theta < 45$-deg. failure is governed by the high interlaminar shear stress near the edges, which decreases with the angle θ. As the angle θ gets smaller the laminate behavior approaches that of the unidirectional lamina under longitudinal tension. When $\theta = 45$-deg. failure results from progressive lamina cracking over the whole specimen. When $\theta > 45$-deg. lamina cracking occurs early and is more localized resulting in low ultimate strains. As the angle increases the laminate behavior approaches that of the unidirectional lamina under transverse tension.

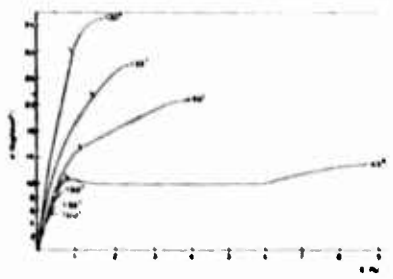


Figure 6. Stress-strain curves of $[\pm\theta]$ angle-ply glass/epoxy laminates (Rotem and Hashin, 1975).

The interaction of failure mechanisms becomes more complex in multi-angle and hybrid laminates having high lamination residual stresses. Residual stresses in laminates are induced during curing as a result of the anisotropic thermal deformations of the variously oriented plies. The influence of residual stresses on failure patterns is vividly illustrated in the case of hybrid angle-ply laminates in Fig. 7. The graphite/glass/epoxy $[\pm 45^C/0^G/0^C]_S$ specimen (where superscripts C and G denote graphite and glass, respectively) failed in a "brooming" fashion after the 0-deg. graphite ply failed first and the isolated layer $(\pm 45^C/0^G)$ curved as shown because of the residual tensile stresses in the 0-deg. glass ply. The same residual stress caused the outer $(0^G/\pm 45^C)$ layer in the $[0^G/\pm 45^C/0G]_S$ specimens to curl outwards after the central 0-deg. glass plies had delaminated.

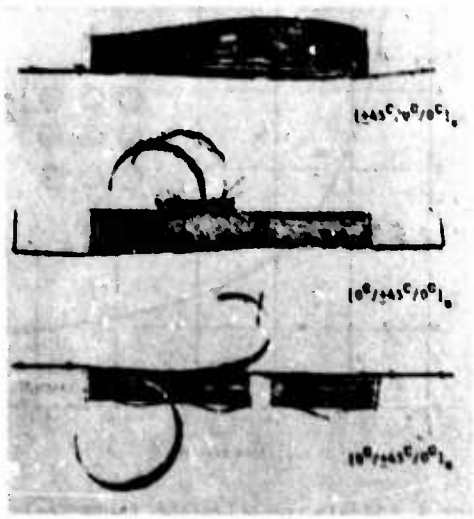


Figure 7. Characteristic failure patterns of three graphite/S-glass/high modulus epoxy specimens under uniaxial tensile loading.

Failure Mechanisms in Laminates with Holes

Of special interest in failure of composites are the failure mechanisms that develop around discontinuities such as holes and cracks, i.e., in the presence of highly nonuniform stress fields. A variety of failure modes, not always predictable by theory, have been observed around notches in boron/epoxy, glass/epoxy and graphite/epoxy composites using experimental strain analysis techniques. The strength and failure modes depend on the type of material, lamination geometry, stacking sequence, hole geometry, hole size, and type of loading.

Uniaxially Loaded $[0/\pm45/0/\overline{90}]_s$ Boron/Epoxy Plate

An experimental strain analysis to failure was conducted for boron/epoxy plates with circular holes using strain gages and photoelastic coatings.[15] Strain distributions in the linear range agree with predictions obtained from linear anisotropic elasticity and finite element analysis. As the load increases a sequence of interacting failure mechanisms consisting of local failure of the 90-deg. ply, local delaminations and finally fiber breakage cause nonlinear strain response, stress and strain redistributions and finally complete failure. The effect of strain redistribution is shown by the strain results of Fig. 8 where the strain near the hole boundary increases nonlinearly at a faster rate and becomes larger than that on the hole boundary. The photoelastic coating fringe patterns of Fig. 9 show that the location of maximum birefringence shifts from θ = 90-deg. (horizontal axis) at low loads to $\theta \cong 67.5°$ deg. near failure. This shift is illustrated by the birefringence variation around the hole boundary for various load levels (Fig. 10). Failure starts at these off-axis points of high birefringence (strain) concentration with nonlinear response. It consists of ply subcracking and local delamination followed by fiber breakage and propagates across the width of the plate to ultimate failure. The failure pattern for this type of specimen is shown in Fig. 11.

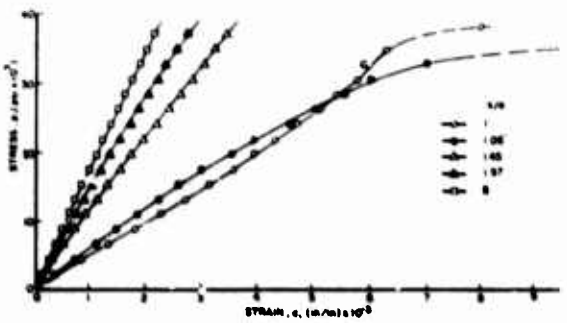


Figure 8. Vertical strains along horizontal axis in $[0/\pm45/0/90]_s$ boron/epoxy specimen with 2.54 cm (1 in.) diameter hole under uniaxial tensile loading.

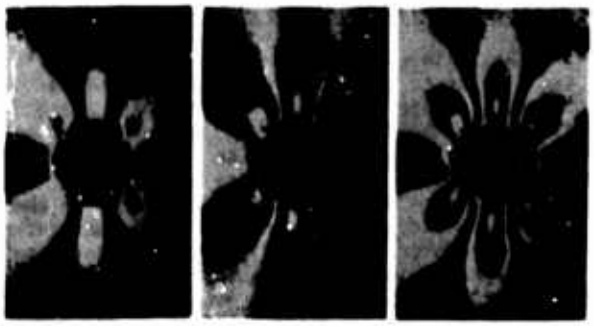


Figure 9. Isochromatic fringe patterns around hole in $[0/\pm45/0/90]_s$ boron/epoxy specimen for applied uniaxial stresses of 166 MPa (24.0 ksi), 225 MPa (32.6 ksi) and 293 MPa (42.4 ksi).

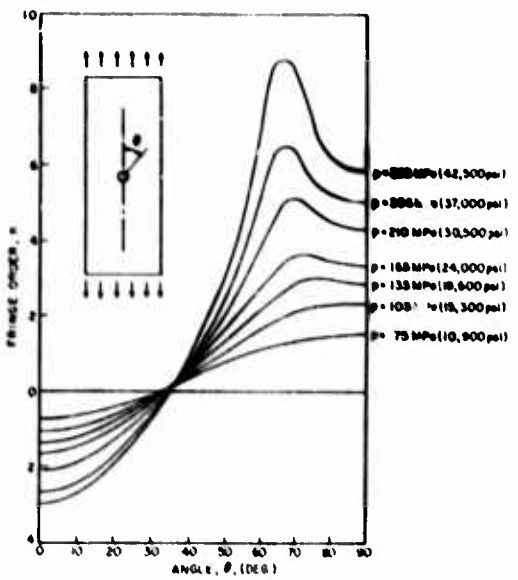


Figure 10. Birefringence distribution around boundary of hole for various load levels in $[0/\pm45/0/\overline{90}]_s$ boron-epoxy specimen.

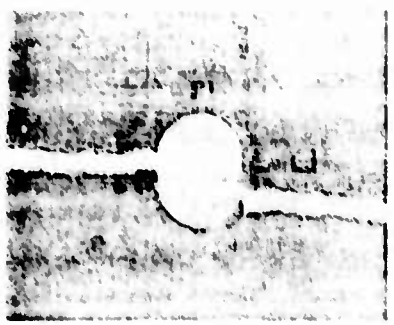


Figure 11. Typical failure pattern around hole in $[0/\pm45/0/\overline{90}]_s$ boron/epoxy specimen under uniaxial tensile loading.

Uniaxially Loaded $[0/\pm45/0/\overline{90}]_s$ Glass/Epoxy Plate

The failure modes in the glass/epoxy plate are similar to those of the boron/epoxy plate above. Failure initiation and propagation are illustrated by the moire fringe patterns of Fig. 12.[16] Cracks start on the hole boundary off the horizontal axis accompanied by extensive delamination. One interesting phenomenon is the seemingly discontinuous propagation of the cracks. They seem to propagate in discrete, discontinuous horizontal steps with a gross direction of fracture at 45-deg. This is possibly due to longitudinal tensile fracture of the outer 0-deg. ply combined with shear delamination of the interior 45-deg. plies. The failure pattern was similar to the one of boron/epoxy but with much more pronounced delamination.

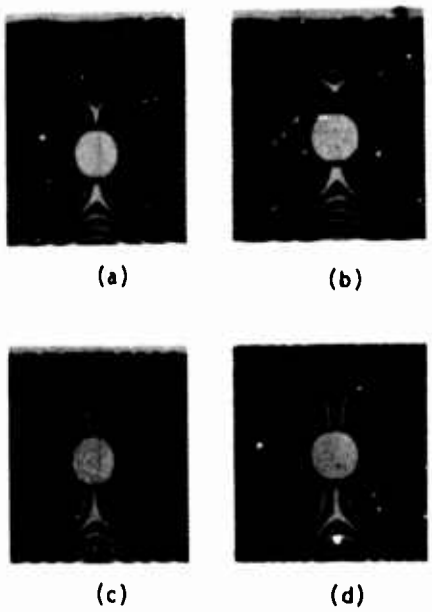


Figure 12. Sequence of moire fringe patterns corresponding to vertical displacements in $[0/\pm45/0/\overline{90}]_s$ glass/epoxy specimen at various applied uniaxial stresses: (a) 198 MPa (28.7 ksi), (b) 206 MPa (29.9 ksi, (c) 206 MPa (29.9 ksi) and (d) 210 MPa (30.4 ksi).

Influence of Laminate Construction

The effect of lamination geometry on failure of plates with holes was studied with boron/epoxy plates of $[0/90/0/90]_s$, $[0_2/\pm45/\overline{0}]_s$, $[0/\pm45/0/\overline{90}]_s$, $[0/\pm45/90]_s$, $[\pm45/0/\pm45]_s$ and $[\pm45/\pm45]_s$ layup.[17] Strain distributions, strain concentration factors, failure modes and strength reduction ratios vary widely with laminate construction. The two extremes of behavior are shown by the fringe patterns for the $[0/90/0/90]_s$ and $[\pm45/\pm45]_s$ plates (Fig. 13). The former shows a sharp strain gradient with a high strain concentration factor (k_ϵ = 4.82) and with all the perturbation dying out within a short distance from the hole boundary. The maximum birefringence remains at the 90-deg. location. The material behaves in a brittle manner. The first sign of nonlinear response is related to failure of the 90-deg. plies. The maximum strain at failure is low (6.6×10^{-3}). The $[\pm45/\pm45]_s$ plate shows a very moderate strain gradient with a low strain concentration factor (k_ϵ = 2.06). The influence of the hole extends through the entire width of the plate. The highest fringe concentration occurs on the horizontal axis at or near the hole boundary. The maximum strain at failure is high ($>25 \times 10^{-3}$).

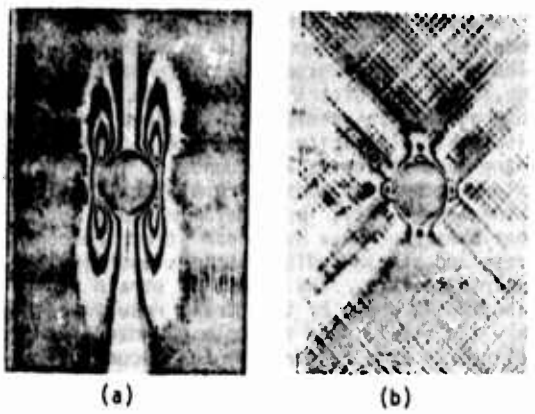


Figure 13. Isochromatic fringe patterns in photoelastic coating around hole in boron/epoxy specimens: (a) $[0/90/0/90]_s$, σ_y = 170 MPa (24.6 ksi), (b) $[\pm45/\pm45]_s$, σ_y = 77 MPa (11.1 ksi).

Failure patterns of the various laminates are shown in Fig. 14. The $[0/90/0/90]_s$ laminate fails in the most brittle fashion through the horizontal axis. The quasi-isotropic laminate $[45/90/0/-45]_s$ failed like the $[0/\pm45/0/\overline{90}]_s$ one discussed earlier, i.e., failure originated on the hole boundary off the horizontal axis, progressed at some angle to the horizontal and finally propagated across the width of the plate in a horizontal direction. Failure in the $[\pm45/0/\pm45]_s$ plate originated off the horizontal axis on the hole boundary and propagated across the width at some angle to the horizontal. The $[\pm45/\pm45]_s$ laminate failed at 45-deg. to the horizontal.

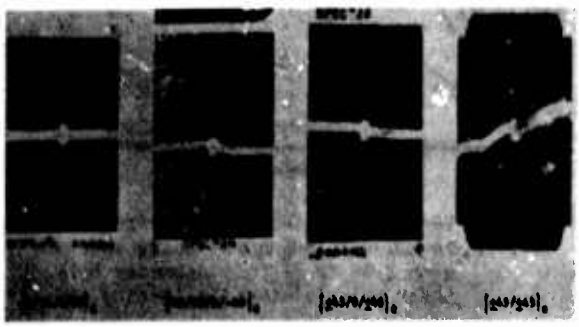


Figure 14. Failure patterns of boron-epoxy panels with holes of various laminate constructions.

The overall laminate strength is related to the number of 0-deg. plies and the strain concentration factor. The strength reduction ratio, i.e., the ratio of the strength of the laminate with a hole to that of a laminate without a hole, was determined for all specimens. In general it is lower for high stress concentration factors. Thus, the $[0/90/0/90]_s$ layup with a stress concentration factor of 4.82 has a strength-reduction ratio of 0.31. At the other extreme, the most flexible layup $[\pm 45/\pm 45]_s$ with the lowest stress-concentration factor of 2.06 had the lowest strength-reduction ratio of 0.91 which means no strength reduction at all based on the net section. Laminates with a mixture of 0, 45, and 90-deg. plies exhibited stress-concentration factors ranging between 3.08 and 3.34 and strength-reduction ratios between 0.47 and 0.39.

The maximum strain on the hole boundary at failure range in most cases between 8×10^{-3} and 9×10^{-3} in./in., except for the flexible $[\pm 45]_c$ construction which witnstood strains up to 37×10^{-3} in./in., and the $[0/90]_c$ construction with a maximum strain at failure of 6.6×10^{-3} in./in. In all cases, the maximum strain at failure on the hole boundary was higher than the ultimate tensile-coupon strain.

Influence of Stacking Sequence

Laminates of the same construction but different stacking sequence may have different strengths due to the interlaminar stresses near free edges. The most influencial of these stresses is the interlaminar normal stress. Whenever the free boundary contains a region of high stress concentration (hole) forcing failure initiation in that region, the effects of stacking sequence variation on strength are further accentuated.

Boron/epoxy laminates with holes of $[\pm 45/0_2/0]_s$, $[0_2/\pm 45/90]_s$, $[+45/90/0/-45]_s$ and $[45_2/-45_2]_s$ layup were investigated.[17] These represent stacking sequence variations of four of the layups discussed before. The most pronounced differences were observed in the pair of $[0_2/\pm 45/0]_s$ and $[\pm 45/0_2/0]_s$ layups. The first one with a measured strain concentration factor of 3.58 was 17 percent stronger than its stacking sequence variation $[\pm 45/0_2/0]_s$ with a measured strain concentration factor of 4.02. The development of interlaminar normal stresses near the boundary is illustrated in Fig. 15. The first layup with compressive interlaminar normal stress is stronger than the second layup where the interlaminar normal stress is tensile.

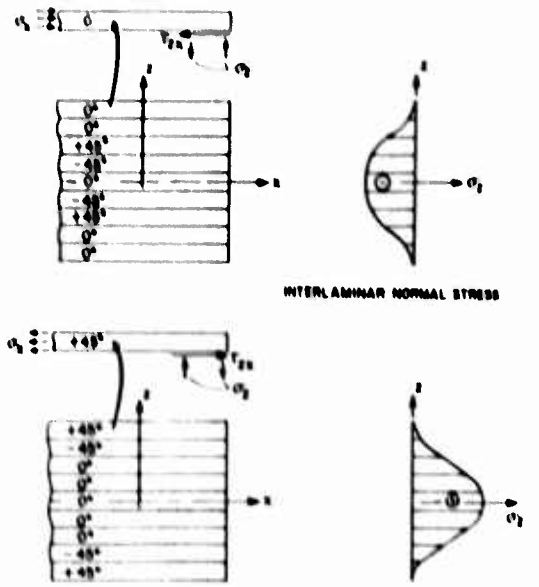


Figure 15. Interlaminar stresses in outer ply and distribution of interlaminar normal stress near the boundary for $[0_2/\pm 45/0]_s$ and $[\pm 45/0_2/0]_s$ laminates under uniaxial tensile loading.

Some of the differences between the two layups are also manifested in the isochromatic fringe patterns in the photoelastic coatings (Fig. 16). The pattern for the first layup is fairly symmetrical, has lower birefringence, and shows a tendency for failure propagation along the vertical tangents to the hole boundary, i.e., parallel to the outer 0-deg. plies. The second pattern is antisymmetrical with higher birefringence concentration. The failures in the first and third quadrants are associated with shear failure of the outer ±45-deg. plies, whereas failures in the second and fourth quadrants are associated with cracking along the subsurface 0-deg. plies. The birefringence variation around the circumference of the hole is shown in Fig. 17. The shift of maximum birefringence from $\theta = 90$-deg. to $\theta = 60$-deg. and $\theta = 65$-deg. is shown as well as the higher peak birefringence for the $[\pm 45/0_2/0]_s$ layup.

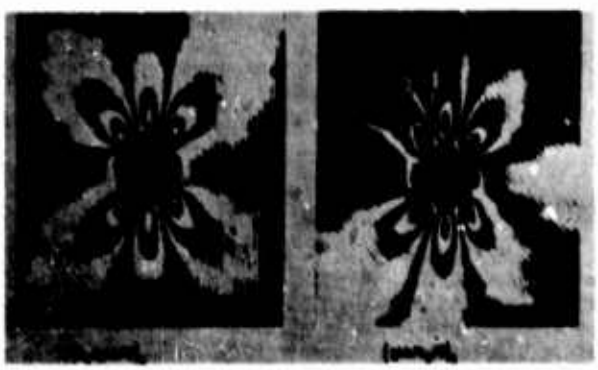


Figure 16. Isochromatic fringe patterns in photoelastic coating around hole in boron/epoxy specimens of two different stacking sequences (σ_y = 392 MPa; 56.8 ksi).

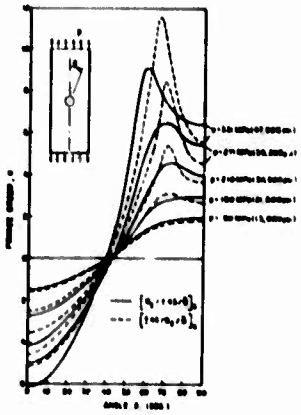
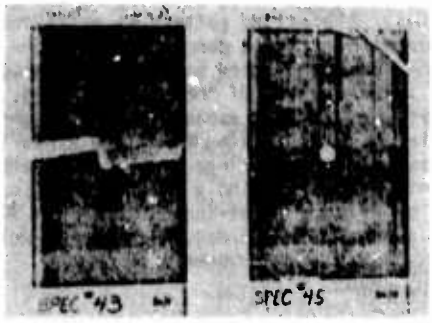


Figure 17. Birefringence distribution around hole boundary at various applied stress levels for two stacking sequence variations.

The stacking sequence variation can affect the failure mode and strength in a dramatic way (Fig. 18). The $[\pm 45/0_2/\bar{0}]_s$ plates tend to fail horizontally through the hole in a catastrophic manner at a relatively low load. The $[0_2/\pm 45/\bar{0}]_s$ plates tend to develop cracking along the vertical tangents to the hole, thus blunting or neutralizing the stress concentration. These specimens subsequently behave like a pair of unnotched laminates and carry a much higher load than the $[\pm 45/0_2/\bar{0}]_s$ specimens.



(a) (b)

Figure 18. Failure patterns of boron-epoxy tensile panels with holes: (a) $[\pm 45/0_2/\bar{0}]_s$, (b) $[0_2/\pm 45/\bar{0}]_s$.

Influence of Hole Geometry

The influence of hole geometry was investigated with $[0/\pm 45/0/\overline{90}]_s$ boron/epoxy laminates containing elliptical and square holes.[18] Isochromatic fringe patterns in photoelastic coatings show the characteristic birefringence concentration at points off the horizontal axis for the elliptical holes (Fig. 19). Failure initiates at these points as in the case of the circular hole (Fig. 20). The plates with elliptical holes having the major axis in the vertical and horizontal directions, are only 25 percent stronger and 20 percent weaker, respectively, than plates with an equivalent circular hole. Laminates with a 2.54 cm (1 in.) square hole were slightly stronger than those with a 2.54 cm (1 in.) diameter circular hole.



(a) (b) (c)

Figure 19. Isochromatic fringe patterns in photoelastic coating of $[0/\pm 45/0/\overline{90}]_s$ boron/epoxy laminates with elliptical and square holes under uniaxial tensile loading. (a) σ_y = 361 MPa (52.3 ksi), (b) σ_y = 241 MPa (34.9 ksi), (c) σ_y = 331 MPa (48.0 ksi).

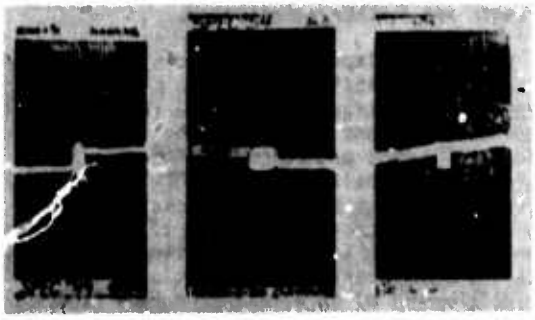


Figure 20. Failure patterns of $[0/\pm 45/0/\overline{90}]_s$ boron-epoxy laminates having elliptical and square cutouts.

Influence of Hole Diameter

Graphite/epoxy plates of $[0/\pm 45/90]_s$ layup with circular holes ranging in diameter between 0.02 cm (0.008 in.) and 2.54 cm (1 in.) were tested under uniaxial tension.[19] The response was similar to that of the quasi-isotropic boron/epoxy specimens discussed before. Strains at and near the hole boundary become nonlinear at a strain corresponding to initial failure of the 90-deg. plies. Maximum measured strains on the hole boundary can reach values up to twice the ultimate strain of the unnotched laminate. Regions of high

strain concentration with nonlinear response develop at four characterisitic locations 22.5-deg. off the horizontal axis. Failure initiates at these points where the interlaminar and membrane shear stresses reach maximum values. The laminate strength decreases with increasing hole size. There is a critical hole size below which the laminate becomes notch insensitive. The strength reduction ratio is plotted as a function of hole radius in Fig. 21. The effect of hole diameter on strength can be satisfactorily explained using the average stress criterion.[20] According to this criterion total failure occurs when the axial stress averaged over a characteristic distance (approximately 4mm) from the hole boundary equals the strength of the unnotched laminate.

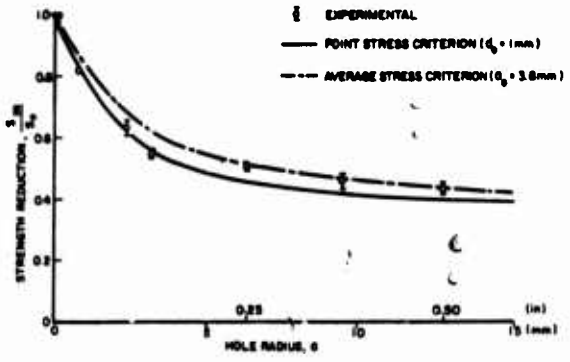


Figure 21. Strength reduction as a function of hole radius for $[0/\pm45/90]_s$ graphite/epoxy plates with circular holes under uniaxial tensile loading.

The effect of hole diameter was also studied with $[0_2/\pm45]_s$ graphite/epoxy plates with holes ranging in diameter between 0.04 cm (0.016 in.) and 2.54 cm (1 in.).[21] Typical strain variation along the horizontal axis are illustrated in Fig. 22 where two levels of nonlinear response are evident. The first one corresponds to a stress redistribution following the nonlinear response of the material under compressive stress at the 0-deg. location. The second level of pronounced nonlinearity occurs as a result of stress and strain redistribution produced by localized compressive failure (delamination) around the 0-deg. location. Failure patterns for specimens with holes of various diameters are shown in Fig. 23. Two failure modes can be discerned. In the case of larger holes failure initiates at locations of the hole boundary approximately 72-deg. from the load axis. In the case of smaller holes the outer 0-deg. plies through the hole tend to separate and, thus, reduce or eliminate the effects of stress concentration. There is a critical hole diameter (approximately 1.6 mm) below which the laminate becomes notch-insensitive. The strength reduction ratio is plotted as a function of hole radius in Fig. 24. The effect of hole diameter can be satisfactorily described using the average stress criterion.

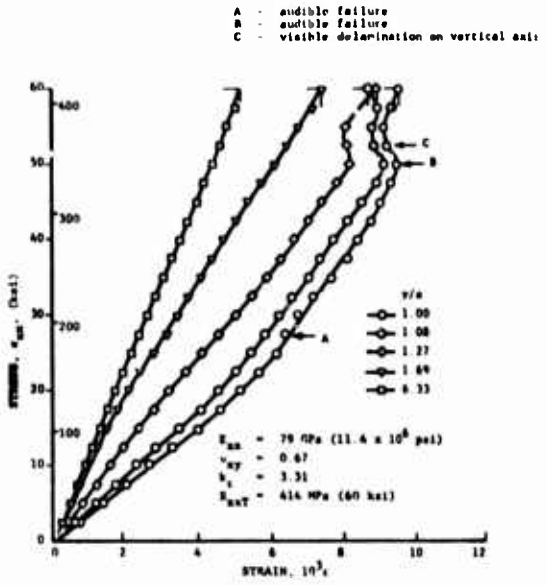


Figure 22. Vertical strains along horizontal axis of $[0_2/\pm45]_s$. Graphite/epoxy specimen with 1.91 cm (0.75 in.) diameter hole under uniaxial tensile loading.

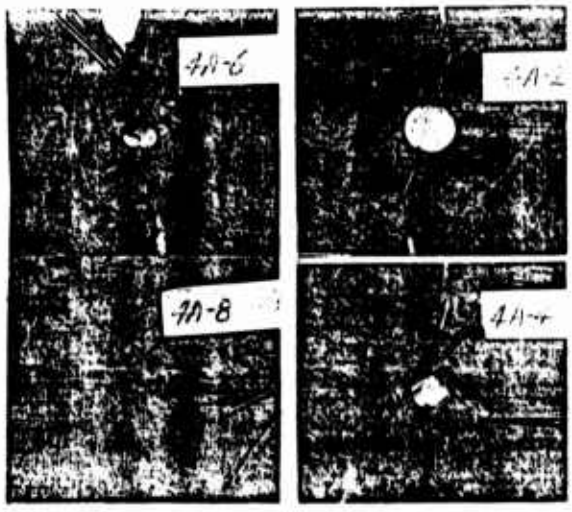


Figure 23. Failure patterns in $[0_2/\pm45]_s$ graphite/epoxy specimens with holes of various sizes under uniaxial tension. (Hole diameters are 2.54 cm (1 in.), 1.91 cm (0.75 in.), 1.27 cm (0.50 in.) and 0.64 cm (0.25 in.).

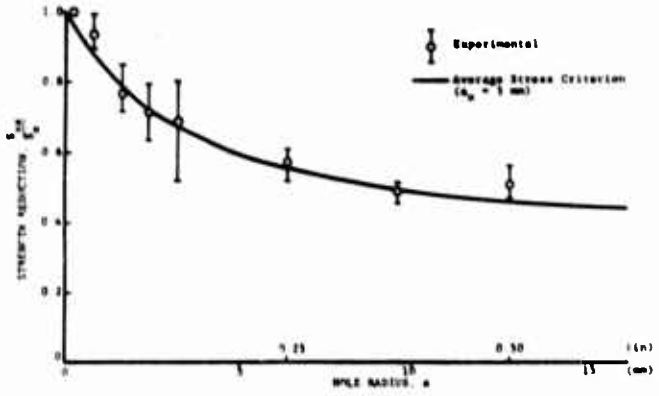


Figure 24. Strength reduction as a function of hole radius for $[0_2/\pm45]_s$ graphite/epoxy plates with circular holes under uniaxial tensile loading.



Figure 26. Failure pattern in $[0/\pm45/90]_s$ graphite/epoxy specimen with 1.91 cm (0.75 in.) diameter hole under equal biaxial tensile loading.

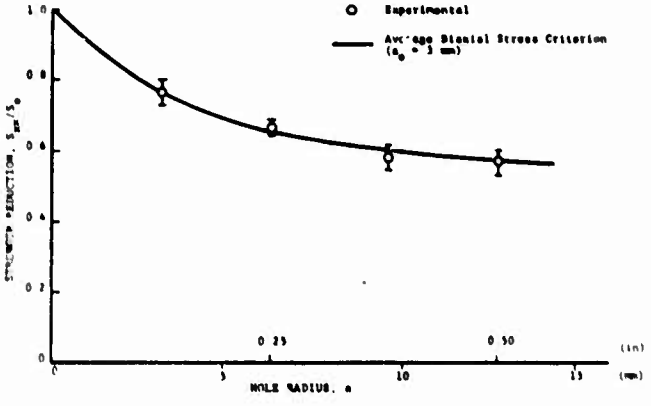


Figure 27. Strength reduction as a function of hole radius for $[0/\pm45/90]_s$ graphite/epoxy plates with circular holes under 1:1 biaxial tensile loading.

Effect of Biaxial Stress and Hole Diameter

These effects were studied by testing $[0/\pm45/90]_s$ graphite/epoxy laminates with holes of diameters ranging between 0.64 cm (0.25 in.) and 2.54 cm (1 in.) under equibiaxial tension.[19] As in the case of uniaxial loading, regions of high strain concentration with nonlinear response develop at eight chracteristic locations approximately 22.5-deg. off the fiber axes as illustrated by the isochromatic fringe patterns of Fig. 25. Failure initiates at one or more of these points. A typical failure pattern is shown in Fig. 26 with cracking and delamination initiated at three locations on the hole boundary. The variation of strength reduction ratio with hole radius was satisfactorily described by using an average biaxial stress criterion (Fig. 27).

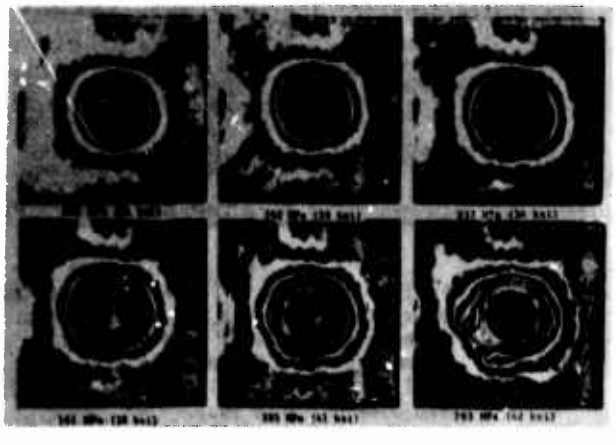


Figure 25. Isochromatic fringe patterns in photoelastic coating of $[0/\pm45/90]_s$ graphite/epoxy specimen with 2.54 cm (1-in.) diameter hole under equal biaxial tensile loading (far-field biaxial stress marked).

Failure Mechanisms in Laminates with Cracks

Uniaxially Loaded $[0/90/0/\overline{90}]_s$ Glass/Epoxy Plate

The failure mechanisms around notches in a crossply glass/epoxy laminate are elucidated by the moire fringe patterns of Fig. 28.[22] A high vertical tensile strain-concentration factor, approximately 5, exists at the tip of the crack. This peak strain remains nearly constant for some distance along a vertical line normal to the axis of the crack. This line represents a boundary between high tensile strain in front of the crack and high shear strain behind the tip of the crack. The high in-plane shear stress near the crack tip causes splitting of the 0-deg. plies along the fiber direction, thus producing the discontinuity in the fringe pattern. This failure is accompanied by delamination and horizontal tensile failure with crack propagation along the subsurface 90-deg. plies. The delaminated and sheared outer 0-deg. ply behaves like a bundle of independent fibers; hence, it is under nearly uniform strain in the segment-shaped region it occupies. The affected zone consists of a square region around the hole expanding into circular segments ahead of the crack. As the load is increased the original

vertical shear crack grows in length and new ones appear ahead of the crack.



(a) (b) (c)

Figure 28. Moire fringe patterns around crack in glass-epoxy composites $[0/90/0/\bar{9}0]_s$ at three levels of applied stress, (a) σ_y = 76 MPa (1.0 ksi), (b) σ_y = 102 MPa (14.8 ksi), (c) σ_y = 128 MPa (18.5 ksi).

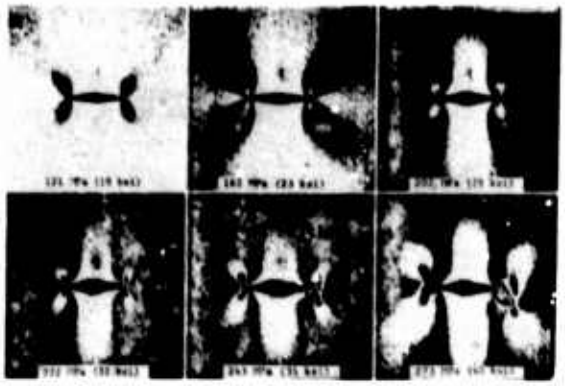


Figure 29. Isochromatic fringe patterns in photoelastic coating around 1.27 cm (0.50 in.) crack of $[0/\pm45/90]_s$ graphite/epoxy specimen at various levels of applied stress.

Uniaxially Loaded $[0/\pm45/90]_s$ Graphite/Epoxy Plate - Effect of Crack Length

The deformation and failure of graphite/epoxy plates with cracks of different lengths were investigated with experimental techniques.[19,23] Crack lengths between 0.64 cm (0.25 in.) and 2.54 cm (1 in.) were investigated. Measured strains near the crack tip show two points of rate change at levels of 0.002 and 0.006. The latter corresponds to failure of the 90-deg. plies. Failure at the tip of the crack takes the form of a damage zone consisting of ply subcracking along fiber directions, local delaminations and fiber breakage. The growth of this damage zone is illustrated by the isochromatic fringe patterns of Fig. 29. The damage zone was measured and correlated with the stress intensity factor ($K_I = \sigma\sqrt{\pi a}$) as was done by Mandell et al.[24] Results of this correlation are shown in Fig. 30. The damage zone increases linearly with the square of the stress intensity factor K_I^2 up to a certain value of K_I, which is nearly constant with crack length. Thereafter, this zone increases linearly at a faster rate, which is independent of crack length. Final failure occurs when the damage zone reaches some critical size. The effect of crack length on strength was satisfactorily described using the average stress criterion (Fig. 31). By comparing these results with those obtained from similar specimens with holes (Fig. 27) it was found that strength was independent of notch geometry, i.e., specimens with cracks and holes of the same size had the same strength (Fig. 32).

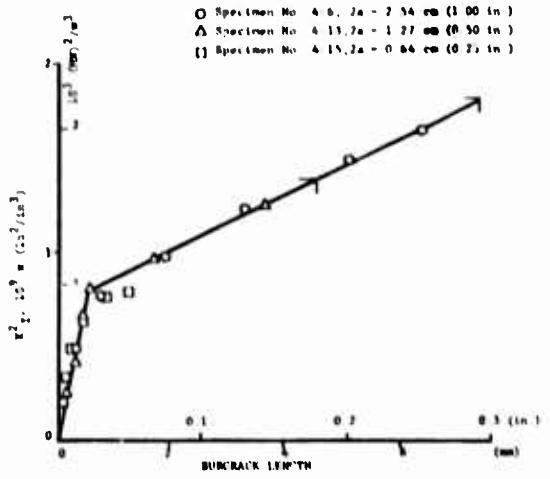


Figure 30. Variation of length of subcrack with square of stress intensity factor for uniaxially loaded $[0/\pm45/90]_s$ graphite/epoxy plates with cracks.

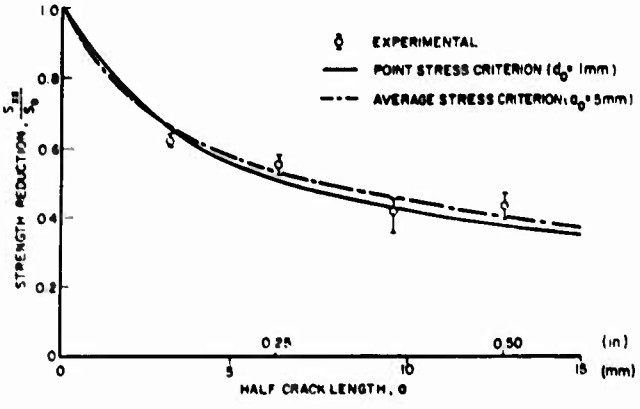


Figure 31. Strength reduction as a function of crack length for $[0/\pm45/90]_s$ graphite/epoxy plates with horizontal cracks under uniaxial tensile loading.

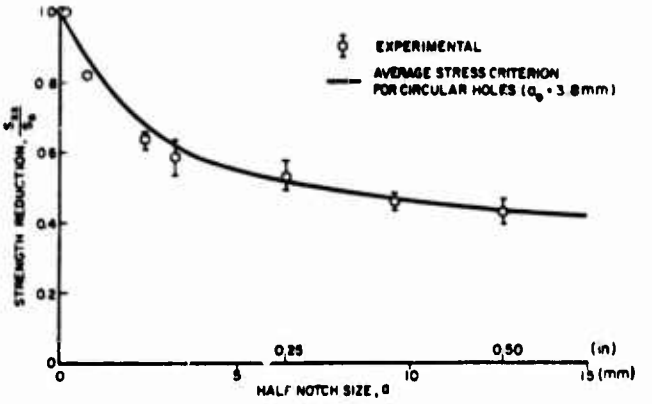


Figure 32. Strength reduction as a function of notch size for $[0/\pm45/90]_S$ graphite/epoxy plates with circular holes and cracks under uniaxial tensile loading.

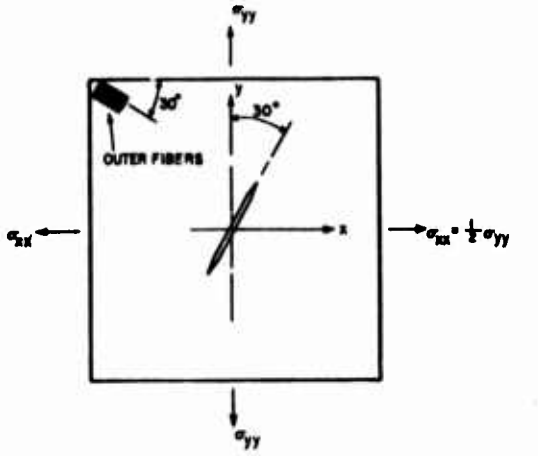


Figure 33. Biaxial loading of $[0/\pm45/90]_S$ graphite/epoxy specimens with cracks.

Effect of Biaxial Stress

Failure mechanisms in biaxially loaded $[0/\pm45/90]_S$ graphite/epoxy plates with cracks were investigated for various crack lengths.[19] Plates with inclined cracks were loaded under 2:1 biaxial tension producing a substantial shear stress along the crack in addition to the crack opening stress. (Fig. 33.) The crack direction was perpendicular to the outer fibers. The shear stress contributes appreciably to the development of the damage zone. The initial crack extension seems to be at 45-deg. to the original crack direction. Thereafter, the damage zone consisting of subcracks parallel to the fibers of the various plies, delaminations and sometimes fiber breakage along the subcracks of the adjacent plies, propagates normally to the crack direction in most cases. Some failure modes are illustrated by the isochromatic fringe patterns of Fig. 34. The size of the damage zone is limited up to a stress of 260MPa (37.7 ksi), then an abrupt jump takes place before the stress level of 278 MPa (40.3 ksi). In addition to the primary damage extension normal to the initial crack, there is secondary crack extension along the original crack direction probably along the fibers of the central plies of the laminate. At the tips of these subsurface cracks tertiary cracks appear normal to the original crack direction as seen in the fringe patterns. A typical failure pattern of a biaxially loaded plate with an inclined crack is shown in Fig. 35.



Figure 34. Isochromatic fringe patterns in photoelastic coating around 1.27 cm (0.5 in.) crack in $[0/\pm45/90]_S$ graphite/epoxy specimen under biaxial loading $\sigma_{yy} = 2.03\sigma_{xx}$ at 30-deg. with crack direction.



Figure 35. Biaxial specimen with 1.91 cm (0.75 in.) long crack after failure.

Conclusion

Failure mechanisms in fiber reinforced composites were discussed from the micro-, mini- and macroscopic points of view. All failure mechanisms in composite laminates can be explained in terms of fundamental modes such as tensile, compressive or shear fracture of the matrix, failure of the fiber-matrix interface and tensile or compressive (buckling) failure of the fibers. Failure of the first (weakest) ply in an angle-ply laminate can be predicted theoretically and ascertained experimentally. Subsequent behavior of the laminate following first ply failure is of greater interest and is more difficult to predict. The presence of notches produces a combination of interacting failure mechanisms which are best studied experimentally. Basically, the initial damage zone around notches consists of ply subcracking along fiber directions, delaminations and fiber breakage in adjacent fibers along the initial subcracks. Unlike homogeneous brittle materials, composite laminates tend to be notch insensitive. Cases were discussed where the strength was independent of notch geometry and where a threshold notch size exists below which the laminate becomes notch insensitive.

In structural applications of composites it is important to be able to ascertain the presence, nature and extent of damage by nondestructive techniques. Knowledge of the physical failure mechanisms will enable one to select or develop one or more nondestructive techniques. Knowledge of the physical failure mechanisms will enable one to select or develop one or more nondestructive techniques for better correlation of physical damage and NDE data. Failure criteria, empirical or theoretical, can be used to correlate extent of damage with residual strength of a component. Thus, NDE has the potential of directly determining the residual strength and remaining useful life of a composite structure.

References

1. B. W. Rosen, N. F. Dow and Z. Hashin, "Mechanical Properties of Fibrous Composites," NASA CR-31, April 1964.

2. J. Mullin, J. M. Berry and A. Gatti, "Some Fundamental Fracture Mechanisms Applicable to Advanced Filament Reinforced Composites," J. of Composite Materials, Vol. 2, January 1968, pp. 82-103

3. C. C. Chamis, "Micromechanics Strength Theories," in "Fracture and Fatigue" Vol. 5, (ed. by L. J. Broutman), Composite Materials (ed. by L. J. Broutman and R. H. Krock), Academic Press, New York, 1974.

4. L. B. Greszczuk, "Consideration of Failure Modes in the Design of Composite Structures," AGARD-CP-163, Specialists Meeting on "Failure Modes of Composite Materials with Organic Matrices and Their Consequences on Design," 1975, Section 12.

5. R. L. Foy, "Structural Composites," North American Aviation, Columbus Division, Contract No. AF33(615)-5150, Quart. Reports, No. 1, 2, 3, Sept. 1966, December 1966, March 1967.

6. D. F. Adams and D. R. Doner, "Transverse Normal Loading of a Unidirectional Composite," J. Composite Materials, Vol. 1, 1967, pp. 152-164.

7. I. M. Daniel, "Micromechanics" in "Structural Airframe Application of Advanced Composite Materials," AFML-TR-69-101, Vol. II, September 1969.

8. R. H. Marloff and I. M. Daniel, "Three-Dimensional Photoelastic Analysis of a Fiber-Reinforced Composite Model," Exp. Mechanics, Vol. 9, April 1969, pp. 156-162.

9. S. W. Tsai, "Strength Characteristics of Composite Materials," NASA-CR-224, April 1965.

10. S. W. Tsai and E. M. Wu, "A General Theory of Strength for Anisotropic Materials," J. Composite Materials, Vol. 5, 1971, pp. 58-80.

11. P. V. McLaughlin and B. W. Rosen, "Combined Stress Effects Upon Failure of Fiber Composites," Materials Sciences Corp., Final Report to Naval Air Development Center, TRF/7404/1112, April 1974

12. S. W. Tsai and H. T. Hahn, "Failure Analysis of Composite Materials," ASME Symposium on Inelastic Behavior of Composite Materials, Houston, Texas, 1975, AMD-Vol. 13, pp. 73-96.

13. R. B. Pipes and N. J. Pagano, "Interlaminar Stresses in Composite Laminates Under Uniform Axial Extension," J. Composite Materials, Vol. 4, October 1970, pp. 538-548

14. A. Rotem and Z. Hashin, "Failure Modes of Angle Ply Laminates," J. Composite Materials, Vol. 9, April 1975, pp. 191-206.

15. I. M. Daniel, R. E. Rowlands and J. B. Whiteside, "Deformation and Failure of Boron/Epoxy plate with Circular Hole," Analysis of the Test Methods for High Modulus Fibers and Composites, ASTM STP 521, American Society for Testing and Materials, 1973, pp. 143-164.

16. R. E. Rowlands, I. M. Daniel and J. B. Whiteside, "Stress and Failure Analysis of a Glass-Epoxy Plate with a Hole," Experimental Mechanics, Vol. 13, January 1973, pp. 31-37.

17. I. M. Daniel, R. E. Rowlands and J. B. Whiteside, "Effects of Material and Stacking Sequence on Behavior of Composite Plates with Holes," Experimental Mechanics, Vol. 14, January 1974, pp. 1-9.

18. R. E. Rowlands, I. M. Daniel and J. B. Whiteside, "Geometric and Loading Effects on Strength of Composite Plates with Cutouts," Composite Materials: Testing and Design (Third Conference), ASTM STP 546, American Society for Testing and Materials, 1974, pp. 361-375.

19. I. M. Daniel, "Biaxial Testing of Graphite/Epoxy Composites Containing Stress Concentrations" - Part I, AFML-TR-76-244, December 1976.

20. J. M. Whitney and R. J. Nuismer, "Stress Fracture Criteria for Laminated Composites Containing Stress Concentrations," J. Composite Materials, Vol. 8, July 1974, pp. 253-265

21. I. M. Daniel, "Biaxial Testing of Graphite/Epoxy Composites Containing Stress Concentrations," Part II, AFML-TR-76-244 June 1977.

22. I. M. Daniel, R. E. Rowlands and D. Post, "Strain Analysis of Composites by Moiré Methods," Experimental Mechanics, Vol. 13, June 1973, pp. 246-252.

23. I. M. Daniel, "Strain and Failure Analysis of Graphite/Epoxy Plates with Cracks," presented at SESA Spring Meeting, Dallas, Texas, May 15-20, 1977.

24. J. F. Mandell, Su-Su Wang and F. J. McGarry, "The Extension of Crack Tip Damage Zones in Fiber Reinforced Plastic Laminates," J. Composite Materials, Vol. 9, July 1975, pp. 266-287.

CHARACTERISTICS OF ACOUSTIC EMISSION SIGNALS FROM COMPOSITES

L. J. Graham and R. K. Elsley
Science Center, Rockwell International
Thousand Oaks, California 91360

ABSTRACT

Certain characteristics of acoustic emission (AE) signals from graphite-epoxy composite specimens were correlated last year with the mechanical behavior of the materials. Moisture degradation, which reduced the ultimate strength, resulted in a change in the AE amplitude distribution early in the loading history. Also, AE having distinct frequency spectral types tended to occur at or near singularities in the load curve. In order to transform those observations into a viable NDE tool, two things needed to be done: (1) develop a quicker and more objective method for extracting the pertinent correlations from the data, and (2) develop the statistical relationship between the AE characteristics and some mechanical strength parameter such as ultimate strength or remaining lifetime. The approach taken was to use computer pattern recognition techniques to analyze the data. A problem which was faced in this was the huge amount of data that are available in raw form from a single acoustic emission test. To reduce the amount of data, an intermediate feature extraction step was required and several ways of doing this, based on the prior work, were tried. As a result, the previous correlations between the acoustic emission signal characteristics and the mechanical condition of the composite were confirmed on a more objective basis. This now provides a tool for methodically studying and identifying the specific failure modes which occur in composite materials under various conditions.

Introduction

Certain characteristics of acoustic emission (AE) signals from graphite-epoxy composite specimens were correlated last year with the mechanical behavior of the materials. Moisture degradation, which reduced the ultimate strength, resulted in a change in the AE amplitude distribution early in the loading history. Also, AE having distinct frequency spectral types tended to occur at or near singularities in the load curve. Those observations were at best objective because of the broad range approach taken experimentally to identify useful correlations. In order to transform those observations into a viable NDE tool, two things need to be done: (1) develop quicker and more objective methods for extracting the pertinent correlations from the data, and (2) develop the statistical relationship between the AE characteristics and some mechanical strength parameter such as ultimate strength or remaining lifetime.

This year the work concentrated in these two areas. Particular characteristics of the AE signals were extracted in digital form and then processed on a minicomputer using special "pattern recognition" routines developed for this purpose.[1] The experimental methods were essentially the same as used last year except that the specimens were loaded in 4-point instead of 3-point bending to alleviate some minor problems experienced with the later configuration. Also, the specimen material was restricted to one type, the one designated as B-1 material last year,[2] and was chosen as being the most representative of actual structural materials. This was a graphite-epoxy laminate constructed by bonding several plies of the uncured material into sheets about 1/4 inch thick, with the graphite fibers all lying in the same direction. Its thermomechanical properties and details of its fabrication may be found in Reference 3. The features of the AE signals which were studied in detail were the distribution in time of the frequency spectral types and the amplitude distribution of the AE.

Frequency Spectral Types

In the previous work frequency spectral analysis was done by recording all the AE generated during a specimen test on a modified video tape recorder having a 3 MHz bandwidth and then doing a "stop action" spectral analysis manually on a representative number of individual AE signals. Pattern recognition by this method is all done in the head of the experimenter, and, due to the large amount of data involved, is necessarily fairly subjective. Typical results of this effort are shown in Figs. 12 and 13 of Ref. 2.

In the present work the same video tapes were played at full speed and a transient recorder (Biomation, Model 8100), under computer control, captures the first 40 μs of an emission at a 5 samples/μs rate. This waveform is stored in disk memory for later processing. In the work reported here, the computer/transient recorder captured 3000 emissions from a 25-minute, 3-point bending experiment on a piece of graphite-epoxy having event rates from several seconds per useable event to beyond the system's maximum capacity of 20 useable events/second. Due primarily to limitations in data transfer rates and in dynamic range, only about 1/8 the total number of AE events recorded were captured and stored by this method. They should, however, form a sufficiently large and unbiased sample of the total number to provide for valid classification if there are indeed different classes present.

In order to study general trends in the frequency spectra, we selected as features the maximum amplitude in each of several frequency bands, as well as the time of occurrence of the emission. The bands, 400 kHz wide and spaced 315 kHz apart, were chosen to be relatively broad so as to suppress structure due to sample and transducer resonances and the effect of emitter location on the fine structure of the spectrum. The maximum amplitude found in each band was used in an attempt to

remove the convolved effects of multiple signal paths.

In order that emissions with the same frequency content but different amplitudes be treated as similar, we normalized the amplitudes by the amplitude in the f = 0 frequency band, yielding 7 normalized frequency components. These 7 spectral components and the time of occurrence form an 8-element feature vector for each emission, so that each emission is represented by a point ("event") in an 8-dimensional vector space.

With this done, we can then start asking questions of the type, "What is the most common type of event?", by finding the event with the largest density of nearby points in the vector space defined above. Figure 1(a) shows the three highest density events during a part of the test. These events have the common "white noise" (WN) spectrum as defined in Ref. 2 (Fig. 12).

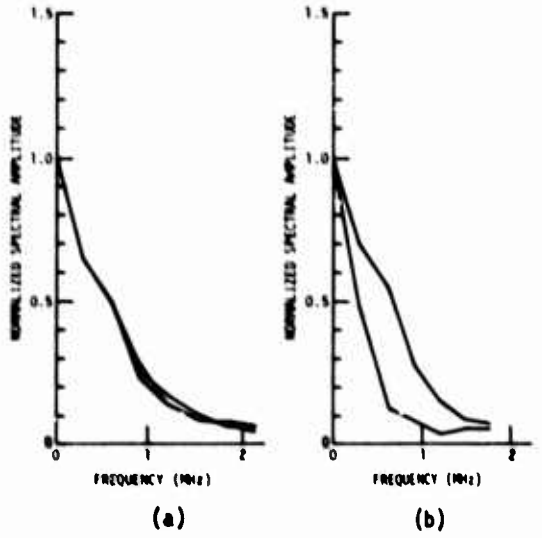


Figure 1. (a) Most common type of emission; (b) two well-separated categories of emissions.

We may further ask, "Are there distinct classes of events?", by looking for well-separated maxima in density. During much of the test, the answer is no. Except for the large maximum of density and some "foothills" probably due to statistical chance, there are so few, widely scattered events that it is not justified to call them separate classes. However, during one part of the test, there were a large number of emissions with very little high frequency energy. Here, the emissions separate easily into two regions of maximum density. Figure 1(b) shows the spectra of the highest density events in these two categories. Low frequency events occur during a 1-1/2 minute period immediately preceeding a period of massive emission event rate and substantial load drop. This type of event was called Type I in Ref. 2.

To see if certain emission classes correlate with the load history of the specimen, we have looked at the emissions occurring in the vicinity of a small sudden load drop early in the test. In order to see if there are types of events which, despite being too few in number to show significant maxima in the event density, are nonetheless informative about what was happening, we asked the question, "Which events are most unique to this time interval?", or in other words, which events are more likely to be found here than at other times during the test? Figure 2(a) shows the events in the vicinity of the small load drop with the highest uniqueness and Fig. 2(b) shows those with the lowest. There is a clear pattern of emissions with substantially more than the usual amount of energy in the 300-900 kHz region, and also even at 2 MHz. This is the high frequency Type II emission of Ref. 2. Even the least unique emissions have more high frequency energy than the more common emissions shown in Fig. 1(a).

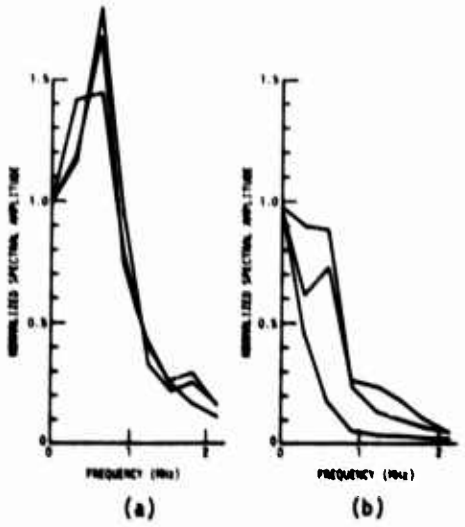
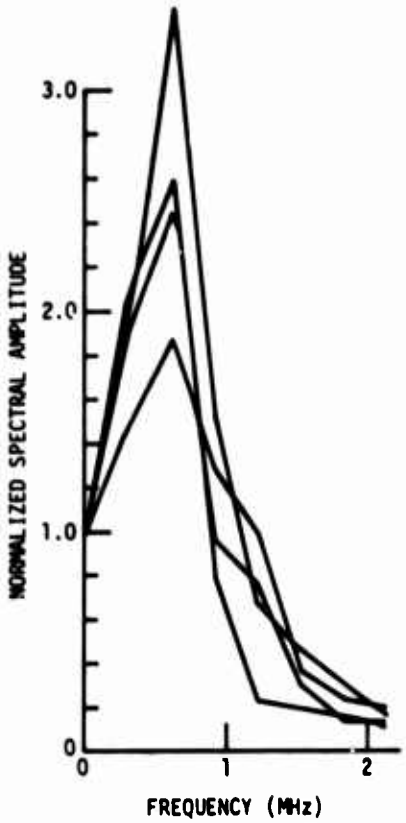
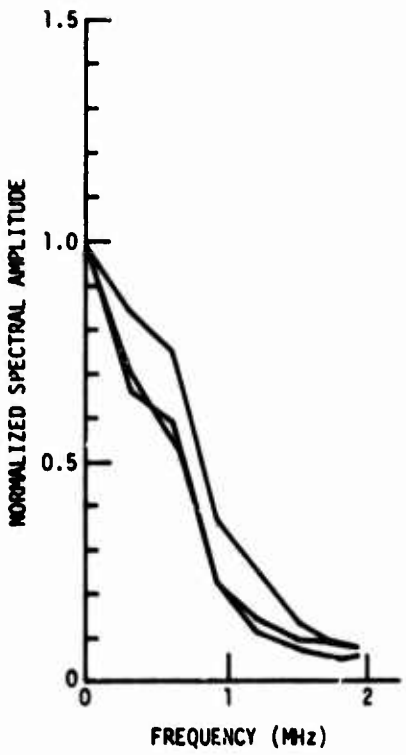


Figure 2. (a) Emissions most unique to the time period of a load drop; (b) emissions least unique to the load drop.

A similar technique can be used even without knowledge of an external feature such as the load. We may ask the question, "Which events are least uniformly distributed throughout the test?" Figure 3(a) shows the most nonuniformly distributed emissions during the first part of the test and Fig. 3(b) shows the least nonuniformly distributed ones. Again, emissions with more high frequency (or less low frequency) energy are the least uniformly distributed. Note the scale change in Fig. 3(a). This spectrum is like the Type III spectrum of Ref. 2.



(a)



(b)

Figure 3. (a) Emissions most non-uniformly distributed throughout the test; (b) emissions least non-uniformly distributed throughout the test.

In these preliminary experiments we have demonstrated:

(1) That a minicomputer based data acquisition system can, in real time, capture a significant number of acoustic emission signals;

(2) That the minicomputer can rapidly classify them according to type, taking into account a variety of signal features; and

(3) That the computer can also discover relationships between the features of the emissions and what is known about the process going on in the specimen.

It is gratifying to find substantial agreement in the frequency spectral classifications made using this objective approach with those made previously by visual observations.

Amplitude Distribution Analysis

The previous amplitude distribution analyses had been done by recording the AE signals on the video tape recorder and then playing the tape back many times through a counter, each time changing the trigger level of the counter. This suffered two drawbacks; there were electrical noise spikes due to tape imperfections which were counted along with the recorded emission signals and the dynamic range was limited to that of the recorder. Both problems could be circumvented to some degree but the accuracy of the data suffered.

In the present work the first 200 μs of each AE signal was captured directly by the digital recorder during a specimen test at a 5 μs/sample rate, and the value of the maximum amplitude digital point and the time of occurrence of the emission event stored in the computer. To effectively increase the dynamic range of the measurements, both input channels of the digital recorder (Biomation, Model 8100) were utilized by taking the AE at two different signal levels from the amplifier chain. If the amplitude of an emission event exceeded the dynamic range of the digitizer on the most sensitive channel, its amplitude was determined by the value on the less sensitive channel times a constant multiplying factor. The dynamic range of the system, after reducing the quantization errors at the low amplitude end to < ½ dB and allowing for some range overlap, was 45 dB. At low AE event rates essentially all the emission events were captured and throughout an entire test of a specimen to fracture about 95% of the events were captured.

The specimens were bend bars 3.0 inches long with a square cross section of 0.250 inches. The surfaces were ground smooth, flat, and parallel and then a rectangular reduced cross section was formed at mid-length by cutting a 0.020 inch wide slit in from two opposite sides with a diamond saw leaving a 0.090 inch wide web. The specimens were loaded in bending so that a crack would advance down this web along its ¼ inch dimension. The specimen orientations with respect to the plate material were such that the maximum tensile stress due to bending was either along the fibers (L-direction) or transverse to them (T-direction) and the crack propagation direction was either through the plate thickness (S-direction) or in the T-direction. Specimens having LS, LT, TS, TL orientation

were tested, where the first letter designates the tensile stress direction and the second letter the crack propagation direction. An Instron machine crosshead speed of 0.005 cm/min was used throughout the study. Hydrothermal aging of the specimens was done by immersion in 100°C distilled water for various lengths of time.

Conventional AE count data were also recorded during the tests. Figure 4 shows typical loading curves for an unaged and a fully aged specimen. Also shown are the cumulative event count, N_E, cumulative emission count, N, and the incremental ratio of these two numbers over successive one-minute time intervals. This ratio is the average number of oscillations in each AE burst during the time interval and is a measure of the average amplitudes of the emission events. The trends are the same as determined previously[2] and show that the average amplitudes of the emission events in the aged material are lower throughout the loading history.

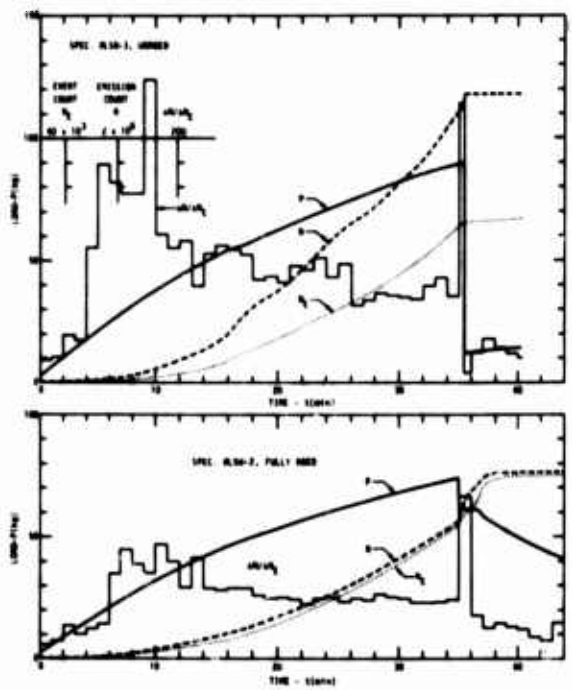


Figure 4. Typical load and acoustic emission vs. time histories for unaged and moisture degraded graphite-epoxy composite bend specimens.

The results of a second type of test are illustrated in Fig. 5. In these tests the load was cycled between successively higher load levels while continuously counting the number of emission events which occurred. These results indicate a depletion of AE generation sites with increasing load (Kaiser effect) which may be an important consideration when trying to establish the mechanical state of a composite structure at some point in its service life from the characteristics of the emission signals produced during proof loading. It will be shown in the following that information about the amount of moisture in the composite is contained in the cumulative amplitude distribution of the emission events throughout the loading history (as might also be implied from the results shown in Fig. 4). Further, only a small load increment above the previous high load is necessary to extract the information.

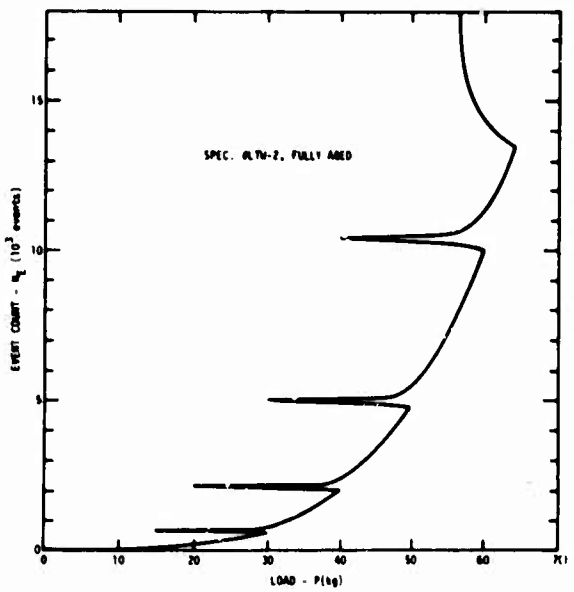


Figure 5. Load cycling results in a depletion of AE generation sites with increasing load (Kaiser effect).

Post-test analysis of the AE amplitude data which is stored in the computer can be done between any two points in the test either on the basis of event number or time. In Fig. 6 are the amplitude distributions of the first 500 emission events which occurred during the testing of unaged and fully aged LT-orientation specimens. For this orientation the direction of crack growth is across the fibers and parallel to the laminate plies. The key features of these distributions are that the emissions appear to fall in at least two distinct amplitude ranges and that the relative number of emissions in the low amplitude range is much greater for the fully aged material. These observations suggest the simultaneous occurrence of more than one AE generation mechanism and also a difference in activity of the mechanisms with aging. It is hypothesized that the mechanism which produces the low amplitude emissions is crazing of the epoxy matrix which is more predominant when the matrix is weakened by exposure to moisture. This hypothesis is unsupported at present, but regardless of the mechanism, if the shape of the amplitude distribution at the low amplitude end is related to moisture content of the composite, this phenomenological observation can be used to indicate the state of the material. Since the effect of moisture on ultimate strength is known,[3] this observation is also an indirect measure of that parameter.

The shapes of the amplitude distributions at the high amplitude end were found to be more sporadic, reflecting the statistical variability in the more macroscopic fracture processes with position in the material. Although there is believed to be a great deal of information about these processes contained in the amplitude data, no clear-cut correlations with the condition of the material has as yet emerged from the analyses.

Shown also in Fig. 6 is the amplitude distribution of the electronic amplifier noise and its amplitude relative to the amplitudes of the emission signals detected. Another way of illustrating this relationship is by the emission count rate produced by decreasing the counter trigger level (or increasing the amplitude gain) in successive 1 dB increments. At the trigger level used during the tests the event count rate was about 0.02 counts/sec, while lowering the trigger level in 1 dB increments produced count rates of 0.8, 14.0, and 106.2 counts/sec.

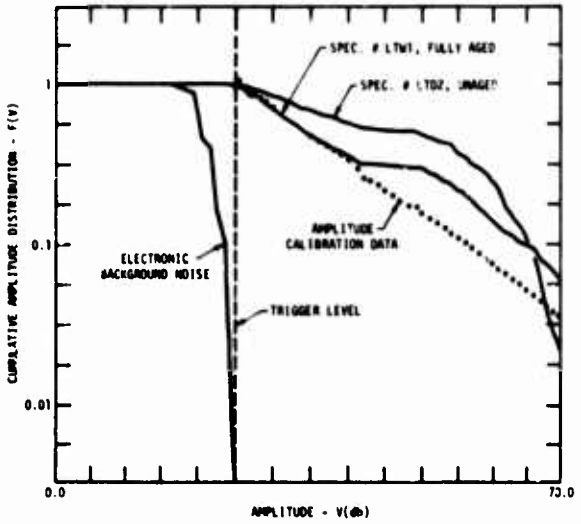


Figure 6. Typical cumulative amplitude distribution curves for unaged and fully aged specimens of the graphite-epoxy composite. Also shown is the electronic amplifier noise relative to the trigger level of the AE event detection circuitry and the system amplitude calibration data.

The remaining data in Fig. 6 are system amplitude calibration data obtained by injecting 50 μs duration bursts of 500 kHz signals at a repetition rate of 1 Hz into the input of the AE system preamplifier. These signals were treated as AE signals and their amplitudes measured and stored in the computer as the input amplitude was changed by 1 dB increments over a wide dynamic range. The pulse amplitudes in the computer were then plotted as if they had a specific power-law number distribution with the result shown in Fig. 6. It is seen that the plotted points all fall on a straight line, as they should, except for a slight deviation at the point of overlap of the two digital recorder channels. This deviation was considered insignificant to the results presented here and no effort was expended to find its cause.

The amplitude data for 14 specimens in the LT- and LS-orientations having various hydrothermal treatments were analyzed during various time periods of the tests. Additional specimens in the TL- and TS-orientations (crack propagation parallel to the fibers) failed in a brittle manner at loads which were 2-5% of the loads sustained by the other specimens. There were less than 50 AE produced during the loading of these specimens and so not much could be done in the way of data analysis.

A summary of the amplitude distribution data for the LS-orientation specimens is shown in Fig. 7. Here are plotted the slopes of the low amplitude portions of the amplitude distribution curves, such as shown in Fig. 6, as a function of water content of the composite determined gravimetrically. A relationship was clearly seen to exist between these two parameters at any stage in the loading history although the data for only four time periods are shown here.

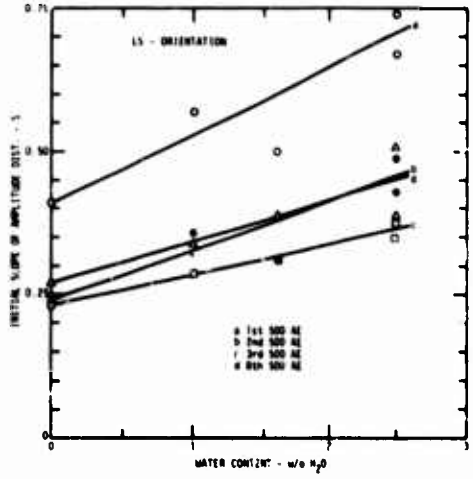


Figure 7. Dependence of the slope of the low amplitude end of the AE amplitude distribution on water content at various points in the loading of graphite-epoxy composite specimens in the LS-orientation.

A different result was found for the LT-orientation specimens as shown in Fig. 8. For these specimens the only correlation with the water content that was found was early in the loading history. At any time after the first few hundred emission events were generated, no dependence on water content was seen in the initial slope of the amplitude distribution.

We interpret this result as meaning that different fracture processes predominate in this load geometry. These specimens also failed at lower loads and with fewer AE generated at comparable times in the loading history than the LS-orientation specimens. These observations provide clues as to the identity of the fracture (AE) processes, but their identification, which was not a goal of this study, required considerably more effort.

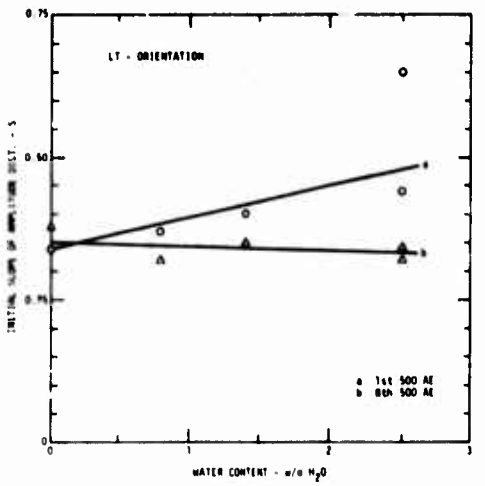


Figure 8. The LT-orientation bend specimens only showed a dependence of the amplitude distribution on water content early in the loading history.

Since the ultimate strength of a composite material has previously been shown to depend upon moisture content,[3] and a relationship has now been shown to exist between the moisture content and the initial slope of the AE amplitude distribution, then this AE parameter should also provide a measure of the ultimate strength of the material. Data for the limited number of specimens of this study which are plotted in Fig. 9 show just such a relationship. This result, which was anticipated from the previous qualitative observations, has now been established quantitatively, although a statistical validation is still required before an NDE useage can be established.

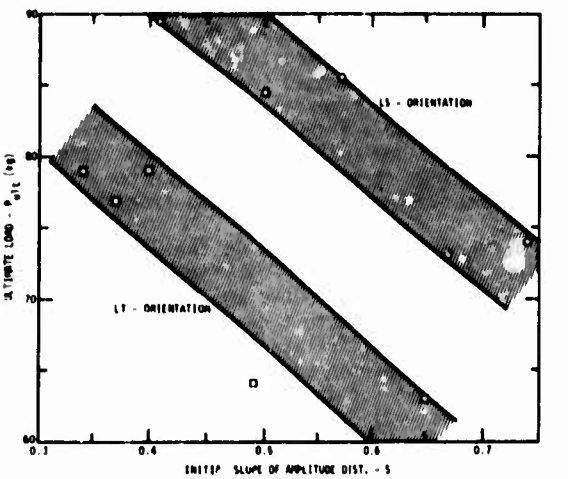


Figure 9. Relationship between the initial slope of AE amplitude distribution for the first 500 emission events and the ultimate fracture load for LS- and LT-orientation specimens with different amounts of hydrothermal aging.

Conclusions

In the current year's work it has been firmly established that at least two characteristics of the AE signals which are produced during the loading of a graphite-epoxy specimen contain information about the current mechanical state of the material. This information can then be used to estimate such parameters as the ultimate strength of the material or its remaining lifetime, if other information such as anticipated loading history is known. Emission signals having specific frequency spectral types were objectively correlated with singular points on the loading curve using computerized pattern recognition techniques. Also, the distribution in amplitude of the emission signals was quantitatively related to the moisture content of the composite material and to the ultimate strength of a given specimen. It was further shown that a minicomputer based data acquisition system can, in real time, capture a significant number of AE signals, rapidly and objectively classify them according to type taking into account a variety of signal features, and discover relationships between the features of the emissions and what is known about the process going on in the material.

Although we feel that these results are a significant advance toward providing an NDE tool for use during structural proof tests, more work needs to be done in relating the distinctive AE characteristics to specific microscopic fracture processes such as fiber fracture, matrix crazing, interlaminar matrix fracture, fiber-matrix debonding, and fiber pull-out. Identification of the statistical mix of these processes at any given time is considered to be essential to the useful interpretation of the acoustic emission data. We believe the tools are now available for doing this.

Acknowledgement

This research was sponsored by the Center for Advanced NDE operated by the Science Center, Rockwell International, for the Advanced Research Projects Agency and the Air Force Materials Laboratory under contract F33615-74-C-5180.

References

1. R. K. Elsley, Science Center, Rockwell International, deserves special credit for developing this software.

2. L. J. Graham, "Microstructure Effects on Acoustic Emission Signal Characteristics," in Interdisciplinary Program for Quantitative Flaw Definition, Special Report Second Year Effort, AFML Contract No. F33615-74-C-5180, Science Center, Rockwell International, August, 1976, pp. 297-320.

3. D. H. Kaelble and P. J. Dynes, "Methods for Testing Strength Degradation in Composites," (same report as Ref. 2), pp. 269-296.

MOISTURE DIFFUSION ANALYSIS OF COMPOSITE STRENGTH DEGRADATION

D. H. Kaelble
Science Center, Rockwell International
Thousand Oaks, California 91360

ABSTRACT

Moisture diffusion analysis (MDA) has been developed as a new non-destructive evaluation methodology to monitor the strength degradation of graphite-epoxy composite materials. Studies of composite strength degradation due to high moisture identify reversible strength loss due to current moisture content and irreversible strength loss related to prior moisture exposure with microstructure damage. MDA measures current moisture content, directional diffusion coefficients, and moisture concentration profiles. MDA measurement utilizes an electrolytic cell to concurrently record cumulative moisture content and moisture effusion rate. Extension of the diffusion analysis of Shen and Springer isolates directional diffusion coefficients and indicates a high sensitivity of MDA to moisture degradation of the fiber-matrix interface. Extension of the methodology to analyze non-Fickian diffusion shows that MDA can be applied to locate regions of composite strength degradation related to hydrothermal cycling effects. Studies which correlate MDA with ultrasonic response, and interlaminar shear strength of composite laminates subjected to localized moisture damage, show that MDA can be applied to map and locate low strength regions of a composite structure.

Introduction

Recent studies by McKague, Halkais, and Reynolds[1] showed that the moisture diffusion properties of graphite-epoxy composites are substantially altered by hydrothermal (separate or combined exposure to high moisture and temperature) cycling which simulates the service conditions of supersonic aircraft. Augl and Berger[2] also report that thermal cycling of unidirectional graphite-epoxy composites previously exposed to moisture increased the moisture diffusion coefficient yet did not reduce the flexural or shear strength. In both studies the increase in diffusion coefficient is attributed to microcrack formation. In studies designed to investigate methods for detecting moisture degradation in graphite-epoxy composites, Kaelble and Dynes[4] recognize that ultrasonic acoustic response and moisture diffusional analysis (MDA) combine as a new methodology for nondestructive evaluation of moisture exposure effects.

One of the important objectives in nondestructive evaluation (NDE) of composite materials is to clearly document and correlate the dependence of a primary performance property such as strength with other physical responses which can be evaluated nondestructively. This report details the completed results of a study of hydrothermal cycling effects upon the ultrasonic velocity and attenuation, transverse dilation, moisture diffusion kinetics, and interlaminar shear strength of a uniaxial graphite-epoxy (Hercules AS Graphite-3501-5 Epoxy) composite. A portion of this study is detailed in a published report[3] and will be briefly discussed here to bring the complete result into sharper focus.

Experimental

As described in an earlier report,[3] a uniaxial reinforced panel of 48 plies of Hercules AS graphite fiber in 3501-5 epoxy matrix was fabricated and cured according to production optimized procedures. The resulting composite displayed a fiber volume fraction $V_f = 0.60$ and void volume fraction $V_v \leq 0.01$. This earlier report also details the chemical composition, moisture degradation mechanisms, strength loss, and NDE results for this composite designated SC4. That study showed that very precise measurement of ultrasonic wave velocity C_L and spatial attenuation α_L are required to directly detect moisture content. The longitudinal sound velocity C_L (Km/s) and spatial attenuation α_L (neper/cm) are determined by the following standard relations:

$$C_L = T/\Delta t = T/(t_2 - t_1) \quad (1)$$

$$\alpha_L = T^{-1} \ln(A_1/A_2) \quad (2)$$

where T is composite thickness, Δt is delay time, and (A_1/A_2) is the signal amplitude ratio. The parameters t_1, t_2 and A_1, A_2 are the respective arrival times (μsec) and amplitudes (V) without sample (subscript 1) and with sample (subscript 2). In this study water is used as the acoustic coupling material between the ultrasonic transducer and sample using ultrasonic C-scan measurement at 2.25 MHz and 23°C following the methods described by Tauchert.[5]

In order to precisely evaluate varied hydrothermal cycling effects, a special experiment was designed for which a precisely machined bar of composite SC4 of dimension L by W by T = 12 by 1.0 by 0.20 in. with fibers parallel to the L axis was prepared. This bar was exposed to four simultaneous conditions of moisture exposure as shown in the schematic of Fig. 1. These varied zones of hydrothermal exposure develop a gradient of moisture content along the L axis of the bar. Subsequent to aging for 1128 hrs. in the conditions described by Fig. 1, the bar was characterized by ultrasonic C-scan at 2.25 MHz and 23°C. Additionally, precision measurements of specimen thickness T which enter calculations of Eq. (1) and Eq. (2) were conducted in conjunction with ultrasonic response at 0.5 in. (1.25 cm) intervals along the sample length.

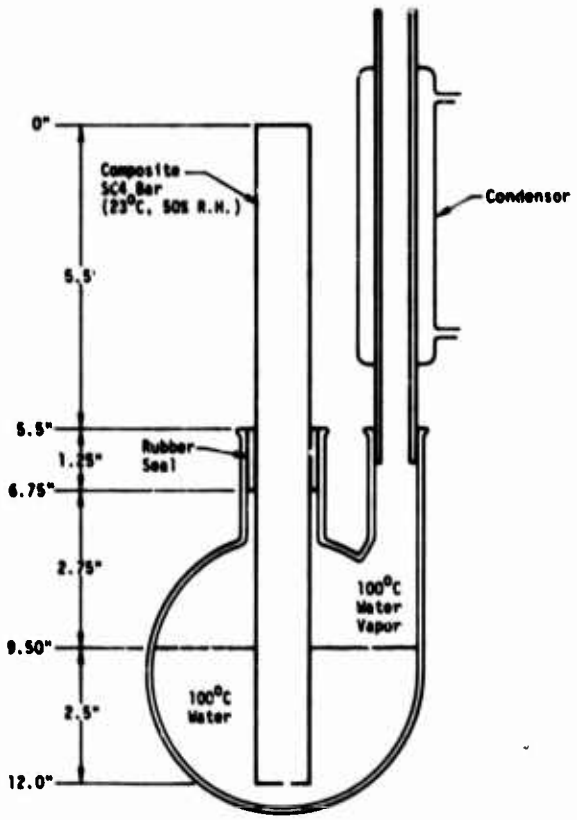


Figure 1. Schematic of variable moisture exposure of composite SC4 aged for 1128 hours.

Subsequent to this initial length characterization, a series of thermal shocks were then imposed on the bar in which the time-temperature history was uniform along the length of the bar. Measurements of T, C_L, α_L were repeated as described above along the length of the bar subsequent to each thermal shock. For each thermal shock cycle the bar was wrapped in aluminum foil to enhance heat transfer and the preheated platens of a hydraulic press were closed against the L by W = 12 x 1 in. faces of the bar with a compressive stress of 100 psi. After 5 or 10 minutes the press was opened and the bar was immersed in 23°C water with repeat measurements of T, C_L, and α_L.

The first two thermal cycles were restricted to the recommended service temperature limit of 177°C (350°F). The third and fourth thermal shock cycles involved progressively higher temperatures of 204°C (400°F) and 232°C (450°F) which approach the glass transition temperature $T_g \simeq 250$°C of fully cured dry composite SC4.

Subsequent to the four thermal shock cycles, the bar received a final length evaluation of T, C_L, α_L and was then dried at 110°C in vacuum and sectioned to provide 48 test specimens of dimensions L by W by T = 1.50 by 0.50 by 0.50 cm with a group of four from each 1 in. section of the bar length. A group of three specimens at bar length positions L_1 = 0.5, 1.5, 2.5, 111 11.5 in. were tested for interlaminar shear strength at 23°C and zero moisture using the compressive shear test of the earlier study.[3] The fourth specimen was subjected to moisture diffusion analysis.

A related study of composite SC4 by moisture diffusion analysis (MDA) describes the use of the DuPont moisture evolution analyzer (Model 902H).[4] Prior to MDA the twelve test specimens were first desiccated to provide a common initial condition of zero moisture. The samples were then exposed to 1800 min. water immersion at 75°C with periodic weighing to evaluate the kinetics of water absorption by weight change measurements. After 1800 min. water immersion at 75°C the samples were individually inserted into the 75°C dry atmosphere ($\simeq$ 0 R.H.) sample chamber of the DuPont Moisture Evolution Analyzer. Measurement of water release rate $dW(H_2O)/dt$ versus time t and determination of moisture content is automatically carried out by the instrument.

Results

A graphic summary of the effects of variable moisture exposure (see Fig. 1) and subsequent thermal cycles on the 23°C values of ultrasonic properties α_L, $_L$ and thickness L is shown in Figs. 2, 3, and 4, respectively. For ease of inspection, the curves are separated by application of a vertical shift factor K to the measured data values as indicated in the graphs. The lower curve of Fig. 2 shows that α_L remains relatively constant with position even though moisture exposure varies with the length abscissa of Fig. 2. The 177°C (350°F) thermal shock cycles of Fig. 2 also show nearly level α_L values with position. With subsequent thermal shock cycles 3 and 4 where the thermal exposure exceeds the recommended service limit of 177°C (350°F) the upper curves of Fig. 2 show notable increases in α_L in the sections previously exposed to high moisture where L = 6 to 12 in. The high attenuation due to internal microstructure degradation in cycle 4 reduced A_2 to low values characteristic of α_L > 12 neper/cm with visible evidence of internal microcrack formation and delamination in the high moisture region L = 6 to 12 in. Conversely in the low moisture region L = 0 to 6 in. the thermal shock cycles 1 through 4 are seen to leave α_L substantially unchanged.

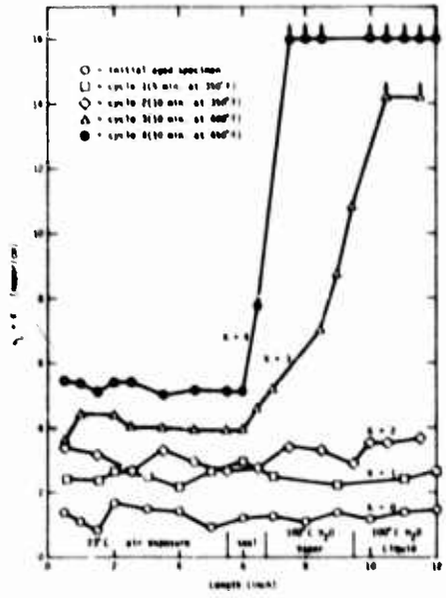


Figure 2. Effects of varied moisture exposure and subsequent thermal cycles on the acoustic attenuation α_L of composite SC4.

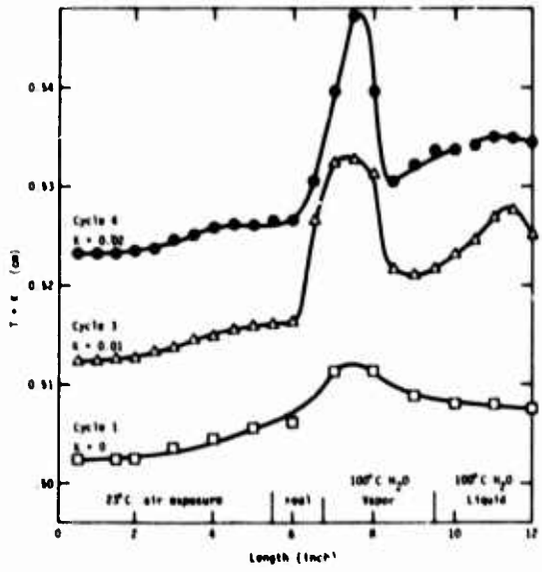


Figure 4. Effects of varied moisture exposure and subsequent thermal cycles on the thickness T of composite SC4.

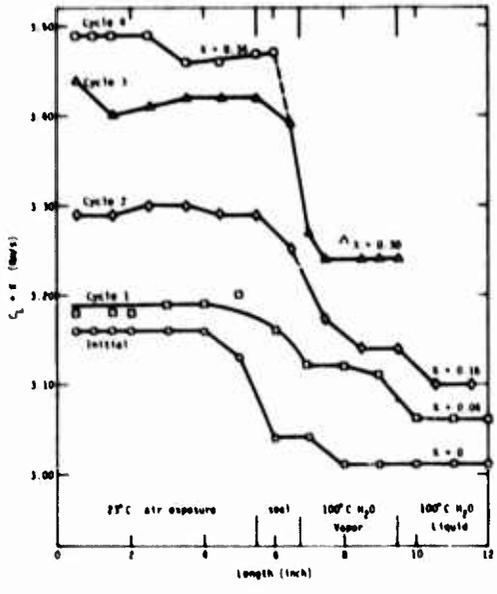


Figure 3. Effects of varied moisture exposure and subsequent thermal cycles on the ultrasonic velocity C_L of composite SC4.

Inspection of Fig. 3 shows that ultrasonic velocity at 23°C and 2.25 MHz is very sensitive to moisture content as indicated by the variation in C_L with L shown in the lower curve. Thermal shock cycles to 177°C (350°F) show the middle section region of C_L versus L is broadened. Thermal shock cycles 3 and 4 show more abrupt changes in C_L in the length region L = 5.5 to 6.75 in. (14.0 to 17.1 cm) where a transition occurs from low to high moisture. Signal loss prevents C_L measurement for L > 6.5 in. (16.5 cm) subsequent to cycle 4 due to internal crack formation.

The curves of Fig. 4 show that the precise thickness T measurements which accompany this ultrasonic characterization are quite informative in identifying the locus of large defect development. The progressive sample thickness maximum where L = 6 to 9 in. (15.2 to 22.9 cm) is evident following the first thermal cycle. Subsequent thermal cycling to higher temperatures increases this local thickness T maximum due to progressive internal crack growth and delamination.

The cured dry material for composite SC4 shows an ultrasonic wave velocity C_L = 2.92 Km/s as compared to C_L = 1.49 Km/s for bulk water at 23°C and 2.25 MHz. The sound velocities shown in Fig. 3 are evidently dominated by the matrix and moisture constituents of the composite. Thus, regions of the composite with high moisture will display a lower sound velocity as shown in Fig. 3. The data of Fig. 3 show that sound attenuation α_L is primarily sensitive to internal defects rather than moisture content. Thus sound velocity is sensitive to current moisture content and attenuation to degree of microstructure degradation. The degree of interlaminar dilation as measured by T in Fig. 4 is also an evident monitor of internal damage.

Following the nondestructive inspection summarized in Figs. 2-4, the composite bar was desiccated to a dry state and sectioned as described above to provide both interlaminar shear and moisture diffusion analysis (MDA) specimens. The MDA specimens were subjected to moisture absorption studies with measurement of weight fraction of water M versus liquid water immersion time t at 75°C. These typical types of moisture absorption curves are shown in Fig. 5. All MDA samples where L = 0.5 to 5.5 characteristic of low moisture exposure (23°C, 50% R.H.) prior to four thermal shocks show classical Fickian moisture absorption. A linear M_A versus $t^{\frac{1}{2}}$ curve which extrapolates to $(M_D)_A = 0$ at $t = 0$ and provides a constant initial slope characteristic of an apparent absorption diffusion coefficient $\bar{D} = 3.78 \cdot 10^{-8}$ cm²/s is shown by the lower curve of Fig. 5.

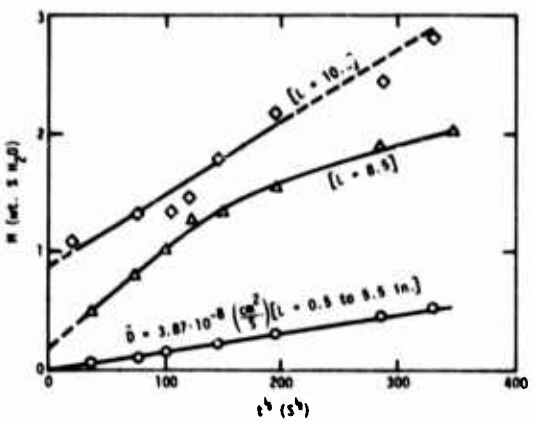


Figure 5. Typical Fickian (lower curve) and non-Fickian (upper curves) moisture absorption at 75°C.

The two upper curves of Fig. 5 show non-Fickian absorption with $(M_D)_A > 0$ indicative of physical penetration of bulk water into surface exposed microcracks at t = 0. A nonlinear M_t versus $t^{\frac{1}{2}}$ response shown in the upper curves of Fig. 5 indicates a more complicated diffusion and moisture saturation along shorter diffusion path lengths which form the microcrack structure.

Moisture effusion rate measurements as shown in Fig. 6 show that the effusion rate dM/dt versus effusion time t is highly reproducible for low moisture exposure elements of the test bar with L = 0.5 to 5.5 in. In the region of high moisture exposure L = 6.5 to 11.5 in., the effusion rate at constant time t is dramatically higher indicative of desorption enhanced by the presence of microcrack structure within the test specimen.

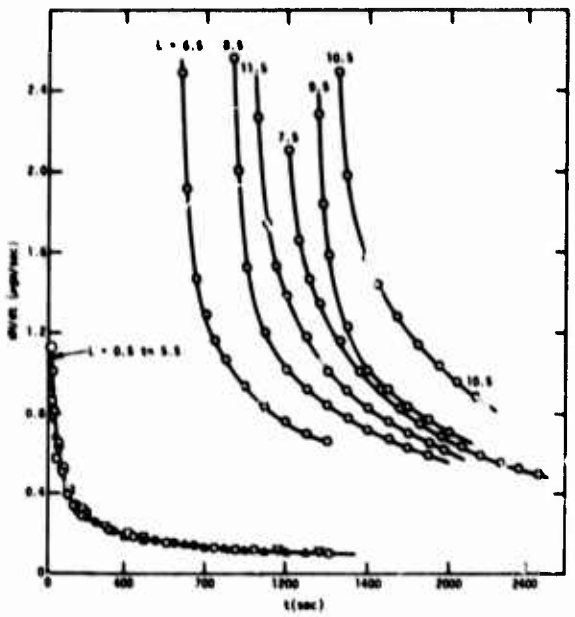


Figure 6. The effusion rate of 3501-5/AS composite bar at 27°C.

Table 1 summarizes the length L dependent values of interlaminar shear strength λ_b (average and std. dev.) the intercept $(M_D)_A$ and initial slope $dM_A/dt^{\frac{1}{2}}$ for absorption. For desorption the initial moisture content $(M_D)_D$ at cycle initiation (subsequent to 1800 min. water immersion at 75°C and the desorption time t_d at 75°C and 0% R.H.) required to reduce effusion rate to a constant level $dM_D/dt = 1.0$ μgm/s (see Fig. 6) are also tabulated in Table 1.

Table 1: Length Dependence of Interlaminar Shear Strength and Moisture Absorption-Desorption Response

L in.	λ_b kg/cm²	$(M_D)_A$ wt %	$(dM_A/dt^{\frac{1}{2}})$ (wt %/s$^{\frac{1}{2}}$)	$(M_D)_D$ (wt %)	t_D (s)
0.5	1081 ± 129	0	$1.5 \cdot 10^{-3}$	.96	20
1.5	943 ± 280	0	$1.6 \cdot 10^{-3}$	.97	20
2.5	891 ± 118	0	$1.4 \cdot 10^{-3}$	.95	20
3.5	980 ± 106	0	$1.5 \cdot 10^{-3}$	1.11	20
4.5	1027 ± 110	0	$1.5 \cdot 10^{-3}$	.93	20
5.5	963 ± 29	0	$1.5 \cdot 10^{-3}$	1.14	20
6.5	481 ± 30	0.40	$6.87 \cdot 10^{-3}$	2.68	945
7.5	814 ± 30	0.35	$8.30 \cdot 10^{-3}$	3.04	1570
8.5	636 ± 260	0.20	$7.90 \cdot 10^{-3}$	2.91	1210
9.5	488 ± 202	0.48	$8.30 \cdot 10^{-3}$	3.16	1610
10.5	520 ± 319	0.86	$6.45 \cdot 10^{-3}$	3.17	1990
11.5	236 ± 53	0.55	$7.30 \cdot 10^{-3}$	2.97	1420

The length profiles of absorption parameters $(M_D)_A$ and $dM_A/dt^{\frac{1}{2}}$ are shown in Fig. 7 and show dramatic and easily recognized increases when L > 5.5 in. characteristic to high moisture exposure prior to thermal cycling. The length profiles of desorption parameters $(M_D)_D$ and t_D shown in Fig. 8 display equivalent large increases when L > 5.5 in. characteristic of prior hydrothermal damage to composite microstructure. The curves of Fig. 7 for moisture absorption and Fig. 8 for moisture release show that low moisture exposure, L = 0.5 to 5.5 in. followed by four thermal cycles, produce no evidence of change in composite microstructure and this result is consistent with the ultrasonic properties shown in Figs. 2 and 3.

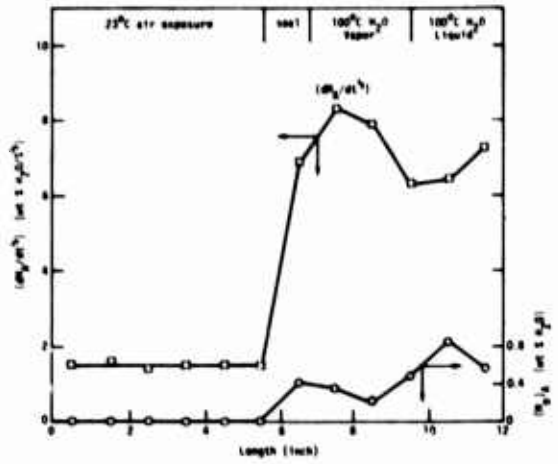


Figure 7. Length profile of moisture absorption.

Ultrasonic measurements in the high moisture region, L = 6.5 to 12 in., of exposure fail due to high signal attenuat-on in thermal cycle 4. The data of Table 1 and curves of Figs. 7 and 8 show that MDA remains a quantitative measuring method over the whole bar length and continues to function after thermal cycle 4. The range of MDA measurement of microstructure degradation is, therefore, potentially broader than possible with ultrasonic measurements.

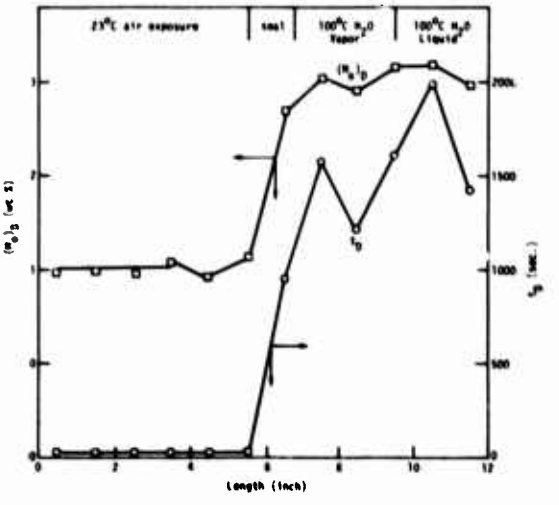


Figure 8. Length profiles of moisture desorption.

The length L dependence of average interlaminar shear strength λ_b is indicated by the data points and dashed curve of Fig. 9. As shown in Fig. 9, the schematic of the compressional interlaminar shear specimen used in this study generates a limited shear stress zone between the side notches. It is not surprising, therefore, that both ultrasonic (Figs. 2 and 3) and MDA (Figs. 7 and 8) which measure a volumetric response of the total sample should only show a qualitative correlation with λ_b. The step curve of Fig. 9 assumes that all strength values from L = 0.5 to 5.5 in. are length independent and form one statistical population. A similar assumption of length independent strength values for L = 6.5 to 11.5 in. assumes that water vapor and liquid water degrade λ_b strength values in similar fashion. The MDA curves of Figs. 7 and 8 also suggest a similar step function change in composite microstructure at L = 6 to 7 which coincides with the seal region between ambient and high moisture aging (see Fig. 1).

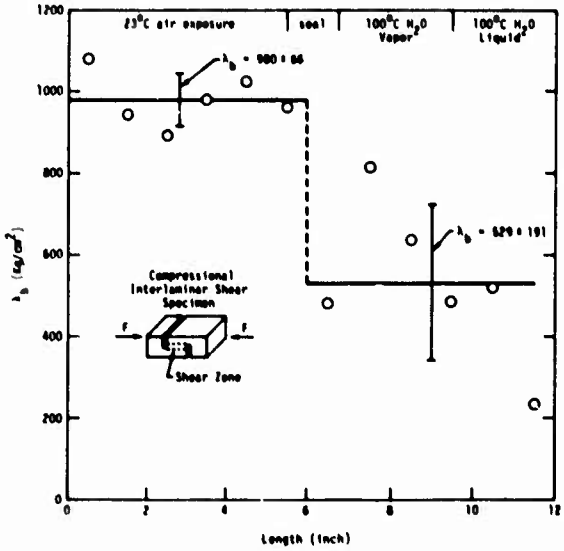


Figure 9. Effects of moisture exposure and four subsequent thermal cycles on the interlaminar shear strength of composite SC4.

The detailed tabulation of λ_b values at varied values of L along the test bar in Table 2 permits a more detailed statistical analysis. Inspection of the two data sets, λ_b for L = 0.5 to 5.5 for low moisture and L = 6.5 to 11.5 in. for high moisture conducted by the Weibull (extreme values) statistics,[6] produces the interesting curves shown in Fig. 10. A special statement of the Weibull argument for this shear test data states that the probability of survival S is related to applied interlaminar shear stress λ by the following relation:[3,6]

$$S = \exp\left(-\lambda/\lambda_0\right)^m V \qquad (3)$$

where V is the volume for uniform shear loading and λ_0 and m are Weibull parameters. For these test data the volume is constant with V = 1.0. By taking logarithms we obtain the following:

$$\ln(-\lambda n\ S) = m[\ln\lambda - \ln\lambda_0] \qquad (4)$$

which predicts a plot $\ln(-\ln S)$ versus $\ln\lambda$ with slope m an intercept $\lambda = \lambda_0$ when the survival probability $S = e^{-1} \simeq 0.37$. The test data of Table 2 for L = 0.5 to 5.5 and L = 6.5 to 11.5 are separately arranged serially j = 1,2,...N in increasing order of λ_b and the survival probability is defined as:[3]

$$S = 1 - F = 1 - \frac{j - 0.50}{N} \qquad (5)$$

where N is the number of observations and F is the failure probability. The upper curves of Fig. 10 show the cumulative distributions plotted as S versus λ_b or $\ln\lambda_b$ for the two aging conditions. The lower curves of Fig. 10 show these same data linearize well on Weibull plots and conform to Weibull analysis.

Table 2: Experimental Values of λ_b for Composite SR4 Tested Dry at 23°C After Described Hydrothermal Aging and Thermal Cycle 4

L(in)	λ_b (Kg/cm^2)			Moisture Aging
0.5	984,	1032,	1228	23°C, 80% R.H., 1128 hr
1.5	1220,	660,	948	
2.5	758,	986,	928	
3.5	1079,	992,	868	
4.5	1092,	1088,	900	
5.5	933,	964,	992	
6.5	632,	412,	400	100°C, 100% R.H. or liquid H_2O, 1128 hr
7.5	836,	792,		
8.5	492,	936,	480	
9.5	696,	476,	292	
10.5	824,	548,	188	
11.5	197,	272		

The data and curves of Fig. 10 show that high moisture exposure, where L = 6.5 to 11.5, combined with thermal cycling to 232°C (450°F) reduces shear strength λ_0 by 43 percent at survival probability S = 0.37. The corresponding decrease in m which broadens the distribution shows that at a higher survival probability S = 0.95 of greater interest to a design engineer, the high moisture exposed length L = 6.5 to 11.5 shows λ_b is reduced by 79% as compared to low moisture length L = 0.5 to 5.5.

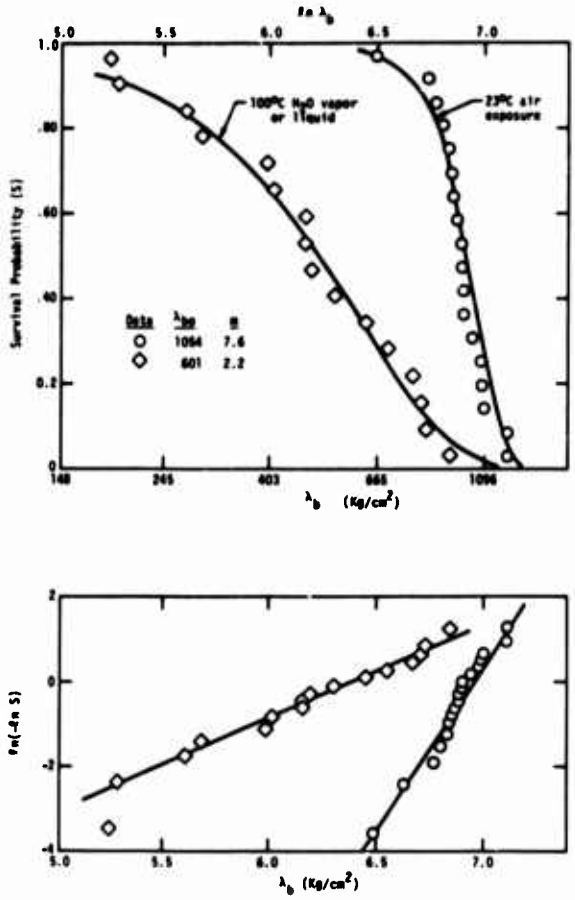


Figure 10. Cumulative distribution function of survival probability.

Summary and Conclusions

This study clearly shows that MDA (moisture diffusion analysis) can be effectively applied to scan the area or length of a composite panel and locate regions of microstructure degradation and resultant loss in internal strength. In this study a one dimensional variation of moisture exposure and subsequent hydrothermal damage was imposed. The results obtained in the present study should also be demonstrated with more complex localizations of moisture exposure to either limited area (two-dimensional) or area plus depth (three-dimensional). When composite SC4 is thermally cycled beyond the recommended service ceiling temperature of 177°C (350°F) the region of high moisture exposure (100°C, water vapor or liquid, 1128 hr.) clearly exhibits microstructure and strength degradation.

Ultrasonic acoustic properties, thickness profiles, and MDA profiles in both adsorption and desorption modes are highly sensitive to the structure degradation. In regions of extensive internal damage, ultrasonic inspection becomes limited as a quantitative tool by high acoustic attenuation and resultant loss of signal. MDA in this instance becomes highly sensitive as a profiling method. Regions of internal microcrack formation display easily detectable non-Fickian moisture diffusion properties wherein bulk water penetrates the open capillary structure and subsequently diffuses by shortened path lengths between adjacent microcracks.

Further analysis of these newly recognized non-Fickian diffusional regimes appears to be a promising new method for anlayzing the details of microstructure degradation. This type of extended MDA analysis combined with statistical analysis of strength degradation as graphed in Fig. 10 appears as the direct approach to coupling MDA and ultrasonic surveillance to quantitative predictive criteria for residual strength and service life of the composite material in critical primary structure applications.

Acknowledgement

This research was sponsored by the Center for Advanced NDE operated by the Science Center, Rockwell International, for the Advanced Research Projects Agency and the Air Force Materials Laboratory under contract F33615-74-C-5180.

References

1. E. L. McKague, J. E. Halkais, and J. D. Reynolds, "Moisture in Composites: The Effect of Supersonic Service on Diffusion," J. Composite Matls., 9, 121 (1975).

2. J. M. Augl and A. E. Berger, "Moisture Effect on Carbon Fiber Composites," Natl. SAMPE Tech. Conf. Series, 8, Society for Advancement of Materials and Process Engineering, 1976, pp. 383-427.

3. D. H. Kaelble and P. J. Dynes, "Methods for Detecting Moisture Degradation in Graphite Epoxy Composites," Matls. Eval., 35 (4), 103 (1977).

4. D. H. Kaelble and P. J. Dynes, "Moisture Diffusion Analysis of Graphite-Epoxy Composites: Part 1, Directional Coefficients," to be published.

5. T. R. Tauchert, "Internal Damping in a Fiber Reinforced Composite Material," J. Composite Matls., 8, 195 (1974).

6. N. R. Mann, R. E. Shafer and N. D. Singpurwalla, "Methods of Statistical Analysis of Reliability and Life Data," Wiley, New York (1974).

Nomenclature

A_1, A_2	acoustic signal amplitudes (v)
C_L	longitudinal sound velocity (km/s)
$\bar{D}$	apparent absorption diffusion coefficient (cm^2/s)
F	failure probability defined by Eq. (3) (dimensionless)
j	Weibull observation index defined by Eq. (5) (dimensionless)
L	length of specimen (in.)
m	Weibull parameter defined by Eq. (3) (dimensionless)
M_A	weight fraction of water in absorption (%)
$(Mo)_A$	weight fraction of water in absorption at time = 0 (%)
M_D	weight fraction of water in desorption (%)
$(M_o)_D$	weight fraction of water in desorption at time = 0 (%)
R.H.	relative humidity (%)
s	survival probability defined by Eq. (3) dimensionless
t	time (sec)
t_D	time required to reduce moisture desorption to 1 μgm/sec (sec)
t_o, t_2	acoustic signal arrival times (μsec)
T	thickness of specimen (in.)
v	volume for uniform shear loading = 1 (dimensionless)
λ_o	Weibull parameter defined by Eq. (3) (Kg/cm^2)
λ	interlaminar shear stress (Kg/cm^2)

OVERVIEW OF RELIABILITY IN STRUCTURAL CERAMICS

A. G. Evans
Science Center, Rockwell International
Thousand Oaks, California 91360

ABSTRACT

The failure prediction requirements and the pertinent accept/reject criteria for structural ceramics are derived, and the available failure prediction techniques are examined, vis-a-vis the failure prediction relations, in order to highlight the capabilities and limitations of each technique. The need for additional techniques is thereby demonstrated. The capabilities of the ultrasonic technique are extensively evaluated in order to determine its ability to satisfy the deficiencies in the existing failure prediction repertoire. The prospects are shown to be very encouraging, but the results of several key studies must be awaited before defining the ultimate role of ultrasonic failure prediction techniques.

I don't intend to emphasize particular failure prediction techniques--that is the intent of the Poster Session and the subsequent talks--but I wish to indicate at the outset that there are several ways of predicting failure in ceramics. It is convenient to separate these into two groups. One group consists of direct techniques, where the defect is detected directly and the fracture mechanics analysis is applied to the defect to predict failure; these include, ultrasonics, microfocus x-radiography, microwaves (see Poster Session) and, of course, dye penetrants. The other group consists of indirect techniques that are particularly pertinent to ceramics. These include overload proof testing (see Poster Session), flaw statistics, and intriguingly, ultrasonic attenuation.

In attempting quantitative failure prediction, we recognize that the defects are irregular in shape and that the defect size range of concern is 10 to 100 microns. What defect features need to be characterized to enable us to predict failure effectively? The first parameter is the defect size, especially the maximum dimension of that defect. The realization that the size distribution of defects in most materials generally has an extreme value form can also be used to good effect. The second defect characteristic is its orientation; normally, in ceramics, the distribution of orientations is essentially random. The third parameter is the aspect ratio of the defect; for which a normal distribution seems reasonable. The fourth feature of great importance, perhaps even more important than the aspect ratio and the orientation, concerns the physical properties of that defect, e.g., the elastic properties, and the thermal expansion coefficient.

The sequence involved in predicting failure is in three parts: firstly, we would like to characterize the defect, then the crack evolution from the defect, and finally, the slow crack growth.

I shall describe an approach based on a fairly quantitative inspection technique and a more qualitative technique. Starting with a series of samples or actual components containing defects of known size and geometry, we can relate the actual defect size to the interpreted defect size through a specific model and signal analysis procedure (Fig. 1). Of course, this isn't just a line through the origin; because, for different types of defect the inferred size can be different for a specified actual size. Also, there is a lower limit for each type of defect and inspection technique.

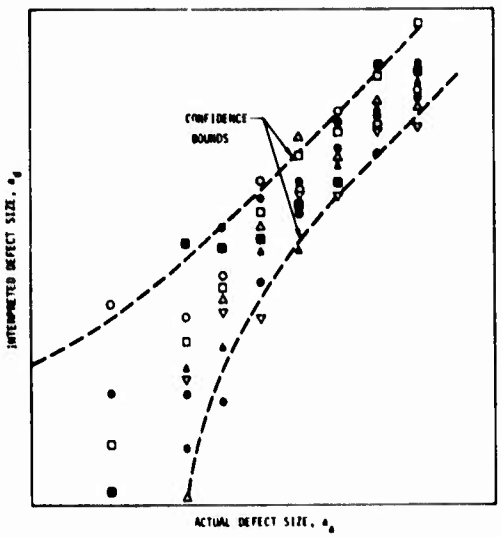


Figure 1. A plot illustrating a probable relation between the actual and detected defect sizes for a quantitative ultrasonic flaw detection method.

For a more typical technique (e.g., microfocus x-rays or a conventional ultrasonic method), certain types of defects will never be detected, regardless of their size, and there is a wide range of inferred defect sizes (Fig. 2). For illustration, some data obtained on a silicon nitride material, containing several types of defect, using high frequency ultrasonics and using microfocus x-radiography, are summarized in Table I.

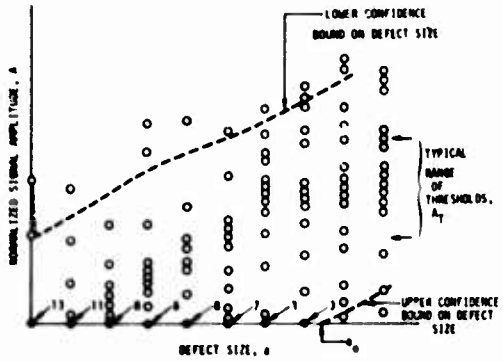


Figure 2. A typical test sequence relating the ultrasonic signal amplitude to the actual defect size. The sequence involves taking samples containing defects of the same size, but of different type (i.e., voids and various inclusions) and measuring the signal intensity from each defect. This process is repeated for a range of defect sizes.

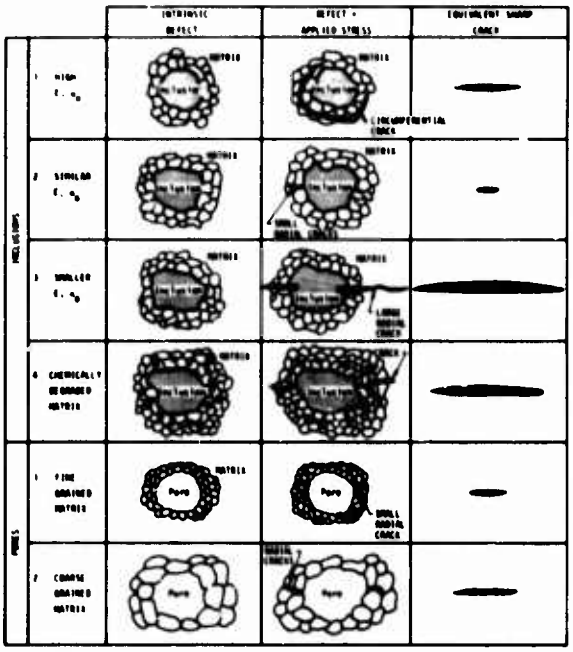


Figure 3. A schematic indicating the relative severities of typical defects in structural ceramic matrices.

Table I. Experimental and Theoretical Scattering from Boron Nitride Defects in Silicon Nitride

Diameter	Experimental Return Signal Amplitude	Theoretical Return Signal Amplitude
500 μm	-18.4 dB	$-19.8+10\log_{10} r^2$
250 μm	-26.7 dB	$-25.8+10\log_{10} r^2$
125 μm	-30.8 dB	$-31.8+10\log_{10} r^2$
25 μm	-36.0 dB	$-45.8+10\log_{10} r^2$

For the second aspect of the failure prediction, cracks will not evolve from all defects of a given size at the same stress level (Fig. 3). The equivalent size of a sharp crack depends upon the type of defect relative to the properties of the matrix. If the elastic properties of the inclusion are similar to the matrix, there would be no stress concentrations and the defect is relatively innocuous, especially if its thermal expansion coefficient is similar to that of the matrix (so that no stresses will develop during cooling from the fabrication temperature). However, when both the elastic modulus and the thermal expansion coefficient of the inclusion are lower than that of the matrix, the equivalent crack size can be many times the inclusion size. It isn't clear how the expansion coefficient can be deduced non-destructively, but hopefully, it might be inferred from the acoustic impedance for a limited set of possibilities.

Because of the characteristics summarized in Fig. 3, when a sample is stressed to failure, e.g., at a constant stressing rate, then for a given defect size the fracture stress would not be a unique quantity (Fig. 4).

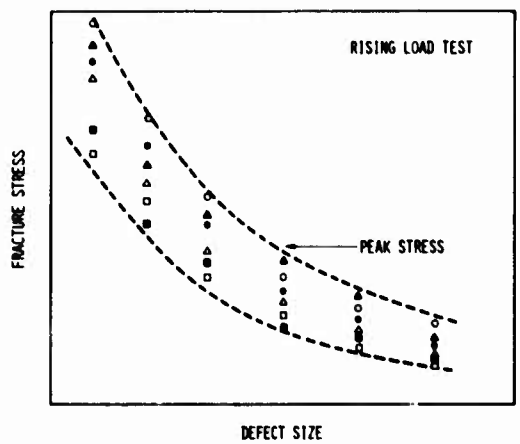


Figure 4. A typical variation of the fracture stress with defect size and type.

If probabilities are now assigned to the interpreted defect size $P(a_i)$ and the fracture strength $P(\sigma_j)$, these probabilities can be combined to obtain the probabilities of fracture that correspond to each interpreted defect size (Fig. 5). Then, by combining with some a priori distribution of defect sizes, we can also derive the rejection probability for satisfactory parts (Fig. 5). What does this mean? It means that if the application specifies that only a certain proportion of components are allowed to fail in-service (the maximum allowable failure probability) there is a corresponding interpreted defect size, and rejection probability (Fig. 5). If the inspection technique is not very quantitative, many components which really would have performed quite well in-service would be rejected (Fig. 5), and that may be economically intolerable. However, for a more quantitative inspection technique, it is evident from Fig. 5 that the rejection probability can be substantially reduced into the realm of economic viability.

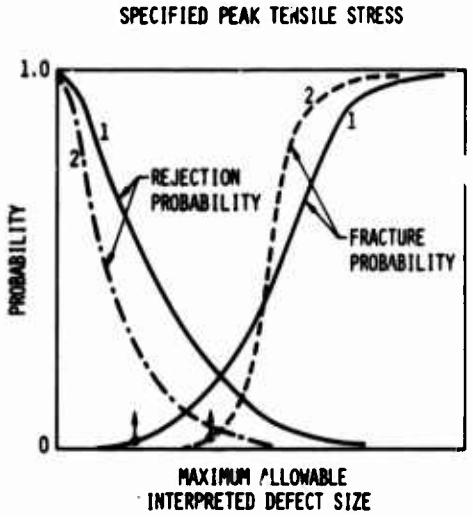


Figure 5. Fracture and rejection probabilities as a function of integrated defect size for two inspection techniques: 2 is superior to 1.

The third aspect of predicting failure, which I haven't described in detail because it's relatively well understood, concerns the slow crack growth.

I shall conclude by quickly describing a few indirect techniques. Certain ceramics, because of either a coarse grain structure, or porosity, are not amenable to high frequency ultrasonic inspection because their attenuation is too large. What do we do then to characterize small defects? It's a real problem. But one possibility, which is rather intriguing, is the use of acoustic attenuation. We have developed a theory of acoustic attenuation based on extreme value statistics, wherein only the largest grains (pores) are considered to contribute significantly to the attenuation. We also know that the large size extreme of voids in porous materials, or grains in large grained materials, are the fracture origins (see Poster Session). So, because both the attenuation and fracture are related to the extremes of the microstructure, there is a potential that by measuring the frequency dependence of the attenuation we should be able to infer the actual fracture strength (or the fracture probability) of that component (Figs. 6 and 7).

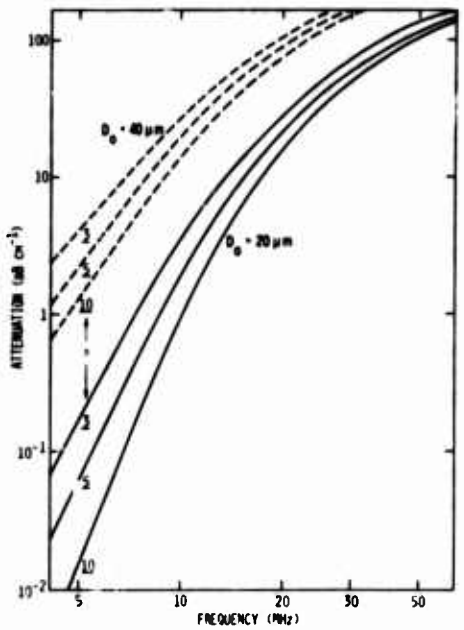


Figure 6. The prediction variation of attenuation with frequency for two grain size distributions.

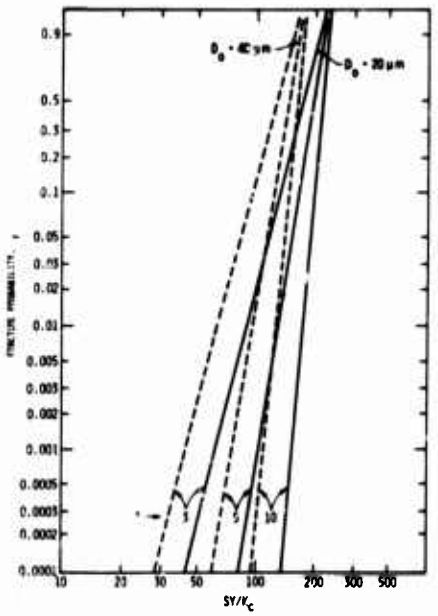


Figure 7. The predicted relation between fracture probability ϕ and strengths for two grain size distributions.

The statistical method has been traditionally used for predicting failure in ceramics. The method is as follows. You can measure the strength of, say, 50 or 100 or 1000 ceramic bars and find the probability of fracture as a function of strength, using order statistics. This probability of fracture is related both to the basic distribution of flaw strengths (of the distribution of flaw sizes) and to the volume of the part. Very recently, techniques for deriving the flaw strength distribution have been devised, and we feel quite comfortable now about this aspect of the process. However, there are still problems associated with failure prediction. Firstly, we find that there are usually several populations of flaws; for example, in bend test, fracture typically occurs from surface cracks produced by machining, giving one population. But in tensile tests, internal defects (inclusions and voids) offer control fracture, giving another population with a lower strength level. So to characterize the flaw population at the strength level that the components will experience, very expensive tensile tests will be required, and it very quickly becomes economically intractable because of the large number of experiments involved. The other problem is that on a batch-to-batch basis the populations can change. Every batch of material will thus have to be re-characterized.

In conclusion, there are a number of techniques available for detecting defects in ceramics; but it is not sufficient to detect defects, we must also characterize their size and infer something about the properties of that defect. The most effective technique for this purpose could be material specific and component specific.

Acknowledgement

This work was sponsored in part by the Center for Advanced NDE operated by the Science Center, Rockwell International, for the Advanced Research Projects Agency and the Air Force Materials Laboratory under contract F33615-74-C-5180; in part by the Office of Naval Research under contract N00014-76-C-0624; in part by the Rockwell International Independent Research and Development Program.

HIGH FREQUENCY ULTRASONICS

G. S. Kino, B. T. Khuri-Yakub
Stanford University
Stanford, California 94305
and
B. R. Tittmann
Science Center, Rockwell International
Thousand Oaks, California 91360

ABSTRACT

A high frequency 250 MHz A-scan system has been used for flaw detection. We have been able to detect 25-500 μm defects of different types (C, Si, SiC, BN, Fe, WC) in a Si_3N_4 plate. Since it is difficult to determine the defect type and size from the amplitude of the backscattered signal, we have carried out Fourier transforms of the backscattered signal to obtain reflectivity as a function of frequency, and used that information to characterize the size and type of defect. Our early experiments have been with voids in glass and Si_3N_4 and we are able to predict the size of the defects we detect.

The objective of ultrasonic nondestructive evaluation of ceramics is the detection of defects in the 10-100 μm range. The aim is to detect the defects and determine their location, size, and possibly the type of inclusions within these flaws. Prior to this program of very high frequency testing, no technique existed where such an evaluation could be made.

The longitudinal wave velocity in ceramics is typically of the order of 10,000 m/sec. So, in order to obtain a maximum reflection from defects, we have decided to work in the frequency range of 150 MHz to 500 MHz, or with acoustic wavelengths in the range from 70-20 μm. For this purpose, we have constructed the A-scan system shown in Fig. 1. This system operates at frequencies 5-10 times higher than those that have been used before in the NDT field.

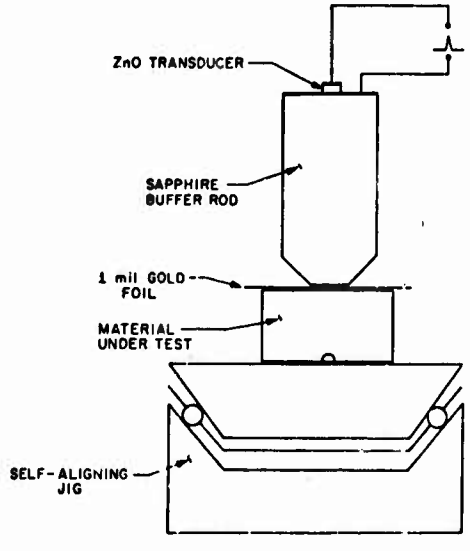


Figure 1. Schematic of A-scan system.

The system consists basically of a piezoelectric transducer on a sapphire buffer rod. This is placed in contact with the ceramic under study. The piezoelectric transducer consists of an 8 μm rf sputtered zinc oxide film on a 2000 Å gold film that is used as a back contact of the transducer. The top contact is formed by normal photolithographic techniques; typically, we use a top contact that is .75 mm in diameter. Such a transducer resonates at a center frequency of 250 MHz, and has a useful bandwidth of 300 MHz. We use a 1 cm long saphhire buffer rod which is tapered to a diameter of 2 mm at its lower end in order to ease the problem of contacting to the ceramic. A 25 μm gold foil is used as the contacting material between the sapphire and the ceramic. Gold is soft and has an acoustic impedance comparable to those of the sapphire and the ceramic; so it makes a good contacting material. A self-aligning jig is used to help make good reproducible contact. The system is used in a pulsed echo mode. A 20 volt, 2 nsec pulse excites the transducer, and we look for reflected pulses from defects in the time range between the echoes corresponding to the front and back surfaces of the ceramic under study. The acoustic pulses obtained are of the order of 2 ns wide between 3 dB points, as shown in Fig. 2.



Figure 2. A demonstration of the depth of resolution obtained by measuring the thickness of a 134 μm glass slide.

The theoretical two-way insertion loss of the transducer is 26 dB, which includes 6 dB of diffraction loss in the sapphire buffer rod. Typically, we measure a round trip insertion and propagation loss of the order of 28-30 dDs. We calculate that 90% of the power incident on the gold foil passes through it to the ceramic; experimentally, we measure a reflection coefficient at the fold foil of 0.1. Typically, we measure the propagation loss in the ceramic to be of the order of 4 dB/cm at 200 MHz for the fully dense hot pressed silicon nitride. A theory has been developed to predict the propagation loss;[1] this is in excellent agreement with the experimental measurements on which it has been checked.

The depth resolution of the system is demonstrated, as shown in Fig. 2. We measure the thickness of a nominally 134 μm glass slide. Our experimental measurement yields a thickness of 132 μm. Notice that we can easily resolve the thickness of the gold foil, which is 25 μm thick. We can then determine the location of a defect tc an accuracy of a couple of microns.

In order to test for the sensitivity of the system, we have looked for defects in the seeded sample shown in Fig. 3. This Si_3N_4 plate had six different types of supposedly spherical inclusions (Si, SiC, Fe, WC, BN, and C) of four different sizes (500 μm, 250 μm, 125 μm, 25 μm). We have been able to detect all the defects in the sample with ease, even SiC that has material constants very close to those of Si_3N_4. Typical reflections from two different inclusions are shown in Fig. 4. Notice that a 180 degree phase shift of the reflected pulse indicates whether the inclusion has a higher or lower acoustic impedance than the host material. We have also measured the amplitude of the echoes coming back from these defects and compared them to the echo from the back side of the ceramic. These measurements agree well with a simple theory which predicts that the reflected power is proportional to the square of the diameter of the defect, at least for the 125 μm, 250 μm, and 500 μm defects, but gives larger scattering than we would expect from the smallest defects (25 μm) as seen in Table I. This is due to the fact that the defect materials were actually sprinkled into the sample. So, we could have been irradiating more than one 25 μm defect.

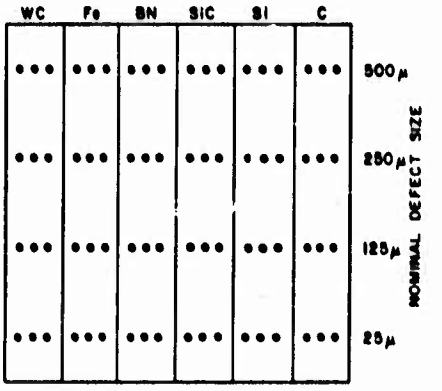


Figure 3. Schematic of Si_3N_4 seeded plate.

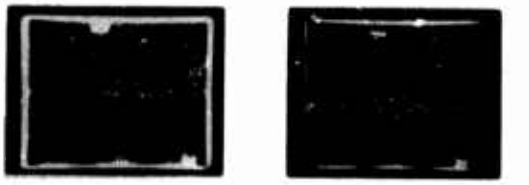


Figure 4. (a) The signal obtained from a 125 μm C defect; (b) the signal obtained from a 25 μm WC defect.

Table I. Experimental and Theoretical Scattering from Boron Nitride Defects in Silicon Nitride

Diameter	Experimental Return Signal Amplitude	Theoretical Return Signal Amplitude
500 μm	-18.4 dB	$-19.8 + 10 \log_{10} \gamma_2^2$
250 μm	-26.7 dB	$-25.8 + 10 \log_{10} \gamma_2^2$
125 μm	-30.8 dB	$-31.8 + 10 \log_{10} \gamma_2^2$
25 μm	-36.0 dB	$-45.8 + 10 \log_{10} \gamma^2$

In addition, the value of the reflected power from the defects, compared to that from the back side of the ceramic, was higher than expected. The discrepancy between theory and experiment made it clear that it is very difficult to use the echo from the back side of the ceramic as a reference signal. This is because misalignment that results in a 6 μm tilt across the transducer at 200 MHz results in large changes of the signal level coming from the back of the ceramic. We demonstrated this point by looking at the echoes coming back from hemispherical voids polished in the back side of a ceramic piece. Two hemispherical voids 200 μm and 400 μm in diameter gave echoes differing by 6 dBs, an excellent agreement with theory. The alignment problem becomes non-critical as the reflecting surface is spherical.

In order to tackle the problem of recognizing the type of inclusion within the defect, we turn to the frequency domain and look at the response of the defect as a function of frequency. The idea here is that different defects have different signatures, as seen in the theoretical calculations of Fig. 5. Notice the difference responses of the void and the WC inclusion in Si_3N_4. Our first problem was to be able to read the nanosecond pulses involved into a digital computer to carry out the Fast Fourier Transformation (FFT) required. This was done using a sampling oscilloscope to give a slowed down version of the pulse in the set up shown in Fig. 6. A typical FFT of the zinc oxide transducer response is shown in Fig. 7. The useful bandwidth of the transducer is 300 MHz. The wide bandwidth and the extremely symmetric trans-

ducer response is a result of the good acoustic match of the piezoelectric ZnO transducer into sapphire. In order to obtain the frequency response of a scatterer, we divide the FFT of the pulse echo obtained from the flaws by that of a transducer, and thus eliminate the effect of the response of the transducer. To check our experimental procedures, we first carried out such an analysis on the reflection from a gold foil; the result is shown in Fig. 8. This result agrees very well with theory. By this technique, we measure the frequency minima, which yield a gold foil thickness of 22 μm for a nominally 25 μm foil; the decrease in the thickness of the foil is due to the pressure applied to it. We have also carried out Fourier analysis on some unknown defects in a SiC sample. Typical results are shown in Fig. 9. We cannot, as yet, infer the type of inclusion that we are looking at, because of incomplete theoretical information at the present time. However, we know that different defects have different signatures.

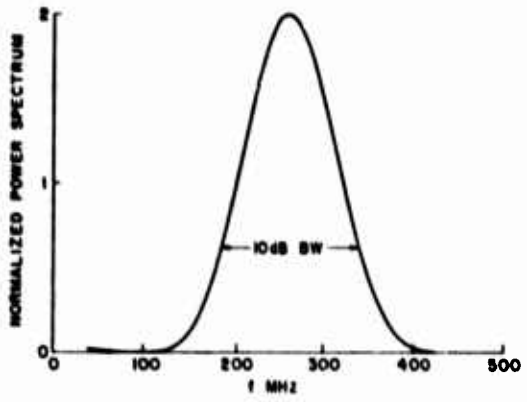


Figure 7. Power spectrum of ZnO/Al_2O_3 high frequency transducer.

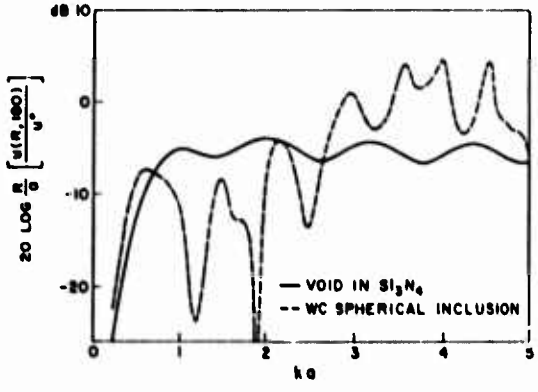


Figure 5. Theoretical backscattered spectra of a spherical void and a WC inclusion in Si_3N_4.

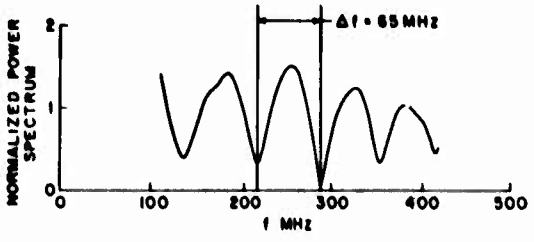


Figure 8. Measured reflection power spectrum of a 25 μm Au foil.

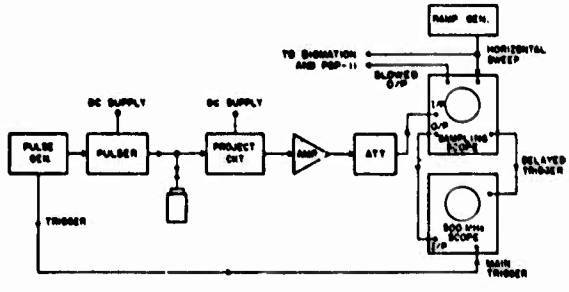


Figure 6. Schematic of setup used to digitize high frequency pulses.

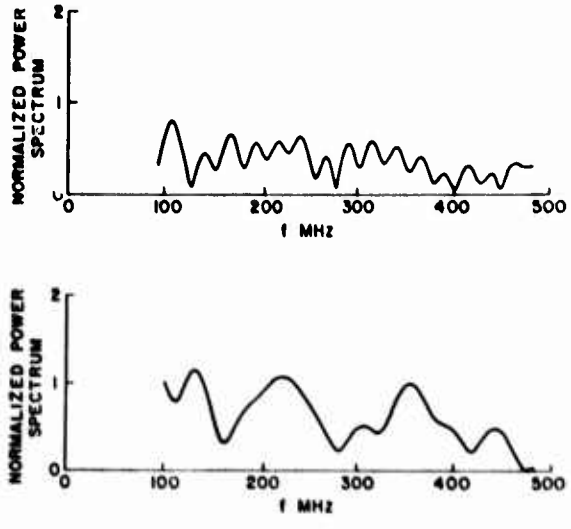


Figure 9. Experimental backscattered power spectra for unknown inclusions in SIC.

We have shown that, using high frequency ultrasonics, it is possible to detect defects in the 10-100 μm range in ceramics. The location of the defect is determined with high accuracy. We are presently working on several techniques to speed up and characterize the observation defects. We are making a 16 element B-scan system that is designed to speed the process of defect detection. We are establishing a catalog of defect responses. We measure the defect response, then, by sectioning, we characterize the defect; thus associating it with its response. We are also carrying out simplified scattering to see whether or not more information can be obtained from the response of the defect in the time domain or the frequency domain.

Acknowledgement

This research was sponsored by the Center for Advanced NDE operated by the Science Center, Rockwell International, for the Advanced Research Projects Agency and the Air Force Materials Laboratory under Contract F33615-74-C-5180.

References

1. A. G. Evans, G. S. Kino, B. T. Khuri-Yakub, and B. R. Tittman, "Failure Prediction in Structural Ceramics," Materials Evaluation, 35, No. 4, pp. 85-95, April 1977.

HIGH RESOLUTION REAL TIME ACOUSTIC MICROSCOPY

L. W. Kessler and D. E. Yuhas
Sonoscan Inc.
Bensenville, Illinois 60106

ABSTRACT

A commercially available scanning-laser-acoustic-microscope (SLAM) has been developed which provides new and unique analytical capabilities for materials science and non-destructive testing. By employing 100 MHz acoustic waves to create images, the "elastic microstructure" of complex materials is visualized directly. The "acoustic micrographs" which contain 2 x 10^4 image points, are displayed on a real time TV monitor. The sample remains accessible to the investigator during the procedure and stressing fixtures can be employed. Dynamic activities can be recorded either on movie film or video tape. There are two acoustic imaging modes which appear to be essential for flaw and defect characterization. The first mode displays the acoustic transmission level through the sample (normal mode) and the second mode displays fringes related to the acoustic phase (interference mode). The presence of a defect within a sample may be evidenced by a change in transmission level or a change in phase or both. The nature of the defect (e.g. high density inclusion or void) can be determined through the combined analysis of the interference and normal mode micrographs. The SLAM technique has been applied to a wide variety of materials including ceramics, metals, glasses, polymers, etc. Defect localization down to 25 μm has been achieved. Samples can be systematically searched, area by area, by simply repositioning the part on the stage of the microscope and observing the acoustic image on the TV monitor.

Introduction

Modern analytical instrumentation has played an important role in materials analysis and non-destructive testing. Microscopy, for example, has broadened our knowledge of fine structure and our understanding of structural components. Ultrasonic equipment has enabled flaw detection at the millimeter size level. The most recent addition to the arsenal of analytical instrumentation is the acoustic microscope. This instrument produces an entirely new and unique view of fine structure. While the optical and electron microscope techniques differentiate the visual, molecular and ultrafine features of a specimen, acoustic microscopy can differentiate structure on the basis of physical properties which are not accessible by the other techniques. In materials science, "mechanical" properties are of prime importance in the service behavior of metals, ceramics, etc., influencing such important phenomena as crack initiation and propagation. The acoustic microscope provides access to the internal "microelastic" structure rather than the "visible" aspects at a surface crossection. Furthermore, structures can be differentiated within thick, optically opaque samples since acoustic wave propagation does not suffer the same restrictions as electromagnetic wave propagation.

The Basic Technique

The SONOMICROSCOPE 100 is a commercially available scanning laser acoustic microscope (SLAM) which produces optical and acoustic micrographs simultaneously. The frequency of ultrasound is 100 MHz and has also been extended to 400 MHz for certain applications in very thin materials. The configuration for viewing specimens is analogous to that used in optical microscopy, in that the sample is placed on a stage where it is both insonified and illuminated. The invisible pattern of sound transmitted through the specimen is detected by means of a rapidly scanning laser-beam-microphone. This pattern, which is the acoustic micrograph, is displayed on a TV monitor. An optical image of the sample is also derived from the laser scan and this is displayed on the adjacent TV monitor. The micrographs are produced in real time, thereby permitting dynamic activity (such as fracture phenomena) to be studied. A block diagram and photograph of this instrument are shown in Figs. 1 and 2, respectively.

With reference to Fig. 2, the 100 MHz acoustic signal is produced by a piezoelectric material bonded onto an applicator stage. The specimen placed upon the microscope stage is coupled via a fluid film at the interface. The energy transmitted through the sample modulates the focused laser beam as it rapidly scans the field of interest. The reflected laser beam is received at a photodetector whose output consists of two signals; one signal depends upon visual features of the surface and the other signal is proportional to the acoustic amplitude. The signals are filtered separately amplified, and converted to video signals for display on the TV monitors. Thus optical and acoustic images appear simultaneously. This technique achieves high resolution, high sensitivity, and real time TV images.

If the specimen is not optically reflective a mirrored coverslip may be placed on top of it and acoustically coupled by means of a drop of fluid. The acoustic signal causes minute displacements to the coverslip surface, thereby modulating the laser beam.

There are two types of acoustic amplitude pictures. First are amplitude pictures made at a single ultrasonic frequency. These acoustic micrographs are generally characterized by high contrast and could also be subject to coherent speckle. The amount of speckle is related to the degree of scattering in the specimens, and this provides some indication of both the mode of acoustic losses, as well as the elastic microstructure of the material under investigation. The second type of amplitude picture is obtained by continuously sweeping the frequency over a selected range. This eliminates coherent speckle and may reveal low contract features which could have been masked.

In addition to displaying the acoustic amplitude distribution throughout the field of view, the SLAM provides an acoustic interference mode of operation. Acoustic interferograms show a series of alternating light and dark stripes. For acoustically homogeneous samples, these bands, or interference fringes, are parallel to one another and are equally spaced. For samples that have variations in acoustic index of refraction or variations in thickness the interference lines will be shifted accordingly. Quantitative velocity of sound measurements may be obtained from the interferograms using simple formulas. Because most of the samples investigated have controlled thicknesses the character of the interferograms is determined solely by localized variations in the velocity of sound. These variations arise from either density or compressibility, or both.

The choice of the visualization modes is made by electronic switching, thus no repositioning of the sample is required.

Advantages of Acoustic Microscopy

Acoustic micrographs provide a new and unique perspective of structure, i.e. that which relates to the microelastic features. Some of the advantages that should be considered are listed below:

1) Optical opacity in thick samples of metal, ceramic, etc. can be avoided with acoustic microscopy; internal structures are differentiated on the basis of intrinsic elasticity variations among the structural components.

2) Microstructure within solids can be observed nondestructively without resorting to laborious sectioning, polishing and etching.

3) The real time feature of the technique permits investigation of dynamic behavior, for example, materials under stress can be observed during the formation of plastic zones and during fracture initiation.

4) Physical elastic properties of structure are brought out by acoustic microscopy. Quantitative data on acoustic index of refraction are available with acoustic interference microscopy. The acoustic interferograms are related to the compressibility and density characteristics of the sample on a micro size scale.

5) Simultaneous acoustic and optical micrographs are produced by the scanning laser technique, thus newly revealed acoustic features can be directly correlated with an optical reference image. Two TV monitors operate simultaneously to provide these views and, thus, the sample need not be disturbed in any way.

6) Acoustic microscopy also plays an important role in biomedical research. Soft and hard tissues can be differentiated, details of muscular contraction can be observed, etc. without exposure to ionizing radiation. Interesting studies performed on hard tissues, such as bone and tooth, revealed variations in microelastic properties which seem to play an important role in the overall functional behavior of the body.

Table 1. Example Application Areas

Welding Flaws	Films
Porosity	Epoxy Bonding
Polymerization Defects	Elasticity and Density Variations
Plastics and Polymers	Dynamic Behavior
Paper	Diffusion Bonding Defects
Non-destructive Testing	Delaminations
Microstructural Integrity	Defect & Flaw Localization
Metals and Alloys	Debonding
Internal Fractures	Composite Materials
Inclusions	Coatings
Heat Treatment Effects	Ceramics
Glasses	Anisotropy
Geological Samples	Adhesive Bonds
Fracture Mechanics	

Acknowledgement

This study is described by R. J. Bratton, C. A. Anderson, and F. F. Lange EPRI Report on Ceramics Rotor Blade Development, May 15, 1976, under contract RP 421-1, p. 3-14 to 3-19.

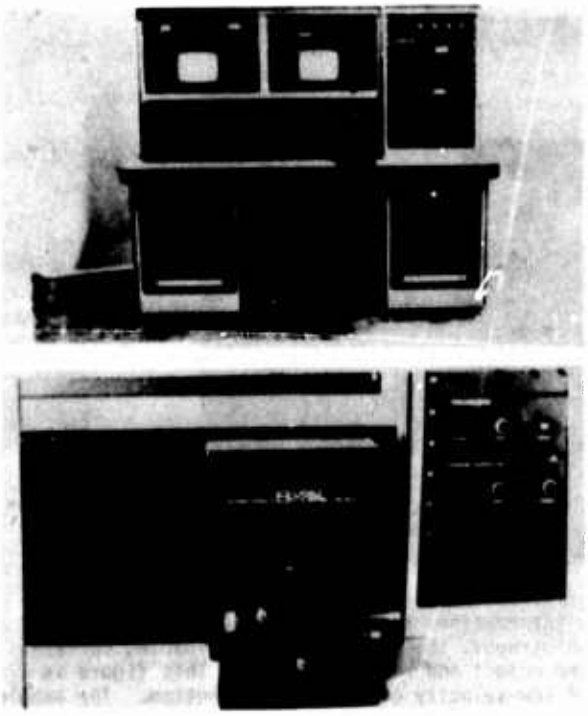


Figure 1. Scanning Laser Acoustic Microscope (SLAM): A commercially available SLAM is shown in the top photo. Two television monitors display the optical and acoustic micrographs simultaneously. A close-up of the stage of isonifying the sample is shown in the bottom photo. The micrometers are used to orient and position the stage and the sample remains accessible to the operator at all times. The operating frequency of this instrument is 100 MHz nominal and specialized stage modules may be dropped in for varying the angle of isonification and the energy mode, i.e., compressional or shear waves.

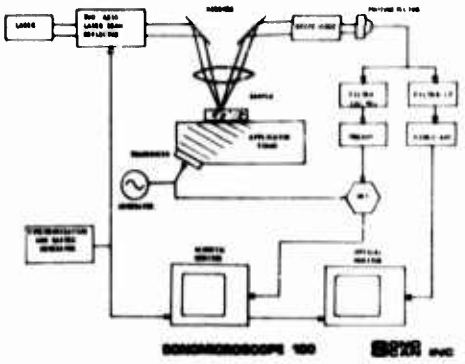


Figure 2. Principle of Operation of the Scanning Laser Acoustic Microscope: A 100 MHz acoustic signal is applied to a specimen placed upon the microscope stage. Acoustic energy transmitted through the sample modulates the non-contacting laser beam as it rapidly scans the field of interest. The reflected laser light is detected by a photodiode whose output consists of two signals; one depends upon visual features of the surface and the other is proportional to the acoustic amplitude. The signals are amplified and displayed on separate TV monitors as optical and acoustic micrographs, respectively. This technique achieves high resolution, high sensitivity, and real time visual displays. If the sample surface does not reflect the laser light then a mirrored coverslip is placed on top of it. The acoustic energy is coupled to the coverslip by means of a drop of fluid.

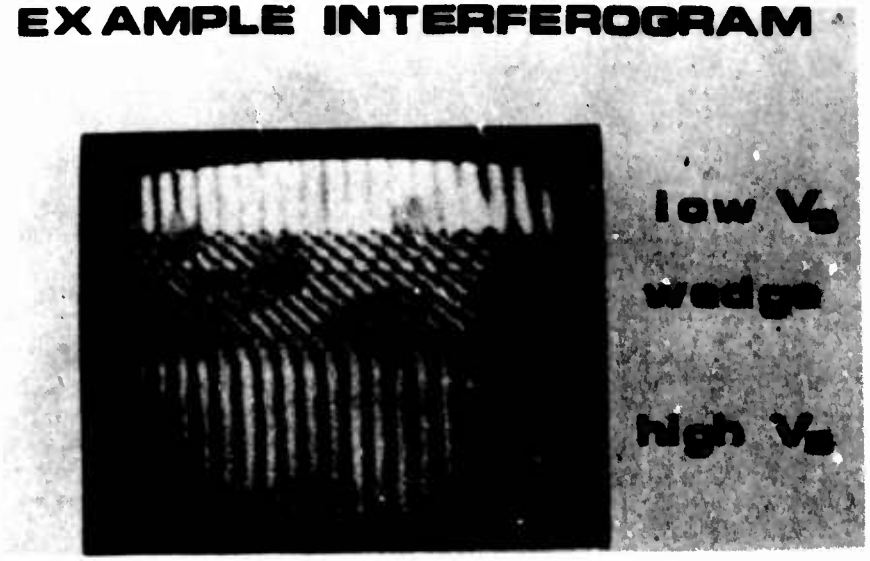


Figure 3. Example Interferogram: An acoustic interferogram displays spatial variations of acoustic transit time in a sample. In order to produce this information, the acoustic transmission signal is combined with a reference signal and, like holography, the resulting fringe spacing corresponds to the spatial angle separation between the object and reference beams. This figure is an interferogram of a 2-phase sample composed of low velocity of sound on the bottom. The sample is uniformly thick and the transition between the materials is shaped as a wedge. Interference fringe shifts to the right indicate less transmission time or higher velocity of sound. The fringe spacing is 80 microns. In an arbitrary specimen, the fringe positions may be readily analyzed to yield velocity of sound data everywhere throughout the field of view.

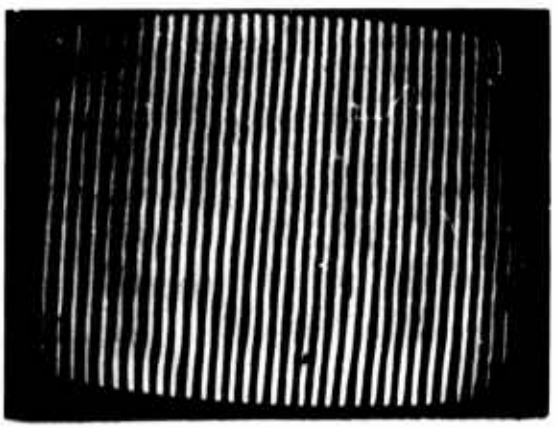


Figure 4. Clean Hot Pressed Si_3N_4: Uniform attenuation and velocity of sound over a field of view is characteristic of "good" hot pressed Si_3N_4. This figure shows an example of such a material. The interference fringes are uniformly straight and evenly spaced.

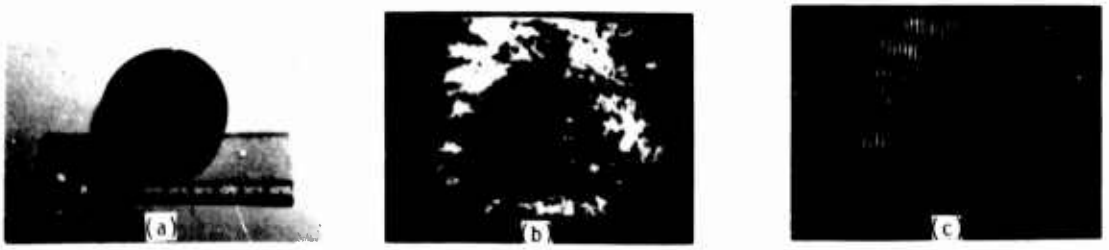


Figure 5. WC Inclusion Within Hot Pressed Si_3N_4: A 2-inch diameter disc, 1/8-inch thick, of hot pressed Si_3N_4 was fabricated with inclusions of known sizes and locations as shown. The actual disc is shown in (a). An acoustic micrograph of a large tungsten carbide inclusion is shown in (b), and the corresponding interferogram fringes are spaced apart by 80 microns. Many of the small dark structures surrounding the large defect are seen to contain phase variations, thus indicating elastic inhomogeniety. Tungsten carbide and boron nitride inclusions were observed on the SLAM down to 50 microns in size. In addition, unintentional heterogeneous elastic variations in the Si_3N_4 were detected at the 50 μ level.

MICROWAVE TECHNIQUES FOR NDE OF CERAMICS

A. J. Bahr
SRI International
Menlo Park, California 94025

ABSTRACT

In recent years, the technology for generating and controlling electromagnetic energy at frequencies of 100 GHz and above has improved considerably, and such components are now readily available. In view of this fact, we have undertaken a program to assess the applicability of this technology to the NDE of ceramic materials and components. We have found that Si_3N_4 is nearly transparent at these high frequencies, which permits the interior of components made from this material to be inspected using microwave energy. The dielectric constant of hot-pressed Si_3N_4 is about 7.5, so the wavelength in this material at 100 GHz is about 1mm. This electromagnetic wavelength is comparable to the acoustic wavelength of 10 MHz ultrasound in this material. Thus, microwave C-scan images will have resolutions roughly comparable to those produced by commercial ultrasonic equipment, but do not require the use of a water bath or other coupling medium in order to achieve rapid scanning. In addition, electromagnetic and ultrasonic scattering will differ for a given flaw, and thus microwave imaging may provide better flaw discrimination in some cases.

Cross-Polarized Transmission Measurements

A block diagram of our experimental arrangement is shown in Fig. 1. The ceramic samples are translated between the sensors in the X-direction via a motor-driven stage, and incrementally in the Y-direction by means of a micrometer positioner.

Broad-flange, open-ended waveguides were used to achieve broadband operation. Since the backward-wave oscillator is capable of being swept over a wide frequency range, we were able to determine the best operating frequency in the neighborhood of 100 GHz for each type of inclusion. Typical frequency responses for four important types of inclusions are shown in Fig. 2. The nominal diameter of these inclusions is 0.020 inches. We note that there are significant variations in these frequency responses, and this fact may prove useful for flaw identification. However, these frequency responses are determined in part by the reflections from the surfaces of the ceramic plate containing the inclusions, and thus it may be difficult to separate the flaw-dependent information from these responses.

C-Scan of Plates

Three different plates of Norton hot-pressed NC 132 containing seeded inclusions and voids were examined using the cross-polarized transmission technique. Figure 3 shows a C-scan of a portion of a plate containing 0.020" and 0.005" inclusions of WC, Fe, Si, and C. Figure 3(a) shows the area covered by the scan and the intended flaw locations. Figure 3(b) shows the portions of the scan area that produce a scattered signal greater than an arbitrarily selected threshold value. Finally, Fig. 3(c) shows the amplitude of the scattered signal as a function of position within the scan area.

Several features of this C-scan are noteworthy. First, all 0.020" flaws are detected. Iron provides the strongest signal, and is the only 0.005" flaw that is clearly detected in this figure. (The other small flaws become more apparent if the frequency is changed.) Second, X-rays show that diffusion of the iron inclusion during hot pressing produces an irregularly shaped scatterer that causes the spatial extent for this flaw to appear overly large in the microwave C-scan. Finally, it appears that a crack-like flaw is present between the 0.020-inch diameter iron and silicon inclusions. Apparently, X-ray, ultrasonic, and dye-penetrant examination by AMMRC did not reveal the presence of such a flaw. If this flaw is indeed found to be real, it would indicate the superior sensitivity of the microwave technique for detecting this type of flaw.

Figure 4 shows a similar microwave C-scan, but for a Si_3N_4 plate containing different types and densities of inclusions. All of the 0.005" inclusions are detected in this scan, but, of course, the closer spacing between inclusions may enhance this detection.

In Fig. 5 we see another scan of the same plate as in Fig. 4, but of only the area containing the 0.001" through 0.010"-diameter silicon inclusions. The sensitivity of our technique for the detection of unreacted silicon appears to be good, and may be better for this purpose than other techniques. This feature could be important in a process-control application.

The data shown in Fig. 6 demonstrates our ability to detect small voids in Si_3N_4, as well as inclusions. The voids were formed in the interior of a 0.250"-thick plate by first drilling small holes in a 0.125"-thick plate, and then diffusion bonding this plate to a second 0.125"-

thick plate. The voids that were not detected by microwaves were also weakly imaged in an X-ray, indicating that these particular holes probably contained some kind of material.

It is interesting to note that partial diffraction pattern produced by the uppermost holes on the left of the scan area. In principle, such a diffraction pattern could provide information about the geometry of the scatterer. The microwave C-scan apparently also shows some inclusions that are not detected in the ultrasonic C-scan.

C-Scan of a Disk

A hot-pressed Si_3N_4 billet in the form of a disk was also examined using microwaves. The main reason for examining this disk was to make a qualitative determination of the effect of the grit-blasted, as-pressed surface on the microwave C-scan. The results obtained before and after the surface of the disk was ground smooth are shown in Fig. 7. The frequency was 94.4 GHz. It can be seen that this amount of surface roughness begins to contribute a significant level of background clutter at this frequency.

After the surface was ground smooth, a microwave C-scan of the disk was made that extended over the edges of the disk. These results are shown in Fig. 8. X-rays showed the presence of an unintended high-density inclusion in the disk, and this flaw is detected in the microwave C-scan. This experiment also shows the effect diffraction near a sharp edge. The cross-polarized scattering from an edge is quite strong, and can be detected at a significant distance from the edge. Qualitatively, we can conclude that flaws near a sharp edge will not be detected with this technique.

Acknowledgement

This work was sponsored by the Army Materials and Mechanics Research Center under Contract DAAG46-76-C-0048.

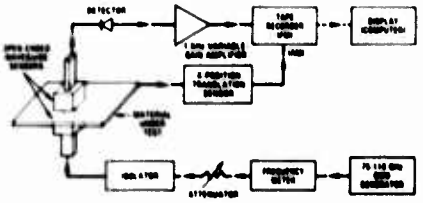


Figure 1. Experimental arrangement for cross-polarized transmission measurements.

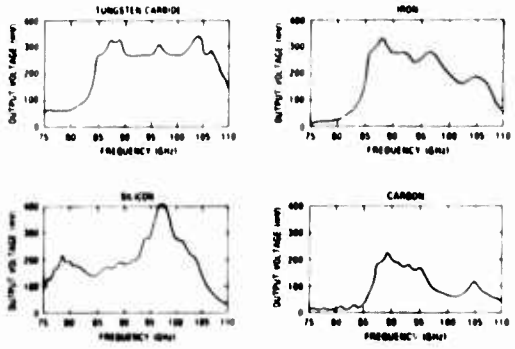
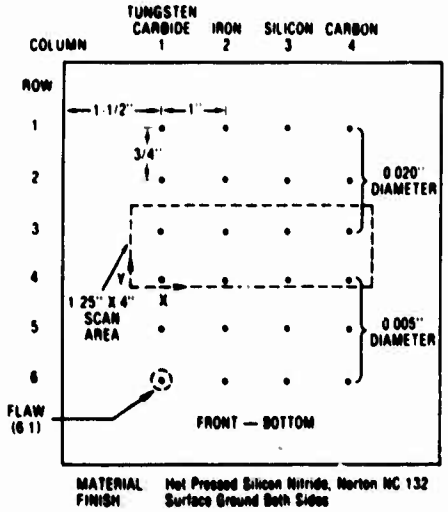
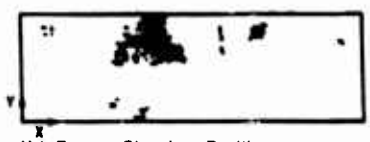


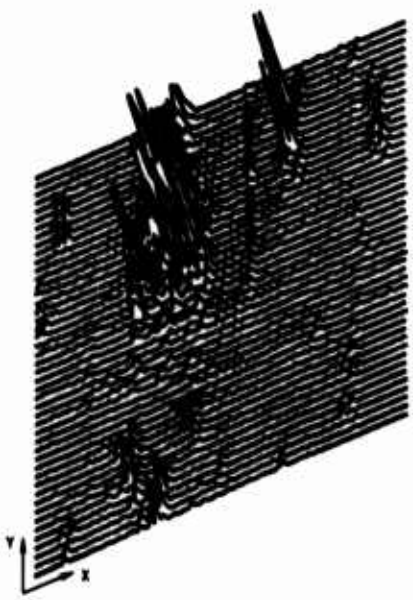
Figure 2. Frequency dependence of the cross-polarized forward scattering from four types of inclusions in a hot-pressed Si_3N_4 plate.



(a) Map of Intended Flaw Locations Showing Scan Area

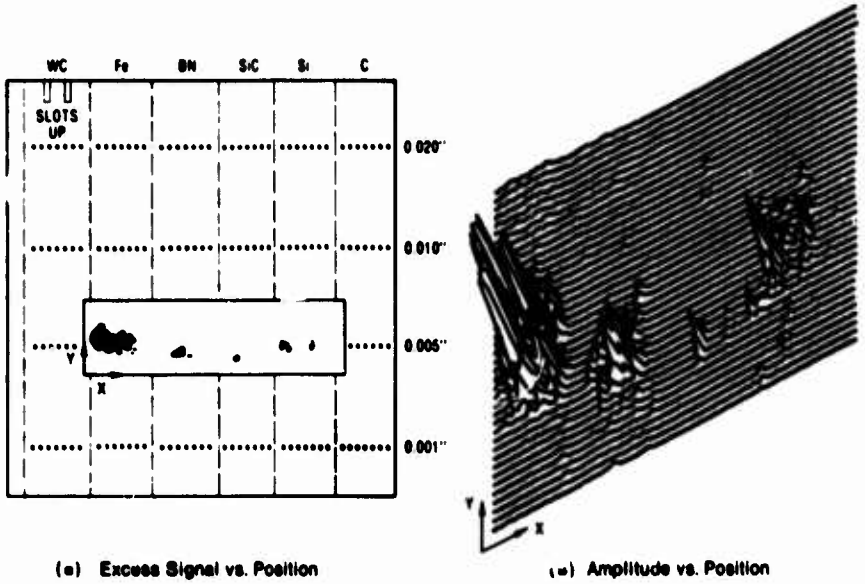


(b) Excess Signal vs. Position



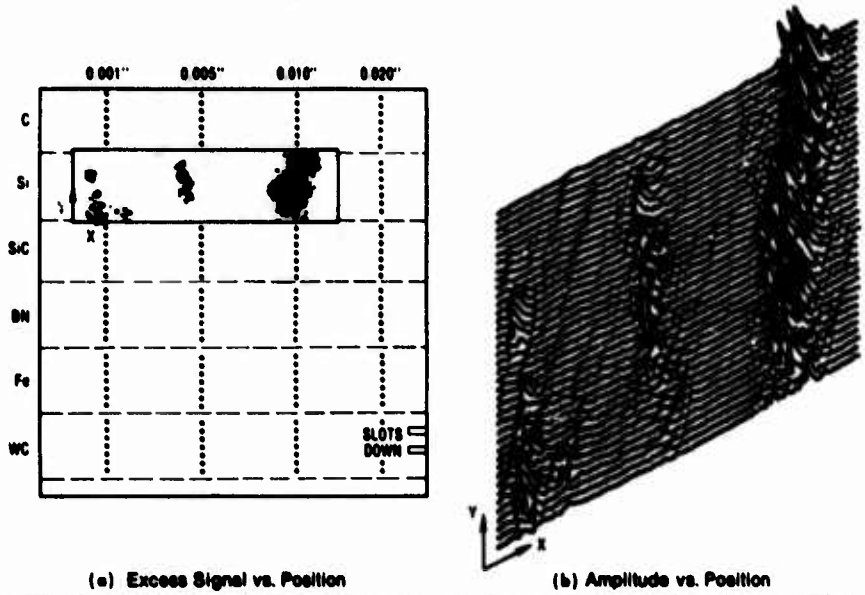
(c) Amplitude vs. Position

Figure 3. Microwave cross-polarized-transmission C-scan of four types of inclusions in Si_3N_4 (frequency = 94 GHz).



(a) Excess Signal vs. Position (b) Amplitude vs. Position

Figure 4. Microwave cross-polarized-transmission C-scan of four types of inclusions in Si_3N_4 (frequency = 91 GHz).



(a) Excess Signal vs. Position (b) Amplitude vs. Position

Figure 5. Microwave cross-polarized-transmission C-scan of silicon inclusions in Si_3N_4 (frequency = 98 GHz).

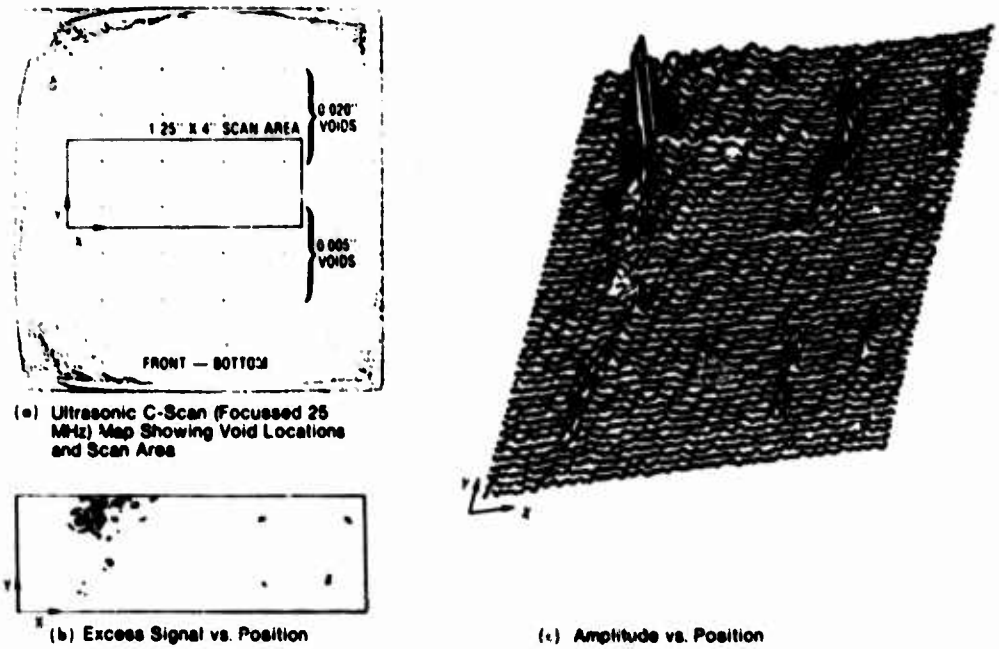


Figure 6. Microwave cross-polarized-transmission C-scan showing voids in Si_3N_4 (frequency = 94 GHz).

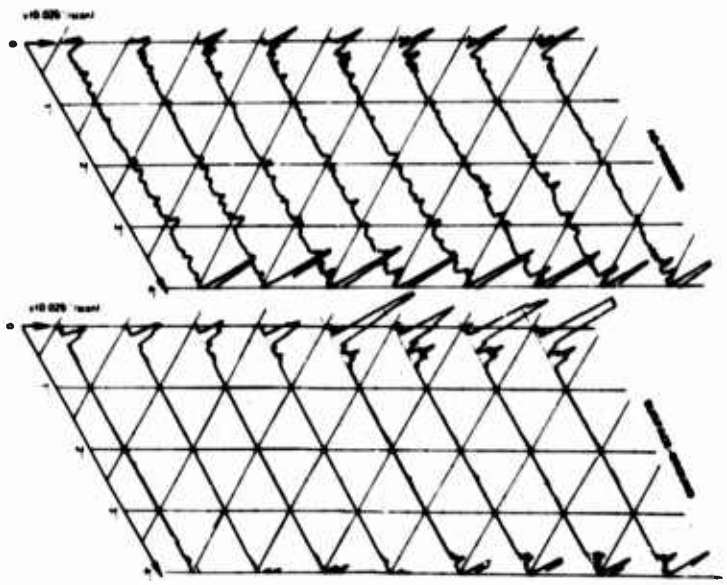


Figure 7. Effect of surface roughness.

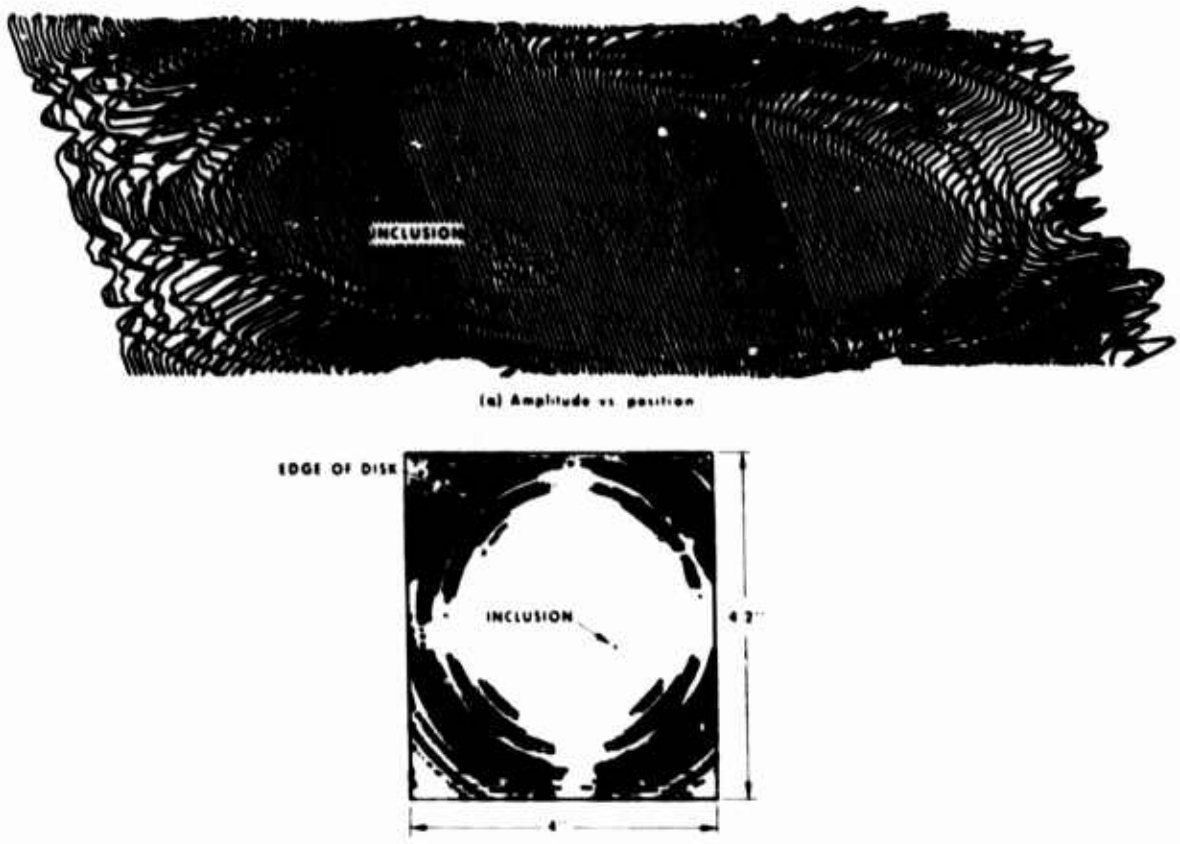


Figure 8. Microwave cross-polarized-transmission C-scan of 4"-diameter hot-pressed Si_3N_4 disk (frequency = 94.4 GHz).

HIGH FREQUENCY LONGITUDINAL AND SHEAR WAVE INSPECTION OF GAS TURBINE CERAMICS

Thomas Derkacs
Thompson-Ramo-Wooldridge
Cleveland, Ohio 44117

ABSTRACT

To assure reliable performance of ceramic materials in gas turbine engines, where performance at 1400°C for up to 10,000 hours is required, it is necessary to screen out material with defects in the size range 10 to 100 μm (0.0004 to 0.004 inches). Investigation of high frequency ultrasonic techniques has led to development of longitudinal and shear wave methods capable of detecting defects at least down to 25 μm in size. The approach is to use a high frequency (45 MHz) ultrasonic pulse-echo immersion mode technique, making C-scan recordings of the results. Inspections have been performed on hot pressed and reaction bonded silicon nitride and hot pressed and sintered silicon carbide. Natural defects, seeded inclusions, and artificial surface cracks have been examined. Reference standards of hot pressed silicon nitride containing seeded defects and laser drilled holes have been developed. Four-point-bend testing and scanning electron microscopy have been employed to establish correlation with ultrasonic results.

This poster describes our NAVAIR sponsored development of high frequency ultrasonic inspection techniques for gas turbine ceramics and also, application of these techniques to the inspection requirements of the AiResearch/NAVSEA program for development of a ceramic gas turbine demonstration engine. The basic goal of the NAVAIR sponsored program was to demonstrate the feasibility of detecting defects in the 10 to 100 μm (0.0004 to 0.004 inch) size range. Selection of high frequency ultrasonics was based on the principle that, for a wave to interact with a defect the wavelength must be of the same order of magnitude as the defect size, or smaller. This dictated the need for a higher frequency than is normally used in ultrasonic inspection to detect the small defects of interest. On the other hand, it was also recognized that if the wavelength approaches the grain size of the material, it will interact causing high background noise and high attenuation. It is the fine grain structure generally found in ceramics such as silicon nitride and silicon carbide which makes it possible to employ high frequency ultrasonics to detect small defects.

The basic technique developed employs an ultrasonic system operating in the pulse-echo mode at 25 to 45 MHz with a focused ultrasonic transducer. Figure 1 shows the arrangement for longitudinal wave inspection. The specimen and transducer are immersed in water with the transducer normal to the specimen surface. The transducer is scanned across the specimen and a C-scan recording is made of the results. We have found that for a 6.4 mm (0.25 inch) thick billet, scans are required at three focal planes to provide complete coverage. Because of the beam orientation, the strongest response is from a defect oriented parallel to the specimen surfaces. This, of course, is not usually the defect orientation of greatest interest. Figure 2 shows the arrangement for shear wave inspection. The same equipment is used, but the transducer is tilted at an angle (11° for hot pressed silicon nitride) in the direction of the scan. This results in a shorter ultrasonic wavelength for a given frequency and provides a beam in the specimen at about a 45 degree angle to the surface. This technique is more sensitive than the longitudinal wave technique and is better applicable to detecting defects which are oriented perpendicular to the specimen surfaces.

The following figures illustrate some of the capabilities of these techniques. The first group of six illustrate some of the work done on the NAVAIR sponsored program. Figure 3 shows a typical C-scan recording of a billet of Ceralloy 147A, hot pressed silicon nitride. This billet contained four seeded defects forming a 25 mm (1 inch) square near corner No. 3. Two of these defects, located on one diagonal, were 125 μm (0.005 inch) diameter simulated voids (SV) consisting of aluminum oxide inclusions. The other two were 125 μm (0.0005 inch) diameter tungsten carbide inclusions (SWC). In addition to these seeded defects, a number of natural defects were detected in the billet. Figure 4 is a composite sketch showing each defect detected in the billet as a dot. The layout of four-point bend specimens is shown with specimen numbers on the outside of each specimen and the height of the ultrasonic pulse from the defect in cm on the inside. The pulse heights were obtained with the beam focused on the defect and are referenced to 4.0 cm for the reference simulated void. Figure 5 shows how each specimen was cut from the billet in order to place the defect near the tensile surface during testing. The 6.4 x 3.2 x 31.8 mm (1/4 x 1-1/4 inch) specimens were cut with the billet thickness as the 6.4 mm (1/4 inch) dimension and with the defect 380 μm (0.015 inches) below the tensile surface.

Figures 6, 7 and 8 show fracture surfaces for specimens that initiated fracture at the ultrasonically detected defects. Figure 6 shows a 25 μm (0.005 inch) tungsten carbide inclusion. The size and material of both these seeded defects were verified by electron microprobe analysis. The portion of the billet containing the other two seeded defects was saved for use as a reference standard as shown in Fig. 4.

To summarize, in the NAVAIR sponsored program TRW has

1) Developed the ability to detect defects at least down to 25 μm (0.001 inch) in size in hot pressed silicon nitriding.

2) Established a reference standard for hot pressed silicon nitride.

3) Demonstrated the ability to correlate ultrasonic inspection results with four-point-bend test data and SEM fractography; and

4) Applied the techniques developed to other materials such as hot pressed and sintered silicon carbide and reaction bonded silicon nitride.

The results of this development program are presently being applied to the AiResearch/NAVSEA program to develop a ceramic gas turbine demonstration engine. The plan calls for TRW to inspect:

1) seeded billets
2) mechanical test specimens
3) prototype blade shapes, and
4) actual blades.

Item 1 is almost complete and items 2 and 3 are in progress. Figures 9 through 12 show some of the results for item 1. Figure 9 shows the C-scan recording of the 45 MHz longitudinal wave inspection of a billet of NC-350, reaction bonded silicon nitride. The billet was seeded with Fe, Si, SiC, low density Si_3N_4, C and pores in sizes ranging from 125 to 1000 μm (0.005 to 0.040 inches) as shown in the margins. Figure 10 shows the corresponding shear wave inspection results. Not only are the defect indications larger in Fig. 10, but there are a number of defect indications in Fig. 10 which do not appear in Fig. 9. This shows the superior sensitivity of the shear wave techniques. Although there are some blank areas where seeded defects are supposed to be, particularly for the low density Si_3N_4 and the smallest size of Si and SiC, there is no way of knowing whether the defects are actually present until the billet is cut up.

Figures 11 and 12 show C-scans of 45 MHz longitudinal and shear wave inspections of a seeded billet of NC-132, hot pressed silicon nitride. In this case the seeded defects are WC, Fe, BN, SiC, Si and C in sizes ranging from 25 to 500 μm (0.001 to 0.020 inches). Once again the shear wave inspection shows more defects than the longitudinal wave inspection. Although the actual defect sizes have yet to be verified by metallurgical evaluation, Fig. 12 offers additional evidence of the ability of high frequency ultrasonics to detect defects at least down to 25 μm (0.001 inches) in size in hot pressed silicon nitride.

In conclusion, the evidence provided, both by inspection of materials containing seeded defects and by SEM examination of ultrasonically detected natural defects, indicates the ability of high frequency (45 MHz) pulse-echo immersion ultrasonic testing using a focused transducer to provide a thorough examination of a large ceramic specimen and to detect defects of a variety of materials at least down to 25 μm (0.001 inches) in size.

LONGITUDINAL WAVE INSPECTION

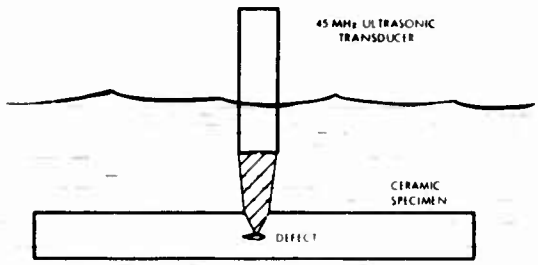


Figure 1. Pulse-echo longitudinal wave inspection is performed at 25 to 45 MHz using a focused ultrasonic transducer immersed in water. C-scan recordings are made of the results. This technique is more sensitive to defects oriented parallel to the surface that is normal to the transducer.

SHEAR WAVE INSPECTION

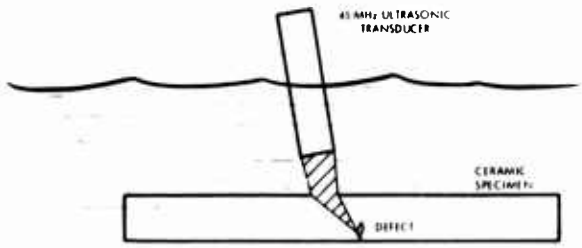


Figure 2. Pulse-echo shear wave inspection is performed using the same equipment, but with the transducer tilted at an angle of about 11° to the surface. This technique is more sensitive to defects oriented normal to the surface.

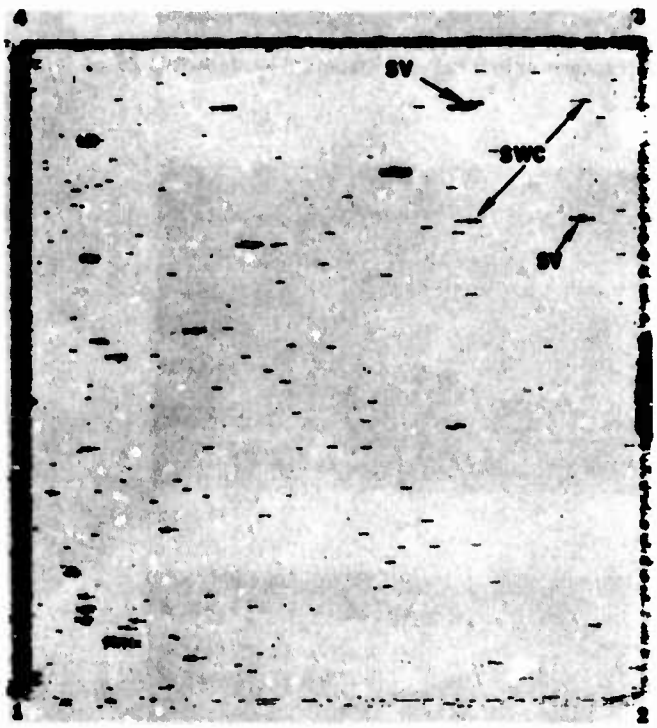


Figure 3. Typical C-scan recording of inspection results for a billet of Cerralloy 147A hot pressed silicon nitride showing seeded low density (SV) and high density (SWC) 125 μm (0.005 inch) defects as well as numerous natural defects.

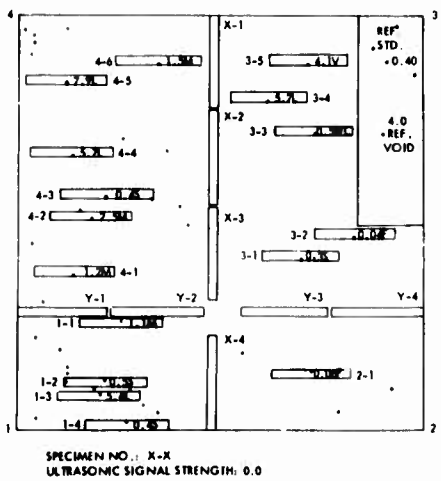


Figure 4. Sketch showing the defects detected in the billet of Cerralloy 147A, the four-point-bend specimens cut from the billet, and the ultrasonic signal strength of the defects located in the specimens.

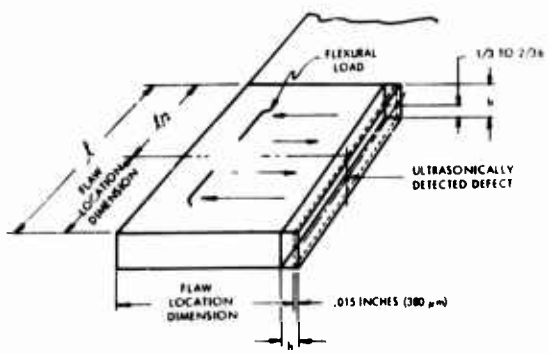


Figure 5. Sketch showing the method by which four-point-bend specimens were cut from the billet of Cerralloy 147A with ultrasonically detected defect located near the tensile surface.

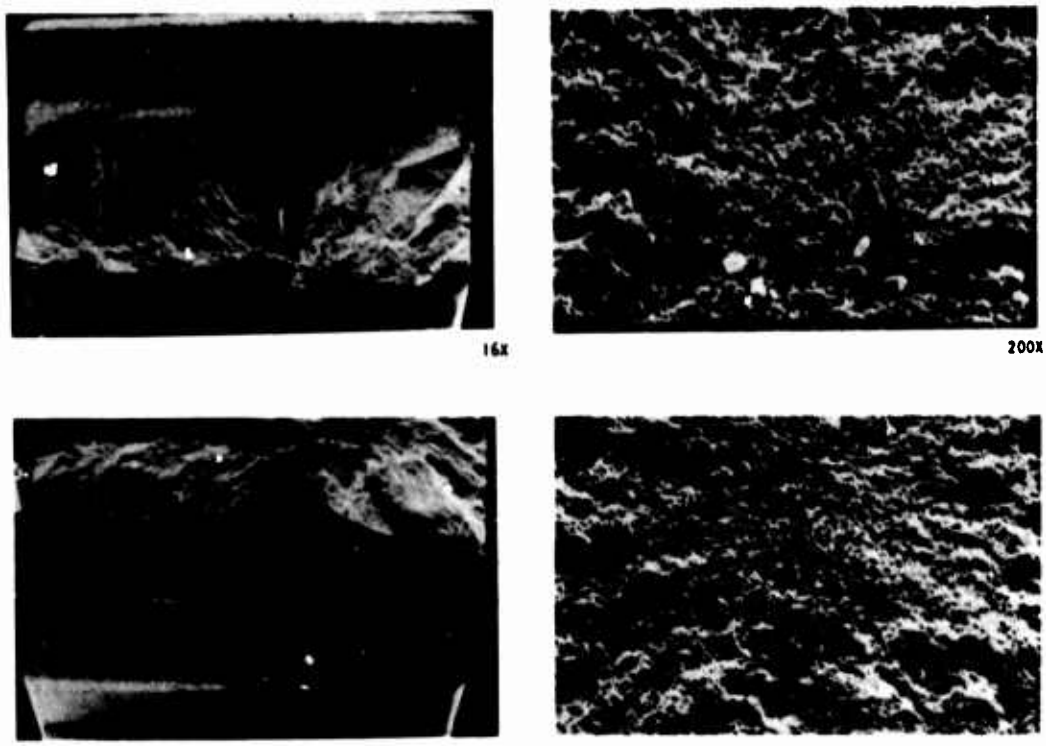


Figure 6. Fracture surfaces of specimen 1-4, showing fracture origin at ultrasonically detected 25 μm (0.001 inch) void.

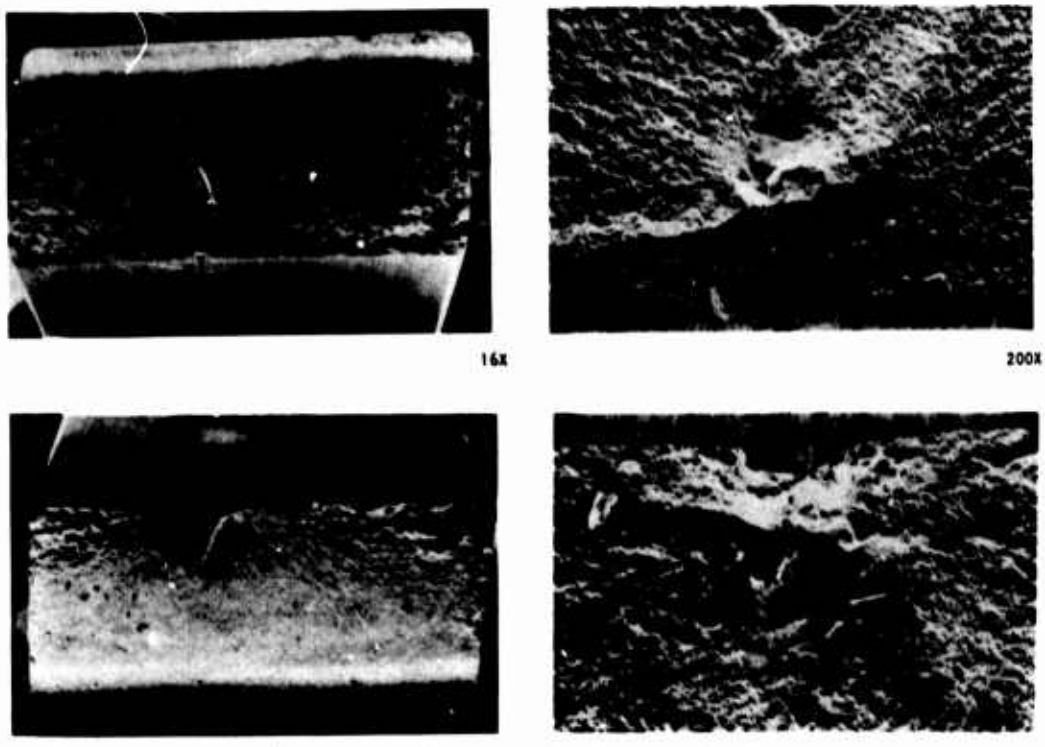


Figure 7. Fracture surfaces of specimen 3-5, showing fracture origin at seeded 125 μm (0.005 inch) simulated void (aluminum oxide inclusion).

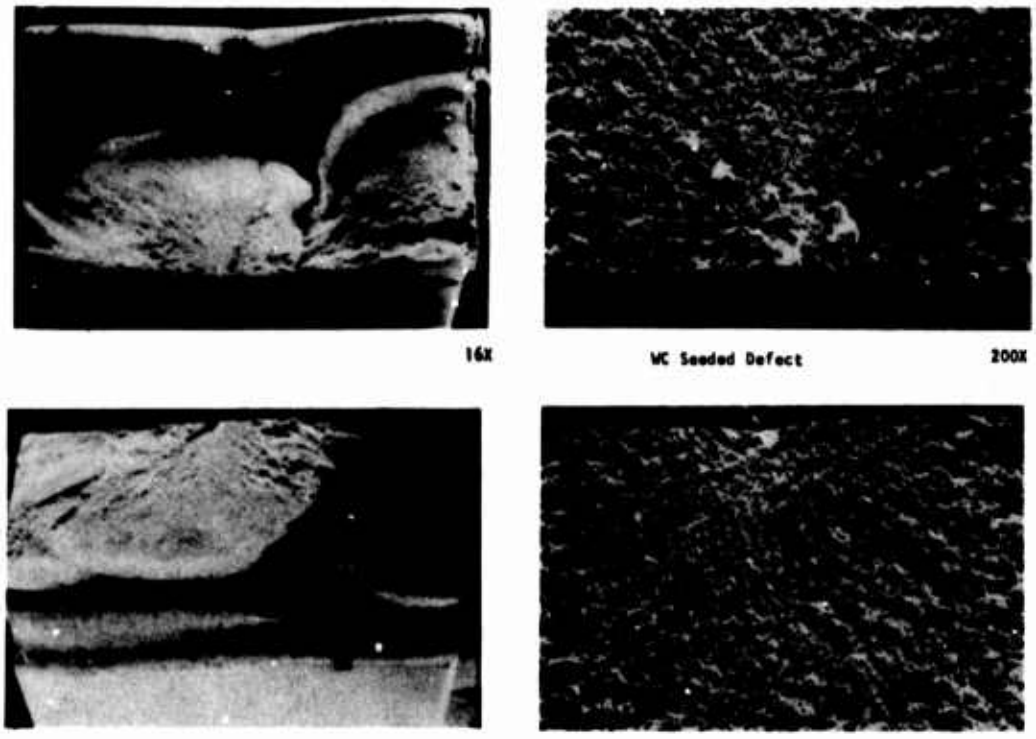


Figure 8. Fracture surfaces of specimen 3-3, showing fracture origin at seeded 125 μm (0.005 inch) high density (tungsten carbide) inclusion.

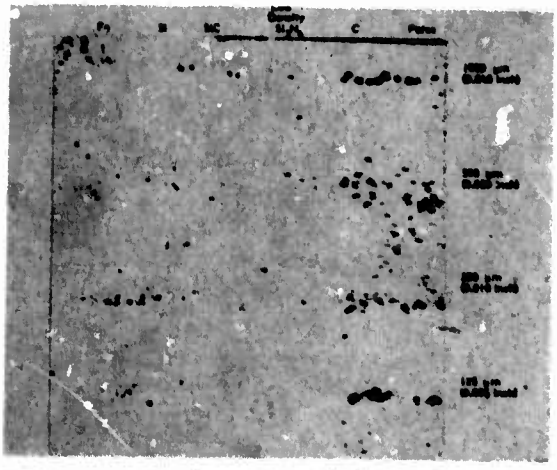


Figure 9. C-scan recording of 45 MHz longitudinal wave inspection results for Airesearch seeded billet of NC-350 reaction bonded silicon nitride.



Figure 10. C-scan recording of 45 MHz shear wave inspection results for Airesearch seeded billet of NC-350, showing superior sensitivity of shear wave technique.

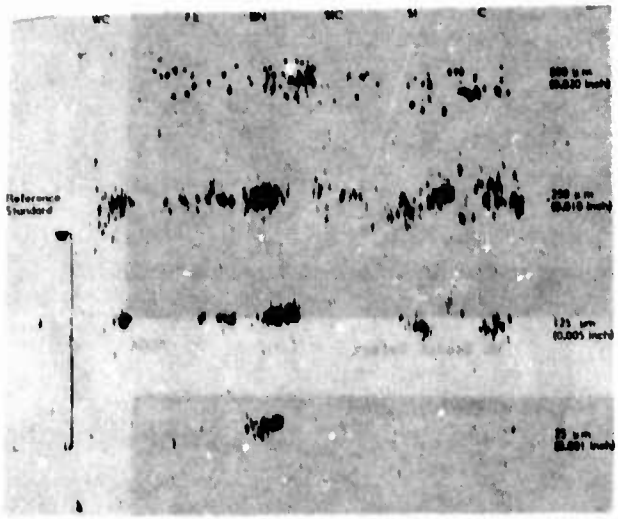


Figure 11. C-scan recording of 45 MHz longitudinal wave inspection results for Airesearch seeded billet of NC-132 hot pressed nitride.

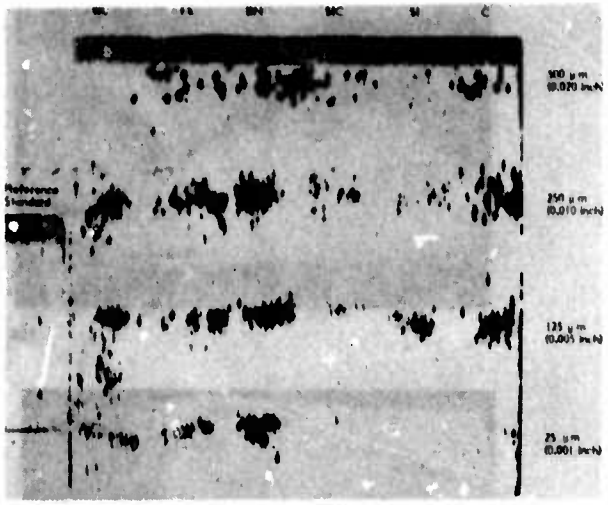


Figure 12. C-scan recording of 45 MHz shear wave inspection results for Airesearch seeded billet of NC-132, showing superior sensitivity of shear wave technique.

FAILURE CAUSING DEFECTS IN CERAMICS: WHAT NDE SHOULD FIND

R. W. Rice, J. J. Mecholsky, S. W. Freiman, and S. M. Morey
Naval Research Laboratory
Washington, D. C.

ABSTRACT

The various types of defects causing failure in a variety of ceramic materials are illustrated. Examples are drawn from such ceramics as piezoelectric, infrared transmitting, and potential turbine materials. Both machining and processing defects are shown as sources of failure. The former are selected to illustrate the effects of machining parameters. Processing defects illustrated include pores, foreign particles and large grains, or clusters of these. Changes in the size of defects with specimen size are also noted.

Introduction

Ceramics are playing an ever increasing role in our modern technology and have the potential for very significant further increases in their utilization. The primary factor pacing this utilization is their mechanical reliability. Successful application of NDE to ceramics coupled with proof testing and improved processing as well as an improved design technology will be the key tools in obtaining increased reliability and, hence, increased utilization. The purpose of this paper is to briefly illustrate the types of failure causing defects in ceramics, and some of the factors determining the size and character of such defects to aid the increased characterization of such defects in ceramics by NDE techniques.

The failure causing defects shown in this paper have all been determined after the fact by fractography. Thus all of the photos (scanning electron micrographs) in this paper, except for a few overall specimen photos, are of the fractures of one or both of the pieces containing the origin. Such fracture origins can be determined from a variety of markings that are generally discernable.* The fracture origins shown in this paper are all in polycrystalline samples. Glasses and single crystal strengths are typically much more heavily dominated by machining flaws which are similar to those in polycrystalline specimens. Note that most of the fractures shown in this paper are in test samples, but examples of hardware fracture origin are shown and discussed.

Types of Failure Causing Defects in Ceramics

Basically, the types of defects that cause mechanical failure of ceramic materials can be divided into three broad categories as shown in Table I.

TABLE I. Types of Ceramic Failure Causing Defects

Processing Defects

1. Pores or porous regions
2. Foreign particles
3. Large grains
4. Combinations of the above or their combination with other types of failure causing defects.

Machining and Handling Defects

Service or Environmentally Induced Defects

Processing Defects

The figures following this text show a variety of the above types of defects and the following comments are intended to put many of these illustrations in a broader context. Pores, either singly, in limited groups, or in clusters of varying gradiation from the average character of the body, are generally the most common source of processing defects in ceramics. Commonly, single pores whose dimensions are several times the grain size are sources of failure as illustrated in Figs. 1, 3, and 4. However, in larger grain bodies pores or groups of pores smaller than a grain size can also be sources of failure as indicated in Fig. 5. One or a few larger pores clustered together or in conjunction with many smaller pores (e.g., as in Figs. 2 and 3b) are also common sources of failure. Local regions somewhat more porous than the average, as indicated in Fig. 6, are also not infrequent sources of failure. Such porous regions may, in fact, be substantially more common as failure sources than we normally detect since in bodies having a fair amount of porosity determination of exact fracture origins is difficult. Such clustering of pores, especially when there is not a significant gradiation between the region causing failure and surrounding matrix, will presumably be extreme challenges for NDE detection.

It should be noted that pores can be quite irregular in shape and they often have a significant anisotropy of shape related to the character of the original processing process as is the case in Fig. 2 and, to a lesser extent, in Fig. 3a.

*For more information on such fracture original determination, see R. W. Rice, "Fracture Topography of Ceramics," pp. 439-472, in Surfaces and Interfaces of Glass and Ceramics, ed. by V. Frechette, W. La Course, and V. Burdick, Plenum Press, NY, 1974.

A fairly common cause of irregular pore shapes is the formation of a partial pore or a series of pores around an agglomerate in the fabrication of body as indicated in Fig. 4. Other major causes of porosity are incomplete powder compaction arising from a variety of sources. Local concentrations of organic matter introduced in the original processing, and subsequently lost during the firing of the ceramic, leaving behind a pore or pores, are a significant source of porosity. This organic matter can be foreign matter, i.e., anything from pieces of tobacco to dandruff, to parts of bugs, lint, etc., to locally high concentrations of organic materials used as binders or lubricants in the processing or many bodies.

Less common, but nonetheless important failure-causing defects are foreign particles such as the graphite and SiO_2 particles illustrated in Figs. 7 and 8. A single large grain or a cluster of large grains (e.g., as illustrated in Fig. 9) can also be important sources of failure provided they are associated with some other defect. Frequently, large grains are the result of a compositional inhomogeneity in the material (i.e., either a localized impurity or a deficiency or excess of additive material. which may be the direct source of the defect associated with the large grains), or may indirectly lead to this due to the generation of porosity. Large grains on the surface are usually preferential locations for failure-causing machining flaws discussed later and stresses from compositional inhomogeneities may aid in the formation of machining flaws.

Machining Defects

The study of machining defects is focused primarily on those from grinding and secondarily from polishing. Both limited study and the nature of the processes suggest that sawing will result in flaws similar to, but more severe than. those due to grinding while lapping will result in flaws similar to, but more severe than, those due to polishing. A fundamental character to be recognized about the above abrasive machining methods is that they will involve abrasive machinine particles being partially imbedded in the surface and moved parallel with the surface. This results in two populations of cracks being generated. The first is a discontinuous series of cracks extending into the material from the bottom of the groove being gouged out by the abrasive particle and usually parallel with the groove, except in single crystal or large grain bodies where the angular variation of the groove from preferred cleavage or fracture planes can be important. The second is a series of cracks generated perpendicular to the direction of particle motion, probably due in part to stick-slip phenomenon as the particle is forced along the surface of the work piece. The latter sets of cracks typically have limited curvature and normally have limited angular variation from the approximate mean of being normal to the direction of particle motion, except in single or large grain bodies where, again, the orientation of preferred cleavage planes can have a significant effect on the orientation of these cracks. However, even a measureable number of such cracks are observed at angles up to nearly 45 degrees from the direction of abrasive motion. Where the directionality of the abrasive particles is continuous over an extensive region as in the typical grinding operation due to the linear motion of the grinding wheel or the workpiece relative to one another, there is thus a significant long-range orientation to the two different sets of flaws. Since the cracks approximately parallel with the groove are often substantially longer than those approximately perpendicular to the groove, there is often a long-range anisotropy to the crack population. Failure of specimens due to stressing parallel and perpendicular to the direction of grinding thus activates each of these flaw populations, resulting in significant strength anisotropy as shown in Fig. 10. In larger grain bodies where flaw and grain dimensions are similar, grain boundaries can provide a constraint on the extent of the machining flaws and, hence, limit the anisotropy of shape and, hence, of strength. However, when the grain size is significantly larger than the crack size, the crack can again exhibit considerable anisotropy but may show greater angular variation from the machining direction due to their following preferred fracture planes within individual grains.

Additional examples of machining cracks and some of their variability in shape are shown in Figs. 11 and 12. Figure 12 simply demonstrates that the concepts discussed above are applicable to grinding of shapes as opposed to flat surfaces. Figure 13 illustrates an important problem that frequently occurs with machining, expecially grinding operations where there are corners or edges involved, especially sharp ones. In such cases there is often a preferential occurrence of cracks, often somewhat larger at the corners or edges of the sample.

Turning next to polishing - if it is not sufficient, then the mechanical behavior will be dominated by cracks left from the prior machining operation. Otherwise, polishing itself introduces the same type of dual crack population as grinding does. However, because typical polishing operations do not have long-range directionality (e.g., due to the typical rotation of both the sample and the polishing wheel) particle trajectories on the surface are effectively random in direction on an overall basis. Thus, strengths are essentially isotropic and failure invariably occurs from the elongated cracks which tend to form parallel with the local particle direction of motion. Again, the extent of elongation of these cracks depends primarily on the interaction with the grain structure. Thus, in a fine grain material, as illustrated in Fig. 14, these cracks are commonly quite elongated as they are in glasses and single crystals (when favorable fracture planes are at not too high an angle to the local direction of particle motion). On the other hand, when the grain size is comparable to the size of the crack, grain boundaries can limit the size of the crack as illustrated in Fig. 15.

Handling and Service Defects

Turning next to handling defects which may occur either in the processing of the specimen or in subsequent service, these can take on a variety of forms such as scratches, spalls and cracks, with one of the most common being cracks due to impact or localized contact. Figure 16 illustrates examples of this in a crystallized glass. It should be noted again that edges and corners are often preferable sites for such damage.

Service induced defects have received relatively little study. The only information presently being generated is on the effects of oxidation on the strength and flaw (crack) character of Si_3N_4 materials. Figure 17 shows failure from oxidation pits which are characteristic of the leading commercial hot pressed Si_3N_4 (NC132). This is not characteristic of Si_3N_4 per se, but appears to be due to a heterogeneous distribution of an impurity possibly reacting with the additive phase. Si_3N_4 compositions have been made which do not show this pitting; however, as illustrated in Fig. 18, initial studies of some of these indicate that failure may preferentially occur from bubbles that form in the oxide surface.

It should be recognized that in view of the limited depths of machining flaws which typically dominate the failure of higher quality ceramics, it takes a relatively limited depth of oxidation or corrosion to completely remove or alter the surface layer containing the machining flaws and, hence, to eliminate them. Thus, one is faced with a completely changed flaw population which poses a problem for both NDE and life prediction techniques. However, it need not be an insurmountable problem, since one can either pre-oxidize or corrode the specimen surfaces to establish the longer term flaw population before putting the part in service, or to adequately characterize the transition between the two defect (flaw) types to make suitable life predictions. However, this aspect of changing of dynamic flaw populations is an important question for the long-term utilization of ceramics which is only beginning to be thought of, let alone experimentally and analytically addressed. Long-term utilization of ceramics at high temperatures or in reactive environments can lead to a number of changes which can make flaws either more severe or less severe, or introduce new flaws which can compete with or become dominant over the previous set of flaws. Thus, for example, internal oxidation can occur in bodies of some porosity, pores can change their size, shape, and distribution due to such oxidation or due to simple diffusional phenomenon, e.g., diffusion of impurities can generate new pores. Correspondingly, impurity particles may either increase or decrease in size depending upon a variety of parameters, and grain growth can occur.

The above examples have been primarily of a single flaw acting by itself. The exception being large grains which require an associated defect for failure. However, other interactions can occur. Thus, for example, in Fig. 1b, one can see a machining flaw has intersected with a pore so that the two together become the combined flaw causing failure. Similarly, there has been some observation of impurity particles associated with flaws generated as a result of machining.

Factors Affecting the Character of Failure Causing Defects in Ceramics

Three general factors should be noted in considering the size and type of flaw character that will control the strength behavior of ceramics in addition to the points made in the previous section. These three factors are the size of the specimen, its shape, and its cost. The introduction of most flaws, whether they be processing defects or machining defects, is a statistically controlled process. Thus, as the specimen size increases the probability of having a more severe, e.g., larger flaw size, increases as schematically indicated in Fig. 19.

Thus, for example, in machining there is a distribution of the size and spacing of the abrasive particles and how they are bonded in the abrasive bonded media as well as the statistical variations of the material they are abrading and the swarf they are generating which can affect the degree of gouging and stick-slip phenomenon. Thus, as the specimen size increases there is an increasing probability of having more serious machining flaws. This is illustrated in Figs. 20 and 21 where machining flaws due to the same machining conditions and the same material result in bigger flaws in the bigger sample. Greater control over the machining parameter such as more frequent dressing of the wheel, smaller depths of cut, may frequently reduce the size effects but probably will not eliminate them.

This size effect can also be observed by comparing fracture origins in actual pieces of ceramic hardware. Figures 22-26 are of failure origins which are typically due to somewhat substantially larger bodies than the test specimens which have been illustrated in Figs. 1-18 and 20. Thus, for example, compare the flaw sizes in piezoelectric materials shown in Figs. 22-24 to those shown in Fig. 1.

Specimen shape can also be an important factor in determining the flaw character. The shape can determine the available machining direction and can also significantly affect the degree of uniformity of the machining. Also, as noted earlier, many processing defects (especially pores and porous regions) exhibit a significant directionality with the character of the processing and hence with the shape of the part. Thus, defects can have different orientations in different parts of the specimen because of different aspects to the forming of these portions, i.e., being more common in areas of more constrained or more turbulent flow in such processes as injection molding.

The introduction of both induced defects and machining flaws can be controlled, but this requires cost. Much of the cost may be in process development, but a reasonable fraction may also be involved in the character of processing used as well as in the quality control. Thus, for example, observe the much larger size of the failure causing defects in the sonar transducer

hardware, Figs. 22-24, in contrast to test bars, Fig. 1. This is a volume, highly cost competitive business in which there are rather limited mechanical requirements for the system. Individual ceramic components sell for on the order of a few dollars. Contrast this with the defects observed in prototype ceramic turbine blades shown in Figs. 25 and 26 with a Si_3N_4 test specimen in Fig. 12. While the lower difference in volume between the component and the test specimen is a factor in the more limited differences in the flaw sizes, the quality of processing is also an important factor and is reflected partly in the cost. The Si_3N_4 component cost is close to three orders of magnitude greater than that of the sonar components.

Summary and Conclusion

We have now achieved a fair understanding of the types and character of failure causing defects that are introduced in the fabrication of a ceramic part and have a general understanding of many of the parameters determining their nature. We are also beginning to gain an understanding of the nature and character of the more important surface induced defects. This understanding gives a clear definition to the ultimate goal of NDE of ceramics. It is our opinion that NDE can be a quite useful tool for ceramics, but that by itself it will not be adequate for complete quality assurance in ceramics because of the imposing difficulties that it must address. Amongst these are: (1) the small flaw sizes in high quality components typically in the ten to fifty micron size range, (2) the background from which they must be detected, e.g., detecting limited variations in the concentration or size of scattered pores and sorting out the orientation of small size machining flaws, (3) the association that may frequently occur with failure causing defects, i.e., the interaction of different types of defects or the importance of defects being associated with large grains, (4) the shape factor in actual components, and (5) the changes in flaw populations that can occur in service. It is thus felt that in the nearer term the primary, but nonetheless, important use of NDE will to sort out particularly weak ceramic parts.

Acknowledgements

Portions of this work have been supported by ONR, NAVAIR, and NAVSEA.

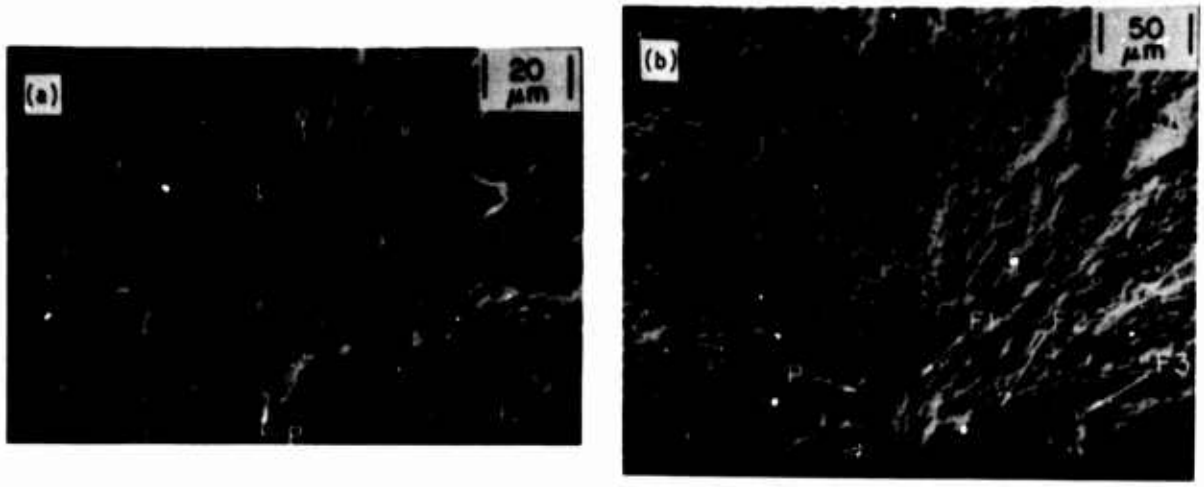


Figure 1. Failure from isolated pores in lead zirconate titanate sonar ceramic test bars. These bars represent some of the highest quality commercial sintered material having strengths respectively of: (a) 17,000 psi, and (b) 15,000 psi. The failure in (a) is from a single, isolated pore (P), and (b) from the interaction between the pore (P) and what appears to be a machining flaw F1. The combination of flaws F2 and F3 does not appear to have contributed to the failure, in part because of the spacing between F1 and F2, and because of the angular difference between F1 and F2.

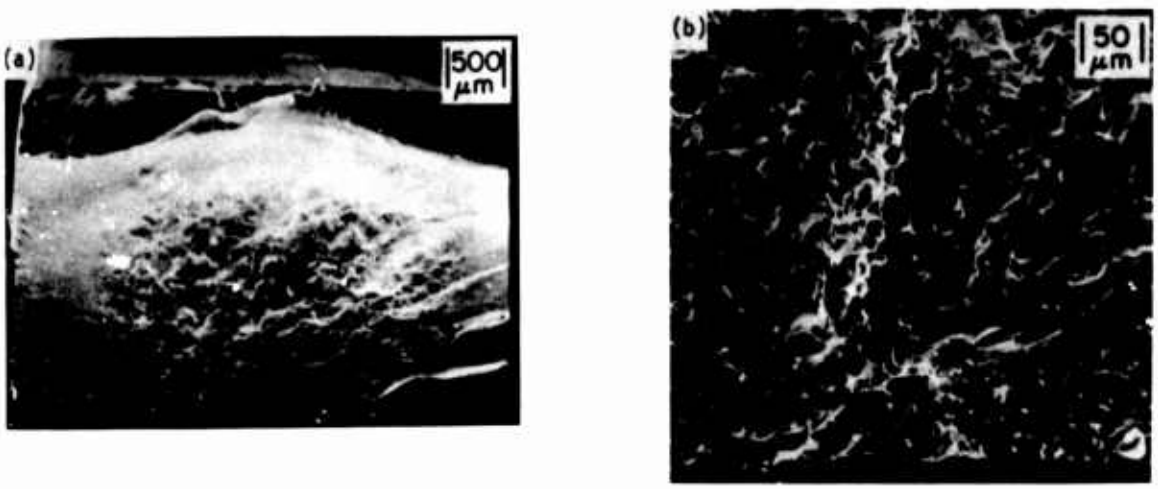


Figure 2. Failure of an experimental $BaTiO_3$ (+ LiF + MgO) sample from a large pore and associated smaller porosity. (a) Lower magnification. (b) Higher magnification of the fracture initiating pore. Note the highly elongated character of the pore which is not too uncommon; its orientation suggests it represents a laminar defect in the original hot pressing. The relative high strength of this specimen (~19,000 psi) is due to the pore being oriented in a less unfavorable orientation.

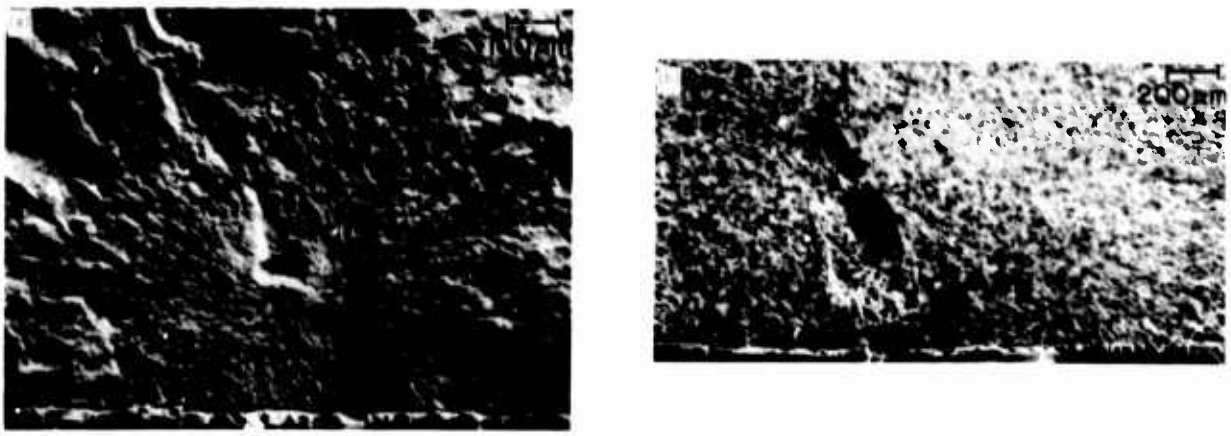


Figure 3. Failure of reaction sintered Si_3N_4 (NC350) from pores; (a) from a single isolated pore of some limited anisotropy in shape, (b) from two larger pores and associated porosity (between arrows).

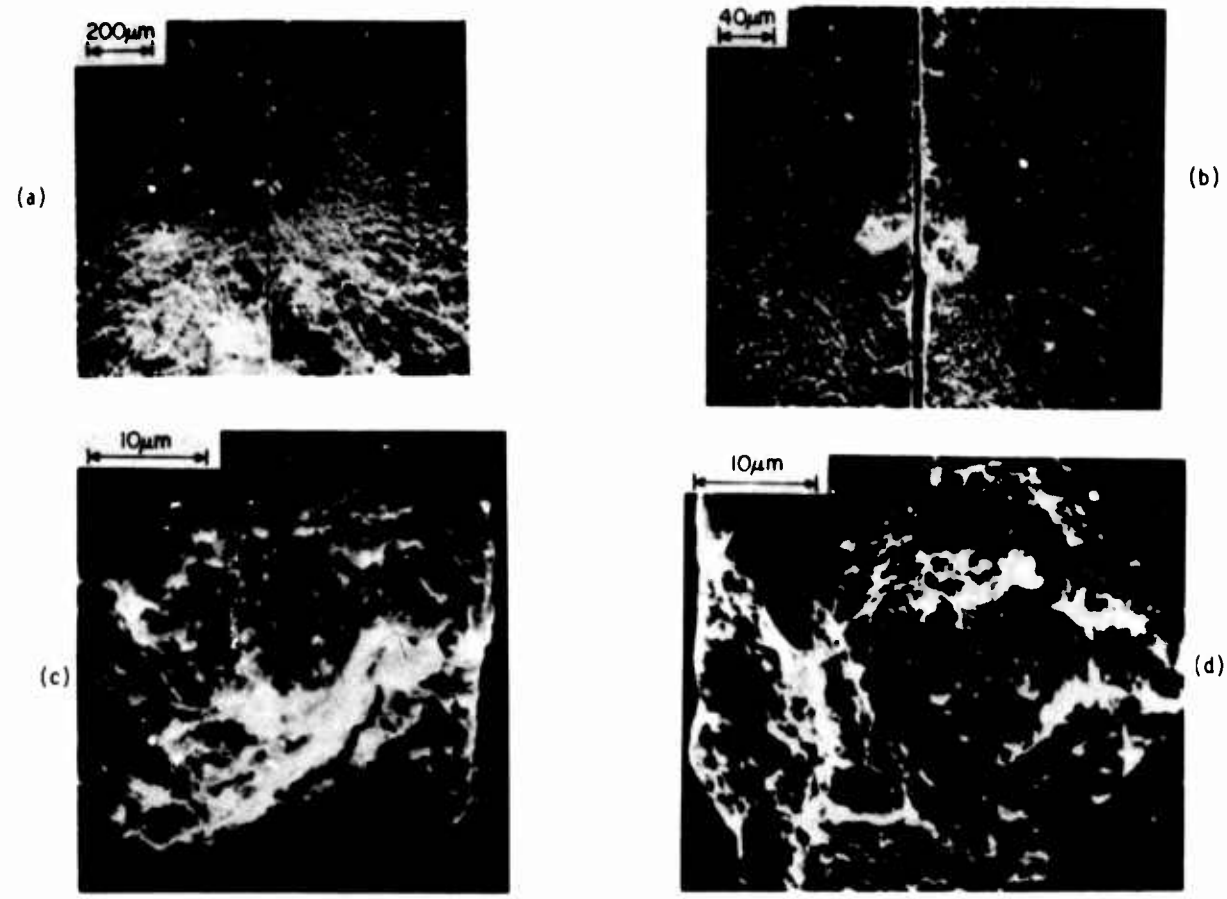


Figure 4. Failure from a crescent shaped pore around an agglomerate in sintered Al_2O_3. (a) and (b) each show both matching fracture halves in the vicinity of the fracture origin at two different magnifications, and (c) and (d) show each half of the failure initiation site. Fracture stress = 94,000 psi.

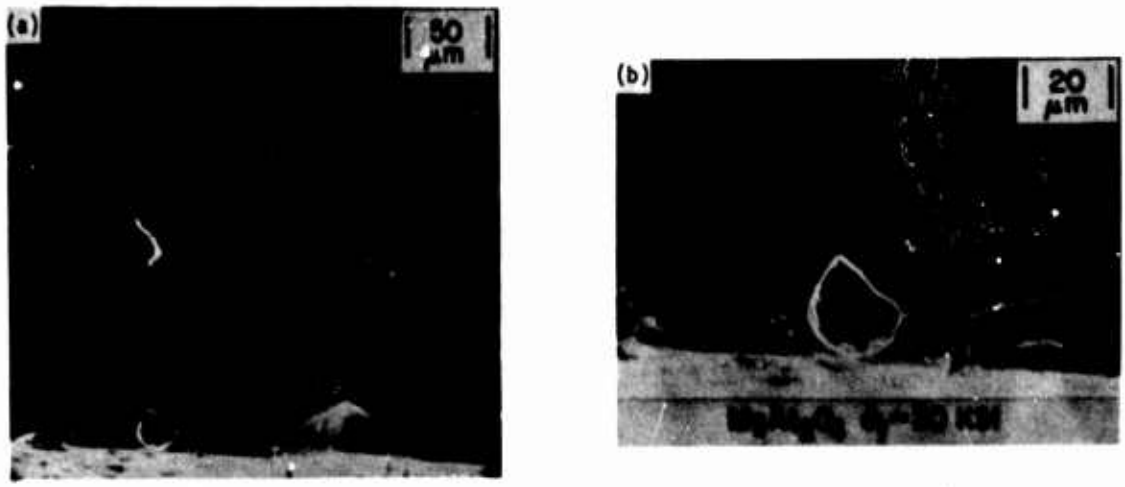


Figure 5. Failure from an isolated pore smaller than the grain size. (a) Lower magnification showing larger view of the fracture initiating region; (b) higher magnification showing primarily the pore which is about 1/5 the grain size. Whether the pore was the sole cause of failure or whether its being partly located along a grain boundary at the immediate tensile surface of the specimen also aided in its being a source of failure is uncertain.

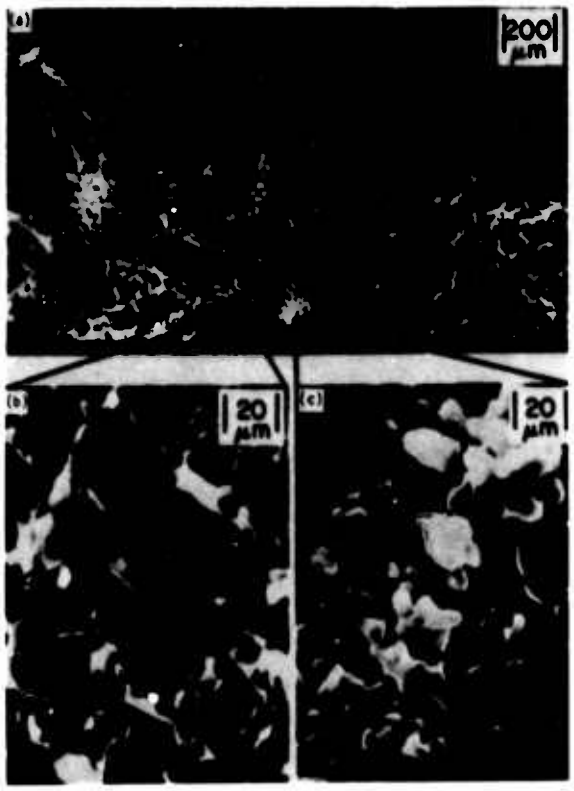


Figure 6. Failure from a porous region in hot pressed Si_3N_4. (a) Lower magnification photo of much of the fracture surface. Most of the material is theoretical density with well bonded, hihgly angular grains as shown in (b) whereas the region within the origin of failure has poorly bonded, still fairly rounded grains as shown in (c). Most of the other white patches in (a) are the result of crack propagation effects and not to poor bonding.

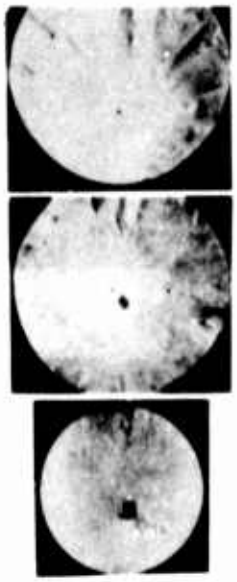


Figure 7. Failure of Al_2O_3 specimens from foreign particles (graphite). The upper two specimens' fracture surfaces are approximately 1/2 inch in diameter while the lower one is approximately 0.2 inches in diameter. These particles most likely occurred due to spallation from the graphite dies used in hot pressing.

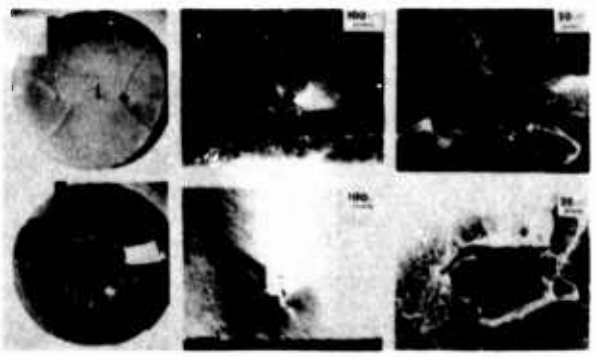
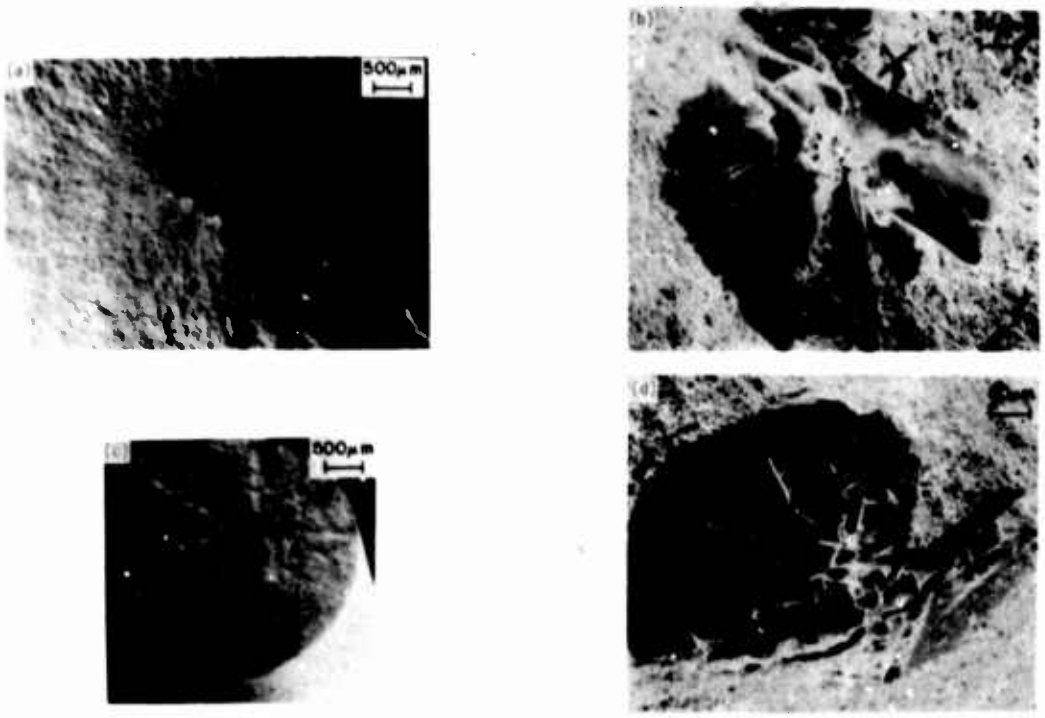


Figure 8. Failure of hot pressed MgF_2 infrared optical material from foreign particles (SiO_2). The upper series of photos from left to right show first a low magnification picture of an approximately 3" diameter test disc after fracturing under biaxial flexure. The photos to the right of this one show the fracture origin at two different magnifications. Note the foreign particle and the crack that had propagated upward from it as well as a crack that had propagated down onto the tensile surface as well as some associated porosity. The lower series of figures is another higher strength disc failing from a smaller particle that was not located as close to the tensile surface.



σ_f = 34.2 ksi Al_2O_3 σ_f = 30.8 ksi

Figure 9. Failure from large grains in hot pressed Al_2O_3. (a) and (b) show a sample failing from an internal cluster of large grains. Note the central porous region seen in (b). (c) and (d) show a sample failing from a large grain cluster at the surface. Note the chipping and cracking of these large grains near the edge.

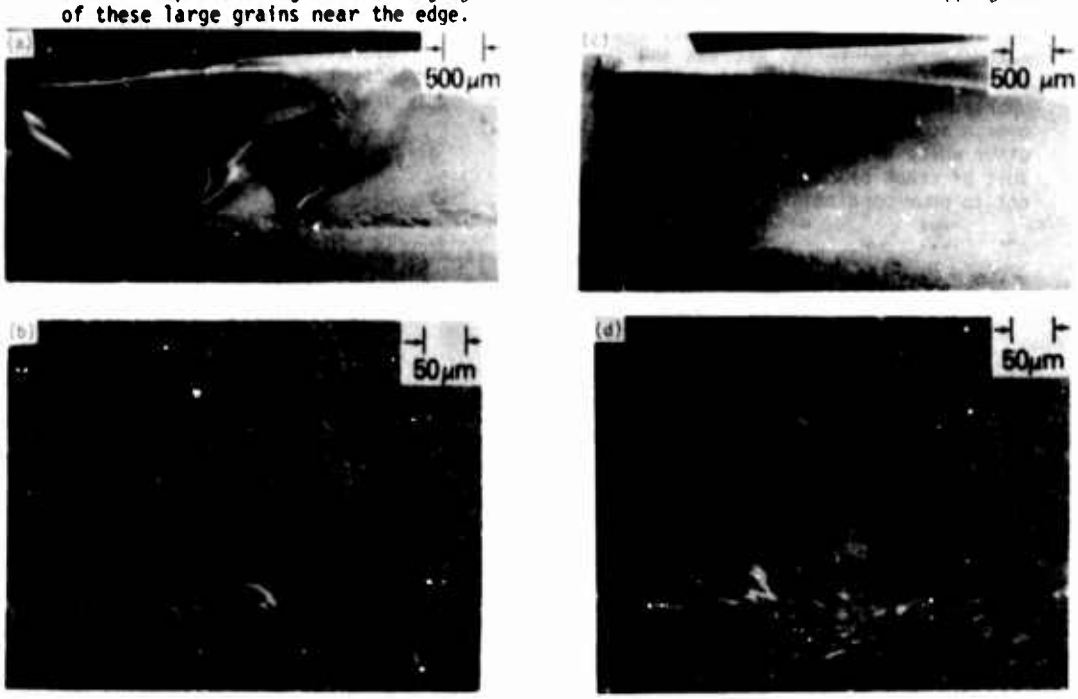


Figure 10. Failure of hot pressed MgF_2 infrared optical material maching flaws illustrating the effect of grinding direction on flaw character. (a) and (b) show the fracture initiating area of a specimen ground parallel with the tensile axis so that the flaws activated are those formed perpendicular to the direction of abrasive particle motion. Note the approximate semi-circular nature of the flaw. (c) and (d) show a specimen of the same material machined at the same time with the machining direction perpendicular to the tensile axis of the specimen. Note the substantially elongated character of the flaw causing failure in (d). Note that the strengths of these two samples, that of (a) and (b) 12,000 psi and of (c) and (d) 6,000 psi, are representative of the strength anisotropy resulting from the dual population of directional grinding flaws.

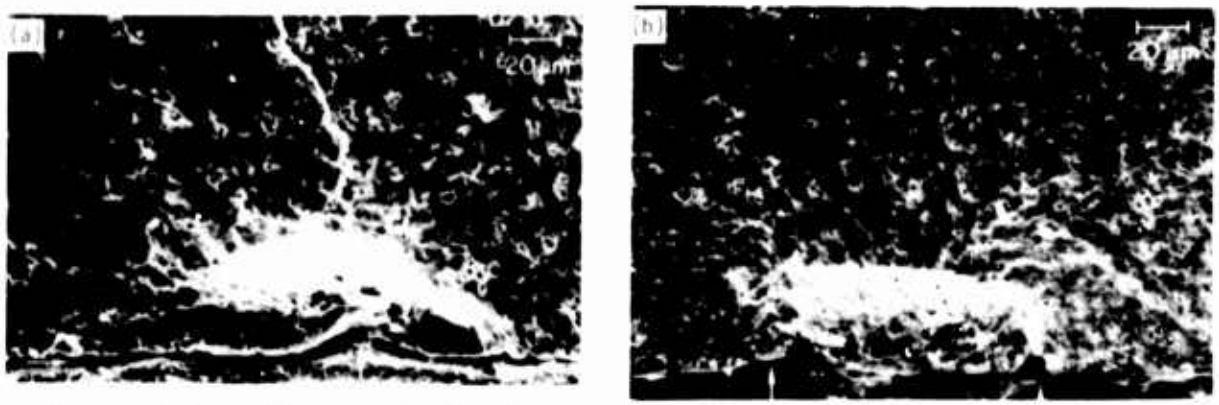


Figure 11. Examples of machining flaw failure origins in reaction sintered Si_3N_4. Note the somewhat irregular and out of plane character to the flaw shown in (a) from grinding parallel with the tensile axis. Note the deeper grinding gouge (vertical arrow) associated with this machining flaw. (b) shows a more elongated flaw from machining parallel with the tensile axis. The longer character of this flaw for machining parallel with the tensile axis is apparently due to its extension between two deeper grinding gouges (vertical arrows). Note in both of the above photos that the horizontal arrows mark the demarkation between the fracture surface and the tensile surface.

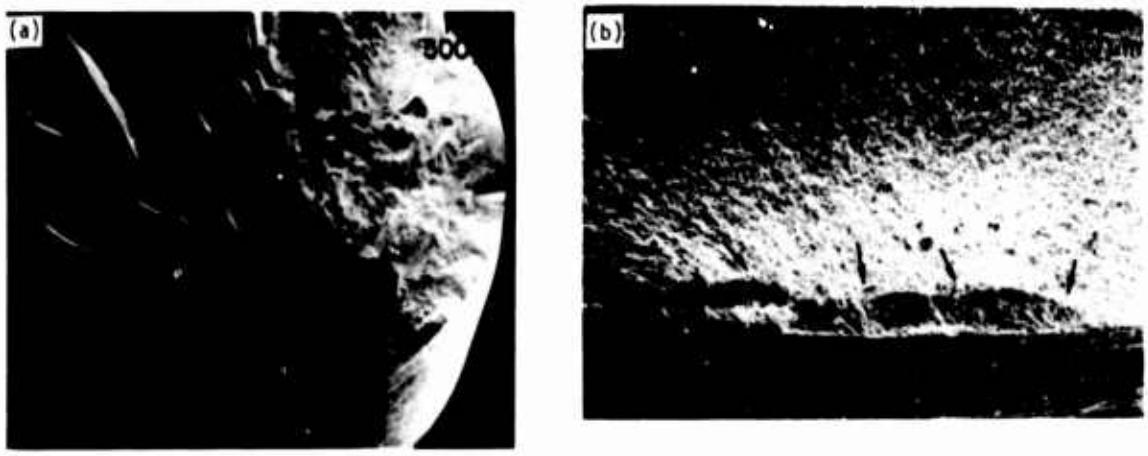


Figure 12. Machining flaw fracture origin in hot press Si_3N_4 (HS130). Note that the circumferential machining of this round tensile specimen is again perpendicular to the tensile axis and even on a shaped specimen results in an elongated flaw shown in (b).

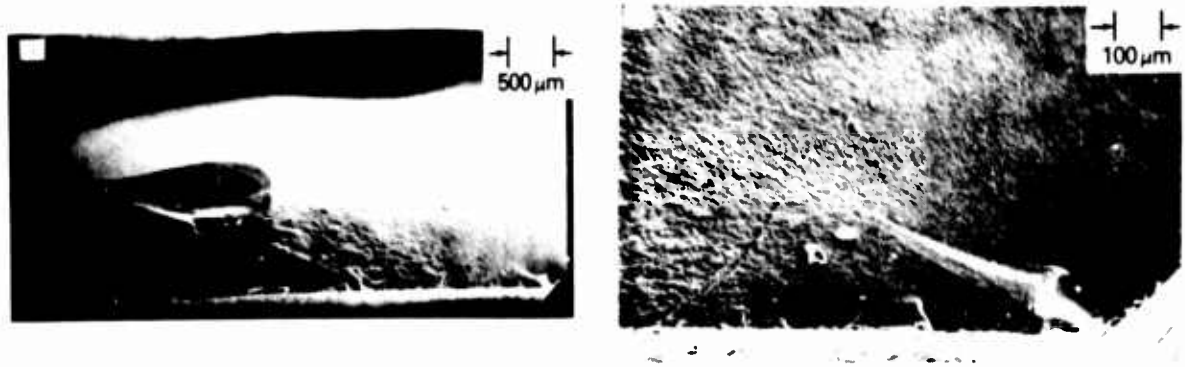


Figure 13. Failure of hot pressed MgF_2 infrared optical material from a machining flaw located at the corner. The approximate semi-circular flaw is located at the intersection of the beveled edge and the tensile surface in the lower right-hand corner of both (a) and (b). The elongated feature extending towards the upper left corner from this flaw is due to the non-planar character of the flaw and its subsequent effect of the fracture first occurring on two planes which subsequently join together.

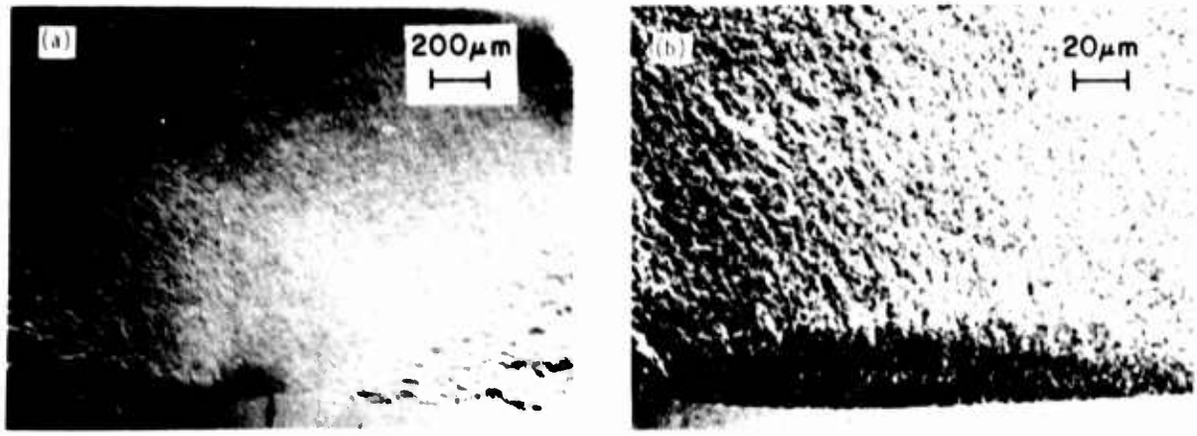


Figure 14. A fairly characteristic flaw from polishing of hot pressed MgF_2 infrared optical material. (a) Lower magnification showing more of the fracture surface with the polishing flaw located between the two arrows. (b) Higher magnification of the polishing flaw. Note the characteristically relatively smooth and continuous nature to the flaw as opposed to the often irregular, somewhat interrupted nature of elongated grinding flaws.

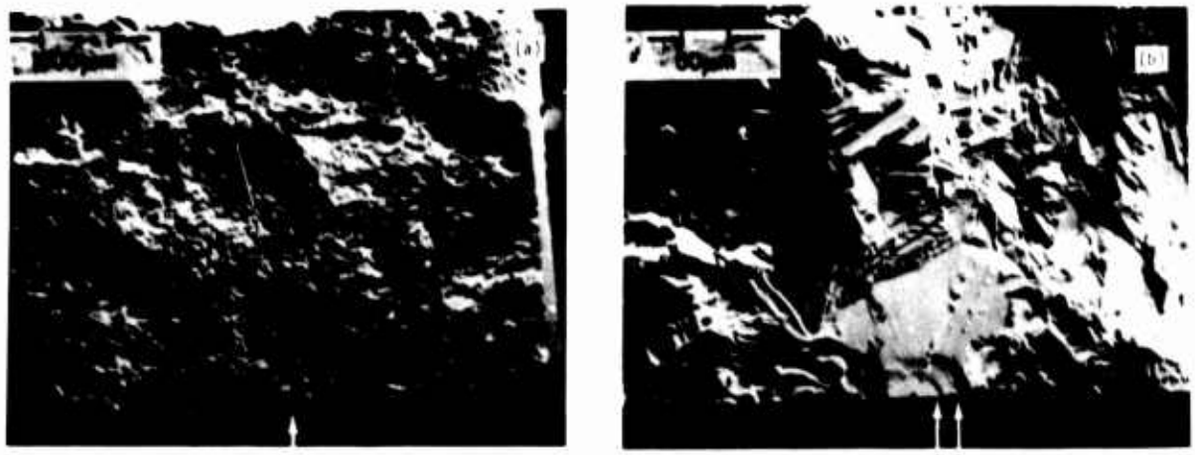


Figure 15. Polishing flaw in larger grain CVD ZnSe laser window material. (a) shows an overview of much of the fracture surface with the white arrow indicating the point of fracture initiation and the other arrows the direction of crack propagation. (b) shows the immediate area of fracture initiation where one can see approximately semi-circular flaw that apparently developed in at least two stages. Both stages are bounded on the left by the grain boundary, while the right-hand edges (white arrows) do not reach the other side of the grain until the flaw is fully developed.

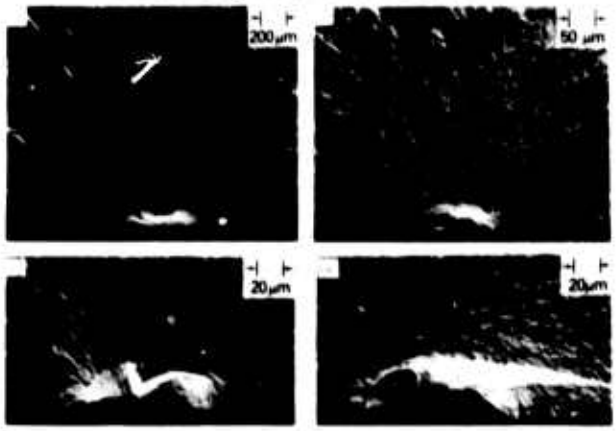


Figure 16. Fracture origins in crystallized glass rods resulting from impact of the rods prior to testing. These four photos show four different fracture origins illustrating the varying character of flaws that can occur due to impact damage. These impacts occurred due to the tumbling of the rods against one another with abrasive grit prior to testing. Note the flaws are frequently at substantially varying angular orientations relative to the specimen surface and the tensile axis.

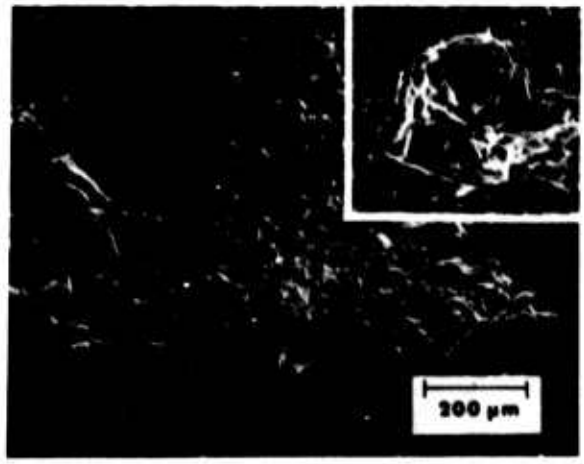


Figure 17. Failure initiation in hot pressed Si_3N_4 (NC132) from a pit as a result of oxidation. This pit is marked by an arrow and also shown in higher magnification in the insert. At this stage oxidation has removed most or all of the machining flaws in the original surface and has generated this new population of flaws, apparently due to the presence of impurities, and possibly their interaction with the hot pressing additives.

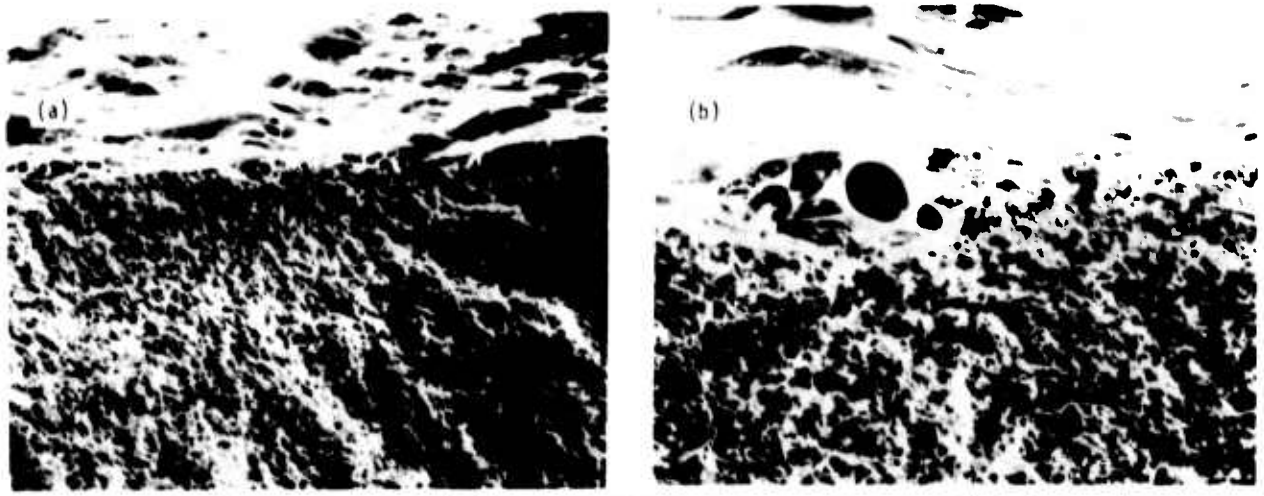


Figure 18. Fracture initiation in experimental hot pressed Si_3N_4 (+ 2 W/O ZrO_2 used as a hot pressing aid). The fracture initiating region is shown at lower magnification in the upper photo and higher magnification in the lower photo. It is relatively common to observe one or more pores in the oxide layer in the vicinity of fracture initiation as seen in this photo of a specimen which has been oxidized for 100 hours at 1250°C. Again, the oxide layer has consumed more than the thickness of the original layer containing machining flaws.

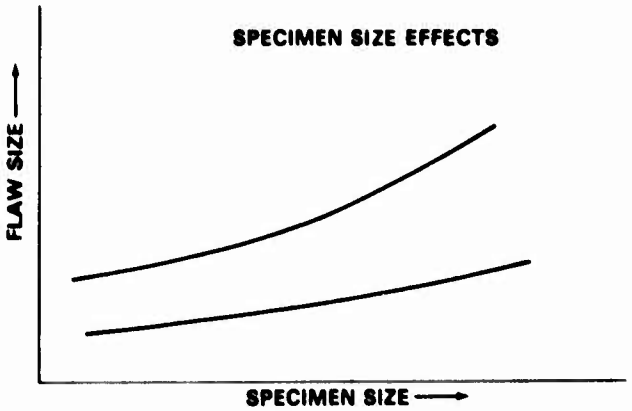


Figure 19. Schematic illustration of the effects of specimen size on flaw size. Because most, if not all, sources of flaws are associated with probablistic or statistically controlled phenomenon, flaw sizes generally increase with specimen sizes. The degree of this increase depends upon a variety of parameters including both the character of the material as well as the nature of theprocessing. Shape effects can also be important in the different variation of flaw size with specimen size which are in turn related to the variation of strength with specimen size and shape.

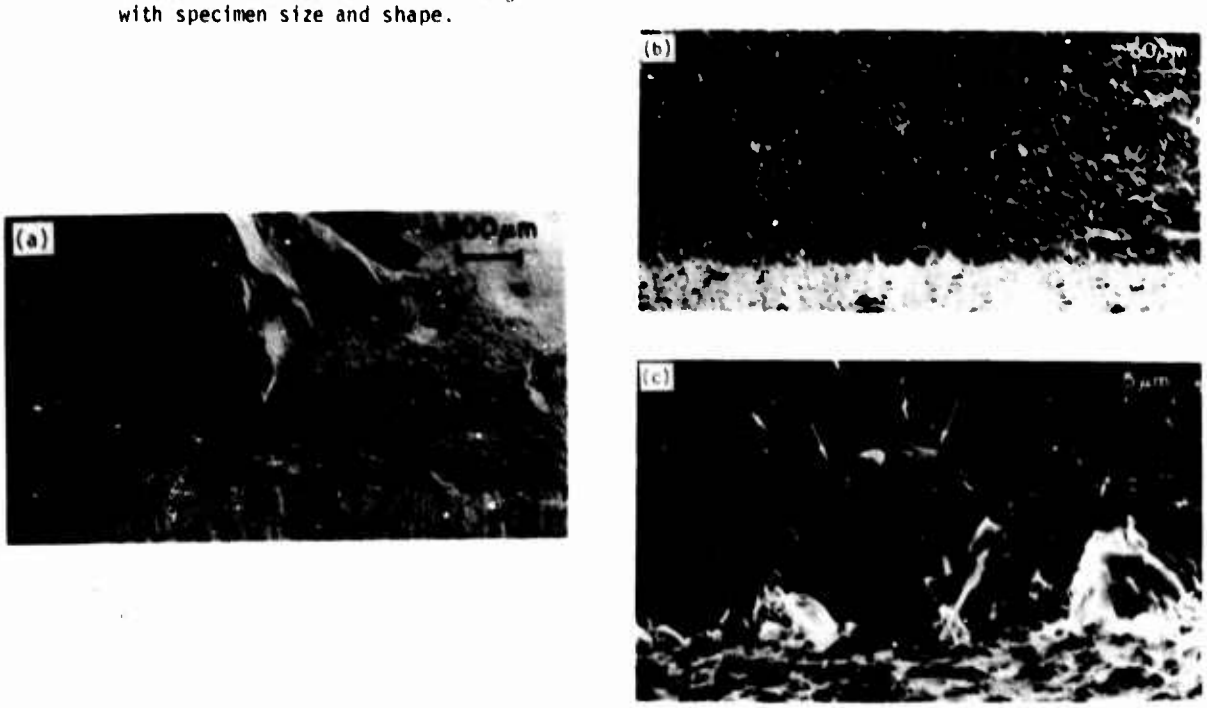


Figure 20. Effect of specimen size on machining. These three figures show progressively higher magnifications of a machining flaw (arrows) resulting from machining parallel with the specimen and tensile axis of a small flexure bar having approximate cross-sectional dimensions of .1" by .2". The failure stress of this hot press B_4C specimen was approximately 61,000 psi. Contrast this with the larger bar machined in the same fashion from the same material in Fig. 21.

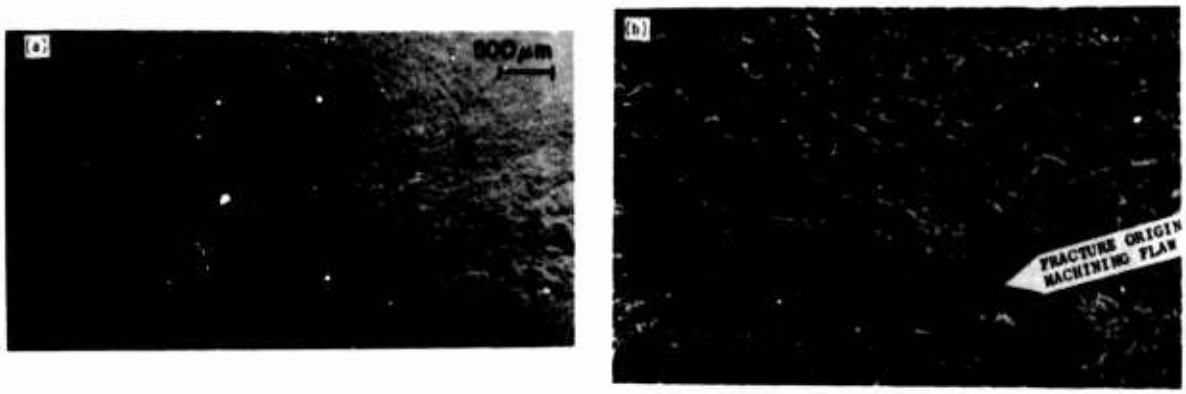


Figure 21. Failure of a larger B_4C machined test bar. The material and machining are essentially the same as that in Fig. 20, however the specimen was substantially larger having cross-sectional dimensions of approximately .25" x .5" with a proportionate increase in the flexure span length. It failed from a substantially larger machining flaw (arrows in (b)) and at a substantially lower stress, approximately 29,000 psi.

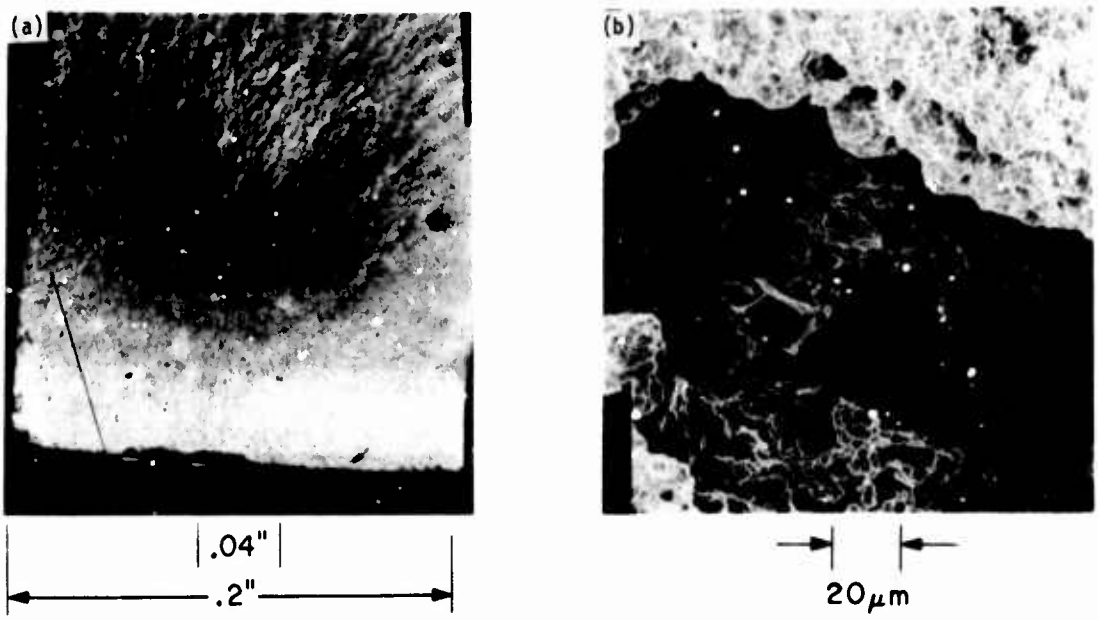


Figure 22. Failure origin in an actual production lead zirconate titanate sonar ring. (a) Low magnification showing much of the fracture origin and a large crack-like void causing failure. (b) Higher magnification of a portion of this void. This ring, which was about 3 inches in diameter and cross-sectional dimensions of ~ 0.2" x 0.5" failed dynamically in hoop expansion at ~ 2,500 psi. Note the elongated character of this pore; probably reflects laminar effects from cold pressing.

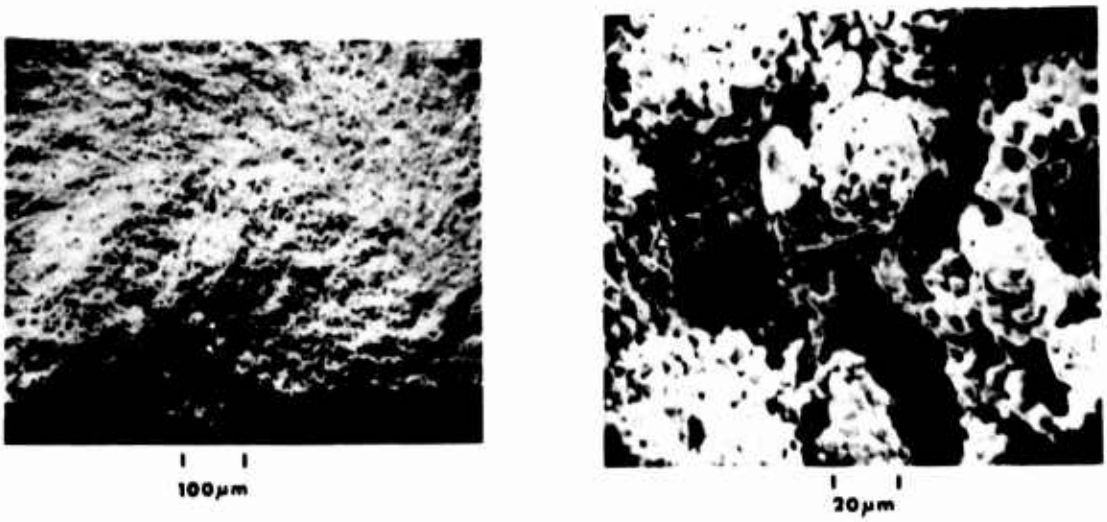


Figure 23. Failure of a commercial lead zirconate titanate sonar transducer ring failing from a highly porous region. (a) Lower magnification of complete porous region plus some surrounding fracture. (b) Magnification of part of the porous region. This ring failed under dynamic loading at approximately 3,100 psi.

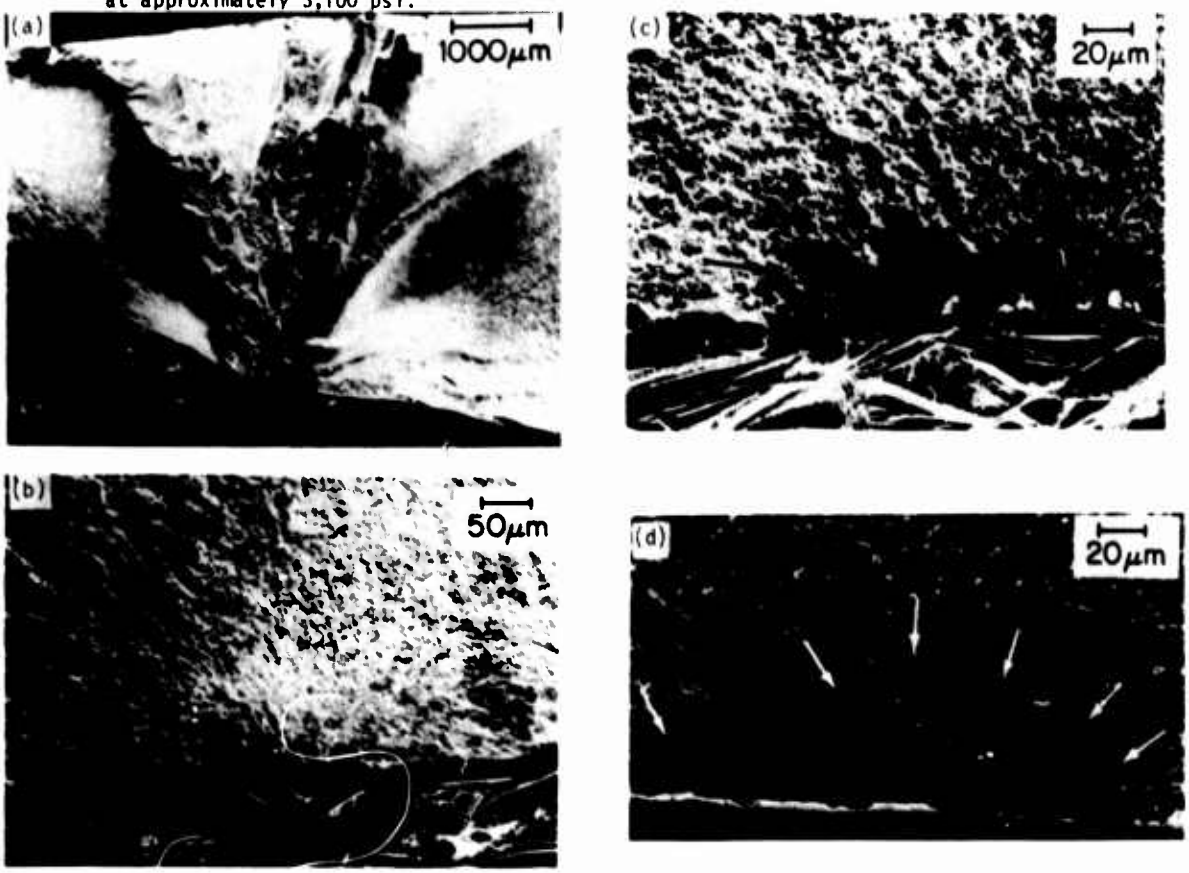


Figure 24. Failure of a hot pressed Si_3N_4 (NC132) prototype turbine blade. This blade failed in the attachment region in a spin test at an estimated stress of approximately 70,000 psi. The fracture origin shown at various magnifications in (a) through (d) was determined to be a machining flaw which is seen most clearly in the view shown in (d). The size and character of this machining flaw is quite similar to that observed in test samples.

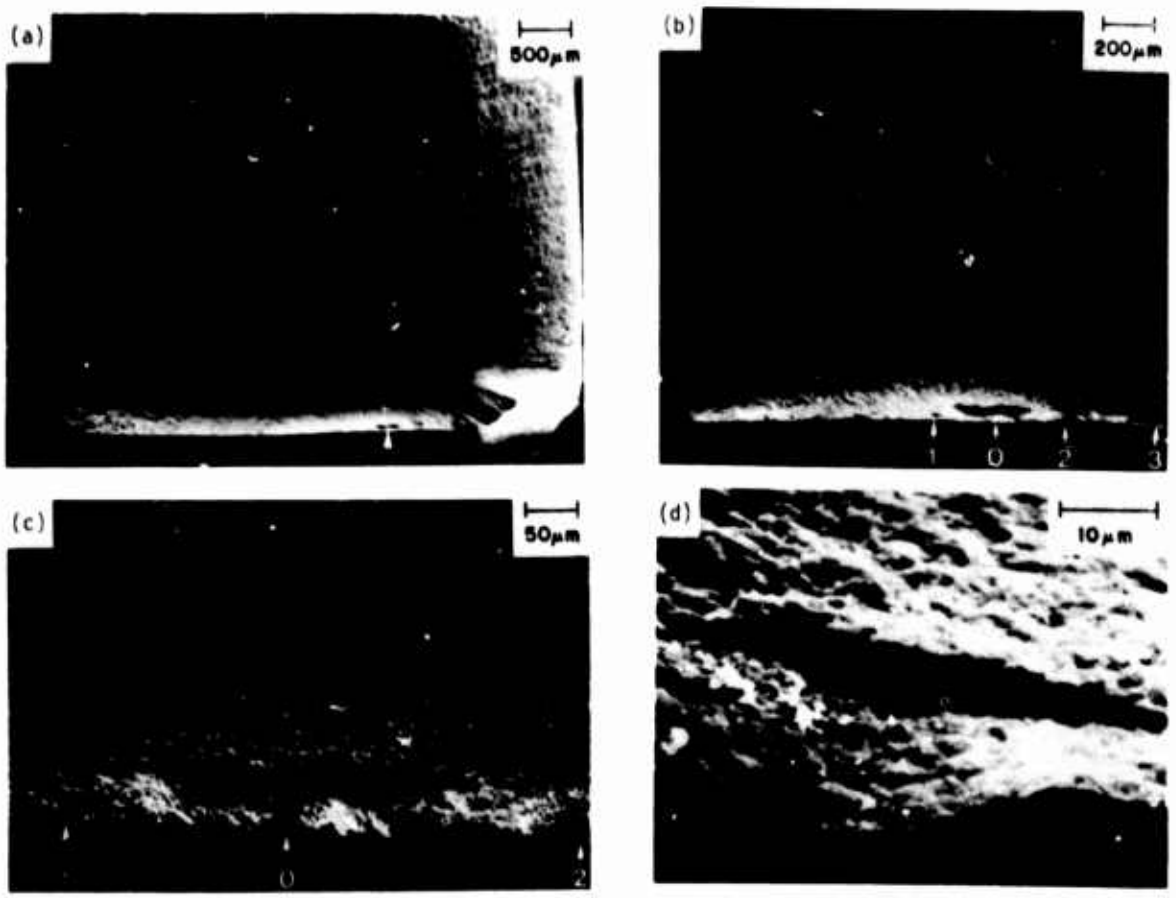


Figure 25. Fracture origin in a hot pressed Si_3N_4 (NC132) prototype turbine blade. (a) through (c) show increasing magnifications of the fracture origin in a blade that failed after a number of spin testing cycles. The failure origin was a laminar defect (from the original hot pressing) indicated by an arrow at (a) and a 0 in (b) and (c). (d) shows a higher magnification of another part of this lamination (marked 1 in photo (b)) not immediately associated with failure.

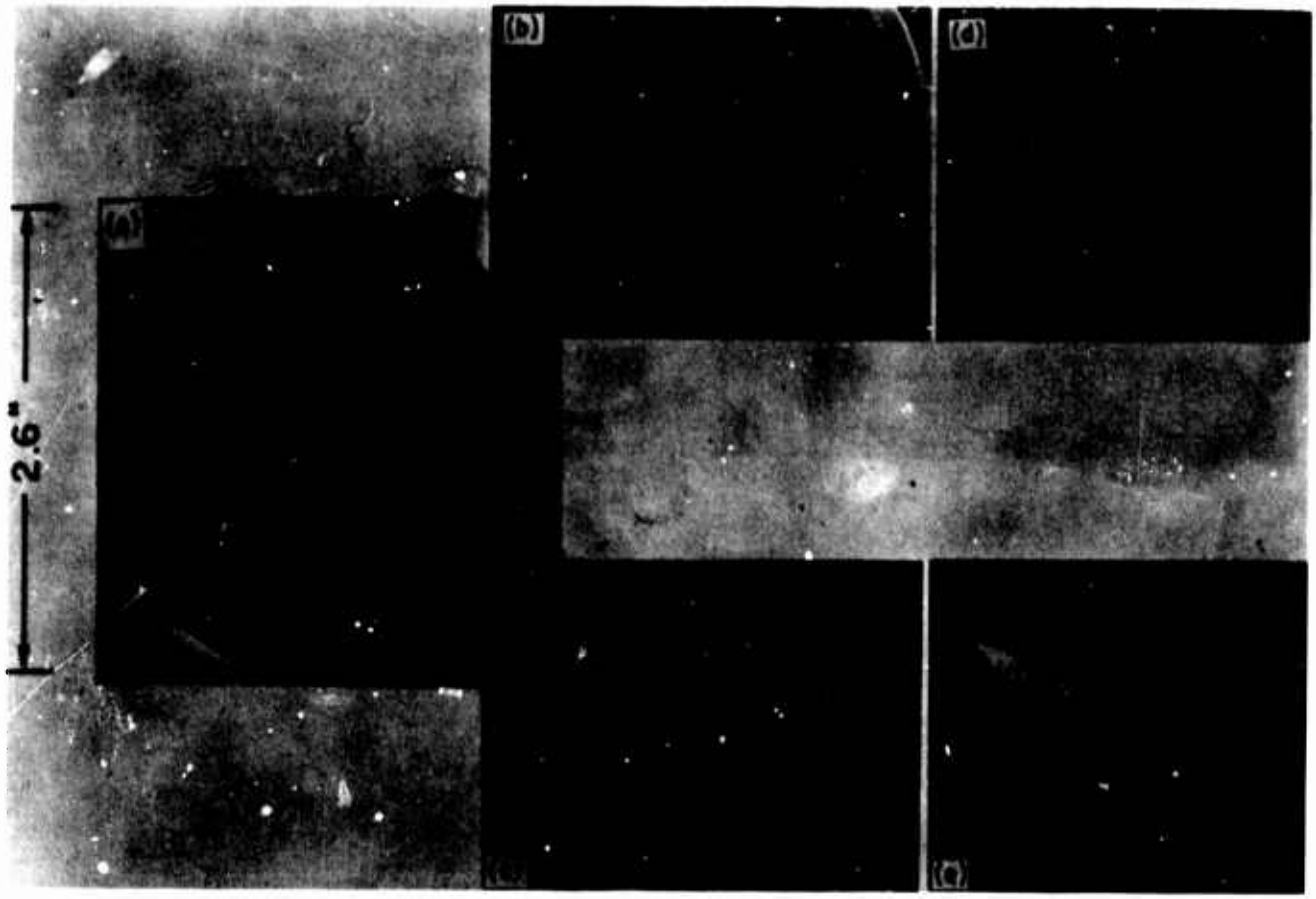


Figure 26. Fracture initiation in actual MgF_2 Irdome. (a) is an overall photo of the dome that failed from thermal stress. Failure initiated between the two pieces marked 1 and 2 in (a). (b), (c), (d), and (e) are higher magnifications on both fracture halves having the actual fracture origin which is believed to be a polishing flaw on the inside surface of the dome. The failure stress predicted from both the fracture markings and the size of the flaw of 9,000 to 10,000 psi agreed well with the analytical predictions from a thermal stress model and the test conditions.

PANEL DISCUSSION

QUANTITATIVE FAILURE PREDICTION: ARE ALL THE WICKETS COVERED?

A. G. Evans, Moderator
Science Center, Rockwell International
Thousand Oaks, California 91360

Panel Members: Nancy Mann from Rockwell International Science Center (an expert in statistics, especially extreme value statistics), Ed Lenoe from Army Mechanics and Materials Research Center (with expertise in reliability and ceramic turbine development), Tom Derkacs of TRW (he's been using ultrasonics to detect defects in ceramics), Roy Rice from the Naval Research Lab (an expert on fracture initiating defects in ceramics), Norm Tallan from the Air Force Materials Laboratory (with a major interest in ceramics for structural applications), and John Schuldies from Aresearch (the NDE expert at Airesearch with a lot of experience using current NDE techniques).

A. G. Evans, Moderator (Rockwell International Science Center): To initiate the proceedings, I shall pose the questions that this evening's discussion is intended to address.

As indicated at the outset of the session today, we want to find out: (a) where are we with the use of NDE techniques to predict failure in ceramics, (b) what do we have to do to quantify those techniques, and (c) what approaches are on the horizon for improving our capability for failure prediction. More specifically, is the failure prediction sequence I described in my talk a complete one, or are there some features in the failure prediction process that we are missing? What are the optimum NDE techniques, recognizing they can be material or component specific? I'd like those who had posters, and who have special techniques, to feel free to come up and discuss their techniques, in order to address how well the techniques can really answer the questions--how big is the defect, what type of defect is it, and so on. Finally, we must recognize that when you get involved with programs of this character they don't have infinite numbers of dollars, therefore a limited number of tests have to be performed and hence, what sort of statistical planning should we use in designing our tests to maximize the pertinent information. Those, then, are the questions we will be asking. Before we get into specifics, Norm Tallan has volunteered to give a very short description of the program the Air Force is about to start in ceramic turbines and put a perspective on some of the questions we just raised.

Norm Tallan, Panelist (AFML): The Air Force is extremely interested in ceramic components for turbine engines, particularly for small limited life applications and we've been looking very carefully at the work that ARPA has been doing in the past both in the Ford/Westinghouse program and more recently in the Garrett program, and we are about to launch our own manufacturing methods program which will pick up on the technology that has evolved from those programs and try to address, particularly, the questions of producibility, cost, and reliability. I emphasize, particularly for this meeting, the question of reliability because the current Garrett program, for example, has demonstrated that as far as designing with brittle ceramic materials concerned, we can accurately predict the temperatures and stresses in components, and rig tests have borne out that those designs are reasonable. We have ample evidence that the materials that we need both for the vanes and blades are probably good enough, in fact I'd say are almost certainly good enough for at least the limited life applications we have in mind for many military systems (where the lifetimes would probably be under 100 hours). But even though we are talking about these relatively short life applications where perhaps we don't have to worry about very slow stable crack growth rates, we do want to know that first of all the components will not fail under initial loading, and also that they will not fail by any unexpected failure mechanisms that we haven't considered. In terms of reliability in our program, I think it very important that we consider all the aspects--the system requirements, the materials that we would use, the kinds of components we have in mind, and what the likely costs are going to be. As an example of some of these factors, consider the inlet guide vanes that we would use in the first stage turbine. The material that's most likely to be used is reaction bonded silicon nitride which, as we know, is a porous material that may dictate some of the techniques we would use. But, furthermore, one of the reasons we are specifically interested in reaction bonded silicon nitride is that we can make it to shape, and if we are going to test that by NDE, we are going to have to test it on a complex shaped surface. On the other hand, the vane itself is probably one of the inexpensive components to make and even if we are talking about a real engine application two or three years from now, we could probably predict that we could buy vanes for, say, $30 apiece and if we have a 30-vane starter, we're dealing with about $1,000 component and we can afford in a case like that to throw many of those away. If we do the NDE and there is any uncertainty at all about the quality, we could probably throw them away. On the other hand, if the material does not have slow crack growth (as it appears right now), then perhaps we can proof test those components: one of the normal reasons for hesitancy about proof testing being that we may damage the part. Also, since the stresses will largely be thermal in origin we can probably proof test them easily by a rig test. So, I think there are really

some cost and potential damage tradeoff's to be made in reaction bonded silicon nitride. These would be entirely different from the blade material, which is likely to be hot-pressed. Here we would probably start with a hot-pressed ingot, which could easily have smooth surfaces that could be inspectable; in fact, the ingot form is still relatively inexpensive compared to the machined component. Each blade at the moment is probably going to cost somewhere on the order of $500-$1,000, so if we have a 30-blade rotor, we are considering $15,000-$30,000 for the components. It's really critical, therefore, that we have some good assurance technique, particularly before we put that rotor together. And maybe its feasible to really do the nondestructive inspection on the ingot before we do the machining, to look for the volume flaws. Then, after we've got the complex surface, which is hard to inspect, inspect only for machining damage. In any event, I think whatever we do in our program we are going to be most concerned that we not only have consideration of the materials that we are going to use, and as many good techniques that we can apply to these, but that we in fact have some reasonable program for actually making a decision - a go/no-go decision - on these components before we put them in an engine. And I think that the position that Tony took this morning is one that we would be very interested in; essentially, a probabilistic approach where perhaps you could use the NDE techniques available in the near term to at least reject those components which we know are bad enough that they will not make the application and not bother to proof test those. Perhaps we can, in the NDE initial screening, decide that there are some components which are so likely to be good that we wouldn't subject them to the potential damage of the proof test; and only proof test those in the uncertain region. In any event, I would say that the program that we are undertaking in manufacturing ought to be an ideal proving ground for many of the NDE techniques that would be developed under the ARPA program. I would certainly hope that we could apply those and get some real experience in the manufacturing program to see how well they work.

A.G. Evans: I think that gives a nice perspective that we should keep in mind when discussing techniques and their use in actual components. Does anyone have any specific comments based on Norm's brief discussion? In that event, what we'll do now is throw open the question that I asked firstly. Is the failure prediction sequence that I presented a complete one? The sequence was: (a) we firstly infer something about the defect size (b) we then break samples containing defects to measure the fracture strength under fairly well defined boundary conditions (like a constant stress rate experiment), then (c) combine those two behaviors, in a probabilistic fashion, to obtain a relationship which is a fracture probability vs inspection size and a rejection probability vs inspection size and then use those graphs for a final comparison of NDE techniques. Also, add in (when necessary) that the cracks will grow slowly in the environment of the turbine (or whatever other component we are interested in) to the critical size.

Roy Rice, Panelist (Naval Research Lab): I don't know whether this would be a different approach but one thing that I haven't heard discussed, at least specifically, is an addition to your indirect techniques. For example, if you have a teacup and you want to know whether or not its in good shape, simply hold it on your finger or a piece of wood and ring it. If it doesn't have a high enough pitch, you know it's got a defect in it - you don't know the size and you don't know where. I think this is indicative of class of inspection that may be feasible. For example, on a complex shaped part, if you ultrasonically excite it, is it possible by its modes of vibration to tell whether or not that part is outside the normal spectrum. It's an indirect technique but I don't think it was specifically mentioned and I'm wondering what opportunities there are for this.

Ed Lenoe, Panelist (Army Mechanics and Materials Research Center): Well, first of all, I return to the question that was posed; is the formalism adequate, are there any things that are missing from the life prediction? The formalism that has been described is certainly rational but it's fair to say there are alternate approaches. At least in the turbine area, critical demonstration tests are underway precisely to explore the adequacy of these various analytical treatments. There is one major deficiency and I hate to try to get specific because the question is so general and I think you have to deal with the component and the kind of material. But let's consider reaction sintered materials. One major deficiency which hasn't really been thoroughly studied are materials instability, such as oxidation, phase changes, dimensional variations that are introduced by environmental exposure. We have some techniques to understand that and screen that out, but there are certain temperature regimes where this to me will be the critical limitation on a particular component in a turbine environment. Some limited studies suggest that kind of a phenomena may be stress/diffusion controlled. That hasn't really been looked into at all except on a limited basis. If that kind of thing happens, that means the fracture toughness may change in certain ceramic materials and perhaps the creep properties, and so forth. Actually, before I saw your questions, I had written down some feelings with regard to the entire meeting that relate to this session. While during the meeting a number of speakers as well as audience participants have stated that we must know what we are looking for and I would like to explore that notion a little bit from several viewpoints - first from the structures viewpoint and then from the fabrication or processing viewpoint. It's well to recall that the definition of a critical flaw size in any application must be determined by stress analysis techniques. This critical flaw is necessarily related to the structural geometry and the service stresses. Obviously the NDE techniques applied must be aimed at examination of the designated critical areas and volumes of the structure. So far, in much of the work that has been presented here, at least in the ceramics area, nondestructive evaluation has seemed to emphasize simple geometries, and in some cases perhaps irrelevant, defects. Now, in addition to what I said about the structural geometry and stress viewpoints, definition of the flaw or defect is a complicated iterative procedure. It cannot be viewed strictly as a microstructural thing. It cannot be viewed as an impurity. That impurity and the definition of that defect must be related to service requirements in the component that you are dealing with. Actually, the NDE techniques have

to follow in parallel with the fabrication or processing. Often in producing a ceramic part, for instance, we introduce cracks and flaws and voids and so forth, that are controlled more or less predominantly by the process itself. In a number of instances, such flaws and folds will occur in virtually non-stressed areas. Therefore, they are not critical defects even though they look horrendous. Thus, from the process viewpoint, NDE techniques suitable for various sub-steps of the fabrication must also be available. Then, we can also mention just in passing residual stresses.

As far as application of the advanced NDE techniques, I think its interesting to consider the results of a recent study conducted by the Society of Nondestructive Testing. What they were after was to review the qualifications of currently employed technicians in the representative industries. Generally they were appalled by the results. These technicians were found to be relatively poorly trained with only modest understanding of what the kind of measurements were that they were dealing with. Now, if the techniques for sophisticated data interpretation were to actually ever be used by the average technician, we have to develop absolutely fool-proof software, and equipment and transducers that are totally reliable. I don't mean that to downgrade the technicians, they just happen to be ill-trained and doing a job for low wages. So I hope that the talented and highly trained engineers working at the forefront of this quantitative utilization of NDE bears this in mind. In addition, some effort should be made to isolate technologically interesting machine and structural components and subsequently develop specialized transducers and analytical techniques which account for the hardware complexities.

I was talking basically about rotor fabrication. The rotor can be fabricated in a variety of ways. Under the ARPA/Ford program, we started out using a slip casting and injection molding and obviously, as you go through this process, you want to have various controls. Potential defect introduction in the process of making a so-called multi-density rotor - this is where the blade ring and the blades are combined in a composite ceramic wheel occurs: in the process of removing the blade rings from the molds, you can introduce cracks at the base of the blades: in the process of drying out, you can introduce high oxygen content which can have disastrous effects on long-term stability.

A.G. Evans: You are quite right, all of those are real problems that have to be borne in mind, especially the very specific character of the techniques and the knowledge that we don't need to inspect the whole part. I'm glad you emphasized those. Now I think we're at the point (since we have the NDE Community with us) of trying to acquire the information we need to select techniques that will be most pertinent to ceramics.

I think we're at the stage now where we'd like those people who feel they have something to offer to the ceramics community in terms of quantitative NDE techniques to try and address the questions we raised earlier; that is, how well can you characterize the size of small defects, and can you possibly tell something about their character?

Bob Gilmore, General Electric: I want to address this question to Ms. Mann. We have talked for three days now about characterizing an indication that we have found and I think that one of the things that has been skillfully skirted in every single discussion is "let's talk about the one's that we miss every now and then." We talk about cutting humans out of the loop, but the fact remains that if you perform one test that's a routine scan you may miss a certain percentage of indications that could or couldn't be critical. If you perform a second test (so that your scan lines don't follow the same groove) you'll get a certain number more. And, I think the thing that we haven't discussed in ceramics or anything else is detection probability, and by this I mean if we have a population field of 2,000 defects which could or could not be critical to maybe 20,000 parts, how many parts didn't we take out by the system.

Nancy Mann, Panelist (Rockwell International Science Center): First, you mentioned another important point; that is, how do you characterize what it is that's the important factor that will cause failure? Here we've talked about size, very conveniently, as if everything else would be held constant; but actually, you're going to get a signal and from that signal you're going to enquire whether there is something about that signal that's important (that will tell something about strength). It's much simpler, of course, if the only thing that you're varying is size. But, if it's the real world, and you're simply looking at a material that has some kind of a defect in it, and you don't know what kind of a defect it is, then there are many things about it that vary from sample to sample. So, that's the first question that I see as an important one. Then, given that, suppose you do decide to manufacture samples and nothing varies. Then we have the kind of problem you spoke about, where there is a probability distribution and there is the probability of not detecting the defect at all. I don't know how to address that problem yet.

John Schuldies, Panelist (Airesearch): I certainly agree with the comments that were made, but let me say something that I think we're all missing. There needs to be more of a working relationship between the fabrication of the ceramic and the NDE. What I mean by that is both types need to be disciplined in the other's area of expertise. Firstly, if you have a working knowledge of what goes on when a part is either injection molded or slip cast or machined, you can second-guess where the major flaws are going to lie. If you are made aware of that problem, you concentrate on it and eliminate it. For example, in the green bodies which Ed Lenoe referred to previously, not enough work has been done in that area.

Roy Rice: I'd like to follow up on some comments that Ed made. He briefly alluded to changes in the population of defects. Even in the short time that Norm was talking about (100 hour lifetime), we have

to consider the possibility of a dynamic population of defects in ceramic materials. Also, to put this in perspective, I'd like to emphasize the importance of surface flaws. We have found, even in direct tension testing of silicon nitride, the predominant source of failure to be machining flaws. Correspondingly, we are now finding in the improved reaction sintered silicon nitrides something like 75% of our failures are from machining flaws rather than processing defects. It also turns out that the stresses in a turbine vane or blade are a maximum on the surface. Now, these surface flaws have had very limited detectability. I am very encouraged by the one talk given here; in fact, I believe it's the first time that a surface crack has been detected in a ceramic. However, there is a significant population of surface cracks in a ceramic and we have to sort out the worst one, which may be only 5 microns deeper than the remaining 95% of them; and those flaws are typically in a range of 20 to 50 microns in depth. Then, depending upon the character of the material, within a matter of a few ten's of hours to a few hundreds of hours, the surface that contains those defects has been totally oxidized and essentially disappeared. Now we have a modified population of defects, introduced by the oxidation itself. In addition, as time progresses, the nature of the processing defects will have changed. Some may have become more benign but others may have become significantly more severe. So we have to keep in mind that there is a dynamic situation. Also, one other point that I'd like to make is that many of the defects that we are dealing with are not random. A significant percentage, in fact in many cases, a majority of the defects, both processing and machine defects, have a significant orientation depending upon the nature of the processing we are dealing with. That may be a help and in some cases it may be a problem. Also, many of the defects we are looking for, we're looking for in areas that are most difficult to inspect. I am encouraged by the progress, but I think we've got to keep in perspective some of these additional challenges that we have to meet.

H. Burte: I feel a little bit like Alice in Wonderland. As encouraged as I am by the progress, as enthusiastic as I am with the potential, I have a feeling that we haven't fully addressed the key issue. The tough problem is not how to find a smaller crack or a smaller flaw in the laboratory. That's tough enough but that's not the toughest question. The real problem is that there is a probability of finding a flaw (or some parameter relating to the severity of the flaw) and the probability curve has a sigmoidal shape, where the plateau may or may not be up around 100%. The problem is not to drive this curve down to smaller sizes, but to change the shape of the curve towards a step function. In metals, we're having problems under production conditions finding flaws which are one or two orders of magnitude larger than the 4 mil flaws you've been talking about. Now I'll be the first to agree that the job should be easier in ceramics than in metals, but I think you should go down the litany of the things that can go wrong and then check off why it won't go wrong in ceramics; or if it will go wrong, what you have to do to prevent it.

Ed Van Reuth: I guess I am emminently qualified, because I have lost more nights' sleep over ceramics, I guarantee you, than anybody in this room. And I'm coming to a conclusion which just frightens me. Let me paint a little bit of background to this. When I first got frightened about ceramics, a pacifier was quickly thrust in my mouth in the form of finite element analysis and "hey, don't worry about it, we know everything that's going on in every one of these little cubes in this material!" But there was a gnawing question in the back of my head going, "How do they know that? How do they know that, how are they going to prove it?" Well, it's quite simple, we'll do a proof test. Now with ceramics which are non-forgiving materials, of course, you should know the stress in every one of these finite elements to a certain probability and a certain degree of confidence. Now suppose we don't. We go into something that we think is a proof test (normally in a rig which is supposed to simulate engine conditions) and we find out something went wrong with a part - I have lost millions of dollars in rig tests with the final answer being told to me, well, the proof test wasn't realistic. That's the problem. A proof test must be very well quantified in ceramics because they are non-forgiving materials and we can't simply have false hopes based on numbers which are given to us by people who are performing finite element analyses. The numbers may be right, but then we must be careful that the proof test is right.

Tom Derkacs: I have accumulated several comments here which I hope I can relate back to the original question. First of all, I agree that all NDE techniques have a probability curve, and there is no reason to believe that any technique that is developed for ceramics is going to be any different. Secondly, as far as Roy Rice's comments on surface cracks, we have evidence to indicate we can detect surface cracks down to 40 microns. As far as the comment on reliability, the question that kind of bothers me a little bit is that nobody has said anything about how well we have to characterize the defect. There's an uncertainty in predicting failure and there is also an uncertainty in characterizing the defect and we ought to have some idea of how good we have to be able to do those things. The other comment I want to make is with respect to reliability, it's very difficult to determine what the reliability of a technique is when it's the only technique that's available to detect the defect. In comparing our inspection results, for instance, with the Air Research microfocus x-rays, we get excellent agreement on the defects that we can both see; but the question is, what about the ones that one of us or both of us can't see. How do you find those things out. I'd like to suggest that one way might be to work out an arrangement where before any specimen is tested, it's inspected by the best techniques that are available, so that we can build up a body of data on the reliability of the inspection techniques. I think that's the only way to do it and it's going to take a long time and a lot of expense.

Roy Rice: Obviously I'm biased. I think that the only way to test the technique is break the samples afterwards and see if they broke from what you thought you saw in the first place.

Tom Derkacs: The problem with that technique, and that's what we tried to do, is that it's very expensive to make a ceramic specimen. If you make 100 ceramic specimens, how many are going to have detectable defects in the high stress region? The probability is probably fairly low unless you deliberately seed them, which is not in my experience exactly comparable to looking for natural defects. So, the other alternative you take is to take a billet and inspect it and then make the specimens around the defects. Then, of course, you have the problem of how accurately you can do that, but either way is expensive. I agree that that's the way to do it, if you can afford it; but so far, I haven't seen anybody with enough money that wants to pay for that.

Norm Tallan: Another approach to the same question would be (in the initial phase of the manufacturing method program) to take real components, where we know the processing is often different than test bars, and wherever we get an NDE indication, cut out the test specimen and subject that then to a fracture stress - we don't have to look only at the ones that are in the high stress region of a component. Then, see that they fracture at the NDE indication, study the origin of the fracture, see what kind of a flaw it was and relate it back to the NDE indication. Then, try to get some idea of what the signatures really mean in terms of effective severity of inclusions.

Roy Rice: Better yet, we need to build up a history of establishing what flaws actually cause failure of components. The worst thing that could happen is for someone to have a failure of a component then throw the pieces away.

C. Jakus: A few months ago I read a news brief in an electro-optical trade journal in which a person stated that optical surface holography is coming to be a serious NDE tool again, with the development of fast films. But the commentator didn't explain what the technique was and what it is used for. But my question to the panel, or to the audience, is that would anybody know whether such a technique would be applicable to ceramics, considering that the surface defects are very crucial?

Dave Kupperman: We have a small program at Argonne to look at various nondestructive testing techniques for silicon nitride rotors for the vehicle program with Ford. One of the techniques that we are looking at is holographic interferrometry. We make a hologram, and the film is developed in place so that we can see the interference pattern generated. We can see flaws by this technique which cannot be detected by x-rays or a microscope. The hardest flaw to see is one at the root of the blade and right now, although we've only done some preliminary work, we can see blade cracks as small as 250 microns. That's our present state of the art. One other technique that we find very interesting is a technique where we use a dye which absorbs x-rays much more strongly than does the ceramic, and by analysis through neutron radiography, we can again see surface cracks of flaws. They are quite clear.

Roy Rice: Also there was a Navy funded program a few years ago which was, in part, the basis of one of my earlier comments. At TRW a holographic technique was applied to ceramic materials and they could, for example, put a surface scratch in a piece of glass and while they could not detect the specific location, they could detect the general location. They could tell the difference between a scratched and unscratched plate holographically by the difference in deflection under very low stress levels and that, as I said, I think is an example of a class of inspection techniques that don't tell you specifically what the flaw is, but you can indirectly correlate it with being a bad part.

R. Gilmore: I'm like a broken record, as usual, but I guess if I looked at NDT, I'd call it "detection, characterization, and analysis." The detection problem, I think, is going to have to receive just as serious, just as long-term, and just as much money as quantitative interpretation of something that you've found. Although ceramics is relatively new, believe me you are going to encounter every problem that any other material has encountered; they may be a little different, but they're all going to be there, residual stress on down.

Gordon Kino: Somebody mentioned the subject of looking at green ceramics and it seems like a very good idea to try and get at these materials at as early stage as possible in the production process. But I was just wondering if anybody has done any measurements on green ceramics, acoustically or otherwise, so some of the parameters are known. It would be very useful to know whether its worth even to try.

John Schuldies: While I was at Ford, conventional radiography was employed. Ultrasonics was employed on a limited basis. Velocity measurements were made on green silicon nitride, injection molded silicon test coupons. As I remember it, the velocity was on the order of maybe something like graphite and it was extremely attenuative; very difficult to get a signal into and out of. So, when you start talking about those kinds of problems and that kind of application, then we compound the material aspects all that much more, and it makes the inspection much more rigorous. But I still feel that with a good knowledge of how you form that part you can second-guess the orientation and the type of defect.

Roy Rice: A few follow-up comments on that. First of all, I think there's very serious danger in that type of inspection doing as much or more damage, if you're not careful in the handling of the green parts. The other thing, of course, is that I recall that a number of the processing techniques that we are using or that we may potentially use are not really amenable to that. For example, when we hot-press materials, we start with powder, put it in a dye and pull it out a solid piece. There is very limited inspection that I think you could do on the powder fill in the dye. Also, I think we're

going to probably see more usage of chemical vapor deposition and here we put in gas and we take out a solid part. With respect to the hot-press material, there are things going on right now that are addressing that problem. For instance, typically a nine-inch billet is made from which is fabricated a number of individual parts. The first thing you can do is to radiograph it. Then, if you can't see the kinds of defects that you are interested in, all you need do is machine off the surfaces, and its amenable to high frequency ultrasonics. Then you can slice this thing up to contain the envelope for the rough blades and do an NDE job on that again, and you're going to still eliminate all kinds of defects and defective material from passing on to a different point in the fabrication sequence.

C. Jakus: One of the recognized problems of proof testing is that you may do damage to the part and you don't know how much damage you have done. Can an ultrasound field do damage to ceramic parts?

A.G. Evans: If the ceramic is fairly anisotropic and prone to microcracking, yes, it does happen; acoustic fatigue is the official title for it. However, it doesn't happen in the sorts of materials we are considering here.

Jerry Hilbrick: I'd like to give some scope to this thing, something I deal with every day in the metals area and composites area. If I'm looking for 20 and 40 and 50 micron internal type cracks or defects, undefined at this point, and I call that a needle, then the size of the thing that I'm looking in is about the size of this building (and that's one heck of a haystack). And the cost of looking through that haystack, needles width by needles width, is expensive and I can see a $30 vane costing me a thousand dollars to inspect when I've got everything worked out. Also, we do an awful lot of rig testing, and traditionally this is the response of the builder of the rig leaving a nut inside the rig when he's all finished, or a washer, or the end of his wrench. But even more so, from the standpoint of if we have one out of thirty blades that is below test, you miss the defect in it and it fails. What do you destroy? Well, you'll destroy all of the 29 blades, which I did. You'll destroy the disc and you'll probably destroy the rig which costs you ten to twenty thousand dollars and six months to rebuild. You'll actually tear up the whole system and again, this is an economic thing.

A.G. Evans: I think the sorts of things you were describing go into that cost quantification that I tried to indicate in my talk and they are important parameters.

Gordon Kino: I grant you the problem of looking at the 50 micron flaws over a large piece is horrific, but I don't think it's quite as bad as you paint. The scanning is not done on a 50 micron scale. What you're doing is using a milimeter diameter beam and are scanning the whole centimeter in a couple of microseconds, if you are prepared to do things electronically. Then, if you find a flaw, you've got to examine it more closely.

Tom Derkacs: The point I'd like to make is really two-fold. One is that in scanning the parts that we have looked at to date, we have looked at 6" square billets of silicon nitride, for instance. As I said before, we can't guarantee 100% reliability but based on what we've done, both by making repeated scans of the same billet and also by scanning seeded billets, it appears that we have fairly high reliability as far as covering the whole material and detecting the defects. Now, the second comment I'd like to make is that I envision an inspection system for ceramic parts to be nothing at all like the common C-scan tank and instrument; but rather, a computerized system, possibly using several different transducers at the same time. And then, compare those defects and their locations with a pre-programmed stress field based on how the part is going to be used. I think that kind of inspection of a whole blade, for instance, could be done in maybe 20 minutes or something like that, which is not very expensive. Now, you might pay $250,000 or a half a million dollars for the system but once you've bought that, the time and the man-hours to inspect the part is not going to be very great.

Norm Tallan: I think the question of proof testing was brought up by Ed. I think it's true that a proof test has to be designed every bit as carefully as the original stress analysis of the component, and we have to design it in such a way that in fact we know that the proof stress is reached at the critical parts of the components. But with regard to the question again of where we put our emphasis in the components, a point I was trying to make earlier with regard to the $30 vane is that here is a component which is probably emminently suited to a proof test. We can probably do it by some kind of a standard burner rig test with a thermal stress imposed and reasonably well assure that we're not going to harm the component during the proof test. In fact, the thermal exposure may even be beneficial in some ways in terms of healing some of the surface. We can afford to throw away a lot of parts, we can weed out some of the ones perhaps by microfocus x-ray before we pass them on, all that sort of thing. The thing we would be concerned about again is the blade, which is likely to be much more damaging to mission accomplishment than a vane failure. We're worried about tearing up a rig, we're even worried about putting it in a small test engine and tearing up the whole engine. But that's still a relatively small investment (whether it be a $20,000 turbo-jet engine or a $100,000 small turbo-fan engine) compared to the risk of actually either tearing up a whole system (whether it be a cruise missile or anything else) or having that missile not perform its mission. And, I think we ought to focus on the whole system, not only the cost but the application we have in mind. What is the most critical component, the most critical problem, overall. And keep in mind that it's not only an NDE problem but also a material problem and a design problem and get all these people together to solve this.

Roy Rice: Ed briefly touched on it and I want to bring up the point again. Of course we are focusing legitimately here on NDE. I think a lot of this ultimately rests on the processing capability in ceramics and I think we can do a great deal there. I think what we really want are the NDE techniques that allow us to help feedback to improve our processing. If we can improve our processing sufficiently, then it's not necessarily a question of inspecting every single component; but to assure us that we are repeating from batch to batch, the same quality that we had in previous successes. So I think let's not lose sight of the possibilities of taking care of a lot of our problems by process improvement, not just inspection and throwing away components.

A.G. Evans: I'll make a summarizing statement if I'm able to; if anybody objects vehemently, say so. The essence I got from the discussion was that NDE should be viewed as a fairly comprehensive process which iterates back to fabrication. We should recognize that NDE can be used in various stages in the fabrication and a different technique might be pertinent to a different stage in the making of a part. We must keep our eyes open for the comprehensive nature of NDE and be aware of any new techniques that will be emerging, to use the available techniques to the best of our capabilites, and to use them quantitatively.

R. Crane: One thing that you should recognize is again what Harris pointed out. That is, each one of those techniques has a curve associated with its ability to detect flaws. A very important concept.

A.G. Evans: I'm glad that you re-emphasized that point. I think we have cleaner systems than metals--- I think we can do a better job, but that remains to be seen.

COMMENTS ON NDE

Prof. Dr. P. Höller
Fraunhofer-Gesellschaft
Institut für Zerstörungsfreie Prüfverfahren
Saarbrücken, Germany

I have prepared some comments for some specific topics we touched upon yesterday. We have a lot to learn toward perfecting nondestructive testing in any area. The Federal Government of Germany has funded us for approximately five years. The Institute for Nondestructive Testing started experimental work about three years ago. We are covering different topics, mainly keeping in mind the application to heavy section materials--the nuclear industry, the steel industry--but to some extent, recently work has also been started on smaller sections and ceramics. We consider nondestructive testing not as just a method for depicting and describing defects, but more as a general method to judge the material, its structure, and the state of stress. Furthermore, the society to whom we belong (the Fraunhofer Society) is heavily devoted to technology aspects. That means that we must regard nondestructive testing as a technology and become involved in the more practical difficulties that arise. In practice, we follow the development of the technology until industry takes over. That is roughly the scope of work at our institution.

Let me give you a brief overview on our work. We have already heard so much about ultrasonics that I will not talk about it for the moment. One field we are heavily involved in is the eddy current technique. Starting with the basic ideas given by Libby at Battelle, Northwest, we have developed a device for multifrequency eddy current testing, and we have also developed the software to calculate what is going on in the material during eddy current testing which includes the design and the optimization of equipment parameters to design the coils. This work has been published and is very advanced. We are now cooperating with industry to get this technique applied in the nuclear industry as well as in the steel industry.

Anotner method uses a dc current to detect and to quantify defects. It is a very simple method using two electrodes on a work piece, which might have a very complicated shape. Measuring the change of the potential drop at the surface one is able to say sometning about the size and presence of a crack. To apply this method, which is particularly sensitive to deep cracks, we have developed a finite element program covering any geometrical shape. This method has been applied successfully to different cases.

Coming back to the eddy current technique, I would like to mention that it is not only able to detect defects but also useful for judging the structure of materials. Those of you who are familiar with the impedance curves know that the permeability and the conductivity are sensitive to the materials' structure. Using a multifrequency eddy current technique one is able to determine permeability and conductivity on any piece of metal of any shape. This is particularly important for weld inspection since permeability depends strongly on the demagnetization factor, that means on the size of the delta ferrite particles.

Furthermore, we are developing a theory of the magnetic leakage. You may know that this method normally is used with powder indications, but you can also use a magnetic tape, place it on the surface and afterwards scan the tape for the presence of cracks. One may also calculate the geometry of the crack, thus having a quantitative basis for application of the magnetic leakage method which is very sensitive to narrow and small cracks. Very recently we started with magnetic noise measurements, where we have two things in mind; the stress--I think some people in the auditorium have already worked in that field--and small inclusions or small precipitates below one micron in diameter. This is very important, for instance, during annealing at temperatures of about 650°C, some carbides and nitrides determine the strengths and the toughness of the materials. Ultrasonic methods are not capable of giving information on these very small precipitates. Magnetic noise, however, is very sensitive because the size of these precipitates is comparable to the thickness of magnetic domain walls.

Let us talk now about ultrasonics. Again, we are trying to determine the materials' structure, defect sizes, and the stress. With regard to materials' structure, we have done a lot of scattering work but not scattering in the sense it was discussed and presented yesterday. We have determined grain scattering, or scattering of single and multiple inclusions. The grain scattering is caused by the anisotropy of the grains yielding a method for an absolute and quantitative determination of an average grain size. Important with regard to application to fracture mechanics is the fact that not only the size of the crack and the materials' strength have to be known, but also the specifics of the matrix immediately around the crack. This latter aspect is particularly important for weldments which may have a completely different structure than the parent material.

A second topic in the ultrasonic field is the electrodynamic excitation of ultrasound. The basic advantage of this method is contact-free generation of sound. Not all of the physically possible wave modes have been utilized yet. We have developed probes for tube testing and multimode plate testing. Different probes generate different wave types and a dynamic range of 50 decibels has been obtained.

Other work deals with ultrasonic holography. One may simply use equipment which has been developed in the U. S. Not only at our place, but also at other institutions in Germany, work is going on to develop procedures for numerical reconstruction of holograms. In conclusion, let me say that it is nice to see the basic scattering work proceeding which is necessary to interpret defect sizes and shapes and that a very important part

of this research is going on here. I think it is a good area for complimentary cooperation. I am sorry that I could not go into more details on the ongoing efforts in Germany in these few minutes.

Thank you very much.

STEADY STATE REQUIREMENT FOR TECHNOLOGY TRANSITION

F. Kelley
Air Force Materials Laboratory
Wright-Patterson AFB
Dayton, Ohio 45433

ABSTRACT

Much has been said in recent years regarding the transitioning of new results from the research laboratory to operating practice, a step of key importance in the acquisition of new technology. However, relatively little has been said concerning the steady state requirements necessary to sustain a timely flow of new results. It is the purpose of this talk to outline several features that are necessary to ensure a continuing transition.

After that elusive title, I think it's important to tell you that, when Don Thompson contacted me about coming to this meeting, he basically said to say what's on my mind, and that's essentially what you're going to hear. I'll certainly weave in that theme and I hope that it sets the stage for the papers that follow and the Poster Session.

Today I'd like to talk briefly about the place of quantitative NDE in the materials reliability or life management process as a key element to decision-making, and I'd also like to suggest how research and its useful product, technology, enters the realm of practical application as part of that decision-making process. My premises are these: first, that today's complex problems, such as systems reliability and life management, can be solved when the decision-making system is understood, is functional, and has been validated. My second premise is that useful technology transitions because the user wants it and because it is easy to use. The third point; that a coherent research base is necessarily a continuing part of the process, but maintains its vitality by being an integral part of a system which solves problems. Now those are the premises I will touch on at the end of what I have to say this morning. I could stop there, but really would like to tell you a story.

In the summer of 1967 at Hill Air Force Base in Utah, a Minuteman missile was disassembled that had been in the silo for seven years, and underwent a periodic inspection--x-ray, ultrasonic, etc. A technician removed the igniter from the front port of the first stage, looked inside with a hand-held mirror, and discovered some cracks about an inch and a half long in each one of the star valleys in that grain design. These cracks were located in a position difficult to see and easily missed by x-ray. They were, however, quite predictable in their location by looking at the stress analysis. The existence of real, field-generated defects led to a momentary paralysis of the system which was designed to anticipate and react to just such a problem. The planning for the occurrence had been elaborate. (I had been part of that planning.) It was based on generalities and abstractions, and it was tied to a level of understanding that was, unfortunately, over ten years old. The following questions were immediately generated: How serious was a crack in that location; is it critical? Can the size and location be assessed for an OK or not-OK decision? If it's currently OK, will it grow to a critical size? How many of the missiles in the thousand-missile force were so affected? How may the force be conveniently and quickly inspected when the missiles are out in the silos? How can a conclusive demonstration of an OK or not-OK condition be conducted, and at what cost? Finally, why weren't we ready for this?

These and many other questions couldn't be answered with the data and methods we had at the time--we couldn't answer the specific question, for instance, of how does a crack, which is burning, behave? Does the combination pressurize inside the crack and mechanically force it open so that it splits like a watermelon? Or, does it burn the tip of the crack and blunt it, and therefore just burn normally to the case, being quite predictable through the burning rate laws? We couldn't figure out how to inspect the missile in the silo for this condition. The cost of opening up the silo at that time was around $25,000 and disassembly was another $20,000. We couldn't even do a decent cost estimate. A massive, highly technical and complex program was undertaken to get answers to these questions.

I selected this example because I believe it's somewhat foreign in specific content to most of the audience in this session, and thereby might provide some stimulation. I also selected it because I was part of the technical community which had formed some ten years earlier to create a resurgent technology base in the highly complex area of solid rocket structure integrity. We had garnered the resources and had established a research center or two with long-range ambitions. We had spread programs throughout the nation in universities and research institutes to work a number of intriguing problems, sustained the program for nearly ten years, and met at least annually to exchange information. We found that (with a real need for answers in a situation which could have been predicted) to get the answers we had to generate a whole new set of oriented and integrated programs. Now you may see a parallel with this particular community.

I have a personal conviction and determination not to let that happen to me again if I can help it. I'm not saying that nothing of value had been produced in the technology programs in the previous years, but the key element which has stayed with me through the years is the realization that a lot of scattered work on obvious pieces of a perceived general need are of little value without integration into a workable decision-making system. I almost feel like saying that again, because it sticks in my mind. A second or subordinate realization which should have been obvious, and I still don't know why it wasn't, was that our early program thinking should have presupposed the occurrence of defects and we should have asked the questions: How critical? How to measure? How to decide? It wasn't that those questions hadn't been asked, it's just that they hadn't really been worked conscientiously as though they were related to real problems.

I'd like to generalize a moment and look at Fig. 1. I've grown fond of this slide because I spent a lot of time trying to simplify the structural design process in which the elements are described, and the information flow is directed toward reaching a conclusion; i.e., a structural safety margin. This flow chart was developed in concert with a lot of design engineers. I wanted to understand the fundamental elements of the design process and relate them to structural failure. It ought to be obvious, but what we have attempted to do is have, as a central idea, the analysis--a stress analysis. We're interested in how loads are converted into stresses, taking into account the geometry and the material properties. Material properties here have been split simply into "response" and "limit"--for example, the ultimate properties. There are generally small deformation properties such as modulus, some sort of fracture property, or an ultimate stress. The stress analysis provides a distribution of stresses and strains in the particular object and when one compares the output with a failure criterion that says if you exceed this value you get failure and if you stay within this value you don't, it includes, of course, all of the probabilistic qualifications and concern with statistical distributions of properties. A major job of the designer is to conduct a strength analysis and come up with a margin of safety.

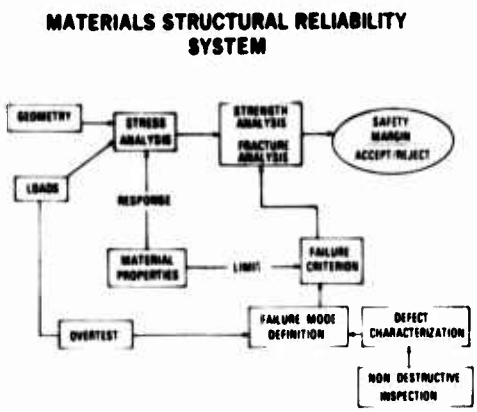


Figure 1. Schematic representation of Materials Structural Reliability System.

When one assumes pre-existing defects, an analytical predictive process may be used if a quantitative characterization of the defect is available. Such an analysis is generally based on the idea that whatever flaws are present are very small and are quite reproducible; therefore, we don't even pay any attention to them. Let me get into the fracture analysis realm where, assuming defects are there, we are concerned with the characterization of those defects. By this I mean knowing where the flaw is, how big it is, how it is oriented, and examining how it interrelates with the stress field. We are then able to deal with the question,--under geometrical, load, and environmental conditions--"Will the crack grow?" Will it grow to an unacceptable limit?

This particular conceptual overview of the design process, integrating the existence of defects, has some new terms, or has some terms that I still have to describe. These terms essentially form the basis upon which the Minuteman service life analysis is now conducted and has been conducted for the last ten years. Actually, it took about two years to react to the defect problem and this conception was the sort of thing which eventually popped out of that reaction.

Let me breathe a little life into this story by describing some of these terms and then I'll come back to the conclusions. Figure 2 shows that the first thing necessary is to define the loads. Loads are hard to define, especially in a dynamic environment. Missiles are handled a lot. They go in and out of silos, they get inspected, and then they are used. A motor fires for about a minute, so it's used in a severe environment for only about a minute, but it sees a lot of time sitting around with its own body forces acting, usually vertically in the silo. Determining loads and, as we like to say, stresses which must be calculated from the loads is the initial problem. The concept of a structural test vehicle is to define the load and to validate analysis is a rather important concept.

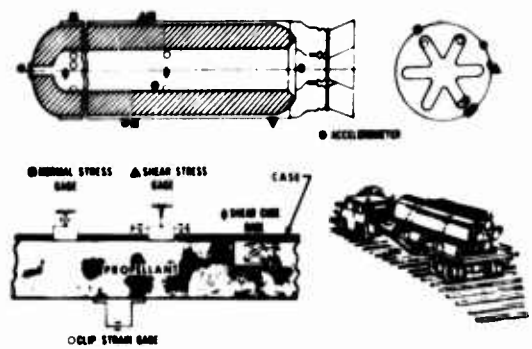


Figure 2. Definition of loads.

This, by the way, is a fair drawing of what the Minuteman first stage looks like. As many of you know, the grain is contoured down the center perforation to get a certain burning profile and a certain pressure-time behavior and, thereby, the thrust-time behavior. It has four nozzles, and you can see the immensity of the problem of trying to inspect for a crack which is up in this region, radially outward from one the the star valleys, and thirty feet up the port, since you can't get access to the front end. Its standing vertically and there are four nozzles on the base, which requires two right-angle turns to get an inspection device up in there. Coming up with a nondestructive device that would extend up and look down the valley in the front end was almost impossible. But that was only the first challenge; to see how one could inspect in the silo from the inside. I won't dwell on this much more, other than to say that the definition of loads is one element and in Fig. 3 you get yet another element on the chart, that is, the concept of "over-test." I find quite frequently, in serving on panels that try to assess the viability of a system, that if one projects that things are getting serious and that we really ought to take these things out of the field and put new ones in, the question always asked is, "Have you ever failed one?" Usually the answer is no. Thus, the idea of defining a limit test. This is kind of a healthy empirical approach to life. Defining a failure mode by purposely breaking something with a somewhat exaggerated, but realistic load is an important part of the process. It's fairly expensive, but this is the sort of thing one does. One purposely breaks the motor by such techniques as plugging the nozzle and pressurizing with inert gas. The intention here is to simulate the loading environment which takes place on ignition, which is one of the more important loading environments.



Figure 3. Schematic for "over-test" arrangement.

Figure 4 gets into material properties. The great concern in this type of system is to make sure that the material properties which one integrates into that decision-making process are real. What we see here is a cutter that was designed to set the rocket motor on top of it and bore a hole in the side to go in there and extract samples as in-situ properties. In fact, you can get the gradient properties going from the case of the rocket in through to the port. Cutting propellant is kind of a dangerous thing, but cutting samples out and running the normal characterization test to get the material properties, for both response and failure, is an important part of this process.

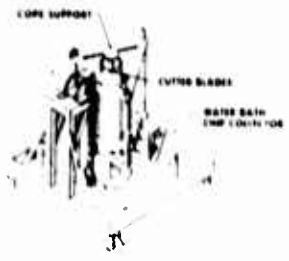


Figure 4. Cutter arrangement for determination of material properties.

In order to validate the analysis and to get some statistical data, some sort of smaller test object needs to be created. Figure 5 shows an analog motor. It is essentially a small cylinder containing propellant with a certain kind of notch. One can then have a predictable corner condition, do some calculations, and then break the motor, the point being that you can break lots of these so that you can get some sort of statistical data base. Figure 6 shows how one attempts to reproduce the particular stress field, the corner condition which one might find in a motor, and conduct the same kind of stress analysis of this condition that one does in the motor. Then by performing the transformation one can conclude that, under the loading conditions and with these particular materials, one can predict the growth of the flaw.

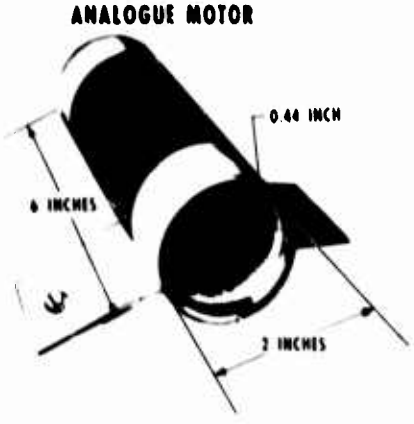


Figure 5. Analog motor for the operation of data base.

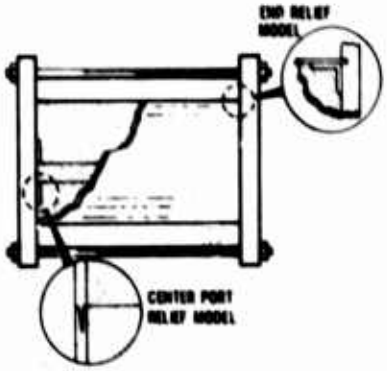


Figure 6. Model for reproduction of corner stress condition.

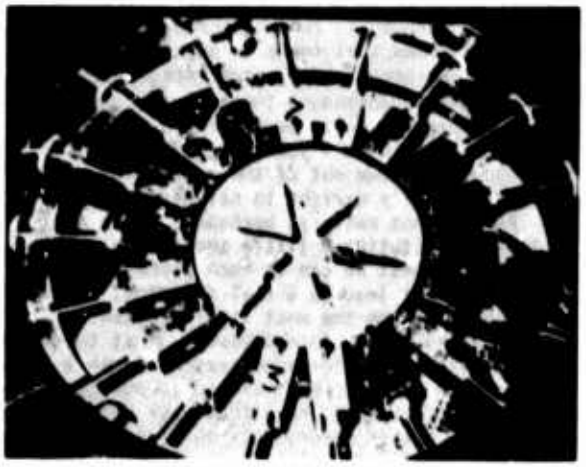


Figure 8. Same as Fig. 7. Note crack growth.

Figure 7 shows an elaborate test used to get the failure criterion. Shown is a sort of plane specimen, a cross-section in which we are applying biaxial loading which is the thermal stress condition pulling on the outside. There is a thermal mismatch between the propellant and the case. When the temperature changes what you get is a tendency when the temperature is low for the propellant to pull away from the wall to which it is bonded. What sets up is essentially a hoop stress condition around the centerport. Figure 8 shows the consequences of that condition; you grow a crack. These are the sorts of tests one runs to validate analyses, but you see, analysis was central to that flow diagram and one of the problems we had was that it is too easy to believe in analysis once it's completed.

Figure 9 shows what is an unfortunate combination of things. What it essentially says is that one finds, from overtesting to the various loading conditions, the kinds of failures which can take place. The thing that's unfortunate is that it doesn't indicate what the consequences of cracking might be. The consequences of cracking might be burning to the case wall if there is a crack there, or fire getting in and burning perhaps too large an area thus creating over-pressurization. Certain failure criteria based on the continuum mechanics approach to life had been reasonably well established. Unfortunately, this did not include a fracture mechanics approach which was so necessary.

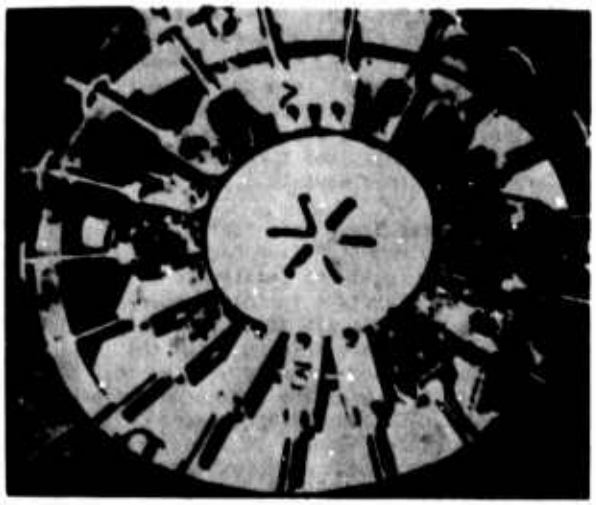


Figure 7. Model test for determination of failure criterion.

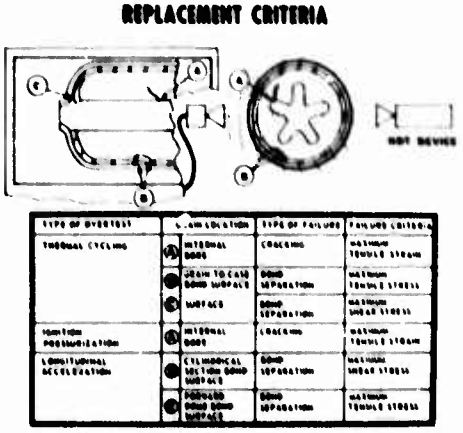


Figure 9. Replacement criteria from "over-test" results.

Next, I'd like to get back to my initial thoughts. My purpose in running through these examples is to show that there is nothing mysterious about an organized program integration and to show how to introduce the analysis and experiment when a problem is to be solved. I guess the last thing I want to tell you about Fig. 1 is that somehow I've come out of the experience with the belief that it's alright to naively push ahead. Perhaps not naively, because I think that we sell our institution a little short. We push ahead doing the best we can in each element of a process which will lead to a real decision, taking into account what are the most likely causes of failure. I also think, in retrospect, that this is all so obvious, but for some reason we ran a program for ten years without all those obvious things becoming apparent and without our doing much more than making compromises on what would be realistic tests and realistic problems because they cost too much. Each piece of the technology underlying research has a place in the scheme of things and has a vital role in the final decisions and solutions of these problems.

Now to move into the technology transition subject which is shown in Fig. 10. The point I want to emphasize here is that this is a kind of technology flow chart. (I meant to write that word "need" a little bigger.) This flow is driven by need. It's nice to have something driven by opportunity, but if you really want to get some acceleration it ought to be driven by need. The point I want to emphasize here is the coherence in the upper-left corner; the coherent research and technology base. I don't know how to get that point across other than to say that I think in terms of the previous chart. I think in terms of the pieces of the problem. I think in terms of the interfaces and making sure that those interfaces really represent the flow of analytical information, i.e. that they represent the flow of numbers which are useful in an input/output sense. That coherent research and technology base essentially takes the previous system apart and asks the question, "Which are the defective elements in this system that produced a useless answer?", or "Is the system all there?" If I view Fig. 10 as a decision-making machine, then, if all the elements are there, I can turn the crank and an answer will come out. The answer might be poor, but at least the machine works. If I've established that basis and then moved back to ask in a kind of sensitivity analysis approach--which of the elements is most defective and is fouling up my answer most--then I'm prepared to deal with that framework as a constant, as an invariant. I can then deal with the elements in an upgrading fashion, perform a sensitivity analysis which isolates those elements which are most deficient, and concentrate resources there. That's essentially the picture. The picture shows that new knowledge is required and that it's coherent in the sense that you know what to do with the knowledge in terms of the final decision.

ELEMENTS OF TECHNOLOGY TRANSITION FOR NDE

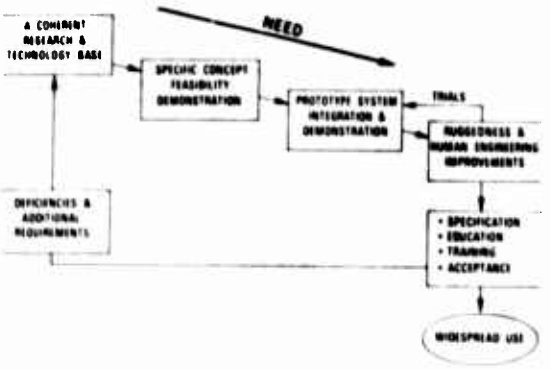


Figure 10. Elements of Technology Transition for NDE. Need is an important driver.

If you've evolved the concept, conducted a feasibility demonstration, and done the system integration, you get into an element here which we have sort of taken as a new focus in our applications program in NDE, that is, the problem of transitioning to the field in a real way through field trials. We generally stop too soon with our programs. In our typical program we demonstrated the concept, made a few prototypes, then gave them to people and said, "Go to it." The real thing to do is to get these prototypes out there, get them used, and then deal with what are important reliability problems.

New devices are unreliable primarily because there are a lot of complicated electronics in some things. What we find out, unfortunately, is that the reliability of the device is, for quite a while, much worse than the reliability of the thing we are inspecting. Then, what drives it into widespread use? If we specify that people must use this integrated systems approach, then they need to be brought into the thing in a cultural sense. That is, people are generally suspicious of the new, are sure that it's going to give them trouble, don't know how to use it and aren't sure they want to.

While I have drawn this "deficiencies and additional requirements" line back toward the start, it would really be legitimate to draw a line to almost any stage in this process because deficiencies exist in all stages. I think, since in this meeting we are talking about that coherent research and technology base, that the continual input of what the real problems are and what the real deficiencies are, based on that kind of systems picture, is what is necessary so that you know you are a part of something which is producing a real and valuable answer.

I'd like to get into that specific embarassing example of where we didn't do this job well, just as a final point. Figure 11 is a picture of some people using a Roto-Scanner. Its purpose is to detect and define the defects; cracks underneath installed fasteners in the wing. Some of you are familiar with the problem, and maybe with the device. We developed the device through Boeing and it did a decent job, at least in our early indications. It would detect a 30 mil radial crack coming out from a fastener while the fastener is installed under one layer. Figure 12 shows the various kinds of readout procedures on the oscilloscope. The upper right, where one gets essentially a circumferential plot of the signal coming back from around that fastener, one gets a little notch in that plot when there is a defect there. We made a prototype and then, with the help of some other agencies like the C-5 and a particular reliability and maintainability program office at Wright-Patterson (PRAM), four or five of these were made, re-engineered to a degree, and given to the inspection centers. Their assessment of it is shown in lower left. It's pretty good in principle, but it has some serious shortcomings in terms of operation in the field environment. The guide system for the head is unreliable; it kept losing the index and then didn't know where the defect was once you got an indication. The transducer mounting plate had problems which concerned the angles of the transducer and the particular thickness of the layer being inspected. Since the thicknesses varied, there were some problems involving moving that mounting plate around. There are some problems in the electronics. I won't go into them greatly, except to say that this was not the best electronic system for this device. I guess one thing we could say as technologists is, "We stop there and it's your problem from here on out." The people who have to use these things see these problems as, "Gee whiz, you've got to hold it up with your left hand and look under your armpit and flip the knob." There are some human engineering aspects as well as some electronic aspects to the problem of dealing with the next step. That's what we're asking the people to do, take one more step. Try to get out there and make the user a part of the process that evolves the re-engineered design. Then, once feasibility has been demonstrated, one can get into usability, and if those people were part of that process then they own it and are more willing to transition it. Enough on that point.



Figure 11. Ultrasonic examination with Roto-Scanner.

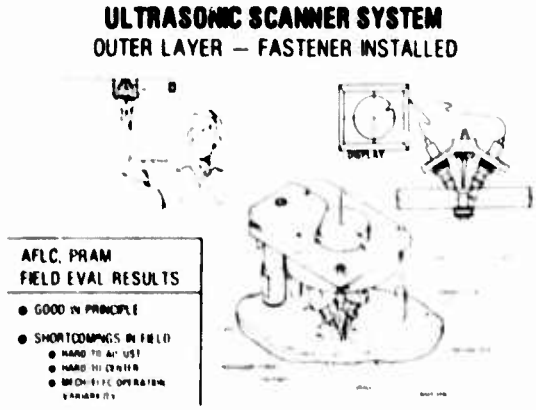


Figure 12. Test results from Roto-Scanner.

I'd like to go back to Fig. 10 on the "Elements of Technology Transition for NDE" again to emphasize my starting points and conclude my remarks. If we're going to maintain this coherent research technology base as a kind of continual source to pump the system which is driven by need, I think it's critically important, of course, that the resources be maintained. The resources to continually support a generalized subject are hard to come by. Therefore, I think the future vitality of this particular kind of activity--not from the standpoint of having meetings, but from the standpoint of maintaining the momentum and the coherence which has been built up--has a lot to do with constantly injecting this particular arrow, the feedback from the real problems or needs. Also, I think the rump session which Don Forney held the other night with several of you on the C-5 problem, in which researchers from various institutions were brought together and brainstormed a real problem, is the greatest way to do that. So, I'd advocate a couple of things for the future for, at least, your consideration. One is that you "design-in" rump sessions like that--they won't be brought to these meetings which are well-defined and important. Line up a few people to talk about the problems. Another way might be to hold a meeting in the places where the guys use these things and get out there and walk around--that was always an eye-opener to me--seeing the environment. Although, while people are polite to you, if you go in on a one-to-one basis you soon get the feeling that you're not trusted which either turns you off and you leave the field entirely, or you say I'm going to beat this problem and I'm going to work with these guys. That's the sort of thing that gives you such great stimulation with regard to continuing your work and I think that resources follow. It's one thing to put in front-end money to get a community going. It's another thing to sustain it, and I believe the thing that will sustain it is constantly getting involved with those real problems and understanding your part in the overall scheme of things. That's why I tried to display that design system with the consideration of defects.

I'd like to stop here because I'm out of time anyway. Thank you.

DISCUSSION

Larry DeVries (University of Utah): What was the outcome of the cracked Minuteman story?

F. Kelley (Air Force Materials Laboratory): That's such a fascinating story that it would have taken all morning to go into it. What we found out was that it was really a fail-safe thing and we could live with those cracks. The analysis which was done--the fracture mechanics analysis, which is kind of tricky on a viscoelastic material, as Larry well knows--indicated that propagation of the crack would go longitudinally rather than radially and we did some over-testing in which we carved out four-inch-deep cracks in each of the star valleys and fired the motors and they fired normally. Our calculations showed that the cracks should not go more than an inch and a half deep; under the worst stress field they would grow longitudinally to the end of the motor. We over-cooled the motor and split it, and it did indeed grow to the end. Therefore, what we have is essentially verification of the analysis that says you can live with those kinds of cracks. Now there have been other kinds of problems while dealing with unbonding about which you come to a different conclusion.

K. Salama (University of Houston): I was glad to see that you mentinned training and education as parts of the progress of NDE. Do you know of any educational training programs on the university level?

F. Kelley: Let me say, honestly, that I don't know of any university program that purposely sets out to teach the subject. If there is, it's probably known to this crowd here. I know that there are kinds of training courses; maybe Don Forney could answer better than I. I think that you may or may not have been exposed to it. Dr. Burte and I did a survey of the science base in materials processing over the past year to year and a half, and visited many, many campuses to talk about what we perceived as the real needs in terms of unsolved problems for the Air Force. Nondestructive evaluation was brought out as one of the most critical science needs. By implication or directly, in that environment one talks about what the educational program is doing for this need. If any of you have started a program in this area, I think it would be important to bring it out. We have a number of people from the universities represented here. Has anybody got one...there's one.

(Speaker not identified): There are a number of survey courses, but the only degree program in NDT that I know of is at Lowell Technological Institute; Steve Serabian's program. It goes to a Master's level.

F. Kelley: Do you know much about that course?

(Speaker not identified): Other than that it's in the Mechanical Engineering Department, Lowell Technological Institute is in Lowell, Massachusetts, near Boston, and it uses all the NDT measurements. It seems to emphasize radiography and ultrasonics, but I have never taken the course.

F. Kelley: I was wondering if anybody used a type of systems concept that integrates the measurement of flaws with the eventual decisions that must be made about them, and whether or not a course had been structured like that.

(Speaker not identified): I know of a number of survey courses at RPI that are in development--having been given on a one-time basis--but I don't know of any formalized course of instruction such as you describe. There are several two-year schools that do this kind of thing, but they are more or less aimed at generating specialists and technicians. An example is Hutcheson Vocational Institute in Hutcheson, Minnesota.

F. Kelley: It might be useful to get someone who is attending one of the sessions for teaching those courses to describe them.

"NEW" CANDIDATES FOR ULTRASONIC NDE STANDARDS AND CALIBRATIONS

George Birnbaum
National Bureau of Standards
Washington, DC 20234

ABSTRACT

The National Bureau of Standards program in acoustic-ultrasonic calibrations and standards, aimed at solving some of the immediate problems, is reviewed. Work on acoustic emission transducers is directed at the determination of sensitivity and spectral response by the use of a reproducible stress impulse. Also in the area of acoustic emission is a program to develop a theoretical basis for acoustic emission signal analysis to characterize moving cracks or defects. Work on the characterization of ultrasonic transducers which should lead to formal calibration services in the near future includes determination of spectral characteristics by measuring the pressure of the ultrasonic radiation field, determination of the radiation pattern from near field measurements and total power by calorimetry. Although the current NBS program is oriented toward standards and calibrations, instrumentation problems are being addressed including the improvement of signal-to-noise ratio by methods such as pulse compression and signal averaging, and the characterization of the important variables in ultrasonic instrumentation. The reliability of flat-bottom hole aluminum reference blocks, which are in wide use, has been improved and a calibration service is now available. Further directions for this effort will include calibration services for steel and titanium blocks, the development of material independent blocks and the development of well-characterized fatigue cracks that could provide calibration for many NDE tests. The use of theoretically characterized scattering from spheres as a standard has recently come into prominence, and Rockwell and NBS have begun to explore this possibility. However, many other standards and calibration procedures for ultrasonic NDE have been proposed or are in use. To provide a fresh look at this area, particularly as it applies to DoD systems, NBS has initiated a program funded by ARPA to assess the status of the field, determine current and future needs, and propose a plan for realizing these needs.

Introduction

A program in nondestructive evaluation (NDE) was formalized in 1975 at the National Bureau of Standards, although various segments of the program had been in existence prior to then. This program, coordinated by the Institute for Materials Research, is aimed at assisting industry and government agencies to make effective use of NDE by improving its reliability and making it more quantitative through standardized NDE measurement procedures. This includes the improvement and development of standards and calibrations, procedural documents such as recommended practices, characterization of instruments, development of improved techniques, and the assessment of the NDE measurement on material performance. Current emphasis in the program is on acoustic emission, ultrasonic measurements, x-ray and neutron radiography, electromagnetic methods (eddy current, visual inspection, microwave methods), penetrant testing, wear debris analysis and thermal testing.[1]

This paper discusses the NBS program in acoustic-ultrasonic standards and calibrations. Certain elements of this program were initiated with medical applications in mind while others address some current standards and calibrations problems in NDE. Since ultrasonic NDE depends so vitally on transducer performance, much effort has been devoted to its characterization, and a formal calibration service is planned in the near future. Transducer characterization includes determination of spectral characteristics by measuring the pressure of the radiation field, determination of the entire radiation pattern from near field measurements, and measurements of the total radiated power by calorimetry and an electrical method. Work on acoustic emission transducers is directed at the determination of sensitivity and spectral response by the use of a reproducible stress impulse. The reliability of flat-bottom hole aluminum reference blocks has been improved to the point where a calibration service has been established.

In addition to the work discussed here, many other standards and calibration procedures for ultrasonic NDE have been initiated or are in use.[2-4] To provide a fresh look at this area, particularly as it applies to DoD systems, NBS has proposed a program partly funded by ARPA[5] to assess the status of the field, determine current and future needs for standards and calibrations, and propose a plan for realizing these needs.

Calibration of Ultrasonic Transducers

This section deals with various techniques which have been developed for characterizing ultrasonic transducers.

Ultrasonic Calorimeter[6]

Calorimetric equipment, schematically shown in Fig. 1, was designed to measure ultrasonic beam power from 1 mW to 10 W, at frequencies from 1 to 15 MHz with uncertainties less than ± (7% + 0.2 mW).

The equipment will accommodate ultrasonic beams having diameters as large as 26 mm, sufficient for a wide variety of medical diagnostic and therapeutic transducers, and for many transducers used for NDE. Twin vessels are provided so that the temperature rise due to the ultrasonic energy absorbed in one vessel can be compared rapidly with accurately measured dc electrical power supplied to a heater in the other vessel. Liquid, whose temperature is equalized by a heat exchanger, enters each vessel near the input port. Twin temperature sensors, located in the output flow from the vessels, are connected to an electrical bridge circuit. The advantage of a twin series-flow calorimetric method is a decreased need for accurately controlling the flowrate and temperature rise. In addition, ambient temperature effects are minimized and insulation requirements are not stringent as in single flow systems. By using a solid as the principal absorber and a liquid to transfer the heat to the sensor, the vessel size, the effective volume of the liquid and the effective volume-displacement time could all be reduced.

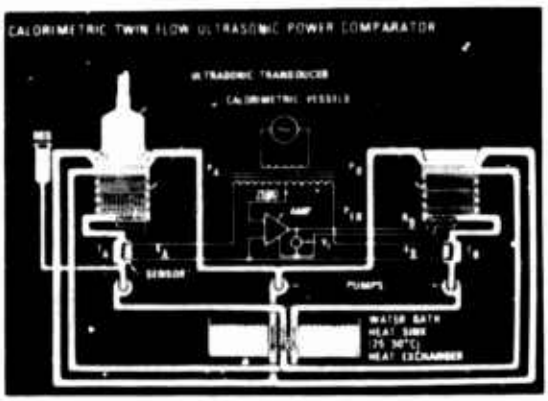


Figure 1. Calorimetric twin flow ultrasonic power comparator.

Power Output by Modulated Radiation Pressure[7]

The spectral characteristics of transducers are determined by measuring the pressure of the radiation field. In this method the input to the transducer is modulated at a low frequency (~39 Hz) and the total output power is intercepted by an absorbing target which experiences a force at the modulating frequency. For a perfectly absorbing target in a collimated beam, the total radiation force equals the incident power divided by the speed of sound in the medium. For propagation in water this force is roughly 67 mg per watt.

The target is mounted on the armature of an electromagnetic microphone provided with an independent coil through which a current at the modulating frequency is adjusted in amplitude and phase (manually or automatically by feedback) to arrest the motion of the armature. The force then depends only on the current, and the apparatus can be calibrated absolutely using direct currents and dead weights. The carrier frequency may be swept over any part of the range 1-80 MHz while a recording of power output versus frequency is made.

The apparatus is stable and easy to use, and the results are absolute. The sensitivity is very high, ~7μW; the uncertainty varies from 2 percent at 1 MHz to 12 percent at 30 MHz.

Transducer Calibration by an Electrical Method[8]

In this method of calibrating specially designed half-wave resonant, air-backed, quartz piston transducers, a highly accurate twin-T null circuit is employed for the measurement of its electrical conductances under certain loading conditions. This permits calculation of the equivalent resonant radiation conductance, which when multiplied by the square of the applied voltage, yields the emitted ultrasonic power into a load. A wide range of accurately known ultrasonic power levels (±5 percent in the range from to 5 MHz) can be obtained by quartz transducers, which thus characterized, can be used for calibrating or checking ultrasonic power measuring equipment.

Measurement of Beam Profiles[9]

Apparatus has been developed for determining the planar distribution of voltage amplitude and phase of ultrasonic transducers. Experimental results are shown in Fig. 2. Given a known receiving probe, this work shows that a single planar scan in the near field of a moderately directive radiator is sufficient to provide relative distributions of quantities such as pressure, particle velocity, energy density, and intensity in accordance with theory.[10] The addition of careful electrical measurements on the transmitter and receiver provide a means of precisely determining absolute field quantities and the related, forward-radiated, acoustic power.

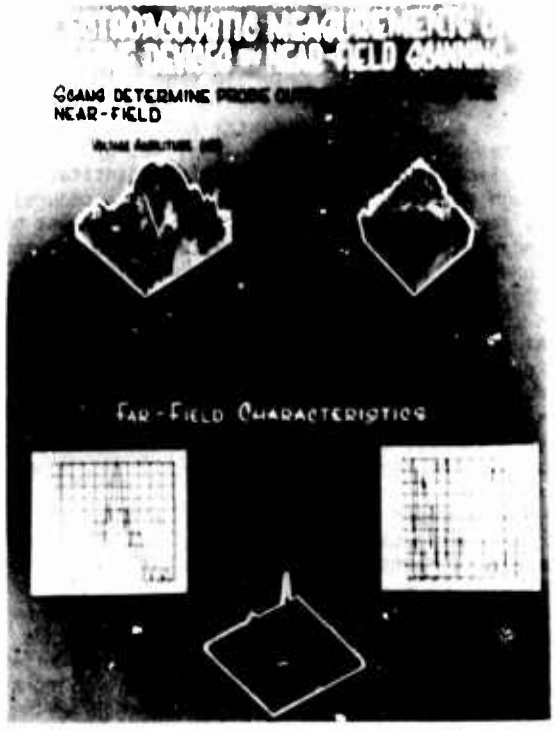


Figure 2. Planar distribution of voltage amplitude and phase measured in the near and far fields.

Calibration of Transducer Power by Measuring Average Near Field Pressure[11]

If a transducer can be found which responds linearly to the total incident force, (not the radiation force) the field amplitude pattern of directive transducers can be measured directly in the near field. This follows from a theory showing that the integrated complex pressure has the same magnitude over parallel planes within the fluid surrounding arbitrary transducers.[10] Further, the magnitude of this force is related by a simple proportionality to the far field amplitude in the direction normal to the planes. Preliminary experimental results, shown in Fig. 3, comparing the far field pattern determined directly and the pattern found from near field measurements, indicate the validity of the theory. The feasibility experiments were accomplished with a 3 mm test transducer (transmitter) separated by about 1.3 cm from a quartz, air-backed, receiving transducer. Care was taken to ensure that all of the power of the transmitter was intercepted by the receiver.

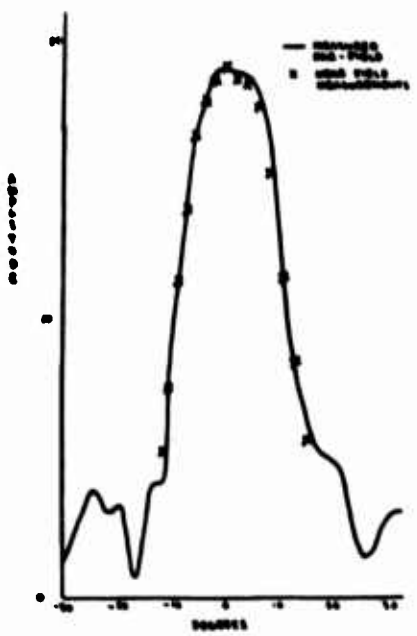


Figure 3. Amplitude distribution of a transducer measured in the far-field compared with the far-field distribution determined from near-field measurements.

A Reproducible Stress Impulse for the Calibration of Acoustic Emission Transducers[12]

In order to interpret acoustic emission signals, the spectral characteristics of the transducer should be known. This is accomplished by applying a reproducible step function of force by breaking a capillary[12] or a lead pencil[13] at a point on, and normal to the plane surface of a semi-infinite isotropic solid and measuring the vertical displacement of the surface. Explicit solutions to this problem first theoretically studied by Lamb[14] have been given.[15] The excellent agreement between theory (Fig. 4) and experiment (Fig. 5) for a transducer located on the same face as the step impulse, but some distance removed, may be seen by comparing Fig. 4 and 5. The electrostatic transducer used to obtain this result, which has a flat wide-band response, then becomes the standard transducer against which is compared the output of test transducers for the same standard seismic event. It becomes very easy, therefore to detect variations in sensitivity and frequency response and to ascertain the effects of changes in clamping force and couplant on response.

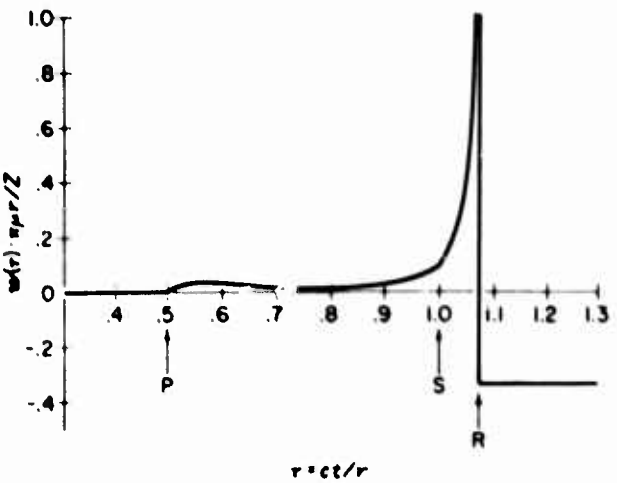


Figure 4. Vertical displacement of surface, W, measured at a distance r from impulse is calculated from an expression of Pekeris[15] for Poisson's ratio equal to 0.25. P, S, and R show arrivals of the longitudinal, shear, and Rayleigh waves, respectively. The speed of the shear wave is c and the shear modulus is μ. Z is the amplitude of the impulse.

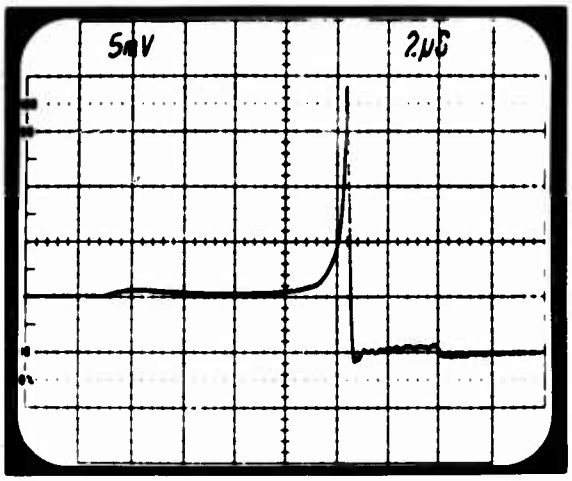


Figure 5. Oscillogram showing result of impulse surface pulse for aluminum-alloy block, Poisson's ratio equals 0.343, 6.3 cm thick and 17.8 cm in diameter. The breaking of a glass capillary 0.15 mm in diameter is the source. Electrostatic transducer is located 5.03 cm from source. Each division or abscissa equals 2μ sec.

Ultrasonic Reference Blocks

Of major concern to the producers and users of ultrasonic reference blocks is the large variability of response from nominally identical standards. In response to this concern, a program to achieve near-term improvements in the reliability of ASTM-type ultrasonic reference blocks (flat-bottom hole) was undertaken. Pulse-echo response of 22 sets of ultrasonic reference blocks of aluminum, steel, and titanium alloys were taken to quantify the variability in response from nominally identical blocks. Techniques for residual stress and microstructural measurements were refined and applied to reference blocks rejected by manufacturers during fabrication in order to evaluate the effect of metallurgical condition on block response. The effects of certain dimensional variables on block response were studied as were the effects of measurement system variables.[16]

As a result of this work a service for the calibration of ASTM E-127-type ultrasonic reference blocks has been established at NBS.[17] A single well-characterized reference block, carefully chosen to be as close as possible to "typical" or "nominal", has been designated as an interim standard against which other blocks can be compared. At present these measurements are primarily comparative due to the lack of a precise mathematical model that describes in a physically meaningful way all the complex interactions that are taking place. However, recent developments in computing the scattering from spheres,[18-20] for example, may make it possible to remove such a limitation. In any case, we plan to examine the role of theory and its implications for standards and calibration procedures.

An Approach to a Rational System of Ultrasonic NDE Standards

In addition to the standards and calibration procedures mentioned here, a great many others have been proposed or are in use. The following statement made in 1962 is still true today: "While it [is] admitted that a number of ultrasonic standards are in use today, none of these has general application; standards either apply to some specific product or material, or they are issued by a particular body or inspection authority and are limited in application." It is clear to standards organizations such as ASTM as well as to the general scientific and user community that the present ultrasonic measurement system is less than ideal and even chaotic in large measure due to an inadequate reference system.

In view of this situation a program sponsored by ARPA has been initiated at NBS to examine in detail the problem of realizing a compatible and traceable system of standards and calibrations for ultrasonic NDE. The steps to be taken include: assessing the current status of ultrasonic NDE standards, determining current and future needs for such standards, and suggesting an approach for realizing them.

No one standard or calibration procedure will be sufficient for the many different types of NDE ultrasonic inspections, different methods, and different parts of the NDE instrument. To deal with such diversity of use and the possibilities that must be considered, a list or criteria for evaluating possible standards and calibrating procedures must be developed. Such criteria include, for example: functional adequacy (will the standards reliably and adequatley accomplish their intended use?), versatility (how many reference standards are needed to carry out calibrations of various instruments for different test objects?), ultimate cost, and compatibility with existing standards. The list, of course, is far from complete but illustrates the complexity of the problem.

In order for such a study to accomplish its objectives, we need the involvement of as many people and groups as possible concerned with these problems. We welcome your inputs to this particular program and to our NDE ultrasonic program.

Acknowledgement

The author thanks Mr. H. Berger, Drs. D. G. Eitzen, N. Hsu and E. B. Miller for many helpful discussions.

References

1. Nondestructive Evaluation Program at the National Bureau of Standards, U. S. Dept. of Commerce, NBS, March, 1977.

2. Panian, F. C., and Van Valkenburg, H. E., "Development of ASTM Standard Reference Blocks for Ultrasonic Inspection", Proc. ASTM 59 (1959).

3. Legge, R., and Carson, H., "The Calibration of Equipment Used in Ultrasonic Flaw Detection in Steel", Nondestructive Testing 1, 35 (1967).

4. Rawding, H. "Ultrasonic Testing Standards", Ultrasonics, 1, 35 (1963).

5. ARPA Contract No. 3374.

6. Zapf, T. L., Harvy, M. E., Larsen, N. T., and Stoltenberg, R. E., "Ultrasonic Calorimeter for Beam Power Measurements", NBS Technical Note 686, Sept. 1976.

7. Greenspan, M., Breckenridge, F. R., and Tschiegg, C. E., "Ultrasonic-transducer Power Output by Modulated Radiation Pressure", J. Acous. Soc. Am. 60, Supplement No. 1, S99 (1976); paper in preparation.

8. Zapf, T. L., "Calibration of Quartz Transducers as Ultrasonic Power Standards by an Electrical Method", Ultrasonics Symposium, Milwaukee, 1974. Proceedings IEEE, p. 45 (1974).

9. Miller, E. B., "Probe Corrected Near-Field Measurements on Electroacoustic Transducers", J. Acoust. Soc. Abstract CC1, April (1976).

10. Kerns, D. M., "Scattering-matrix Description and Nearfield Measurements of Electroacoustic Transducers", J. Acoust. Soc. Am. 57, 497 (1976).

11. Yaghjian, A. A., and Miller, E. B., "Method for Calibrating Electroacoustic Transducers by Measuring the Average Near-field Pressure", J. Acoust. Soc. Am. Abstract C4 April (1976); paper in preparation.

12. Breckenridge, F. R., Tschiegg, C. E., and Greenspan, M., "Acoustic Emission: Some Application of Lamb's Problem", J. Acoust. Soc. Am. 57, 626 (1975).

13. Hsu, N., "Acoustic Emissions Simulator", U. S. Patent 4018084 (1977).

14. Lamb, H., "On the Propagation of Tremors over the Surface of an Elastic Solid", Philos. Trans. Roy. Soc. A203 (1904).

15. Pekeris, C. L., "The Seismic Surface Pulse", Proc. Nat. Acad. Sci. 41, 469 (1955).

16. Suskinsky, G. F., Eitzen, D. G., Chwirut, D. J., Bechtoldt, C. J., and Ruff, A. W., "Improved Ultrasonic Standard Reference Blocks", NBSIR 76-984, National Bureau of Standards, Washington, D. C. 20234 (1976).

17. Chwirut, D. J., Sushinsky, G. F., and Eitzen, D. G., "Procedure for the Calibration of ASTM E-127-Type Ultrasonic Reference Blocks", NBS Technical Note 924, National Bureau of Standards, Washington, D. C. 20234 (1976).

18. Cohen, E. R., "Analysis of Ultrasonic Wave Scattering for Characterization of Defects in Solids", AFOSR-TR-76-0754 May (1976).

19. Gubernatis, J. E., Domany, E., Krumhansl, J. A., and Huberman, M., J. Appl. Phys. 48, 2804, 2812 (1977).

20. Tittmann, B. R., Thompson, D. O., and Thompson, R. B., "Standards for Quantitative Nondestructive Examination", ASTM STP 624, p. 295 (1977).

TRI-SERVICES NDE CAPABILITIES REQUIREMENTS
AIR FORCE/ARMY/NAVY

D. M. Forney, Jr.
Air Force Materials Laboratory

S. Lorber
Army Material Development & Readiness Command

J. J. Kelly
Naval Material Command

D. M. FORNEY, JR.: I imagine that most of you would agree that it is a very difficult task to conclude what the military services--the Army, Navy and Air Force--have established as their major NDE requirements toward which research projects could be focussed. What we are going to try to do in the next few minutes, then, is present a short view of what, in our best judgement, these requirements are and what are the long range capabilities that we would like to see developed. We hope that by doing this, you will get a better picture of the key NDE research objectives within the DoD.

First let me put the NDE activity in the Air Force into perspective. While both daily in-service NDE support activity and R&D work have been ongoing for many years, these functions were not described as a formal USAF program activity until the issuance of Air Force Regulation 66-38, "Nondestructive Inspection Program," in 1966. AFR 66-38 established the authority and assigned responsibilities for various NDE functions to specific commands as outlined in Fig. 1 and detailed in Ref. 1.

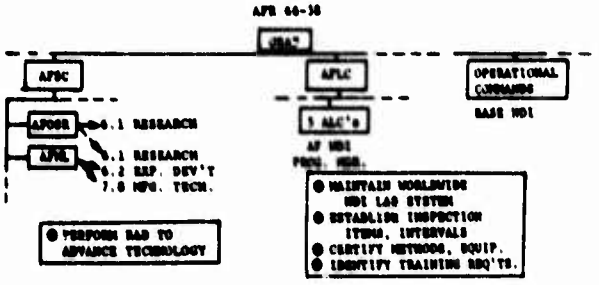


Figure 1. NDI/NDE Program Responsibilities.

The Air Force Logistics Command (AFLC) oversees a worldwide NDE laboratory system with inspection groups at over 195 bases and at the 5 Air Logistics Centers (maintenance depots). Furthermore, AFLC establishes inspection schedules and approves NDE procedures and equipment, and finally, identifies personnel training needs. An Air Force NDE Program Manager is assigned to coordinate all of these activities. The R&D responsibility is assigned to the Air Force Systems Command (AFSC). The program is conducted through two organizations primarily: the Air Force Office of Scientific Research (AFOSR) which manages the 6.1 Basic Research work and Air Force Materials Laboratory (AFML) which conducts the 6.2 Exploratory Development and 7.8 Manufacturing Technology NDE efforts. As shown, some 6.1 funding is transferred directly to AFML by AFOSR for the performance of specific basic research projects on behalf of OSR.

A key advantage in the USAF program lies in the fact that all NDE R&D and Manufacturing Technology work is planned and conducted by two specific compatible organizations (AFOSR and AFML) within one single command.

The USAF NDE development program performs two major types of functions:

1. Research and Development

   New Fundamental Technology
   Technology Applications
   Manufacturing Technology

2. Quick Reaction Engineering Support to other USAF organizations.

The major thrusts in these two functions will be reviewed in a moment.

Program activities are focussed on several types of problems:

- Specific problems--solution of a special problem and specific requirements. For example, improved techniques and instrumentation tailored to solve the C-5A wing fastened joint inspection problem.

- General problems--solution of a specific type of problem with application to hardware in general. For example, the early detection of hidden corrosion.

- Generic problems--development of new technology to increase NDE capabilities to apply to a wide range of requirements. For example, improvements in the various aspects of the ultrasonics method in order to increase the probability of detection of flaws in hardware under field conditions--a fairly general but serious problem.

The 6.1 Basic Research program being conducted by AFOSR is concentrating on two particular areas which are shown along with several examples of specific programs therein:

- Advanced Acoustics Science
  - EM Acoustic Transducer Concepts
  - Acoustic Emission
  - Particle Emission
  - PVF_2 Film Transducers

- New Physical Methods

  - Positron Annihilation
  - Optical Detection Methods
  - X-Ray Strain Probes for Composites
  - Nuclear Magnetic Resonance Techniques

OSR is concentrating on the development of new knowledge of acoustics which may lead to fundamental improvements in the ultrasonics NDE method. The thrust on new physical methods is exploring phenomena which may offer new ways to detect flaws early in their formation by measuring subtle physical changes that can be related to the fracture process. The remaining part of the USAF NDE R&D program (6.2 and 7.8) which is conducted by AFML, has undergone a change in overall philosophy which is summarized below:

1. Concentrate resources on a few key development requirements.

2. Emphasize improvement in in-service NDE reliability.

3. Include field implementation phase in development programs.

4. Continue focussed fundamental NDE program--initial thrust: ultrasonics.

The number of development needs have grown to the point where resource availability is far outstripped. Thus, rather than attempt to deal with most of the problems, many inadequately, a few of the most critical problems will receive proper resourcing to assure timely results and lesser priority programs will be postponed.

A significant portion of program resources will be assigned to increase the reliability, sensitivity, and general flaw detection capabilities of the major techniques. Current emphasis is on the improvements of ultrasonic equipment capabilities during the next 2-3 years. The next major emphasis will probably be on eddy current techniques.

As Dr. Kelly mentioned earlier, the weakness of many past programs has been due, in part, to an inadequate job of technology transfer to the field, including the development and testing of prototypes and/or procedures and the reworking of prototype designs or procedures as part of the program to yield a well engineered model truly ready for routine productions. Present and future programs will, therefore, feature a strong phase to complete this development cycle.

Finally, we consider the continuation of the strong fundamental NDE program, epitomized by the ARPA/AFML program being reviewed at this conference, to be a vital step toward the creation of sensitive, accurate and reliable NDE.

The AFML program is organized into two program areas: The Technology program using 6.2 funding plus some 6.1 funding from AFOSR; and the Applications program using 6.2 and 7.8 funds. The program thrusts of each program area are shown in general order of priority:

Technology

- Quantitative Ultrasonics
  - Transducers
  - Signal Acquisition
  - Signal Processing
- Quantitative NDE of Surface Flaws
  - Surface Wave Ultrasonics
  - Electromagnetics
  - Optical
- NDE of Advanced Materials
  - Composites
  - Adhesive Bonds
  - Ceramics

Applications

- NDE of Fastened Joints
- Field NDE Reliability Improvement
- Composite In-Service Inspection Methods
- NDE of Complex Shapes
- Adhesive Bond Evaluation Methods

Discussion

The details of the Technology program thrusts are being covered in these proceedings. In the Applications program, the NDE of Fastened Joints thrust contains work to develop instrumentation capable of detecting 0.1 inch radial length cracks from fastener holes, both in outer and interior joint layers, without fastener removal: The Field NDE Reliability thrust deals with the design and manufacturing technology of new, advanced state-of-the-art ultrasonic equipment (pulser-receiver, transducers, signal processing) capable of higher reliability flaw detection under in-service conditions; the Composites In-Service Inspection Methods thrust will produce improved, semi-automated inspection processes/equipment for reliable composite structure NDE under service conditions; the NDE of Complex Shapes thrust supports NDE equipment/technique developments for computer-aided flaw and metrology evaluation of complex-shaped airframe structures and engine hardware (disks and blades); the Adhesive Bond Evaluation thrust is completing work on NDE methods to assess pre-bonding surface conditions and to detect strength-degrading disbonds in high performance bonded structure.

In the area of Quick Reaction NDE Engineering Support (Systems Support) the AFML provides several types of technical service including:

- NDE advice to Weapon System Program Offices (SPO's)
- Technical aid to field organizations with NDE problems
- Development and improvement of USAF NDE specifications
- Special NDE method improvement projects and new method evaluations

One final word on some projections of the future technology requirements of interest to the USAF. Among the more important ones are:

- Automation and computer-aided decision processes
- Major advances in eddy current capabilities
- New/improved radiography capabilities and roles (e.g., neutron radiography if an on/off generator is developed)
- Improved ultrasonic techniques useful in finding interior layer defects
- "Clean", consistent transducers
- Detection methods for small, tight surface flaws
- Quantitative flaw growth monitoring in a real time

One last comment. The AFML is conducting a detailed program roadmap review for all interested groups--industry, academia, government--in Dayton, Ohio, on 19-21 July 1977. At this review, the FY77, FY78 and FY79 program activities will be described in detail. Attendees will receive a report of the details discussed.

In the short space available, I have attempted to summarize the main features of the USAF NDE development program and plans, highlighting the factors shaping the major thrusts. I shall be happy to elaborate further upon request.

Reference

1. Forney, D. M., "NDI in the U. S. Air Force," British Journal of NDT, May 1976, pp. 72-81.

S. LORBER: Good morning, gentlemen--lady and gentlemen, Nancy. It's indeed a pleasure to be here and your agenda is very impressive. I wish I could understand it. The coffee breaks I understand, and the lunch. The money and the other subjects are indeed interesting to you, I'm sure, but I'm on the other end of the stick. I'm the Director of Product Assurance in the Readiness Command--Materiel Development and Readiness Command, and my purpose is to use the results of your experiments and that's what they are, experiments. Until they are applied, practically, repeatably, and in the field, they are just experiments. I need solutions, I need them today. Now my objective is very simple. Now this is an old chart (Fig. 1), but I always use it to remind myself what my job is. And that's to satisfy that man, a very simple man, a soldier. Last Tuesday I received a flasher report from Europe; we had a premature in a 81 mm mortar shell, two soldiers were killed, several injured seriously We make millions of 81 mm mortar shells, it's fired by an infantry man, he carries it around with him, puts it in the back of his truck. Fortunately or unfortunately, depending on your point of view, one in a million might be good or bad, but that's my job and I'm looking for the techniques that you are developing that will at least assure that man that the material I'm fielding will not premature, that it will work as intended. That's my job and I need your help to do it but I need your help today. I need your help today to find a way that I can solve that problem today because we're making them today--we're issuing today in large quantities.



Figure 1. The user that must be satisfied.

Okay, now let's look at the Materiel Command briefly and what are our problems. This is the way we approach our problem. I use the Army's Materials Mechanics Research Center (AMMRC) spider chart technique (Fig. 2) and this is to show you the mission areas that we're concerned with in DARCOM. It covers the whole gammit of Army material, anything you would expect the Army to have. We carry out our program through eight development commands, about forty project managers, two laboratories, and five readiness commands--about 101,000 civilians and 16,000 military. Incidentally, there are twelve depots involved where we do our overhaul work towards the issue. So you see, the areas that we are concerned about--everything--and some of it rather exotic, some of it rather simple. For example, road wheels--rubber on aluminum, on tanks--well you know if you lose your road wheel on a tank, the tank is immobile and that's almost as bad as a premature in combat and if you've ever been in combat.... I've had the bad fortune or misfortune of looking at all the tanks that were killed in Israel during the 1973 war. It's quite frightening when you look at what happens to a tank crew when their tank is immobile. When you're hit by one of the shells, you're just literally cooked inside that tank. So just losing something like a road wheel can be very serious to a tanker. Not as exotic as some of the aircraft, but a very real problem for us in the Army and we need your techniques to make sure that we can produce those road wheels so that they meet our needs. That's just one item. Talk about fuzes...that's the front end of the 81 mm mortar. It's a probable cause of that premature. You make fuzes for rounds of ammunition anywhere from the smallest round, 20 mm, on up to the largest. What can I do to make sure that those fuzes are assembled properly? Simple, something as simple as that--assembled properly, that's what causes prematures. What techniques can you give me to solve that problem? Well, the way we go about trying to identify problems--and this is what Dr. Kelly, I think, was driving at--I'm on the other end; I have to identify the problems and find some way to force your fraternity to help me solve them. But I can't blame you unless I can identify them and force you to look at them. That's my job and I'm not doing it too well--I'm not doing it too well. I am not identifying the needs. For some reason we think that we have to have a solution before we can identify the needs. I'm not worried about that anymore. I am looking just for the problem so that I can force you to address those issues. And what I've tried to do is get the people you see in the center here, our project managers and our development commands, to set up a program for each of their major systems; a review at the beginning of the development. I'm talking about the XM-1 tank, I'm talking about the new ammunition, the new mortar, the new artillery piece. The project manager who is responsible for developing and fielding that item as a part of his development effort to identify the issues concerning inspection and test that he faces so that he can force the community to solve those problems as part of his development effort. And I'll show you one example at the end. But we're asking him to do it so he can force the laboratories and force the people in technology fields to help him solve his problem--bring the needs to you and help you solve them.

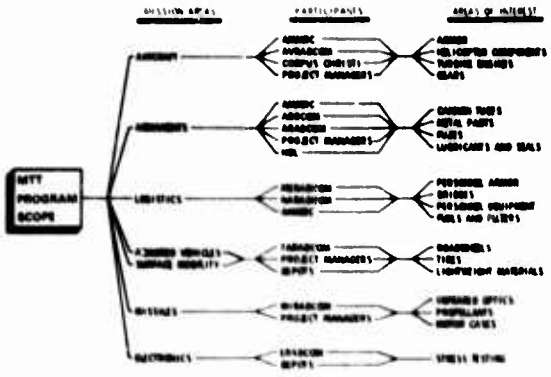


Figure 2. Spider chart showing DARCOM mission areas.

Our first attempt using the spider chart technique is shown in Fig. 3. I've asked the people at AMMRC--here are the mission areas we talked about earlier--I've tried to identify the basic inspection needs that I have, and then on top I have indicated the techniques that are essentially available for me to use and on the bottom a first cut of what we think we need in terms of some research so that we will have the techniques available to the field. Now I'm not going to try to tell you what they are. You know more about those techniques than I do, but this is what I'm trying to do as a user of your techniques to bring to you my needs and force you to address them. I say that rather forcibly, but you know what I'm really saying--that if those are my needs and I've identified them, then I have to find some resources to help you to solve the problem. It's easier to get resources when I know there is a need. Now, thinking about the problem that Dr. Kelly raised earlier and then thinking about my point, you know what I guess I'm looking for is a matchmaker, someone to bring us together, that's our problem. We've got to do more of that. We have to break down those walls and force the technology people to get involved with the people who have needs. In this symposium, how many people here are users of these techniques? That's part of our problem. I have my meetings and you don't attend those meetings, but how can we get together so that we can better identify needs to help solve the problems facing us today. Well, I guess I said part of it. I said that within the Army the first solution is the top one--how can I bring together the people who have problems, the project managers, the development command, to identify basic needs, highlight them and do it at an appropriate time so that I can get funds out to do the research necessary to develop the tools. That's our problem and we're trying to work on it.

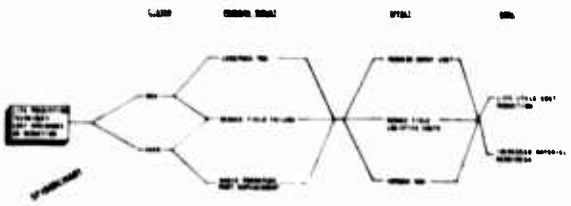


Figure 3. Goals for mechanical predictive technology.

Within the second area, what are my drivers? (See Fig. 4.) They are twofold and very simple. One I have already mentioned (to assure the reliability and safety of Army material) and, second, obviously, I think, to increase the productivity of the industry that supports us and I think NDE does both and does it well if we apply it properly. Third, we are on our way to trying to identify the needs so that we can put our money to solving our most pressing problems. One other approach that we are using is trying to marry NDI with our reliability effort. What we are trying to find out is whether there is some way that we can improve the life of our end items in our major components and we believe that by the application of proper reliability techniques coupled with the NDI techniques we can actually: (1) predict more accurately the life; (2) properly monitor our equipment and extend life without going into planned overahul. So that's another effort, and you can see some of the efforts underway.

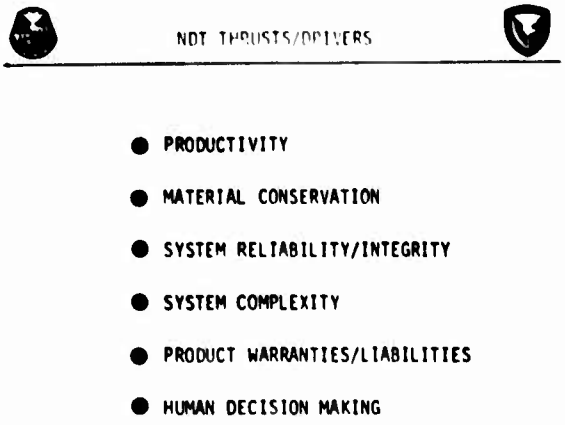


Figure 4. Drivers of DARCOM activities.

This is a somewhat similar chart (Fig. 5) I think I've seen earlier, but this is the approach we are using: determine the wear and failure mechanisms as part of our development effort; use the techniques that we can for proper determination and for proper monitoring in the field (you see it here); continue the selected techniques, confirm them in our depots and manufacturing plants, and as our confidence increases, increase the life of our equipment. But this is an approach we're trying to get together on with the experts in the field. I have only one example (Fig. 6) of how this can be used and we have high hopes for this application--the screening of 105 shells. We make about 60,000 shells a day when we are in production on this item and we have about 15 plants making these shells. Obviously, we are not making that many now; we're not at war, thank God. But when we are, we have 15 plants making shells, loading, and inspecting. Why do we inspect them? A crack in the metal parts or an improper fill leads to a premature that I mentioned earlier. We have a technique that is almost real time now which we'll put into our production line and it will actually screen these shells 100% for this defect. No plates. This is some of the work that you have been doing and I think some of the people here could talk to you about it. I'm not really that much of an expert in the technique used, but it's very promising. It will be going into our first modern plant, I think, in about six months. This will give us greater assurance that the ammunition is safe. It is a natural output of some of the work that has been done by your people. Now the one point problem I have with this system--I'm not satisfied yet. It solves my reliability problem and it solves my safety problem, but what I need to do now is find some way to couple that with the manufacturing process so that I really can adjust the process properly and not make bad materials. It doesn't solve many problems to sort if the output isn't great. I've got to find a way of putting this kind of equipment into the line to make it manage the line; actually manage the line to preclude the manufacture of bad materials. That's the next step, but I have a good screening technique. Now, I have some advice for you--I use it quite often but it helps. Thank you very much.

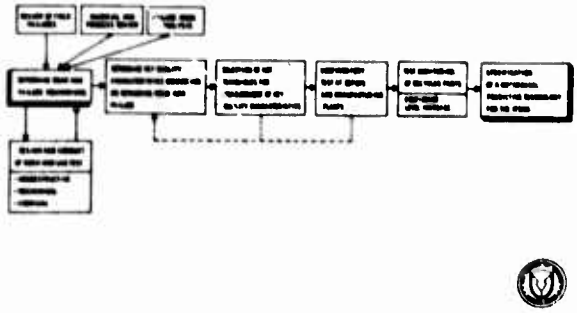


Figure 5. Mechanical predictive technology program schematic.

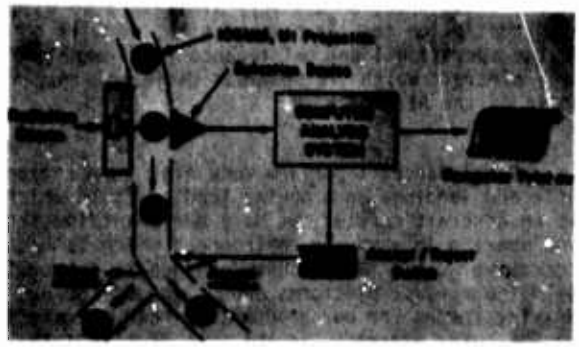


Figure 6. Automated inspection device for explosive charge in shell (AIDECS) conceptual model.

J. J. KELLY: The Navy is a multi-mission type of service and uses a variety of platforms to accomplish these missions. As you can see, we are in the air with aircraft, and using conventional warships like a carrier, and have an advanced type of high performance craft like a hydrofoil. For those of you who are not familiar with these crafts, we also have surface effect type ships, and amphibious craft which travel over both land and water which are air-cushioned landing craft, the artist's concept of these craft operating over the waves. We also have submarines which we saw before and missiles, both strategic and tactical. So we have a wide range of platforms to be concerned with.

The Navy is definitely concerned with flaws and their detection in these platforms from at least two points of view. One, from the concept of the construction and repair phase - what do we have to detect at that stage; and secondly, during the operation and maintenance phase with the equipment. I will discuss the major NDE requirements for each platform in terms of these two categories. However, since the Air Force and Navy requirements in aircraft construction are very similar, I've eliminated that slide for the sake of time and will go on to the operational and maintenance requirements for Navy aircraft which are somewhat different than those of the Air Force.

Naval aircraft perform very high impact take-offs and landings on a moving landing field which is an aircraft carrier; we have different loadings and operate in a marine environment which is highly corrosive. This latter consideration is common to all of our naval platforms and is one of the driving forces for our programs, either in materials or NDE. For aircraft, in the area of structures, we are concerned with fatigue, fatigue-induced cracks and the growth of cracks, delamination of composites caused by minor impacts like dropping tools and wrenches on the wing of the craft which are basically undetected by visual examination, and also corrosion under the painted surfaces. There are a number of NDT techniques which are listed in Fig. 1 and which are commonly used for the detection of these flaws.

The major limitations that are shown can be applicable to one or more of the NDE techniques - they are not in a line-by-line relationship. For example, safety limitation really applies only to the x-ray restrictions that are imposed with the use of the equipment, while operator sensitivity limitation is applicable to eddy current and ultrasonics in terms of the skill of the operator who uses the equipment, and also for the interpretation of the results. I've used this same type of limitation throughout my discussion. Also, since we're dealing with built-up fabricated structure, accessibility with the use of NDE equipment is a very, very vital concern to us and a serious limiting factor.

In the propulsion area, we are concerned with the small flaws on the order of 10^{-5} inches. These are in the ceramic materials used in gas turbines and I think you heard enough on the paper in the Poster Session by Rice from NRL and some of the work discussed last night to cover this aspect.

In the conventional ship area, a major area of concern is the adequacy of steel welds during the construction repair phase. I've listed some of the problem areas that would be of concern in Figs. 2 and 3. The biggest problem that we have is that we are dealing with thousands of feet of welds so a speedy NDE capability is vital. We have to have sufficient area coverage, if it is possible; and safety, as I mentioned before, is a problem of cost associated with safety requirements. We have to clear areas when we begin to do x-rays. That holds up on the actual construction work. In terms of the hull coating quality, this is a critical area for the Navy with conventional ships. For the large areas that we have to deal with, our best inspection technique is visual observation and a fingernail test - stick it under the paint and see how well it maintains its adhesion. We have a large problem in this area in terms of scheduling. The last item usually on a ship-building schedule is the painting, and that's when everybody is pushing the ship out so you don't really have too much time to take a good look at it.

AIRCRAFT	REQUIREMENT	CURRENT CAPABILITY	LIMITATIONS
STRUCTURE	• FATIGUE CRACKS IN METALS AND COMPOSITES (.005 TO .05 INCHES) • CRACK GROWTH IN METALS AND COMPOSITES	ULTRASONICS EDDY CURRENT X RAY ACOUSTIC EMISSION PENETRANTS HOLOGRAPHY	• SAFETY • OPERATOR SENSITIVE • CRACK SIZE AND LOCATION • ACCESSIBILITY
	DELAMINATION OF COMPOSITES CAUSED BY MINOR IMPACT	X RAY ULTRASONICS COIN TAP	• SAFETY • OPERATOR SENSITIVE
	CORROSION OF PAINTED METAL STRUCTURE	EDDY CURRENT ULTRASONICS NEUTRON RADIOGRAPHY VISUAL	• SAFETY • OPERATOR SENSITIVE • LIMITED COVERAGE • ACCESSIBILITY
PROPULSION	• FATIGUE CRACKS IN TITANIUM AND CERAMIC COMPONENTS • CRACK GROWTH IN TITANIUM AND CERAMICS	SAME AS FOR STRUCTURES	SAME AS FOR STRUCTURES

Figure 1. U. S. Navy NDE requirements of operation and maintenance, aircraft.

CONVENTIONAL SHIPS	REQUIREMENT	CURRENT CAPABILITY	LIMITATION
STRUCTURE	ADEQUACY OF STEEL WELD QUALITY • LACK OF FUSION • LACK OF PENETRATION • COLD CRACKING • POROSITY • INCLUSIONS	X RAY ULTRASONICS PENETRANTS MAGNETIC PARTICLE EDDY CURRENT	SAFETY OPERATOR SENSITIVE SPEED DEFECT SIZE AREA COVERAGE
	HULL COATINGS QUALITY • HOLIDAYS (.005 INCHES) • ADHESION STRENGTH • SURFACE ROUGHNESS • THICKNESS	VISUAL MAGNETIC EDDY CURRENT CAPACITANCE	OPERATOR SENSITIVE SPEED AREA COVERAGE
PROPULSION	SUBSURFACE CRACKS VOIDS IN PROPELLER BLADES AND VALVES	X RAY ULTRASONICS	SAFETY DEFECT SIZE

Figure 2. U. S. Navy NDE requirements construction-repair, conventional ships.

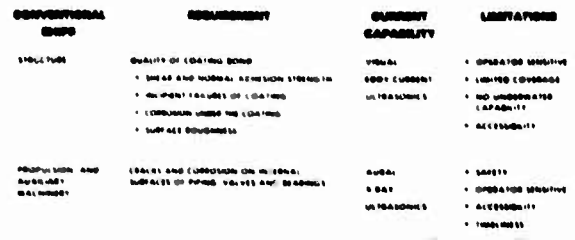


Figure 3. U. S. Navy NDE requirements operation-maintenance, conventional ships.

In the area of propulsion we are looking for subsurface cracks and voids in the propeller blades and waterjet impellers. I'd say we have the NDE capability and techniques for this particular application. It's just that some of them are troublesome in terms of the limitations I've shown.

I've listed other limitations where applicable. In terms of the propulsion machinery area, we have no way of monitoring in-situ the material condition of valves and bearings - there is some effort using fiber optics for examining the condition of the bearings. We are looking at various parameters now, but it's still not a fully implemented system in the field. Right now we rely more on the ear of an experienced crewman. If the valve doesn't sound right, something's wrong and that is the first level of detection. Accessibility, of course, is a problem here.

High performance ships are fabricated from a thin gauged material, 3/8" to 1" thick. It has thousands of feet of welds and is typical of some of the construction that we have. Conventional NDE techniques are used and we have problems. For the thin gauge aluminum alloys, x-rays provide poor quality radiographs. We have problems due to the lack of standards in this area and the possibility of using composite structure for some of the high performance ships adds to our problems. With composite structures, I think we have the same problems that everybody else has been pointing out except we will use them in a marine environment which will aggravate it to some extent.

In the area of propulsion, we have the same kind of problems with the gas turbines that we had on the aircraft except now we are working at higher temperatures and closer to the highly corrosive, marine environment. We have subsurface cracks and voids in the valves and piping systems and in bearings that are difficult to detect.

For high performance craft, in terms of operation and maintenance, we are concerned with fatigue cracks or grout crack growth in some of the structures. We have some of the capability in terms of NDE. However it is not adequate enough for us. Accessibility and the lack of an NDE underwater capability are problem areas. Detection of delamination, disbonds and composite-metal interfaces integrity where we're joining composites to metal interfaces in the structures are major items of concern. We do have a good sensitivity for small defects in this area. Accessibility is a critical problem. The quality of coatings I have already discussed.

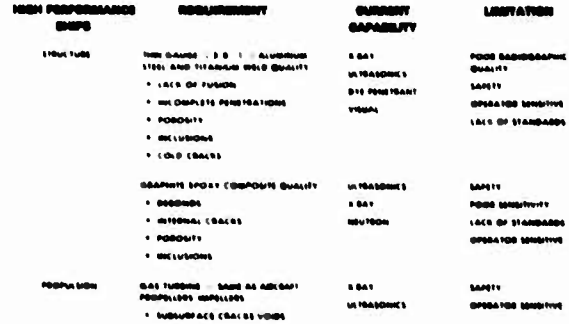


Figure 4. U. S. Navy NDE requirements construction-repair, high performance ships.

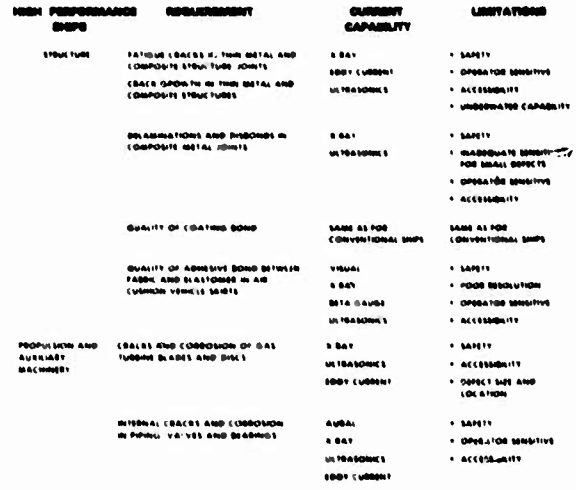


Figure 5. U. S. Navy NDE requirements operation-maintenance, high performance ships.

For air-cushioned vehicle skirt systems, assessment of the integrity of the adhesive bond between the rubber and the reinforcing fabric is vital. We have problems in finding out just how good a bond we have and how it performs in service or in test. We have no really good handle on this right now. We ran some x-rays and basically, all we could see was where the gross failure is and that's all. We know no more than that. We couldn't find out anything from it and yet we know there is damage taking place in other parts of the test specimen as indicated by changes in the physical properties. In the area of propulsion per-

formance, we are concerned with cracks in gas turbine blades - we are looking for NDT capabilities there and for detection of internal cracks and corrosion in the piping systems. This is the same problem as found in conventional ships. For submarines there are a number of problems which I will not discuss at this unclassified meeting. I'll just say that some of the problems are similar to what I've shown for some of the other areas. For example NDE requirements for submarine hull coating and those of conventional ships are not very much different.

In the area of missiles, these are some of the problems - which I think Frank Kelly addressed earlier. Our particular problem is that we are looking at a number of different type nose tips for these missiles, and in the case of the graphite composite we know that we do not want a defect any larger than .006 inch crack. That's one criteria we have. For the carbon-carbon composite we do not have a defect level established yet. Basically, there's no real problem with the NDT capabilities that are available right now except for the obvious one. We just haven't been able to relate the defect size to the performance that we get except in that one case. For missile structure, I'm not going to go into that really too much - it's self-explanatory. For the motor case and liner and interface voids, I think Dr. Kelley addressed that before.

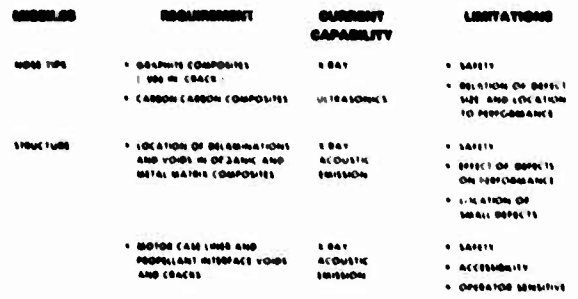


Figure 6. U. S. Navy NDE requirements construction-repair, missiles.

In this summary chart the covered area relates to thickness range which we are interested in. I have basically summarized what the requirements are we have been looking at.

In terms of NDE needs, I would think that our first requirement would be reliability of the equipment, followed by safety. I don't think you have any idea of the cost for doing NDE inspection in the field or a shipyard. We don't do 100% inspection, only the critical areas and it still drives costs up. The other need is the reduction in required skill level. We need NDE equipment for field use where we do not have to rely on a highly skilled operator. For example, we have used electronic technicians, who are fairly well educated in the Navy systems, with eddy currents and evaluations. The results were erratic. They found fatigue induced cracks in ship structure that would indicate near term failure. When an experienced radio eddy current inspector performed the same evaluation, he didn't find the same flaws and those that he did find were not that large. Because of the problem of accessibility, there is a need for more compact equipment.

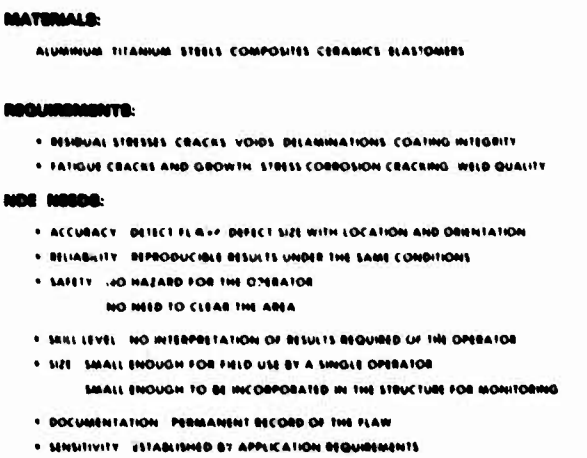


Figure 7. U. S. Navy NDE requirements.

NEW TECHNOLOGY FROM ARPA/AFML

D. O. Thompson
Science Center, Rockwell International
Thousand Oaks, California 91360

and

H. M. Burte
Air Force Materials Laboratory
Wright-Patterson Air Force Base
Dayton, Ohio 45433

D. O. Thompson (Science Center, Rockwell International): My purpose in this talk is to introduce the Poster Session that follows. We believe that most of the work presented in that session is ready for the next step of development. One of the key elements in this step is to find the "window" which can make use of these new pieces of technology. I truly appreciate the opportunity to hear the talks from the Air Force, Navy, and the Army which will help to identify some of these slots. I'd like to give a bit of our program philosophy that is important in this regard. On Wednesday, you heard some of the fundamentals of the ultrasonic work that we have been doing; work that has resulted in procedures which now are capable of producing numbers that characterize a defect. In achieving this capability, there are a number of improvements in various elements of the ultrasonic apparatus that have a useful identity of their own, i.e., they have a spinoff capability Thoseare the elements that we wish to talk about this morning and to identify as having reached a proof-of-principle plateau, and, if you will, are ready now for the next question. In the context of Dr. Frank Kelley's remarks and the needs identified by the Tri-Services, we must now seek to put them into specific problems for evaluation. As indicated also by Dr. Kelley, this is a very important step in developing a technology flow within the DoD. However, research must continue in order that future results may also be harvested. With this background in mind, I'd like to introduce some of the topics that you'll see in the Poster Session that have been developed under ARPA/AFML sponsorship.

The first package of elements that we have pursued in achieving a quantitative capability is concerned with items providing options for improved ultrasonic reliability; fidelity, improved spatial resolution, processing, and so on. One of the posters you will see is by Professor R. M. White who has been developing ways to provide inverse filtering for ultrasonic NDE systems. He has adopted two approaches, the first being a SAW compensated device, and the second an approach utilizing CCD device technology. Key points that can be provided by this technique are summarized in Fig. 1. The second topic in this area has been developed by Prof. V. Newhouse and associates at Purdue. This work has not been a direct part of the current program, but funded under a separate ARPA/Air Force program. He has demonstrated a proof-of-principle utilizing deconvolution processes which permit another approach to the defect characterization problem through signature comparison techniques. He utilizes both adaptive and minimization procedures which have to make some assumptions about the nature of the object. A summary of his work is provided in Fig. 2. A third topic in this group has been developed by Prof. Ken Lakin of the University of Southern California. One of the things that we have found in our efforts to develop quantitative information from ultrasonic return defect signals is the problem of not knowing really what the transducer does and what its characteristics are. He has developed a technique that allows one to do transducer modelling using the complex impedance and conversion efficiency to derive the acoustic output from measured electrical parameters, including a way to define and measure the effective gain of a transducer. Effective gain in this context is used in an overall sense. His system provides a convenient way to characterize the radiation patterns of the transducer and the displacements on any plane in the beam profile, including the surface of the transducer. This feature includes techniques to provide imaging of both the amplitude and phase response of the transducer plate. We believe that a standardized facility to look at transducers would go a long way toward providing ways to write better transducer specifications and improving ultrasonic reliability. This work is summarized in Fig. 3. Another topic in this group is a series of computer aided signal processing techniques, or software packages. A number of them are summarized in Fig. 4; these are available for use. These include procedures for transducer normalization, various windowing functions to improve the effect of signal-to-noise ratios, size estimation procedures, automatic classification of acoustic emission signals, and other topics. In addition to this work, which was specifically designed to aim at some of the quantitative problems associated with signal acquisition and sorting, the Adaptronics work is well known and very effective. It has produced a number of new results as a result of this program, although it existed well in advance of the start of the current effort. Finally, Fig. 5 gives a summary of a new concept for ultrasonic standards that has emerged from the quantitative scattering work in this program. The concept utilizes the sample preparation work done by Neil Paton, some of the theoretical work by Dick Cohen of the Science Center and Prof. Krumhansl and his associates at Cornell, and measurement procedures that have been developed by Bernie Tittmann. It is one of our beliefs that if we are going to make good quantitative ultrasonic measurements we must be

able to provide a system calibration. That is an essential and basic experimental concept. There are certain features in the suggested approaches that are quite different from standard flat-bottom hole approaches. Our work starts really with the recognition of the similarity between the solid state ultrasonic problem and the radar problem. Certain features that come out of this approach we believe to be advantageous and provide a way to separate unwanted transducer effects and materials variability from a true signal return. The concept introduces the utilization of theoretically developed signal returns. We believe this to be important, for it provides an operator with a set of expectation values for his calibration process, and thus, fills a gap in our current practice.

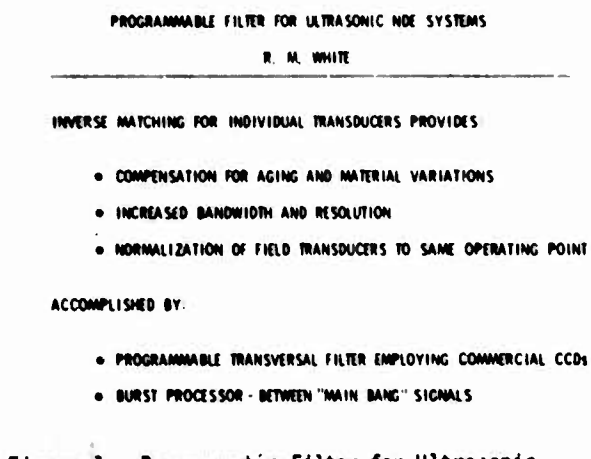


Figure 1. Programmable Filter for Ultrasonic NDE Systems.

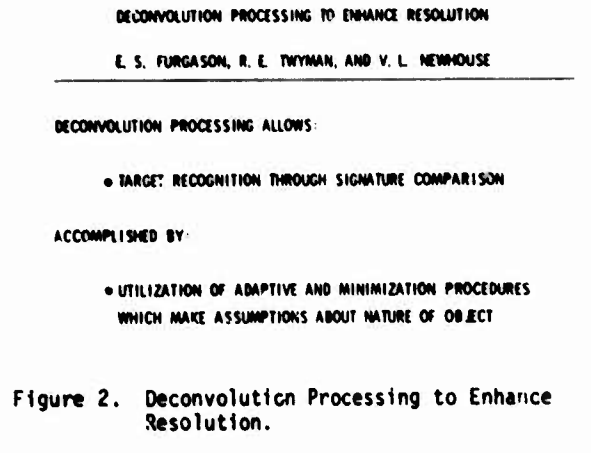


Figure 2. Deconvolution Processing to Enhance Resolution.

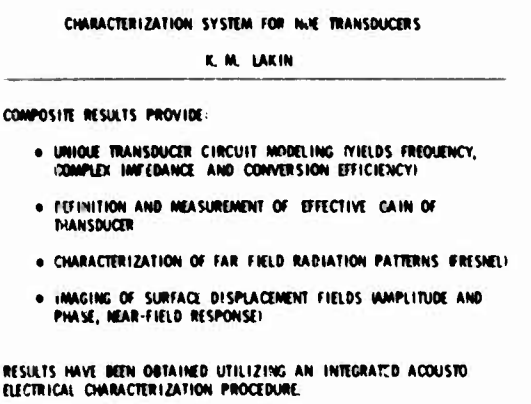


Figure 3. Characterization System for NDE Transducers.

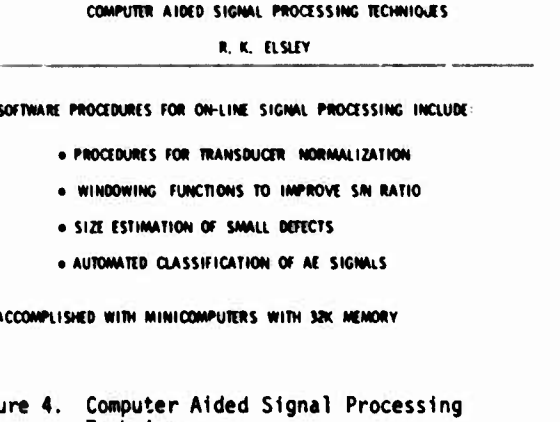


Figure 4. Computer Aided Signal Processing Techniques.

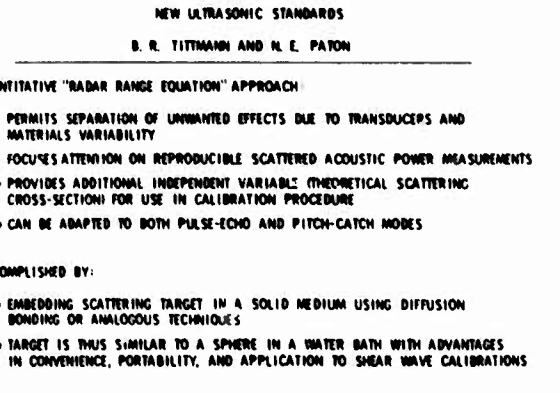


Figure 5. New Ultrasonic Standards.

Another part of the program that has turned out to be exceedingly rich in new thoughts and capabilities is that of the non-contact ultrasonic transducer (EMAT). Improvements made in this area by a number of authors are summarized in Fig. 6. Also shown in the Poster Session this morning are some applications that have been developed in parallel programs. One of these, sponsored by the American Gas Association, applies to the inspection of buried natural gas pipelines. Another one, sponsored by the Army, applies to the inspection of projectiles. A third one sponsored by EPRI pertains to the inspection of heat exchanger tubing. A fourth one, sponsored by Rockwell International, relates to the high temperature inspection of weldments.

OPTIMIZATION AND APPLICATION OF EMATs

R. B. THOMPSON, C. M. FORTUNKO, C. VASILE, G. ALERS, T. MORAN

PROVIDES CAPABILITY FOR NONCONTACT ULTRASONIC TRANSDUCTION:

- HIGH SPEED OPERATION (20 mph DEMONSTRATED)
- HIGH TEMPERATURE OPERATION (600 F DEMONSTRATED)
- REMOTE CONTROL AND AUTOMATION APPLICATIONS
- GENERATION OF NEW WAVE TYPES SUCH AS HORIZONTAL SHEAR
- GENERATION OF CODED WAVEFORMS FOR RESOLUTION IMPROVEMENT
- GENERATION OF ELECTRONICALLY CONTROLLED ANGLE BEAMS
- RESIDUAL STRESS DETECTION IN FERROMAGNETIC MATERIALS

IN-PROGRESS APPLICATIONS:

- BURIED NATURAL GAS PIPELINES
- 155 mm ARTILLERY PROJECTILES
- STEAM GENERATOR TUBES
- HIGH TEMPERATURE WELDS

Figure 6. Optimization and Application of EMAT's.

Another poster presented in the sessions gives the results of work by Prof. Kino and his students at Stanford in ultrasonic imaging. This work represents a transfer of technology that they had developed for the medical field into the materials area. They've achieved a number of things in this area which are summarized in Fig. 7, including transmission images of epoxy bonded boron fiber reinforced laminates, with significant hundred-speed increases while maintaining a resolution comparable to that of the current C-scan systems, and have produced images with a variety of ultrasonic wave types; i.e., Rayleigh waves, Lamb waves, longitudinal and shear waves.

ULTRASONIC IMAGING SYSTEM

G. S. KINO, T. M. WAUGH, AND D. COHL

IMAGING OF FLAWS PROVIDES A RAPID INDICATION OF FLAW POSITION, SIZE, SHAPE AND ORIENTATION. HAVE OBTAINED:

- TRANSMISSION IMAGES OF EPOXY BONDED BORON FIBER REINFORCED LAMINATES WITH 10⁵ FOLD SPEED INCREASE AND RESOLUTION COMPARABLE TO THAT OF MECHANICALLY SCANNED SYSTEMS
- FOCUSED REFLECTION IMAGES WITH RESOLUTION OF 2λ
  - RAYLEIGH WAVES
  - LONGITUDINAL WAVES
  - LAMB WAVES
  - SHEAR WAVES
- MEASUREMENTS OF LENGTHS OF CRACKS WHEN CRACKS NOT PARALLEL TO ARRAY BY DEFINING POSITION OF LINE SCATTERS AT ENDS

ACCOMPLISHED BY:

- ELECTRONICALLY SCANNED AND FOCUSSED IMAGING DEVICES PRODUCING REAL TIME IMAGES

Figure 7. Ultrasonic Imaging System.

The adhesive bond work has demonstrated proof-of-principle for both cohesive and the adhesive characterization in simple systems. Further work is needed in the case of complex, two-phase adhesive systems. This work is summarized in Fig. 8.

STRENGTH MEASUREMENT OF ADHESIVE BONDS

P. L. FLYNN, G. A. ALERS, AND R. K. ELSLEY

PROVIDES PROCEDURE FOR:

- PREDICTING COHESIVE STRENGTH OF ADHESIVE MATERIAL WITHIN BOND LINE
- PREDICTING STRENGTH OF ADHESION AT METAL-TO-ADHESIVE INTERFACE

ACCOMPLISHED BY:

- SIGNAL ANALYSIS OF ULTRASONIC PULSES REFLECTED FROM ADHESIVELY BONDED STRUCTURES
- ESTABLISHING A THEORETICAL MODEL FOR INTERACTION OF ULTRASOUND WITH LAYERED MEDIA
- RAPID COMPARISON OF THEORY AND MEASUREMENTS IN A COMPUTER

Figure 8. Strength Measurement of Adhesive Bonds.

Finally, proof-of-principle has been demonstrated for the non-destructive measurement of moisture in composites. One of these methods is demonstrated in Fig. 9. This work is based upon a direct measurement of the effusion rates of moisture from a composite material. Using these results and measured diffusion coefficients, the inverse problem has been solved to yield a quantitative map of the water concentration profile as a function of depth in the material. From this, a strength profile can be obtained.

MOISTURE DIFFUSION ANALYSIS (MDA) FOR COMPOSITES

D. H. KAELBLE

PROVIDES ANALYTIC CAPABILITY TO ASSESS

- DIRECTIONAL OR AVERAGED MOISTURE DIFFUSION COEFFICIENTS
- WATER CONCENTRATION VALUES AND CONCENTRATION PROFILES
- MICROSTRUCTURE AND STRENGTH DEGRADATION DUE TO WATER ABSORPTION

ACCOMPLISHED BY

- MEASUREMENT OF EFFUSION RATES
- INVERSION OF DIFFUSION EQUATION TO OBTAIN CONCENTRATION PROFILES

Figure 9. Moisture Diffusion Analysis (MDA) for Composites.

H. M. Burte (AFML): I want to identify two areas for additional comment that particularly intrigue me. One of these is the adaptive signal processing work in which available theory is used either to help train the network or at least to help define what experimental data are most important to acquire and feed into the network. This is a very powerful tool which we will be able to use increasingly as we define the windows for it. Next I want to re-emphasize the fact that, as Don said, our ability to describe the scattering from a flaw is growing significantly. We're even beginning to develop a meaningful capability of doing the inverse problem. More uses for this capability (beyond the subject of standards that both Don and George Birnbaum talked about) should be sought.

Finally I want to focus attention on the most serious problem we now face. As I have mentioned before, this is concerned with the reliability of flaw detection. If we plot the probability of detection with any NDE technique against a flaw size parameter, we always find a result that shows a zero probability at zero size slowly transitioning to almost 100% at some much larger size. The closer we can come to a step function which occurs at a selected size on the flaw size axis, the better off we will be and the more efficiently we can use our NDE methods. To what extent can our growing quantitative capability impact this particular problem?

As the number of practical inferences which can be drawn from our growing knowledge continues to increase, it becomes more and more important to start focusing relatively more attention, as several people have been saying and as Don has said, at defining what at Asilomar I called the specific window to use these possibilities. These are the real current needs with definable objectives and payoffs which can make use of the new technologies. These windows can stimulate not only a valid specific product, but they can provide the initial signposts to guide reduction to practice efforts into broad areas of use for the new knowledge. They generate enthusiasm and they also provide direction to the continuing research base. The work of the theorists can also be greatly helped if they know what they are looking for, what questions they are expected to answer. I challenge all of you, both scientists and technologists, to increase your efforts to define the specific ways our emerging knowledge can be put to use. And I thank you for what I think has been a very stimulating and effective symposium.

D. O. Thompson: Thank you, Harris. I would simply like to add that all of us in the program have benefited significantly from the guidance that our monitors, yourself, and your staff have provided. We consider it a privilege to be provided with an opportunity to utilize science in the solution of problems.

Again, I would like to take this opportunity to express our appreciation to the people at Cornell who have made so many efforts to cooperate with us. These include, of course, Professor Herb Johnson and his assistants, Mr. Noel Desch, and Mrs. Sharon Wellman. I'd like to thank all of our colleagues who contributed to the presentation of the program. Professor Jim Krumhansl, who has been a member of our program from the start, made the initial suggestion that we hold the meeting at Cornell this year. We are certainly grateful for the invitation, Jim. Finally, I'd like to express our thanks to our hostesses, Diane Harris from the Science Center, who has effectively coordinated most of the meeting from the Science Center end, and Ms. Kris Molt from Cornell who has operated as her counterpart here. We certainly do appreciate all these efforts and I hope that you all have a good meeting.

PROGRAMMABLE FILTER FOR ULTRASONIC NDE SYSTEMS

Richard M. White
Department of Electrical Engineering and Computer Sciences
and the Electronics Research Laboratory
University of California, Berkeley, California 94720

ABSTRACT

Transversal filters based on the charge-coupled device (CCD) technology may be applied to processing received signals in an ultrasonic NDE system. Filters having a fixed response (fixed tap weightings) could be used to compensate for the characteristics of a given ultrasonic transducer. A more flexible arrangement allowing programmability employs a CCD delay line whose tap electrodes are accessible externally for weighting. The response of this device can be altered by changing a set of resistors mounted on a printed circuit board which can be plugged into a socket connected to the CCD. Proper response for a given ultrasonic transducer is obtained by plugging in the proper circuit board. Because present commercial CCD's allowing programmability have clock frequencies too low for direct processing of ultrasonic NDE signals, the filter is preceded by a CCD video delay line which quickly stores the return signal and then outputs it more slowly for processing during the time between successive excitations of the ultrasonic transducer.

Burst Processor System

The filter system that has been designed and constructed is illustrated schematically in Fig. 1. The signal from the NDE ultrasonic transducer is input to the "Analog Data Acquisition System" which consists of the Fairchild CCD321 analog shift register, a driver circuit board, and the necessary integrated circuitry to generate charge-transfer clocks of the desired frequencies. The NDE transducer signal is sampled at a high rate and stored in the CCD video delay line while the fast clock is supplied to the line. After storage, the clock generator drops to a lower rate and the stored signal is clocked out of the delay line and into the CCD transversal filter whose charge transfer is at the slow clock rate. As shown in the timing diagram at the bottom of Fig. 1, this entire sequence occurs between successive excitations of the ultrasonic system.

Analog Data Acquisition System - The heart of this system is the Fairchild 321 CCD analog shift register. This device was designed for the storage of 455 or 910 samples representing a line of a television picture. The device can accept clock inputs at up to 20 MHz; because of the rather demanding requirements on the clock signals (17 volts with as short as 10 ns rise and fall times for transfer, as short as 5 ns rise and fall for sample voltages) we purchased the complete Fairchild 321M module containing CCD and driver circuitry. A locally-designed circuit board was built for generation of the clock signals and the various required timing signals (see Fig. 2). This circuitry utilizes a 20 MHz crystal as its master clock and provides that frequency to the 321M as the fast clock signal. Dividers produce the slow clock signal which we chose as 100 kHz, allowing for a division by two on the circuit board of the CCD transversal filter (in other words, the actual transfer frequency in the transversal filter is 50 kHz, or the time per transfer there is 20 microseconds). Thus about 500 signal samples could be processed between excitations of a typical NDE system operating at 1000 pulses per second.

The sampling/storing/readout-out cycle is illustrated in Fig. 3 with high frequency sawtooth waveforms at fundamental frequencies of 1, 2.5, and 5 MHz respectively (top to bottom). The samples read out at the low rate are clearly seen in the major part of the photograph; input sampling occurred during the first 7% of the trace, at the far left where the waveform is blurred. On the bottom trace of Fig. 3 one sees the loss of detail--loss of the higher frequency components--as the fundamental frequency is raised and the sampling theorem dictates increasingly poorer fidelity of the sampled representation of the waveform.

When we first operated the data acquisition system in the burst mode, we found unexpected signals appearing in the output. The signals are apparent in Fig. 4, an oscilloscope display of the output when a sawtooth waveform is input to the video delay line circuit. One notices, in addition to the samples' waveform (which appears smooth here because of the large number of samples per cycle of the sawtooth), eight samples which are displaced from the sawtooth and appear as isolated dots in the figure. Eventually, the following was learned about the origin and treatment of this affliction of the CCD video delay line: The voltage spikes are caused by the different structure of the CCD circuit on its silicon chip at the points where the charge-transfer path turns corners. The CCD321 is being redesigned by Fairchild engineers to correct this problem and a new device is expected to be available within a few months. The spikes do not appear if the clock rate is not changed, and so the phenomenon was not noticed early in development and distribution of the CCD321 because burst processor use was not examined. The amount of added charge producing the corner-turning spikes is roughly proportional to the amount the clocking frequency is changed. The spike amplitude can be reduced (from the 0.5 volt observed here) by carefully maintaining proper time relations between the newly initiated transfer clock and the sampling waveforms; an "enable" terminal and circuitry for synchronization exists on the

321M circuit module board.

Even with the use of the enable synchronizing circuit the spikes are large enough to interfere with samples' waveforms, so the new CCD321 device will be welcomed. Further, use of the enable circuit prevents one from using multiplexed operation of the CCD321. When it can be used, multiplexed operation provides an effective doubling of the clock frequency for transfer in the video delay line: waveform samples are taken on each phase (+ and -) of the input clock, and alternate samples progress through two independent charge-transfer lines to be "interleaved" to form the output. (The multiplexed output is also relatively free of the large clock spikes which appear on the outputs of the two independent lines themselves.)

It is hoped that the redesign of the CCD321 itself and modification of its driver circuitry can permit burst operation in the multiplexed mode without the interfering spikes. In such a mode, operation with an effective clock frequency of 40 MHz and signal bandwidth approaching half that would be possible.

Experiments

The Analog Data Acquisition System is shown in Fig. 5. The device can be operated in a free-running mode or it can be operated in a triggered burst mode from either a remote or an internally-supplied local trigger signal. The real view of the instrument is included as it suggests some of the flexibility of the system. The A and B channels can be used independently or their inputs may be paralleled for multiplex ("mux") operation. Inputs are provided for A and B channels with signals no greater than one volt; otherwise the protected signal inputs (such as "a signal in") are used, though they are slightly less desirable because of a 4:1 signal amplitude decrease caused by the voltage divider in the protective circuitry.

The transversal filter having switches and adjustable resistors for tap weighting is shown in Fig. 6. The TAD32 is the large integrated circuit in the center of the circuit board. Most tests were made with this circuit.

Figure 7 shows a transversal filter circuit designed to use tap weighting supplied by resistors on small circuit boards (Fig. 8). The TAD32 is on one side of the 4 inch x 8 inch circuit board; weighting networks plug into a 40-pin zero-insertion-force socket on the opposite side of the board. Figure 9 shows a view of the entire setup.

The tap weights are related to the reference reflection waveform. For example, if one wanted to make a matched filter using the transversal filter, one would weight taps so that the transversal filter had an impulse response which was the time reverse of the reference waveform. Thus for the matched filter one might take sample values of the reference function (for example, using an oscilloscope display, or a digital voltmeter and a sample-and-hold circuit on the output of the data acquisition system), reverse the order of the sample values, and set tap weights proportional to those values. Figure 10 shows the reference waveform output from the data acquisition system and the output of a transversal filter, matched to this function, when the reference signal is fed into it.

To obtain the tap weights for an inverse filter (previously when using a SAW implementation we obtained the reference waveform), we took its frequency spectrum, inverted and weighted it with a windowing function, and then computed the impulse response of the filter to be fabricated. In a SAW filter there is a simple correspondence between the impulse response and the placement and length of each transducer electrode; hence it was relatively simple to design the SAW transversal filter from the impulse response.

With the CCD approach to transversal filtering, we at first employed different approaches--based on computer programs which yielded tap weights to achieve a given frequency response with a given optimized error. When we tested filters having tap weights adjusted to the computed values we found they did not yield improvement comparable to that seen with the SAW filter. We now believe this is either because phase information was necessarily lost in the process (owing to the nature of the programs used), or because the design responses were not closely enough approached by the optimized responses. These suppositions can be checked with more computer experiments, but a more fruitful avenue appears to be to design the CCD transversal filter directly from the impulse response itself (rather than from the frequency response) as was done with the SAW filters.

The reasoning behind this statement is that any filter which has an impulse closely similar to the design impulse response must perform the deconvolution correctly and. hence, produce the desired improvement of spatial resolution. With the CCD taps we have full freedom in weighting, but no freedom in the placement of taps along the delay line; taps will be equally spaced along the line because the manufacturer put them there. We noticed earlier that the impulse response "called for" some unequal spacings in the SAW electrodes, and so we would expect to be able to approximate such an impulse response with the CCD only by "sampling" the impulse response somewhat densely with CCD taps (for example, with four taps per cycle of the waveform).

Remedies which should enable one to obtain a close approximation to the design impulse response are: (a) using two TAD32 devices in series (they are designed to operate in this fashion), and (b) "reconstituting" the slowed-down signal as it is clocked slowly out of the acquisition system by lowpass filter (eliminates the clock frequency components) and sample it at a suitable rate by the TAD32 circuits driven with a clock whose frequency can be varied. In this way a sufficient number of cycles of the impulse response could be sampled with CCD taps, whereas now at a given instant each tap of the TAD32 is responding to only a single sample of the ultrasonic return signal from the acquisition system sampler. Even though the constraints of the sampling theorem

are being observed with regard to the input signal sampling in the acquisition system, the sampling of the desired impulse response for tap weighting is too sparse for an adequate representation. However, there appear to be no fundamental limitations which will prevent the fabrication of a programmable filter which will provide improved spatial resolution in ultrasonic test signals and which will provide a way to help "normalize" ultrasonic test procedures.

Acknowledgement

This work was sponsored by the Center for Advanced NDE operated by the Science Center, Rockwell International, for the Advanced Research Projects Agency and the Air Force Materials Laboratory under contract F33615-74-C-5180.

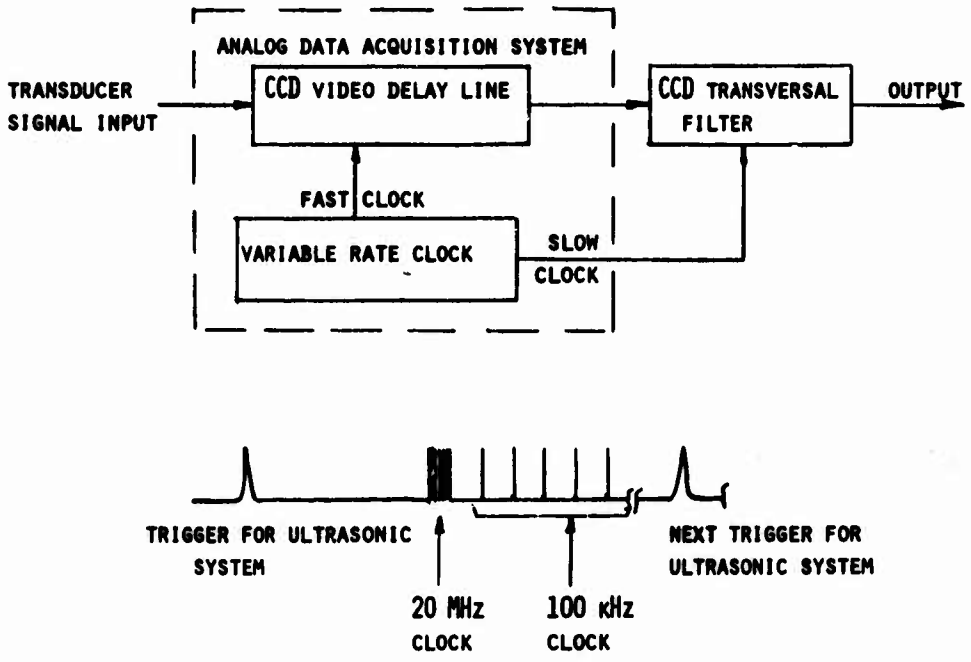


Figure 1. Burst processor system. (Top) Block diagram showing arrangement of analog data acquisition system which samples signal from NDE transducer using the fast clock from the variable rate clock generator. After acquisition, the clock generator frequency drops and lower frequency clock is supplied to the CCD video delay line, clocking out the stored samples slowly, and to the CCD transversal filter, whose output is slowed and filtered version of the signal input. (Bottom) Timing diagram for burst processor system.

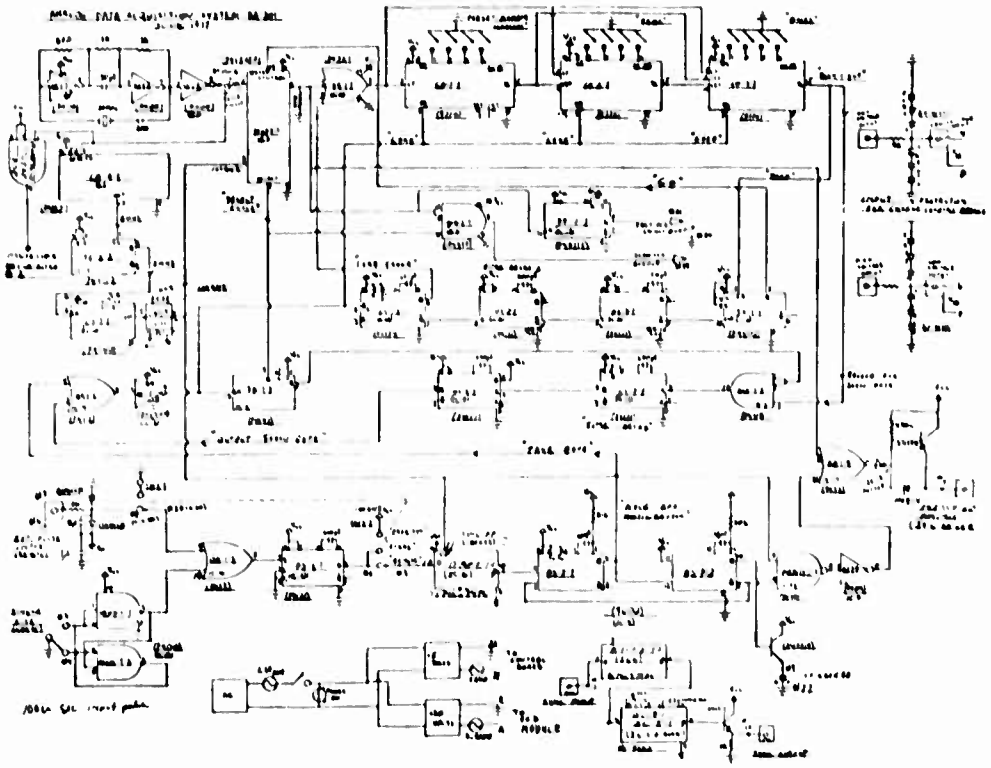


Figure 2. Schematic diagram of the circuit board supplying clock signals to the video delay line and the transversal filter.



Figure 3. Display of sawtooth waveforms (fundamental frequencies 1, 2.5, and 5 MHz) samples and then slowly clocked out of video delay line. (Horizontal scale 50 microseconds/major division.)



(→ time)

Figure 4. Output of the data acquisition system showing "corner-turning-spikes" which result when the clock rate is changed substantially (being corrected by the manufacturer).

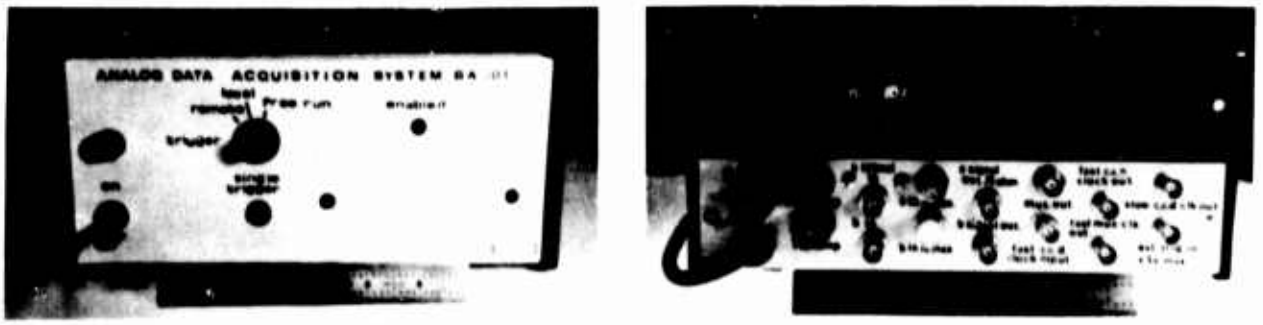


Figure 5. Front and rear views of analog data acquisition system.

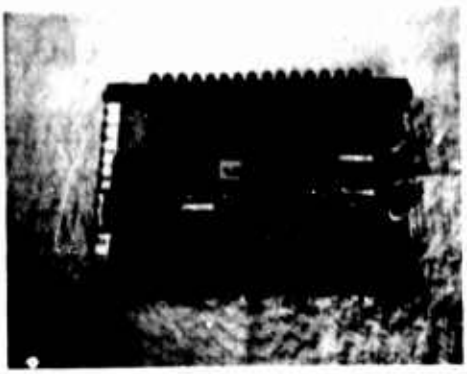


Figure 6. Transversal filter employing switches and variable resistors to adjust tap weights (built by Frederick Pack).



Figure 7. CCD transversal filter employing interchangeable weighting networks to change response. (a) 4 inch x 8 inch circuit board showing clock and signal inputs on left, TAD32 in center, output at right. (b) Rear of board showing zero-insertion-force socket which accepts plug-in weighting network board.

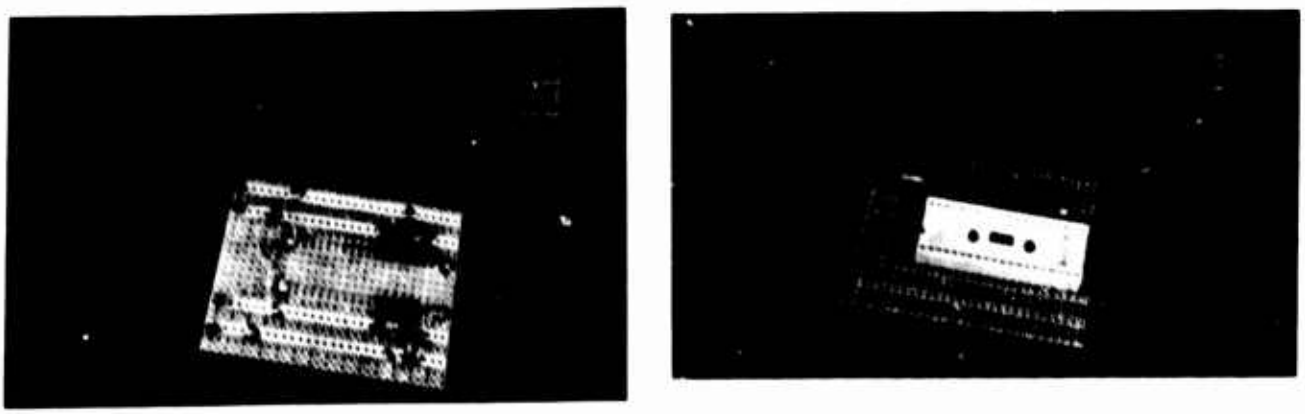


Figure 8. Top (right) and bottom (left) views of plug-in weighting network.



Figure 9. Photograph of burst processor system. From left to right are: power supply for transversal filter; transversal filter with switches and resistors; analog data acquisition system (with amplifier on top of it); pulse generators for adjusting triggering of ultrasonic system and oscilloscope; test block with its transducer; commercial (Panametrics) pulser/receiver/oscilloscope.

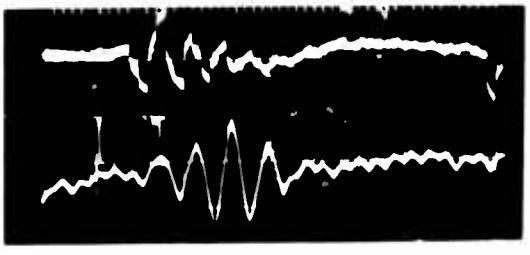


Figure 10. (Top) Output of analog data acquisition system when reference reflection waveform at around 5 MHz is input. (Bottom) Output of CCD transversal filter when taps are set for matched filter operation (filter matched to upper waveform) and reference function is input. (Horizontal scale 50 microseconds/major division.)

DECONVOLUTION PROCESSING FOR FLAW SIGNATURES

E. S. Furgason, R. E. Twyman, and V. L. Newhouse
Purdue University
West Lafayette, Indiana 47907

ABSTRACT

The ultimate resolution of all ultrasonic flaw detection systems is limited by transducer response. Although the system output contains detailed information about the target structure, these details are masked by the system characteristics. Since the output can be described as the convolution of the target response and the impulse response of the system, it should - in principle - be possible to reverse this operation and extract the target response. In practice, it is found that the presence of even relatively small amounts of noise make the deconvolution process impossible. If, however, the flaw detection system has an extremely high output signal-to-noise ratio it is possible to use estimation techniques in the deconvolution process to achieve a good approximation to the actual target response. Results are presented that demonstrate these techniques applied to both simulated and experimental data. Coupling deconvolution processing with feature extraction is shown to yield an order of magnitude increase in range resolution.

Introduction

The output of a linear flaw detection system, $y(t)$ can be represented as the convolution of the target response, $x(t)$, and the impulse response of the system, $h(t)$.

$$y(t) = x(t) * h(t) = \int_{-\infty}^{\infty} x(\tau)\, h(t-\tau)\, d\tau \quad (1)$$

For this type of system the convolution process can be reversed to remove the effects of the system and obtain detailed information about the target. Since the impulse response of the system can be measured, extraction of the target response from the convolution integral by straight-forward deconvolution is achieved by taking Fourier transforms

$$Y(\omega) = X(\omega) \cdot H(\omega)\,, \quad (2)$$

dividing, and taking the inverse transform

$$x(t) = F^{-1}\,(Y(\omega)/H(\omega))\,. \quad (3)$$

However, in the case of real experimental data, the output $y(t)$ is contaminated by the presence of noise, $n(t)$, so that the measured output is

$$\hat{y}(t) = x(t) * h(t) + n(t). \quad (4)$$

If straight forward deconvolution of the noise contaminated output, $\hat{y}(t)$, is attempted, we obtain

$$\hat{x}(t) = F^{-1}\left(\frac{Y(\omega)}{H(\omega)} + \frac{N(\omega)}{H(\omega)}\right) \quad (5)$$

where the first term is the desired target response and the second term is the noise contribution. Since the functions $N(\omega)$ and $H(\omega)$ are unrelated, their zeros can not in general coincide. Thus it is usually the case that the noise term dominates, completely obscuring the desired target response.

In an actual system the noise, $n(t)$, is an unknown random function. Thus examination of Eq. 5 reveals that straight forward deconvolution actually generates an entire set S of possible solutions in which each noise function yields a different approximation $\hat{x}(t)$. Virtually no useful information can be extracted from this simple processing technique. This result clearly demonstrates the desirability of obtaining the largest possible output signal-to-noise ratio. However it does not follow directly that a high signal-to-noise ratio implies a good approximation to the actual target response in straight forward deconvolution.

For detection systems which possess a high signal-to-noise ratio, the following estimation technique can be used to advantage. If we know that the noise is bounded and assume that all the signals exist only in a finite time interval such that

$$\int_{-\infty}^{\infty} n^2(t)dt \le \epsilon^2\,, \quad (6)$$

we can select a particular solution $\hat{x}_s(t)$ from the set S of all possible solutions such that[1,2]

$$\int_{-\infty}^{\infty} [c(t) * \hat{x}_s(t)]^2 dt = \min_{\hat{x}\in S} \left(\int_{-\infty}^{\infty} [c(t) * \hat{x}(t)]^2 dt\right) \quad (7)$$

where $c(t)$ is a constraint operator which forces the particular solution to meet predetermined criteria for smoothness. The original applications of this technique in radiography[3] utilized the second difference operator, $\delta''(t)$, to yield

smooth responses. In the following, we will utilize the identity operator, $\delta(t)$, as the constraint. Thus Eq. 7 becomes

$$\int_{-\infty}^{\infty} |c(t) * \hat{x}_s(t)|^2 dt = \int_{-\infty}^{\infty} \hat{x}_s^2(t) dt = \min_{\hat{x} \in S} \left(\int_{-\infty}^{\infty} \hat{x}^2(t) dt \right) \quad (8)$$

which requires weaker a priori assumptions about the smoothness of the unknown target function, i.e. it allows for the presence of delta functions.

Phillips and Twomey have shown that the constraint given by Eq. 7 is, for the case of discrete functions, equivalent to

$$\frac{\partial}{\partial \hat{x}_k} \left\{ |H\hat{x} - \hat{Y}|^2 + \gamma \hat{x}^* C \hat{x} \right\} = 0 \quad (k = 1,2,\ldots N) \quad (9)$$

where H and C are the matrices that represent the system response and the constraint, respectively, and γ is a Lagrangian multiplier.

Hunt demonstrated that the solution of Eq. 10 can be represented in terms of discrete Fourier transforms as

$$X(k) = \frac{\hat{Y}(k) H^*(k)}{|H(k)|^2 + \gamma |C(k)|^2} \quad (k = 1,2,\ldots N) \quad (10)$$

where the Lagrangian multiplier is chosen to satisfy the condition of noise energy (Eq. 6)

$$\sum_{k=1}^{N} \frac{|\hat{Y}(k)|^2}{\left[\frac{|H(k)|^2}{\gamma |C(k)|^2} + 1 \right]^2} \simeq \frac{\varepsilon^2}{N} \quad (11)$$

Figures 1 through 3 demonstrate the application of the constrained deconvolution technique to simulated data. The first figure shows the assumed system impulse response contaminated with a small amount of noise. Figure 2 shows the type of system output expected from a target containing two parallel plane surfaces that are too close together to resolve. The constrained deconvolution of this noisy output signal, displayed in Fig. 3, shows a dramatic increase in resolution. For comparison Fig. 4 presents the results of a straight forward deconvolution applied to the trace in Fig. 2.

Figures 5 through 11 represent the application of this technique to experimental data on aluminum targets. Figure 5 is the system impulse response, obtained from a target consisting of a single plane surface. Figures 7 and 10 are the constrained deconvolutions of the output from the stepped plane surface targets shown in Figs. 6 and 9. For comparison, Figs. 8 and 11 display the results of deconvolution by straight forward division of Fourier transforms.

Target misalignment can have adverse effects on the deconvolution output. If the target is not parallel to the transducer face, the target will no longer appear to the sound beam as a plane surface; instead it will appear to be a distributed target, causing the reflected energy to be spread over a longer time interval. In contrast to the delta function obtained from the plane surface, the target deconvolution of the tilted surface will appear as a spread version of the delta function. Therefore, spreading in the deconvolution output suggests that the target is at a greater angle with respect to the transducer than the reference target. This effect is demonstrated in the simulated deconvolution shown in Fig. 12 where the target is at 2° to the face of the transducer and the reference target is parallel to the face of the transducer. The presence of damped oscillations in a deconvolution trace suggest reference target misalignment, as demonstrated in the simulated deconvolution in Fig. 13. For this case the target to be deconvolved in parallel to the face of the transducer while the reference target is tilted 2° to the face of the transducer.

Deconvolution of Known Targets

The previous section presented a general approach to the problem of deconvolving the response of a target about which little or nothing was known. If the target response is known in advance the deconvolution problem is significantly altered. In this case the objective is simply to identify and locate a particular target(s) in an output containing information about many targets.

Assuming that the target of interest has a reflectivity function (signature) $g(t)$, a general system output containing several targets may be written as

$$y(t) = \left| \sum_k \alpha_k g(t - t_k) \right| + x(t) * h(t) + n(t) \quad (12)$$

where α_k are the relative amplitudes of the desired targets, $x(t)$ is the response of all other targets, and $h(t)$ is the impulse response of the system. If a generalized response is defined as

$$\tilde{h}(t) = g(t) * h(t) \quad (13)$$

the system output can be rewritten as

$$\hat{y}(t) = \left| \sum_k \alpha_k \delta(t - \Delta t_k) \right| * \tilde{h}(t) + |x(t) * h(t) + n(t)| \quad (14)$$

Thus all the information about the desired targets is now contained in the experimentally measurable function h(t) and the problem is reduced to identifying delta functions in the output.

A processing method that we have used with some success begins as straight forward deconvolution by forming the ratio of transforms

$$\frac{Y(\omega)}{H(\omega)} = \sum_k a_k e^{-j\omega\Delta t_k} + \frac{X(\omega)H(\omega) + N(\omega)}{H(\omega)} . \quad (15)$$

In this ratio each of the desired targets is represented as a complex exponential whose frequency is proportional to the location of the target. A nonlinear pattern recognition routine is then employed to identify the complex exponentials and suppress the remaining terms in this expression. Finally the function resulting from this nonlinear process is inverse transformed to yield the deconvolution output.

Figures 14 through 19 demonstrate the capability of this processing technique to enhance resolution. The experimentally measured response, h(t), of a single plane aluminum surface is shown in Fig. 14. The system output corresponding to the two parallel plane surfaces forming a 24 mil step in an aluminum block is displayed in Fig. 15. Figure 16 shows the deconvolution of the stepped target response. The deconvolved output can be seen to provide a significant increase in resolution with the width of each delta function corresponding to less than 1 mil.

Figures 17 through 19 show the target responses and deconvolved outputs for a series of step targets of decreasing step height. From these figures it is clear that even as the step height decreases below the resolution limit of the flaw detection system, the deconvolution process is still able to accurately locate both surfaces of the step.

Discussion

Two approaches to the problem of deconvolution have been investigated. Both methods apply computer processing to flaw detection outputs which possess extremely high signal-to-noise ratios to remove the effects of the ultrasonic transducer which tends to obscure the details of the target under investigation.

The first processing scheme attached the general problem of deconvolving the response from an unknown target. Experimental results were presented which demonstrated that this procedure could be used to enhance the resolution of the detection system and provide more detailed information about the structure and orientation of the target.

The second technique dealt with the related problem of identifying and accurately locating known targets. By combining deconvolution processing with a pattern recognition procedure, it was experimentally demonstrated than an order of magnitude increase in resolution could be realized. When examining unknown targets it may be possible to use the first technique to identify target structure. This information can then be used with the second technique to provide optimum target resolution.

Another possible application of the pattern recognition deconvolution procedure is in conjunction with a library of flaw signatures. This should make it possible to characterize flaw type as well as enhance resolution. It should be stressed that both the above procedures are most effective when used on the outputs of system providing considerable initial signal-to-noise ratio enhancement to the flaw echo signal.

Acknowledgement

This work supported by Advanced Research Projects Agency, Project No. F33615-75-C-5252.

References

1. D. Phillips, "A Technique for the Numerical Solution of Certain Integral Equations of the First Kind," J. Assoc. Comput. Mach., Vol. 9, pp. 97-101 (1962).

2. S. Twomey, "The Application of Numerical Filtering to the Solution of Integral Equations Encountered in Indirect Sensing Measurements," J. Franklin Inst., No. 279, pp. 95-109 (1965).

3. B. Hunt, "The Inverse Problem of Radiography," Math. Biosci., Vol. 8, pp. 161-179 (1970).

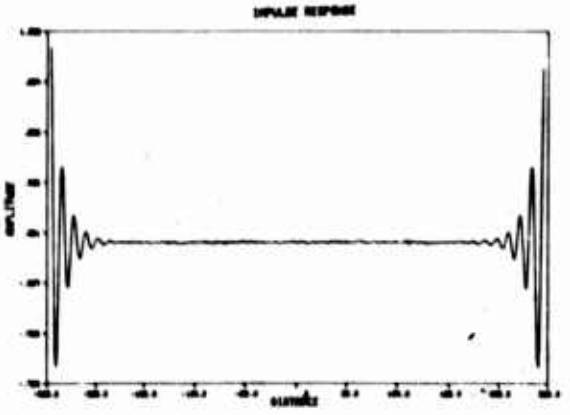


Figure 1. Simulated impulse response (reference signal) of a parallel (parallel to the face of the transducer) plane surface reflector superimposed with uniform density noise 0.7% of the maximum value of the reference signal.

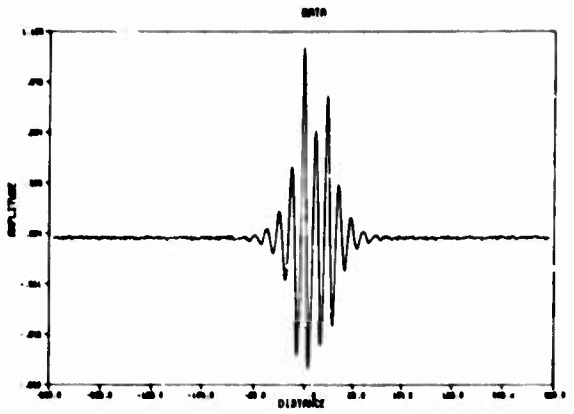


Figure 2. Simulated system output containing two parallel plane targets (relative amplitudes 1.0 and 0.7) separated by 25 points on a 512 point data sample, superimposed with uniform density noise 0.7% of the maximum value of the target signal.

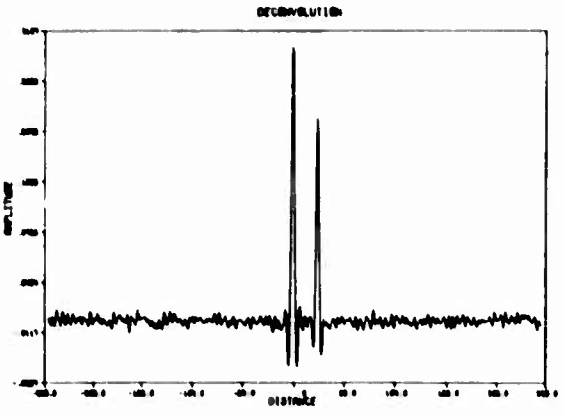


Figure 3. Constrained deconvolution of Fig. 2 by optimization of smoothing function using the impulse response of Fig. 1.

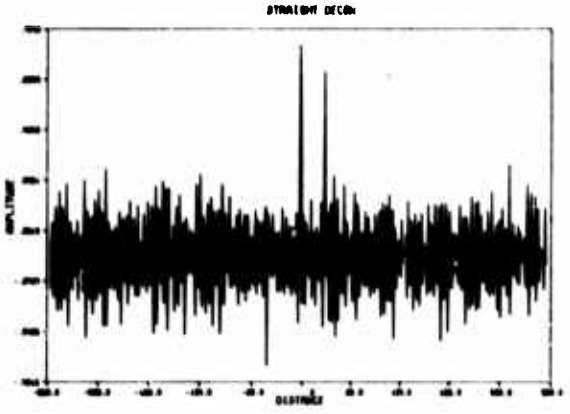


Figure 4. Deconvolution of Fig. 2 by straightforward division of Fourier transforms using the impulse response of Fig. 2.

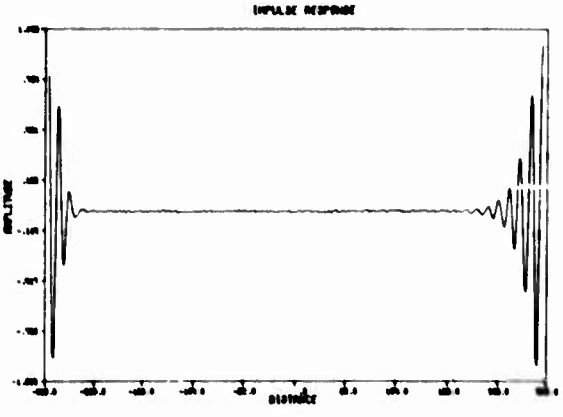


Figure 5. Actual system impulse response taken from a plane surface aluminum target assumed to be parallel to the face of the transducer.

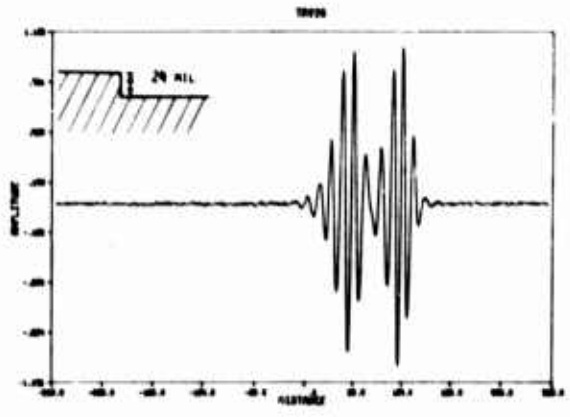


Figure 6. Actual system output of a plane surface aluminum target, containing a 24 mil step and assumed to be parallel to the face of the transducer.

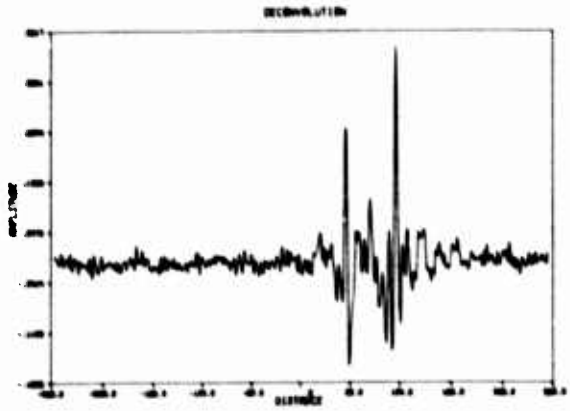


Figure 7. Constrained deconvolution of Fig. 6 using the impulse response of Fig. 5, showing locations of the two plane reflectors and suggesting that the stepped target and the reference target are at approximately the same angle to the face of the transducer.

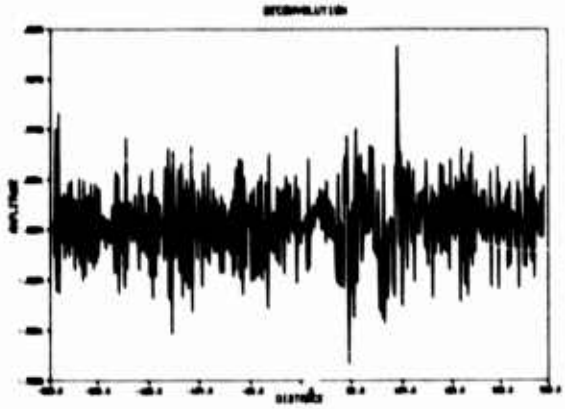


Figure 8. Deconvolution of Fig. 6 by straightforward division of Fourier transforms using the impulse response of Fig. 5.

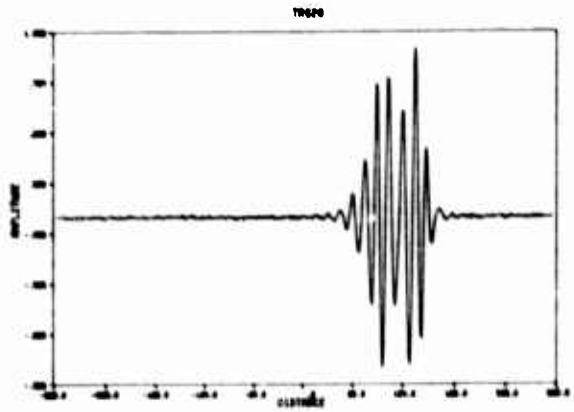


Figure 9. Actual system output of a plane surface aluminum target containing a 15 mil step and assumed to be parallel to the face of the transducer.

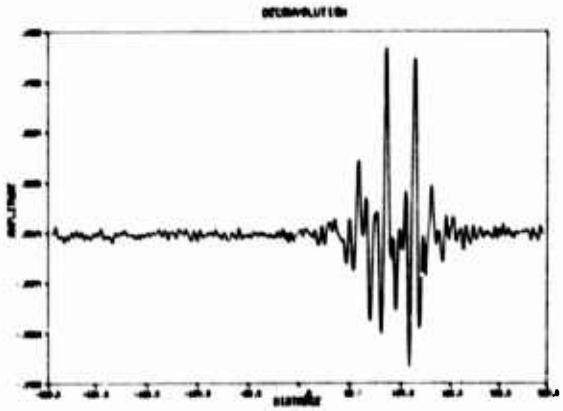


Figure 10. Constrained deconvolution of Fig. 9 using the impulse response of Fig. 5, showing locations of the two plane reflectors and indicating that the stepped target and the reference target are at approximately the same angle.

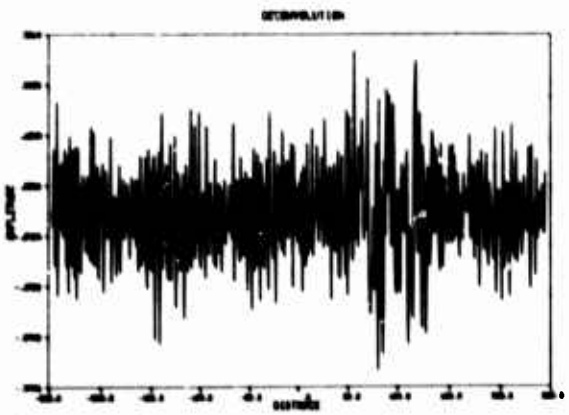


Figure 11. Deconvolution of Fig. 9 by straightforward division of Fourier transforms using the impulse response of Fig. 5.

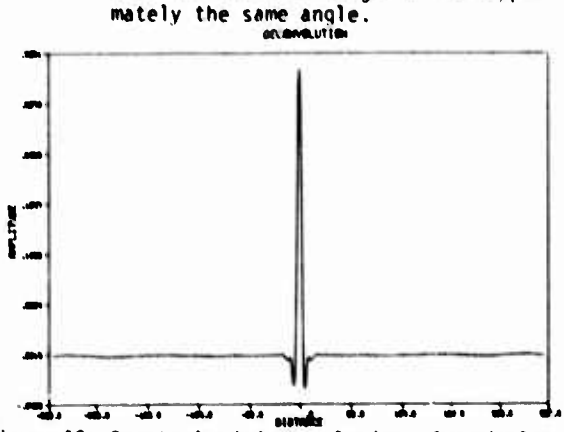


Figure 12. Constrained deconvolution of a simulated system output from a plane target that is tilted 2° to the face of the transducer and using an impulse response from a plane target that is parallel to the face of the transducer.

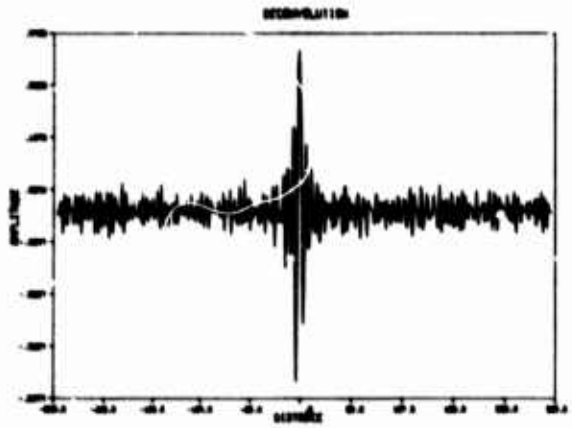


Figure 13. Constrained deconvolution of a simulated system output from a plane target that is parallel to the face of the transducer and using an impulse response from a plane target that is tilted 2^{0} to the face of the transducer.

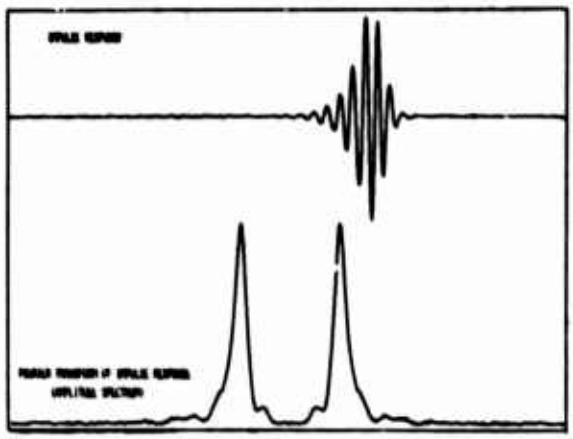


Figure 14. Actual system impulse response taken from a plane surface aluminum target showing the amplitude spectrum of the Fourier transform.

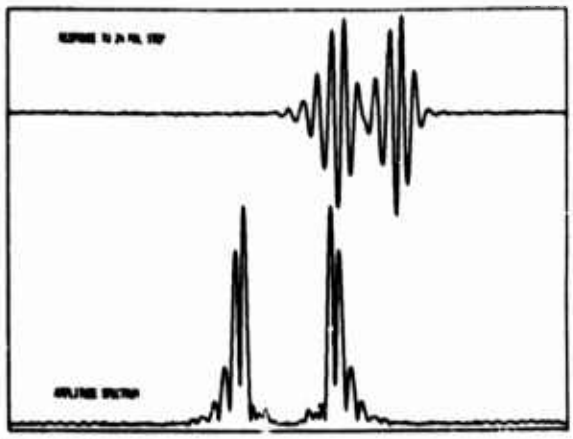


Figure 15. Actual system output of a plane surface aluminum target containing a 24 mil step showing the amplitude spectrum of the Fourier transform.

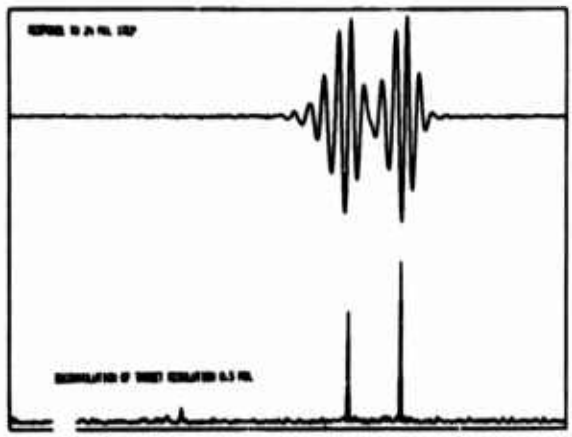


Figure 16. Actual system output of a plane surface aluminum target containing a 24 mil step which is the same as Fig. 6 and 15, and also shows the pattern recognition deconvolution of the stepped target using the impulse response of Fig. 14.

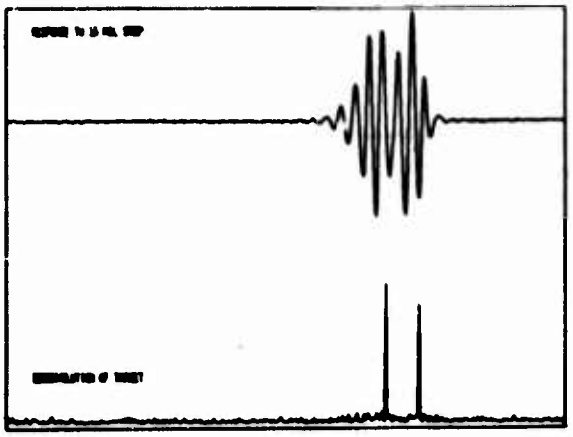


Figure 17. Actual system output of a plane surface aluminum target containing a 15 mil step, which is the same as Fig. 9, and also shows the pattern recognition deconvolution of the stepped target using the impulse response in Fig. 14.

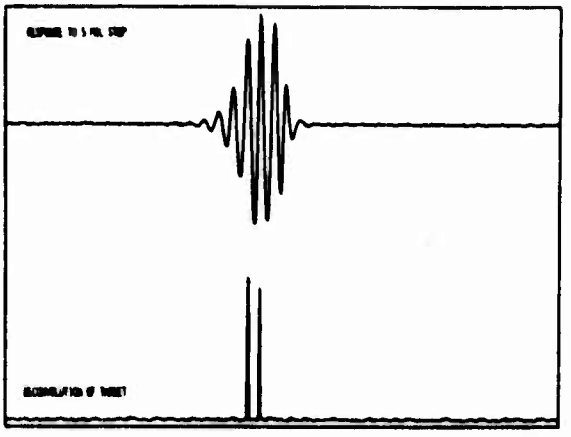


Figure 18. Actual system output of a plane surface aluminum target containing a 13 mil step and also shows the pattern recognition deconvolution of the stepped target using the impulse response of Fig. 14.

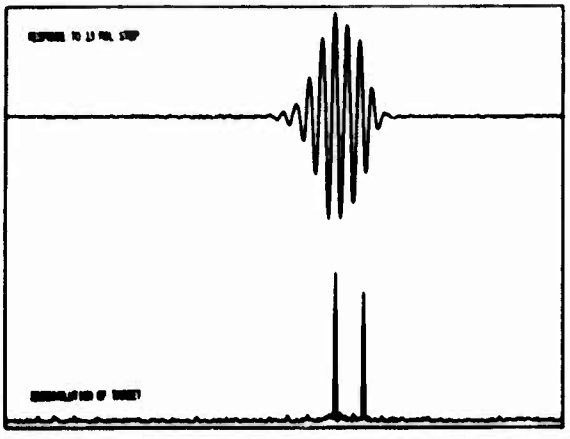


Figure 19. Actual system output of a plane surface aluminum target containing a 5 mil step and also shows the pattern recognition deconvolution of the stepped target using the impulse response of Fig. 14.

CHARACTERIZATION FACILITY FOR NDE TRANSDUCERS

K. M. Lakin
University of Southern California
Los Angeles, California

ABSTRACT

The characterization of NDE transducers involves an assessment of the bidirectional acousto-electric conversion between electrical and acoustic terminals and an evaluation of the near and far-field radiation patterns. The internal details of the transducer are largely unknown and, consequently, the traditional techniques for analyzing the structures cannot be applied. Instead, the transducer may be characterized as a hybrid two-port network whose parameters may be determined by relatively simple measurements taken at the electrical port when the acoustic loads are known. The radiation pattern involves measurement only in the region exterior to the transducer. There are several techniques which may be used to accomplish this task. Our approach has been to measure the acoustic field in the far-field region and then to reconstruct the field at the face of the transducer. Once we have the field at the transducer, an evaluation of the source may be readily determined from amplitude and phase contour plots or from gray scale or pseudo-color images.

Introduction

The characterization of NDE transducers is a problem which could be greatly aided by determining the fields at the surface of the transducers. Such information would be useful not only for directly characterizing the transducer, but also as a check on the predictions of theoretical models of the transducers.[1] The fields at the surface of the transducer or in any intermediate plane can be reconstructed from measurements of the amplitude and phase of the radiation pattern. This measurement and reconstruction process is basically holography.[2]

Previous attempts at reconstructing images of acoustic radiators or scatterers have involved recording the radiation pattern on film and reconstructing the image optically.[3] Such recordings are Gabor or on-axis holograms. As such, the reconstructed image is degraded by a second defocused image of the object superimposed on the desired image. In the work done here, the radiation pattern is scanned and the resultant data is processed with a digital computer to generate an image free of any degrading secondary images.

The total system consists of an analog electronic recording system, A/D conversion, and digital processing. The transducer is placed in water and driven with a constant frequency (5 MHz) signal. A second transducer scans the radiation pattern measuring amplitude and phase. Here an oscillator (5 MHz) is used as a reference signal in order to extract the phase. The data points are recorded in the Fresnel diffraction zone. By multiplying the data with a quadratic phase term, we obtain the equivalent of the Fraunhofer diffraction pattern.[1] The data are also multiplied with an apodizing factor which will be discussed later. Given the Fraunhofer diffraction pattern, the fields at the surface of the transducer are found by taking the inverse Fourier transforms of the data.[1] These steps can be better visualized by looking at a totally optical analog of this system as shown in Fig. 1. Multiplying with a quadratic phase factor in (a) is equivalent to placing a collimating lens in the scanning plane. The discrete Fourier transform (DFT) has its parallel in the second lens. It is well known that the field in the back focal plane of a lens is equal to the Fourier transform of the field present in the front focal plane.[4] Thus lens L2 performs a Fourier transform of the radiation pattern. The combination of collimating lens L1 and Fourier transform lens L2 is seen to form a simple imaging system which images the transducer.

Apodization

If one takes all the data points in the Fourier plane, weights them equally, and then does the inverse Fourier transform, the resultant image exhibits ringing at any sharp edges. This is a manifestation of the Gibb's overshoot phenomenon associated with truncating Fourier series. This effect can be minimized without significant loss of resolution by applying appropriate weights to the data points. This is equivalent to placing an apodization filter in the optical system of Fig. 1. A test was made to compare several different apodization functions. For the test, a square pulse was used. The pulse function was Fourier transformed (digitally), the resultant spatial frequency samples were multiplied with the apodization function, and then an inverse Fourier transform was performed (again digitally). Figure 2 shows the results of this procedure for several different apodization functions. On the scale of these plots, the square input function had a width of 32. The heights have been normalized to 200. Figure 2(a) shows the ringing that results when no apodization is used. Four cases were then evaluated (Figs. 2(b) - 2(e)). The last three cases (Figs. 2(c) - 2(e)) all give very good and approximately equivalent results. These filters respectively have the forms: Gaussian, A+cosine, and $\sin(x)/x$. Figure 3 shows reconstructions of the intensity on the surface of a transducer with and without apodization. The smoothing of the overshoot on the edges is apparent

Although the apodization, in principle, does not result in any information loss, it does result in an effective signal loss. Thus the three above-mentioned apodization filters which gave essentially equivalent results under noise-free conditions, may perform differently in the presence of noise.

Aspects of the Imaging System

Distortion - In general, an imaging system will introduce depth distortion in the image of a three-dimensional object. The longitudinal magnification, M, of a single lens imaging system is a nonlinear function of position along the axis of the system. If one wishes to image curved surfaces without longitudinal distortion, one must carefully choose the imaging system. Figure 4 shows a telecentric imaging system for which the longitudinal magnification is a constant M = f2/f1, where f1 and f2 are the focal lengths of the two lenses L1 and L2. For the imaging system used in this project (see Fig. 1) the longitudinal magnification is, in general, not constant.

$$M = f1.f2/|x1(f2 - f1) + f1|^2 \qquad (1)$$

Here, f1 and f2 are again the focal lengths of the lenses and x1 is the distance of the object plane from the front focal plane of lens L1. We note, however, that if f1 = f2, the longitudinal magnification becomes a constant, in fact, unity. So for the particular case, the system shown in Fig. 1 gives distortion-free imaging at unit magnification.

Depth distortion is only a problem when one considers displaying three-dimensional data. Of the three-dimensional display techniques discussed later, depth distortion affects primarily the optical holographic technique.

Lateral Distortion - In the work done thus far, the collected data has been multiplied with a quadratic phase factor before being Fourier transformed (Fig. 1). The effect of this phase factor is analogous to that of a collimating lens. The quadratic phase factor is an approximation to the ideal phase correction. The approximation is only valid for paraxial rays, or in other words, when the dimensions of the scanned area and of the imaged area are small compared to the distance between the object plane and the scan plane. Since the computer has replaced the lens, it is possible to improve this approximation so that the only remaining restriction is that the object field must be small in terms of the solid angle it subtends at the measurement plane. The size of the measurement plane itself is unrestricted.

This relaxation of the restrictions on the system is achieved by using the exact phase factor for imaging a point source as predicted by Huygen's theory. This new phase factor constitutes an "ideal lens" for a point source located on the axis. This ideal lens is simply a spherical phase;

$$\phi(x,y) = 2\pi/\lambda \sqrt{x^2 + y^2 + R^2}\ , \qquad (2)$$

where λ is the wavelength of radiation in the given medium (e.g., water), x,y are the coordinates in the measurement plane, and R is the distance from the point source to the measurement plane. This exact phase factor can be used instead of its paraxial approximation in Fig. 1.

$$\phi'(x,y) = \frac{\pi}{\lambda}\left(\frac{x^2+y^2}{R}\right) + \text{constant} \quad \text{if } R>>(x^2+y^2). \qquad (3)$$

Although the new solution is only exact for the point on axis, it also reduces the distortion in the images of off-axis points.

Three-Dimensional Presentation

A major concern of this program is the visualization of an ultrasound transducer or scatterer. In particular, a means of presenting any three-dimensional structure of the source is important. There are several possible ways of displaying three-dimensional information that have been studied in regard to this project. These methods are described below.

Optical Holographic Reconstruction - This method involves the creation of a hologram from the recorded data. This hologram could then be reconstructed optically to give an exact three-dimensional image of the original source. This would be an ultimate presentation in terms of the amount of information in the display. Virtually all of the available three-dimensional information is retained. However, this is an extremely involved process. The recorded data must be converted into an optical hologram. The amplitude information recorded in the Fresnel zone can be converted to a transparency by means of a plotting microdensitometer. The phase information is more difficult. To get the phase directly, we have to record an intensity related to the phase on film, and then bleach the film to convert the intensity variations to phase variations. Such a phase recording combined with the previously mentioned amplitude transparency produces an on-axis phase-and-amplitude hologram. Alternatively, the phase could be encoded as intensity variations by "interfering" the phase front with a reference phase front and recording the resulting fringe pattern. This could be used to produce an off-axis type of hologram. Although the off-axis approach avoids the problems associated with bleaching film to create a phase record, it requires a higher spatial resolution on the phase record; thus, it puts more severe requirements on the plotting microdensitometer.

Another problem with the holographic display approach is that the data tends to cover an extremely large dynamic range (see Fig. 5). Computer holograms, however, are only capable of recording fairly small dynamic range objects. A number of techniques were explored to overcome this difficulty. One such technique was an iterative technique whereby the object was first reconstructed digitally, then a random phase was imposed on the reconstruction. This was Fourier transformed to get a first approximation to the desired hologram. In this hologram the phase information was retained but the amplitude was set equal to some predeter-

mined function with low dynamic range requirements. Both a constant function and a Gaussian function were used in this regard. From this modified Fourier transform, a reconstruction was made. Here also the phase was retained, but the amplitude was set equal to the original amplitude in the reconstruction. This process was repeated after each Fourier transform, setting the amplitude equal to the predetermined values, until a hologram was obtained whose amplitude deviated only slightly from the desired function. This technique was successful, particularly when the Gaussian amplitude was applied to the holograms. However, it is time-consuming and, furthermore, is only suitable for planar or nearly planar objects. The resultant holograms are shown in Fig. 6. It should be noted that all of these holograms are of the Lohmann type.[5] The amplitude of the field is encoded through a type of pulse width modulation while the phase is encoded through pulse position modulation.

A second method consisted of digitally precompensating the data to reduce its dynamic range. This could be done, for instance, by multiplying it with an appropriately scaled inverse Gaussian. A hologram was generated from this compensated data. Then upon reconstruction, the hologram was illuminated with a nonuniform beam which restored the original dynamic range. If the compensation function was an inverse Gaussian, which proved most practical, the natural Gaussian profile of a laser beam in the TEM mode could be used to illuminate the hologram. The main problem with this technique is that there are strict alignment requirements in the reconstruction stage.

A third technique of avoiding the dynamic range problem promised to overcome some of the difficulties of the other two, but lack of time prevented its thorough investigation during this project. In this approach, an arbitrary plane near the object is reconstructed digitally. From this reconstruction an image plane hologram is generated. By recording in the image plane, the problem of extremely large dynamic range signals are avoided. The image plane hologram is then viewed through a coherent spatial filtering imaging system to convert the interference fringe information into phase information. Figure 7 shows a preliminary version of an image plane computer-generated hologram. For practical utilization a higher carrier frequency would be desirable. This approach is suitable for arbitrary three-dimensional objects and does not have the severe alignment problems of the previously mentioned technique.

Digital Reconstruction of Individual Planes - By multiplying the data with a given quadratic phase factor and performing a digital Fourier transform (DFT), we obtain an image of a given plane. The position of this plane along the "viewing axis" is determined by the quadratic phase factor. Thus by varying this phase factor we can scan through the depth of the object. By imaging several such planes we obtain a three-dimensional picture of the object in layers. Although this is the simplest method to implement, it gives the least satisfying presentation of information. Each contains an in-focus image of the section of the object which lies in that particular plane, but also all other planes are in the picture but out of focus. This method is computationally time-consuming if several planes are to be imaged.

One particular instance arose during the project in which this approach did prove quite useful, suggesting an important potential in evaluating transducers. A focused transducer was used as a test object. Since we have the capability of imaging any plane, it is possible to search for the focal plane of the transducer. This not only allows one to determine accurately and easily the focal plane from just one set of measurements, but it also allows one to measure the performance of the transducer by examining the quality of the point image in the focal plane. Figure 8 shows plots of the field intensity in various planes in front of a focused transducer.

Stereo Imaging - In this approach the measured data is used to generate a stereo pair of images. Stereo imaging is a simple means of conveying a large amount of information about an object. Stereo imaging has received renewed attention as a research subject in recent years.[6] To generate the stereo pair the recorded data is split into two groups; all data points recorded to the left of an imaginary center line being grouped in the "left hologram" and the points lying to the right of the line going into the "right hologram." Each hologram is used to generate an image of the object by means of a DFT. The two images form a stereo pair. The appropriate viewing system allows the observer to see a three-dimensional image. This approach has several advantages. It is considerably easier to implement than the optical holography approach. It is computationally preferable to the strictly digital method described above since it requires only two DFT's. It also gives a presentation that is easily digested by the human observer. The necessary software has been developed for this approach. A means of simultaneously displaying the two stereo images in the form of a green and a red image has been developed. These images can then be viewed through anaglyph glasses for a stereo image. Experiments on test data have demonstrated the feasibilities of this approach.

Phase Contours - The above techniques are well suited to displaying depth information of a few wavelengths or more. However for variations of a wavelength or less, another approach is much more fruitful. This method consists of displaying contours of constant phase. Preliminary results in this area are very promising. Figure 9 is a picture of the reconstructed phase at the surface of a focused transducer. The surface is approximately spherical with a depth variation of about one wavelength (.03 cm). The phase variations are recorded here as intensity variations. The vertical fringe system is due to the fact that the transducer was tilted slightly, producing a linear phase variation across the face of the transducer. The curvature of the fringes indicates the spherical curvature of the transducer face.

Acknowledgements

The authors wish to thank Mr. A. Hsueh for his part in developing much of the software used in this work. Professor A. Sawchuk is also to be thanked for many helpful discussions and suggestions during the course of this project.

This research was sponsored by the Center for Advanced NDE operated by the Science Center, Rockwell International, for the Advanced Research Projects Agency and the Air Force Materials Laboratory under contract F33615-74-C-5180.

References

1. K. Lakin and A. Fedotowsky, IEEE Transactions Sonics and Ultrasonics, SU-23, 317 (1976).

2. B. P. Hildebrand and B. B. Brendon, Introduction to Acoustic Holography, Plenum Press, New York, 1972.

3. K. Preston, Jr., and Kreuzer, Applied Physics Letters, 10, 150 (1967).

4. J. W. Goodman, Introduction to Fourier Optics, McGraw-Hill, New York, 1968.

5. A. W. Lohmann and D. P. Paris, Appl. Opt., 6, 1739 (1967).

6. A. A. Sawchuk and H. C. Andrews, J. Opt. Soc. America, 66, 1111 (1976).

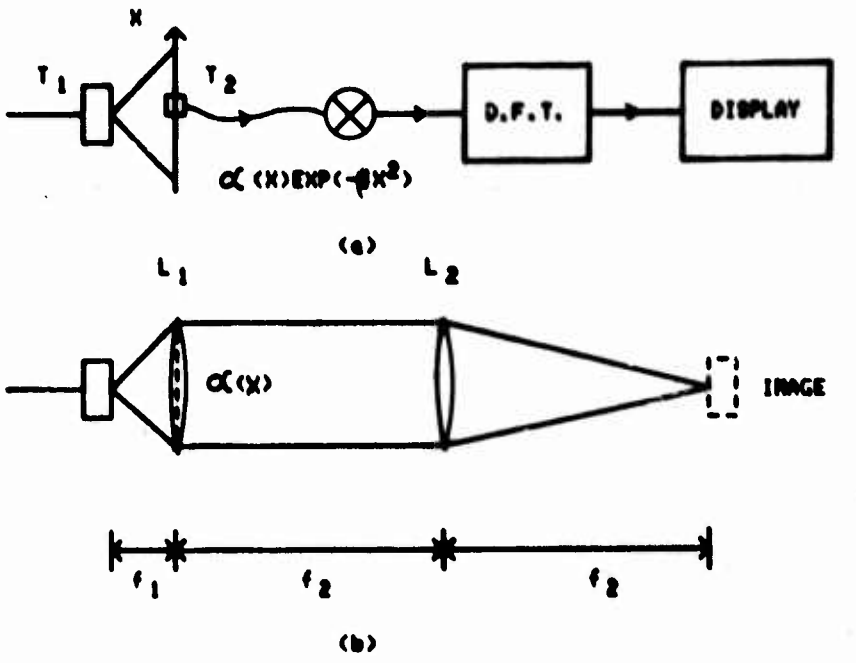
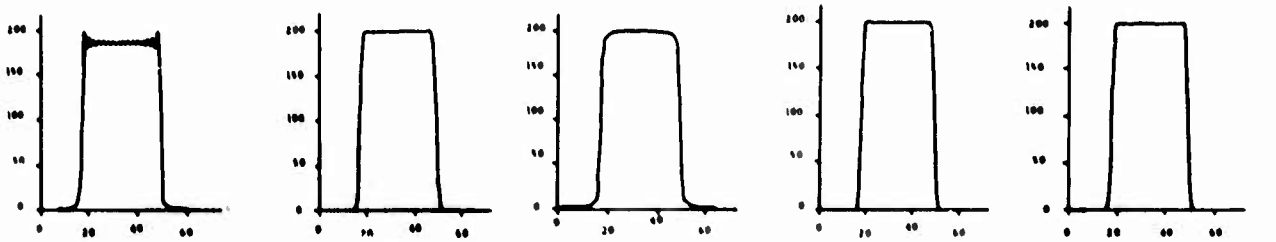


Figure 1. Digital imaging system: (a) Actual system. T_1 is the acoustic transducer being studied, T_2 is a transducer used as a scanning detector, $\alpha(x)$ is the apodization factor, $\exp(-i\beta x^2)$ is the quadratic phase factor, D.F.T. represents a discrete Fourier transform; (b) Optical analog to the system shown in (a). L_1 is a collimating lens which corresponds to the quadratic phase factor, $\alpha(x)$ is the apodizing filter, and L_2 is a Fourier transforming lens. f_1 and f_2 are the focal lengths of L_1 and L_2, respectively.



(a) Without apodization. (b) Triangle function apodization. (c) Gaussian apodization. (d) (A+Cosine) apodization. (e) Sinc function apodization.

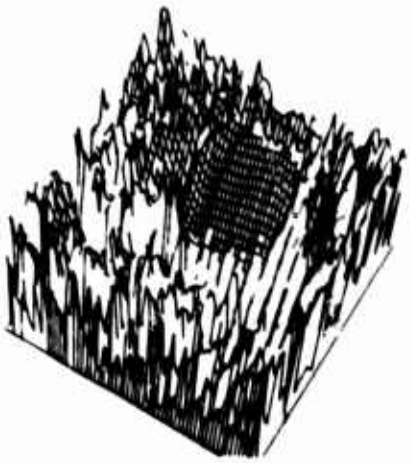
Figure 2. Effect of apodization. A test object consisting of a square pulse was low-pass filtered with various apodization filters to eliminate ringing.



(a) No apodization, grey scale images of amplitude.



(b) No apodization, perspective plot of amplitudes.



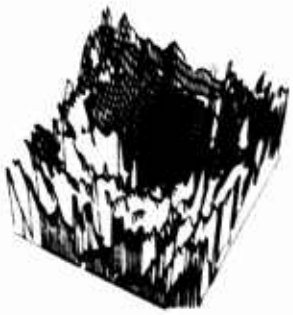
(c) No apodization, perspective plot of phase.



(d) Reconstruction of a transducer with apodization.



(e) With apodization, perspective plot of amplitude.



(f) With apodization, perspective plot of phase.

Figure 3. Effects of apodization on reconstruction of a transducer's amplitude and phase.

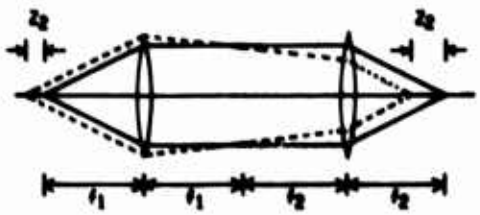


Figure 4. Telecentric imaging system. f_1 and f_2 are the focal lengths of lenses L_1 and L_2, respectively. For this system, displacements along the optical axis are imaged without distortion, i.e., $z_2 = (f_2/f_1)z_1$.

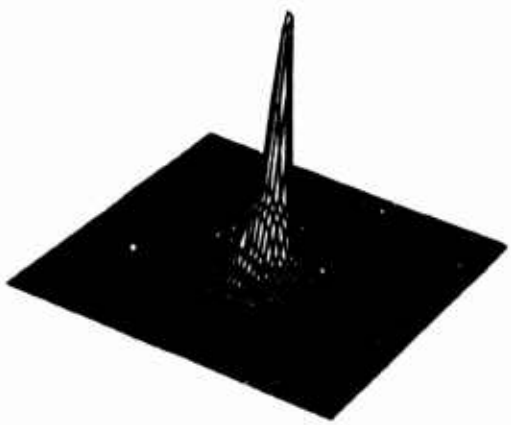


Figure 5. Plot of the field amplitude in the measurement plane.



(a) Uncompensated hologram. Limited dynamic range of the plotting system causes only the central peak to be plotted.



(b) Compensated hologram. Amplitude has been forced to be approximately constant by the iterative method.



(c) Compensated hologram. Amplitude has been forced to approximate a Gaussian by the iterative method.

Figure 6 Binary computer-generated holograms of the data.

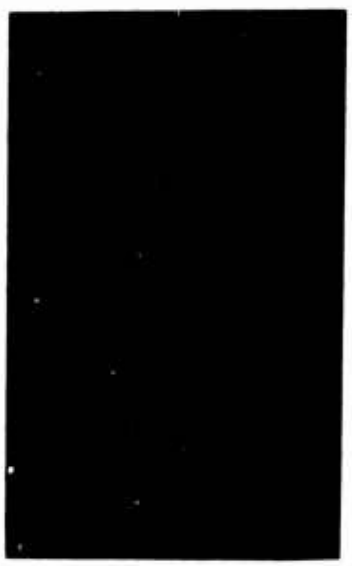


Figure 7. Binary computer-generated image-plane hologram.

(a) Image of the transducer surface.

(b) Image of a plane 9.6 cm in front of the transducer.

(c) Image of a plane 21.6 cm in front of the transducer. This is approximately the focal plane.

(d) Image of a plane 30.2 cm in front of the transducer.

Figure 8. Images of various planes in front of a focused transducer.



Figure 9. Phase contours on the surface of a focused transducer. Each intensity represents a constant phase. The fringes are due to a slight tilt of the transducer causing a linear phase variation across the face of the transducer.

COMPUTER AIDED INTERPRETATION OF NDE SIGNALS

R. K. Elsley
Science Center, Rockwell International
Thousand Oaks, California 91360

ABSTRACT

In order to improve NDE reliability, it is important to recover as much as possible of the useful information in NDE waveforms. An on-line minicomputer is ideally suited to both the collection of data and the performance of sophisticated signal processing tasks. Using a variety of signal processing techniques, including windowing, self-normalization (of transducer properties and far-field diffraction effects), transformations (Fourier magnitude and phase transforms, autocorrelations, cepstra), feature extraction and pattern recognition, it has been possible to obtain information about very small defects, strength of adhesive bonds and acoustic emissions which are not available by conventional means. Examples of these various capabilities are given.

In the past, the ultrasonic signals from nondestructive testing apparatus have been processed in only one simple way: the waveforms are rectified and converted into a "video" signal and displayed on an oscilloscope. A peak in this video signal is taken to be an indication of a defect at the location corresponding to the arrival time of the signal, and the amplitude of the peak is taken as a measure of the defect's size.

This method ignores a great deal of the information present in the ultrasonic signals: no use is made of variations in the frequency content of the signals, phase relationships between parts of the signal are ignored, and long duration signals, such as an echo train from a layered structure, are not treated as one signal.

In order to use more of the information present, first, ultrasonic RF waveforms have to be captured; second, preprocessing operations which enhance the usable information have to be performed, and third, features of the signals which best predict defect type and size have to be determined.

Figure 1 shows a laboratory minicomputer-based signal processing facility. The entire RF waveform is recorded digitally, and the computer performs a wide variety of signal processing operations using Rockwell's interpretive signal processor language.

Figures 2 and 3 show how the properties of the particular ultrasonic transducer and associated electronics used can be removed from the signal in order to allow direct comparisons between experiments, standards and theoretical predictions. In particular, Fig. 3 shows that some signals contain the information needed to "self-normalize" themselves.

Figure 4 shows that the use of a simple gate to pick out a part of a signal can be improved upon by using instead a window of carefully selected shape.

Figure 5 shows that the size of defects no larger than one wavelength of sound can be accurately determined by looking at appropriate properties of the signals.

Figure 6 shows the results of automatic pattern recognition experiments in which the computer learned what features of acoustic emission signals are indicative of what is going on within a part.

Finally, Fig. 7 lists the areas in which the computer system has made contributions to nondestructive evaluation research.

By using more of the information present in ultrasonic signals, it is now possible to answer questions about defects that it was not possible to answer before.

Acknowledgement

This research was sponsored by the Center for Advanced NDE operated by the Science Center, Rockwell International, for the Advanced Research Projects Agency and the Air Force Materials Laboratory under contract F33615-74-C-5180.

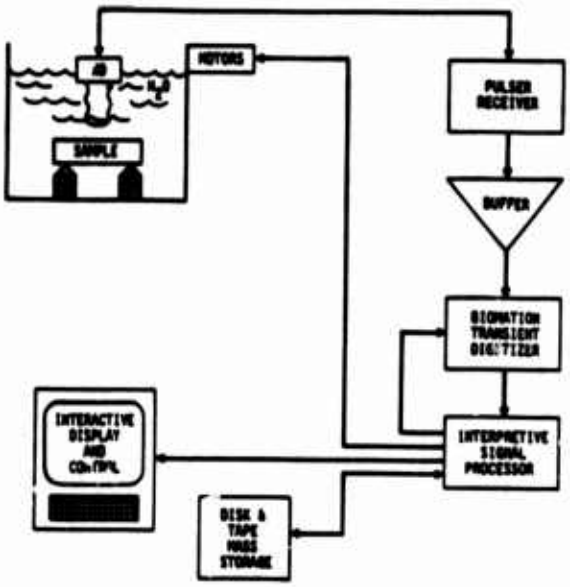


Figure 1. Laboratory minicomputer-based signal processing facility.

WHEN MAKING BROADBAND SPECTRAL MEASUREMENTS, THERE ARE 2 DISTINCT FREQUENCY-DEPENDENT EFFECTS ASSOCIATED WITH THE TRANSDUCER.

1. RESONANT ELECTROMECHANICAL RESPONSE OF TRANSDUCER AND PULSER: NOT MUCH ENERGY AT VERY LOW OR HIGH FREQUENCIES.
2. DIFFRACTION DUE TO FINITE SIZE OF TRANSDUCER: LOW FREQUENCIES ARE IN FAR FIELD, HIGH FREQUENCIES ARE IN NEAR FIELD.

USING A REFERENCE WAVEFORM (e.g. FROM A REFERENCE BLOCK OR BACK SURFACE), ONE CAN NORMALIZE OUT THE TRANSDUCER RESPONSE AND THE FAR FIELD DIFFRACTION.

THE RAW (UNNORMALIZED) SPECTRUM IS THEREBY CONVERTED TO A NORMALIZED SPECTRUM WITH FLAT FREQUENCY RESPONSE WHEREVER SUFFICIENT SOUND ENERGY IS PRESENT.

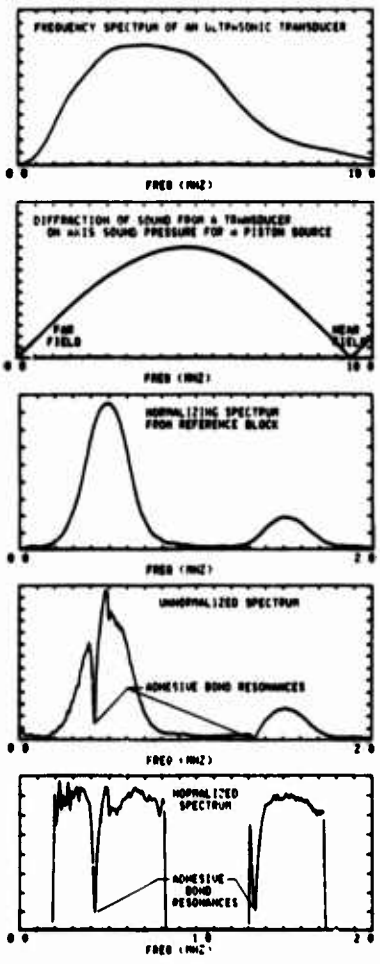


Figure 2. Removing transducer effects I.

IN SOME CASES EACH ULTRASONIC WAVEFORM CAN NORMALIZE (i.e. CORRECT) ITSELF.

THIS REMOVES NOT ONLY TRANSDUCER AND PULSER PROPERTIES AT THAT MOMENT, BUT ALSO TEST PART IRREGULARITIES SUCH AS WARPAGE OR MISALIGNMENT AT THAT POSITION ON THE PART.

- IN PULSE-ECHO TESTING OF ADHESIVELY BONDED ALUMINUM STRUCTURES, THE FRONT SURFACE ECHO IS USED TO NORMALIZE (CORRECT) THE ENTIRE WAVEFORM.

- RAW (UNCORRECTED) FREQUENCY SPECTRA ARE VERY DIFFERENT FOR DIFFERENT TRANSDUCERS.

AFTER SELF-NORMALIZATION, SPECTRA ARE IDENTICAL FROM 1 TO 18 MHz.

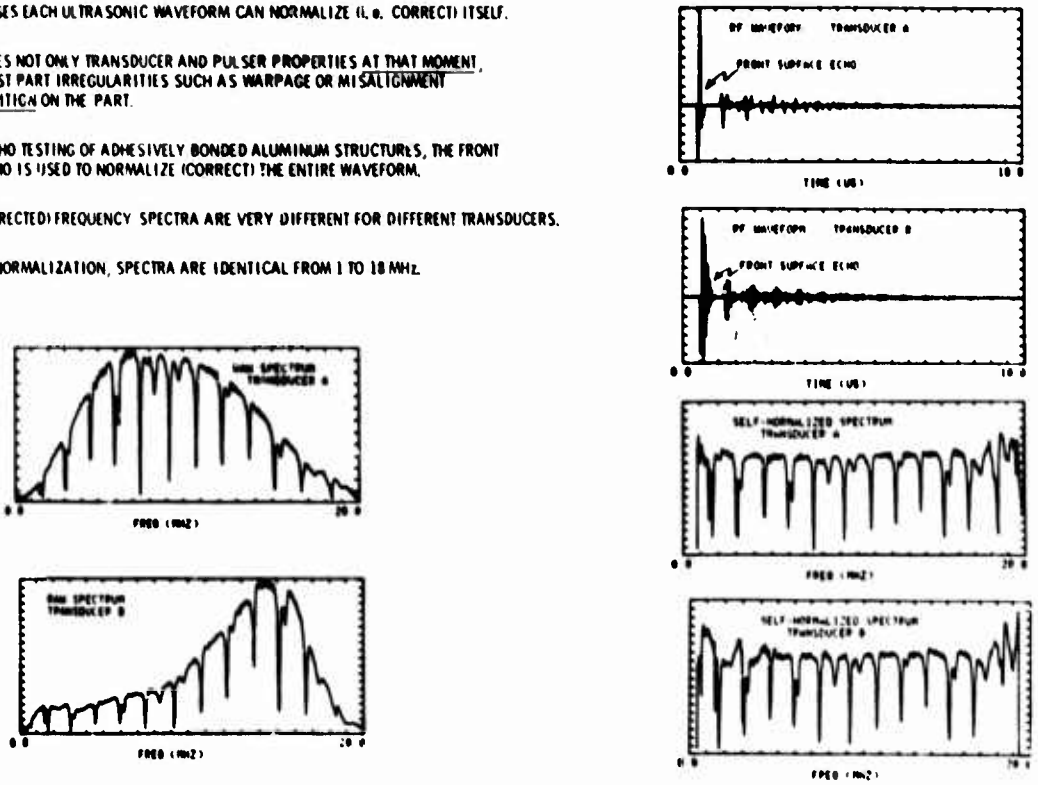
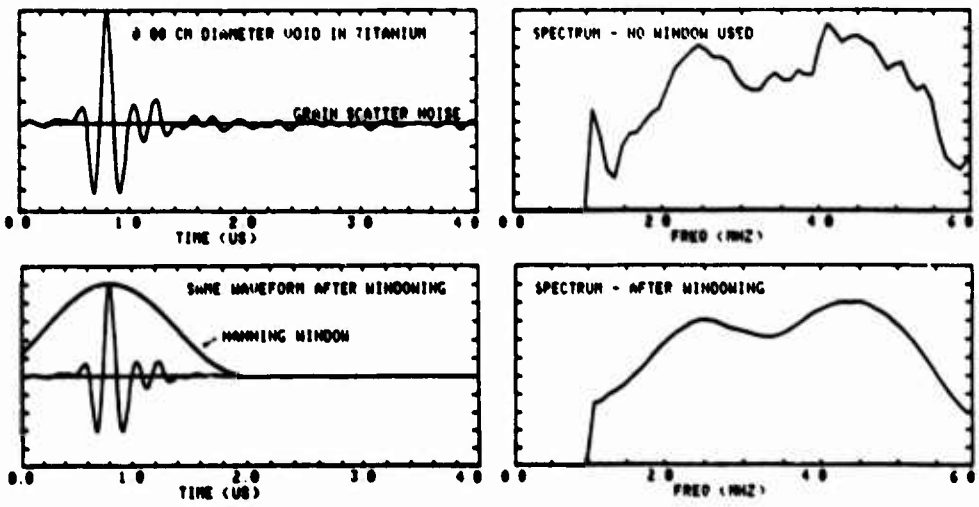


Figure 3. Removing transducer effects II. Self-normalization.



- IF A DEFECT SIGNAL IS ACCOMPANIED BY COHERENT GRAIN BOUNDARY SCATTERING, THE LATTER WILL DISTORT THE FREQUENCY SPECTRUM

- WHEN A SUITABLY SHAPED WINDOW IS MULTIPLIED BY THE WAVEFORM BEFORE FREQUENCY ANALYSIS, THE GRAIN NOISE IS REDUCED WITHOUT INTRODUCING RINGING INTO THE SPECTRUM

Figure 4. Windowing to recover defects from grain noise.

- SEVERAL TECHNIQUES HAVE BEEN DEVELOPED FOR ESTIMATING THE SIZE OF SMALL DEFECTS

  FOR VOID DEFECTS WHICH ARE ROUGHLY SPHERICAL, CHANGING SIZE MERELY STRETCHES FREQUENCY SCALE. THUS ANY FEATURE OF FREQUENCY SPECTRUM, SUCH AS PEAK POSITION, GIVES AN ESTIMATE OF DIAMETER

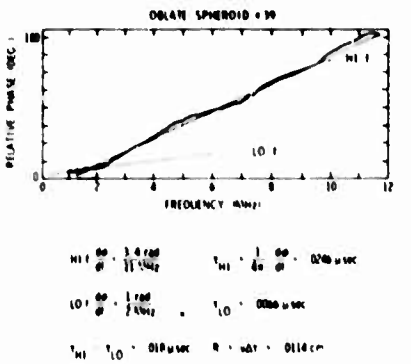
- MORE GENERALLY, SLOPE OF PHASE PART OF FREQUENCY SPECTRUM TELLS ABOUT SIZE AS FOLLOWS

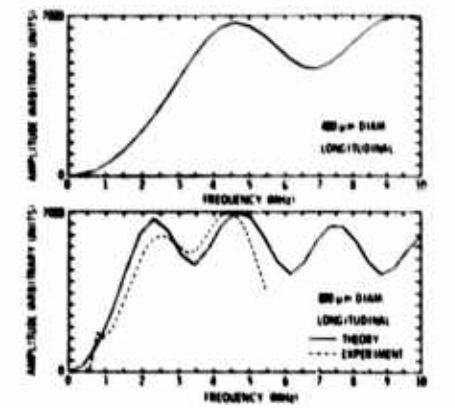
  SLOPE OF PHASE GIVES ARRIVAL TIME OF PULSE

  AT HIGH FREQUENCY, SLOPE GIVES ARRIVAL TIME FROM FRONT OF DEFECT

  AT LOW FREQUENCIES, SLOPE GIVES ARRIVAL TIME FROM CENTER OF DEFECT

  THE DIFFERENCE GIVES A MATERIAL INDEPENDENT MEASURE OF SIZE FOR INCLUSIONS





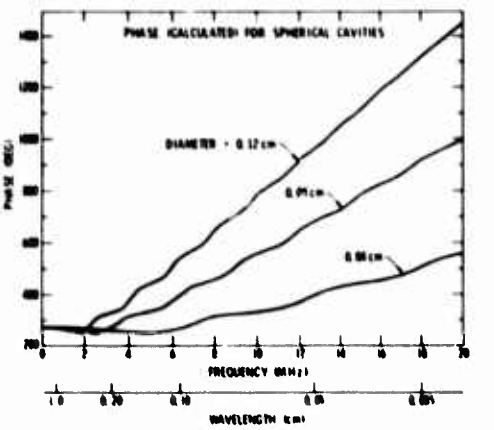


Figure 5. Size of small defects.

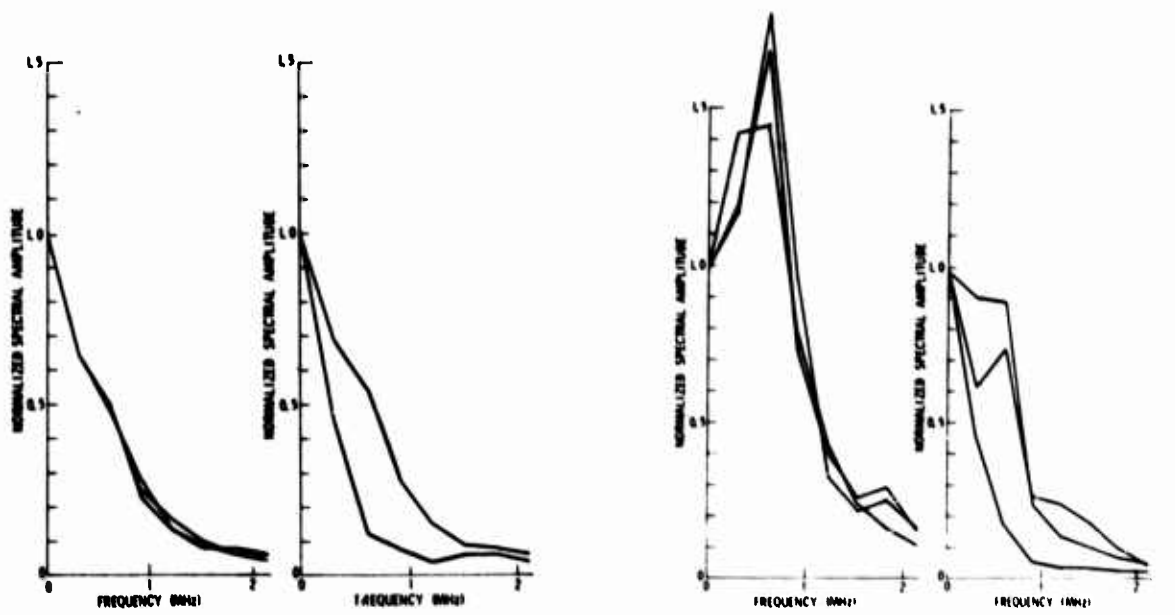
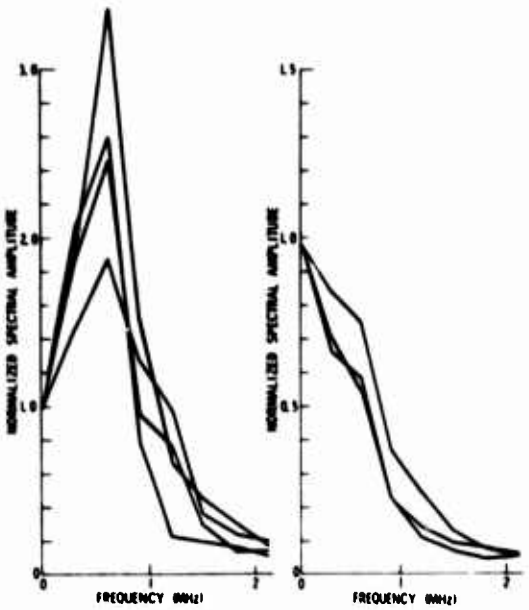


Figure 6. Results of automatic pattern recognition experiments.



(e) (f)

Figure 6. (Continued)

THE MINICOMPUTER SIGNAL PROCESSING SYSTEM HAS BEEN APPLIED IN THE FOLLOWING AREAS:

- ANALYZE BROADBAND DATA FROM SMALL VOIDS AND INCLUSIONS IN TITANIUM
- CALCULATE THEORETICAL SOLUTIONS FOR SCATTERING FROM SMALL DEFECTS
- ESTIMATE SIZE AND IMPEDANCE OF SMALL SCATTERERS
- ANALYZE BROADBAND DATA FROM ADHESIVELY BONDED ALUMINUM PARTS
- CALCULATE THEORETICAL PULSE ECHO DATA FOR ADHESIVELY BONDED PARTS
- DETERMINE STRENGTH RELATED FEATURES OF ADHESIVE BOND SIGNALS
- COLLECT AMPLITUDE-TIME DATA FOR EVERY ACOUSTIC EMISSION IN A TEST
- COLLECT WAVEFORMS AND SPECTRA FOR MOST ACOUSTIC EMISSIONS IN A TEST
- AUTOMATICALLY IDENTIFY VARIOUS TYPES OF ACOUSTIC EMISSION SPECTRA
- MEASURE VELOCITY, THICKNESS AND ATTENUATION OF COMPOSITES
- ANALYZE CLEAN SURFACES BY ELLIPSOMETRY, SURFACE POTENTIAL DIFFERENCE AND PHOTOELECTRON EMISSION
- MEASURE BONDING OF VERY INHOMOGENEOUS SPACE SHUTTLE INSULATION TILES
- DISPLAY CHLADNI FIGURES OF HONEYCOMB SANDWICH PANELS
- SIGNAL AVERAGE NON-CONTACT ELECTROMAGNETIC TRANSDUCER WAVEFORMS

Figure 7. Applications

NEW ULTRASONIC STANDARDS

B. R. Tittmann and N. E. Paton
Science Center, Rockwell International
Thousand Oaks, California 91360

ABSTRACT

Standard samples containing defects of known size, shape, and location are requirements for the evaluation and calibration of NDE test equipment. Here we review the methods developed for producing such samples from selected metallic alloys and ceramics. In the work with metallic alloys, the method of diffusion bonding Ti-6Al-4V is presented in some detail and is illustrated for a large number of samples containing a variety of defects ranging from spherical cavities and inclusions, to prolate and oblate spheroids, to thin discs and simulated cracks. In the work with ceramics, the method of hot pressing of glasses with cavities and inclusions is illustrated for a variety of defects. The presentation demonstrates how these samples may be applied in a procedure for calibrating ultrasonic systems by employing a recently proposed characteristic equation for the system and a figure-of-merit for the transducers in analogy to the gain of a radar antenna.

Figure 1 suggests a new approach to ultrasonic standards for use in the calibration of ultrasonic systems. The approach focuses attention on "calibration standards" exclusively, and introduces a single equation which characterizes the ultrasonic system and allows a step-by-step accounting of the effect such as those from transducers, material availability, etc.

The equation shown in Fig. 2(a) (ultrasonic range equation) gives a detailed accounting of all of the steps involved, from the transmitted electrical signal all the way through the scatterer to the received electrical signal. A calibration procedure is demonstrated which achieves a calibration by comparing the experimentally determined parameter, $S_{experimental}$, to its independently obtained and invarying counterpart, $S_{theoretical}$. This is demonstrated in Fig. 2 under the heading of "Calibration Procedure" and here we show a comparison over a range of scattering angles through experimental $(S)_{dB}$ values which are shown in data point open circles and theoretical expectation values to solid lines. One can see that you get very good agreement for this particular demonstrating experiment. Figure 2(b) is a photo of the fixture used to calibrate the ultrasonic system. It shows, in detail, the polygonal sample of Ti-6Al-4V alloy with a spherical tungsten carbide inclusion. Also shown are the typical commercial transducers used in the experiment. To get the graph shown in Fig. 2(c), we have to carry out the detailed calculations indicated in Fig. 2(a) for the ultrasonic range equation. The new standard is obtained by inserting a scattering target in a solid medium by using diffusion bonding or analogous techniques. This is demonstrated in Figs. 3, 4, and 5.

Metallurgical Aspects of Diffusion Bonding

In order to produce ultrasonic reference standards for calibration purposes, samples were diffusion bonded as shown in Fig. 3(a) and some of the types of defects in defect arrays are shown in Figs. 3(b) and 3(c).

The bonding process is illustrated in Fig. 4 with stringent requirements on lapping, cleaning, and diffusion bonding methods in order to create a bond with no defects or impurities, and yet produce a sound diffusion bond without gross deformation in the sample which would cause a change of shape of the defect. The sample assembly is also shown in Fig. 4, along with defects of various geometries that have been fabricated.

Figure 5 illustrates some of the requirements in the diffusion bonding process where calculations have shown that good surface preparation is essential to obtain a metallurgically sound bond at low pressure so that distortion of the desired defect is avoided. In order to calculate the desired bonding pressure and bonding time, elevated temperature flow stress measurements are made on the material out of which the sample is to be produced.

Figure 6 illustrates some of the measurements that have been made on ceramic standards. These are produced by fabricating a sample with a sphere of either nickel or some other suitable material inserted into a glass matrix. Advantages of such processes are low cost, low attenuation, low noise from the ceramic sample, and optical transparency in the glass so that the location of the defect can be found independent of the ultrasonic measurements. The overall philosophy is thus to use a target similar to a sphere in a water bath with the advantages and convenience of portability and application to shear wave calibration. The standard can be adapted to both pulse echo and pitch methods. The approach introduces a new figure-of-merit for transducers (a factor G) in analogy to the gain of the radar antenna. Thus, scattering theory plays an all-important role, because: (1) it can be introduced into the software to normalize out transducer characteristics, (2) it describes "defects" in terms of scattering cross sections, and (3) it has transferability between laboratories and inspection stations.

What we have done is defined in Fig. 7. The calibration standard is an ultrasonic standard solely employed to insure equipment is functioning according to specifications, and is in distinct contrast to the so-called reference standard which is simply a library of scatters of different shapes used to aid in the identification of an unknown

defect after ultrasonic systems have been calibrated. The objective of this work has been to develop an overall system calibration and to develop a technique that has sufficient dynamic range so that systems can be calibrated and compared to theoretically known expectations. The new feature is the ultrasonic range equation, which encourages separation of transducer effects, material reliability effects, propagation losses, and scattering in standard defects. It introduces the concept of a self-consistent calibration, i.e., the use of an additional independently-determined invariant parameter against which a system can be calibrated. It also suggests new procedures in materials for fabricating essentially material-independent calibration standards, and introduces a concept of transducer G factor as a figure-of-merit in analogy to antenna gain in radar, and, finally, it permits the theory as an aid in primary standard calibration and an aid in developing software for accurate ultrasonic testing and system calibration.

Acknowledgement

This research was sponsored by the Center for Advanced NDE operated by the Science Center, Rockwell International, for the Advanced Research Projects Agency and the Air Force Materials Laboratory under contract F33615-74-C-5180.

SUMMARY

THIS POSTER SUGGESTS A NEW APPROACH TO ULTRASONIC STANDARDS FOR USE IN THE CALIBRATION OF ULTRASONIC SYSTEMS.

THE APPROACH FOCUSES ATTENTION ON "CALIBRATION STANDARDS" EXCLUSIVELY, AND

INTRODUCES A SINGLE EQUATION WHICH CHARACTERIZES THE ULTRASONIC SYSTEM AND ALLOWS A STEP-BY-STEP ACCOUNTING OF EFFECT SUCH AS THOSE FROM TRANSDUCERS, MATERIAL AVAILABILITY, ETC.

A CALIBRATION PROCEDURE IS DEMONSTRATED WHICH ACHIEVES A CALIBRATION BY COMPARING AN EXPERIMENTALLY DETERMINED PARAMETER, S_{exp}, TO ITS INDEPENDENTLY OBTAINED AND INVARIANT COUNTERPART, S_{th}

THE NEW STANDARD IS OBTAINED BY EMBEDDING A SCATTERING TARGET IN A SOLID MEDIUM BY USING DIFFUSION BONDING OR ANALOGOUS TECHNIQUES

THE TARGET IS THUS SIMILAR TO A SPHERE IN A WATER BATH WITH ADVANTAGES IN CONVENIENCE, PORTABILITY AND APPLICATION TO SHEAR WAVE CALIBRATION

THE STANDARD CAN BE ADAPTED TO BOTH PULSE-ECHO AND PITCH-CATCH MODES

THE APPROACH INTRODUCES A NEW FIGURE-OF-MERIT FOR TRANSDUCERS, THE "TRANSDUCER GAIN FACTOR G," IN ANALOGY TO THE GAIN OF A RADAR ANTENNA

SCATTERING THEORY PLAYS AN ALL IMPORTANT ROLE BECAUSE IT:

(1) ALLOWS THE DEVELOPMENT OF SOFTWARE TO NORMALIZE OUT TRANSDUCER CHARACTERISTICS

(2) INTRODUCES THE SCATTERING CROSS SECTION

(3) HANDLES RIGOROUSLY MATERIALS TRANSFERABILITY AND VARIABILITY

Figure 1. New approach to ultrasonic standards for use in the calibration of ultrasonic systems.

ULTRASONIC RANGE EQUATION
(ANALOGOUS TO RADAR RANGE EQUATION)

$$(A_R)_{dB} = (A_T)_{dB} + (G_T)_{dB} + (P_f)_{dB} + (S)_{dB} + (G_R)_{dB} + (F)_{dB}$$

$(A_R)_{dB}$ - RECEIVED ELECTRICAL SIGNAL AS SEEN ON CRT

$(A_T)_{dB}$ - TRANSMITTED ELECTRICAL SIGNAL

$(G_T)_{dB}$ - TRANSMITTER TRANSDUCER G-FACTOR

$(P_f)_{dB}$ - PROPAGATION LOSSES

$(S)_{dB}$ - SCATTERING FUNCTION

$(G_R)_{dB}$ - RECEIVER TRANSDUCER G-FACTOR

$(F)_{dB}$ - GAIN OF RECEIVER AMPLIFIER

CALIBRATION PROCEDURE

COMPARISON OVER A RANGE OF SCATTERING ANGLES BETWEEN THE EXPERIMENTAL $(S)_{dB}$ VALUES (DATA POINTS) AND THE THEORETICAL EXPECTATION VALUES (SOLID LINE)

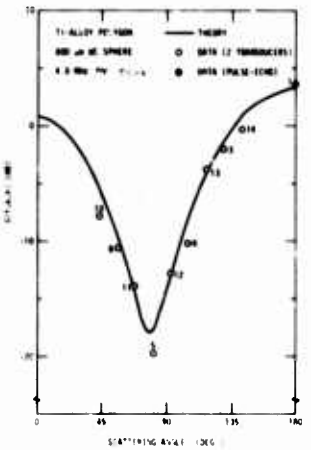


PHOTO OF FIXTURE USED TO CALIBRATE ULTRASONIC SYSTEM.

(1) COMMERCIAL TRANSDUCER

(2) POLYGONAL SAMPLE OF Ti-6Al-4V ALLOY WITH SPHERICAL TUNGSTEN CARBIDE INCLUSION (0.030 cm DIAMETER)

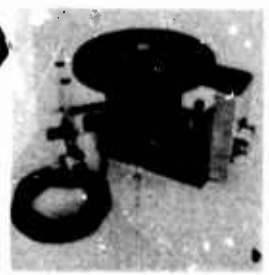


Figure 2. Ultrasonic range equation, calibration fixture, and calibration procedure.

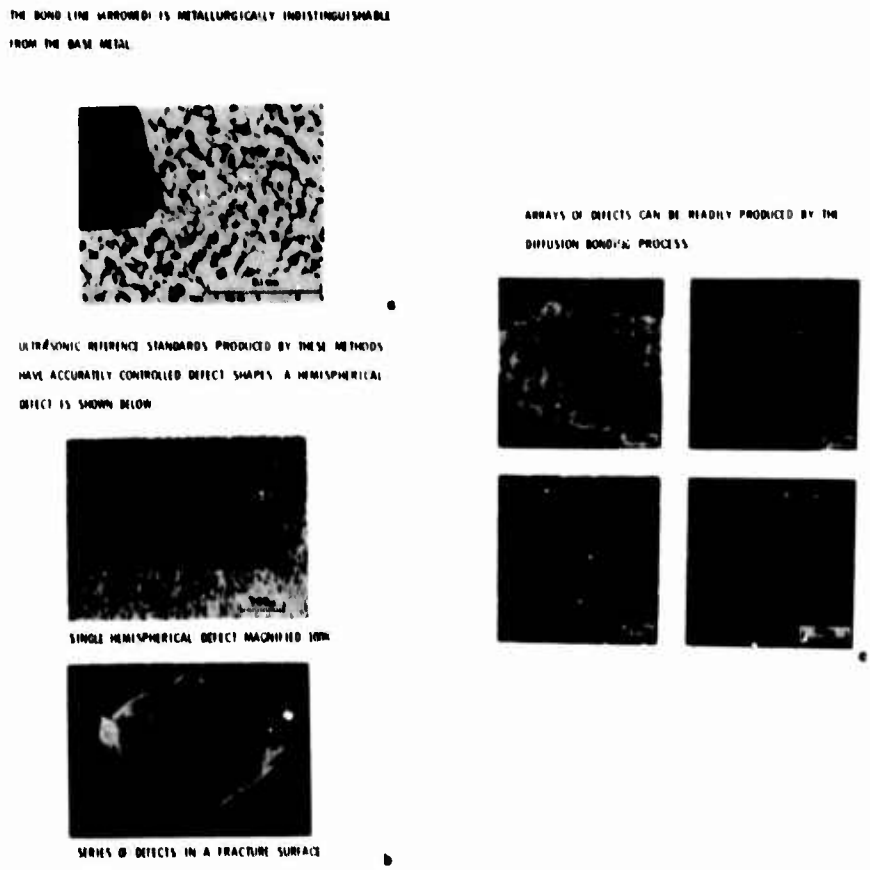
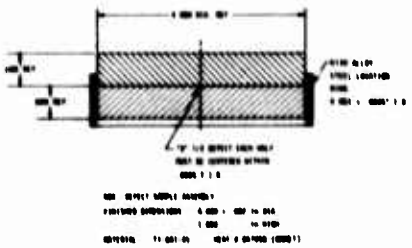


Figure 3. (a) Diffusion bonded sample; (b) and (c) types of defects and defect arrays.

THIS TABLE SHOWS THE SURFACE PREPARATION AND DIFFUSION BONDING PROCEDURES USED FOR Ti-6Al-4V.

LAPPING	SURFACE GROUND AND LAPPED TO 4 FINISH FLAT TO WITHIN FOUR OPTICAL BANDS	
CLEANING	1. WASH IN ACETONE	
	2. WASH IN ALKALINE CLEANER 80-100 C	15 MIN.
	3. RINSE IN DISTILLED WATER	5 MIN.
	4. PICKLE 60% BY VOLUME HNO_3	
	10% g/LITER $NH_4F \cdot HF$	
	BALANCE H_2O	
	5. RINSE IN RUNNING DISTILLED WATER	5 MIN.
	6. PASSIVATE 10% HNO_3	1.5 MIN.
	7. RINSE IN DISTILLED WATER	5 MIN.
	8. AIR PRESSURE RINSE	
	9. RINSE IN DISTILLED WATER - 6 TIMES	1-2 MINS EACH
	10. OVEN DRY - 90-120 C	15 MIN.
DIFFUSION BONDING	1. HEAT IN VACUUM OF BETTER THAN 10^{-5} TORR TO SPECIFIED TEMPERATURE 1600 OR 1750 C.	
	2. LOAD TO 500 psi FOR 30 MINS	
	3. COOL IN VACUUM	

SAMPLE ASSEMBLY FOR 4 INCH DIAMETER SPECIMEN



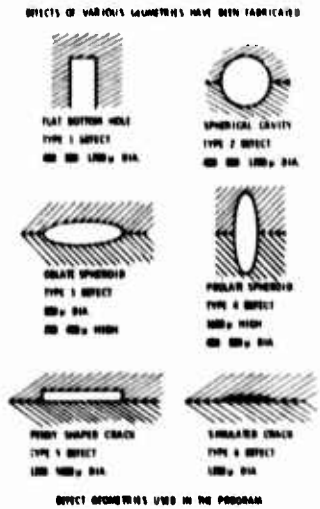


Figure 4. Illustration of bonding process.

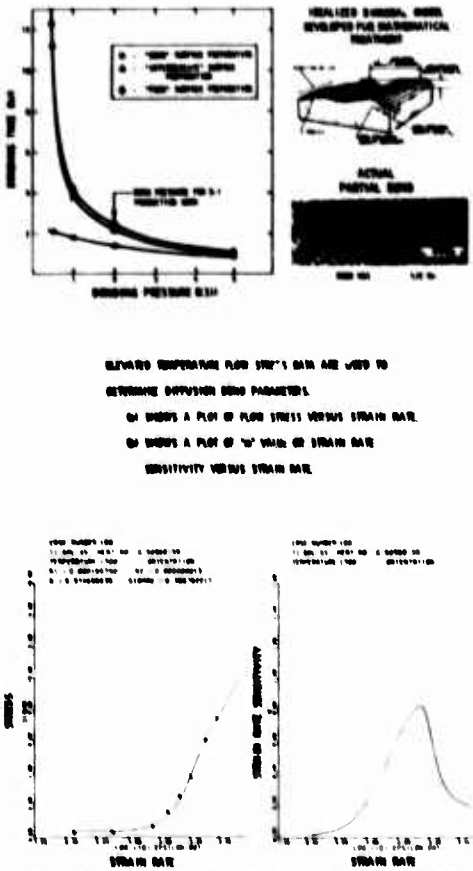
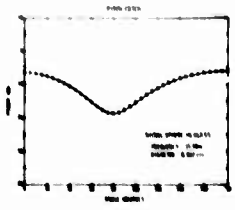
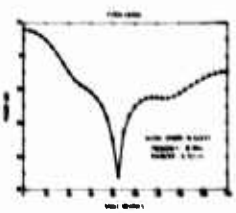


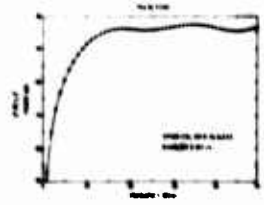
Figure 5. Sample requirements in the diffusion bonding process.

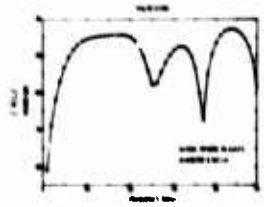
ADVANTAGES

- LOW COST
- LOW ATTENUATION
- LOW CERAMIC NOISE
- OPTICAL TRANSPARENCY
- DURABILITY
- HOMOGENEITY ISOTROPY
- STABILITY (NO DISLOCATIONS)
- REPRODUCIBILITY
- LIGHT WEIGHT (PORTABILITY)









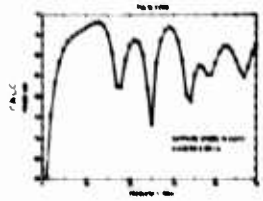


Figure 6. Measurements made on ceramic standards.

DEFINITIONS

CALIBRATION STANDARD

- ULTRASONIC STANDARD SOLELY EMPLOYED TO ENSURE EQUIPMENT IS FUNCTIONING ACCORDING TO SPECIFICATIONS

REFERENCE STANDARD

- LIBRARY OF SCATTERERS OF DIFFERENT SHAPES USED TO AID IN IDENTIFICATION OF AN UNKNOWN DEFECT AFTER ULTRASONIC SYSTEM HAS BEEN CALIBRATED.

OBJECTIVES

- DEVELOP AN OVERALL SYSTEM CALIBRATION
- DEVELOP A TECHNIQUE THAT HAS SUFFICIENT DYNAMIC RANGE SO THAT LINEARITY CHECK IS MEANINGFUL WITH NO DEGREES OF FREEDOM
- DEVELOP A TECHNIQUE SO THAT SYSTEM CAN BE CALIBRATED AND COMPARED TO THEORETICALLY KNOWN EXPECTATIONS

NEW FEATURE: ULTRASONIC RANGE EQUATION

- ENCOURAGES SEPARATION OF TRANSDUCER EFFECTS, MATERIAL RELIABILITY EFFECTS, PROPAGATION LOSSES AND SCATTERING FROM STANDARD DEFECT.
- INTRODUCES CONCEPT OF "SELF-CONSISTENT CALIBRATION," (i.e. THE USE OF AN ADDITIONAL INDEPENDENTLY DETERMINED, INVARIANT PARAMETER AGAINST WHICH A SYSTEM CAN BE CALIBRATED.)
- SUGGESTS NEW PROCEDURES AND MATERIALS FOR FABRICATING ESSENTIALLY MATERIAL INDEPENDENT CALIBRATION STANDARDS
- INTRODUCES CONCEPT OF TRANSDUCER G-FACTOR AS FIGURE-OF-MERIT IN ANALOGY TO ANTENNA GAIN IN RADAR
- PERMITS USE OF THEORY AS AID IN FABRICATION, AID IN "PRIMARY STANDARD" CALIBRATION, AID IN DEVELOPING SOFTWARE FOR RAPID, INEXPENSIVE FIELD CALIBRATION.

Figure 7. Results

DIGITALLY CODED ELECTROMAGNETIC TRANSDUCERS

T. J. Moran
Air Force Materials Laboratory
Wright-Patterson AFB, Ohio 45433

ABSTRACT

Electromagnetic transducers had previously been shown to be capable of acting as pulse compressors to achieve improved range resolution. Compression was achieved using pairs of transducers designed to produce or detect a burst with a linear frequency variation. An alternate approach, which is also easier to fabricate, is to impress a digital phase code on single frequency coils. One such code with good autocorrelation properties is the 13 bit Barker coder. Coils with this code were fabricated and evaluated. It will be shown that the operation of these devices is very similar to the coils with dispersive designs. The waveforms, compression ratio, and sidelobe levels to be expected from these devices are described.

Introduction

In a previous paper[1], it was shown that one inherent problem with electromagnetic surface acoustic wave transducers (SAW EMT's) is poor range resolution due to the long tone burst outputs of the devices. One solution to the problem is the use of pulse compression techniques which were developed originally for radar applications to achieve an output pulse from the receiving transducer which is comparable to the broadband pulse normally used for NDE ultrasonic inspections. In the previous work, the pulse compression scheme chosen for evaluation was the use of a transducer designed to produce a chirp signal which is a tone burst within which the frequency varies linearly with time. When such a signal is received by an identical transducer, it is compressed by an amount equal to the pulse width-bandwidth product.

One problem with the chirp design is the difficulty of fabrication since the high frequency segment of the chirp normally requires very narrow line spacings which are near the limit of resolution of the present photoetch production technique. An alternative scheme which is very much easier to fabricate is to digitally phase code[2] the output waveform of a transducer which is basically a single frequency device. Of the large number of codes available[2], the 13 bit Barker code was selected for use with SAW EMT's because it was best able to give the required performance within the constraints imposed by the physical nature of the EMT. These constraints were as follows: First, for ease of fabrication, the bits should be composed of complete cycles with each bit at 0° or 180° phase difference. Second, the largest number of lines which can be effectively utilized with the permanent magnets available is on the order of 30. Since line spacing is 1/2 wavelength, two lines are required for the minimum length bit, the maximum number of bits is on the order of 15. Third, the code should have minimum sidelobe levels.

The Barker codes fulfill the third constraint very well. This class of codes has sidelobe levels at 0 or 1 with the main peak at level N where N is the number of bits[2]. A 13 bit code is the maximum length code in the Barker class and this code would require a 26 line EMT coil if each bit is one cycle. Thus, this code fulfills all the constraints.

Design and Operation

The coil design for the Barker 13 bit phase coded EMT is shown in Fig. 1. The thick outside lines are current return paths which are not meant to generate significant acoustic amplitude. In the first design these lines were of the same thickness as the lines in the active part of the coil. It was found that the acoustic signals from these lines were of the same order of magnitude as those generated in the active region. When they were made very thick, however, the current density was lowered and the frequencies at which they could couple to acoustic waves were shifted low enough that no signals were detected from these lines during subsequent tests.

Coils were constructed which were designed to operate at fundamental frequencies of 4 and 7.25 MHz. The output waveform of the 4 MHz coil when it is driven with an approximately 50 n sec wide pulse and exciting surface waves in aluminum is shown in Fig. 2. In this case the receiving transducer is a 10 MHz Panametrics broadband wedge transducer. The permanent magnets were set roughly 1/8" apart since this distance produced the largest output pulse. As can be seen from the figure, the magnet configuration produces a rather strongly peaked field and the acoustic amplitude as a function of position is correspondingly peaked.

When the waveform shown in Fig. 2 is received by an identical transducer the compressor output pulse as shown in Fig. 3 results. The resulting sidelobes do not have the uniform level one would expect for the ideal case. An elementary analysis showed that the peaking of the output pulse gives rise to two effects in the sidelobes. First, the amplitude of the sidelobes increases as the central maximum is approached and second, the points which would normally be zeros reach a finite amplitude. In this case it should be noted that only the sidelobes adjacent to the central maximum are greater than 1/13 of the peak which is the magnitude of all the sidelobes in the ideal case. Thus, the nonuniform amplitude only harms the performance

near the central peak. The width of the compressed pulse is slightly greater than 400 n sec, yielding a compression ratio of greater than 7.

An attempt was made to determine the effect on the performance if a more uniform amplitude output were obtained. Rough uniformity in the magnetic field was obtained by inserting a 1/4" spacer between the magnets, considerably reducing the field strength. This magnet configuration produced the output signal shown in Fig. 4 and the corresponding compressed pulse in Fig. 5. As can be seen from these figures, the output pulse is close to the theoretically desired and the sidelobes have much less structure. However, the sidelobe amplitudes still increase as the central maximum is approached and the amplitude of the central peak is reduced by approximately 35% from the previous case.

The Barker 13 bit phase coded coils with the 7.25 MHz fundamental frequency were investigated in a similar manner. The output signal from the pulse excited coil is not shown here because the bandwidth of the piezoelectric transducer receiver was not sufficient to reproduce the rapid phase changes between bits. However, the amplitude was found to be peaked as in Fig. 2 for a similar magnet configuration. The compressed output signal from the transducer pair is shown in Fig. 6. The main difference in this waveform as compared to the output of the 4 MHz units is a reduction in the pulse width. In this case, the compressed pulse is on the order of 200 n sec wide. This pulse width is comparable to that obtained with the 4 MHz bandwidth chirp transducers used in the previous study[1].

Conclusions

It has been shown that a digitally phase coded EMT will perform in a manner comparable to the chirp EMT with the advantage of being easier to fabricate. One distinct disadvantage of this design is the sidelobe levels. With the digital coding there is little one can do to reduce these levels in contrast to possible reductions one can obtain in the chirp case with suitable spectral weighting[2].

References

1. T. J. Moran, 1976 Ultrasonic Symp. Proc., IEEE Cat. #76 CH1120-5SU, p. 26 (1976).

2. C. E. Cook, M. Bernfeld, and C. A. Palmieri, Microwave Journal, pp. 73-81, Jan. 1965.



Figure 1. Coil design for 13 bit Barker coded EMAT.

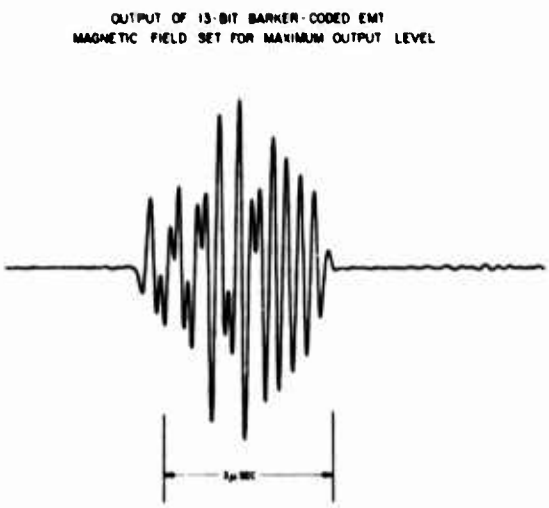


Figure 2. Output of a single 13 bit Barker coded EMAT which is pulse excited. Signal propagated on aluminum and received with a piezoelectric transducer, f = 4 MHz.

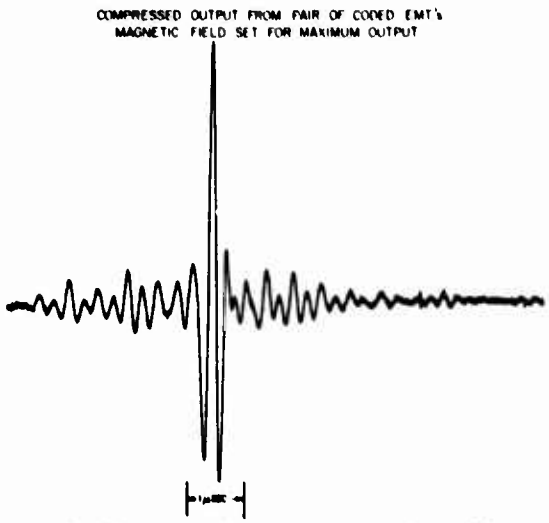


Figure 3. Response of an identical 13 bit Barker coded EMAT to the signal shown in Fig. 2.

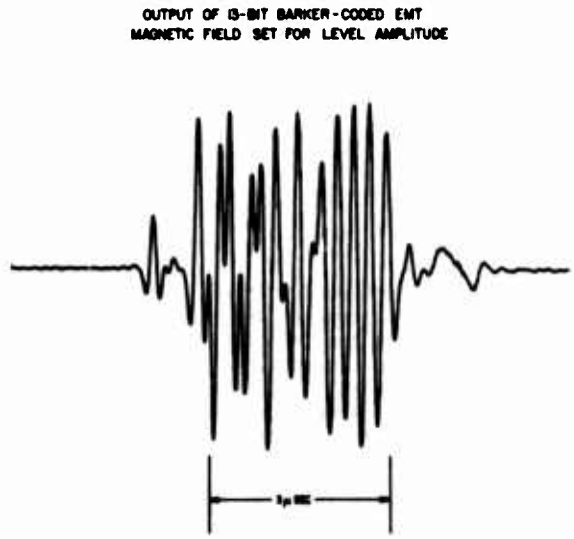


Figure 4. Nearly uniform amplitude output signal from a 13 bit Barker coded EMT achieved by using magnets with a wider spacing between the pole faces. Piezoelectric receiver.

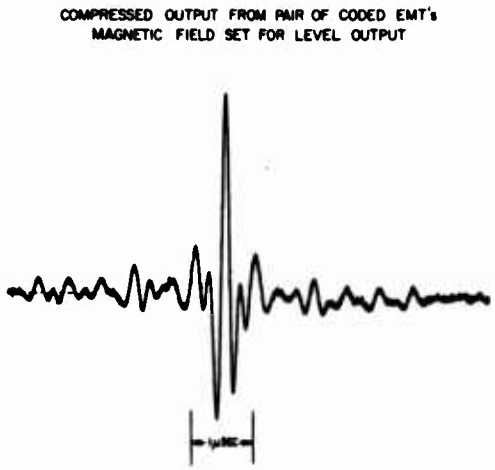


Figure 5. Response of an identical 3 bit Barker coded EMT to the signal shown in Fig. 4. Note the decrease in the number of sidelobes.



Figure 6. Response of a pair of 13 bit Barker coded EMT's operating with a fundamental frequency of 7.25 MHz. Note the narrowing of the compressed pulse as compared to the MHz devices.

NEW ELECTROMAGNETIC TRANSDUCER APPLICATIONS

R. B. Thompson
Science Center, Rockwell International
Thousand Oaks, California 91360

ABSTRACT

A number of recently identified applications of electromagnetic transducers (EMAT's) are identified. These have been made possible by the development of optimized electronics which allow one to obtain high signal-to-noise ratios in EMAT systems despite the fact that the transduction efficiencies are somewhat lower than those of piezoelectric transducers. It has been demonstrated that EMAT's can be used to excite horizontally polarized shear waves which have the property that the particle motion is always parallel to the surface of the part in which they are excited, independent of the direction of propagation. Such waves have a number of attractive features. They do not mode convert on reflection from obstructions parallel to the shearing motion, they are not accompanied by the excitation of surface waves, they can be scanned in angle with little change in amplitude by varying the drive frequency, and they can be excited and detected at surfaces that may be irregular, painted or at high temperatures. Application of these transducers to the inspection of welds in thick plates at welding temperatures is discussed. An ultrasonic ellipsometer, which excites a shear wave of controlled, elliptical polarization which can be used in a fashion analogous to optical ellipsometry to measure the properties of thin layers, such as adhesive bonds, is presented. The use of EMAT's to detect residual stress in ferromagnetic materials is also reviewed.

This poster summarizes a number of new ultrasonic inspection capabilities that have been made possible by electromagnetic-acoustic transducers (EMAT's) and that represent advances that contribute to the well-known advantages of non-contact operation.

Figure 1 shows that optimum transducer systems have been developed by combining the development of sensitive, dedicated electronics with analysis of radiation properties. This analysis is particularly appropriate for EMAT's since the coupling is very reproducible.

Figure 2 illustrates that horizontally polarized angle shear beams can be excited, as opposed to the vertically polarized beams produced by angled incidence of a compressional wave excited by a piezoelectric transducer. Several of the advantages of the horizontal shear waves are enumerated.

Figure 3 demonstrates one use of this new transducer in the high-temperature, electronically-scanned inspection of welds.

Figure 4 carries this idea one step further by indicating that shear waves of arbitrary elliptical polarization can be excited using the periodic permanent magnet EMAT. This makes possible the construction of an elastic wave ellipsometer having high sensitivity to surface conditions, analogous to an optical ellipsometer.

Figures 5 and 6 show that, on ferromagnetic materials, EMAT's can be used to measure residual stress. This occurs because magnetostriction is very stress sensitive. EMAT efficiency is determined by magnetostrictive properties, and specific parameters in the field variation of transducer efficiency can be selected as stress indicators. The properties of a device built on these principles are indicated.

In Fig. 7, a number of the many advantages of EMAT's are summarized.

Acknowledgement

This research was sponsored by the Center for Advanced NDE operated by the Science Center, Rockwell International, for the Advanced Research Projects Agency and the Air Force Materials Laboratory under contract F33615-74-C-5180, and the Rockwell International Independent Research and Development program.

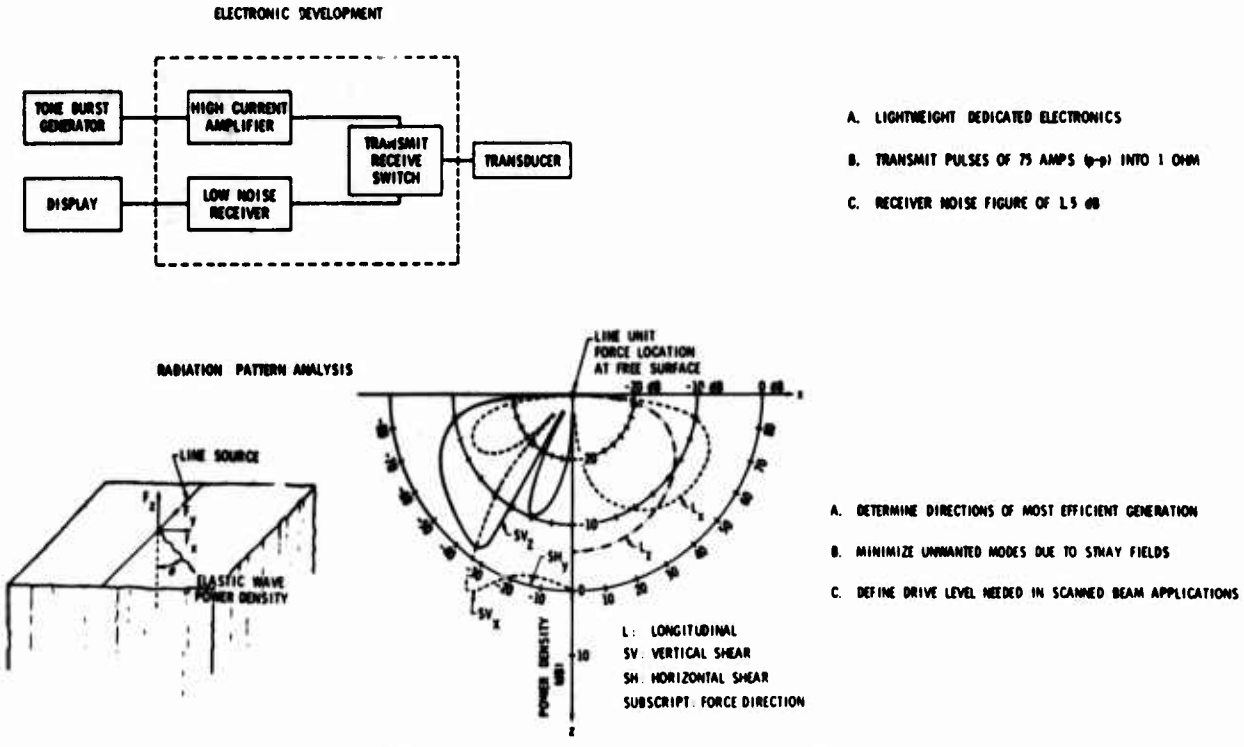


Figure 1. Optimized transducer systems.

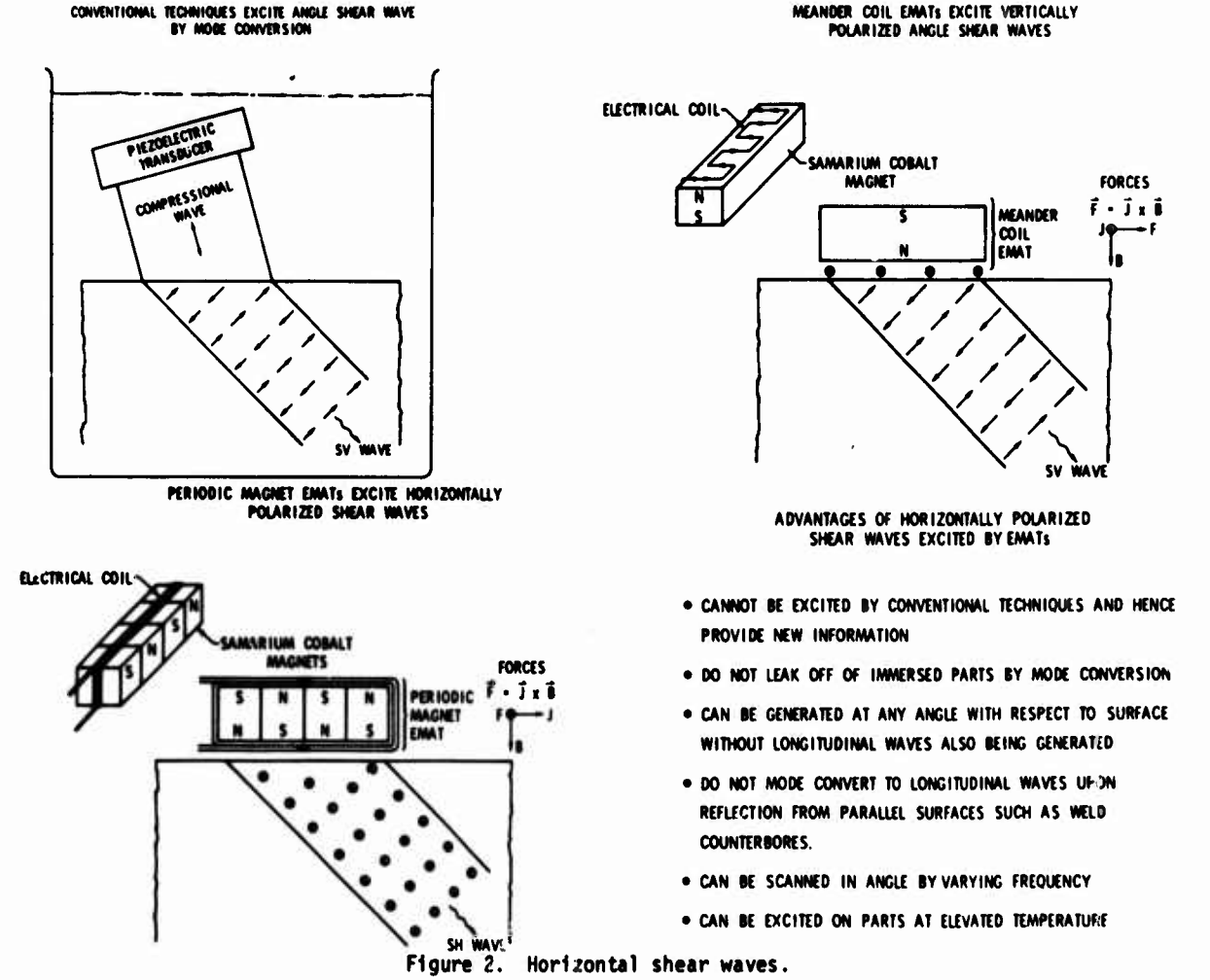


Figure 2. Horizontal shear waves.

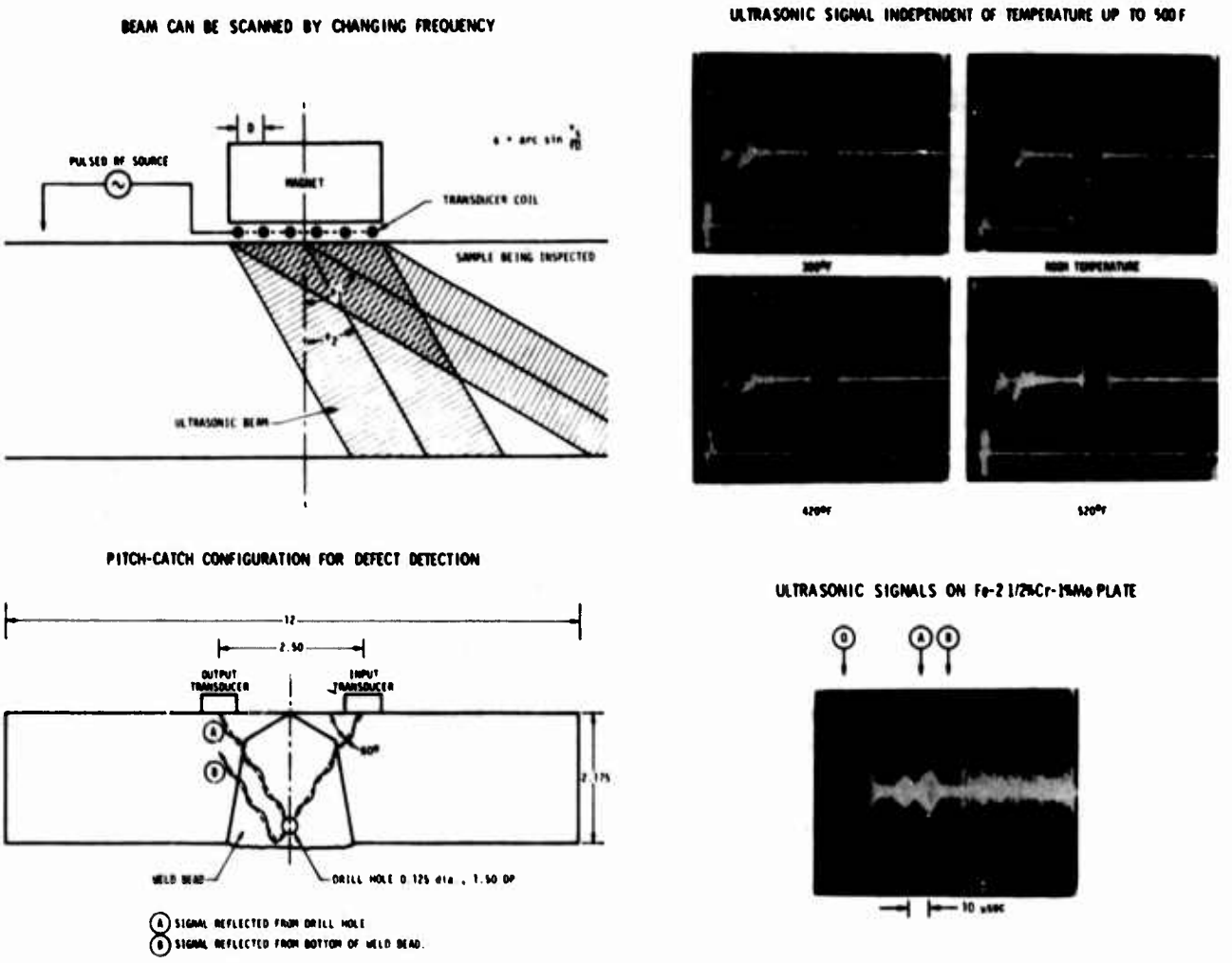


Figure 3. High temperature electronically scanned weld inspection.

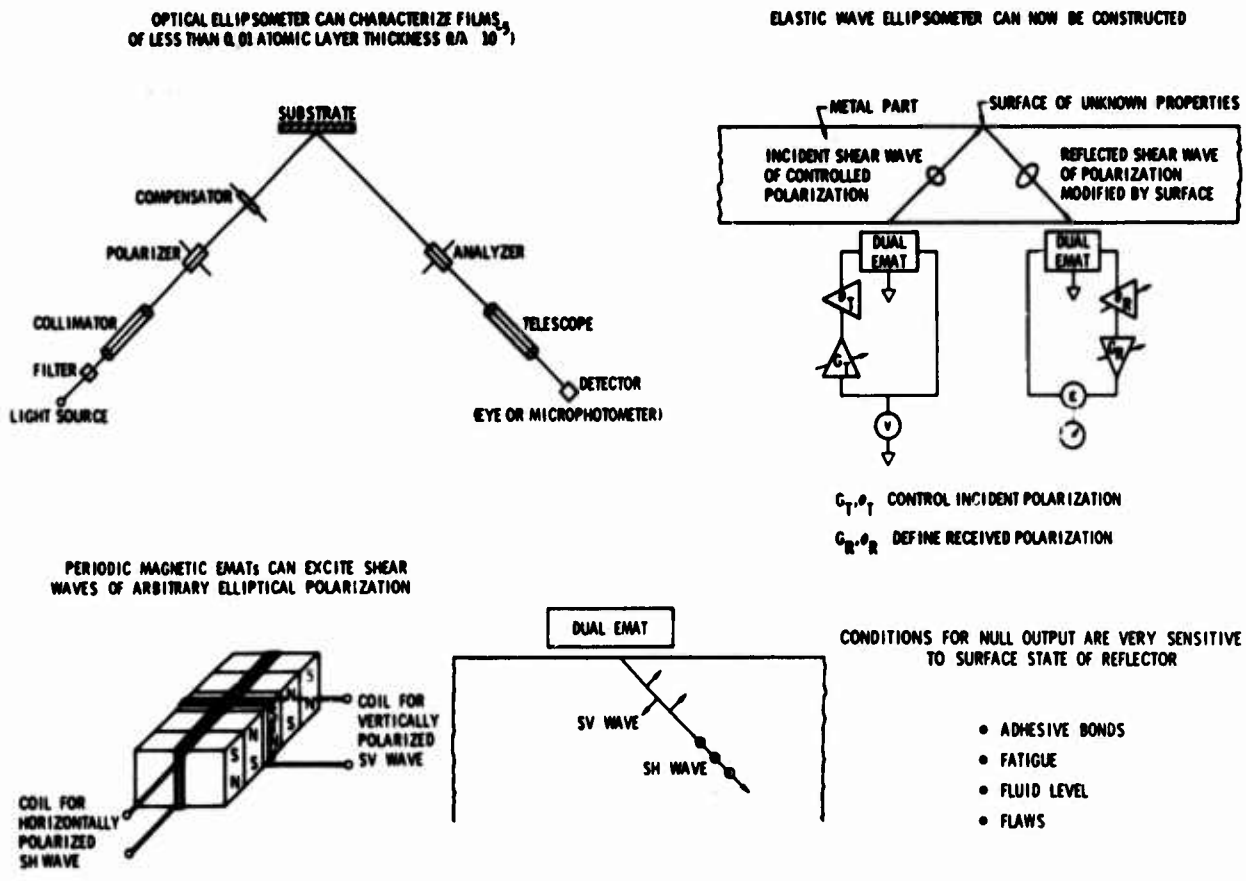


Figure 4. Elastic wave ellipsometer.

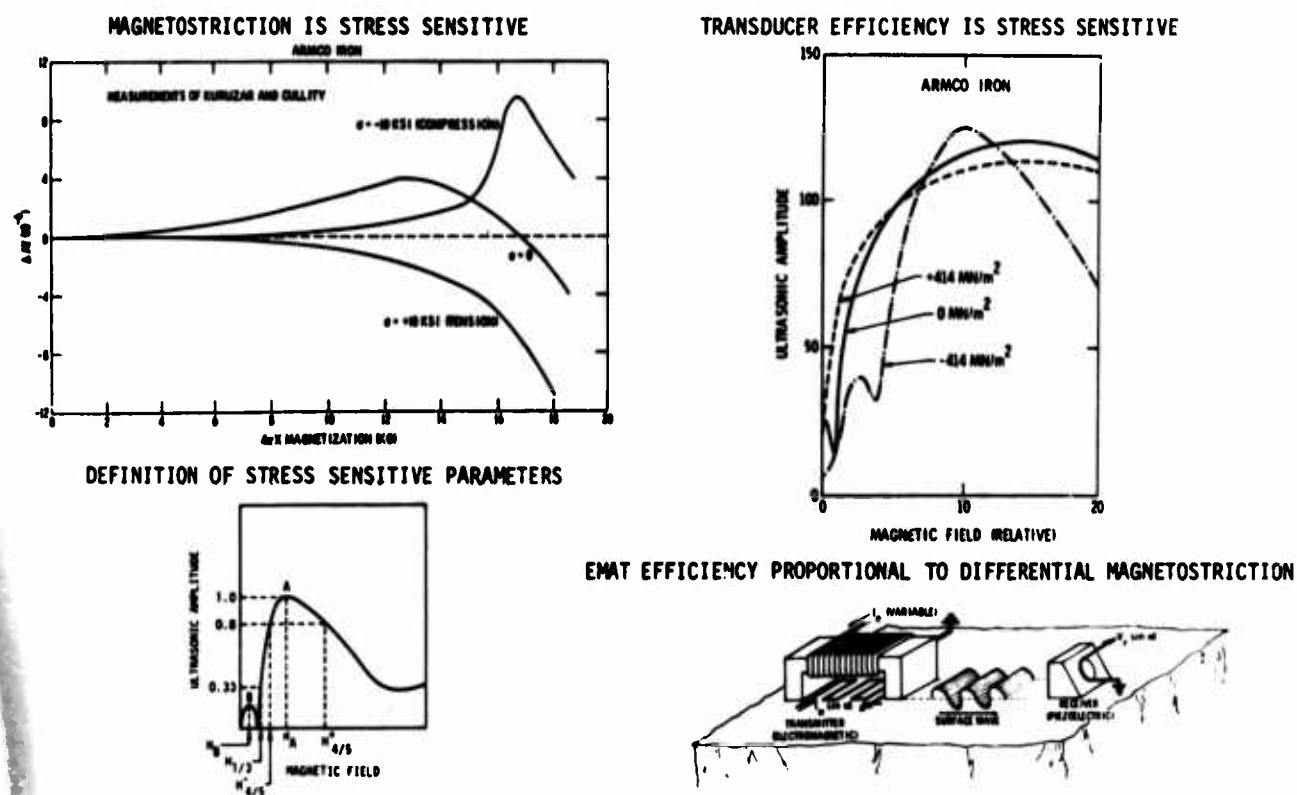
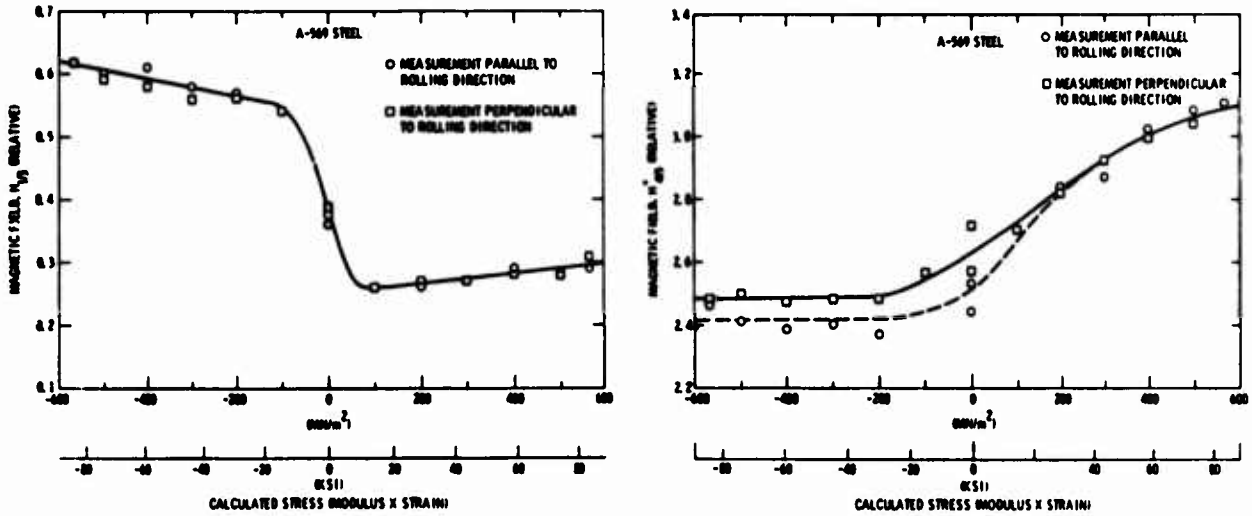


Figure 5. Stress detection in ferromagnets.



SUMMARY OF CHARACTERISTICS

- LIGHTWEIGHT, PORTABLE PROBE
- OPERATION ON PAINTED AND ROUGH SURFACES
- MEASUREMENT AVERAGES STRESSES OVER ELECTROMAGNETIC SKIN DEPTH
- PRELIMINARY EXPERIMENTS INDICATE FATIGUE DETECTION POSSIBLE
- MULTIPLE PARAMETERS USEFUL IN DISTINGUISHING STRESS EFFECTS FROM MATERIAL VARIABILITIES

Figure 6. Experimental data showing behavior of different parameters.

- ELECTROMAGNETIC TRANSDUCERS PARTICULARLY USEFUL
  - AT HIGH SPEED
  - AT HIGH TEMPERATURE
  - IN REMOTE LOCATIONS
  - FOR ELECTRONICALLY CONTROLLED BEAM SCANNING
- ELECTROMAGNETIC TRANSDUCERS CAN PRODUCE NEW WAVE TYPES
  - HORIZONTALLY POLARIZED SHEAR WAVES
  - SHEAR WAVES OF CONTROLLED ELLIPTICAL POLARIZATION
  - RADIALLY POLARIZED SHEAR WAVES
- ELECTROMAGNETIC TRANSDUCERS CAN BE USED TO DETECT STRESS IN FERROMAGNETIC MATERIALS

Figure 7. Conclusions.

ARTILLERY PROJECTILE INSPECTION WITH EMAT'S

C. M. Fortunko
Science Center, Rockwell International
Thousand Oaks, California 91360

ABSTRACT

A technique for ultrasonically inspecting 135 mm artillery projectiles has been demonstrated. Non-contact EMAT's placed on the outside of the projectile excited 2.25 MHz surface waves and 1.8 MHz angle shear waves which were used to detect EDM slots on both the inner and outer surfaces. The defect locations and sizes, 0.051 cm (0.020 in.) deep and 0.508 cm (0.200 in.) long were chosen on the basis of fracture mechanics analysis. Each was detected with signal-to-noise ratios in excess of 30 dB. These results indicate that it is feasible to construct a system for full inspection of projectiles at normal production line rates. Among the desirable features of such a system are the absence of an ultrasonic couplant, the resulting potential for high speed operation, and the convenience with which multiple transducers can be incorporated to achieve high coverage and to gain additional information for defect characterization.

This poster presents the results of a recently completed study which demonstrated the feasibility of inspecting artillery projectiles for critical defects with electromagnetic transducers. The purpose was to show that the non-contact feature of EMAT's could be used to advantage in the design of a high-speed system for 100%, on-line inspection.

Figure 1 shows a longitudinal cross-section of a M107 projectile on which the locations of defects that were studied are indicated. These were placed in regions where high stresses are produced during firing.

Figure 2 shows in addition a circumferential cross-section showing one possible location of transmitting and receiving transducers.

A photograph of the laboratory test-bed is shown in Fig. 3. The large electromagnet provides the necessary bias field. The transducer coils are seen on top.

Figure 4 shows that the same transducers can be used to inspect the exterior with 2.25 MHz surface waves or the entire wall, including interior surfaces, with angle shear waves at 1.8 MHz, traveling circumferentially around the shell.

Figure 5 shows the ultrasonic surface wave signals reflected from a 0.020 inch deep, 0.200 inch long EDM notch on the exterior. Note that the signals propagating completely around the shell are observed and that the flaw is easily detected at any point in the circumferential belt interrogated by the transducers.

Figure 6 shows similar results for the angle shear mode. In this case, the full circumferential signals are not seen as clearly because the inner surface is not parallel to the exterior surface of the projectile wall. However, the defect signals again have high signal-to-noise ratios.

Figure 7 shows an artist's concept of an on-line inspection system, which would include a raster of transducers of the type shown in Fig. 3 positioned along the length of the projectile. Included are the conclusions of this successful feasibility demonstration, which indicate that high-speed on-line inspection should be possible with this technique.

Acknowledgement

This work was supported by the U. S. Army, Frankford Arsenal, Philadelphia, Pennsylvania under contract number D AAA25-76-C-0381.

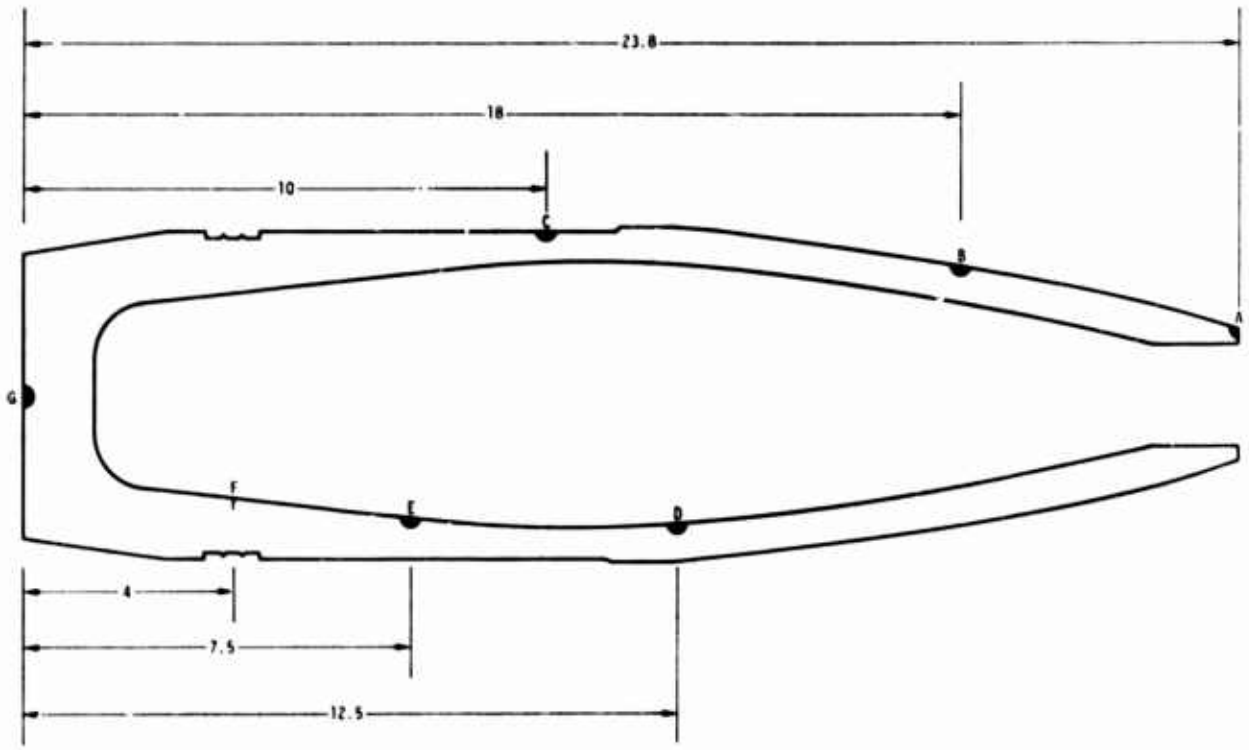
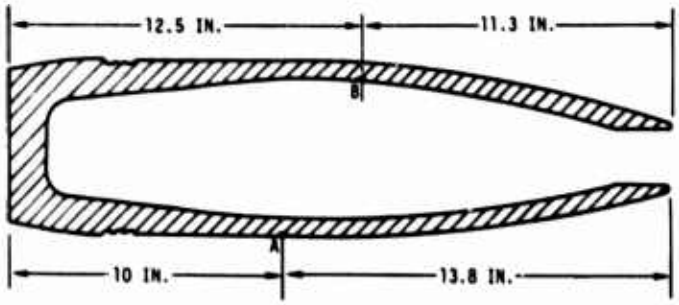


Figure 1. Cross sectional view of a 155 mm artillery projectile with EDM slots machined in exterior and interior surfaces.

LOCATION OF SLOTS IN 155, M107 PROJECTILE

(EDM SLOTS 0.020 INCH DEEP, 0.200 INCH LONG)



EXPERIMENTAL SETUP

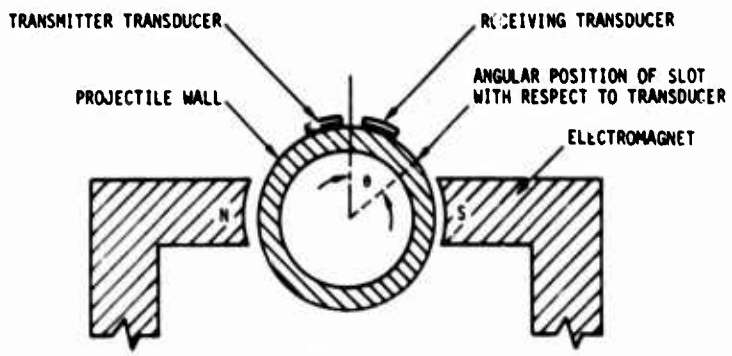
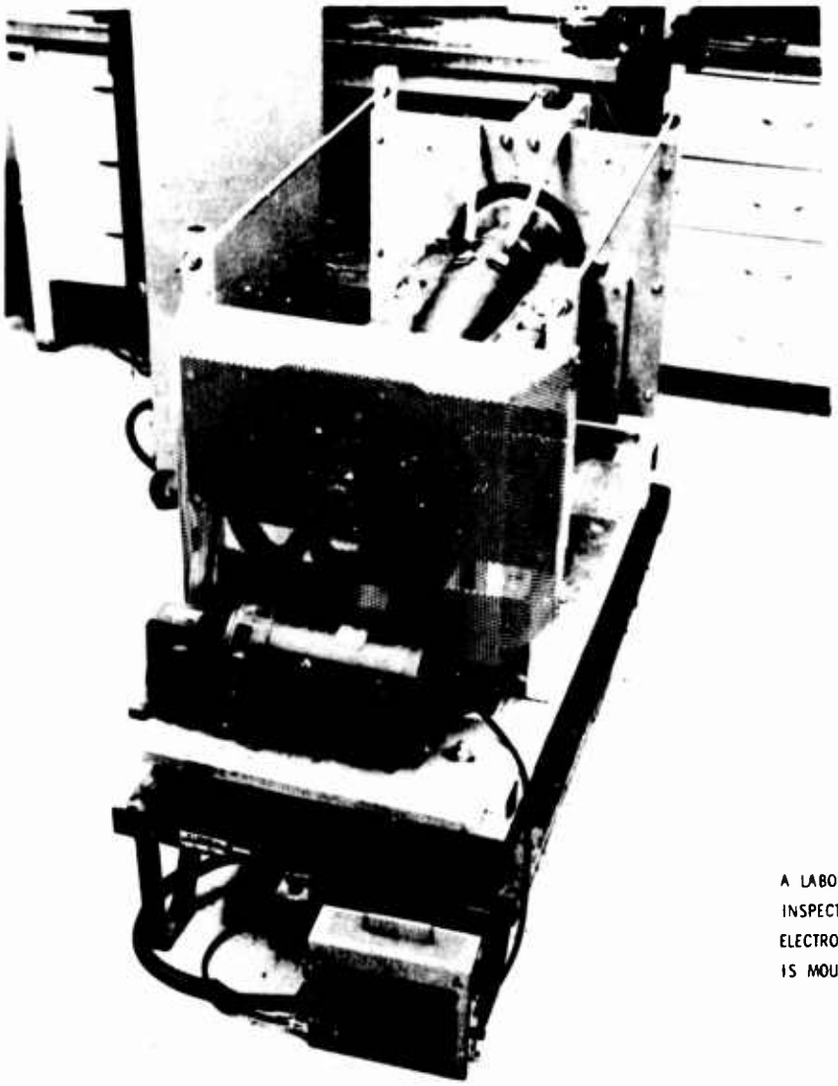


Figure 2. Circumferential cross section of a M107 projectile (155 mm) showing one possible location of transmitting and receiving transducers.



A LABORATORY TEST-BED FOR ARTILLERY PROJECTILE INSPECTION, INCLUDING TWO MEANDER COIL ELECTROMAGNETIC TRANSDUCERS. THE PROJECTILE IS MOUNTED IN THE GAP OF AN ELECTROMAGNET

Figure 3. Laboratory test bed.

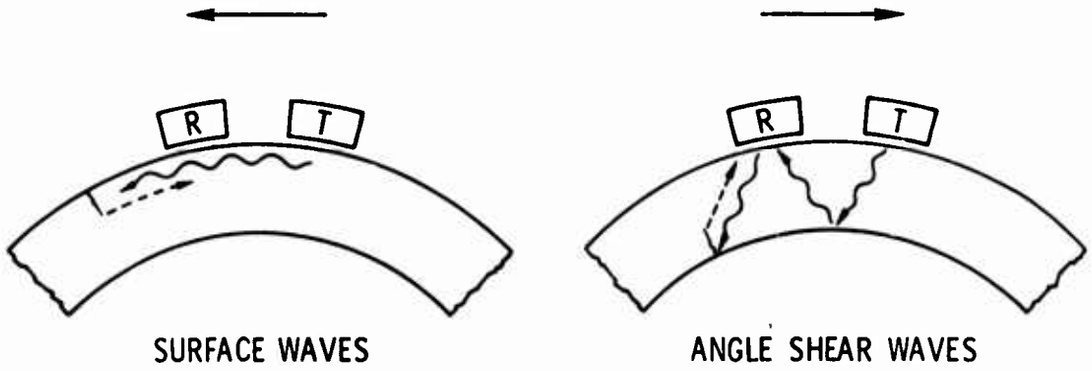
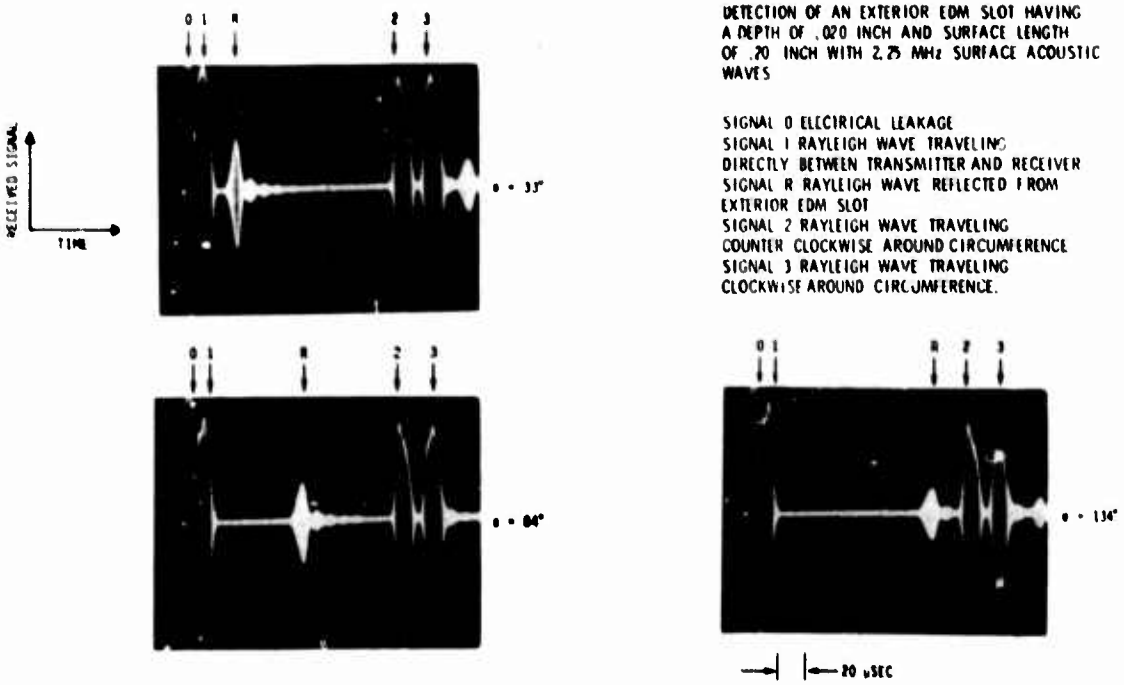


Figure 4. Inspection of projectile wall.



DETECTION OF AN EXTERIOR EDM SLOT HAVING A DEPTH OF .020 INCH AND SURFACE LENGTH OF .20 INCH WITH 2.25 MHz SURFACE ACOUSTIC WAVES

SIGNAL 0 ELECTRICAL LEAKAGE
SIGNAL 1 RAYLEIGH WAVE TRAVELING DIRECTLY BETWEEN TRANSMITTER AND RECEIVER
SIGNAL R RAYLEIGH WAVE REFLECTED FROM EXTERIOR EDM SLOT
SIGNAL 2 RAYLEIGH WAVE TRAVELING COUNTER CLOCKWISE AROUND CIRCUMFERENCE
SIGNAL 3 RAYLEIGH WAVE TRAVELING CLOCKWISE AROUND CIRCUMFERENCE.

Figure 5. Detection of an exterior EDM slot with 2.25 MHz surface acoustic waves.

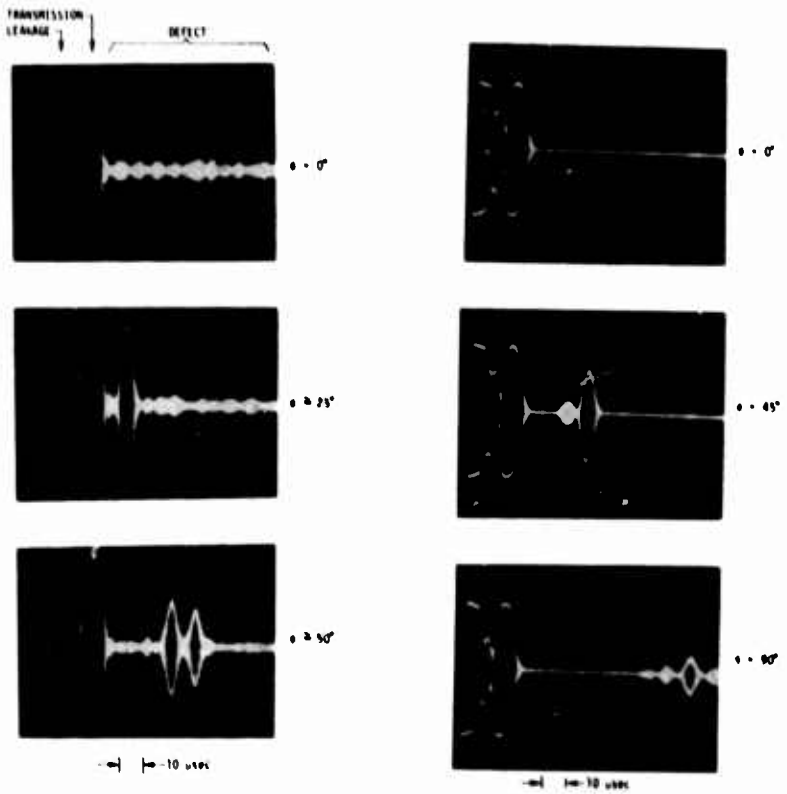


Figure 6. Detection of exterior and interior defects with 1.8 MHz angle shear waves.

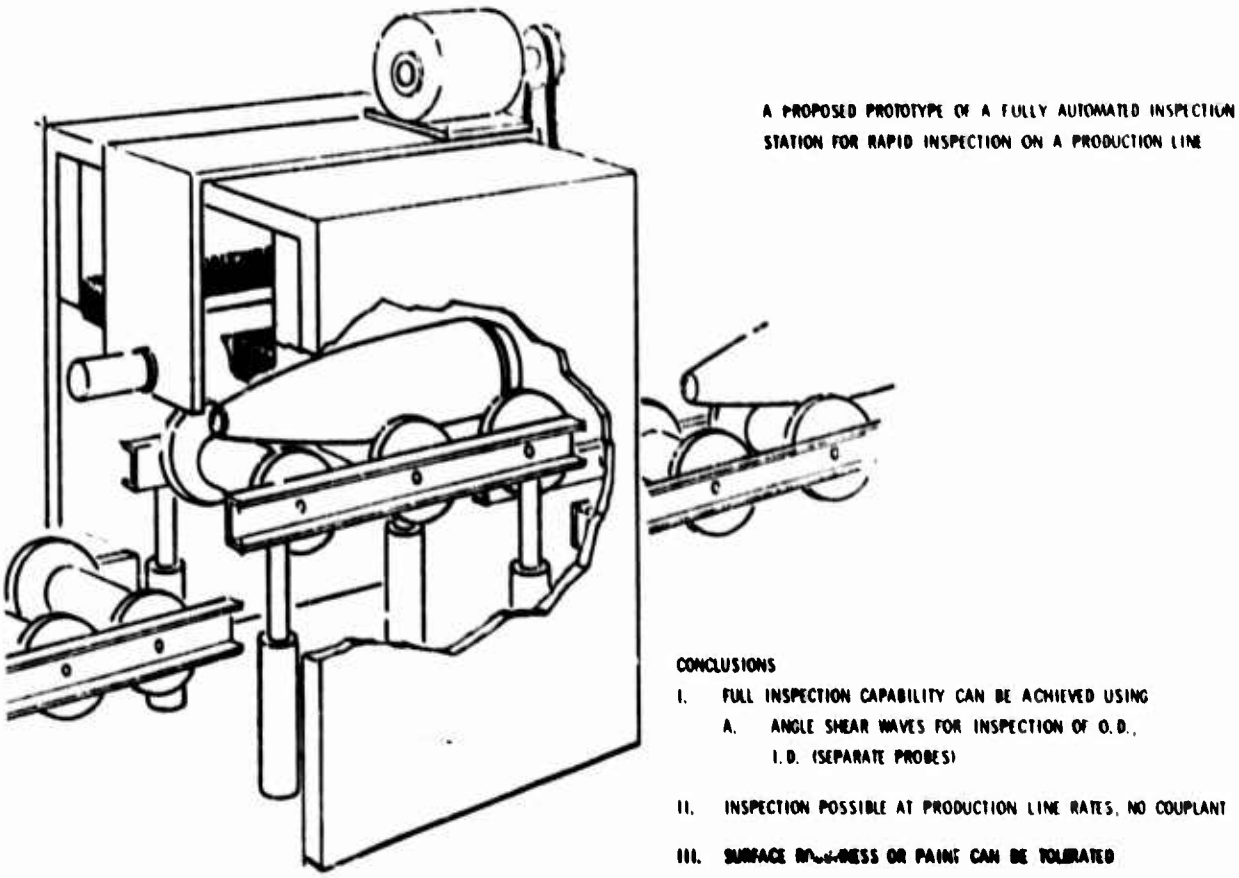


Figure 7. Artist's concept of an on-line inspection system.

STEAM GENERATOR TUBE INSPECTION WITH EMAT'S

C. F. Vasile
Science Center, Rockwell International
Thousand Oaks, California 91360

ABSTRACT

A brief summary of newly developed techniques for ultrasonic inspection of small diameter tubes using EMAT's is given. The technique employs a periodic-permanent magnetic torsion wave transducer which fits inside and can be quickly translated through the tube. Both dominant and higher order ultrasonic modes traveling longitudinally along the tube can be individually excited by varying the transducer design parameters. Experimental results are presented which define transduction efficiencies in aluminum, Inconel, and steel and the sensitivities of the various wave types to different defects. The ability of these techniques to detect flaws in difficult regions such as U-bends and dents is reported.

This poster presents the results of a recently completed study that demonstrated the feasibility of inspecting steam generator tubes in a pressured water reactor for commercial electrical power generation. The purpose was to show that compact EMAT's can be constructed which operate efficiently from within the 7/8 in. OD, 0.050 in. wall Inconel tubes and hence make possible ultrasonic inspection at comparable rates to those exhibited by the presently used eddy current systems.

Figure 1 presents a more detailed statement of the objective, problem, and proposed solution.

Figure 2 contains a schematic sketch of the periodic permanent magnet EMAT developed to generate torsional modes of the tube. Also shown is a photograph of some of the probes and a schematic of a pitch-catch configuration used in the study.

Figure 3 presents the elastic wave dispersion curves for a flat plate of the same thickness as the tube wall and indicates the operating points of the transducers.

Figure 4 shows the ultrasonic signals from a variety of machined defects in aluminum tubes as pictured. Note that the end reflections which clutter the A-scans would be absent in the 70 meter long steam generator tubes.

Figure 5 shows that defects can be detected in regions where the tubes have been dented, a problem that occurs in steam generators as a result of corrosion products building up where tubes pass through support plates.

Figure 6 is a tabulation of the measured reflection coefficients for a wide variety of defects for both the $n = 0$ and $n = 1$ tube modes.

Figure 7 presents the conclusions of this work.

Acknowledgement

This work was supported by the Electric Power Research Institute, Inc., Palo Alto, California under Project ERPI RP698-1.

OBJECTIVE:

ACCURATE DEFECT CHARACTERIZATION IN INCONEL OR FERRITIC STEAM GENERATOR TUBING IN ORDER TO PROVIDE A BASIS FOR PLUGGING UNSERVICEABLE TUBES.

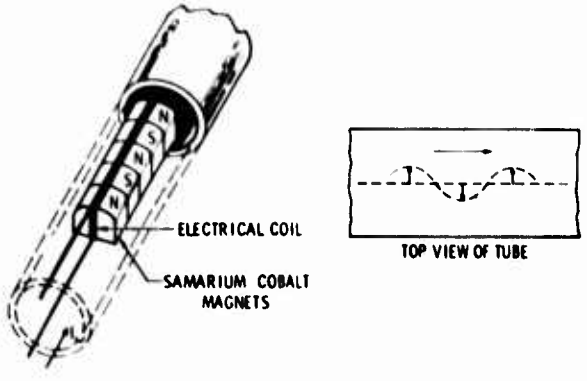
PROBLEMS:

1. LARGE NUMBER OF TUBES
2. RADIATION CONTAMINATION
3. LIMITED ACCESS
4. FAST PULLING RATES REQUIRE LOW-DRAG-NON-CONTACT PROBES
5. REGIONS WHERE ESTABLISHED EDDY CURRENT INSPECTION TECHNIQUES ARE NOT RELIABLE.

SOLUTION:

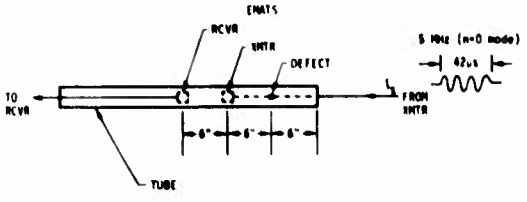
NEW NON-CONTACT ULTRASONIC TORSION WAVE TRANSDUCER TO COMPLEMENT ESTABLISHED EDDY CURRENT INSPECTION TECHNIQUES.

Figure 1. Statement of objective, problems, and solution.



SKETCH OF TORSIONAL WAVE TRANSDUCER

TOP VIEW OF TUBE



SKETCH ILLUSTRATING EXPERIMENTAL TEST SETUP



PHOTOGRAPH OF EXPERIMENTAL TRANSDUCERS

Figure 2. Torsional wave.

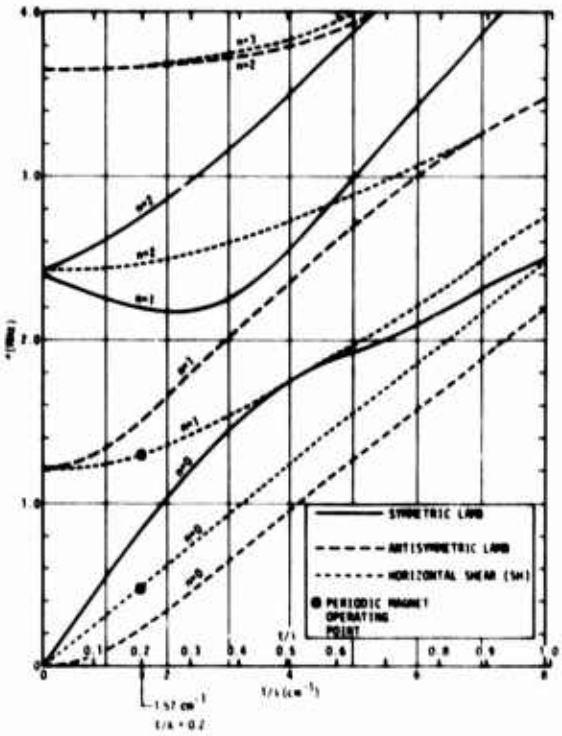


Figure 3. Dispersion curves for a 0.05 in. (0.127 cm) thick inconel plate.

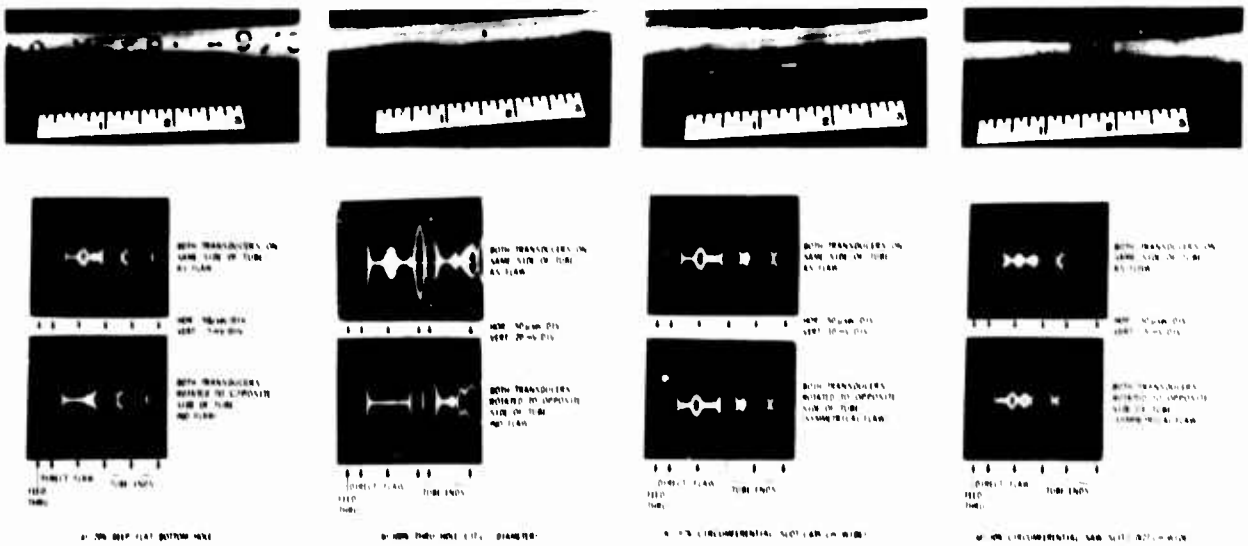


Figure 4. Defect detection in aluminum tubing.

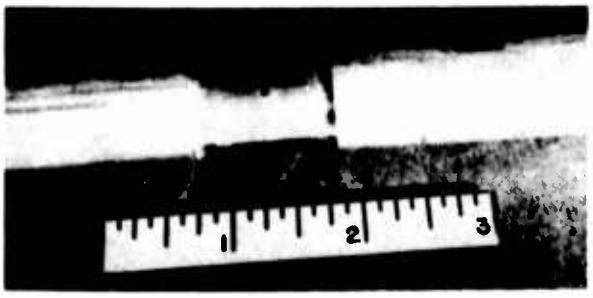


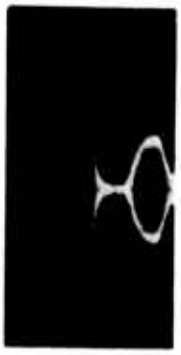
PHOTO OF DENTED SECTION
AND DEFECT .17cm DIAMETER HOLE



50% DEEP



80% DEEP



NO HOLE



30% DEEP



60% DEEP



100% DEEP

DEFECT GROWTH IN A DENTED REGION (7% REDUCTION IN DIAMETER)

Figure 5. Detection of defects in dented tubes.

REFLECTION COEFFICIENTS FOR MACHINED DEFECTS

DEFECT	AMPLITUDE RATIO		dB	
	n=0	n=1	n=0	n=1
A. ALUMINUM TUBES 7/8" O.D. .049" WALL				
1) .188" DIAM .010" DEEP FLAT BOTOM HOLE	.02	.107	-34	-19
2) .109" DIAM .03" DEEP FLAT BOTTOM HOLE	.016	.093	-36	-21
3) .067" DIAM THROUGH HOLE	.15	.087	-17	-21
4) .25" WIDE .005" DEEP CIRCUMFERENTIAL SLOT	.05	.62	-26	-4
5) .005" WIDE .005" DEEP CIRCUMFERENTIAL SLOT	.019	.07	-35	-23
6) .25" WIDE .005" DEEP 2" LONG AXIAL SLOT	.008	.1	-42	-20
7) .011" WIDE .005" DEEP .2" LONG AXIAL SLOT	.01	.03	-40	-30.5
B. STEEL (4130) TUBES 7/8" O.D. .049" WALL				
8) .067" DIAM THROUGH HOLE	.24	.138	-12.4	-17
C. INCONEL TUBES 7/8" O.D. .049" WALL				
9) .067" DIAM THROUGH HOLE	.35	.073	-9	-23
10) .3" LONG .03" WIDE .02" DEEP TRANSVERSE V-GROOVE	-	.093	-	-21

Figure 6. Summary of measured defect signals.

1. NEW TYPE OF NON-CONTACT ELECTROMAGNETIC TRANSDUCER HAS BEEN DEVELOPED FOR INSPECTION OF TUBES FROM INTERIOR OR EXTERIOR.

2. TRANSDUCERS MAKE TUBE INSPECTION FEASIBLE IN GEOMETRICALLY DIFFICULT REGIONS.
    a. DENTS AT TUBE SUPPORTS
    b. U-BENDS

3. TRANSDUCERS ALLOW NEW INFORMATION TO BE OBTAINED THAT IS COMPLEMENTARY TO EDDY CURRENT DATA.
    a. CIRCUMFERENTIAL DEFECTS
    b. THINNING AND WALL THICKNESS MEASUREMENT POSSIBLE WITH HIGHER ORDER MODE

4. PROBES WORK WELL IN FERRITIC TUBES.

ACKNOWLEDGEMENT

WORK SUPPORTED BY EPRI PALO ALTO CALIFORNIA UNDER CONTRACT NO. EPRI RP 698-1.

Figure 7. Conclusions.

BURIED GAS PIPELINE INSPECTION WITH EMAT'S

G. A. Alers
Science Center, Rockwell International
Thousand Oaks, California 91360

ABSTRACT

The electromagnetic, noncontact transducer (EMAT) is particularly well suited to ultrasonic inspection problems where it is difficult or impossible to couple the sound into the object being tested through a liquid or grease layer. For inspecting buried natural gas pipelines, the inspection process must be carried out by a self contained instrument package blown through the pipe by the gas stream. This demands that the transducers move with speeds of 10 to 20 mph along the pipe and give continuous operation over distances of 50 to 100 miles. Under the sponsorship of the American Gas Association, it has been demonstrated that EMAT's designed to launch and detect Lamb waves which propagate around the circumference of the pipe can meet these inspection requirements. The special transducers designed for this purpose used conductors laid down in a meander line configuration with the spacing between the adjacent lines chosen to be equal to one half of the wave length of the first antisymmetric Lamb wave mode of the pipe wall (a flexure wave) at the operating frequency of 130 KHz. These Lamb waves were focused into a beam of energy and directed around the pipe circumference so that when they encountered a longitudinal stress corrosion crack or a region of pit corrosion, the reflection of energy could be used to detect the location and approximate size of the defect. Both transmitters and receivers were fabricated and the detection of simulated defects machined into the outside surface of a 36-inch dia. by 40-foot long section of pipe buried at the Science Center has been demonstrated. In addition, special experiments were performed to demonstrate that the EMAT's performed satisfactorily when the metal moves past them at speeds up to 20 mph (27 ft/sec, 1/3 inches/millisecond).

Natural gas pipelines that have been buried for some time are subject to corrosion and stress corrosion cracking which may cause leaking after extended service. In order to find areas where leaking may soon occur, it is desirable to inspect the pipeline periodically with a self-contained instrument package that can be blown through the pipe by the gas stream and which can record the presence and location of potentially weak areas. Current devices to accomplish this inspection use magnetic flux leakage techniques to detect localized thinning of the pipe wall, but these turn out to be insensitive to longitudinal stress corrosion cracks and to non-localized regions of generalized corrosion. Recently, the American Gas Association has sponsored a program at the Science Center to determine if the new ultrasonic technology based on Electromagnetic Acoustic Transducers (EMAT's) could be used in the remote environment of a buried gas pipeline and give new and different information on the defects in the pipe wall.

Figure 1 lists the requirements set down by the gas association which any ultrasonic inspection device must meet in order to be useful. It also gives the characteristics of the EMAT based system which make it a viable concept for this application.

Figure 2 shows the basic principles of operation. A meander coil EMAT is placed between the poles of a permanent magnet (or an electromagnet) and held in proximity to the ID of the pipe. There it excites ultrasonic Lamb waves in the pipe wall which propagates around the circumference of the pipe in both a clockwise and a counterclockwise direction. If a defect lies anywhere on the circumference, it will reflect a portion of the Lamb wave energy back toward the transmitter. By placing a meander coil receiver transducer between the poles of the same magnet as was used for the transmitter, it can pick up the reflection from the defect in the typical ultrasonic pulse-echo mode of inspection. One magnet with a receiver and a transmitter could, in principle, inspect the entire pipe circumference, but attenuation and beam spreading make it more practical to utilize three transducer pairs positioned at equal angular intervals around the circumference as is shown on the right-hand side of the figure.

Figure 3 shows that two types of Lamb waves can be excited in the pipe walls at the low frequencies for which the wave length is comparable to the pipe wall thickness. At the single frequency of 130 KHz, these two Lamb waves have quite different propagation velocities and the different distortions shown on Fig. 3. The differing velocities of propagation mean different wave lengths so that the spacing of the meander coils in the transducers is only about 3/8 inches for the flexural wave and about 5/8 inches for the longitudinal wave case.

Figure 4 shows an example of the pulse-echo signals resulting from some simulated defects machined into the pipe wall. In this case, separate transmitter and receiver transducers and magnets were used. The numbers labeling each RF pulse signal displayed on the oscilloscope photographs are associated with the wave paths shown in the drawing of a cross-section of the pipe. Figure 5 shows photographs of the top and bottom views of the experimental inspection system as it entered a 40-foot long section of a 36-inch diameter test pipe.

Figure 6 lists the accomplishments attained by the Science Center program to date. It can be concluded that the EMAT type of transducer can be used to detect longitudinal stress corrosion cracks and generalized pipe wall thinning in buried pipelines. It now becomes necessary to install this technology on an inspection device designed to operate in real pipelines of several miles in length.

Acknowledgement

This work was supported by the American Gas Association, contract PR-73-57.

REQUIREMENTS

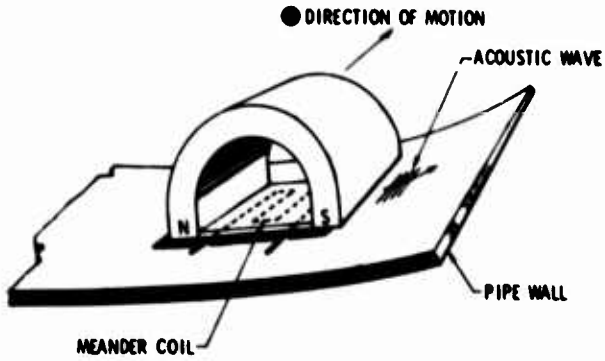
- DETECT EXTERNAL DEFECTS FROM AN INTERNAL SENSOR
- INSPECT ENTIRE LENGTH (20 - 100 MILES) AND CIRCUMFERENCE (18 - 48 IN. DIA.)
- ACCOMMODATE SHARP TURNS
- TRAVEL AT GAS FLOW SPEEDS (10 - 20 MPH)
- SELF-CONTAINED DATA PROCESSING AND RECORDING
- DEFECT CHARACTERIZATION

ULTRASONIC INSPECTION SYSTEM

- EMATs OPERATE AT HIGH SPEED
- CIRCUMFERENTIAL LAMB WAVES SENSITIVE TO LONGITUDINAL CRACKS
- FEW TRANSDUCERS NEEDED TO INSPECT ENTIRE CIRCUMFERENCE
- MAGNETIC FIELD NEEDED ONLY AT TRANSDUCERS
- COMPACT SHAPE POSSIBLE FOR SHARP TURNS
- ULTRASONIC SIGNAL ANALYSIS FOR DEFECT IDENTIFICATION

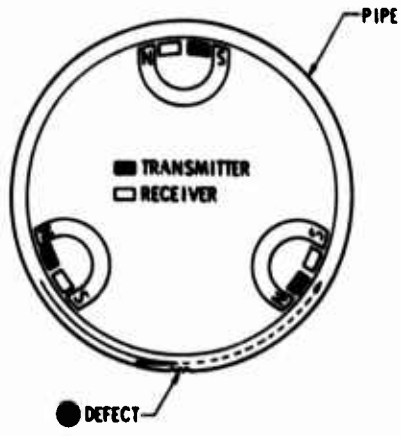
Figure 1. Gas Association requirements for ultrasonic inspection devices and characteristics of EMAT based system.

NONCONTACT ELECTROMAGNETIC TRANSDUCER



HIGH SPEED MOTION POSSIBLE

INSPECTION PRINCIPLE

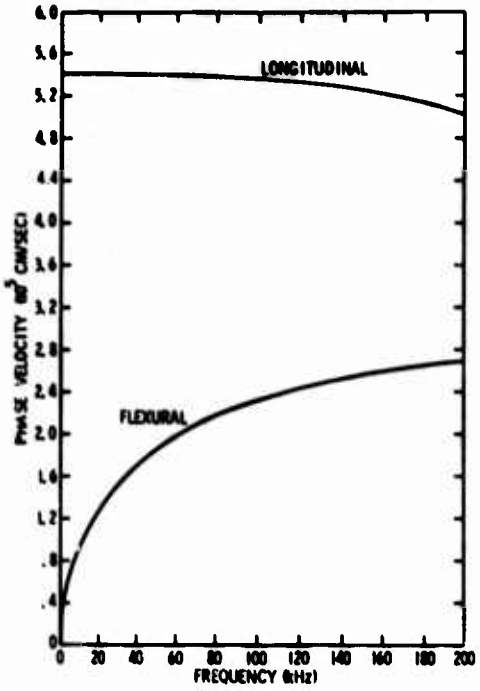


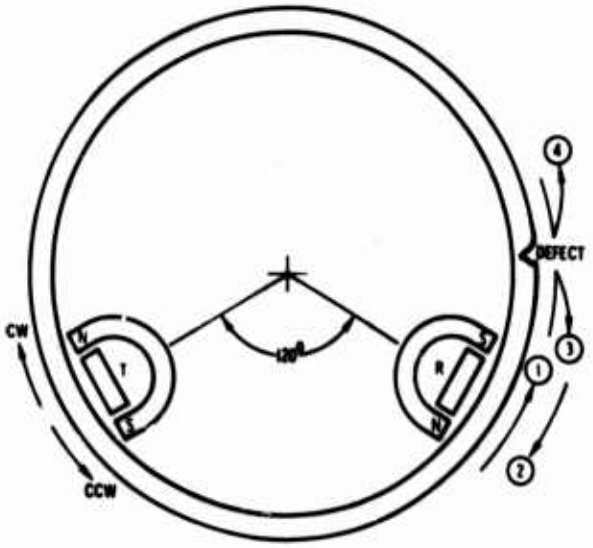
DEFECT CHARACTERIZATION POSSIBLE

LAMB WAVES LAUNCHED AND DETECTED AT EACH MAGNET

- DEFECTS LOCATED BY PULSE-ECHO REFLECTION TECHNIQUES
- AT 20 MPH TRANSDUCERS MOVE 0.3 INCHES/MILLISECOND

Figure 2. Basic principles of operation for an EMAT based system.

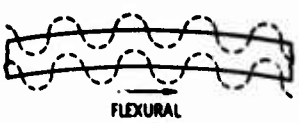




- EMAT'S GENERATE CLOCKWISE AND COUNTERCLOCKWISE LAMB WAVES
- FULL CIRCUMFERENCE SIGNALS USEFUL FOR NORMALIZING SIGNALS











- LAMB WAVES ARE VIBRATIONAL MODES OF A PLATE IN WHICH THE ENERGY IS TRAPPED BETWEEN THE TWO BOUNDARIES OF THE PLATE

- FOR PIPELINE INSPECTION A FREQUENCY OF 130 kHz EXCITES LAMB WAVES THAT HAVE A WAVE LENGTH COMPARABLE TO THE PIPE WALL THICKNESS

Figure 3. Lamb waves.

Figure 4. Pipe echo signals.



PHOTOGRAPH OF VEHICLE ENTERING A 36 INCH DIAMETER PIPE
TWO EMAT's LOCATED AT 4 AND 8 O'CLOCK



UNDERSIDE OF ONE EMAT MAGNET SHOWING A RECEIVER BETWEEN
THE POLE PIECES AND A TRANSMITTER UNDER ONE POLE PIECE

Figure 5. Experimental inspection vehicle.

CONTRACT SPONSORED BY THE AMERICAN GAS ASSOCIATION

PHASE I	DEMONSTRATION OF FEASIBILITY OF USING EMATs AND LAMB WAVES
PHASE II	DEMONSTRATE OPERATION FROM A MOVING PLATFORM IN A BURIED PIPE
PHASE III	DEMONSTRATE TECHNIQUES FOR DEFECT CHARACTERIZATION AND HIGH SPEED OPERATION
PHASE IV	OPTIMIZE SYSTEM COMPONENTS AND DEMONSTRATE OPERATION ON REAL DEFECTS
PHASE V	CONSTRUCT EXPERIMENTAL INSPECTION SYSTEM WITH ON-BOARD RECORDING
PHASE VI	GENERATE QUANTITATIVE DATA FOR SENSITIVITY DETERMINATIONS

Figure 6. Accomplishments.

ULTRASONIC IMAGING SYSTEMS

G. S. Kino, T. M. Waugh, and D. Corl
Stanford University
Stanford, California 94305

ABSTRACT

The use of ultrasonic imaging systems for non-destructive evaluation is increasing, with particular interest being paid to research into real time and quasi-real time imaging systems. Photos are shown which were taken using an electronically scanned and focused real time ultrasonic imaging system. The system can be operated with longitudinal waves, shear waves, Rayleigh waves, and Lamb waves in the 1.5 MHz to 3.5 MHz frequency range, and has been successfully used on composite materials (boron fiber epoxy on titanium) and on a number of metals (steel, aluminum, and titanium). This system has been operated in both transmission and reflection modes; examples of each are shown.

Results Obtained on an Electronically Scanned and Focused Imaging System

During the last three years, a new type of electronically scanned and focused acoustic imaging system has been demonstrated for use in non-destructive testing applications. The system has been operated in A-scan, B-scan, and C-scan testing modes and has demonstrated increases in speed of as much as 100 times that of an equivalent mechanically scanned system while producing images which are easily recognizable by a human operator and which produce information on the two-dimensional location of its size and shape. As far as we are aware, this is the first electronically scanned and focused imaging system that has been used in NDT applications.

Consider the application of the system in a C-scan mode. With a normal mechanical scan, illustrated in Fig. 1, a focused receiver and transmitter would be used to obtain definitions of the order of 1 mm. It might take many hours to scan a raster to produce a visual display of a large object. In an equivalent electronically scanned system, illustrated in Fig. 2, arrays of as many as 100 transducer elements are employed in the transmitter and receiver. By electronic signal processing, the beam can be focused and scanned along a line parallel to the array in less than 60 μsec. The method employed makes use of surface acoustic wave technology, and employs a surface acoustic wave delay line with one tap per element of the array. By this means, a phase reference is introduced which is equivalent to the action of a physical lens. The electronic lens behaves like a physical lens which scans a line in the x direction parallel to the array at a rate comparable to the acoustic velocity in the medium; the focal length of this lens can be changed electronically, at will. At the present time, the definition in the perpendicular direction, the y direction (parallel to the array surface) is controlled either by a slit in front of the object or by a physical lens, or, alternatively, by the width of the beam itself. Scanning in the vertical direction is still arranged mechanically, but now, because of the use of 100 elements in the array, the basic scanning speed has been increased by 100 times.

An acoustic image of a boron fiber reinforced epoxy laminate laid down on titanium, supplied to us by E. Caustin of the Los Angeles Division, Rockwell International, is shown in the upper display of Fig. 3 with an illustration of the voids in the original panel. It will be seen that the device picks out most of the defects very clearly.

The system can also be operated with electronic scanning in both the x and y directions by using crossed arrays. We have done relatively little with this mode of operation. For completeness, a result taken of the letter "S" cut into a piece of rubber is shown in Fig. 4.

Most of our work has been devoted to B-scan imaging. The basic operation of the system is illustrated in Fig. 5. In this mode of operation, the array focusing system can be regarded as a moving lens which is scanned at a velocity comparable to the acoustic velocity in the medium itself. The system is first operated as a transmitter. It is focused on a line a distance z from the array, and, thus, scans this line. At a time 2T later, where $T = z/v_a$ and v_a is the velocity of an acoustic wave in the medium, the device is operated as a moving receiver lens, so that it picks up a signal from a point which has been illuminated at a time 2T before. A signal arriving from a more distant point will arrive after the lens has moved past the received beam, so that there will be good range definition. Similarly, a signal arriving from a different point on the scan line will not be seen, because of the good transverse definition of the lens. Thus, the device has good transverse and range resolution. In practice, the system is used to scan along a line, as shown in Fig. 6, then refocused and the time delay between transmit and receive changed so as to scan a line at a different distance z from the array until a complete raster normal to the array has been scanned.

A simple picture of a step block in water is shown in Fig. 6. It will be noted that both the transverse position and longitudinal position of the steps can be clearly seen; the steps being approximately 8 mm apart and 5 mm wide, the results being taken at an acoustic frequency of 2 MHz.

During the last year the system has been used to take images with various types of waves in metals. As an illustration, we have used 3 MHz longitudinal waves in aluminum to obtain an image of a flat bottomed hole. The results are shown in Fig. 7, where it will be seen that the top surface of the hole can be observed, as well as

the front and back walls of the metal sample. The hole has a diameter of 3 mm and a length of 25 mm. It will be noted that the diameter and length of the hole can be measured directly by this technique, without further interpretation of the results. Because the surface of the hole is a specular reflector, we only observe its top surface, a point of great importance in NDT problems. A further point which is important to realize is that, in contradistinction to our earlier imaging system results, we are now able to obtain images of small reflectors very near to large reflectors, like the wall of a sample; the basic difficulty in doing this is that the relatively weak sidelobes of the image from strong reflectors can "swamp out" the weak reflection from a small neighboring flaw. To eliminate this difficulty, we have adopted a method known as "gating the pulse," which makes it possible to look only at the image corresponding to the main lobe of the reflector of interest. This slows the scan rate considerably, but proves feasibility for the rapid scanning system which we are now developing, and is a valid technique for examining small flaws and is still much quicker and more accurate than mechanical scanning.

As a second illustration, in Fig. 8 we show how a shear wave is excited in an aluminum sample, with the shear wave propagating along the axis of the sample, and focused and scanned in a direction perpendicular to the paper. A series of holes cut into the sample are shown in the same figure, and it can be seen that both the transverse and longitudinal position of these holes can clearly be observed.

A similar technique can be used to excite Rayleigh waves and Lamb waves in target plates, as shown in Fig. 9. Some results obtained for Lamb waves are shown in Fig. 10.

Another set of results for Rayleigh waves is shown in Fig. 11. In the first photo, the top and bottom edge of the plate can be seen, for the Rayleigh wave passes over the top surface of the plate and around the edge to the bottom surface. By changing the image intensity, three small 0.5 mm D holes 9 mm from the edge can also be seen.

Finally, we show Rayleigh wave images of an artificial crack 1 cm long, ~100 μm side, eloxed in a metal sample. This sample can be rotated in the surface wave field, so that the crack can be aligned at an angle to the transducer array. When the crack is parallel to the array ($\theta = 0$), the crack is clearly seen, as shown in Fig. 12(a). Because the crack is a specular reflector, when it is turned at an angle no signal will be returned to the array from the middle of the crack; only the two ends of the crack will be observed. The results for $\theta = 0°$, 45°, and 90° are shown in Figs. 12(a), 12(b), and 12(c), respectively. The scattering from the crack ends can clearly be seen. A similar set of results is shown in Fig. 13 for two holes whose diameters are the same as the width of the crack. The results will be seen to be almost indistinguishable from those of a crack, except for the $\theta = 0$ case. But more precise analysis does show differences in amplitudes between the two cases, so that one might expect that a more detailed study would show up considerable differences between a crack and two holes.

These studies confirm the results obtained in theoretical work on this program of scattering from cracks. The two ends of the cracks behave like sources, and the imaging technique shows the presence of the sources directly, rather than resting on an indirect inference based on the interference phenomenon between the two sources, as would be obtained with simple plane wave transducers.

The Design of a New Imaging System

After working with the present imaging system in NDT applications during the last three years, we have obtained considerable insight into its advantages and disadvantages. The advantages are the basic ones to be expected; good definition in two directions, high speed, and large field of view in the direction normal to the array. The disadvantages are, a relatively limited field of view in the direction parallel to the array because of the limited number of array elements used in our research system, complexity, higher sidelobe levels than we would like, at least in the high speed operating mode, a relatively small aperture, so that the range of viewing angles is relatively small thus tending to give ppor images of specular reflectors, and operation at a lower frequency than optimum (2.5 MHz).

In order to eliminate most of these difficulties, we have been examining and experimenting with component parts of a new imaging system. The new system is eventually intended to employ a very long array of elements, perhaps several hundred, or, alternatively, a small hand held array with perhaps 20-30 elements which can be moved by hand over the surface of an object. In each case, only 20-30 elements will be used at a time, thus making the electronic problems of the control circuitry, amplifiers, and other components of the system much simpler. In the purely electronic system, the equivalent of mechanical scanning will be carried out by a multiplexing arrangement to switch the electronic circuits along the way.

The system will be arranged so that from any 30 elements a focused beam will be obtained, which scans over a circular sector of the order of ±40° or more, and yields a complete dynamically focused image of this sectorial region of radius up to 20 cm. The process will then be repeated for each position along the long array, or each mechanical position. Equivalent points in the multiple images will be computed and placed at the same point on the cathode ray screen. This is like the operation of the present medical B-scan imaging system, systems which are unfocused and purely mechanically scanned. In that case, the radial sector scanning is obtained by tilting the transducer and relying on the flexibility of the body surface. The operating system will emit a pulse, or train of pulses, from a single highly efficient transducer element, receive the reflected echoes back at the same transducer, and then use an A to D converter to digitize the received signals. The device will then store the digital

signals from one transducer element in a RAM and then repeat the process for 29 more elements. With the information stored in the RAMS, we can obtain a complete image of one sector, either by using special purpose CCD's being developed in our own integrated circuit laboratory, or by programming the output taps of the RAMS to compute the image, an operation which can be carried out in real time, if the programs are stored in ROMS. We will then convert the output to analog form, and, thus, produce an intensity display of the image. After moving along the array one step, or changing its mechanical position and keeping track of the position with a support arm of the type used in medical systems, we will then repeat the process, and superimpose the images obtained, using either a scan converter of the type presently available, or its digital form, a type presently coming on the market.

We have tested some of these concepts; an efficient transducer array, the RAM circuitry, simple transmitter and receiver circuits, and inverse filtering circuits, so that we can use long pulse trains to obtain a higher energy in the transmitted signal. All the concepts appear to be feasible. So, we have begun to build a new electronically scanned and focused system which we believe will have a low sidelobe level, be close to real time operation, and operate initially with a maximum frequency of 5 MHz, and eventually at 10 MHz.

Conclusions

We have shown that imaging techniques are very powerful ones for determining the position of the flaw, and for finding information on its size and shape. Careful attention to the design of these imaging systems is necessary to keep the side lobe levels low enough, so that small flaws can be observed in the neighborhood of a large scatterer, such as a metal wall. Feasibility demonstrations of this mode of operation have been made. The operation of these devices is quick and simple, and provides an increase in speed on the order of 100 times over that of a purely mechanically scanned system. In B-scan operation, the transverse definition in these systems is comparable to the range definition, a major advance in capability over present systems.

A new system is being designed which shows promise of being capable of eliminating most of the difficulties associated with our first research system. The concept involved makes use of digital circuitry and memories, which are dropping in price all the time, so it should eventually lead to an inexpensive enough and flexible enough system to make it eventually possible to construct an electronically focused system with full three-dimensional focusing and dynamic scanning.

Acknowledgement

This research was sponsored by the Center for Advanced NDE operated by the Science Center, Rockwell International, for the Advanced Research Projects Agency and the Air Force Materials Laboratory under contract F33615-74-C-5180.

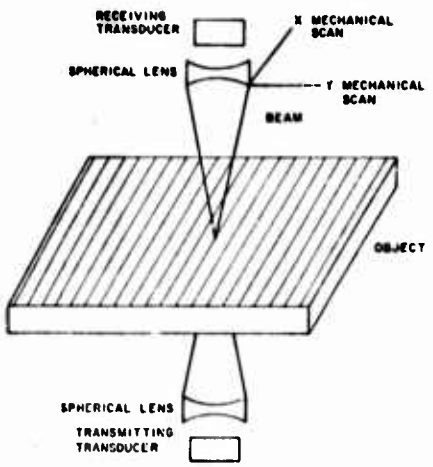


Figure 1. Illustration of typical mechanically scanned transmission system used for nondestructive testing.

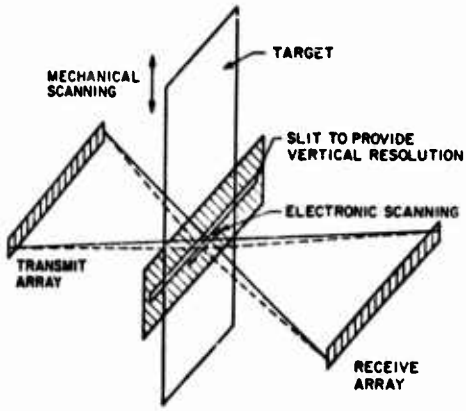


Figure 2. Illustration of system used for electronically scanned transmission imaging.

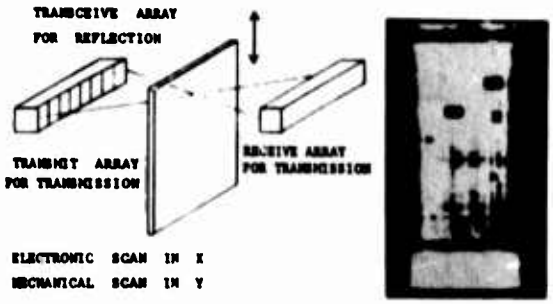
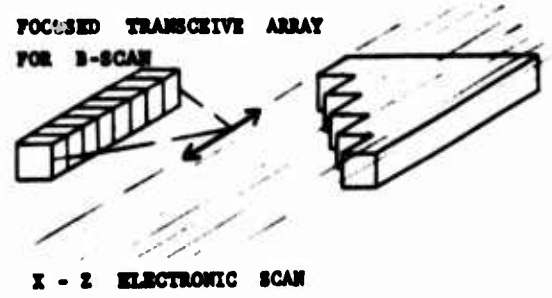


Figure 3. Transmission image of bonded boron fiber reinforced epoxy laminate laid down on titanium, illustrating debonded regions.



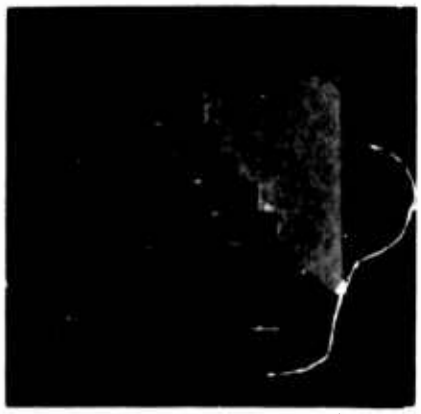


Figure 6. A B-scan image of a stepped sample compared with its optical image. The small steps are 5 mm wide with 8 mm distance between them.



Figure 4. A completely electronically scanned and focused C-scan system, used to image a letter S cut in a piece of rubber.

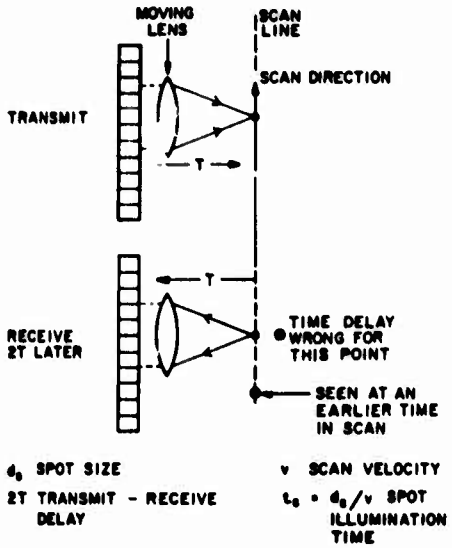


Figure 5. Illustration of the operation of the B-scan system, where it is regarded as a moving lens.

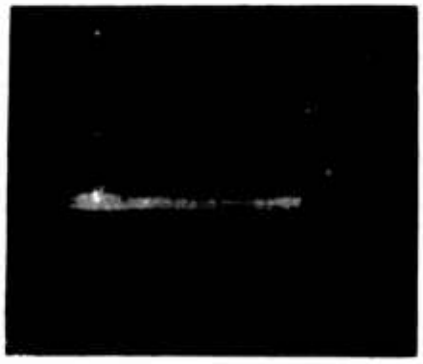
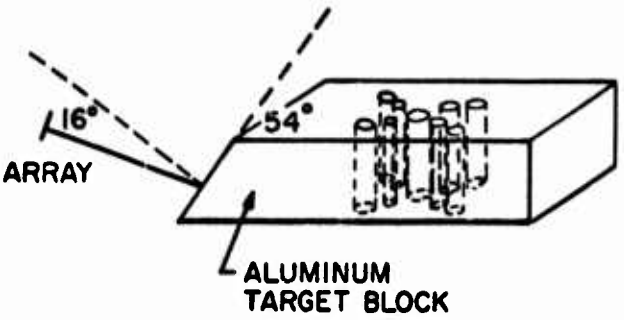


Figure 7. An acoustic image of a flat bottomed hole (3 mm dia. x 25 mm deep) using 3 MHz longitudinal waves in an aluminum sample.



(a)



(b)

Figure 8. 2.75 MHz shear wave B-scan imaging in aluminum. (a) Picture of 2 mm diameter holes in aluminum block. Hole is roughly 25 mm x 50 mm. Center hole is 150 mm fron end of block. (b) Schematic of setup to excite shear waves in aluminum block.

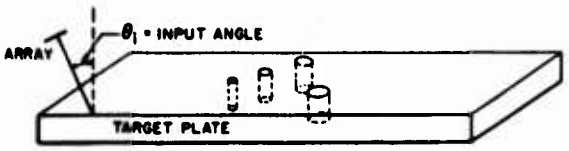


Figure 9. Schematic of setup to excite Rayleigh waves and Lamb waves in target plates. For Rayleigh waves in aluminum $\theta = 28^{o}$.

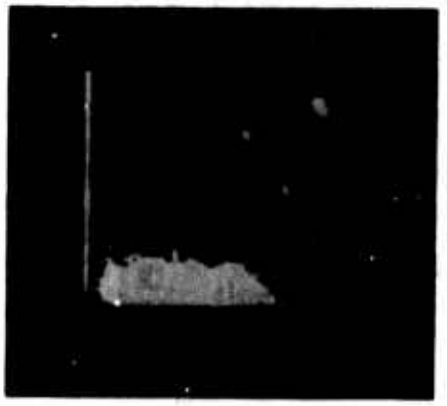


Figure 10. B-scan Lamb wave image. Holes range in size from 1.5 mm diameter to 10 mm diameter. Spacing between holes is on the order of 30 mm.

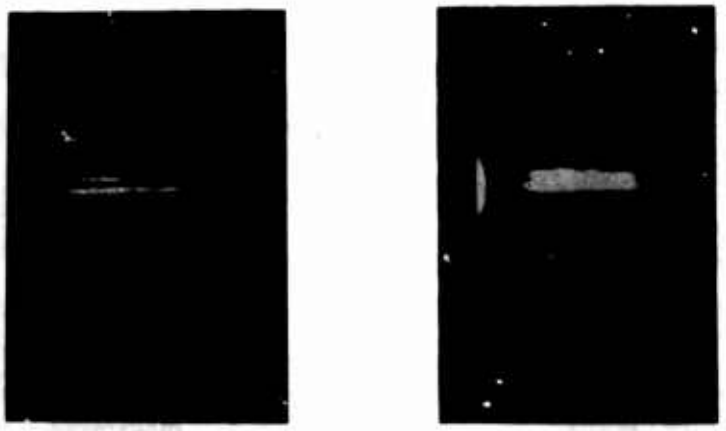


Figure 11. Rayleigh wave imaging in an aluminum target plate. The holes are 1 mm in diameter and 9 mm from the edge of the plate, spaced on 12.5 mm centers on a 1/4 inch thick plate.

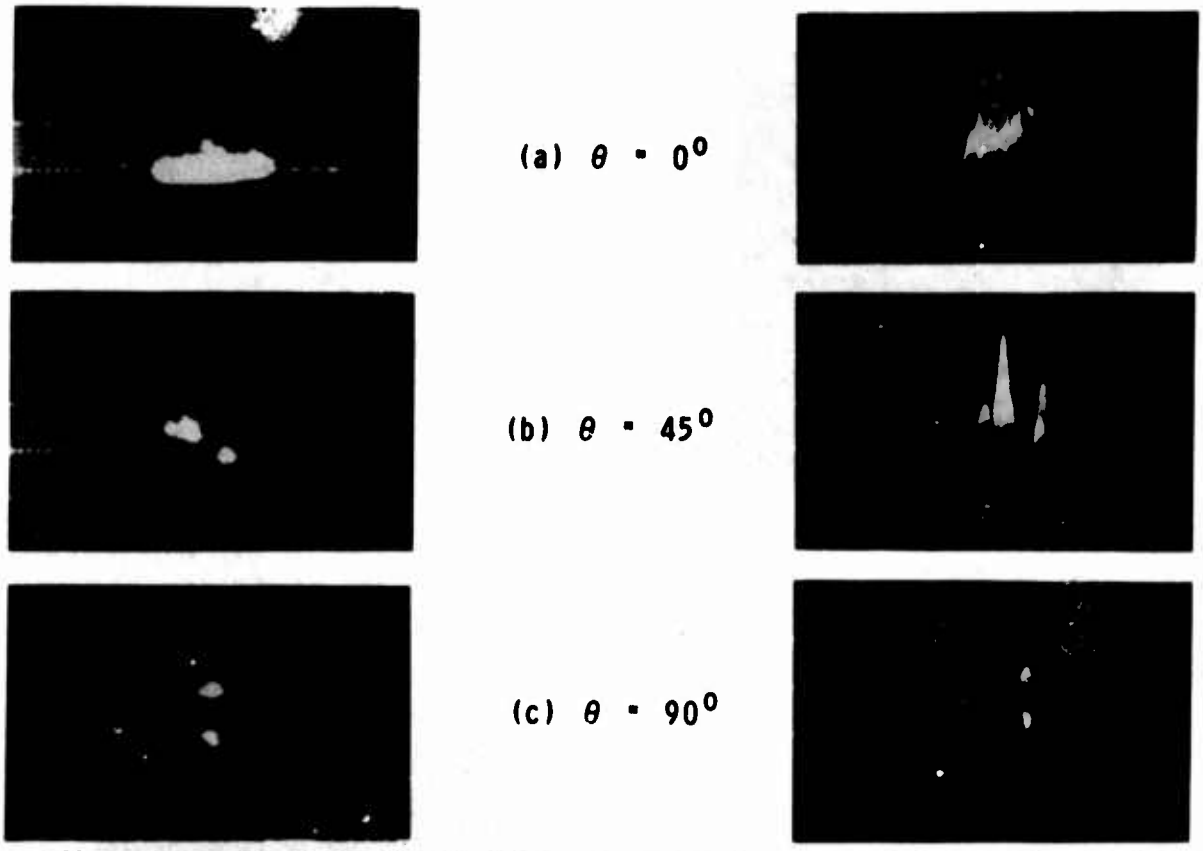


Figure 12. Intensity images and amplitude images of a crack taken with the crack at various angles to the array. The amplitude is reduced by 10 dB in Fig. 8(a) for comparison with the other results.

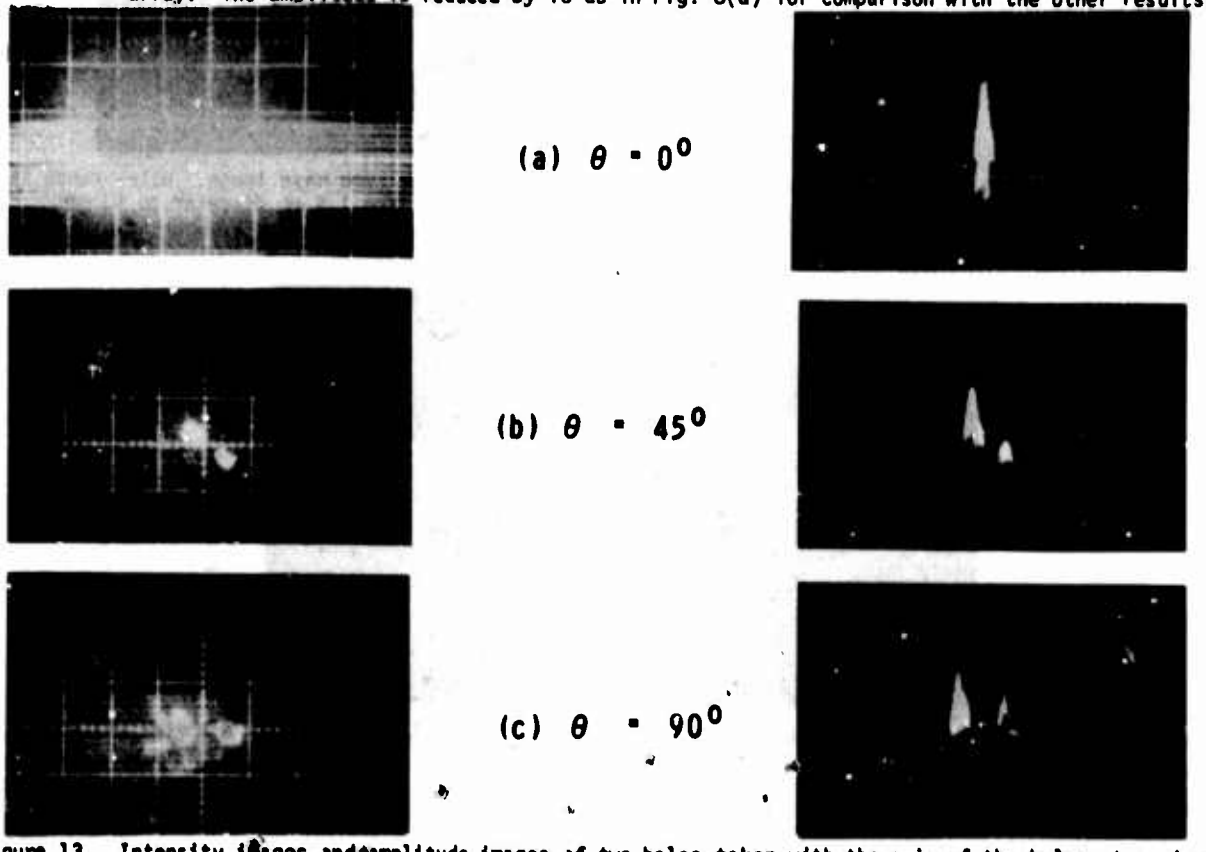


Figure 13. Intensity images and amplitude images of two holes taken with the axis of the holes at various angles to the array.

MEASUREMENT OF STRENGTH OF ADHESIVE BONDS

G. A. Alers and R. K. Elsley
Science Center, Rockwell International
Thousand Oaks, California 91360

and

P. L. Flynn
General Dynamics
Fort Worth, Texas 76101

ABSTRACT

In order to predict the strength of an adhesive bond between two metal sheets, it is necessary to measure the physical state of the adhesive layer that mechanically joins the two pieces of metal. This requires rapidly performing a detailed analysis of the ultrasonic echoes reflected from the entire structure when it is immersed in a water bath for a normal ultrasonic pulse-echo inspection. To achieve this result, computer-operated ultrasonic inspection systems have been assembled and equipped with special signal processing routines so that particular features of the ultrasonic echo in both the time domain and the frequency domain can be extracted in a time short enough to meet the requirements of a production inspection system. Such features as the relative amplitude of the signals reflected from the top and bottom of the adhesive layer and the frequencies for which standing waves are excited in the adhesive and in the metal adherends are of particular interest for making the strength predictions. It is also important that the interrogating ultrasonic pulse be of very short time duration so that the echoes from the various interfaces in the sandwich-like joint can be resolved in the time domain display. This requires the use of special high frequency pulse generators coupled to broad band transducers and amplifiers. Special procedures are also needed to insure the accuracy of the analog-to-digital conversion at the input to the computer and the subsequent transformations to and from the frequency domain.

The measurement of the strength of a completed adhesive bond between two pieces of metal stands as one of the most important NDE problems in the aerospace industry. Without such a test, this very light, inexpensive and efficient method of joining two metals can only be used in secondary structures. Two aspects of the problem must be attacked because the bonds can fail both by cohesive failure within the bulk adhesive itself and by adhesive failure at the interface between the metal and the polymer used as the adhesive. The detection of both of these basic failure modes has been the subject of the current program being carried out at the Rockwell International Science Center and at General Dynamics.

In both laboratories, the approach has been to utilize extensive digital processing on the ultrasonic signals reflected from a metal-adhesive-metal joint purposely prepared with either poor cohesive bond strength or with poor adhesion at the metal interface.

Figure 1 shows the ultrasonic data acquisition system used. It consists of a transducer in a water bath directing its beam at normal incidence against a sandwich structure consisting of two relatively thick metal sheets on each side of a thin adhesive layer. Also shown are the broad band (narrow time duration) echo signals reflected by the structure. Signal R_1 is large and arrives first because it is reflected from the top surface of the first metal adhered. Signal R_2 is much smaller and arises from the reflection at the top metal to adhesive interface. Immediately thereafter, the reflection from the bottom of the adhesive layer (signal R_3) appears followed by the reverberations of signals reflected more than once by all of the interfaces in the joint. In order to separate these reverberations and extract quantitative information from them, the echo train is put into digital format and a Fourier transform is calculated by the computer.

Figure 2 shows the results of such transformations. The smooth, bell shaped amplitude versus frequency curve in the upper left is the transform of the front surface echo alone and is used to define the band pass characteristics of the transducer and electronics. The transform of the entire echo train is shown in the lower left where many well defined dips can be seen to be superimposed on the band pass curve of the transducer. The dips correspond to the frequencies at which standing acoustic waves can be established within the various layers. By correcting the wave train transform for the transducer response, the reflection spectrum shown in the upper right can be obtained. It represents the experimental reflection coefficient of the adhesive bond sandwich that would be obtained if a truly flat frequency response transducer had been used. Fortunately, the reflection of plane acoustic waves by a layered medium is a soluable mathematical problem, and the theoretical reflection amplitude versus frequency curve is shown in the lower right for comparison. The excellent agreement between theory and experiment shows that a detailed comparison between the observed and calculated responses can be used to find abnormalities which may correlate with the mechanical strength.

Figure 3 shows photographs of the computerized ultrasonic adhesive bond inspection systems which have been assembled at the Science Center and at General Dynamics. The block diagrams

show that different individual pieces of ultrasonic and data processing equipment were used at each laboratory even though the results of the analysis are very similar.

Figure 4 shows the possible methods that can be used to measure the strength of a completed adhesive bond. For the present program, most of the mechanical strength data was obtained from the small compression shear type of specimen obtained by cutting small coupons out of larger bonded strips or plates of aluminum. Examples of the peel specimen and the compression shear specimen after failure are shown on the right.

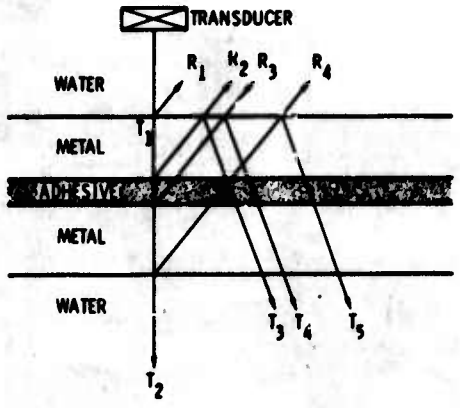
In order to control separately the cohesive and adhesive bond strength of the specimens during the sample preparation cycle, two methods were used as described on Fig. 5. For the cohesive bond strength tests, two 6-inch square aluminum plates were bonded together using a commercial adhesive, FM 400, with different curing temperatures. After ultrasonic scanning, these plates were cut up into many small compression shear specimens and their shear strengths measured destructively. The different curing temperatures resulted in different degrees of crosslinking and hence a systematic variation in cohesive strength of the adhesive material itself. For the adhesive interface bond tests, both lap shear and peel type specimens were prepared with a thin layer of contamination applied to the aluminum surfaces prior to bonding. By changing the thickness of the layer of contamination, samples exhibiting differing strengths of adhesion were prepared.

Figure 6 shows the results of correlating the measured cohesive bond strength with two physical properties of the bulk adhesive deduced from the ultrasonic measurements in the frequency and time domains shown in Figs. 1 and 2. The two physical properties of the adhesive layer were the attenuation and the sound velocity in the adhesive. For a model adhesive, which contained no scrim cloth and very little bubble type porosity, the correlation was excellent as shown on the left-hand side of the figure. For the commercial adhesive which contained a scrim cloth and had bubbles formed by the evolution of volatiles during the cure process, the correlation is poor because of the large scatter in the data. Much of this scatter has been traced to the fact that the scrim cloth and the porosity dominate the attenuation and, to a lesser extent, the velocity so that the measured physical properties are not closely related to the condition of the adhesive material itself.

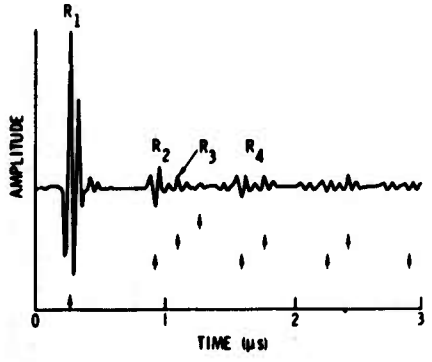
Figure 7 shows the results obtained for the samples with thin layers of stop-cock grease at the metal to adhesive interface. For these tests, lap shear specimens were used and an obvious difference in the Fourier spectra of the echo signals can be seen in four specimens whose strengths were different. The different strengths of these samples are recorded in the upper left-hand corner of each spectrum. A graph correlating the measured shear strength with the highest frequency at which splitting was observed in the dips of the reflection amplitude versus frequency graphs show a promising technique of predicting the strength of adhesion in a completed bond. Theoretical analysis of the spectra shows that the splitting arises from the fact that the upper and lower metal plates can be considered as separate oscillators whose thickness resonant modes are coupled together through the adhesive layer. The absence of splitting can be interpreted as showing that no high frequency acoustic energy is transmitted through the interfaces from the top metal sheet to the bottom sheet, and a standing wave is set up only in the top plate at high frequencies.

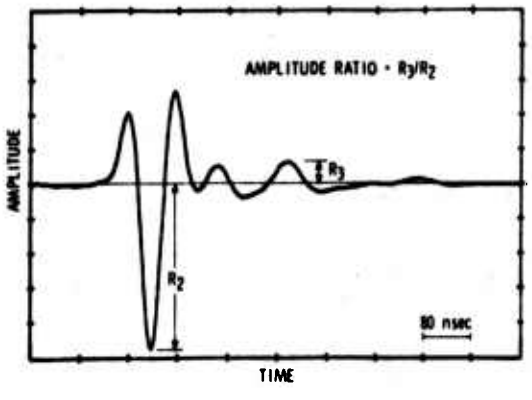
Acknowledgement

This research was sponsored by the Center for Advanced NDE operated by the Science Center, Rockwell International, for the Advanced Research Projects Agency and the Air Force Materials Laboratory under contract F33615-74-C-5180.



ULTRASONIC INSPECTION
WITH NORMAL INCIDENCE WAVES

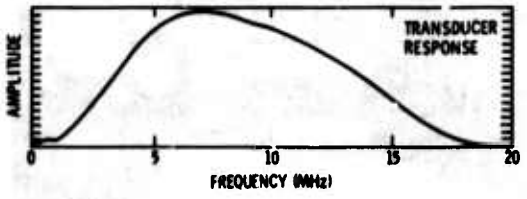


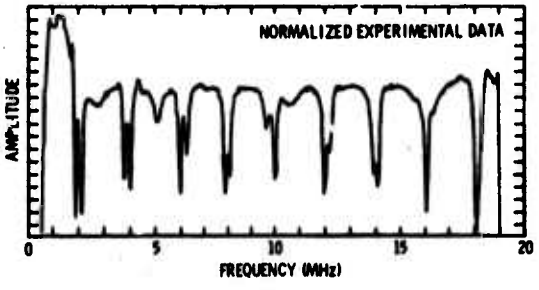


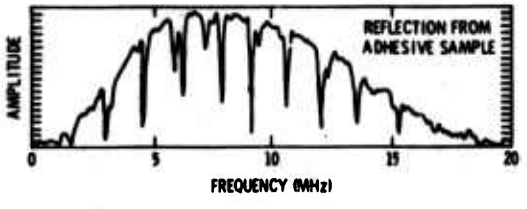
TIME DOMAIN PRESENTATIONS OF SIGNALS

Figure 1. Data acquisition.

FOURIER TRANSFORMATION OF DATA BY A COMPUTER YIELDS FREQUENCY DEPENDENCE OF ULTRASONIC WAVE INTERACTIONS







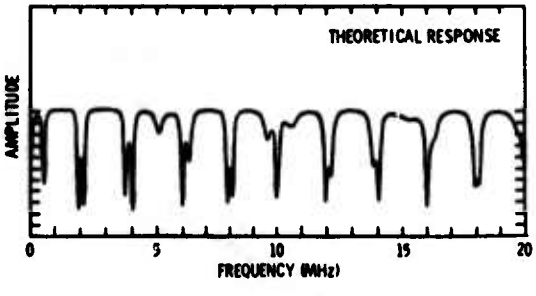
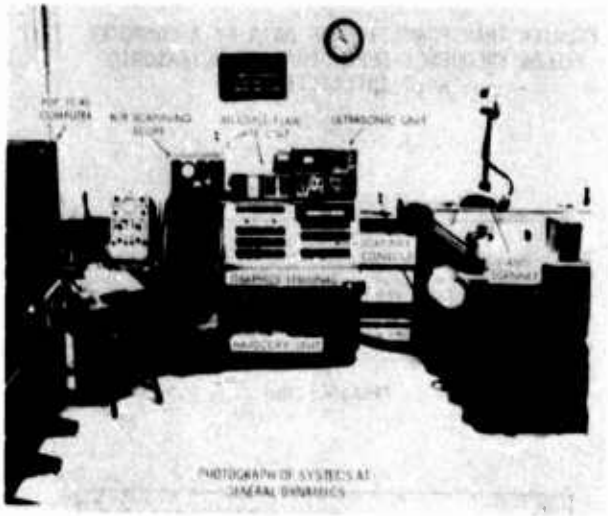
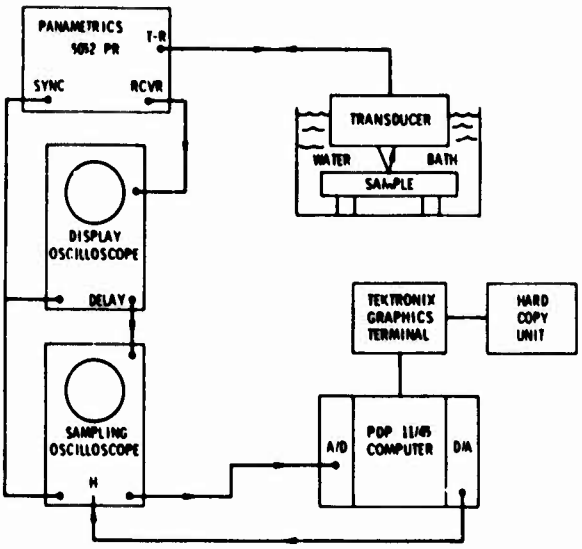


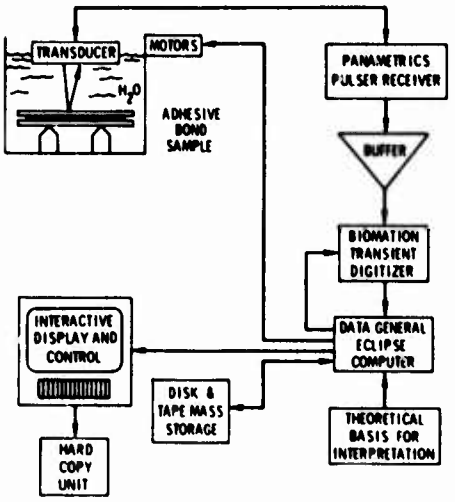
Figure 2. Signal processing.





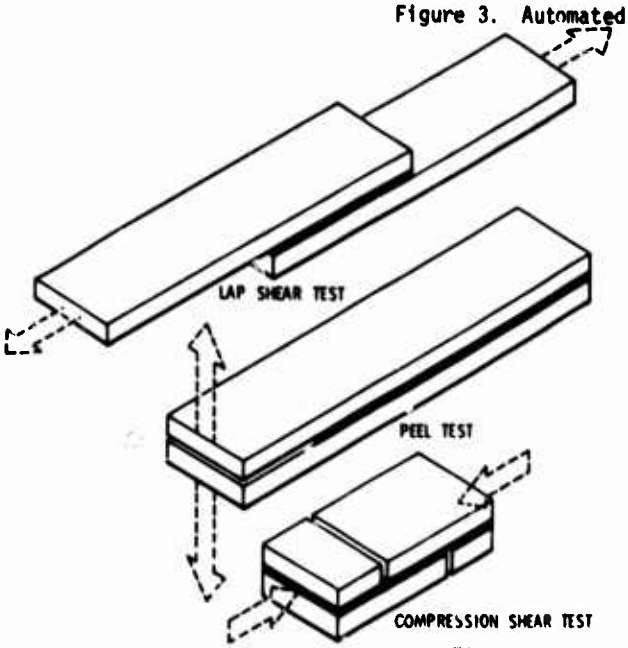


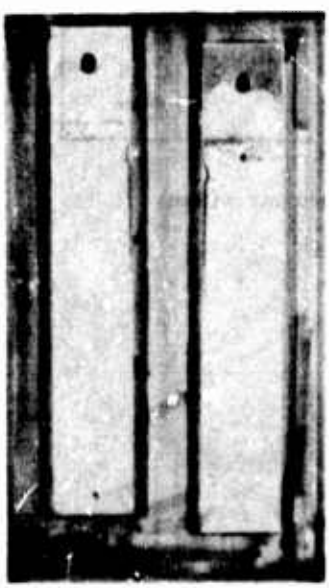
GENERAL DYNAMICS SYSTEM



SCIENCE CENTER SYSTEM

Figure 3. Automated inspection system.





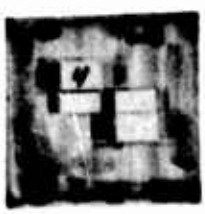


Figure 4. Specimen testing.

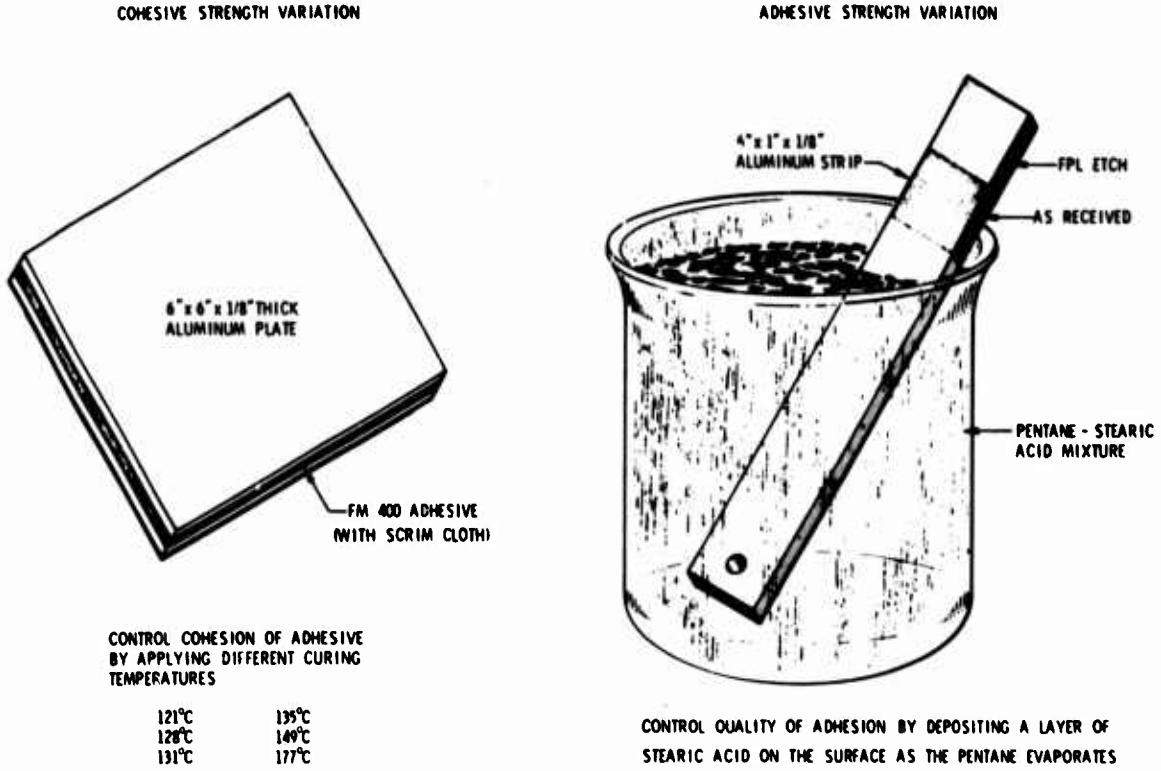


Figure 5. Specimen fabrication.

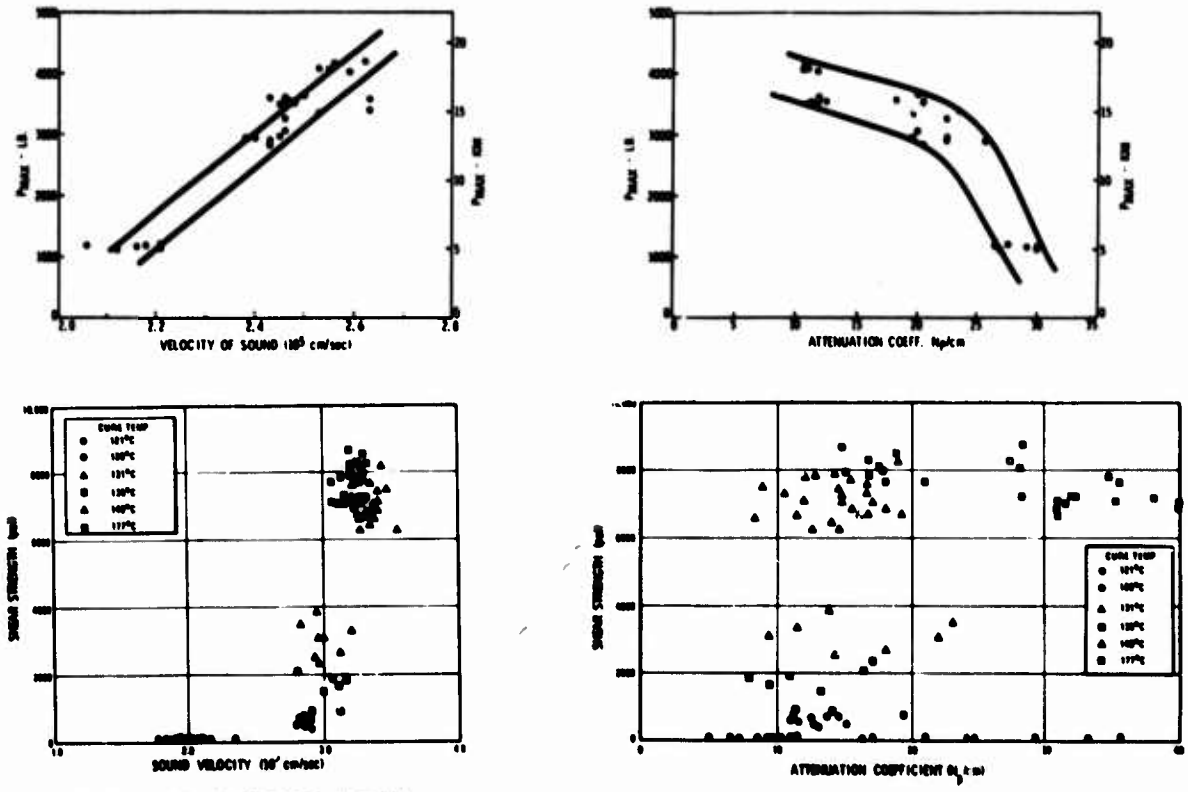
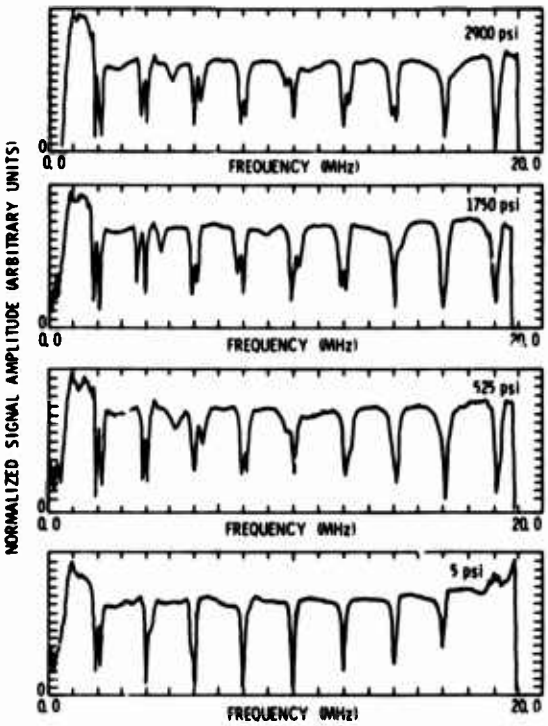
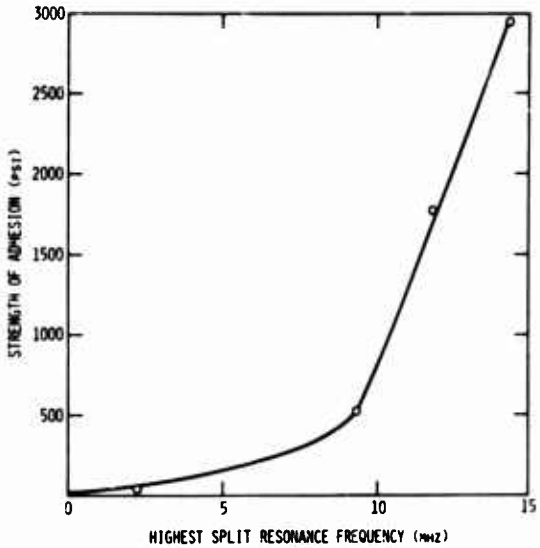


Figure 6. Cohesion strength measurement.



EXPERIMENTALLY OBSERVED SPECTRA OF ULTRASONIC SIGNALS REFLECTED FROM BOND LINES HAVING THE DIFFERENT BOND STRENGTHS INDICATED.



THE SPLITTING OF THE STANDING WAVE RESONANCES IN THE SANDWICH STRUCTURE INDICATES THE QUALITY OF THE METAL-TO-ADHESIVE INTERFACE

Figure 7. Adhesion strength measurement.

WETOMETER FOR MEASUREMENT OF MOISTURE IN COMPOSITES

D. H. Kaelble
Science Center, Rockwell International
Thousand Oaks, California 91360

ABSTRACT

A combined experimental and analytic approach to moisture diffusion analysis (MDA) has evolved in proof of principle form as a new instrument termed a moisture profilometer. The objective in moisture profilometry is the quantitative analysis of the spatial distribution of moisture within composites and definition of localized internal stress fields. An electrolytic cell is utilized to record cumulative moisture evolution and moisture effusion rate. Variation of cell geometry accommodates either laboratory analysis of small composite damage control specimens or field inspection of limited surface areas of composite structure in an area scanning mode. An important new aspect of moisture profilometry is calculation of the depth profile of moisture concentration from measurement of surface effusion and rate with time. Statistical estimation theory is applied to this problem and preliminary results indicate that concurrent calculations can generate moisture concentration profiles during the course of moisture effusion measurements. Results of initial instrument design and computational analysis will be demonstrated and discussed.

Introduction

Moisture is known to degrade the strength and stiffness of graphite-epoxy composites and the results of recent studies summarized in several workshop proceedings.[1-3] Several detailed studies of uniaxial graphite fiber reinforced epoxy resins[4,5] show that ultrasonic acoustic properties are sensitive to both current moisture content and prior microstructure damage due to moisture absorption-desorption cycling. This discussion briefly outlines the development of a new NDE methodology for direct measurement of moisture concentration and moisture diffusion properties in composite materials. This new nondestructive measurement is termed moisture diffusion analysis (MDA) and provides a quantitative tool for direct evaluation of moisture in composites.

Measurement Methodology

The upper left view of Fig. 1 shows the moisture evolution analyser (DuPont Model 902H) employed in the current studies. This instrument uses an electrolytic measurement and feedback control loop shown in the upper right view of Fig. 1 to measure both the rate of moisture release to a dry carrier gas at controlled temperature. The lower right view of Fig. 1 shows the higher rate of directional moisture release measured on the transfibrous surface of a uniaxial composite where moisture diffusion is along the fiber axis. The lower left view of Fig. 1 shows the conventional full enclosure sample chamber supplied with the instrument. New surface sampling chambers such as the sleeve type for bar specimens and the face plate type for plate specimens are presently under development and testing. These latter sampling chambers permit small area sampling of large composite structure to provide surface mapping for moisture content and moisture diffusion response.

Directional Diffusion Coefficients

Using the fully enclosed sampling chamber, the three principal diffusion coefficients of the uniaxial composite can be evaluated as shown in Fig. 2. The upper left view of Fig. 2 shows the three sample geometries which provide the enhanced diffusion along each of the three composite principal axis. The upper right view of Fig. 2 shows the typical absorption (A) and desorption (D) kinetics of moisture in the pure epoxy matrix at 75°C. for two successive cycles of exposure and drying. The lower left view of Fig. 2 shows that three successive cycles of moisture absorption and desorption along the fiber axis produces a substantial increase in diffusion coefficients D_2 parallel to the fiber axis. The lower right view of Fig. 2 shows that the temperature dependence of diffusion coefficients parallel to fibers (D_1 in upper curve) and transverse to fibers (D_3 in lower curve) are directionally different. Precise evaluation of the directional diffusional coefficients and their dependence on temperature and moisture cycling is essential for calculations which predict moisture concentration profiles.

Moisture Profilometry

The inversion of the Fickean diffusion equations can be applied to develop a numeric analysis of moisture profiles as shown in the upper left view of Fig. 3. Typical experimental data utilized in this analysis are tabulated in the upper right view of Fig. 3. These data cover an effusion time t_m range which describes the effusion rates J_m for moisture escaping from the surface $t_m \simeq \Delta$ to approximately 20% into the sample thickness at $t_m \simeq 50.5$ min. The lower left view of Fig. 3 shows that the computed concentration profile correctly estimates the fully saturated moisture concentration near the sample surface at 32000 ugm H_2O per cc composite. At greater depths, where $0.2 < X/L_x < 0.8$ where experimental data are unavailable, the lower left view of Fig. 3 shows that the analytical estimator produces a cyclic response. The lower right view of Fig. 3 shows that synthetically smoothed moisture effusion data produce the correct moisture profile much farther into the fractional thickness (X/L_x) of

the composite. This analytic approach to moisture diffusion analysis provides for three-dimensional moisture mapping by combining the depth profiling shown in Fig. 3 with the surface area mapping using the face plate sampling chamber described in Fig. 1.

Microstructure Degradation

A summary of MDA analysis of microstructure degradation is illustrated in Fig. 4. The upper left views show a 12-inch bar of graphite epoxy composite aged so as to develop a gradient of moisture concentration with maximum moisture at the lower extremity which is immersed in boiling water for 1132 hours and relatively low moisture in the upper 5.5 inches which is exposed to ambient air. Following the moisture exposure cycle, this bar was thermally cycled between 23°C. and temperatures above the service ceiling temperature of 177°C. (350°F.). The regions of the composite which experience the combined high moisture and high temperature exposure exhibit microfracture. The lower left view of Fig. 4 shows that the length profile of moisture desorption properties is sharply modified at L≈6. The upper right view shows that profiles of moisture absorption response are similarly modified at L≈6 which coincides with the seal region between the zones of low and high hydrothermal damage. The changes in MDA shown in Fig. 4 correlate with microcrack and craze structure where $6 \leq L \leq 12$ inch due to hydrothermal degradation. Evaluation of interlaminar shear strengths as shown in the lower right view of Fig. 4 shows that samples exposed to high moisture (100°C. H_2O vapor or liquid) display a lower average strength λ_0 and broader strength distribution indicated by lower m in the Weibull cumulative strength distribution. This strength loss correlates with the microcrack formation produced by hydrothermal damage and measured by MDA.

Summary

The results shown above illustrate the development and application of moisture diffusion analysis and as a new multi-purpose NDE tool for moisture and microstructure characterization of composite materials.

Acknowledgement

This research was sponsored by the Center for Advanced NDE operated by the Science Center, Rockwell International, for the Advanced Research Projects Agency and the Air Force Materials Laboratory under contract F33615-74-C-5180.

References

1. Proceedings of Workshop on Durability Characteristics of Resin Matrix Composites, sponsored by AFFDL and AFML, Battelle Memorial Institute, Columbus, Ohio, Sept. 30 - Oct. 2, 1975.

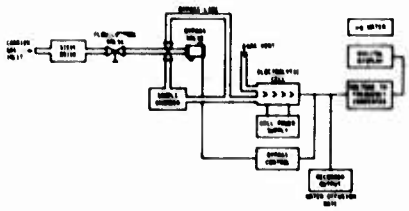
2. Proceedings of Workshop on the Role of the Polymer Substrate Interphase in Structural Adhesion, sponsored by AFOSR and AFML, University of Dayton, Dayton, Ohio, Sept. 9-10, 1976.

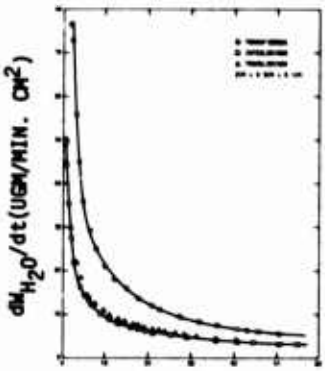
3. Transactions of the Workshop on The Effects of Relative Humidity and Elevated Temperature on Composite Structures, editors: J. R. Vinson, R. B. Pipes, W. J. Walker, and D. R. Ulrich, Air Force Office of Scientific Research Tech., Report AFOSR 77-0030

4. D. H. Kaelble and P. J. Dynes, "Nondestructive Tests for Shear Strength Degradation of a Graphite-Epoxy Composite," ASTM STP 617, American Society of Testing and Materials, Philadelphia (1977), pp. 190-200.

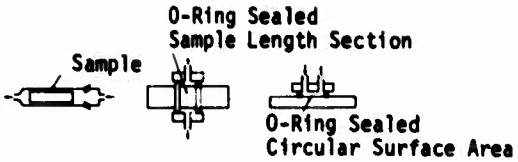
5. D. H. Kaelble and P. J. Dynes, "Methods for Detecting Moisture Degradation in Graphite-Epoxy Composites," Materials Evaluation, 35 (4), (1977), pp. 103-108.







○ Transfibrous
□ Interlaminar
△ Translaminar
2cm x 0.5cm x 0.1cm



Full Enclosure
Sample Chamber

Face Plate for
Single Surface
Plate Specimens

Sleeve Type
for Bar Specimens

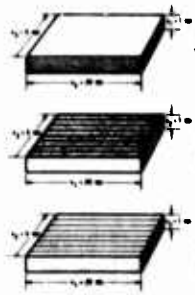
Method:

1. Use moisture evolution analyzer (Du Pont Model 902H)
2. Analyze digital display of total water release for moisture content.
3. Analyze recorder output of moisture effusion rate for depth profile of moisture concentration.
4. Provide special specimen cell designs to isolate small volumes or surfaces on large specimens.

New Results:

1. Can measure and analyze directional diffusion coefficients.
2. Can map local microstructure degradation and predict strength changes in large composite structures.
3. Can measure depth profile of moisture concentration for internal stress analysis.

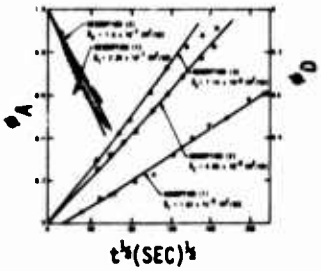
Figure 1. Measurement methodology

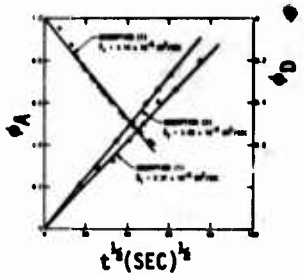


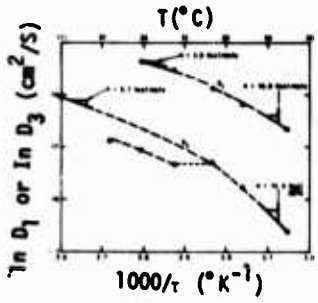
Interlaminar surface (i = 1)

Transfibrous surface (i = 2)

Translaminar surface (i = 3)







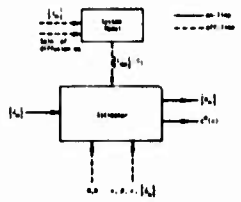
Method:

1. Prepare test specimens in three principal axes of composite (i = 1, 2, 3).
2. Analyze cyclic diffusion of pure matrix.
3. Analyze cyclic diffusion along composite principal axes i = 1, 2, 3.
4. Temperature dependence of diffusional coefficients D_1, D_2, D_3.

New Results:

1. Can isolate principal axis diffusion coefficients D_1 D_2 D_3 for both absorption (A) and desorption (D).
2. Initial moisture absorption is non-Fickian and relates to microstructure or internal stress relaxation.
3. Initial cycles of moisture absorption and desorption produce 3 to 4 fold increased absorption coefficients $(Di)_A$.
4. Comparison of experimental and theoretical diffusion coefficients shows simple laminate theory does not describe important diffusional properties.

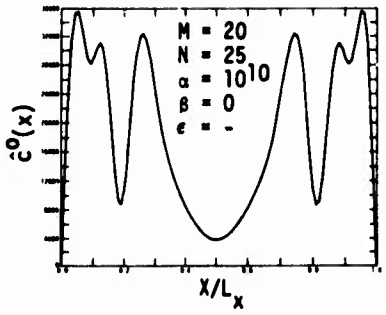
Figure 2. Directional diffusion coefficients

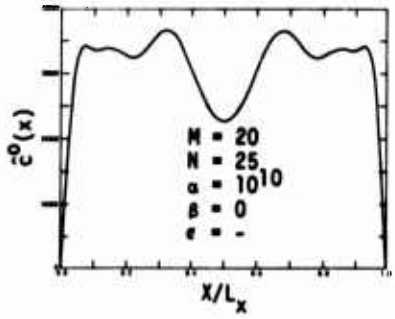


M = number of measurements
N = number of estimations
c_μ = concentration of water in the composite corresponding to the chemical potential μ
α = a priori bias against large amplitude $c^o(x)$
β = a priori smoothness which is applied to $c^o x$ in the range $\epsilon\pi$, $(1-\epsilon)\pi$
ϵ = numeric range factor $0 < \epsilon < 0.5$
$\{\bar{a}_n\}$ = observationally conditioned average for a_n

Table 1: Experimental Data

m	t_m(min)	$\tilde{J}_m$(μgm min^{-1})
1	1.5	80.6
2	2.2	62.6
3	3.0	49.7
4	4.5	37.4
5	5.5	32.7
6	6.4	30.3
7	7.0	27.6
8	9.2	23.1
9	11.2	20.3
10	13.2	18.2
11	16.0	16.0
12	17.7	15.0
13	19.5	14.0
14	21.2	13.1
15	25.5	11.8
16	29.3	10.6
17	35.7	9.40
18	40.7	8.52
19	44.3	8.18
20	50.5	7.20





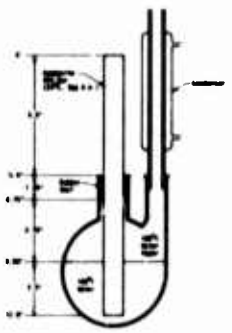
Method:

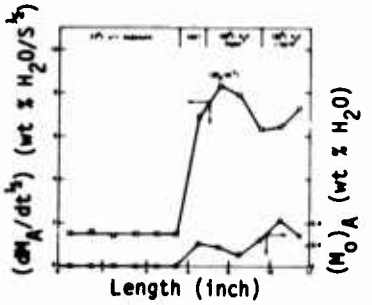
1. Measure moisture effusion rate versus time.
2. Develop numeric estimation theory for calculation of moisture concentration versus depth.
3. Graph estimated concentration profile based on experimental data.
4. Graph estimated concentration profile based on synthetic smoothed data

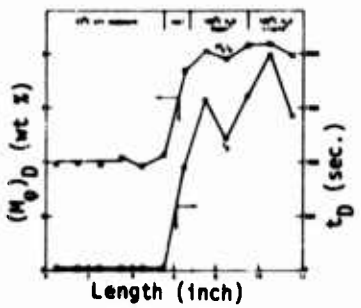
New Results:

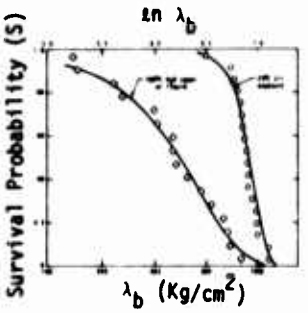
1. Calculated moisture concentration agrees with independent experiments.
2. Concentration profile based on experimental data indicates internal structure.
3. Proof of concept for moisture profilometry is demonstrated.

Figure 3. Moisture profilometry

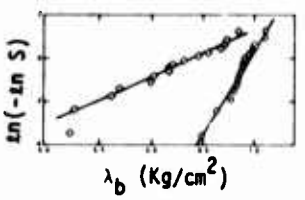








Data	λ_{bo}	m
○	1054	7.6
◇	601	2.2



Method:

1. Apply variable moisture exposure along the length L of composite bar then subject to uniform thermal cycling.
2. Map the initial absorbed moisture $(M_o)_D$ and characteristic absorption time t_D versus length.
3. Map the initial moisture of desorption $(M_o)_D$ and characteristic absorption time t_D versus length.
4. Define variable moisture aging effects upon microstructure and shear bond strength.

New Results:

1. Moisture <u>absorption</u> kinetics highly sensitive to microstructure degradation.
2. Moisture <u>desorption</u> kinetics highly sensitive to microstructure degradation.
3. Mapping of microstructure and strength degradation demonstrated using moisture diffusion analysis.
4. MDA is a new tool for service inspection of composite structures.

Figure 4. Microstructure degradation

ATTENDEE LIST

REVIEW OF PROGRESS

IN

QUANTITATIVE NDE

CORNELL UNIVERSITY

JUNE 14-17, 1977

Dr. J. D. Achenbach
Department of Civil Engineering
Northwestern University
The Technological Institute
Evanston, Illinois 60201

Dr. Laszlo Adler
Department of Physics
University of Tennessee
Knoxville, Tennessee 37916

Dr. George Alers
Rockwell International Science Center
1049 Camino Dos Rios
Thousand Oaks, California 91360

Dr. Frank V. Ammirato
General Electric Company
Knolls Atomic Power Laboratory
P. O. Box 1072
Schenectady, New York 12301

Dr. B. A. Auld
Ginzton Laboratory
Stanford University
Stanford, California 94305

Dr. Michael Avioli
Drexel University
32nd & Chestnut Streets
Philadelphia, Pennsylvania 19104

Dr. Alfred J. Bahr
Stanford Research Institute
333 Ravenswood Avenue
Menlo Park, California 94025

Mr. D. B. Ballard
Supervisor, NDT Division 9351
Sandia Laboratories
Albuquerque, New Mexico 87115

Mr. John Baron
Ontario Research Division
800 Kipling Avenue
Toronto, Ontario, Canada

Dr. Willard D. Bascom
Adhesives and Polymer Composites Section
Code 6120
Naval Research Laboratory
Washington, DC 20379

Mr. Jack Becker
Pratt and Whitney Aircraft
P.O. Box 2691
West Palm Beach, Florida 33402

Dr. Arden L. Bement, Jr.
DARPA
1400 Wilson Boulevard
Arlington, Virginia 22209

Mr. Alan J. Bennett
General Electric Company
Research & Development Center
P. O. Box 8
Schenectady, New York 12301

Dr. George Birnbaum
National Bureau of Standards
Mail Station 223/A3C3
Washington, DC 20234

Mr. John L. Bjorkstan
University of Washington
Department of Electrical Engineering
Seattle, Washington 98195

Dr. Norman Bleistein
Department of Mathematics
University of Denver
University Park
Denver, Colorado 80208

Dr. D. B. Bogy
Department of Mechanical Engineering
University of California-Berkeley
Berkeley, California 94720

Mr. John P. Bosko
Rockwell International
Rocketdyne Division
6633 Canoga Avenue
Canoga Park, California 91304

Prof. Peter F. Braunlich
Department of Physics
Washington State University
Pullman, Washington 99164

Dr. Otto Buck
Rockwell International Science Center
1049 Camino Dos Rios
Thousand Oaks, California 91360

Dr. Michael J. Buckley
Defense Advanced Research Projects Agency
1400 Wilson Boulevard
Arlington, Virginia 22209

Mr. Morris Budnick
U. S. Army Natick Research & Development Command
Kansas Street
Natick, Massachusetts 01760

Dr. Harris M. Burte
Chief, Metals & Ceramics Division
Air Force Materials Laboratory, AFML/LL
Wright-Patterson Air Force Base
Dayton, Ohio 45433

Dr. Peter Cannon
Rockwell International Science Center
1049 Camino Dos Rios
Thousand Oaks, California 91360

Mr. J. Stephen Cargill
Pratt & Whitney Aircraft
P. O. Box 2691, Loc. B-08
West Palm Beach, Florida 33402

Dr. Richard F. Chance
Grumman Aerospace Corporation
Mail Stop A01-10
Bethpage, New York 11714

Dr. Francis H. Chang
General Dynamics
Fort Worth Division
P. O. Box 748
Fort Worth, Texas 76101

Dr. William T. Chen
IBM Corporation
Glendale Drive
Endicott, New York 13760

Prof. Marvin Chodorow
Director
Ginzton Laboratory
Stanford University
Stanford, California 94305

Dr. E. Richard Cohen
Rockwell International Science Center
1049 Camino Dos Rios
Thousand Oaks, California 91360

Dr. Dorothy Comassar
General Electric Company
Mail Drop E-45
Evendale, Ohio 45215

Mr. Douglas Corl
Ginzton Laboratory - 9
Stanford University
Stanford, California 94305

Dr. Robert Crane
Air Force Materials Laboratory
Wright-Patterson Air Force Base
Dayton, Ohio 45433

Dr. Benjamin T. Cross
Rockwell International
Atomics International Division
Rocky Flats Plans, Bldg, 777B
P. O. Box 464
Golden, Colorado 80401

Mr. A. E. Crouch
AMF Tuboscope Co., Inc.
P. O. Box 808
Houston, Texas 77001

Dr. Isaac M. Daniel
IIT Research Institute
10 W. 35th Street
Chicago, Illinois 60616

Mr. Henry Dardy
Department of Navy
Naval Research Laboratory
Washington, DC 20375

Dr. S. K. Datta
Department of Mechanical Engineering
University of Colorado
Boulder, Colorado 80302

Mr. Thomas Derkacs, T/M 2429
TRW, Inc.
23555 Euclid Avenue
Cleveland, Ohio 44117

Dr. K. L. DeVries
College of Engineering
University of Utah
Salt Lake City, Utah 84112

Dr. Steven R. Doctor
Battelle-Northwest
P. O. Box 999
Richland, Washington 99352

Mr. J. E. Doherty
Pratt & Whitney Aircraft Group
Plant M
400 Main Street
Middletown, Connecticut 96457

Mr. D. P. Dolbey
Ontario Research Division
800 Kipling Avenue
Toronto, Ontario, Canada

Dr. Eytan Domany
Department of Physics
University of Washington
Seattle, Washington 98195

Mr. Louis Dragonette
Department of Navy
Naval Research Laboratory
Washington, DC 20375

Dr. B. E. Drony
Bethlehem Steel Corporation
Homer Research Lab
Bethlehem, Pennsylvania 18016

Mr. T. F. Drumwright
Aluminum Company of America
Alcoa Technical Center
Alcoa Center, Pennsylvania 15069

Mr. John C. Duke, Jr.
Mechanics and Materials Science Department
Johns Hopkins University
Baltimore, Maryland 21218

Dr. Robert Dukes
Admiralty Materials Laboratory
Holton Heath
Poole, Dorset, England

Dr. Richard Elsley
Rockwell International Science Center
1049 Camino Dos Rios
Thousand Oaks, California 91360

Mr. R. C. Ervin
Northrop Aircraft
3901 West Broadway
Hawthorne, California 90250

Dr. Anthony G. Evans
Rockwell International Science Center
1049 Camino Dos Rios
Thousand Oaks, California 91360

Mr. Charles Fechter, Dept. 457 - Level 107
McDonald Douglas/Astronautics
P. O. Box 516
St. Louis, Missouri 63166

Mr. Charles Federman
National Bureau of Standards
Building 233, Room B-106
Washington, DC 20234

Mr. Frederick J. Fitzsimmons, DRDAR-QAS
Commander
U. S. Army Armament
Research & Development Command
Dover, New Jersey 07801

Dr. Paul L. Flynn
Applied Research Laboratory
General Dynamics
P. O. Box 748
Fort Worth, Texas 76101

Mr. D. M. Forney, Jr.
Air Force Materials Laboratory
AFML/LLP
Wright-Patterson Air Force Base
Dayton, Ohio 45433

Dr. Christopher M. Fortunko
Rockwell International Science Center
1049 Camino Dos Rios
Thousand Oaks, California 91360

Mr. Ellis Foster, Jr.
Battelle Columbus Laboratories
505 King Avenue
Columbus, Ohio 43201

Mr. Brian G. Frock
ARMCO Steel Corporation
Research Center
Middletown, Ohio 45043

Mr. Eric S. Furgason
Electrical Engineering Department
Purdue University
West Lafayette, Indiana 47907

Dr. C. Gerald Gardner
University of Houston
Department of Electrical Engineering
Houston, Texas 77004

Mr. Frank S. Gardner
Office of Naval Research
495 Summer Street
Boston, Massachusetts 02210

Mr. Donald A. Gavin
General Electric Company
Knolls Atomic Power Laboratory
P. O. Box 1072
Schenectady, New York 12301

Mr. John R. Gleim
Naval Ship Engineering Center
Washington, DC 20306

Mr. Tom Glispin, D-8434, Bldg. 154
Lockheed-Missiles Systems
P. O. Box 504
Sunnyvale, California 94086

Mr. Matthew J. Golis
Battelle-Columbus Labs
505 King Avenue
Columbus, Ohio 43201

Dr. Alvin E. Gorum
University of Washington
Ceramic Engineering
Seattle, Washington 98195

Mr. Lloyd J. Graham
Rockwell International Science Center
1049 Camino Dos Rios
Thousand Oaks, California 91360

Dr. Robert S. Graham
Rockwell International
Automotive Operations
2135 West Maple Road
Troy, Michigan 48084

Prof. Robert E. Green, Jr.
Mechanics and Materials Science Department
Johns Hopkins University
Baltimore, Maryland 21218

Mr. A. Greer
NTIAC-Southwest Research Institute
Box 28510
San Antonio, Texas 78284

Mr. Robert H. Grills
General Dynamics Corporation
Electric Boat Division
Groton, Connecticut

Mr. G. Gruber
NTIAC-Southwest Research Institute
Box 28510
San Antonio, Texas 78284

Mr. Robert C. Grubinskas
Army Materials & Mechanics Research Center
NDT Advanced Research Branch
Watertown, Massachusetts 02172

Dr. James E. Gubernatis, T-11, MS 457
Los Alamos Scientific Laboratory
Los Alamos, New Mexico 87545

Dr. Steve Gustafson
University of Dayton Research Institute
AFML/LLP
Wright-Patterson Air Force Base
Dayton, Ohio 45433

Mr. Hans E. Guttwein, DRDAR-QAS
U. S. Army Armament
Research & Development Command
Dover, New Jersey 07801

Mr. N. Obuo Hamano
University of Missouri
Department of Nuclear Engineering
Columbia, Missouri 65201

Mr. Stephen C. Hardy
National Bureau of Standards
Institute for Materials Research
Washington, DC 20234

Capt. David Harold
Royal Military College
Ringsten, Ontario, Canada

Mrs. Diane Harris
Rockwell International Science Center
1049 Camino Dos Rios
Thousand Oaks, California 91360

Dr. Edmund G. Henneke
Department of Engineering Science & Mechanics
Virginia Polytechnic Institute
and State University
Blacksburg, Virginia 24061

Dr. Leroy R. Hettche
Engineering Materials Division (Code 6300)
Naval Research Laboratory
Washington, DC 20375

Dr. Joseph S. Heyman
NASA-Langley, MS 499
Ultrasonics Lab
Hampton, Virginia 23665

Dr. B. P. Hildebrand
Battelle Northwest
Battelle Boulevard
Richland, Washington 99352

Dr. Lawrence N. Hjelm
Air Force Materials Laboratory
AFML/LL
Wright-Patterson Air Force Base
Dayton, Ohio 45433

Dr. Edward L. Hoffmann
NASA-Langley Research Center
Mail Stop 188A
Hampton, Virginia 23665

Prof. Dr. P. Höller
Fraunhofer Gesellschaft
Institut für zerstörungsfreie Prüfverfahren
66 Saarbrücken, University (Gebäude 37)
Germany - West

Dr. Nelson N. Hsu
National Bureau of Standards
B118, 223
Washington, DC 20234

Mr. John Bradley Hunter
Applied Mechanics
Stanford University
Stanford, California 94305

Dr. T. Hutchison
Royal Military College
Kingsten, Ontario, Canada

Mr. Jackson H. Hwang
AMF Tuboscope, Inc.
P. O. Box 808
Houston, Texas 77001

Dr. Joseph John
IRT Corporation
7650 Convoy Court
San Diego, California 92111

Mr. George C. Johnson
Stanford University
Applied Mechanics, Durand Building
Stanford, California 94305

Prof. Herb Johnson
Cornell University
Materials Science
Ithaca, New York 14853

Mr. Warren L. Junker
Westinghouse Electric Corp.
Research & Development Center
Churchill Boro
Pittsburgh, Pennsylvania 15235

Mr. David H. Kaelble
Rockwell International Science Center
1049 Camino Dos Rios
Thousand Oaks, California 91360

Mr. Sidney Karlan
U. S. Army Materials Development & Readiness Command
PM Production Base Mod.
DRCPM-PBM-T-PA
Dover, New Jersey 07801

Dr. Frank Kelley
Air Force Materials Laboratory
Wright-Patterson Air Force Base
Dayton, Ohio 45433

Mr. James J. Kelly
Naval Material Command
MAT Code 08T242
Washington, DC 20360

Dr. Lawrence W. Kessler
Sonoscan, Inc.
720 Foster Avenue
Bensenville, Illinois 60106

Dr. B. (Pierre) T. Khuri-Yakub
E. L. Ginzton Laboratory
Stanford University
Stanford, California 94305

Mr. Thomas G. Kincaid
Bldg. 37, Room 5032
Corporate Research & Development
General Electric Company
Schenectady, New York 12345

Prof. Gordon S. Kino
E. L. Ginzton Laboratory - 9
Stanford University
Stanford, California 94305

Mr. Donald Y. Konishi, Mail Code 011-AB61
Rockwell International
Los Angeles Division
International Airport
Los Angeles, California 90009

Mr. Charles G. Kosonen
Naval Ship Engineering Center
SEC 6107, Room 347 NC 4
Washington, DC 20362

Prof. James A. Krumhansl
Department of Physics
Cornell University
Ithaca, New York 14850

Mr. David Kupperman
Argonne National Laboratory
Materials Science Division, Bldg. 212
Argonne, Illinois 60439

Mr. Masao Kuriyama
National Bureau of Standards
Institute for Materials Research
Washington, DC 20234

Dr. Ken Lakin
University of Southern California
Department of Electrical Engineering
University Park
Los Angeles, California 90007

Mr. Frank L. Lederman
General Electric Research & Development Center
P. O. Box 8
Schenectady, New York 12345

Mr. Chin C. Lee
Carnegie Mellon University
Electrical Engineering Department
Pittsburgh, Pennsylvania 15213

Dr. David A. Lee
U. S. Air Force Institute of Technology
AFIT/ENC
Bldg. 640
Wright-Patterson Air Force Base
Dayton, Ohio 45433

Mr. Kent Lewis
Department of Physics
University of Tennessee
Knoxville, Tennessee 37916

Dr. K. Lo
Mechanical Engineering Department
Washington University
St. Louis, Missouri 63130

Mr. S. Lorber
Army Material Development & Readiness Command
5001 Eisenhower Avenue
Alexandria, Virginia 22333

Dr. W. Lord
Electrical Engineering Department
Colorado State University
Fort Collins, Colorado 20523

Mr. Layman A. Lott
EG&G Idaho, Inc.
P. O. Box 1625
Idaho Falls, Idaho 83401

Dr. James F. Lovelace
Bldg. 28, Room 450
General Electric Company
Schenectady, New York 12345

Mr. Jeremiah R. Lowney
Naval Surface Weapons Center
White Oaks Laboratory, 3-208
Silver Springs, Maryland 20910

Dr. Keith C. MacMillan
Lawrence Livermore Laboratory
P. O. Box 808, L-415
Livermore, California 94550

Dr. Robert W. McCoung
Metals & Ceramics Division
Oak Ridge National Laboratories
P. O. Box X
Oak Ridge, Tennessee 37830

Dr. Robert J. McGrattan
General Dynamics Corporation
Electric Boat Division
Groton, Connecticut

Dr. Nancy Mann
Rockwell International Science Center
1049 Camino Dos Rios
Thousand Oaks, California 91360

Mr. T. M. Mansour
Ford Motor Company, Research Staff
24500 Glendale Avenue
Detroit, Michigan 48239

Mr. Connie W. Marvin
Texas Eastern Transmission Corporation
P. O. Box 2521
Houston, Texas 77001

Dr. Bruce W. Maxfield
University of California
Mail Code L415
Lawrence Livermore Labs
Livermore, California 94550

Dr. S. McBride
Royal Military College
Kingsten, Ontario, Canada

Ms. Shirley McDonald, Dept. 8123, Bldg. 154
Lockheed-Missile Systems
P. O. Box 504
Sunnyvale, California 94086

Dr. B. J. McKinley
Lawrence Livermore Laboratory
P. O. Box 808, L-415
Livermore, California 94550

Mr. Joseph Moisis
Air Force Materials Laboratory
Wright-Patterson Air Force Base
Dayton, Ohio 45433

Dr. Thomas J. Moran
Air Force Materials Laboratory
AFML/LLP
Wright-Patterson Air Force Base
Dayton, Ohio 45433

Dr. Anthony N. Mucciardi
Adaptronics, Inc.
Westgate Research Park
7700 Old Springhouse Road
McLean, Virginia 22101

Mr. Julius O. Natwick
U. S. Naval Underwater Systems Center
New London Laboratory
Fort Trumbull
New London, Connecticut 06320

Prof. Vernon L. Newhouse
School of Electrical Engineering
Purdue University
Lafayette, Indiana 47907

Prof. Arthur A. Oliner
Polytechnic Institute of New York
333 Jay Street
Brooklyn, New York 11201

Mr. C. Harvey Palmer
Electrical Engineering Department
Johns Hopkins University
Baltimore, Maryland 21218

Dr. Yih-Hsing Pao
Department of Theoretical & Applied Mechanics
Cornell University
Ithaca, New York 14853

Dr. Emmanual P. Papadakis
Ford Motor Company, Research Staff
24500 Glendale Avenue
Detroit, Michigan 48239

Dr. William J. Pardee
Rockwell International Science Center
1049 Camino Dos Rios
Thousand Oaks, California 91360

Dr. Neil E. Paton
Rockwell International Science Center
1049 Camino Dos Rios
Thousand Oaks, California 91360

Mr. John A. Patsey
U. S. Steel Research Center
125 Jamison Lane
Monroeville, Pennsylvania 15146

Mr. Andrew Perfetto
Sikowski Aircraft
North Main Street
Stratford, Connecticut 06602

Dr. Stuart Pergament
Ocean Environmental Systems, Ltd.
1843 Palmer Avenue
Larchmont, New York 10538

Mr. Gary Petersen
MATEC, Inc.
60 Montebello Road
Warwick, Rhode Island 02886

Dr. Robert Pohanka
Naval Research Laboratory/ONR
Code 6361
Washington, DC 20375

Mr. Jack Raisch
Drexel University
32nd & Chesnut Streets
Philadelphia, Pennsylvania 19104

Mr. John M. Raney
Systems Research Laboratories
2800 Indian Ripple Road
Dayton, Ohio 45440

Mr. Roy Rice
Naval Research Lab
Code 6360
455 Overlook Avenue
Washington, DC 20375

Dr. John M. Richardson
Rockwell International Science Center
1049 Camino Dos Rios
Thousand Oaks, California 91360

Dr. James H. Rose
Department of Physics
Cornell University
605 Clark Hall, LASSP
Ithaca, New York 14853

Dr. Wolfgang Sachse
Department of Theoretical and Applied Mechanics
Cornell University
Ithaca, New York 14853

Dr. Kamel Salama
Mechanical Engineering Department
University of Houston
Hosuton, Texas 77004

Mr. Robert J. Sanford
Naval Research Lab
Code 8431
Washington, DC 20375

Mr. Gerald W. Schrick
Rockwell International
Atomics International-Rocky Flats
P. O. Box 464
Golden, Colorado 80401

Mr. John Schuldies, D/93-393
Airesearch Corporation
P. O. Box 5217
Phoenix, Arizona 85010

Dr. William R. Scott
Department of Navy
Naval Air Development Center
Code 3023
Warminster, Pennsylvania 18974

Mr. Henry J. Scudder, 37-5026
General Electric C. R. & D.
Schenectady, New York 12345

Dr. James A. Seydel
University of Missouri
Department of Nuclear Engineering
Columbia, Missouri 65201

Mr. Ramesh Shankar
Adaptronics, Inc.
Westgate Research Park
7700 Old Springhouse Road
McLean, Virginia 22101

Mr. Ken Shimmin
Air Force Materials Laboratory
Wright-Patterson Air Force Base
Dayton, Ohio 45433

Mr. Stanley Silverstein
Department of the Navy
Naval Sea System Command
Washington, DC 20362

Major Wilbur C. Simmons
AFOSR/NE
Bolling Air Force Base
Washington, DC 20332

Mr. W. A. Simpson, Jr.
Oak Ridge National Laboratories
P. O. Box X
Oak Ridge, Tennessee 37830

Dr. James M. Smith
Industrialized Applications Branch
AMMRC
Watertown, Massachusetts 02172

Mr. Michael L. Stellabotte
U. S. Naval Air Development Center
Code 302C
384 Westfield Drive
Warminster, Pennsylvania 18974

Mr. Ronald D. Strong
Los Alamos Scientific Laboratory
P. O. Box 1663, Group M-1, MS 912
Los Alamos, New Mexico 87545

Mr. William R. Sturrock, 3882/84
Northrop Corporation
Aircraft Division
3901 West Broadway
Hawthorne, California 90250

Dr. Thomas Szabo
RADC/ETEM
Deputy for Electronic Technology
Hanscom Air Force Base
Bedford, Maryland 01731

Mr. T. W. Sze
School of Engineering
University of Pittsburgh
Pittsburgh, Pennsylvania 15261

Dr. Norman M. Tallan
Air Force Materials Laboratory
AFML/LLM
Wright-Patterson Air Force Base
Dayton, Ohio 45433

Mr. Francis M. Taylor
Systems Research Laboratories, Inc.
2800 Indian Ripple Road
Dayton, Ohio 45440

Mr. Cecil M. Teller
Southwest Research Institute
9500 Culebra Road
San Antonio, Texas 78284

Dr. Graham Thomas
Drexel University
32nd & Chesnut Streets
Philadelphia, Pennsylvania 19104

Dr. Robert L. Thomas
Department of Physics
Wayne State University
Detroit, Michigan 48202

Dr. Donald O. Thompson
Rockwell International Science Center
1049 Camino Dos Rios
Thousand Oaks, California 91360

Dr. R. Bruce Thompson
Rockwell International Science Center
1049 Camino Dos Rios
Thousand Oaks, California 91360

Dr. Bernhard R. Tittmann
Rockwell International Science Center
1049 Camino Dos Rios
Thousand Oaks, California 91360

Prof. Chen S. Tsai
Carnegie-Mellon University
Department of Electrical Engineering
Schenley Park
Pittsburgh, Pennsylvania 15213

Mr. Roy E. Twyman
Purdue University
Electrical Engineering Department
West Lafayette, Indiana 47907

Dr. Hendrikus H. Vanderveldt
Naval Sea Systems Command
Department of the Navy
Washington, DC 20362

Dr. Edward C. van Reuth
Advanced Research Projects Agency
1400 Wilson Boulevard
Arlington, Virginia 22209

Dr. H. E. Van Valkenburg
Sperry Products Division
Automation Industries, Inc.
Box 3500
Danbury, Connecticut 06810

Dr. Vasundara V. Varadan
Department of Theoretical & Applied Mechanics
Cornell University
Ithaca, New York 14853

Mr. Vijay K. Varadan
Department of Theoretical & Applied Mechanics
Cornell University, Thurston Hall
Ithaca, New York 14853

Dr. Carmine F. Vasile
Rockwell International Science Center
1049 Camino Dos Rios
Thousand Oaks, California 91360

Dr. John R. N. Viertl
General Electric Research & Development Center
1 River Road, Bldg. 37, Rm. 523
Schenectady, New York 12301

Dr. Shirley L. Wakefield
General Electric - Aircraft Engine Group
I75 & Bypass 50, Mail Drop H-9
Cincinnati, Ohio 53215

Dr. John P. Wallace, 401-2B27
Westinghouse Research Labs
1310 Beulah Road, Churchill Boro
Pittsburgh, Pennsylvania 15235

Mr. James R. Wamsley
U. S. Army Foreign Science & Technology Center
220 7th Street, N.E.
Charlottesville, Virginia 22901

Mr. Jackson Wang
AMF Tuboscope
P. O. Box 808
Houston, Texas 77001

Mr. Shing-kuo Wang
Carnegie-Mellon University
Department of Electrical Engineering
Pittsburgh, Pennsylvania 15213

Mr. Geoffrey R. Webster
Bethlehem Steel
Homer Research Labs
Bethlehem, Pennsylvania 18015

Mr. H. L. Wheley
Babcock & Wilcox
P. O. Box 1260
Lynchburg, Virginia 24053

Prof. Henry W. White
Department of Physics
University of Missouri
223 Physics Building
Columbia, Missouri 65201

Prof. Richard M. White
EECS Dept./TE01
Electronics Research Laboratory
University of California
Berkeley, California 94720

Dr. Thomas Wolfram
223 Physics Building
University of Missouri
Columbia, Missouri 65201

Dr. W. E. Woodmansee
The Boeing Company
MS 73-05
P. O. Box 3707
Seattle, Washington 98124

Dr. Edward M. Wu
Lawrence Livermore Labs
University of California
P. O. Box 808
Livermore, California 94550

Mr. John D. Young
General Electric Company
Corporate Research & Development Center
P. O. Box 8
Schenectady, New York 12301

Dr. John Zurbrick
General Electric
Aircraft Engine Division
Mail Drop M87
Cincinnati, Ohio 45215

*U.S.Government Printing Office: 1978 — 757-080/110